

# **Utilising biomass waste as a fuel for diesel generators**

Zahida Bi Aslam

Submitted in accordance with the requirements for the degree of  
Doctor of Philosophy

The University of Leeds  
School of Chemical and Process Engineering

June 2022

The candidate confirms that the work submitted is his/her own, except where work which has formed part of jointly authored publications has been included. The contribution of the candidate and the other authors to this work has been explicitly indicated below. The candidate confirms that appropriate credit has been given within the thesis where reference has been made to the work of others.

**The work in Chapters 2, and 4-7 is based on the following publication:**

Olanrewaju, F., Li, H., Aslam, Z., Hammerton, J., and Lovett, J., *Analysis of the effect of syngas substitution of diesel on the Heat Release Rate and combustion behaviour of Diesel-Syngas dual fuel engine*. Fuel, **2022**. 312: p. 122842 DOI: 10.1016/j.fuel.2021.122842.

The candidate is a co-author of this publication and conducted the experimental work alongside part of the data processing and analysis. The lead author (Francis Olanrewaju) was involved in the methodology, manuscript writing, reviewing, editing and submission. The other authors contributed to the experimental work, reviewing, and editing this publication.

**The work in Chapter 4 is based on the following publication:**

Aslam, Z., Li, H., Hammerton, J., Andrews, G., Ross, A., and Lovett, J., *Increasing Access to Electricity: An Assessment of the Energy and Power Generation Potential from Biomass Waste Residues in Tanzania*. Energies, 2021. **14** (6): p. 1793 DOI: 10.3390/en14061793.

The candidate is the lead author of this publication, and the conceptualization, methodology, investigation, data processing, writing, reviewing, and editing were conducted by the candidate. The other authors contributed by supervision, visualization, reviewing, and editing of this publication.

**The work in Chapters 5-7 is based on the following publication:**

Aslam, Z., Li, H., Hammerton, J., and Andrews, G.E., "Combustion and Emissions Performance of Simulated Syngas/Diesel Dual Fuels in a CI Engine," SAE Technical Paper 2022-01-1051, 2022, doi:10.4271/2022-01-1051.

The candidate is the lead author of this publication, the other authors contributed by supervising, visualization, reviewing, and editing this publication.

This copy has been supplied on the understanding that it is copyright material and that no quotation from the thesis may be published without proper acknowledgement.

The right of Zahida Bi Aslam to be identified as Author of this work has been asserted by her in accordance with the Copyright, Designs, and Patents Act 1988.

## Acknowledgements

I would like to thank my supervisors, *Dr. Hu Li*, *Prof. Gordon Andrews*, and *Dr. Andrew Ross*, for their support.

Especially, *Dr. Hu Li*, for his guidance, knowledge, and motivation throughout the project, including during Covid-19. This has been invaluable, without which, the completion of this project may not have been possible.

I would like to thank technician *Scott Prichard* for all his assistance, contribution, and not least, his patience in the engine lab.

I also thank the technical staff for their assistance: *Adrian Cunliffe* and *Karine Alves Throne* from SCAPE analytical labs, and *Stuart Micklethwaite* from LEMAS.

I am grateful for the funding that made this research possible from Bioenergy CDT and the Engineering and Physical Sciences Research Council (grant number EP/L014912/1). In addition, from the GCRF grant: Creating Resilient Sustainable Microgrids through Hybrid Renewable Energy Systems (CRESUM-HYRES grant number EP/R030243/1).

I also thank the CDT management team: *James McKay* and *Emily Bryan-Kinns* for their support. I would also like to thank all my colleagues, in particular, *Judith Ford*, *Andrew Price Allison*, *Jason Ferns*, *David Maxwell*, *Aaron Brown*, *James Hammerton*, *Francis Olanrewaju*, and *Scott Wiseman*.

A special thanks to *Nina Ortiz* for her support and positive enthusiasm that kept the momentum alive.

Finally, a special thank you to my family and friends, especially for their support and prayers throughout this journey. A big thank you to my son, *Binyamin*, for bearing with me over the past few years. Also, a thank you to *Zahir* for providing me with the motivation I may not have otherwise found.

This thesis is dedicated to my parents for their continuous inspiration.

## Abstract

The purpose of this study was to research ways whereby biomass waste could be used as a fuel for diesel generators in developing countries for small-scale renewable electricity generation. In particular, by adapting diesel generators to run as gas-diesel dual fuel engines. Biomass waste/residues can be used to produce a gaseous fuel using gasification (syngas) and/or anaerobic digestion (biogas) which can be used to substitute diesel in dual fuel combustion. Tanzania and Uganda were selected as the focus of this study due to their low electrification rates.

This thesis investigated the energy potential of four biomass residue streams (from agriculture, forestry, livestock, and urban human waste) in Tanzania and Uganda. From this, the net electricity generation potential was calculated based on overall efficiencies of 10 and 25% (from biomass to net electricity) for the base year of 2019. This work found that both countries have a plentiful supply of biomass residues; the calculated net electricity generation potential from these combined residues was found to exceed the electrical energy generated nationally for both countries.

This thesis also researched the impact of dual fuel combustion using syngas and biogas. When compared with diesel combustion, the advantages were the lower emissions of nitrogen oxides ( $\text{NO}_x$ ), particulate matter mass, and particle number, alongside reduced diesel consumption. The disadvantages were a reduction in the brake thermal efficiency (BTE), and an increase in the total hydrocarbons (THCs), carbon monoxide (CO), methane ( $\text{CH}_4$ ), and formaldehyde emissions. Higher THC and CO emissions can be mitigated by utilisation of a diesel oxidation catalyst (DOC).

Increasing the hydrogen content of the simulated syngas led to an improvement in the BTE and reductions in the CO, THC,  $\text{CH}_4$ , and formaldehyde emissions; in contrast,  $\text{NO}_x$  emissions increased when compared to the syngas blends with lower hydrogen content.

## Table of Contents

<b>Acknowledgements</b> .....	<b>iii</b>
<b>Abstract</b> .....	<b>iv</b>
<b>Table of Contents</b> .....	<b>v</b>
<b>List of Tables</b> .....	<b>xiii</b>
<b>List of Figures</b> .....	<b>xviii</b>
<b>List of Abbreviations</b> .....	<b>xxv</b>
<b>Chapter 1 Introduction</b> .....	<b>1</b>
1.1 Background and motivation .....	1
1.2 Research aims .....	7
1.3 Thesis outline .....	7
<b>Chapter 2 Literature Review</b> .....	<b>9</b>
2.1 Introduction .....	9
2.2 Energy trilemma in Africa (countries of interest).....	9
2.3 Small-scale electricity generation using renewable energy in Africa.....	11
2.4 Biomass residues in Africa .....	14
2.5 Utilisation of biomass residues in an internal combustion engine for energy generation .....	16
2.5.1 Overall conversion efficiency (biomass to net electricity).....	17
2.5.2 Anaerobic digestion.....	18
2.5.3 Gasification .....	19
2.5.3.1 Stages of gasification .....	20
2.5.3.2 Types of gasifiers .....	21
2.5.4 Syngas composition produced from downdraft gasification .....	24
2.6 A summary of the waste biomass resource assessments reviewed in the literature .....	27
2.7 Fundamentals of a diesel engine .....	27
2.7.1 Overall introduction and working principles .....	27
2.7.2 Four-stroke engine fundamentals.....	28
2.7.3 Combustion phases for a diesel Compression Ignition (CI) engine .....	30
2.8 Emissions from diesel combustion in compression ignition engines.....	32
2.8.1 Carbon monoxide (CO) .....	32

2.8.2 Unburnt Hydrocarbon (UHC) /Hydrocarbon (HC) .....	33
2.8.3 Nitrogen oxides (NO <sub>x</sub> ) .....	34
2.8.4 Particulate Matter (PM)/soot.....	35
2.8.5 Summary of diesel combustion emissions .....	37
2.8.6 Diesel engine after-treatment systems for emission control .....	37
2.9 Dual fuel (DF) engines for small-scale electricity generation using biomass residues.....	38
2.9.1 Addition of gaseous fuel into a dual fuel compression ignition engine .....	40
2.9.2 Reactivity Controlled Compression Ignition (RCCI).....	41
2.9.3 Engine speed selection in dual fuel engines for small-scale power generation .....	41
2.10 Syngas-diesel Heat Release Rate (HRR) studies .....	45
2.11 Syngas-diesel: engine combustion performance and emissions .....	51
2.11.1 Ignition delay .....	51
2.11.2 Peak pressure .....	51
2.11.3 Temperature.....	51
2.11.4 Brake Thermal Efficiency (BTE) .....	52
2.11.5 Carbon monoxide (CO) .....	53
2.11.6 Hydrocarbon / Unburnt hydrocarbon (HC/UHC) .....	53
2.11.7 Nitrogen oxides (NO <sub>x</sub> ) .....	54
2.11.8 Carbon dioxide (CO <sub>2</sub> ) .....	56
2.11.9 Particulate Matter (PM) .....	56
2.11.10 Diesel substitution values for syngas-diesel combustion.....	58
2.11.11 Syngas-diesel combustion: summary of the trends.....	58
2.11.12 The impact of changing the H <sub>2</sub> content of the syngas on dual fuel engine combustion and emissions.....	62
2.11.13 Summary of the syngas-diesel literature reviewed.....	69
2.12 Engine performance & emission studies for biogas/diesel .....	71
2.12.1 Particulate Matter (PM) emissions for biogas-diesel .....	71
2.12.2 Brake Thermal Efficiency (BTE) for biogas-diesel.....	72
2.12.3 Carbon monoxide (CO) emissions for biogas-diesel .....	73
2.12.4 Hydrocarbon (HC) emissions for biogas-diesel .....	74
2.12.5 Nitrogen oxides (NO <sub>x</sub> ) emissions for biogas diesel.....	75
2.12.6 Carbon dioxide (CO <sub>2</sub> ) emissions for biogas-diesel.....	76

2.12.7 Diesel displacement rate for biogas-diesel.....	77
2.12.8 Biogas-diesel Heat Release Rate (HRR) studies .....	77
2.12.9 Summary of the biogas-diesel literature reviewed.....	79
2.13 Knowledge gaps.....	81
2.14 Research questions.....	82
2.15 Refined aims and objectives .....	82
2.15.1 Overall aim .....	82
2.15.2 Specific objectives.....	83
<b>Chapter 3 Methodology for Engine Testing .....</b>	<b>84</b>
3.1 Introduction .....	84
3.2 Fuels for testing.....	84
3.2.1 Red Diesel.....	84
3.2.2 Simulated syngas .....	84
3.2.3 Biogas .....	87
3.3 Engine testing lab.....	87
3.3.1 Engine specification .....	88
3.3.2 Engine-related instrumentation .....	89
3.3.3 Analytical instrumentation and analysis.....	91
3.3.3.1 Particulate analysis .....	91
3.3.3.2 Gaseous emission analysis.....	95
3.4 Health and Safety.....	98
3.5 Data Analysis .....	98
3.5.1 Conversion of genset output to engine output power .....	98
3.5.2 Brake Thermal Efficiency (BTE) .....	99
3.5.3 Brake Specific Fuel Consumption (BSFC) .....	100
3.5.4 Brake Specific Energy Consumption (BSEC).....	100
3.5.5 Air to Fuel Ratio .....	100
3.5.6 Diesel displacement rate ( $Z$ ) .....	101
3.5.7 Equivalence ratio ( $\phi$ ) .....	101
3.5.8 Peak pressure and ignition delay .....	102
3.5.9 Emission Index for gaseous emissions .....	103
3.5.10 Specific Emissions for gaseous emissions.....	104
3.5.11 Particulate Matter Emission Index (PM EI).....	104
3.5.12 Particulate Matter Specific Emissions (PM SE).....	105
3.5.13 Methane slippage.....	105

3.6 Experimental procedure .....	107
3.6.1 Preliminary screening tests .....	107
3.6.2 List of experimental tests conducted .....	107
3.6.3 Lab testing procedure.....	109
<b>Chapter 4 An Assessment of the Energy and Power Generation Potential from Biomass Residues .....</b>	<b>111</b>
4.1 Methodology for the biomass resource assessment .....	111
4.1.1 Quantification of the gross energy potential .....	112
4.1.1.1 Agricultural residues.....	112
4.1.1.2 Forestry residues .....	115
4.1.1.3 Livestock residues.....	116
4.1.1.4 Urban human waste .....	118
4.1.2 Net electrical generating potential of the biomass waste..	118
4.2 The energy potential of the agricultural residues.....	119
4.3 The energy potential of the forestry residues .....	123
4.4 The energy potential arising from the livestock residues.....	125
4.5 The energy potential & biogas yield from the urban human waste.....	129
4.6 The combined energy potential of all four waste streams .....	130
4.6.1 Tanzania .....	130
4.6.2 Uganda.....	132
4.7 Summary.....	133
<b>Chapter 5 Dual Fuel Engine Combustion Performance Analysis .....</b>	<b>135</b>
5.1 Introduction .....	135
5.2 Brake Thermal Efficiency, Brake Specific Fuel Consumption, and the Brake Specific Energy Consumption data .....	135
5.2.1 Diesel baseline data.....	135
5.2.2 Syngas A.....	136
5.2.3 Syngas B.....	137
5.2.4 Syngas C.....	139
5.2.5 Biogas .....	140
5.2.6 Discussion of the Brake Thermal Efficiency and the Brake Specific Energy Consumption results .....	141
5.2.7 Brake Thermal Efficiency data: cross-comparison .....	143
5.2.8 Brake Specific Energy Consumption data: cross- comparison.....	147
5.3 In-cylinder pressure and ignition delay .....	149

5.3.1 Diesel baseline .....	149
5.3.2 Syngas A.....	150
5.3.3 Syngas B.....	152
5.3.4 Syngas C.....	154
5.3.5 Biogas .....	156
5.3.6 Discussion of the ignition delay and peak pressure findings.....	158
5.3.7 Comparison of the ignition delay and the peak pressure data across gas blends .....	161
5.3.7.1 Ignition delay data .....	161
5.3.7.2 Peak pressure data .....	161
5.3.7.3 Peak pressure location.....	164
5.4 Exhaust gas temperature, air-fuel ratio, and the equivalence ratio ( $\phi$ ) .....	165
5.4.1 Diesel baseline .....	165
5.4.2 Syngas A.....	165
5.4.3 Syngas B.....	169
5.4.4 Syngas C.....	169
5.4.5 Biogas .....	170
5.4.6 Discussion of the exhaust gas temperature data .....	171
5.4.7 Cross-comparison of the exhaust gas temperature data..	172
5.5 Summary .....	175
<b>Chapter 6 Gaseous Emission Analysis .....</b>	<b>178</b>
6.1 Introduction .....	178
6.2 Raw emission analysis using MEXA 7100D.....	178
6.2.1 Diesel baseline data.....	178
6.2.2 Syngas A.....	179
6.2.3 Syngas B.....	183
6.2.4 Syngas C.....	186
6.2.5 Biogas .....	188
6.2.6 Raw emission trends during dual fuel combustion .....	192
6.2.7 Cross-comparison of raw emissions for syngas blends....	196
6.3 Specific Emissions, and Emission Index data .....	197
6.3.1 Syngas A.....	197
6.3.2 Syngas B.....	199
6.3.3 Syngas C.....	201

6.3.4 Biogas .....	203
6.3.5 Specific Emission and Emission Index (g/MJ fuel) trends during dual fuel combustion .....	207
6.3.5.1 Specific Emission (SE in g/kWh) trends .....	207
6.3.5.2 Emission index (in g/MJ fuel) trends.....	209
6.3.6 Cross-comparison of Specific Emission and Emission Index trends across syngas types .....	211
6.3.6.1 Total hydrocarbon (THC).....	211
6.3.6.2 Carbon monoxide (CO) .....	214
6.3.6.3 Nitrogen oxides (NO <sub>x</sub> ).....	216
6.3.6.4 Carbon dioxide (CO <sub>2</sub> ) .....	218
6.4 Speciation of gaseous emissions using the FT-IR .....	220
6.4.1 Diesel baseline data .....	221
6.4.2 Syngas A.....	221
6.4.3 Syngas B.....	222
6.4.4 Syngas C.....	222
6.4.5 Biogas .....	223
6.4.6 Methane slippage in the exhaust gases in dual fuel mode .....	223
6.4.6.1 Cross-comparison of the methane slippage for syngas.....	226
6.4.7 Summary of the FT-IR trend data.....	228
6.4.7.1 Ethanol.....	229
6.4.7.2 Formaldehyde .....	230
6.4.7.3 Hexane.....	231
6.4.7.4 Ethane.....	231
6.4.7.5 Ethylene (ethene).....	232
6.4.7.6 Increase in hydrocarbons at loads <55% in dual fuel mode .....	233
6.4.8 Cross-comparison of the formaldehyde and methane emissions across syngas blends.....	233
6.5 Summary.....	235
<b>Chapter 7 Particulate Emissions.....</b>	<b>239</b>
7.1 Introduction .....	239
7.2 Particle number emissions .....	239
7.2.1 Syngas A.....	239
7.2.2 Syngas B.....	241

7.2.3 Syngas C.....	243
7.2.4 Biogas .....	245
7.2.5 Cross-comparison of the Total Particle Number Concentration (TPNC) data.....	247
7.2.5.1 TPNC <i>versus</i> diesel consumption .....	248
7.2.6 Particle emissions summary during dual fuel mode .....	250
7.3 Andersen cascade impactor data.....	251
7.3.1 PM <sub>10</sub> mass data from the impactor.....	251
7.3.2 PM <sub>10</sub> Particle Mass Size Distribution.....	255
7.3.2.1 Syngas A.....	255
7.3.2.2 Syngas B.....	256
7.3.2.3 Syngas C.....	257
7.3.3 Summary of the PM <sub>10</sub> Andersen cascade data .....	258
7.4 Characterisation of PM <sub>10</sub> .....	259
7.4.1 Thermogravimetric Analysis (TGA) .....	259
7.4.1.1 Syngas A: Thermogravimetric analysis data .....	260
7.4.1.2 Syngas B: Thermogravimetric analysis data .....	262
7.4.1.3 Syngas C: Thermogravimetric analysis data .....	264
7.4.1.4 Thermogravimetric analysis trend summary.....	266
7.4.1.5 Cross-comparison of the Thermogravimetric Analysis results across syngas blends.....	267
7.4.2 Energy Dispersive X-Ray (EDX) analysis.....	270
7.4.3 Scanning Electron Microscope (SEM) analysis.....	271
7.4.3.1 Diesel baseline SEM comparison.....	271
7.4.3.2 SEM particle size range comparison for dual fuel combustion.....	274
7.4.3.3 Morphology of the PM collected at each Andersen impaction stage.....	276
7.5 Overall summary .....	279
<b>Chapter 8 Conclusions .....</b>	<b>281</b>
8.1 Major findings from this study.....	281
8.1.1 Net electricity generation potential from biomass residues .....	282
8.1.2 The impact of syngas-diesel dual fuel combustion.....	283
8.1.3 The impact of changing the hydrogen content of the syngas.....	285
8.1.4 The impact of biogas-diesel dual fuel combustion.....	286

8.2 Concluding remarks .....	287
8.3 Limitations and future work .....	288
8.3.1 Net electricity generating potential .....	288
8.3.2 Dual fuel combustion (syngas-diesel & biogas-diesel) .....	289
<b>Appendix A Data related to Chapter 4 .....</b>	<b>291</b>
<b>List of References .....</b>	<b>294</b>

## List of Tables

<b>Table 2-1 Overall efficiency of dual fuel systems for electricity generation.....</b>	<b>18</b>
<b>Table 2-2 Variability in the composition of the syngas generated from various studies.....</b>	<b>26</b>
<b>Table 2-3 A comparison of the diesel genset engine speed.....</b>	<b>42</b>
<b>Table 2-4 The equivalent % GEFs used in the HRR study .....</b>	<b>48</b>
<b>Table 2-5 Summary of the diesel displacement rates in the dual fuel studies reviewed using syngas-diesel.....</b>	<b>58</b>
<b>Table 2-6 Summary of the trends reported for syngas/diesel dual fuel combustion relative to the diesel baseline.....</b>	<b>61</b>
<b>Table 2-7 Literature review summary for syngas dual fuel combustion.....</b>	<b>66</b>
<b>Table 2-8 Literature review summary for effects of varying the hydrogen content of the syngas on dual fuel combustion.....</b>	<b>68</b>
<b>Table 2-9 Summary of the literature reviewed for various biogas-diesel dual fuel combustion studies .....</b>	<b>80</b>
<b>Table 3-1 Results of the analysis of red diesel.....</b>	<b>84</b>
<b>Table 3-2 Summary of the compositional variability of the syngas from the literature review .....</b>	<b>85</b>
<b>Table 3-3 Summary of the composition of the syngas/biogas purchased.....</b>	<b>86</b>
<b>Table 3-4 Summary of the density values calculated for each gaseous fuel .....</b>	<b>86</b>
<b>Table 3-5 Summary of the LHV calculated for each gaseous fuel .....</b>	<b>86</b>
<b>Table 3-6 Engine specifications.....</b>	<b>88</b>
<b>Table 3-7 Other engine-related instrumentation.....</b>	<b>91</b>
<b>Table 3-8 Particle size distribution of each impactor stage .....</b>	<b>93</b>
<b>Table 3-9 MEXA: Principles of analysis &amp; the measuring range per gas.....</b>	<b>95</b>
<b>Table 3-10 Gaseous species analysed using the FT-IR with the detection limits.....</b>	<b>97</b>
<b>Table 3-11 Summary of the experiments conducted and the test conditions.....</b>	<b>108</b>
<b>Table 3-12 Summary of the experimental testing ranges (for engine load and % GEF).....</b>	<b>108</b>
<b>Table 4-1 Perennial plantation crop residue data.....</b>	<b>113</b>
<b>Table 4-2 Agricultural crop residue data.....</b>	<b>114</b>
<b>Table 4-3 Oilseed crop residue data .....</b>	<b>114</b>

Table 4-4 LHV data used for the EP calculation of the forestry residues .....	116
Table 4-5 The EP arising from agricultural residues in Tanzania .....	120
Table 4-6 The EP arising from agricultural residues in Uganda .....	121
Table 4-7 Summary of the electrical generation potential of the agricultural residues in Tanzania .....	121
Table 4-8 Summary of the electrical generation potential of the agricultural residues in Uganda.....	121
Table 4-9 The EP arising from the forestry residues in Tanzania .....	123
Table 4-10 The EP arising from the forestry residues in Uganda .....	124
Table 4-11 Summary of the electrical generation potential from the forestry residues in Tanzania.....	124
Table 4-12 Summary of the electrical generation potential from the forestry residues in Uganda.....	124
Table 4-13 The EP arising from the livestock residues in Tanzania ...	125
Table 4-14 The EP arising from the livestock residues in Uganda .....	126
Table 4-15 Summary of the electrical generation potential from the livestock residues in Tanzania.....	126
Table 4-16 Summary of the electrical generation potential from the livestock residues in Uganda.....	126
Table 4-17 The biogas potential and energy potential available from urban human waste residues in Tanzania .....	129
Table 4-18 The biogas potential and energy potential available from urban human waste residues in Uganda.....	129
Table 4-19 Summary of the electrical generation potential from the urban human waste residues in Tanzania .....	129
Table 4-20 Summary of the electrical generation potential from the urban human waste residues in Uganda .....	130
Table 4-21 Summary of the biomass assessment results for Tanzania.....	131
Table 4-22 Summary of the biomass assessment results for Uganda.....	133
Table 5-1 Summary of the effect of the gaseous fuel composition on BTE .....	144
Table 5-2 Summary of the effect of the BSEC data <i>versus</i> gaseous fuel type .....	147
Table 5-3 The SoC, ID, RPM, and $P_{max}$ data for the diesel baseline ....	149
Table 5-4 The data for SoC, ID, and $P_{max}$ data for SGA-diesel.....	150
Table 5-5 The data for SoC, ID, and $P_{max}$ data for SGB-diesel.....	153
Table 5-6 The data for SoC, ID, and $P_{max}$ data for SGC-diesel.....	155

Table 5-7 The data for SoC, ID, and $P_{max}$ data for biogas-diesel .....	157
Table 5-8 The % change in the ID for each gas fuel type between the highest % GEF and DBL data at all engine loads .....	161
Table 5-9 The % change in the $P_{max}$ value for each gas blend .....	162
Table 5-10 The change in the $P_{max}$ location (in CAD) for each gas fuel type between the highest and lowest % GEF value evaluated across all engine loads .....	164
Table 5-11 The engine EGT, AFR, and the $\phi$ for SGA-diesel .....	166
Table 5-12 The equivalent % GEFs used in the HRR study .....	166
Table 5-13 The engine EGT, AFR, and the $\phi$ for SGB.....	169
Table 5-14 The engine EGT, AFR, and the $\phi$ for SGC.....	170
Table 5-15 The engine EGT, AFR, and the $\phi$ for biogas.....	170
Table 5-16 Summary of the trends noted when cross-comparing data across the syngas blends evaluated .....	176
Table 6-1 Raw emission analysis from MEXA for the diesel baseline runs .....	178
Table 6-2 Raw emission analysis for SGA-diesel.....	179
Table 6-3 Raw emission analysis for SGB-diesel.....	184
Table 6-4 Raw emission analysis for SGC-diesel.....	186
Table 6-5 Raw emission analysis for biogas-diesel .....	189
Table 6-6 Cross-comparison of raw emission data (in ppm).....	196
Table 6-7 Emission Index (EI) data (in g/kg fuel) for SGA-diesel .....	198
Table 6-8 EI (g/MJ fuel) and SE (g/kWh) data for SGA-diesel .....	198
Table 6-9 Emission Index (EI) data (in g/kg fuel) for SGB-diesel .....	200
Table 6-10 EI (g/MJ fuel) and SE (g/kWh) data for SGB-diesel .....	200
Table 6-11 Emission Index (EI) data (in g/kg fuel) for SGC-diesel .....	202
Table 6-12 EI (g/MJ fuel) and SE (g/kWh) data for SGC-diesel .....	202
Table 6-13 Emission Index (EI) data (in g/kg fuel) for biogas-diesel...	204
Table 6-14 EI (g/MJ fuel) and SE (g/kWh) data for biogas-diesel .....	204
Table 6-15 FT-IR emission data for diesel baseline runs.....	221
Table 6-16 FT-IR emission data for SGA-diesel runs .....	221
Table 6-17 FT-IR emission data for SGB-diesel runs .....	222
Table 6-18 FT-IR emission data for SGC-diesel runs .....	222
Table 6-19 FT-IR emission data for biogas-diesel runs. ....	223
Table 6-20 Summary of the cross-comparison methane slippage data from syngas-diesel dual fuel combustion .....	228
Table 6-21 Summary of the FT-IR trends for SGA-diesel.....	228

Table 6-22 Summary of the FT-IR trends for SGB-diesel.....	228
Table 6-23 Summary of the FT-IR trends for SGC-diesel.....	229
Table 6-24 Summary of the FT-IR trends for biogas-diesel.....	229
Table 6-25 Overall trend summary for SGC-diesel at high loads.....	235
Table 6-26 Overall trend summary for biogas-diesel at high loads ....	236
Table 6-27 A reduction in the CO <sub>2</sub> emissions arising from the reduced diesel consumption during SGC-diesel mode.....	237
Table 6-28 A reduction in the CO <sub>2</sub> emissions arising from the reduced diesel consumption in biogas-diesel mode.....	238
Table 7-1 SGA-diesel particle emission data .....	239
Table 7-2 SGB-diesel particle emission data .....	242
Table 7-3 SGC-diesel particle emission data .....	244
Table 7-4 Biogas-diesel particle emission data.....	246
Table 7-5 The % change in the TPNC data (relative to diesel baseline) per gas/diesel blend .....	248
Table 7-6 The % reduction of PM <sub>2.1</sub> per syngas at 10 & 22% GEF.....	254
Table 7-7 % Reduction of PM <sub>10</sub> EI (g/MJ) per syngas at 10 & 22% GEF.....	254
Table 7-8 % Reduction of PM <sub>10</sub> SE (g/kWh) per syngas at 10 & 22% GEF.....	254
Table 7-9 Summary of the mass of PM (mg/m <sup>3</sup> ) equivalent to the various mass fractions at the two particle size ranges for SGA .....	260
Table 7-10 Summary of the PM EI and PM SE data for the various SGA mass fractions equivalent to the particle size of 0- 0.43µm.....	260
Table 7-11 Summary of the mass of PM (mg/m <sup>3</sup> ) equivalent to the various mass fractions at the two particle size ranges for SGB .....	262
Table 7-12 Summary of the PM EI and PM SE data for the various SGB mass fractions equivalent to the particle size of 0- 0.43µm.....	262
Table 7-13 Summary of the mass of PM (mg/m <sup>3</sup> ) equivalent to the various mass fractions at the two particle size ranges for SGC .....	264
Table 7-14 Summary of the PM EI and PM SE data for the various SGC mass fractions equivalent to the particle size of 0- 0.43µm.....	264
Table 7-15 Summary of the range of the measured diameter of the individual primary particle for DBL at each impaction stage per syngas blend.....	273

<b>Table 7-16 The diameter range of the primary particle for SGA.....</b>	<b>274</b>
<b>Table 7-17 The diameter range of the primary particles for SGB.....</b>	<b>274</b>
<b>Table 7-18 The diameter range of the primary particles for SGC.....</b>	<b>274</b>
<b>Table A-1 Raw data of the softwood tree species used for the basic density calculation for Tanzania.....</b>	<b>291</b>
<b>Table A-2 Raw data of the hardwood tree species used for the basic density calculation for Tanzania.....</b>	<b>291</b>
<b>Table A-3 Raw data of the tree species used for the basic density calculation for government plantations in Uganda (23%) .....</b>	<b>292</b>
<b>Table A-4 Raw data of the tree species used for the basic density calculation for private plantations in Uganda (77%).....</b>	<b>292</b>
<b>Table A-5 Data sources used for the calculation of the energy potential from livestock.....</b>	<b>293</b>

## List of Figures

Figure 1-1 The % of the population with access to electricity in Sub-Saharan Africa (from 2010-2020) [2] .....	1
Figure 1-2. Population with access to electricity for 2019 [3] .....	2
Figure 1-3 The % of the population which relies on clean cooking technologies, by region [5].....	3
Figure 1-4 Fuel consumption by region as a result of using generators for energy generation [6] .....	4
Figure 1-5 A comparison of the cost of electricity when using 'Back-Up fossil-fuelled Generators' (BUGS) versus grid supply [6] .....	4
Figure 1-6 The emissions arising from 'BackUp fossil-fuelled Generators' (BUGS) in Africa [6].....	5
Figure 2-1 The World Energy Trilemma profile for Africa [24].....	11
Figure 2-2 Population distribution in Tanzania in relation to the existing power grid and minigrids [37] .....	14
Figure 2-3 Various types of fixed bed gasifiers [81].....	22
Figure 2-4 The basic geometry of a reciprocating ICE [112] .....	28
Figure 2-5 The four strokes of the diesel engine [113] .....	29
Figure 2-6 The rate of heat release for diesel combustion [112].....	30
Figure 2-7 The formation of NO, HC and PM during the two combustion phases in a direct injection diesel engine [112].....	34
Figure 2-8 Diesel exhaust particle size distribution [126].....	36
Figure 2-9 The relationship between the engine speed and the optimum fuel consumption [133].....	43
Figure 2-10 Dual fuel combustion HRR profiles at high and low loads [110] .....	47
Figure 2-11 The combustion performance of syngas-diesel at various loads and syngas substitution ratios [117].....	49
Figure 2-12 The various combustion phases in dual fuel combustion for syngas-diesel [117] .....	50
Figure 3-1 The overall schematic for the genset engine and the related instrumentation .....	87
Figure 3-2 Syngas cylinder configuration.....	89
Figure 3-3 The modified cylinder head to incorporate syngas/biogas .....	89
Figure 3-4 Regression analysis results for the alternator efficiency calculations at various kVA values .....	99
Figure 3-5 A typical P-CAD plot generated at full load during dual fuel combustion with the identified SoC .....	103

Figure 4-1 A visual summary of the biomass resource assessment..	112
Figure 4-2 The % of the total EP available by crop type in Tanzania..	119
Figure 4-3 The % of the total EP available by crop type in Uganda....	120
Figure 4-4 The % of the total EP available from each animal in Tanzania.....	127
Figure 4-5 The % of the total EP available from each animal in Uganda.....	127
Figure 4-6 The raw energy potential (PJ) of each waste stream in Tanzania.....	131
Figure 4-7 The raw energy potential (PJ) of each waste stream in Uganda.....	132
Figure 5-1 The diesel baseline data for BSFC, BSEC, and BTE .....	136
Figure 5-2 BTE <i>versus</i> increasing % GEF of SGA.....	136
Figure 5-3 BSEC data <i>versus</i> increasing % GEF of SGA .....	137
Figure 5-4 BTE data <i>versus</i> increasing % GEF of SGB.....	138
Figure 5-5 BSEC data <i>versus</i> increasing % GEF of SGB .....	138
Figure 5-6 BTE data <i>versus</i> increasing % GEF of SGC.....	139
Figure 5-7 BSEC data <i>versus</i> increasing % GEF of SGC.....	140
Figure 5-8 BTE data <i>versus</i> increasing % GEF of biogas.....	140
Figure 5-9 BSEC data <i>versus</i> increasing % GEF of biogas .....	141
Figure 5-10 A comparison of the BTE values obtained for the different gaseous fuels evaluated at 10% GEF at 76% engine load.....	145
Figure 5-11 BTE data <i>versus</i> the H <sub>2</sub> content at 76% engine load.....	146
Figure 5-12 BSEC data at 76% engine load <i>versus</i> the syngas H <sub>2</sub> content of the syngas blends.....	148
Figure 5-13 The ID at full and 74% engine load <i>versus</i> % GEF of SGA .....	150
Figure 5-14 P-CAD data for SGA at full engine load at various % GEFs.....	151
Figure 5-15 HRR profile for 4kW SGA at various % GEF values [117].....	152
Figure 5-16 HRR profile for 3kW SGA at various % GEF values [117].....	152
Figure 5-17 The ID at full and 72% engine loads <i>versus</i> % GEF of SGB .....	153
Figure 5-18 P-CAD data for SGB at full engine load at various % GEFs.....	154
Figure 5-19 The ID at full & 80% engine loads <i>versus</i> % GEF of SGC .....	155

Figure 5-20 P-CAD data for SGC at full engine load at various % GEFs.....	156
Figure 5-21 ID at full & 80% engine loads <i>versus</i> %GEF of biogas ....	157
Figure 5-22 P-CAD data for biogas at full engine load at various %GEF .....	158
Figure 5-23 P-CAD profiles per syngas blend at full engine load at 46 %GEF (with diesel baseline as a reference).....	162
Figure 5-24 The % $P_{max}$ change <i>versus</i> the $H_2$ content of the syngas.....	163
Figure 5-25 The exhaust gas temperature and $\phi$ for the diesel baseline.....	165
Figure 5-26 Modelled in-cylinder temperatures for SGA at full engine load [117].....	167
Figure 5-27 Modelled in-cylinder temperatures for SGA at 76% engine load [117].....	167
Figure 5-28 Modelled in-cylinder temperatures for SGA at 54% engine load [117].....	168
Figure 5-29 Modelled in-cylinder temperatures for SGA at 30% engine load [117].....	168
Figure 5-30 Normalised EGT data comparison at full engine load across the dual fuel gas types at all the % GEF values tested ...	173
Figure 5-31 Normalised EGT data comparison at 77% engine load of the various dual fuel gas types with increasing % GEF .....	174
Figure 5-32 Normalised EGT data comparison at 54% engine load of the various dual fuel gas types with increasing % GEF .....	174
Figure 5-33 Normalised EGT data comparison at 30% engine load of the various dual fuel gas types with increasing % GEF .....	175
Figure 6-1 Raw $NO_2$ emission data for SGA-diesel <i>versus</i> $\phi$ per load.....	180
Figure 6-2 Raw CO emission data for SGA-diesel at various engine loads .....	181
Figure 6-3 The effect on the dual fuel emissions as a function of the total $\phi$ at variable pilot diesel quantities [276] .....	182
Fig 6-4 SGA: THC levels at full load .....	
Fig 6-5 SGA: CO levels at full load.....	183
Figure 6-6 $NO_2$ v $\phi$ levels for SGB-diesel at various engine loads.....	184
Figure 6-7 CO emission data for SGB-diesel at various engine loads.....	185
Fig 6-8 CO v $\phi$ for SGB-diesel      Fig 6-9 THC v $\phi$ for SGB-diesel ..	186
Figure 6-10 CO emission data for SGC-diesel at various engine loads.....	187

Figure 6-11 NO <sub>2</sub> emission data v $\phi$ for SGC-diesel at various engine loads .....	188
Figure 6-12 CO data for biogas-diesel at various engine loads .....	190
Figure 6-13 THC data for biogas-diesel at various engine loads .....	190
Figure 6-14 NO <sub>2</sub> emission data as a function of $\phi$ for biogas-diesel.....	191
Figure 6-15 CH <sub>4</sub> emission data for biogas-diesel at various engine loads.....	192
Figure 6-16 Raw CO emission data for all syngas blends at 96% load.....	197
Fig 6-17 SE CO for SGA	199
Fig 6-18 SE THC for SGA.....	199
Fig 6-19 SE NO <sub>x</sub> for SGA	199
Fig 6-20 SE CH <sub>4</sub> for SGA.....	199
Fig 6-21 SE CO for SGB	201
Fig 6-22 SE THC for SGB.....	201
Fig 6-23 SE NO <sub>x</sub> for SGB	201
Fig 6-24 SE CH <sub>4</sub> for SGB .....	201
Fig 6-25 SE CO for SGC	203
Fig 6-26 SE THC for SGC.....	203
Fig 6-27 SE NO <sub>x</sub> for SGC	203
Fig 6-28 SE CH <sub>4</sub> for SGC.....	203
Fig 6-29 SE CO (Biogas)	205
Fig 6-30 SE THC (Biogas) .....	205
Fig 6-31 SE NO <sub>x</sub> (Biogas)	205
Fig 6-32 SE CH <sub>4</sub> (Biogas).....	205
Figure 6-33 CO <sub>2</sub> SE data for biogas-diesel at various engine loads....	206
Figure 6-34 SE of CH <sub>4</sub> <i>versus</i> $\phi$ for biogas-diesel.....	206
Fig 6-35 EI CO (Biogas)	209
Fig 6-36 EI THC (Biogas).....	209
Fig 6-37 EI NO <sub>x</sub> (Biogas)	210
Fig 6-38 EI CH <sub>4</sub> (Biogas) .....	210
Fig 6-39 SE THC (96% load)	212
Fig 6-40 EI THC (96% load) .....	212
Fig 6-41 SE THC (77% load)	213
Fig 6-42 EI THC (77% load) .....	213
Fig 6-43 SE THC (53% load)	213
Fig 6-44 EI THC (53% load) .....	213
Fig 6-45 SE THC (30% load)	213
Fig 6-46 EI THC (30% load) .....	213
Fig 6-47. SE CO (96% load)	214
Fig 6-48. EI CO (96% load) .....	214
Fig 6-49 SE CO (77% load)	214
Fig 6-50 EI CO (77% load) .....	214
Fig 6-51 SE CO (53% load)	215
Fig 6-52 EI CO (53% load) .....	215
Fig 6-53 SE CO (30% load)	215
Fig 6-54 EI CO (30% load) .....	215
Fig 6-55 SE NO <sub>x</sub> (96% load)	217
Fig 6-56 EI NO <sub>x</sub> (96% load) .....	217
Fig 6-57 SE NO <sub>x</sub> (77% load)	217
Fig 6-58 EI NO <sub>x</sub> (77% load) .....	217
Fig 6-59 SE NO <sub>x</sub> (53% load)	218
Fig 6-60 EI NO <sub>x</sub> (53% load) .....	218
Fig 6-61 SE NO <sub>x</sub> (30% load)	218
Fig 6-62 EI NO <sub>x</sub> (30% load) .....	218
Fig 6-63 SE CO <sub>2</sub> (96% load)	218
Fig 6-64 EI CO <sub>2</sub> (96% load).....	218
Fig 6-65 SE CO <sub>2</sub> (77% load)	219
Fig 6-66 EI CO <sub>2</sub> (77% load).....	219
Fig 6-67 SE CO <sub>2</sub> (53% load)	219
Fig 6-68 EI CO <sub>2</sub> (53% load).....	219

Fig 6-69 SE CO <sub>2</sub> (30% load)	Fig 6-70 EI CO <sub>2</sub> (30% load).....	219
Figure 6-71 Methane slippage (%) for SGA-diesel.....		224
Figure 6-72 Methane slippage (%) for SGB-diesel.....		224
Figure 6-73 Methane slippage (%) for SGC-diesel.....		225
Figure 6-74 Methane slippage (%) for biogas-diesel.....		225
Fig 6-75 The methane slippage (%) at full load for all syngas blends .....		226
Fig 6-76 The methane slippage (%) at ~78% load for all syngas blends .....		226
Fig 6-77 The methane slippage (%) at ~52% load for all syngas blends .....		227
Fig 6-78 The methane slippage (%) at 30% load for all syngas blends .....		227
Figure 6-79 The formaldehyde concentration for SGA-diesel at various engine loads .....		230
Fig 6-80 CH <sub>4</sub> conc. (96% load)	Fig 6-81 CH <sub>4</sub> conc. (78% load) .....	234
Fig 6-82 HCHO conc. (96% load)	Fig 6-83 HCHO conc. (78% load)..	234
Fig 7-1 PNSD (full load) SGA	Fig 7-2 PNSD (74% load) SGA.....	241
Fig 7-3 PNSD (56% load) SGA	Fig 7-4 PNSD (31% load) SGA.....	241
Fig 7-5 PNSD (full load) for SGB	Fig 7-6 PNSD (76%load) for SGB .	242
Fig 7-7 PNSD (54% load) SGB	Fig 7-8 PNSD (30%load) SGB .....	243
Fig 7-9 PNSD (full load) SGC	Fig 7-10 PNSD (80% load) SGC ....	244
Fig 7-11 PNSD (51% load) SGC	Fig 7-12 PNSD (29% load) SGC....	245
Fig 7-13. PNSD (full load) Biogas .....		
Fig 7-14 PNSD (80% load) Biogas .....		246
Fig 7-15 PNSD (52% load) Biogas .....		
Fig 7-16 PNSD (30% load) Biogas .....		247
Fig 7-17 TPNC <i>versus</i> diesel BSFC at full load for all gas/diesel blends .....		248
Fig 7-18 TPNC <i>versus</i> diesel BSFC at 77% load for all gas/diesel blends .....		249
Fig 7-19 TPNC <i>versus</i> diesel BSFC at 53% load for all gas/diesel blends .....		249
Figure 7-20 Mass of PM collected at various sizes for SGA.....		251
Figure 7-21 Mass of PM collected at various sizes for SGB.....		252
Figure 7-22 Mass of PM collected at various sizes for SGC.....		252
Figure 7-23 The PMSD and the cumulative weight gain up to PM <sub>10</sub> for SGA .....		256

Figure 7-24 The PMSD and the cumulative weight gain up to PM <sub>10</sub> for SGB .....	257
Figure 7-25 The PMSD and the cumulative weight gain up to PM <sub>10</sub> for SGC .....	258
Figure 7-26 Mass conc. (relative to DBL) of the various fractions collected (PS ≤0.43μm) v GEF of SGA-diesel .....	261
Figure 7-27 Mass conc. (relative to DBL) of the various fractions collected (PS 0.43 – 0.65 μm) v GEF of SGA-diesel.....	261
Figure 7-28 Mass conc. (relative to DBL) of the various fractions collected (PS ≤0.43μm) for SGB-diesel .....	263
Figure 7-29 Mass conc. (relative to DBL) of the various fractions collected (PS 0.43 – 0.65 μm) for SGB-diesel .....	263
Figure 7-30 Mass conc. plots (relative to DBL) of the various fractions collected (PS ≤0.43μm) for SGC-diesel .....	265
Figure 7-31 Mass conc. plots (relative to DBL) of the various fractions collected (PS 0.43-0.65μm) for SGC-diesel .....	266
Figure 7-32 The % change in the PM EI (mg/MJ fuel) data of the VOF mass fraction at 10% GEF as a function of the H <sub>2</sub> content of the syngas .....	268
Figure 7-33 The % change in the PM EI (mg/MJ fuel) data of the C mass fraction at 10% GEF as a function of the H <sub>2</sub> content of the syngas .....	268
Figure 7-34 The % change in the PM EI (mg/MJ fuel) data of the VOF mass fraction at 22% GEF as a function of the H <sub>2</sub> content of the syngas .....	269
Figure 7-35 The % change in the PM EI (mg/MJ fuel) data of the C mass fraction at 22% GEF as a function of the H <sub>2</sub> content of the syngas .....	269
Figure 7-36 An example of the EDX spectrum obtained from the analysis of the PM collected during dual fuel combustion .....	270
Fig 7-37 Examples of some primary particles selected for diameter measurements from the SEM image of the particulate matter....	271
Fig 7-38 SEM (≤0.43μm) SGA DBL .....	
Fig 7-39 SEM (≤0.43μm) SGB DBL .....	272
Fig 7-40 SEM (≤0.43μm) SGC DBL .....	
Fig 7-41 SEM (0.43-0.65μm) SGA DBL .....	272
Fig 7-42 SEM (0.43-0.65μm) SGB DBL .....	
Fig 7-43 SEM (0.43-0.65μm) SGC DBL .....	273
Fig 7-44. DBL SGA (≤0.43μm) .....	
Fig 7-45 10% GEF SGA ( ≤0.43μm) .....	
Fig 7-46 22% GEF SGA ( ≤0.43μm) .....	276

<b>Fig 7-47 DBL SGA (0.43-0.65<math>\mu</math>m)</b>	.....	
<b>Fig 7-48 10% GEF SGA (0.43-0.65<math>\mu</math>m)</b>	.....	
<b>Fig 7-49 22% GEF SGA (0.43-0.65<math>\mu</math>m)</b>	.....	<b>276</b>
<b>Fig 7-50 DBL SGB (<math>\leq</math>0.43<math>\mu</math>m)</b>	.....	
<b>Fig 7-51 10% GEF SGB (<math>\leq</math>0.43<math>\mu</math>m)</b>	.....	
<b>Fig 7-52 22% GEF SGB (<math>\leq</math>0.43<math>\mu</math>m)</b>	.....	<b>277</b>
<b>Fig 7-53 DBL SGB (0.43-0.65<math>\mu</math>m)</b>	.....	
<b>Fig 7-54 10% GEF SGB (0.43-0.65<math>\mu</math>m)</b>	.....	
<b>Fig 7-55 22% GEF SGB (0.43-0.65<math>\mu</math>m)</b>	.....	<b>277</b>
<b>Fig 7-56 DBL SGC (0-0.43<math>\mu</math>m)</b>	.....	
<b>Fig 7-57 10% GEF SGC (0-0.43<math>\mu</math>m)</b>	.....	
<b>Fig 7-58 22% GEF SGC (0-0.43<math>\mu</math>m)</b>	.....	<b>278</b>
<b>Fig 7-59 DBL SGC (0.43-0.65<math>\mu</math>m)</b>	.....	
<b>Fig 7-60 10% GEF SGC (0.43-0.65<math>\mu</math>m)</b>	.....	
<b>Fig 7-61 22% GEF SGC (0.43-0.65<math>\mu</math>m)</b>	.....	<b>278</b>

## List of Abbreviations

A	Ampere
ABP <sub>manure</sub>	Amount of biogas from recoverable manure
AC	Andersen Cascade (impactor)
AD	Anaerobic Digestion
AFR	Air Fuel Ratio
AFR <sub>DBL</sub>	Air Fuel Ratio (diesel baseline)
AFR <sub>df</sub>	Air to Fuel Ratio (dual fuel)
AFR <sub>stoic-diesel</sub>	Air to Fuel Ratio (stoichiometric diesel)
AFR <sub>stoic-gas</sub>	Air to Fuel Ratio (stoichiometric gas)
AH	Annual harvest of the crop or product
ARG	Amount of a residue generated annually on a dry basis
atm	Atmosphere
BMEP	Brake Mean Effective Pressure
BP	Brake Power (output in kW)
BSEC <sub>(df)</sub>	Brake Specific Energy Consumption (dual fuel)
BSEC <sub>(diesel)</sub>	Brake Specific Energy Consumption (diesel)
BSFC	Brake Specific Fuel Consumption
bTDC	before Top Dead Centre
BTE	Brake Thermal Efficiency
BUGS	Back-Up fossil-fuelled Generators
BG	Biogas
C <sub>i</sub>	Concentration of a gaseous pollutant
CAD	Crank Angle Degree
cc	Cubic centimetres
CHR	Cumulative Heat Release
CH <sub>4</sub>	Methane
CI	Compression Ignition
CLD	Chemiluminescence detector
CN	Cetane Number
CO	Carbon monoxide
Conc.	Concentration
CO <sub>2</sub> (eq)	Carbon dioxide (equivalent)
C <sub>par</sub>	PM mass concentration
C <sub>p</sub>	Specific heat capacity
CRESUM-HYRES	Creating Resilient Sustainable Microgrids through Hybrid Renewable Energy Systems
CR	Compression Ratio
CV	Calorific Value
daf	Dry ash-free
DBL	Diesel Baseline
DEF	Diesel Exhaust Fluid
DF	Dual Fuel
DI	Direct Injection
DM	Dry Matter (kg/head/day)

DMR	Dry Matter Recoverable from animal manure (kg DM/yr)
DOC	Diesel Oxidation Catalyst
DoC	Duration of Combustion
DPF	Diesel Particulate Filter
DSG	Dynamometer Services Group
EDX	Energy Dispersive X-Ray
EI	Emission Index
EGR	Exhaust Gas Recirculation
EGT	Exhaust Gas Temperature
EoC	End of Combustion
EP	Energy Potential
EP <sub>manure</sub>	Energy Potential of the recoverable manure
EPSRC	Engineering and Physical Sciences Research Council
EP <sub>residue</sub>	Energy Potential of the residue
EUF	Energy Use Factor
$\phi$	Equivalence ratio
$\phi$ df	Equivalence ratio (dual fuel mode)
$\phi$ DBL	Equivalence ratio (diesel baseline)
f	Frequency (Hz)
FA	Fraction Available
FAO	Food and Agricultural Organisation
FID	Flame Ionisation Detection
FIT	Feed-In-Tariff
FR	Fraction of animal manure Recoverable
FT-IR	Fourier Transform Infrared
GCRF	Global Challenges Research Fund
GEF	Gas Energy Fraction
GHG	Greenhouse gas
GSS	Gasifier Simulated Syngas
GWh <sub>(e)</sub>	Gigawatt hours (equivalent)
GWP	Global Warming Potential
H <sub>2</sub>	Hydrogen
HC	Hydrocarbon
HCHO	Formaldehyde
HCCI	Homogeneous Charge Compression Ignition
HHV	Higher Heating Value
HRR	Heat Release Rate
Hz	Hertz
ICE	Internal Compression Engine
ID	Injection Delay
IEA	International Energy Agency
IMEP	Indicated Mean Effective Pressure
IMEP <sub>n</sub>	net Indicated Mean Effective Pressure
IOF	Insoluble Organic Fraction
J	Joule
k <sub>gas</sub>	Conversion coefficient of the gaseous pollutant

kPa	Kilopascal
kT	kilotonne (1,000 kg)
kVA	Kilo-volt-ampere
kW(h)	Kilowatt (hour)
kWe	Kilowatt-electric
kWp	Kilowatts peak
LHV	Lower Heating Value
LHV <sub>biogas</sub>	Lower Heating Value of biogas
LHV <sub>d</sub>	LHV of diesel
LHV <sub>df blend</sub>	LHV of the pilot diesel and gas
LHV <sub>g</sub>	LHV of the gaseous fuel
LHV <sub>residue</sub>	LHV for the biomass residue
μ	Micrometre
MB50	Crank angle at which 50% of the injected fuel was burned
MC	Moisture Content
m <sub>d</sub>	Mass flow rate of diesel for diesel baseline
m <sub>df air</sub>	Mass of air intake in dual fuel mode
M <sub>DBL air</sub>	Mass of air intake for diesel baseline
m <sub>g</sub>	Mass flow rate of syngas/biogas
MJ	Megajoule
m/m	mass/mass
MPa	Mega Pascal
MPD	Magneto-Pneumatic Detection
M <sub>pd</sub>	Mass flow rate of pilot diesel in dual fuel mode
ms	Millisecond
MW	Megawatt
N	Shaft rotation speed (RPM)
NA	Number of animals
NC	No Change
ND	Non-Detected
NDIR	Non-Dispersive Infrared Spectroscopy
NHRR	Net Heat Release Rate
N <sub>2</sub>	Nitrogen
nm	Nanometre
Nm <sup>3</sup>	Normal cubic metre
NO <sub>x</sub>	Nitrogen oxides
NO	Nitrogen monoxide
NO <sub>2</sub>	Nitrogen dioxide
N <sub>2</sub> O	Nitrous oxide
OD	Oven dried (od)
ρ	Density
P	Number of magnetic poles
PAH	Polycyclic Aromatic Hydrocarbons
P-CAD	Pressure <i>versus</i> Crank Angle Degree
PF	Power Factor
PJ	Petajoule

PM	Particulate Matter
PM <sub>10</sub>	Particulate Matter with a diameter of ≤10 micrometres
PM <sub>2.5</sub>	Particulate Matter with a diameter of ≤2.5 micrometres
PM <sub>2.1</sub>	Particulate Matter with a diameter of ≤2.1 micrometres
PM <sub>0.4</sub>	Particulate Matter with a diameter of ≤0.4 micrometres
PM EI	Particulate Matter Emission Index
PM <sub>BC</sub>	Particulate Matter which contains 'black carbon'
PM <sub>OC</sub>	Particulate Matter which contains 'organic carbon'
P <sub>max</sub>	Peak in-cylinder pressure
PM SE	Particulate Matter Specific Emissions
PMSD	Particle Mass Size Distribution (from AC impactor)
PNSD	Particle Number Size Distribution (from DMS)
PoHRR	Peak of Heat Release Rate
ppm	Parts per million
PS	Particle Size
PSD	Particle Size Distribution
PT	Peak Temperature
PV	Photovoltaic
RCCI	Reactivity Controlled Compression Ignition
REA	Rural Energy Agency
RPM	Revolutions Per Minute
RPR	Residue to Product Ratio
RS	Real syngas
SAF	Surplus Availability Factor
SCR	Selective Catalytic Reduction
SDG	Sustainable Development Goal
SE	Specific Emissions
SEM	Scanning Electron Microscope
SG	Specific Gravity
SGA	Syngas A
SGB	Syngas B
SGC	Syngas C
SI	Spark injection
SoC	Start of Combustion
SoI	Start of Injection
SOF	Soluble Organic Fraction
SO <sub>2</sub>	Sulfur dioxide
SMPS	Scanning Mobility Particle Size
SS	Simulated Syngas
t	Tonne
T & D	Transmission and Distribution
TDC	Top Dead Centre
TGA	Thermogravimetric Analysis
THC	Total Hydrocarbon
TPNC	Total Particle Number Concentration
TOC	Total Organic Carbon
UHC	Unburnt Hydrocarbon

UHW	Urban Human Waste
ULSD	Ultra-Low Sulfur Diesel fuel
USD	United States Dollar
V	Volts
$V_{\text{adjusted air fraction}}$	Volume of the adjusted air fraction
v	Versus
$V_{\text{DBL air intake}}$	Volume of the air intake in diesel baseline mode
$V_g$	Gas fuel flow rate (lpm)
VOC	Volatile Organic Compound
VOF	Volatile Organic Fraction
vs.	The fraction of volatile solids in dry matter
VS/DM	Volatile solid/dry matter ratio
wt	Weight
$Y_{\text{biogas}}$	Biogas yield
Yr	Year
Z	Mass-based diesel displacement rate, %

# Chapter 1 Introduction

## 1.1 Background and motivation

According to projections, between 2017 and 2050, it is expected that the global population will increase by 2.2 billion people; half of this population growth is to occur in Africa, which in turn, will increase the energy demand immensely [1]. Electricity is a key factor for economic development and raising living standards. Significant progress has been made in increasing electrification rates globally, with a 15% increase seen in the region of Sub-Saharan Africa over the period 2010 - 2020, as shown in Fig. 1.1 [2].

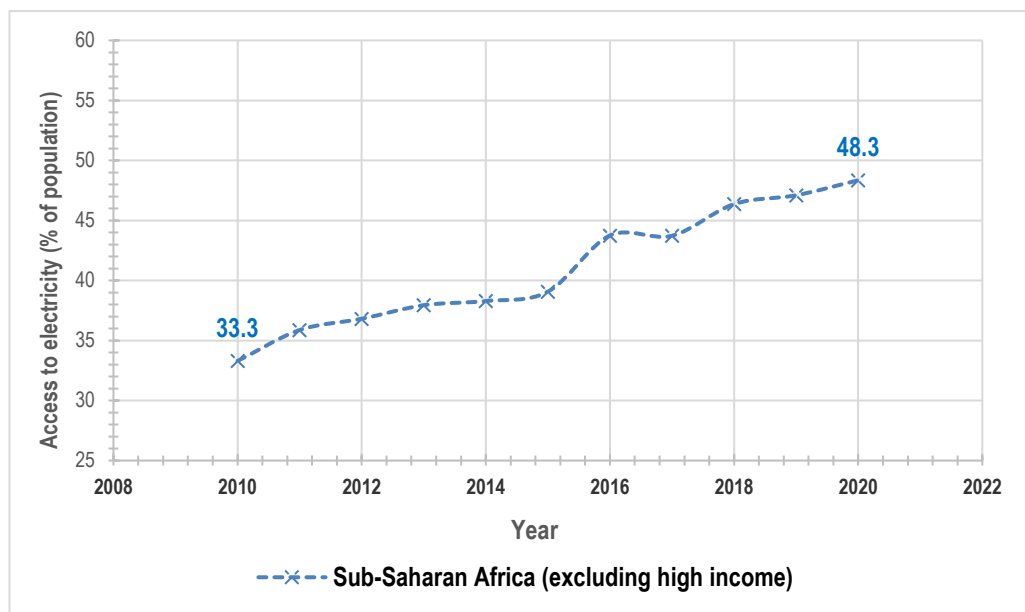


**Figure 1-1 The % of the population with access to electricity in Sub-Saharan Africa (from 2010-2020) [2]**

The national electrification rates are shown for 2019 in Fig. 1.2, the top 20 countries highlighted as 'energy deficit' lie within Sub-Saharan Africa, which include Tanzania and Uganda (the countries of interest for this thesis) [3]. Data for 2020 highlights that globally, Sub-Saharan Africa still has the lowest electrification rate, with only 48.3% of the population having access [2]; this number is considerably lower in rural areas 28.7% [4].

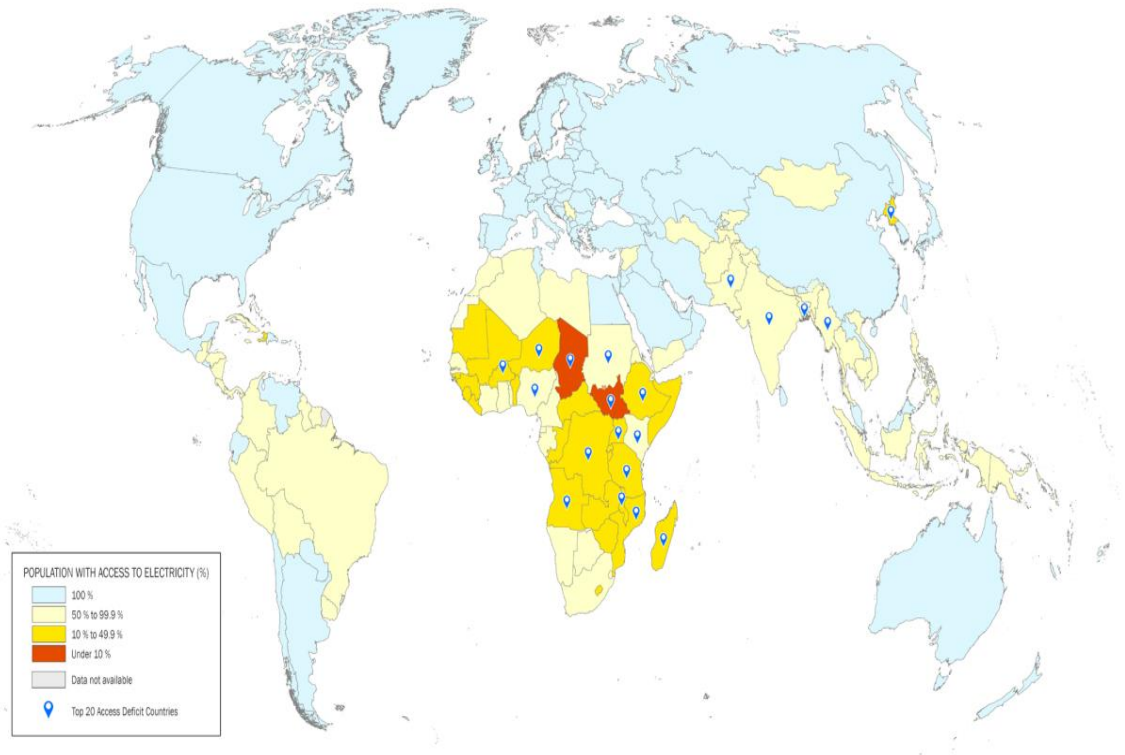


**Figure 1-2. Population with access to electricity for 2019 [3]**

In addition to the low national electrification rates in Sub-Saharan Africa, this region lacks access to ‘clean cooking’ fuels such as gas and electricity and still utilises polluting fuels such as charcoal, kerosene, or fuelwood for this purpose [3]. The increase in the population in Sub-Saharan Africa of those now having access to clean cooking fuels has been limited to urban areas. Only a small increase has occurred in this region over nine years (2005-2014) in terms of the % of the population which has access to ‘clean cooking’ technologies [5] as shown in Fig. 1.3.

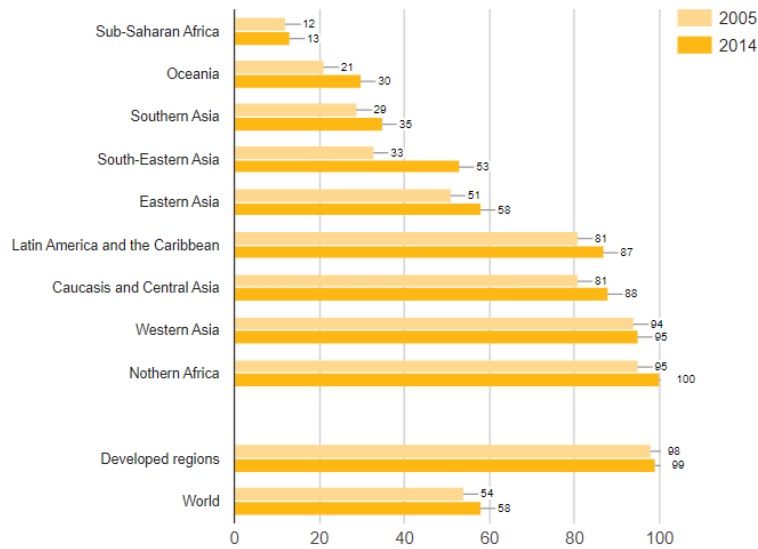


**Figure 1-3 The % of the population which relies on clean cooking technologies, by region [5]**

Most people who lack access to energy and clean cooking solutions reside in rural areas within the Sub-Saharan Africa region and rely on the use of diesel and petrol generators (often referred to as gensets) for their energy. According to The World Bank [6], ~9% of the electricity used in Sub-Saharan Africa was provided by these gensets.

Globally, 5 million small sized diesel gensets (< 60kW) are used for electricity production, which makes up approx. 20% of all diesel generators that are used for a backup supply [6]. Fig. 1.4 illustrates the heavy consumption of diesel fuel due to the reliance on diesel generators for energy generation in Sub-Saharan Africa, this stands at 22% of the total diesel consumption [6]. The cost of electricity produced from these gensets is high due to the high fuel cost, associated with the transport of fuel, alongside fluctuating prices due to a volatile market [6]. The World Bank has compared the cost of electricity per unit (expressed as USD/kWh) arising from operating backup generators versus that from the grid for various regions [6]. Fig. 1.5 highlights the increased cost when relying on backup generators in comparison to the grid supply.

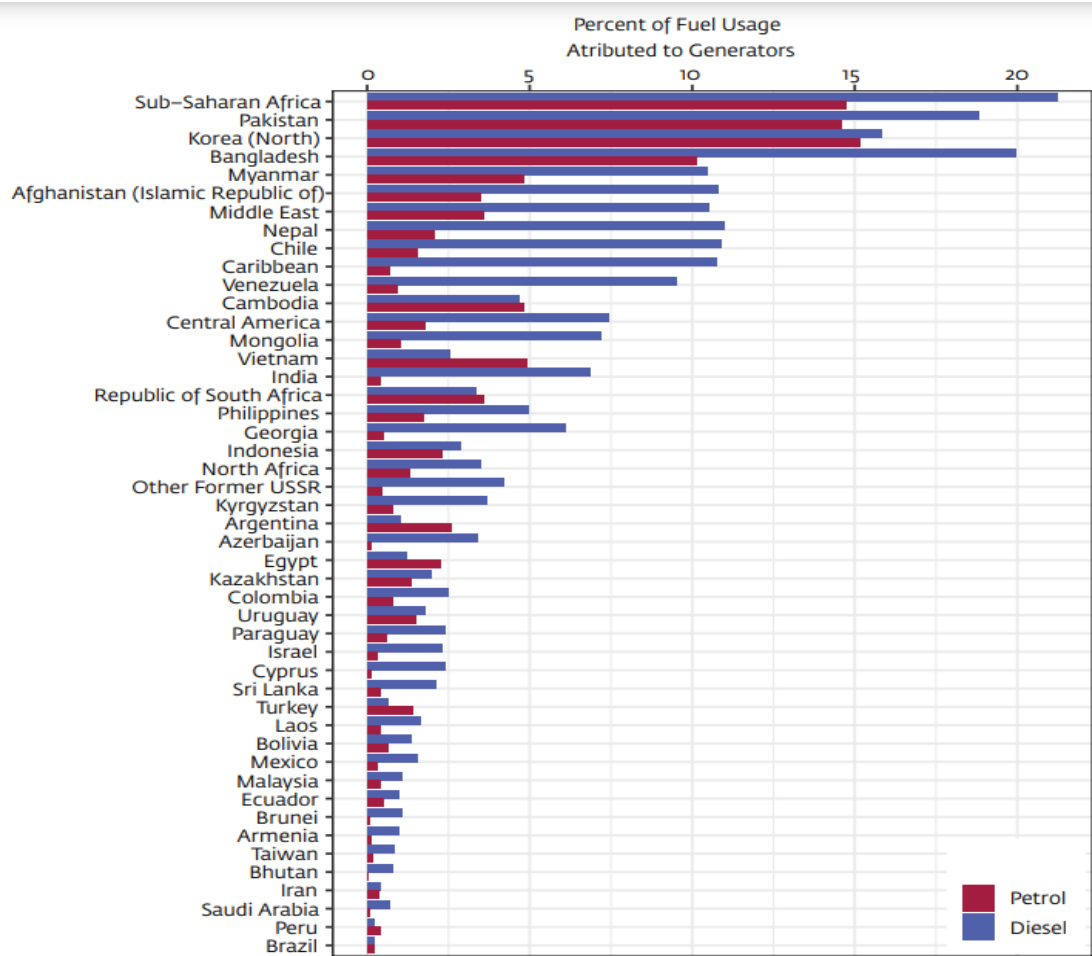


Figure 1-4 Fuel consumption by region as a result of using generators for energy generation [6]

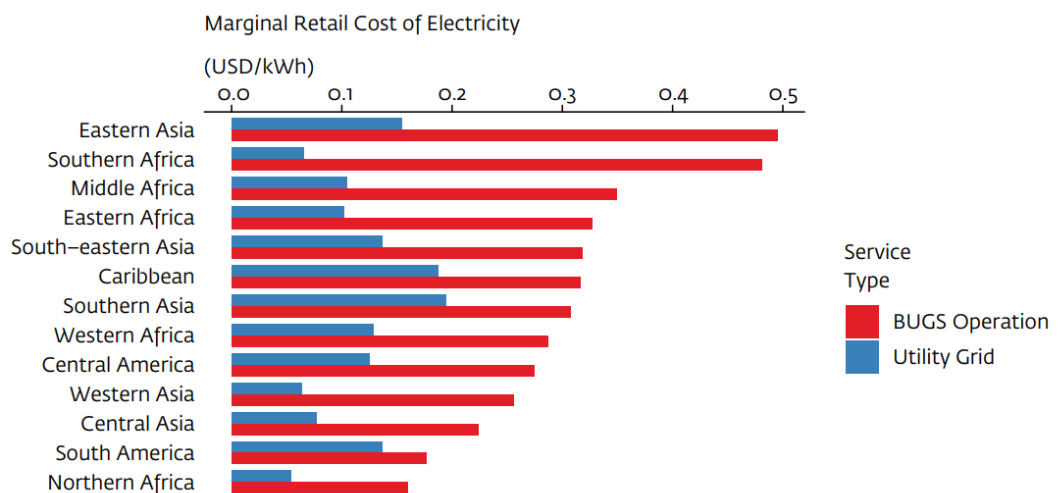
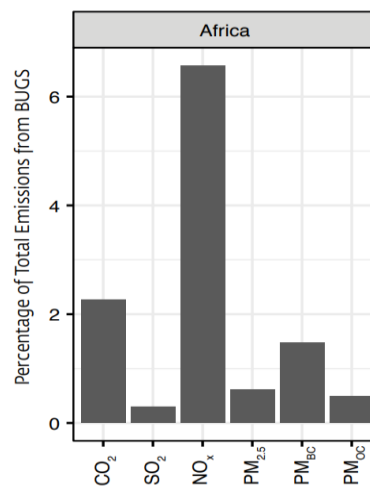


Figure 1-5 A comparison of the cost of electricity when using 'Back-Up fossil-fuelled Generators' (BUGS) versus grid supply [6]

Genset engines produce similar pollutants ( $PM_{2.5}$ ,  $NO_x$ , HC, and CO) as their counterparts used in transport, however, they are usually in closer proximity to people's dwellings in such regions, hence, the health risk may be greater [6]. It is estimated that the nitrogen oxides ( $NO_x$ ), and particulate matter (PM) emissions which are less than 2.5  $\mu m$  in aerodynamic diameter ( $PM_{2.5}$ ), derived from diesel gensets account for the majority of these emissions from the power sector in Sub-Saharan Africa.

Fig. 1.6 illustrates the % of each type of emission produced from the backup generators used in Africa [6]. The PM 'black carbon' ( $PM_{BC}$ ) and PM 'organic carbon' ( $PM_{OC}$ ) are both derived from  $PM_{2.5}$ , both of which contribute not only to health hazards but also directly to the absorption and reflection of solar radiation, thus contributing to climate change [6].



**Figure 1-6 The emissions arising from 'BackUp fossil-fuelled Generators' (BUGS) in Africa [6]**

Fig. 1.6 shows that the dominant pollutants are  $NO_x$  and  $PM_{2.5}$  when using backup fossil-fuelled generators for energy generation in Africa. As discussed in the literature review (Chapter 2, section 2.8), the dominant emissions arising from diesel combustion, compared to a petrol engine are  $NO_x$  and PM, hence, these emissions can be attributed to diesel generators.

One of the United Nations 'Sustainable Development Goals (SDG 7) is to 'ensure access to affordable, reliable, sustainable and modern energy for all', this incorporates the use of renewable energy [3]. It has been globally recognised that to increase national electrification rates where a large amount of the population resides in rural locations, increasing rural electrification rates is imperative.

This is often not economically viable by expanding the national grid due to low population densities and dispersion, alongside many other contributing factors, hence, the utilisation of renewable energy is the key [7]. Utilising a sole source of renewable energy in such regions is not always feasible due to its intermittent nature (such as solar or wind), hence, combining renewable energy with a primary source (a hybrid system) is considered a more reliable and affordable solution for increasing rural electrification rates [7-9]. This can be done by using either minigrids or microgrids ( $\leq 10$  MW) which are standalone solutions [7, 8].

Zebra et al. [7] reported that as the cost of renewable technologies has fallen, hence, are now more viable when considering utilising these to create hybrid renewable systems to increase rural electrification rates. The hybrid technologies considered include biomass, of which it is recognised that this region has an abundant supply [10, 11]. Utilising biomass residues as a fuel for diesel gensets to form hybrid minigrids allows the production of sustainable energy, whilst increasing access to electricity in these regions by broadening fuel choices.

The conversion techniques considered to utilise or convert the energy in the biomass residues were anaerobic digestion (AD) and gasification, both techniques result in the production of gaseous fuel. An existing diesel genset system can be adapted easily and cheaply into a dual fuel engine whereby the diesel engine can use the gaseous fuel to substitute diesel fuel for small-scale electricity generation, thus improving access to energy as the reliance on diesel fuel is reduced.

This research was funded by Engineering and Physical Sciences Research Council (EPSRC) for a Global Challenges Research Fund (GCRF) grant: Creating Resilient Sustainable Microgrids through Hybrid Renewable Energy Systems (CRESUM-HYRES).

The project focused on four developing countries: The Republic of Congo, the United Republic of Tanzania (referred to as Tanzania throughout this study), Uganda, and Indonesia. Tanzania and Uganda were selected for the focus of this thesis as they represent some of the least electrified Sub-Saharan countries in the world.

## **1.2 Research aims**

This study aims to research means of increasing electrification rates in the developing world, specifically, in rural areas where small-scale electricity generation is currently carried out using diesel gensets. In particular, the focus is on the investigation of the operational, combustion, and emission performance of dual fuels (gaseous and liquid fuels) in a small genset. The gaseous fuels could be produced by the thermal or biological conversion techniques such as gasification and/or anaerobic digestion of biomass residues that are available in this region. The gaseous fuel can be used to substitute diesel in a dual fuel engine to generate renewable electricity for small-scale electricity production. The specific objectives are discussed in further detail in Chapter 2, section 2.15 (see p83).

## **1.3 Thesis outline**

This thesis is divided into eight chapters in total which will be discussed here.

Chapter 1: This chapter provides an introduction and background to the research undertaken, an overview of the status of the electrification rate in the Sub-Saharan African region, and the challenges faced when trying to increase electrification in this region. This chapter also introduces the overall aims of the research and provides a thesis outline.

Chapter 2: This chapter provides a review of the literature relevant to this field which includes the biomass waste resource assessments, the technologies utilised to convert biomass waste into a gaseous fuel, and the literature associated with dual fuel combustion and emissions.

Chapter 3: This chapter describes the methodologies and equipment used for the experimental research conducted when investigating the impact of dual fuel combustion.

Chapter 4: This chapter focuses on the waste biomass resource assessments and is made up of two parts: the first describes the methodologies used to conduct the assessments for both countries. The second part presents the waste biomass resource assessment results for both countries.

Chapter 5: This chapter reports the experimental results for dual fuel combustion and compares the impact of dual fuel combustion (of both biogas and syngas) relative to diesel.

Chapter 6: This is the second engine experimental results chapter which reports the gaseous emission for dual fuel combustion. This chapter compares the gaseous emission results from dual fuel combustion (of both biogas and syngas) relative to the diesel baseline.

Chapter 7: This is the final results chapter which reports the particulate emissions findings from dual fuel combustion (for both biogas and syngas) relative to the diesel baseline.

Chapter 8: This chapter concludes the thesis, discusses future work, and puts forward recommendations.

## **Chapter 2 Literature Review**

### **2.1 Introduction**

In this Chapter, the first section focuses on the investigation and quantification of the energy generating potential of biomass residues to produce renewable energy for small-scale electricity generation. The biomass waste streams estimated are those arising from agriculture, forestry, livestock, and urban human waste. The second section looks at the effects of dual fuel combustion using gaseous fuel generated from either gasification and/or anaerobic digestion using biomass residues in an adapted diesel genset engine. The focus is on the engine performance and emissions resulting from dual fuel combustion.

Hence, the first section of this review provides the critical literature review relating to the research regarding the status of electrification in Africa and the waste biomass resource assessments in this region (in particular, for the countries of interest, those being Tanzania and Uganda). Also, is researched, is the typical syngas composition produced from gasification for use in diesel engines. The second section of this review (which incorporates the bulk of this review) investigates the fundamentals of a diesel engine, dual fuel engine combustion performance, and emission formation and generation relative to pure diesel.

### **2.2 Energy trilemma in Africa (countries of interest)**

Access to electricity is a globally recognised requirement to eradicate poverty and has been chosen by the United Nations as a “sustainable development goal”, defined as “Goal 7: ensure access to affordable, reliable, sustainable, and modern energy for all” [5]. Hence, access to electricity is pivotal in achieving this as many basic human activities rely solely on electricity and other forms of energy cannot be used as a substitute. Such examples include lighting, refrigeration, running of household appliances et cetera.

Much effort has gone into increasing electrification rates in Africa which is recognised to be one of the most energy deprived areas in the world. However, Sub-Saharan Africa still has the lowest access to electricity, (expressed as the % of the population), this value has increased by ~2%, i.e. from 46.4 to 48.4% from 2018 to 2020 [12].

Tanzania and Uganda are both poor countries with a similar human development index value of 159 which is classified as having 'low human development' [13]. Tanzania has a large growing population, of which only 35.6% had access to electricity [14] in 2018. In 2018, Tanzania had a rural population of 66.2%, with only 18.6% of this rural population having access to electricity [15, 16].

In comparison, the total % population in Uganda with access to electricity based on 2018 data corresponds to 41.9% [17]. In 2018, Uganda had a rural population of 76.2% [18]; in terms of access to electricity, 32.5% of the rural population had access to electricity [19]. Thus, the lack of access to clean modern energy supplies is most acute in rural areas [20, 21]. Moreover, even for those connected to an electric grid, the supply is often intermittent and unreliable [22, 23].

To focus on the overall energy situation in this region, The World Energy Trilemma Index has been considered, whereby countries and regions are ranked annually on the three defined fundamental dimensions [24]:

- **Energy Security:** this evaluates how well the nation/region can meet its energy demand (current and future). It considers import independence, the diversity of energy generation as well as energy storage.
- **Energy Equity:** this dimension evaluates the nations/regions' capacity to administer basic access to energy that is reliable and affordable.
- **Environmental Sustainability:** this focuses on how well the country/region is at mitigating and avoiding environmental damage during energy generation (including transmission and distribution).

From this assessment, an overall balance grade and trilemma score are produced, and an index ranking is assigned, thus illuminating any challenges in balancing the Energy Trilemma and identifying areas for improvement. An assessment does exist for Tanzania, but not for Uganda, therefore, the overall regional assessment for Africa has been considered instead which covered 29 countries in this region. The assessment results are illustrated in Fig. 2.1. This assessment recognised that this region has made progress in trying to increase access to energy as per the United Nation's SDG 7.

Despite this, out of the six global regions assessed, Africa was in the bottom 25%, and this was concluded as being due to the overall 'energy equity' score remaining low, which mirrors the low electrification rates discussed earlier. Sustainability was also considered to be a challenge in the region alongside volatile energy security [24].

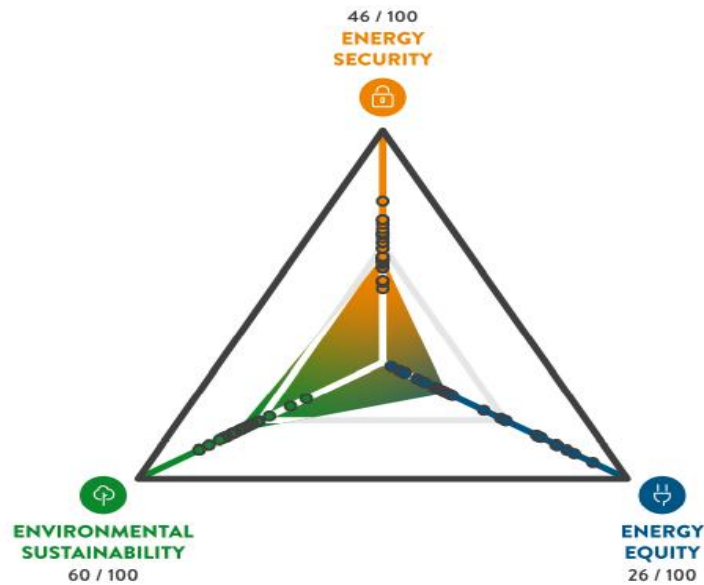


**Figure 2-1 The World Energy Trilemma profile for Africa [24]**

### **2.3 Small-scale electricity generation using renewable energy in Africa**

Many African governments recognise that one of the most economical methods of increasing electrification rates (especially within rural areas) is not by network grid expansions, but by utilising renewable energy sources, specifically mini and off-grid/standalone solutions [7, 20, 23]. To increase electrification in rural Africa, grid extensions are usually considered uneconomically viable due to the remote locations and costs related to extensions, in addition, the number of end-users/ demand potential is often too small when trying to justify the required investment [7, 20].

The diesel genset is still used heavily for electricity generation within existing minigrids and in remote areas [7, 20, 25]. It is recognised that the integration of renewable energy within existing minigrids (hybridisation) leads to reduced costs and environmental pollution whilst increasing energy security [7, 20].

For those relying on electricity generated by off-grid diesel generators, the fuel costs are high, so these off-grid systems have a substantially higher running cost (per kWh) than grid-connected systems [7, 23, 26-29].

The high cost and dependency on fossil fuels used in off-grid diesel generators are impediments to sustainable and economic development, especially in rural areas [7, 26, 29]. In addition, the environmental impact of using fossil fuels associated with running diesel gensets includes greenhouse gas (GHG), nitrogen oxides (NO<sub>x</sub>), and particulate matter (PM) emissions.

Moreover, people in this region still utilise biomass (firewood, charcoal, et cetera) as a source of energy [30-33]. Whether burnt indoors or outdoors, the smoke produced is a pollutant linked to adverse health, in particular, respiratory diseases which disproportionately affect women and children in this region [27, 34]. Those residing in the cooler climate of the southern highland regions of Tanzania, and Uganda, often cook indoors, thus increasing exposure to smoke pollutants [32, 35].

A lack of technical expertise and unfavourable governmental policies have hindered the successful use of new minigrids (10kW -10MW) or stand-alone systems (such as the diesel genset or photovoltaic systems) in this region [7, 20]. For example, Bertheau et al. [26] reported that incorporating photovoltaic (PV) and storage systems with existing diesel-based off-grid systems can lead to significant cost reductions in electricity generation by this method in Tanzania. Furthermore, Zebra et al. [7] concluded that hybrid minigrids which incorporate the diesel genset (as a backup source) are more economically preferential than minigrids based solely on renewable energy. The additional recognisable benefits of including renewable energy on a national level include a reduction in air pollution and GHGs which result in the reduction of fossil fuel usage [20].

The success of the installation of minigrids to increase the electrification rates in this region is variable from country to country. Specifically, in terms of supporting regulatory policies, financial incentives, and public financing availability [20]. Furthermore, to facilitate the uptake of renewable energy opportunities, favourable governmental policies, economics, and training are all required.

However, ensuring the correct supporting policy exists for utilising minigrids is key to increasing rural electrification rates. Supporting policies alongside community involvement have favoured this as seen in countries such as Tanzania and Mali [7, 20]. Both Tanzania and Uganda have implemented the 'Feed-in tariff' policy (FIT) which in principle should favour the uptake of renewable energy [31]. Management of such policies and monitoring the potential investment companies is key to its future success.

In general, energy policies are quite well developed in Tanzania, for example, the minigrid regulatory framework [7]; however, some sectors require further development, particularly, the biomass and off-grid sectors [36]. Government policies and agencies exist in Tanzania which support rural electrification and the use of local renewable energy sources. The Rural Energy Agency (REA) was established in 2005 to focus on rural electrification. In conjunction with other organisations, the REA has promoted off-grid electrification projects as decentralised solutions ranging from 1-10 MW [36]. The Rural Electrification Program Prospectus developed by the REA states that for rural communities, the focus is to increase electrification by using off-grid technologies where isolated minigrids are supplied by renewable energy sources or hybrid systems. The focus is on minigrids associated with hydro and biomass gasifier plants or hybrid PV systems to settlements/villages/households located 10 km or more from the main grid [36]. 6 MW of solar PV has been installed for Tanzanian communities [36]. Other approved small power producer agreements for isolated minigrids were associated with solar (2 MW), three biomass plants (5.1 MW), and two hydropower projects [31].

Fig. 2.2 shows that the existing power grid connects more densely populated urban regions, whereas minigrids are sparsely distributed across rural areas of Tanzania [37].

Uganda currently utilises domestic renewable energy sources for national electricity generation: namely hydropower [38]. The Rural Electrification Agency was established in 2001 in Uganda with its primary goal being to aid the government in increasing the rural electrification rate by using off-grid renewable energy via minigrids or standalone solutions. Some examples of successful biomass-gasification projects supported by this agency in Uganda include a 32 kW biomass gasification project in 2016, an 11 kW biomass-solar hybrid minigrid project in 2016, a 230 kW solar-diesel genset hybrid minigrid project in 2017, a 50 kW biomass gasification project in 2018, and a 100 kWp solar-diesel hybrid minigrid project in 2019 [39].

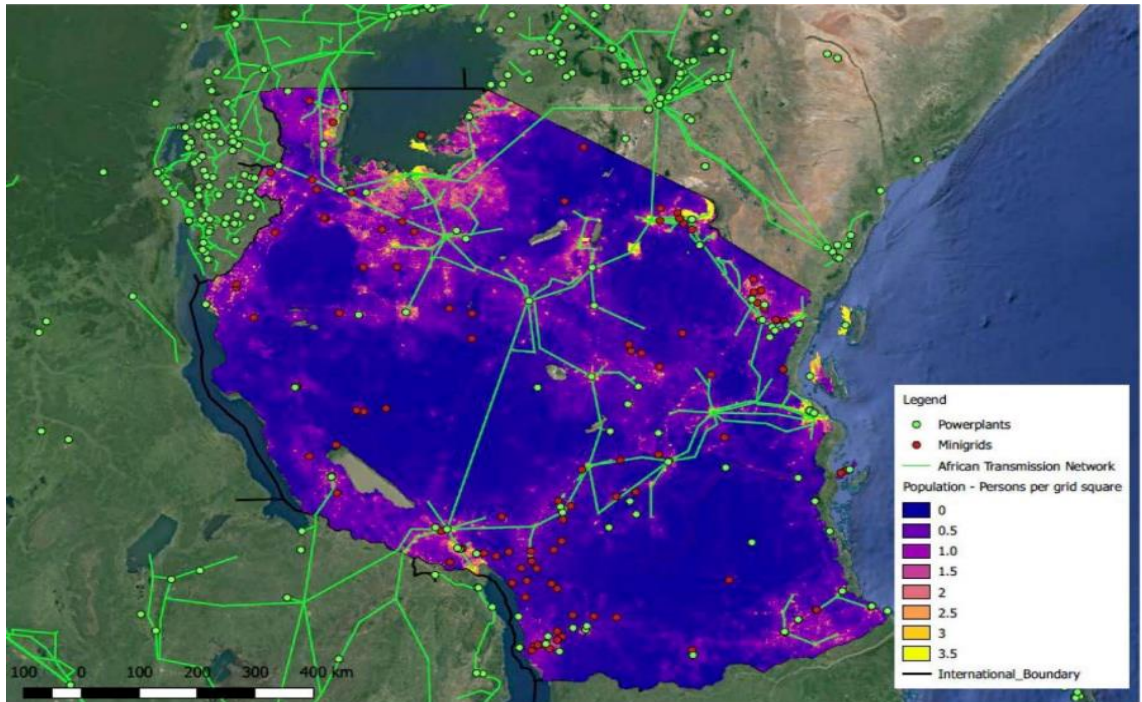


**Figure 2-2 Population distribution in Tanzania in relation to the existing power grid and minigrids [37]**

## **2.4 Biomass residues in Africa**

Biomass residues are underutilised and/or wasted in this region [40]. Open dumping and/or open burning are common methods of waste treatment and disposal in such developing countries [41, 42]. The Food and Agricultural Organisation (FAO) estimated that in 2018 the total amount of dry biomass residues burnt (from maize, rice, sugar cane, and wheat) in Tanzania equated to ~4,164 kT, and in Uganda ~1,141 kT [43], with the majority of this waste residue arising from maize alone (min. 85%) [43]. Using waste biomass as a direct source of “solid biofuels” for energy generation is difficult due to the variable nature of these residues in terms of size, form, moisture content, low density, et cetera [44]. Pre-treatment methods such as pelleting, briquetting, and torrefaction are becoming commonly used to overcome these issues thereby increasing the concentration, density, and heating values [44]. However, this study will focus on methods of using such waste streams in the absence of such enhancement techniques. For the scope of this research, the renewable energy of interest for increasing electrification rates is waste biomass. In comparison to other renewable sources of energy available in this region (solar, wind, hydro, and geothermal) [29, 45], biomass is more uniformly available.

Many waste biomass resource assessments exist in the literature, less so for certain countries in Sub-Saharan Africa. All these vary in terms of methodology, for example, the types of crop residues included, also, for the values used for the following: fraction available (FA), the Residue to Product Ratio (RPR), moisture content (MC), and lower heating values (LHVs). In some cases, some researchers do not account for the moisture content during these waste resource assessment calculations [46-48], whereas other researchers do indeed account for the moisture content [33, 49-53]. It is difficult to make direct comparisons across studies for a specific country due to this data variability and the different methodologies employed.

Lyakurwa [47] quantified the energy potential from the ten main crops grown in Tanzania and that generated from livestock waste whereby the number of live animals and crop production was average data over 51 years from 1961-2012. The moisture content of the crop residues was not accounted for, rather a standard coal conversion ratio figure was used. Lyakurwa [47] concluded that overall, the crop residues had an energy potential of ~5.7 PJ and the livestock, ~ 1.4 PJ; utilisation and management of both these residues in the correct manner could generate renewable electricity, thereby increasing access to electricity thus reducing fossil fuel consumption. Terrapon-Pfaff [51] calculated the energy potential arising from the biomass residues from five key commercial crops in Tanzania. This study concluded that utilising certain agricultural process residues for energy generation could secure the energy supply as well as improve the sustainability of land-use practices in Tanzania. Kusekwa [40] identified all four of these waste streams as having huge energy potential with the potential to be realised using gasification or AD within Tanzania. Furthermore, he stated that converting such biomass residues into energy provides a commercial value to the biomass of interest; however, this author did not quantify the energy potential of these streams. Overall, all the biomass studies of Tanzania [40, 47, 51] have concluded that there is a huge energy potential in the biomass residues generated in Tanzania regardless of the methodology used to quantify this.

Okello et al. [52] quantified the energy potential using census data from 2008/2009 arising from residue streams from crops, forestry, animals, and humans in Uganda.

This study showed Uganda to have a renewable energy potential of 260 PJ/year with the largest single energy stream being from the agricultural sector. This data was calculated using similar methods and accounted for the moisture content of the residues.

Other biomass evaluation studies conducted for Uganda in the literature indicate that biomass has the potential for energy generation; however, these studies focus on one or two of the waste streams identified [29, 38]. Okello et al. [54] state that technologies that utilise biomass such as gasification and anaerobic digestion are present within the country, but their use is not prevalent due to a lack of expertise and high capital costs. However, utilisation of these techniques to produce renewable energy could help provide electricity to those without [33]. As mentioned earlier, utilising some of these residue streams to produce energy can also reduce the serious environmental problems caused by their usual disposal method.

## **2.5 Utilisation of biomass residues in an internal combustion engine for energy generation**

The two electricity generation technologies evaluated for this purpose are gasification and anaerobic digestion (AD). The feedstock for the generation of gaseous fuel is from the processing of the residue streams arising from agriculture, forestry, livestock, and urban human waste. The availability of such feedstock and the suitability of the technologies identified are considered viable for this region [33, 55-57] and can be coupled with existing small-scale electrification equipment.

The agricultural and forestry residues can be processed using gasification technology to produce an energy-rich combustible gas called synthetic gas (abbreviated to syngas). Livestock, urban human waste residues, and any high moisture content crop residues can be processed using AD to produce biogas. AD technology is more feasible for processing waste streams with high moisture content.

These gases can be fed into a dual fuel internal combustion engine, more particularly for this study, an adapted diesel engine whereby the gaseous fuel is used to substitute the diesel. Production of electrical energy by utilisation of biomass residues can provide more affordable and renewable energy due to the decrease in diesel consumption, thus decreasing dependency on fossil fuels whilst increasing access to electricity, especially in rural locations.

This also increases the 'energy equity' dimension of the energy trilemma by improving access to energy that is reliable and potentially more affordable.

Utilising these waste streams for gasification [55] or using AD technology [42, 57] in this manner also provides an alternative waste management solution, thereby mitigating environmental and health issues associated with the current disposal methods [33]. Thus, in summary, utilising biomass residues as feedstock for gasification or AD to produce small-scale renewable energy has additional benefits, especially for rural communities. These include environmental, social, and economic benefits [55, 57, 58]. Other alternatives to produce renewable power from these gaseous fuels involve using a dedicated gas engine or modification of existing internal combustion engines.

There are advantages and disadvantages to both processes when used for small-scale power generation with an internal combustion engine (ICE). For gasification, the waste biomass residues can be easily collected and stored as a natural by-product during harvesting or processing. Whereas for biogas, the residues may be dispersed over larger areas and must be manually collected and stored appropriately for the generation of biogas. Hence, gasification is better suited for larger volumes of biomass residues.

Developing countries that have a plentiful supply of biomass residues [46, 51, 59] can utilise biomass residues as a feedstock for gasification thus enabling the production of more affordable and renewable electricity, especially in rural locations for people who rely on existing diesel genset engines for power production.

### **2.5.1 Overall conversion efficiency (biomass to net electricity)**

When utilising biomass in gasification with a diesel engine for power generation, the overall efficiencies are dependent on the size of the power plant [60, 61].

A review of the literature based on the use of syngas in an ICE by Martinez et al. [62] shows that the overall efficiencies of downdraft gasification units coupled with diesel engines (sized 12 to 20 kW) varied from 11.69 to 25.0% [62-66]. Losses are experienced for various reasons including the thermal efficiency of the engine; however, a further factor that impinges on the overall efficiency is the calorific value (CV) of the syngas produced. This in turn is dependent on the quality and type of the biomass feedstock and the gasification operational parameters.

Dual fuel operation diesel/biogas engines (~1,500 RPM) which are used for small-scale electricity generation typically have a maximum thermal efficiency of 23% [67]. A summary of the overall efficiencies seen in dual fuel engines for electricity generation reviewed in the literature is summarised in Table 2.1.

**Table 2-1 Overall efficiency of dual fuel systems for electricity generation**

Power (kW)	Overall efficiency (%)	Dual Fuel Type	Reference
<10	10	Gasification/diesel	[60]
10-100	10-20	Gasification/diesel	[60]
<50	20	Gasification/diesel	[61, 68, 69]
25-50	>25	Gasification/diesel	[61, 68, 69]
100	18	Gasification/diesel	[61, 68]
12-16	21-24	Gasification/diesel	[62, 63]
15-20	25	Gasification/diesel	[62, 65]
11.44	11.69	Gasification/diesel	[62, 64]
17.5	16.6	Gasification/diesel	[62, 66]
68.4	11.7-20.7	Gasification/diesel	[70]
5.5	Maximum 23	Biogas/diesel	[67]

The literature reviewed shown in Table 2.1 highlights that the overall efficiency of these dual fuel systems (from biomass to net electricity) varies. For future calculations for this study, in Chapter 4, lower and upper values were chosen of 10 and 25%, based on the values quoted in the open literature.

## 2.5.2 Anaerobic digestion

During the process of anaerobic digestion (AD), which involves the breakdown of organic matter using microorganisms in the absence of air/oxygen, biogas is produced. The biogas produced is made up of methane, carbon dioxide, small amounts of water vapour, and other trace gases.

The energy from this biogas comes from methane gas which is the primary component. Biogas can be used to either produce electricity or for cooking. Feedstock for AD can vary from crop residues, animal manure, and the organic fraction of municipal organic waste to wastewater sludge [71]. When considering crop residues, the residues with higher moisture content are more suitable for AD than gasification. Utilising livestock residues and urban human waste residues as feedstock for AD provides a sustainable waste treatment option and mitigates the environmental risks associated with the usual disposal methods.

The methane content of biogas varies dependent on the feedstock, it can range between 45% to 75% vol, with the remainder being predominantly CO<sub>2</sub> [71, 72].

AD technology combined with gas or dual fuel engines is well developed and globally used for energy production [73]. Its success in “newly industrialised countries” has been enhanced by government support in the form of policies, subsidies, tax incentives, and/or feed-in tariffs [56, 73].

Transferring this success to Africa is deemed as potentially promising if the various barriers can be overcome. One of the initial barriers to uptake, (especially on the smaller scale of 1–500 kW), revolves around the initial investment as developers may find these less financially attractive [56, 73, 74]. A small study conducted in northern rural Tanzania indicated that some of the benefits gained by those who adopted AD technology included an increase in farm incomes as well as a reduction in GHG emissions [75], whilst providing flexibility as this technology can be used on a small or large scale [56, 58]. Furthermore, using biogas for cooking mitigates the pollutant issues associated with low-grade fuels used in inefficient cookstoves. In contrast, there are still some issues associated with AD; the effluent generated from AD units needs to be managed.

A study of the feedstocks and effluent from various digesters in Uganda was monitored for standard wastewater and fertilizer [76]. This study highlighted that the effluent produced from micro-scale anaerobic digesters in Kampala did not meet the regulatory standards to enable direct discharge. In the event of direct discharge, the high levels of nitrogen and phosphorus would exacerbate the eutrophication of Lake Victoria. Hence, the effluent arising from the digesters needs management to avoid these potential environmental issues and should be used as land fertiliser or treated further before discharge.

### **2.5.3 Gasification**

Gasification is an old well-established technology that was originally used commercially in the 1800s for industrial and residential heating and lighting where coal and peat were used as the feedstock. During the wars, in particular, WWII, this technology resurfaced due to the lack of fossil fuels. Wood gasification was used to produce producer gas to run car engines.

Gasification is a technology whereby carbonaceous fuel undergoes partial thermal oxidation in the presence of a gasifying agent which can include either air, steam, oxygen, or carbon dioxide (a mixture of these may be used). Typical temperatures for gasification are 500-1,400°C. This produces syngas which is made up of H<sub>2</sub>, CO, CO<sub>2</sub>, N<sub>2</sub>, O<sub>2</sub>, char (solid carbon-based residues), ash, tar, and oils [62, 77].

Gasification coupled with an ICE for energy production has penetrated various countries over a range of scales, especially in India [73, 78]. Small-scale gasification units have the benefit of lower capital costs, thus making them more economically viable. Bhattacharya [79] states that to overcome the barriers associated with this technology on a medium to large scale, using small-scale units that are locally fabricated and can be successfully operated by operators with limited technical experience is the best solution. However, issues remain in terms of the reliability of these units based upon problems associated with a lack of technical expertise as well as with gas quality. This is due to the high tar content of the syngas produced and the contamination of cleaning water [73, 78]. Overall, biomass gasification for producing energy is seen as a good alternative in developing countries for the following reasons [80]:

- A plentiful supply of biomass with some countries having uniform distribution.
- Simple technology with annual availability.
- Potential to mitigate environmental pollution as can be used as a waste management technique for residues otherwise left to decompose.
- Can be used to provide energy to remote rural locations in a carbon-neutral sustainable way, in this case, using dual fuel engines for small-scale energy generation.

Gasification technology is versatile as it can be used to produce syngas, hydrogen, or liquid biofuels which can all be used to produce electricity.

### **2.5.3.1 Stages of gasification**

Gasification occurs via a series of reactions or stages, which are said by many researchers to overlap; there are no clear boundaries between these. These four stages in order, are as follows: heating and drying, pyrolysis, oxidation, and gasification.

### **Heating and drying stage**

The moisture content of biomass is very variable and is very dependent on the feedstock type and what treatment/conditions it has been exposed to. For effective gasification efficiencies, the biomass must have been dried to some extent, in particular eliminating surface moisture.

Ideally, the moisture content should range between 10 to 15% [77]. This stage occurs at typically 100-200 °C and results in a reduction of the moisture content of the feedstock down to values less than 5% [80, 81].

### **Pyrolysis stage**

This stage occurs when the biomass reaches temperatures between 150 and 400°C [77]. The biomass undergoes thermal decomposition in the absence of oxygen/air to produce char (solid carbonaceous waste) and volatile gases. The main gases produced are hydrogen, carbon dioxide, water, hydrocarbons, and in lesser amounts other organic compounds. The mixture of organic compounds produced is referred to as 'tar.'

### **Oxidation stage**

During this stage, partial oxidation occurs via a gasification agent which is usually air. The gases produced from the drying and pyrolysis stages may or may not pass through this oxidation stage as this is dependent on the gasifier design [80]. The energy produced from this stage is used for reactions that occur during the reduction, pyrolysis, and gasification stages.

### **Gasification stage**

During this stage, the char produced during pyrolysis is converted mainly to CO, CH<sub>4</sub>, and H<sub>2</sub> via a series of reduction reactions which are mainly endothermic and occur between 800 – 1000 °C [80]. The amount of tar and gases produced alongside their composition is dependent on a range of factors which include the energy content of the initial fuel, the physical characteristics of the fuel, the gasifier design, and the operational conditions employed.

#### **2.5.3.2 Types of gasifiers**

Generally, there are three types of gasifiers that are classified based on how the biomass, gasifying agent, and how the reagents interact with the gasifier itself [77]. The most common types of gasifiers are fixed bed/moving bed, fluidized bed, and thirdly the entrained suspension gasifier.

The latter type is not conventionally used for biomass such as wood, it was developed for fine coal dust (0.01-0.44mm) [80]. For small-scale applications using biomass, the downdraft reactor has been studied in depth and is considered to be a mature technology [62].

Fixed bed gasifiers are also called moving bed reactors due to the movement of the flow of biomass as it travels through the reactor. As this movement is relatively slow, these types are often referred to as 'fixed bed' reactors. These types of reactors can differ and are further classified into types based on the positioning of the reaction distribution regions [77]. The diagrammatic representation of the three main types of fixed bed gasifiers is depicted in Fig. 2.3.

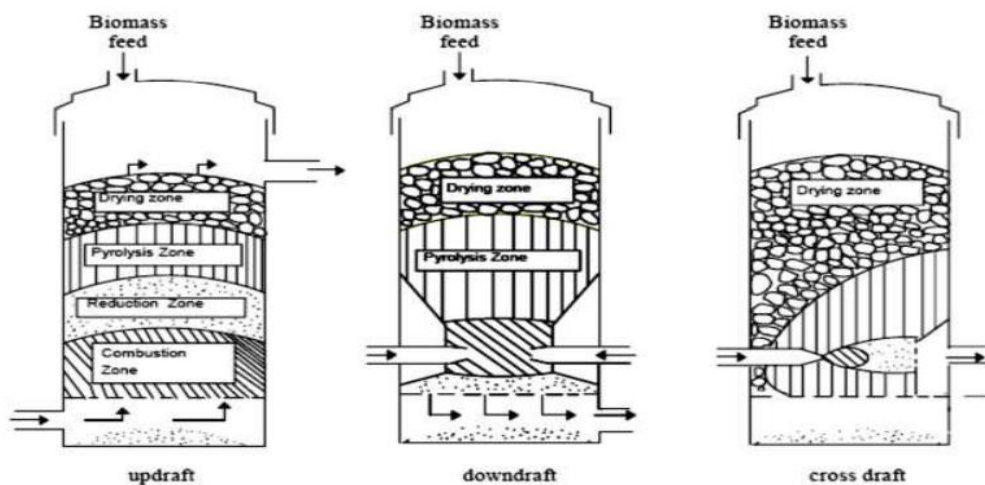


**Figure 2-3 Various types of fixed bed gasifiers [81]**

In summary, the performance of a gasifier is dependent on its design, operational conditions, and fuel properties [82]. Most researchers agree that the updraft gasifier is more suitable for thermal applications and is unsuitable for use with engine applications due to the intensive cleaning operation required to remove the tars [83], whereas the downdraft type is suitable for both thermal and engine applications [83-85].

In a downdraft (concurrent) gasifier, the biomass is fed in from the top, whereas the gasifying agent enters from the bottom or the sides. As the air (gasifying agent) enters, it interacts with the pyrolysis zone. After this, the gases and solids generated both travel parallel downstream through the reactor. Some of the gas generated in the pyrolysis zone is burnt in the gasification area.

Hence, the energy required for the endothermic reactions is provided by the combustion of the pyrolytic gas and this is known as the pyrolytic flame [77]. The zones in an updraft gasifier are arranged differently from those in a downdraft gasifier.

The downdraft gasifier has four distinct zones, from top to bottom being: the drying zone, the pyrolysis zone, the oxidation zone, and the reduction zone. In this design, the products from pyrolysis and the combustion zone travel downwards. These hot gases pass through the hot char where gasification is occurring, thus resulting in a gas that has a lower tar content. This producer gas leaves roughly below the grate of the gasifier which allows partial cracking of the tars produced and therefore, has a lower particulate and tar content (~ 1g/Nm<sup>3</sup> [80]). However, this gas produced has a lower CV because the pyrolytic gases are consumed to provide energy for the endothermic reactions. A further negative is that this type of gasifier has a lower overall thermal efficiency and is not adept at utilising biomass with a high moisture and ash content.

Martinez et al. [62] reiterate that the performance of a downdraft gasifier is affected by various factors. In particular, the producer gas composition, its CV, and the yield and efficiency all depend on the physical and chemical properties of the biomass such as the MC and particle size. Process parameters such as the equivalence ratio ( $\phi$ ) influence the temperature. Furthermore, the design features of the gasifier such as the air inlet locations, the volume of the gasification zone, the design of the grate, et cetera, all influence the performance of the gasifier.

The presence of the tars in the syngas is one of the technical issues which needs to be overcome for further applications. In downdraft gasifiers, this is addressed by making changes in the design of the gasifier, such as the incorporation of a throat in a downdraft gasifier which results in a reduction in the tar content (15 -50 mg/Nm<sup>3</sup>) of the producer gas [82].

However, other technical implications arise from the incorporation of a throat which makes the gasifiers less suitable to handle biomass which is higher in MC (> 25%) and ash (>5%). Such adapted gasifiers now require uniform sized/shaped biomass to avoid blockages as well as to allow the pyrolysis gases to flow downwards as well as allow the heat to flow upwards [82].

Although such design modifications reduce the tar content, totally tar free producer gas is not achievable. Any bridging or channelling of the biomass will increase the tar content as well as short residence times in the combustion zones.

#### **2.5.4 Syngas composition produced from downdraft gasification**

Numerous studies exist in the literature that successfully demonstrate the gasification of biomass using downdraft gasifiers to produce producer gas with low to medium CV. Various biomass types have been used for the feedstock from woodchips to various agricultural residues. Usually, the biomass introduced has been dried, in some studies, it has been pelletized [86] or briquetted to increase bulk density [87]. Olgun et al. [82] utilised wood chips, barks, olive pomace, and hazelnut shells. Zainal et al. [88] used waste furniture wood and wood chips. Patil et al. [89] used wood shavings, Masmoudi et al. [90] utilised almond shells to yield a producer gas with an LHV of 4 MJ/m<sup>3</sup>. Kumar and Randa [91] utilised chir pine needle (leaf) to produce a producer gas with an LHV of around 10 MJ/m<sup>3</sup>. Uma et al. [92] used small pieces of keekar wood as feedstock into a downdraft gasifier.

In addition, the type of gasifying agent affects the CV of the producer gas. Using air as a gasifying agent results in the syngas containing higher levels of nitrogen, thus reducing the overall CV of the syngas [62]. The typical composition of syngas when air is used as a gasifying agent contains 15-20% H<sub>2</sub>, 15-20% CO, 0.5 -2% CH<sub>4</sub>, 10-15% CO<sub>2</sub> with the remaining being N<sub>2</sub>, O<sub>2</sub>, and hydrocarbons (HCs) [62].

A literature review conducted by Martinez et al. [62] on the application of a downdraft gasifier with reciprocating diesel engines states that two types of downdraft gasifiers can be used which are the open and close top designs. The closed top gasifier (of interest) can be either configured as having a straight cylindrical reactor or with a throat in the core (traditionally known as an Imbert gasifier). The height of the reduction zone is said to be especially important for producing high quality producer gas. If this height is too low, this decreases the residence time and therefore, reduces the operational efficiency. To further reduce the tar content in the producer gas which is to be used in reciprocating internal combustion engines, having downdraft gasifiers with a double air supply will facilitate this.

This tar content can be further reduced in downdraft gasifiers by utilising clean up stages prior to the producer gas entering the engine. For example, water scrubbers and special condensers can be employed. Alternatively, the biomass can be pre-treated before gasification to reduce the tar content, however, this is expensive and potentially not feasible when considering the scope of this study [93].

When considering using syngas produced from downdraft gasification in a dual fuel diesel engine, Hasler and Nussbaumer [94] state that for satisfactory performance the particle content must be below 50 mg/Nm<sup>3</sup>, and the tar content below 100 mg/Nm<sup>3</sup>. Other researchers quote a tar range of 10 -1 mg/Nm<sup>3</sup> for successful gasifier-engine system operation [95]. Bhattacharya et al. [95] state the tar concentration in clean syngas after utilising high efficiency scrubber systems is still higher than preferred at 70–75 mg/Nm<sup>3</sup>. Alternative studies such as those reported by Sridhar et al. [96] state that the engine is capable of running at higher tar levels than those quoted by Hasler and Nussbaumer [94]. Thus, as indicated by Martinez et al. [62], this data should be taken as a guide as in each of the studies the values reported are related to specific engine types whereby the design features affect the validity of the results. In summary, the type of syngas most suitable for use with diesel engines is that generated from the downdraft gasification process due to its lower particulate matter (PM) and tar content [84, 97, 98].

Research to date indicates that downdraft gasifiers have been specifically designed to facilitate the gasification of specific types of biomass [99]. This is due to the large variation of the physical and chemical properties in the types of biomass residues available and or suitable for gasification.

The quality and composition of the producer gas generated is also dependent on the operational factors of the gasifier, in addition to the physical and chemical properties of the biomass feedstock such as the moisture content and particle size. As a result, the producer gas composition quoted in the literature is variable as it is based on many factors which differ from study to study.

To gain an indication of the compositional variability, the syngas composition data from various studies available in literature which has been produced predominantly from downdraft gasification of biomass residues [62, 81, 82, 84, 86, 87, 90, 91, 100-109] has been reviewed and is shown in Table 2.2.

**Table 2-2 Variability in the composition of the syngas generated from various studies**

	CO	H <sub>2</sub>	CH <sub>4</sub>	HC	O <sub>2</sub>	N <sub>2</sub>	CO <sub>2</sub>	LHV (MJ/Nm <sup>3</sup> )
Average %	19.7	14.8	2.7	1	0.95	54.2	12.2	5.2
Range	9.4 – 29.6	7- 24.8	0.1 – 8.21	0.2 – 2.4	0.61- 1.61	34.1 - 60.8	8.9- 36.4	3.8- 10.6

Table 2.2 shows the range of each component present in the syngas produced from downdraft gasification using various biomass residues. The largest range in variations that affect the net resulting LHV occurs in the hydrogen and CO content.

To accurately evaluate the combustion performance and resulting emissions of dual fuel combustion using syngas/diesel, a uniform supply of syngas is needed in terms of compositional quality. As we know, the output syngas quality produced directly from a gasification unit is affected by the variation in the MC, the particle size of the feedstock, alongside the operational parameters of the gasification unit, hence this cannot be guaranteed. Using simulated syngas which is reflective of the composition of the individual components found in syngas produced by downdraft gasification, (as shown in Table 2.2) is preferential as it guarantees the compositional consistency during the experimental testing period.

Many researchers have conducted studies whereby the simulated syngas contains just CO and hydrogen as these compounds contain the majority of the energy. However, it is known that diluent gases such as CO<sub>2</sub> and nitrogen (which are present in syngas from gasification) when introduced into the engine charge can alter the state of the mixture during compression [110]. Hence, using syngas that mimics the composition of that produced from gasification which includes nitrogen and CO<sub>2</sub> is preferred when studying dual fuel engine combustion and emission performance, especially when considering NO<sub>x</sub> emissions as these gases can function as NO<sub>x</sub> reducing strategy, similar to Exhaust Gas Recirculation (EGR).

Furthermore, using syngas produced directly from gasification in a compression ignition (CI) engine requires cooling, cleaning/filtering to remove dust, ash, and tars [111]. The extent of the clean-up will reflect the final residual tar content, and this is variable. For this study, simulated syngas blends were used which are ash/dust, and tar free.

Consequently, all the studies reviewed in the literature whereby simulated gasifier syngas was used were also 'tar' free.

## **2.6 A summary of the waste biomass resource assessments reviewed in the literature**

Various waste biomass resource assessments exist in the literature which focus on the countries of interest (Uganda and Tanzania) [40, 47, 51, 52, 54]. However, for Tanzania, there is no single study available in the literature that quantifies the raw energy potential (EP) arising from all four biomass residues which include: agriculture, forestry, livestock, and urban human waste streams. Okello et al. [52] have quantified the raw energy potential of the biomass residues from these waste streams for Uganda but have not further quantified the electrical generating potential. Hence, there is nothing available in the literature that has calculated the net electrical energy generating potential (using gasification or AD) coupled with a diesel genset, i.e., dual fuel combustion using biogas or syngas with diesel from these biomass residues. The gaseous fuel produced can then be used to substitute diesel fuel in small-scale dual fuel gensets; thus, reducing dependency on fossil fuels.

## **2.7 Fundamentals of a diesel engine**

An ICE converts chemical energy (present in the fuel), into mechanical energy via combustion, with the energy release occurring inside the actual engine. ICEs are commonly referred to as reciprocating engines (also known as piston engines) and these include spark-ignition (SI) and also CI or diesel engines. These engines use piston motion to transfer energy and are classified as either four or two-stroke cycles which represents the number of piston strokes required to complete one working cycle.

Most reciprocating engines operate on a four-stroke working cycle whereby each cylinder relies on four strokes of its piston – two revolutions of the crankshaft to deliver one power stroke [112]. For this study, the focus is on a reciprocating piston engine, which is based on a four-stroke CI/diesel engine that is commonly used in diesel gensets.

### **2.7.1 Overall introduction and working principles**

During a working cycle within the engine, the piston moves up and down between two positions known as the '*top dead centre*' (TDC) and '*bottom dead centre*' (BDC).

The piston movement is driven by the crankshaft to complete one clockwise rotation in  $360^\circ$ . The crank angle is the angle at which the crankshaft is positioned during its clockwise rotation, this is measured in units of crank angle degrees (CAD). The simplified geometry of a reciprocating ICE is depicted in Fig. 2.4, whereby TC represents TDC, and BC represents BDC. The movement of the piston is derived from the energy produced from combustion and transfers this power via various mechanical parts to the drive shaft.

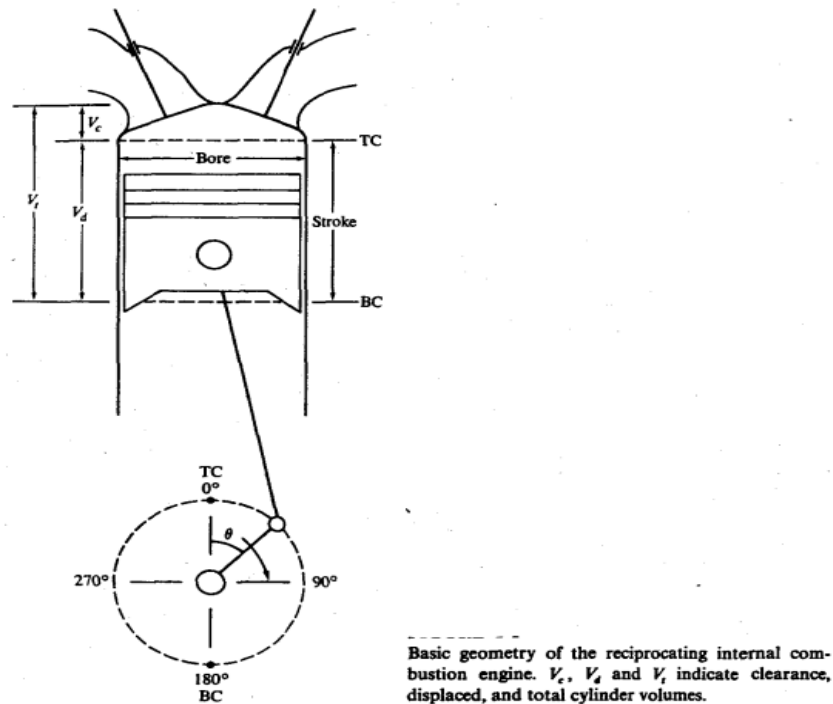


**Figure 2-4 The basic geometry of a reciprocating ICE [112]**

### 2.7.2 Four-stroke engine fundamentals

The four strokes within a diesel CI engine are as follows: the air intake/induction stroke, compression stroke, expansion/power stroke, and exhaust stroke. Each stroke is explained further in detail [112]:

- Intake stroke: the piston moves from TDC to BDC thus creating suction thereby drawing in the air via the inlet valve into the cylinder. During this stroke the inlet valve is open, and the exhaust valve closed, the inlet valve closes after this stroke ends.

- The compression stroke: the air inside the cylinder is compressed by the movement of the piston back to TDC; both valves remain closed during this stroke. At the end of this stroke, the fuel is injected under high pressure, and combustion follows as a result of the autoignition of the fuel-air mixture brought about by the high pressure and temperature, resulting in a rapid increase in the cylinder pressure.
- These first two strokes complete one revolution of the crankshaft (360°).
- The expansion/power stroke: the piston is forced downwards from TDC to BDC because of an increase in temperature and pressure generated from the combustion of the fuel. This results in the rotation of the crank. As the piston reaches BDC, the exhaust valve opens to initiate the next stroke. During this stroke, the thermal power is converted to mechanical power.
- The exhaust stroke: the waste gases are removed from the cylinder by the movement of the piston from BDC to TDC. The exhaust gases are expelled due to differential cylinder pressure: the pressure in the cylinder is higher than the exhaust pressure. As the piston nears the position of TDC, the inlet valve opens again to repeat the cycle.
- These final two strokes complete the second revolution of the crankshaft (360°).

The four strokes of the diesel engines discussed are diagrammatically represented using Fig. 2.5.

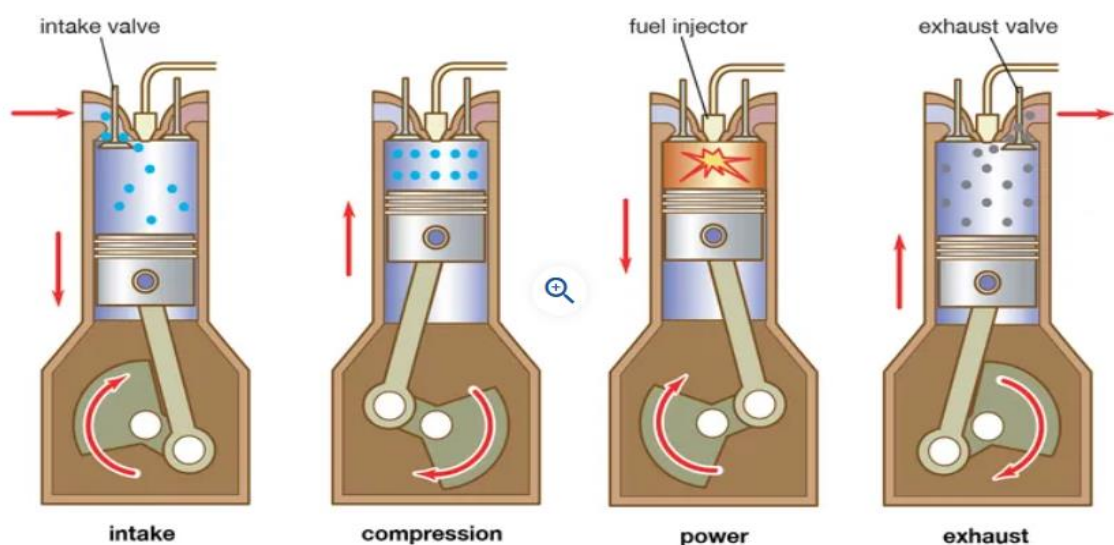
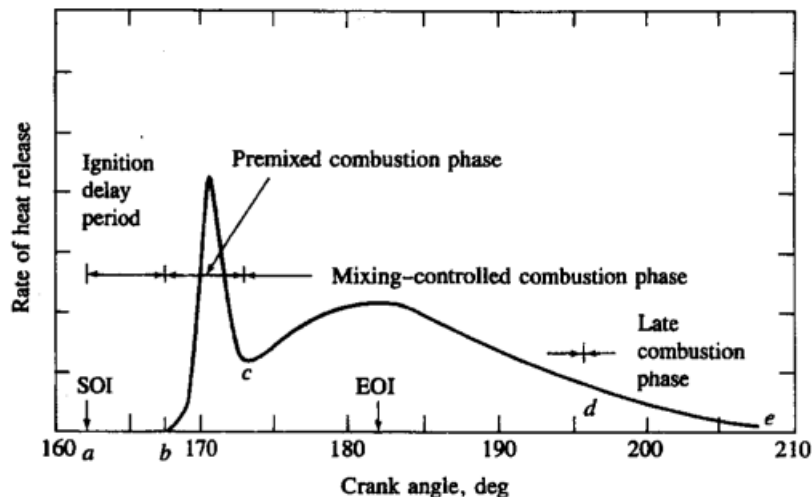


Figure 2-5 The four strokes of the diesel engine [113]

### 2.7.3 Combustion phases for a diesel Compression Ignition (CI) engine

There are various stages defined within the CI diesel combustion engine which are typically identified by studying heat release rate (HRR). The HRR provides vital information regarding the in-cylinder combustion process and its phases. The net HRR (often also referred to as NHRR) is based on the first law of thermodynamics and also by modelling the cylinder as a closed system. It is calculated by using the average data from pressure *versus* crank angle degree (P-CAD) traces. The resulting graphs which show the rate of heat release as a function of crank angle degree (CAD) are good indicators of the stages of combustion as well as the combustion duration. For diesel, these four phases will be discussed in further detail and are illustrated using Fig. 2.6 which shows the HRR diagram for the different diesel combustion phases.



**Figure 2-6 The rate of heat release for diesel combustion [112]**

*Injection delay (ID)*. This stage impacts the following combustion phase heavily. Typically, the fuel is injected via the high-pressure injection system into the cylinder towards the end of the compression stroke, this usually occurs before TDC [112]. The fuel is atomised and vaporised, vaporisation occurs by absorbing heat from the compressed hot air. This vaporised fuel then mixes with the hot pressurised air in the cylinder. As a result, a slight decrease in the cylinder pressure is noted. In addition, the HRR curve often may exhibit negative values as a result of the vaporisation of the fuel, seen just before combustion [114, 115]. During this stroke, the piston is reaching the end of the compression stroke.

Once the autoignition temperature of diesel is reached, the fuel ignites featuring the Start of Combustion (SoC) and the end of the ID period. This also results in a sharp increase in the in-cylinder pressure which is used to determine the SoC when calculating the ID period.

The ID period is calculated from the Start of Injection (Sol) and the SoC and is expressed as CAD or time [112, 115]. The SoC is usually determined by studying the P-CAD traces and/or from the HRR of the P-CAD data [112]. Often first/second derivative data of the P-CAD curves are used to determine the SoC and the ID [116, 117]. There are two stages of the ID period: the chemical delay and the physical delay. The chemical delay is associated with the time involved in the pre-combustion reactions, whereas the physical delay is associated with the time required for the processes involving atomisation, vaporisation, and fuel air mixing. The ID related to diesel is stated to have a strong correlation with ambient temperature and pressure [115]. In addition, the mixing of the air and fuel during ID has a direct impact on the resulting NO<sub>x</sub> and soot emissions [118].

*Premixed or rapid/uncontrolled combustion.* This phase is often referred to as 'rate controlled combustion' and is said to be significant when considering emission controls [118]. This phase involves the combustion of the premixed or accumulated fuel (from the ID period) and occurs quickly within a few CAD [112]. This stage of combustion relates to a high rate of heat release over a very short period, and this heat release has a strong correlation with the amount of fuel-air mixture produced during ID [114]. This combustion phase is associated with peak pressure and temperature, alongside the highest heat release [118]. The mass of the fuel burn in this phase has a linear relationship to engine speed and the ID [114], which is dependent on the fuel mass prepared during the ID period [118]. Typically during this stage, when utilising 'normal cetane number' (CN) fuels such as diesel, <25% of the total energy of the total fuel heat is released [118].

*Mixing-controlled combustion phase.* This phase is often referred to as 'diffusion combustion' and involves the combustion of the fuel/air mixture as it becomes available. The combustion rate during this phase is primarily controlled by the mixing of the vaporised fuel with the air process [112], hence, is referred to as the 'controlled' stage. During this stage, lower rates of heat release rates are experienced in comparison to the previous premixed combustion stage [114]. This combustion phase experiences a bright luminous flame which is typically characteristic of a diffusion flame [114].

*Late combustion phase.* This phase is often referred to as 'after burning.' During this stage, a lower level of HRR continues into the expansion stroke [112]. This phase involves the combustion of any unburnt fuel, further oxidation/complete combustion of any soot, and any other combustion products promoted by mixing. The rate of oxidation/combustion of these products decreases with decreasing cylinder temperatures as a result of the expansion stroke [112].

## **2.8 Emissions from diesel combustion in compression ignition engines**

Overall, it can be said that the process of diesel combustion is primarily controlled by the mixing of fuel and air [114]. Diesel emissions are a direct consequence of the heterogeneous mixing of fuel/air. The fuel is injected towards the end of the compression stroke, hence the mixing of the fuel/air is not considered to be homogenous [112]. Therefore, the emissions formed are dependent on fuel distribution which depends highly on the level of fuel/air mixing [112]. Emissions from diesel engines are a source of air pollution, in comparison to petrol engines, the most problematic emissions in diesel engines are  $\text{NO}_x$  and PM.

### **2.8.1 Carbon monoxide (CO)**

CO is produced as a direct result of incomplete combustion of the fuel due to incomplete oxidation. The CO emissions are more important in SI engines as they operate closer to the stoichiometric ratio, thus producing higher CO emissions. Diesel CI engines run lean (with an excess of air), hence, in comparison, the CO emissions are lower and are not considered problematic [112]. CO emissions in all internal combustion engines are a direct result of the fuel/air equivalence ratio ( $\Phi$ ) [112]. The  $\Phi$  is important for defining the composition of a mixture during combustion and represents the ratio of the actual fuel/air ratio to the stoichiometric fuel air ratio [112]. The production of CO in diesel engines occurs when mixing/swirl/turbulence is reduced or is inadequate in the combustion chamber, or when the fuel droplets are not small enough. Larger droplets have a slower rate of vaporisation, hence, their distribution and velocity will be impacted [112]. How fast CO is oxidised to  $\text{CO}_2$  is limited by reaction kinetics, and enhancing the oxygen availability of the air fuel mixing enhances the combustion process [119].

CO is a toxic gas and if inhaled it impairs the human body's ability to transport oxygen around the body. The level of impairment is dependent on the concentration inhaled.

### **2.8.2 Unburnt Hydrocarbon (UHC) /Hydrocarbon (HC)**

The terminology used for this pollutant is often interchangeable between HC/UHC. Typically low levels of UHCs are produced by a diesel engine, most of which are produced at low engine loads due to lean fuel-air mixing [120]. UHCs are formed from incomplete combustion arising from a lack of homogeneity of the fuel air mixture due to poor mixing [119].

At such operational parameters, the flame speed is reduced, hence combustion may not complete in the combustion stroke resulting in raised HC emissions [120, 121]. Due to this low temperature, especially around the cylinder wall (in comparison to the centre of the cylinder), some of the fuel remains unburnt due to incomplete combustion resulting in the formation of UHCs [120].

UHCs are harmful to human health and the environment as they are directly involved in the formation of smog/ground level ozone. Smog is formed from the reaction between NO<sub>x</sub> and the volatile organic compound (VOC) fraction of the UHCs. A VOC is defined as an organic compound with a boiling point between 50-260°C. Typical examples include formaldehyde, d-Limonene, toluene, acetone, ethanol (ethyl alcohol), 2-propanol (isopropyl alcohol), and hexanal [122].

Fig. 2.7 illustrates how the formation of NO, HCs, and soot are impacted by the injected fuel and flame during the two different combustion phases: the premixed phase, and the controlled phase in a direct injection (DI) diesel engine [112].

Fig. 2.7 depicts a swirl type of mixing occurring and shows that NO is formed in high temperature regions. The soot formation occurs in areas that have a high concentration of unburnt fuel, this is further oxidised by any remaining oxygen thus producing a yellow luminous flame in the controlled combustion phase. The HC is produced from three potential sources: flame quenching (the walls of the combustion chamber act like a heat sink), incomplete combustion, and any fuel that vaporises late in the combustion phase, thus, is not fully oxidised [112].

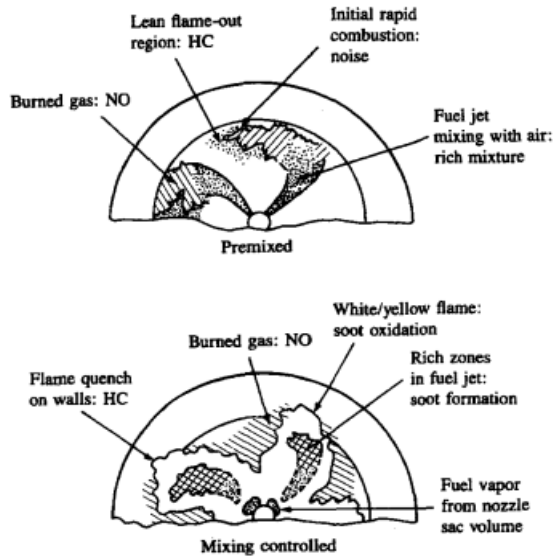


**Figure 2-7 The formation of NO, HC and PM during the two combustion phases in a direct injection diesel engine [112]**

### 2.8.3 Nitrogen oxides (NO<sub>x</sub>)

NO<sub>x</sub> emissions include the gases which are nitric oxides (NO) and nitrogen dioxide (NO<sub>2</sub>). CI engines produce higher levels of NO<sub>x</sub> in comparison to SI engines due to their operating conditions of higher temperatures and pressures which favour NO<sub>x</sub> formation.

NO<sub>x</sub> formation in diesel engines is favoured by high temperatures (>1,600 °C), high availability of oxygen, and the residence time in the cylinder [120]. The majority of NO<sub>x</sub> formation occurs when the flame temperature is at its highest, which is usually when the piston is at the top [120].

NO<sub>x</sub> emissions are considered critical pollutants arising from diesel combustion due to their adverse impact on human health and environmental damage and are linked to acidification, damage to ecosystems, nutrient enrichment, and smog formation [120]. NO, and NO<sub>2</sub> are both toxic gases, but NO<sub>2</sub> is five times more toxic than NO and is linked to lung disease, and respiratory problems [120].

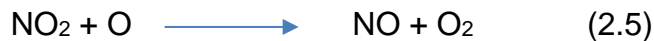
NO is the dominant oxide produced from nitrogen in diesel combustion (~85-90% of all NO<sub>x</sub>) [120]. The nitrogen source for the formation of NO is atmosphere nitrogen (N<sub>2</sub>) [112]. The reactions for NO formation are known as the 'Zeldovich' mechanism [112]. NO is formed in regions where the temperature is high. The simplified equations for this mechanism are shown in Eqs. 2.1-2.3.



NO<sub>2</sub> is typically formed from NO in diesel engines, as shown in Eq. 2.4 [112]:



Furthermore, the NO<sub>2</sub> formed can also react to form further NO, see Eq. 2.5:



This explanation supports the fact that the highest NO<sub>2</sub>/NO ratio occurs at light loads in diesel combustion, as in cooler regions the NO converts back to NO<sub>2</sub> [112]. N<sub>2</sub>O is a GHG with a very high global warming potential (GWP); one kilogram of N<sub>2</sub>O is equivalent to releasing ~298 kg of CO<sub>2</sub> [123]. When this species breaks down into the stratosphere, it acts as a catalyst in breaking down the ozone layer.

Any additional diluent added to the air intake such as exhaust gas recirculation (EGR) results in a reduction in NO, and the resulting NO<sub>x</sub> formations [112]. Hence, any syngas with a high inert component should, in theory, aid in the reduction of NO and NO<sub>x</sub>.

Thus, when assessing the impact of NO<sub>x</sub> emissions in diesel/syngas dual fuel combustion, it is more accurate to consider using simulated syngas with a composition that mirrors that produced during the gasification process, that is, with the addition of any diluents which may affect the formation of NO<sub>x</sub>.

#### **2.8.4 Particulate Matter (PM)/soot**

The definition of PM varies and is determined by the sampling method employed. Most emissions standards define this as the material that is collected by filtration from diluted and cooled exhaust gases [124], therefore, this includes solids and any liquid material which may condense. According to Kittleson [125], the PM is made of solid carbonaceous solids which are highly agglomerated, VOCs, ash, and sulfur compounds (derived from the fuel). Typically the PM is made up of two main fractions, the first being the insoluble organic fraction (IOF) which contains carbon derived soot and any sulfates [114]. The other fraction is commonly known as the soluble organic fraction (SOF), this contains low molecular weight species typically derived from the incomplete oxidation of the fuel and/or lubricant which includes polycyclic aromatic hydrocarbons (PAHs) [114, 125].

Diesel PM is predominantly made up of carbon and is formed in fuel-rich areas which contain unburnt fuel within the flame region [112, 120]. Diesel PM from the engine exhaust contains particles of varying mass, size, and surface area. The typical distribution of diesel PM is illustrated in Fig 2.8.

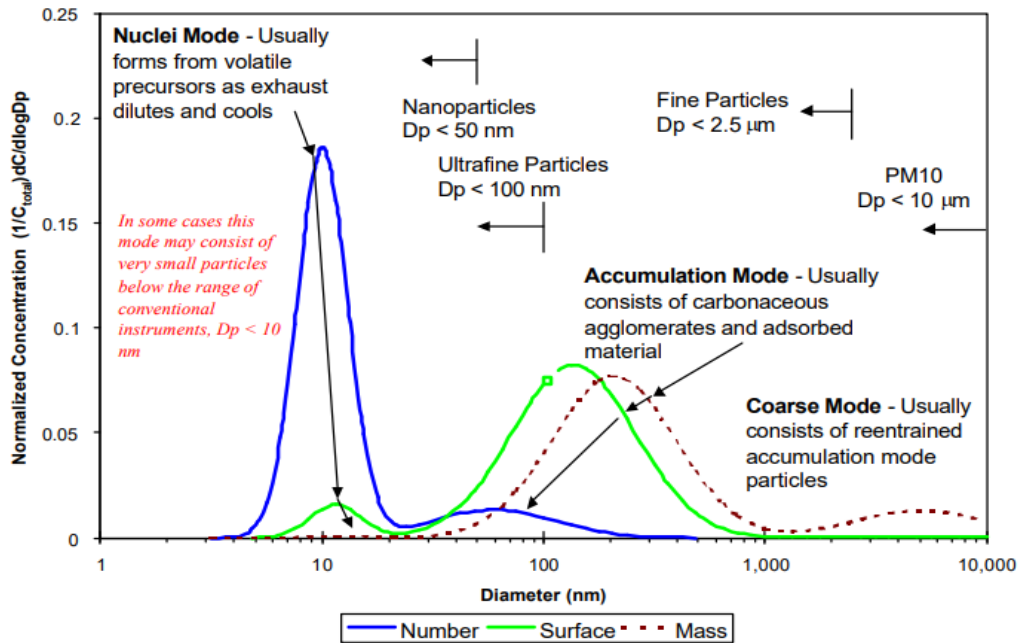


**Figure 2-8 Diesel exhaust particle size distribution [126]**

The particle sizes illustrated in Fig. 2.8 vary in diameter and fall into three modes. The first is the nuclei mode which contains nanoparticles that are the smallest in size with a diameter ranging from 3-50 nm [125, 126]. Typically, the maximum concentration of nanoparticles occurs at 10-20 nm and these particles make up the majority of the total particle number, but only account for 0.1-10% of the total PM mass [125]. Nanoparticles are formed during the process of the exhaust gas being diluted and cooled and are composed of a small amount of carbon and metallic compounds, with the rest being mainly VOCs and sulfur related compounds [126].

The second mode is the accumulation mode which contains particles ranging from 50-500 nm which contribute to the majority of the mass [126]. These particles are made up of carbonaceous matter with adsorbed materials directly from combustion. The particles found in this mode range from fine, ultrafine, and nanoparticle ranges [126].

Finally, the coarse mode contains particles with a diameter greater than 1,000 nm, these particles contribute to 5-20% of the total mass with minimal contribution to the particle number [126]. The particles in this mode are formed from the re-entrainment of accumulation mode particles such as from the cylinder walls [126].

In summary, diesel exhaust emissions produce  $PM_{10}$  which contains particulate matter which is  $<10\mu m$  in diameter. Of that  $PM_{10}$ , some are classified as  $PM_{2.5}$ , i.e., having a particle diameter of  $<2.5\mu m$ . Both PM sizes contain particles that are small enough in size to be inhaled and can enter the respiratory system. Exposure to particles less than  $PM_{10}$  is linked to lung and heart problems which include cancer.  $PM_{2.5}$  are considered a greater risk due to their smaller size which enables them to penetrate deeper and potentially enter the bloodstream, therefore increasing the health risks enormously.

### **2.8.5 Summary of diesel combustion emissions**

The problematic emissions arising from DI diesel engines are PM and  $NO_x$ . To reduce the  $NO_x$  levels, combustion temperatures must be reduced, and in doing so, this affects combustion and thermal efficiency and leads to an increase in soot/PM. To decrease the mass of PM, better combustion is needed which requires higher temperatures, which in turn, potentially increases  $NO_x$  emissions. Hence, this is often referred to as the 'PM and  $NO_x$  trade-off.' In many diesel engines, an EGR strategy is used to reduce  $NO_x$  levels. This works on the principle by which some of the engine exhaust gas is cooled and returned to the combustion chamber. This contains a high level of  $CO_2$  from combustion, thus reducing the oxygen availability or concentration in the combustion chamber as well as the temperature, thus, reducing  $NO_x$  formation.

### **2.8.6 Diesel engine after-treatment systems for emission control**

Often emission control in heavy-duty diesel engines is done using after-treatment systems which include the 'diesel oxidation catalyst' (DOC), diesel particulate filter (DPF), and selective catalytic reduction (SCR) [120].

DOCs are used referred to as 'catalytic convertors,' and they work by oxidising the HC and CO present from incomplete combustion, as well as oxidising the SOF of the PM into carbon dioxide and water, thereby reducing PM emissions.

A DOC is considered a mature, simple, relatively inexpensive technology that required no maintenance. A DOC is stainless steel container, inside which there is a monolith honeycomb structure made up of ceramic or metallic material that contains numerous parallel channels which provide high contact due to the large surface area provided between the monolith and the exhaust gases. This monolith carrier structure is coated with a washcoat and an active noble metal catalyst which is typically either platinum (Pt) or palladium (Pd) [120]. As the exhaust gases pass over the DOC, the oxidation process is catalysed; the pollutants are converted into CO<sub>2</sub> and water.

SCR technology is used to reduce NO<sub>x</sub> emissions, and this system is sighted after the DPF. This system is composed of an SCR catalyst and a liquid tank for the diesel exhaust fluid (DEF), commonly known as Ad-Blue which contains aqueous urea. The DEF is injected into the exhaust system after the DPF, it hydrolyses and mixes with the exhaust gases. These exhaust gases including ammonia next pass over the SRC whereby the ammonia and the NO<sub>x</sub> react with the catalyst to form nitrogen and water. The other advantage of utilising this SCR after-treatment is that the engine design can be further optimised to reduce fuel consumption and maximise torque. The advantage of this after-treatment is its high NO<sub>x</sub> conversion efficiency, however, it is expensive, and to achieve optimum efficiency, good control is needed [120]. Again, the catalyst used for this SCR technology is either Pt or Pd [120].

The DPF aims to remove PM emissions from the exhaust. These trapped solid particles are routinely burned off via the regeneration process. Commonly, DPFs are coupled with the DOC after-treatment systems to remove diesel exhaust PM emissions [120].

The role of after-treatment systems is important in diesel engines, especially when considering the reduction of the pollutants being produced and their impact on the environment and human health.

## **2.9 Dual fuel (DF) engines for small-scale electricity generation using biomass residues**

The diesel CI engine is more able to accept a wider variety of fuels in comparison to the SI engine [110]. This is evident in history whereby the conventional diesel engine has been adapted into a dual fuel engine utilising various gaseous fuels: coal gas, sewage gas, and methane [127].

Hence, as more of these engines are used for stationary small-scale energy generation purposes, adapting these existing engines to utilise gaseous fuels produced from biomass residues makes more economical sense in order to provide more sustainable and affordable electricity, especially in rural areas. Usually, diesel engines that are capable of operating in DF mode are conventional diesel engines that have undergone modifications. The modifications undertaken can vary depending on their end use and the associated operating conditions [110].

For this study, a dual fuel engine is defined as one where an internal combustion engine has the capability of burning two very different fuels in varying proportions simultaneously [110]. Typically, combustion of the gaseous fuel provides the bulk of the energy, whereas the liquid fuel is used mainly primarily for ignition purposes, and may be combusted to provide a much smaller fraction of energy [110]. DF engines have the additional advantage of switching between fuels as required. The other type of DF engines considered are:

*Bi-fuel engines* are engines that use alternate fuel sources whereby ignition is external, using spark ignition as an example. Examples of these engines include diesel engines which have undergone extensive costly modifications which include the reduction of the compression ratio and changing the injection system to allow it to operate as a spark ignition [110].

Another type of dual fuel engine in this category is known as the *gas diesel engine*. Here the gaseous fuel is injected either into the cylinder directly, or late toward the end of the compression stroke. In such engines, autoignition does not occur due to compression, but rather combusts with the aid of the injected liquid fuel injection process [110].

Finally, *multifuel engines* is another terminology often used, this usually refers to the use of multi-liquid fuels. Such engines undergo modifications to enable them to operate using various liquid fuels, including fuels that are different from conventional diesel [110].

### **2.9.1 Addition of gaseous fuel into a dual fuel compression ignition engine**

Dual fuel engines that use a gaseous fuel as the additional fuel can differ in operation depending on how this fuel is introduced. Usually, the simplest and most economical method is to introduce the gaseous fuel through the air intake valve; this is a common practice in SI engines [110].

It is deemed more practical to make minor modifications to enable a conventional compression ignition (CI) engine to run in DF gas/diesel mode. Typically this involves the diesel fuel ignition system remaining intact and can be used fully as the only fuel source, or can be reduced whereby the diesel fuel is used only to provide a consistent/ controlled source of ignition, often referred to as the pilot injection [110]. This is the approach that was taken for this study, and the air intake port was modified to allow the direct addition of the gaseous fuel at this point. In this method, there is no direct control in terms of the gaseous fuel entering the cylinder, indirect control exists whereby the basis is the mass flow meter used to control and monitor the volume of syngas/biogas added into the air intake. A direct control system for dual fuel combustion, as defined for this study, is one whereby the gaseous fuel is added using a dedicated injection system.

In CI engines, other alternative approaches involve introducing the gas at the start of the compression process which allows additional mixing with the air before the pilot injection. Such engines are commonly referred to as *premixed dual fuel engines* and this mode of the gas introduction is known as fumigation [110].

In addition, the gaseous fuel can be injected at high pressure directly into the cylinder. This injection can occur at two points, before or just after the injection and ignition of the pilot liquid fuel. These engines are typically known as *high-pressure direct injection gaseous-fuelled dual fuel engines* [110]. This mode of introduction of the gaseous fuel allows for better control of the combustion process, however, is very costly and involves major modifications. Typically, an additional control system is added for the second fuel to control its injection.

### **2.9.2 Reactivity Controlled Compression Ignition (RCCI)**

RCCI is a terminology given to a dual fuel combustion technology that utilises the blending of two different fuels with different reactivities inside the cylinder [128]. This technology is a version of Homogeneous Charge Compression Ignition (HCCI) and was developed at the University of Wisconsin-Madison Engine Research Centre laboratories [129]. RCCI combustion usually involves the fuel with the lower reactivity (syngas/biogas/petrol) being blended with the air before entering the combustion chamber, and the fuel with the higher reactivity (diesel in this case), being introduced via direct injection through the injection system [128].

RCCI technology often utilises multiple injections to control and optimise the combustion process [129]. The use of RCCI technology in dual fuel engines requires a high degree of premixing which is often achieved by utilisation of port fuel injection systems [128, 130, 131], and also by altering injection timing [131].

By controlling the amount of fuel used, the timing, and by selecting the fuel with the 'required' reactivity, RCCI technology enables combustion performance to be customised to maximise fuel efficiency, and control temperatures, thus controlling/reducing NO<sub>x</sub> emissions, and the equivalence ratio, thus controlling soot formation, hence, reducing the need for any expensive after-treatments [129].

For this study, RCCI technology was not fully utilised as no injection timings were altered, nor was an additional port fuel injection system deployed for the gaseous fuel. Rather, 'dual fuel' combustion was simply used whereby the gaseous was added directly above the air inlet valve. Some level of premixing was achieved, but not a significant amount as required by RCCI technology, hence it could be argued that this technology was only partially employed in this study.

### **2.9.3 Engine speed selection in dual fuel engines for small-scale power generation**

Diesel genset engines which include a fixed speed diesel engine combined with a generator are often used for off-grid power generation, and typically produce an output of 50/60 Hz [132].

To produce a frequency of 50/60 Hz, the relationship of the frequency with the engine speed is shown using Eq. 2.6 [133].

$$f = \frac{P}{120} \times N \quad (2.6)$$

$f$  = the frequency (Hz)

$P$  = number of magnetic poles

$N$  = shaft rotation speed (RPM)

120 = conversion from minutes to seconds, combined with poles to pole pairs

Thus, to generate 50 Hz using a slower speed four pole generator, an engine speed of 1,500 RPM is required. To generate the same frequency using a 2-pole generator, a faster engine speed of 3,000 RPM is required.

Four pole generators are more commonly used for small-scale power generation in rural areas, however, the two-pole generator is utilised for smaller power requirements (<10 kW) [25, 132], and in steady state power plants [97].

Hence, the choice of engine speed for the consumer when purchasing a diesel genset for small-scale power generation is dependent on the user's requirements and economic means. The advantages and disadvantages of the two speed diesel gensets engines are summarised in Table 2.3 [133, 134]. Also, the relationship between engine speed and optimum minimum fuel consumption is illustrated in Fig. 2.9 [133].

**Table 2-3 A comparison of the diesel genset engine speed**

<b>Category:</b>	<b>The engine speed of the diesel genset (RPM)</b>	
	<b>3,000</b>	<b>1,500</b>
<i>Uses</i>	Regular standby/backup power Agricultural applications	Static installation/ daily prime power Standby use
<i>Space</i>	Compact - small home friendly	Larger - less suitable for small homes
<i>Portability</i>	More portable	Less portable due to size
<i>Purchase cost</i>	Cheaper to purchase	More expensive
<i>The typical lifespan if well maintained</i>	2000-3000 hr	10,000+ hours
<i>Fuel consumption</i>	Higher	Lower

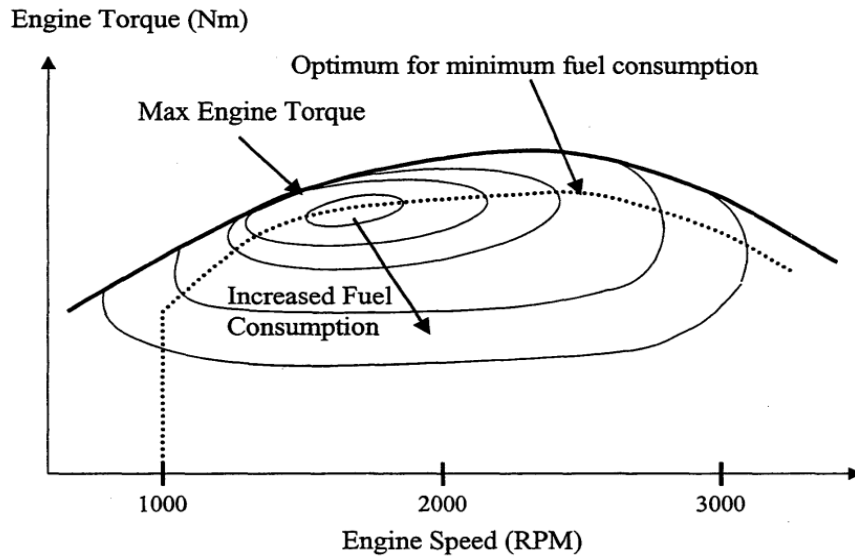


**Figure 2-9 The relationship between the engine speed and the optimum fuel consumption [133]**

Various literature was reviewed to determine the engine speed used for dual fuel combustion using syngas/biogas with diesel.

When utilising biogas with diesel in dual fuel mode, typically the literature reviewed showed that engines of various sizes are used with typical engine speeds ranging from 1,000 to ~1,750 RPM, the mode engine speed was 1,500 RPM [135-140].

When utilising syngas (composed solely of just CO and hydrogen gas), with diesel in dual fuel mode, the typical engine speed used within these literature studies reviewed, varied from 1,300 to 2,450 RPM, and the mode engine speed was 1,300 RPM [128, 130, 131, 141-146].

When utilising syngas (produced directly from gasification), or simulated syngas, (whereby the composition reflects the syngas produced from gasification), with diesel in dual fuel mode, the typical engine speed used within these literature studies reviewed, varied from 910 to 3,000 RPM. The mode speed was 1,500 RPM [70, 85, 92, 95, 97, 102, 111, 117, 128, 147-163].

The studies using 3,000 RPM engines are limited, Rinaldi et al. [97] used a constant 3,000 RPM speed, 4-stroke, 4-cylinder, 2.7 litre, turbocharged diesel test engine equipped with a 160 MPa common rail injection system and a high-pressure EGR circuit. This engine was coupled with an air blown downdraft gasifier syngas using wood chips as its feedstock and the syngas was cooled and cleaned before entering the engine.

Rinaldi et al. [97] investigated the feasibility of operating an automotive turbocharged diesel engine in dual combustion mode using syngas to substitute diesel fuel. These authors reported a diesel substitution rate of 60% at 50Nm and an improved brake thermal efficiency (BTE) at a 27% substitution rate; engine missions were not reported.

The other studies conducted using engine speeds of 3,000 RPM focussed on HRR studies using syngas and diesel. The co-authored study carried out by Olanrewaju et al. [117] used the same engine/lab setup and one of the simulated syngas blends: syngas A (SGA) tested in this work. The focus of this study was specifically on the dual fuel HRR and combustion phasing. The other authors who used a 3,000 RM engine, Rith et al. [163], focussed their technical study around the design and assembly of a combustion measurement instrument for the study of pressure and HRR data in a dual fuel engine using syngas and diesel.

According to Kamimoto and Kobayashi [114], the principal factor which governs diesel combustion is the process of fuel-air mixing. The fuel-air mixing process is in turn affected by the fuel injection system, (which is in turn affected by the engine speed), the gas conditions, which include factors such as air motion, temperature, compression ratio, and any use of EGR, and finally, the shape of the combustion chamber.

Hence, in summary, the engine speed influences many outcomes, one being the rate of injection [114], which in turn affects ID [114], and the resulting combustion phase, which affects resulting emissions greatly [118]. Thus, it is important when considering engine combustion performance and emissions, to compare data for studies that have used similar/identical engine speeds, alongside other factors [118]. Most of the work reviewed above focuses on lower speed diesel engines typically around 1,500 RPM. Furthermore, there are limited works/studies available in the literature that evaluate the engine combustion and emission performance based on a small high-speed dual fuel diesel genset engine of ~3,000 RPM even though these engines are used for small-scale electricity generation. This is important in this study as we are looking at ways to improve affordability and increase energy access using renewable energy sources, in particular biomass waste. Hence, there is potential to convert 3,000 RPM gensets into dual fuel mode with minor, cheap, and affordable modifications.

## 2.10 Syngas-diesel Heat Release Rate (HRR) studies

For comparison, the HRR and combustion phases for pure diesel combustion have been reviewed in subsection 2.7.3.

Garnier et al. [151] studied the effects of dual fuel combustion using simulated syngas (with a composition reflective from gasification) in a 1,500 RPM Litter-Petter diesel engine; their HRR model was derived from Wiebe's Law. These authors reported a decrease in ID with increasing syngas substitution. Additionally, the peak of the heat release rate of the pilot diesel fuel decreased during the premixed combustion stage when the pilot fuel (diesel) was substituted by syngas at values <45–50% [117, 151].

Tuan and Luong [153] also studied the HRR for syngas/diesel using a 3-cylinder, 8.75 kW diesel engine. A simulation model was used for the prediction of combustion characteristics. The syngas used was produced directly via gasification using charcoal as the feedstock. These authors reported that when the indicated mean effective pressure was fixed, the peak rate of heat release increased with increasing syngas substitution relative to the diesel baseline. This was attributed to the impact of the hydrogen content of the syngas having a faster flame speed, thus, resulting in more homogeneous combustion.

The study by Kousheshi et al. [128] numerically investigated the combustion characteristics of syngas/diesel dual fuel combustion using an RCCI, 1,300 RPM speed engine operating with simulated syngas/diesel at constant energy per cycle. Various syngas blends were used, two of these blends had compositions that would have typically been produced from the gasification process, and the third syngas contained just hydrogen and CO. Commercial software (CONVERGE) was used to model dual fuel HRR. These authors reported that as the % of hydrogen content in the syngas increased, so did the resulting peak pressure and peak heat release. This resulted in a shorter ID, a sharper HRR, and the crank angle at which 50% of the injected fuel was burned (MFB50) occurred later. Thus, concluding that to boost combustion efficiency in dual fuel combustion, a hydrogen-rich fuel is preferential.

A further HRR study for syngas/diesel was conducted by Rith et al. [163] using a 5.7 kW, single cylinder, 3,000 RPM, naturally aspirated diesel engine, and simulated syngas whose composition was based on gasification. This study reported that the peak net heat release rate decreased in dual fuel mode and was delayed in CAD timing. The peak net heat release rate became more delayed as the syngas fraction was increased. Also, with increasing syngas fraction, the net heat release rate increased, as seen in other dual fuel studies, [149, 153], which indicated that the syngas combustion was delayed due to the longer ID period and was occurring in the diffusion combustion phase. In addition, the cumulative heat release (CHR) was the lowest for diesel baseline and increased for increasing syngas substitution during dual fuel combustion. The CHR was noted to be higher in the diffusion combustion phase for dual fuel mode relative to diesel, thus indicating a reduction in combustion efficiency in this mode.

In dual fuel mode combustion, the combustion phases occurring after ID as defined by Karim [110] are:

- Stage one occurs as a direct result of the premixed combustion of a small amount of entrained gaseous fuel and ~50% of the pilot diesel fuel [164].
- Stage two in dual fuel combustion is comparable to the premixed combustion phase seen in pure diesel combustion [112]. In dual fuel combustion, the remainder of the pilot diesel fuel burns rapidly alongside the gaseous fuel and is defined as the diffusive combustion phase.
- Stage three in dual fuel combustion is comparable to the diffusion combustion phase seen in diesel combustion [112]. In this stage the remaining premixed fuel-gas-air mixture burns [164].

When utilising a lower flow of gaseous fuel and at lower loads in dual fuel combustion, the three combustion phase peaks produced after the ID period (as discussed above) are distinguishable from one another, and the majority of the energy release is attributed to the pilot and gaseous fuel entrained by the pilot injection as shown in Fig. 2.10 [110, 164]. In comparison, at higher loads, or when using higher gas substitution values, according to Karim [110], the combustion phases merge resulting in the peaks overlapping on the HRR curves, hence producing more stable flame propagation.

In addition, Karim [110] postulated that potentially most of the energy release would occur at stage 3 (diffusion burning phase), this was the case as reported by the HRR study conducted by Rith et al. [163].

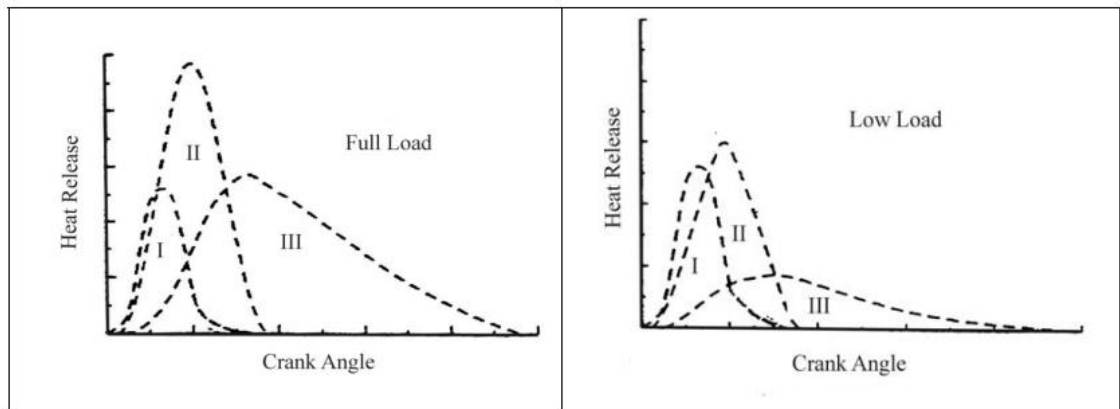


**Figure 2-10 Dual fuel combustion HRR profiles at high and low loads [110]**

A recent combustion study was conducted by Olanrewaju et al. [117] using the same engine/lab setup and one of the simulated syngas blends: syngas A (SGA) tested in this experimental work of this thesis. Due to the relevance of this co-authored study, in terms of syngas composition, and the engine/equipment used, this will be discussed in more detail.

From the combustion study conducted by Olanrewaju et al. [117], various parameters were determined using the HRR profiles, the P-CAD derivative data, and the derived fuel burn profiles which include the Start of Combustion (SoC), the End of Combustion (EoC), the duration of combustion (DoC), and the crank angle at which 50% of the injected fuel was burned (MFB50). For this study, the EoC was defined as the crank angle at which the fuel burn profile began to level off after the MFB50 (and did not include the late combustion phase). The DoC was the difference between the EoC and the SoC. Also, using the pressure, temperature, and HRR profiles generated, the crank angle timings were determined for the peak pressure ( $P_{max}$ ), peaks temperature (PT), and the peak of the heat release rate (PoHRR) for all loads and conditions evaluated.

Due to the differences in the method of calculating the syngas substitution fractions in this thesis and the study by Olanrewaju et al. [117], Table 2.4 shows the equivalent syngas fraction used in this thesis and the co-authored HRR study being discussed.

**Table 2-4 The equivalent % GEFs used in the HRR study**

<b>% Engine/ generator load (kW)</b>	<b>Syngas energy fraction in the HRR study [117]</b>	<b>Equivalent % GEF from this thesis</b>
96 (4kW)	10	10
76 (3kW)	24	22
54 (2kW)	45	38
30 (1kW)	Not evaluated	46

Olanrewaju et al. [117] reported that as the amount of syngas added increased, the HRR profile shifted to the right, away from the diesel baseline reference curve at each engine load tested. This was stated to be a direct effect of the reduction in the CN of the dual fuel mixture which increased with the addition of syngas, thus reducing its tendency to autoignite. This was further corroborated by their ID data which showed that the ID increased with increasing syngas at all loads tested.

This study found that the SoC, MB50,  $P_{max}$ , and the PoHRR (all expressed in CAD timing) all became later with increasing syngas addition relative to the diesel baseline at all the engine loads tested. The findings related to the PoHRR confirmed those as reported by others [163]. Also, the duration of combustion (DoC) increased with increasing syngas addition at generator loads of 1 to 3kW. This was explained as a direct result of the slower and delayed combustion caused by the presence of the CO component in the syngas. At full load (4kW), the DoC did not see this increase, rather a slight decrease was noted with increasing syngas substitution. Hence, it can be said that the DoC in dual fuel combustion for syngas-diesel was load and flow rate dependent.

In terms of the peak in-cylinder temperature and pressure, both these values decreased with increasing syngas fraction relative to the diesel baseline at all load conditions tested. The decrease in peak temperature in this study was said to be related to a reduction in the flame temperature with increasing syngas fraction.

The combustion behaviour in dual fuel mode was compared to pure diesel by comparing HRR profiles by Olanrewaju et al. [117], these are compared in Fig. 2.11 for all testing loads and conditions. Generally, the PoHRR data (expressed as J/CAD) showed a decrease with increasing syngas substitution at all loads evaluated with two exceptions.

A generator loads of 3 and 4kW, the PoHRR values for 10% syngas substitution were higher than the diesel baseline data. One explanation given for this was the premixed combustion of pilot diesel and the premixed combustion of the syngas occurred at the same crank angle, thus merging, and resulting in one single peak, thus indicating an increase and not a decrease as expected.

Also, the HRR curves as presented by Olanrewaju et al. [117] in Fig. 2.11 did show that at low loads and lower gas substitution values, the two peaks representing premixed combustion for dual fuel combustion were more distinguishable than at higher loads, and higher gas flow rates. At higher gas flow rates and loads, these peaks merged as shown in Fig. 2.11, c, and d. The oscillations in the HRR curves in Fig. 2.11 (a to d) are due to the combustion of the remaining pockets of unburnt fuel during the expansion stroke. Also, during the expansion stroke, there is some turbulence being experienced which causes these oscillations. Hence, it is recommended that for future work, data smoothing is conducted on the P-CAD data generated.

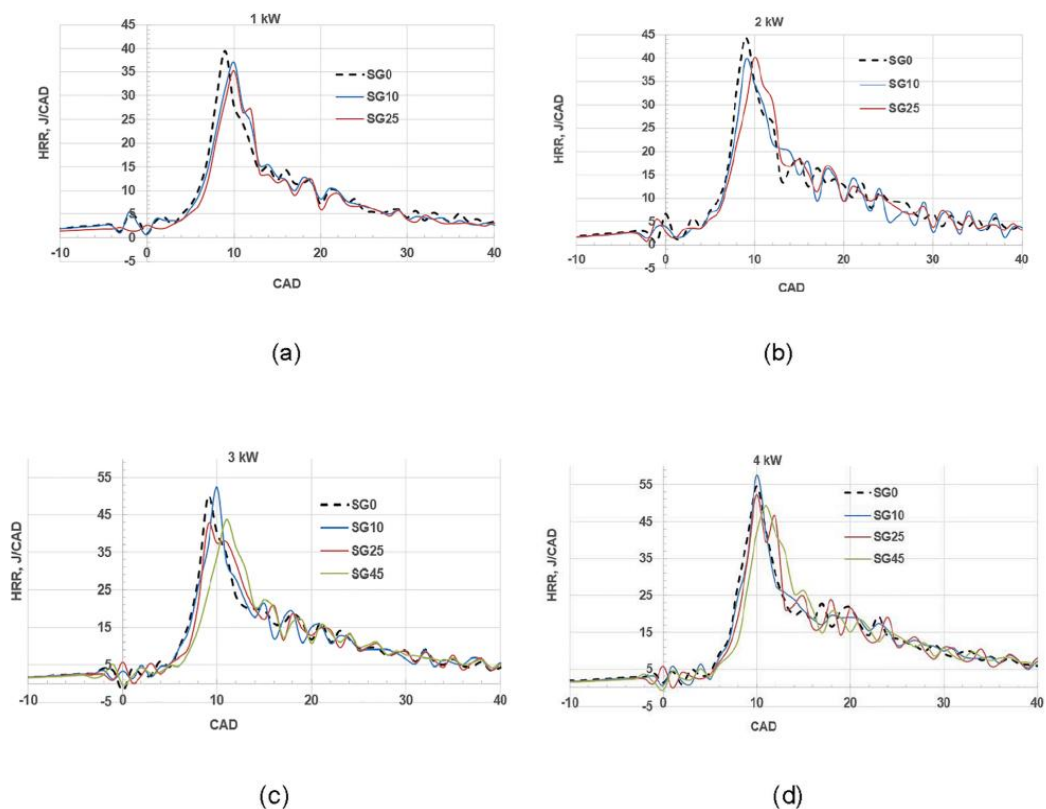


**Figure 2-11 The combustion performance of syngas-diesel at various loads and syngas substitution ratios [117]**

The stages of dual fuel combustion generated are illustrated more clearly using Fig. 2.12 for a generator load of 1kW and syngas energy fraction of 25%. This combustion profile is very similar to that generated by Garnier et al. [151] whereby good agreement was found between experimental data and predicted data.

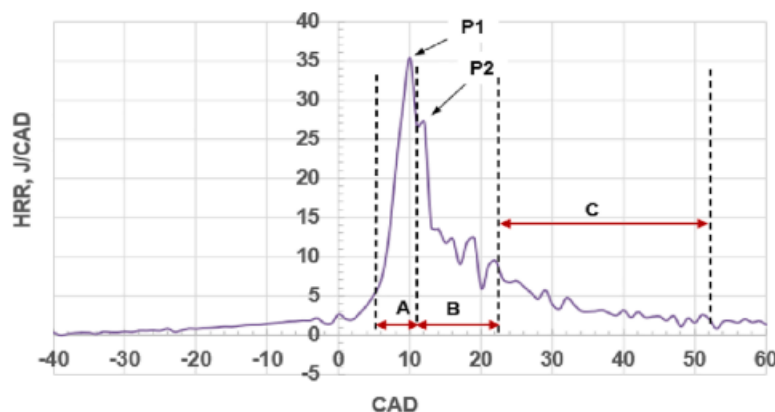


**Figure 2-12 The various combustion phases in dual fuel combustion for syngas-diesel [117]**

Olanrewaju et al. [117] found that the rate of heat release (depicted in Fig.2.12 as 'A') represented the *rapid/premixed combustion phase*, this was the highest and was due to the combustion of the diesel and some of the injected syngas. The corresponding peak for HRR during this combustion phase (represented as P1) was the result of the combustion of pilot injection fuel (diesel).

Stage B in Fig. 2.12 represents the *rapid/premixed combustion phase* for the remaining pilot diesel and the syngas fuel. The second HRR peak (P2) shown in this phase is a direct result of the premixed combustion of syngas. The second peak is lower, due to the lower thermal capacity of the syngas [151].

Stage C represents the mixing-controlled combustion phase, and this appears calmer and more controlled.

In summary, the dual fuel combustion study conducted by Olanrewaju et al. [117] reported that the start of combustion, peak pressure, and peak heat release rate all occurred later in syngas-diesel mode compared to the diesel baseline; these findings agreed with other researchers [153, 163]. This was attributed to a longer injection delay in dual fuel mode [117, 142, 150, 163], which increased with the increasing syngas fraction. Also, in dual fuel mode, a reduction in the peak pressure and peak temperature were noted relative to the diesel baseline.

## **2.11 Syngas-diesel: engine combustion performance and emissions**

### **2.11.1 Ignition delay**

The trends reported in the literature reviewed for the change in ignition delay (ID) in dual fuel mode relative to the diesel baseline are variable. The modelling simulation study conducted by Feng [149] reported that the ID decreased with increasing syngas fraction. Garnier et al. [151] also reported a decrease in ID in dual fuel mode relative to diesel. In contrast, the majority of other researchers reported an increase of ID in dual fuel mode when using syngas-diesel relative to the diesel baseline [117, 142, 150, 163]. Also, the ID was reported to increase with increasing syngas fraction [117, 150, 163].

### **2.11.2 Peak pressure**

The peak pressure ( $P_{\max}$ ) in dual fuel mode combustion using syngas-diesel relative to diesel was reported to decrease in the majority of studies reviewed [117, 150, 163].

However, in some of the literature reviewed, contradictory trends were reported. Feng and Mahmood et al. [149, 165] both reported an increase in the  $P_{\max}$  values. Guo et al. [150] reported that with increasing syngas fraction addition, the  $P_{\max}$  increased. Rinaldi et al. [97] reported that the in-cylinder pressure traces for pure diesel and syngas-diesel were similar.

### **2.11.3 Temperature**

It was reported that dual fuel combustion results in an increase in the exhaust gas temperature (relative to the diesel baseline), and this increased with increasing syngas fraction [102, 111, 142, 157]. The increase in the exhaust gas temperature (EGT) is said to be a reflection of later burning [157].

The peak in-cylinder temperature (PT) in dual fuel mode combustion using syngas-diesel relative to diesel was reported to increase in one study [165], which also reported a corresponding increase in  $P_{\max}$ . In another study, this was reported to be similar to the diesel baseline data [97], and in the remaining studies reviewed, this was reported to decrease [117, 150, 153].

#### 2.11.4 Brake Thermal Efficiency (BTE)

The BTE is a measure of the engine's performance which calculates how efficiently the energy from the fuel is converted into mechanical energy/work. Most dual fuel studies reviewed reported a decrease in BTE in dual fuel mode when using syngas-diesel relative to diesel.

This includes studies where just CO and H<sub>2</sub> have been used to represent the syngas [142, 145], also, studies that have used simulated syngas (with a composition that mimics gasifier syngas) [149, 150], and finally, studies where real syngas (produced from a gasification unit coupled with the diesel engine) has been used [70, 92, 102, 111, 147, 152, 158, 160, 162]. The BTE is reported to decrease with increasing syngas fraction [102, 149, 150].

The reason for a lower BTE value in dual fuel mode versus pure diesel is due to the poorer combustion characteristics (especially at lower loads) which result in incomplete combustion, therefore, causing unburnt syngas to pass out into the exhaust [142, 145].

Contradictory results have been reported which state that BTE increases in dual fuel mode relative to the diesel baseline, however, these are fewer in number [97, 159, 165]. One dual fuel study that reported an increase in BTE was conducted by Malik and Mohapatra [159] who investigated the emissions and performance of an engine coupled to a gasification unit using cotton stalks as feedstock. The increase in the BTE was attributed to the high methane content (~49%) of the syngas produced from the gasifier. The other study to report an increase in BTE was conducted by Rinaldi et al. [97] who stated that the increase in BTE was due to faster combustion of the syngas-diesel fuel relative to diesel.

Both these studies used engines coupled with gasification units. If the composition of the syngas gas produced was non-uniform during the testing experimental procedure, then this could lead to inaccurate BTE calculations whereby it appears that the overall BTE value increases and not decreases relative to diesel. The modelling study conducted by Mahmood et al. [165] also reported an increase in BTE in dual fuel mode relative to the diesel baseline. These authors studied the combustion characteristics of syngas-diesel dual fuelling whereby numerical simulations were conducted on a single-cylinder Ricardo-Hydra 2,000 RPM diesel engine. Simulated syngas (containing 50:50 H<sub>2</sub> & CO) was evaluated at various ratios ranging between 10 to 50% at a lambda value of 1.6.

Brake specific energy consumption (BSEC) is inversely proportional to BTE. If it is to be assumed that BTE is reduced in dual fuel mode, then the resulting BSEC (expressed as MJ/kWh) is expected to increase in DF mode, which was as reported by the majority of the literature reviewed [70, 92, 102, 152, 153].

### **2.11.5 Carbon monoxide (CO)**

All the dual fuel studies reviewed for this thesis, unanimously reported that the CO emissions were greater in DF mode relative to diesel, irrespective of the syngas composition type used [70, 92, 102, 111, 142, 147, 149, 150, 152, 153, 157-159, 162, 165], and that the dual fuel CO emissions increased with increasing syngas addition [102, 145, 149, 150, 153, 159, 162].

An interesting trend was noted by Guo et al. [150], whereby in dual fuel mode, at low loads the CO levels increased, but at medium load conditions, the initial introduction of syngas lead the CO emissions to increase, but after this, further addition of syngas did not affect the CO emissions. This was thought to be a direct function of the  $\Phi$ .

The increase in CO emissions in DF mode is reflective of more incomplete combustion of the premixed mixture [147, 159], which is reflected by the decrease in BTE. When syngas is added, this displaces the air, thus reducing the oxygen availability in the premixed mixture, thus favouring incomplete combustion. CO emissions are said to generally increase with increasing syngas addition, thus using higher syngas flow rates reduces oxygen availability further, thus further reducing cylinder temperature and peak pressure, thereby resulting in lower combustion efficiencies [166].

Furthermore, syngas has a lower adiabatic flame temperature coupled with a lower mean effective pressure which can lead to higher CO emissions in dual fuel mode [147].

### **2.11.6 Hydrocarbon / Unburnt hydrocarbon (HC/UHC)**

Of the literature reviewed, all these studies reported an increase in the hydrocarbon or unburnt hydrocarbon (HC/ UHC) emissions in dual fuel mode (for all syngas composition types used) relative to the diesel baseline [142, 147, 158, 162]. Generally, the UHC emissions increased with increasing syngas addition [162].

Similarly, to CO emissions, UHCs are a direct consequence of incomplete combustion caused by a lack of mixing.

Typically, a higher amount of HCs are present at lower loads. The HC emissions are also sensitive to the pilot diesel quantity, especially at low loads, a lower amount of pilot diesel is used which results in poorer atomisation, a lower flame temperature, poorer mixing, and poorer ignition of the gas-air mixture thus, leading to poorer combustion and increased HC emissions [147, 167, 168].

Uma et al. [92] reported that at optimum engine load (of 80%), the HC emissions were marginally lower in dual fuel mode relative to the diesel baseline. At low loads (30-40 kW), DF combustion produced higher HC emissions (in g/kWh). Hence, the trends reported in HC emissions in this one study, relative to the diesel baseline were engine load dependent.

### **2.11.7 Nitrogen oxides (NO<sub>x</sub>)**

The NO<sub>x</sub> emissions are dependent on temperature and oxygen availability. The NO<sub>x</sub> emissions reported in DF mode for syngas-diesel combustion relative to the diesel baseline in the literature reviewed all differed.

Some studies reported that NO<sub>x</sub> emissions increased in DF mode relative to the diesel baseline [145, 146, 151, 153]. One study reported that the NO emission increased in DF mode relative to the diesel baseline, thus, one would expect the resulting NO<sub>x</sub> emissions to be greater in DF mode [165].

Other studies reviewed reported that the NO<sub>x</sub> emissions were significantly reduced in DF mode combustion relative to the diesel baseline [70, 92, 111, 142, 147, 149, 150, 158, 159, 162] and NO<sub>x</sub> emissions increased with increasing syngas addition [147, 149-151, 159, 162].

Bika et al. [145] reported that the NO<sub>x</sub> emissions in DF mode were dependent on the operating parameters. At 2bar IMEP<sub>n</sub>, the NO<sub>x</sub> levels were unaffected and remained constant for all test conditions. At 4bar IMEP<sub>n</sub>, the NO<sub>x</sub> emissions increased with increasing syngas substitution and were greater than the diesel baseline. These NO<sub>x</sub> results were also contradictory to those who reported a decrease in dual fuel mode. The reason for this is unclear, it is difficult to speculate why, as the engine types, design, geometry, compression ratio, et cetera, all differ from study to study as does the syngas composition used. Additionally, these authors reported that the NO<sub>2</sub>/NO ratio doubled with syngas substitution and was higher than the diesel baseline for all the test conditions evaluated. This was attributed to an increase in the amount of HO<sub>2</sub> radicals which react with the NO to form NO<sub>2</sub>.

Tuan and Luan [153] also reported an increase in NO<sub>x</sub> emissions in DF mode, and these emissions increased with increasing syngas addition. The NO<sub>x</sub> increase in DF mode is contradictory to other findings in similar studies as discussed earlier. In this study, these emissions were modelled using a reaction kinetic model. The increase in NO<sub>x</sub> emissions was explained by the increase seen in the in-cylinder temperature with increasing syngas fraction. The findings in this study were contradictory as the in-cylinder temperature graph which illustrated the change in temperature with increasing syngas fraction showed a decrease.

Hernandez et al. [161] demonstrated that the use of EGR in dual fuel mode combustion (syngas/diesel) could be used to further reduce NO<sub>x</sub> emissions, hence, suggesting this is a viable method in improving the NO<sub>x</sub>-PM trade-off, especially in dual fuel combustion.

Hassan et al. [111] studied the effects on engine emissions in dual fuel operation using two modes: *supercharged syngas addition* as well as *premixed syngas addition*. Real syngas was used in a four-stroke, single-cylinder, direct injection diesel engine with a speed of 1,600 RPM. The syngas was supercharged by this method: the syngas directly from the gasification unit was compressed and mixed with compressed air at the air intake before addition. The pressure of the supercharged syngas was maintained at 200 kPa. It was reported that in the supercharged syngas addition mode (relative to premixed syngas addition), the supercharged mode resulted in higher BTE, lower specific energy consumption, and lower CO emissions, but higher NO<sub>x</sub> emissions alongside considerably higher EGTs. Hence, it was concluded that supercharging for syngas diesel dual fuel combustion is effective in reducing CO emissions and increasing efficiency, with the penalty being the increase in NO<sub>x</sub>.

In summary, the reduction in NO<sub>x</sub> emissions during dual fuel mode combustion is brought about by the reduction in the in-cylinder mixture caused by the intake of syngas [117, 153]. This results in a reduction in the in-cylinder peak pressures [117, 142, 163], and the reduction in peak pressure ( $P_{max}$ ) was due to the longer IDs [117, 142, 150] which lead to a shorter duration of combustion in dual fuel mode [142, 149]. Overall, from the literature reviewed, the trend in NO<sub>x</sub> emissions in dual fuel mode when using syngas-diesel (relative to the diesel baseline) remains unclear; contradictory results have been reported.

### **2.11.8 Carbon dioxide (CO<sub>2</sub>)**

Typically, the CO<sub>2</sub> emissions were said to increase during dual fuel combustion relative to the diesel baseline [102, 151, 152, 165], and with increasing syngas addition [151]. This was due to the CO<sub>2</sub> content of the syngas passing through into the exhaust, as well as additional CO<sub>2</sub> being formed from the complete oxidation of the methane and carbon monoxide components of the syngas.

### **2.11.9 Particulate Matter (PM)**

The techniques used for measuring PM in these studies have varied. Ramadhas et al. [102] reported a reduction in the smoke density in dual fuel mode when using real syngas directly from gasification relative to the diesel baseline, the smoke density increased with increasing syngas fraction. This was measured using a NASSALCO branded smoke meter. A further study reported that syngas-diesel dual fuelling reduces the particulate emissions when conveyed as a filter smoke number; dual fuel combustion leads to a 90% decrease in the in-cylinder peak soot production [130]. Chuahy et al. [146] conducted an experimental study (using syngas containing H<sub>2</sub> and CO) and reported reductions in transient soot emissions in DF mode; the soot emissions were expressed as a % opacity and were measured using an AVL 439 opacimeter.

Other studies have looked at the PM mass (expressed as specific emissions in units of g/kWh), and have reported a reduction in PM mass in dual fuel mode relative to the diesel baseline [92, 149, 153, 161, 162, 165]. The reductions in soot emissions, (expressed in g/kWh) decreased with increasing syngas addition [149, 150, 153, 162], and were all lower than the diesel baseline. This was thought to be due to the fact that when using higher rates of syngas, less diesel is being burnt, hence reducing the likelihood of PM formation. This combined with the fact that at higher syngas flow rates, there is a higher rate of mixing, thus more homogenous combustion is achieved, leading to overall PM reductions [153].

Hernandez et al. [161] conducted a dual fuel study in 2014 using an AVL 501 single-cylinder, 1,500 RPM, DI engine, equipped with EGR and a common rail injection system. The syngas used had a composition resembling that produced from steam gasification of de-alcoholised marc of grapes.

The particle number and size distribution were determined using a Scanning Mobility Particle Size (SMPS) which measured the particle diameter size up to 100 nm with, and without, the use of EGR. This study concluded that in dual fuel mode, the PM mass and concentration were lower than the diesel baseline data, alongside a reduction in the particle mean diameter. Both the PM mass and concentration decreased with increasing syngas fraction. This reduction was thought to be due to a reduction in the use of diesel fuel (the source of particulates). In addition, a higher concentration of OH radicals is present which are derived from the hydrogen content of the syngas. The OH radicals are thought to promote soot oxidation. Also, the volatile organic fraction of the PM was reported to increase whilst the PM mass decreased in dual fuel mode. This was said to be possibly due to the extra adsorbed unburnt CO and CH<sub>4</sub> on the porous soot. This is the only study reviewed that has looked at the particle number and particle size distribution (PSD) in syngas-diesel combustion using syngas which contains more than just CO and hydrogen.

A combined experimental and computational study by Chuahy et al. [131] looked at the particle size distribution (PSD) in syngas-diesel using reformat, i.e. syngas containing hydrogen and CO. The particle measurements were analysed using an SMPS analyser. This study showed that in dual fuel operation (using energy fractions as low as 25%), the PSD curves changed when compared to pure diesel. In dual fuel mode, the particle concentration related to the accumulation mode decreased while the nucleation mode particle concentration increased. These changes in the PSD were attributed to reductions in fuel stratification and not due to changes in the soot surface chemistry. It was also stated that areas with a high  $\phi$  lead to the formation of larger soot particles. In summary, lower  $\phi$  and temperatures were the two factors identified as the cause of lower particulate formation in dual fuel mode.

Overall, the literature reviewed indicates that the majority of studies have reported a reduction in PM mass, smoke density, and concentration in dual fuel mode using syngas-diesel relative to the diesel baseline.

There are limited studies that have looked at the change in the PM mass and PSD when using gasifier-based syngas (real or simulated). Even so, the findings from the study by Hernandez et al. [161] cannot be directly compared to the experimental work from this thesis due to the differences in the engine speed and engine operational conditions.

### 2.11.10 Diesel substitution values for syngas-diesel combustion

The % mass of diesel displaced as a direct result of syngas-diesel dual fuel combustion varied in the literature reviewed from 50 to 86% as shown in Table 2.5. This varies as the thermal efficiency will depend on the engine design, size, performance, injection system et cetera, as well as the composition of the syngas used.

**Table 2-5 Summary of the diesel displacement rates in the dual fuel studies reviewed using syngas-diesel**

<b>% Diesel displacement rate</b>	<b>Reference</b>
Maximum 59%	[142]
60	[153]
60	[97]
67-86	[92]
50	[159]
~75	[70]
62-64	[160]
57	[140]
50	[102]
80	[157]

Rinaldi et al. [97] reported that the maximum diesel substitution rate was limited by the production rate of the syngas from the connected gasifier, therefore higher powers were not reached. However, technically, the limitations caused by the production rate of the syngas from the gasifier can be overcome by storing and compressing syngas for the application of small-scale power generation [128].

### 2.11.11 Syngas-diesel combustion: summary of the trends

Various studies exist in the literature for dual fuel syngas/diesel combustion, and upon review, the following key points were found:

The composition of the syngas used in these studies is variable. The composition of the syngas produced from gasification is also variable (see Table 2.2). Of the literature reviewed, only one study used gasifier simulated syngas that contained a trace amount of oxygen [153].

The studies discussed above, and their findings in terms of the effect of dual fuel mode, (relative to the diesel baseline) are summarised for various engine combustion performance parameters and emissions in Table 2.6.

The composition of the syngas used per study was highlighted to show the variability in the literature reviewed.

The syngas composition in each study has been identified as either:

- '*Simulated Syngas*' - contains solely CO and H<sub>2</sub>; denoted as 'SS'.
- '*Real Syngas*' - derived from biomass gasification, denoted as 'RS.'
- '*Gasification Simulated Syngas*'- simulated syngas with a composition of gasifier syngas, denoted as 'GSS.'

To summarise, the trends in syngas-diesel dual fuel combustion from the literature reviewed (as shown in Table 2.6) show the following:

- The majority of authors have reported a decrease in BTE and an increase in BSEC in dual fuel mode relative to the diesel baseline.
- In terms of ID, combustion duration, and peak pressure, contradictory results have been reported in the literature reviewed for dual fuel syngas-diesel combustion relative to the diesel baseline. The change in the combustion duration appears to be load dependent [117]. Also, from the studies reviewed, when defining the EoC, it is unclear whether the late combustion phase has been included or not. Hence, different methodologies used will affect the results reported.
- There is good consensus in the literature that states that the exhaust gas temperatures increase in dual fuel syngas-diesel combustion relative to the diesel baseline, with increasing syngas fraction. This is indicative of late burning and reduced combustion efficiencies [117, 157].
- Most researchers have reported that the peak in-cylinder temperatures decrease in dual fuel syngas-diesel combustion relative to diesel.
- There is good agreement in the reporting of the CO, CO<sub>2</sub>, and UHC emissions in dual fuel syngas-diesel combustion, whereby all the authors reviewed reported an increase in these emissions.

- The NO<sub>x</sub> emissions reported are unclear; it cannot be definitively said if these emissions increase or decrease during dual fuel syngas-diesel combustion relative to diesel. The studies reviewed that used syngas containing just CO and hydrogen (i.e., free of diluents) all reported an increase in NO<sub>x</sub> emissions relative to diesel, but equally so did other studies where simulated syngas was used which did contain the diluents. Therefore, there is no apparent trend regarding the change in the NO<sub>x</sub> emissions being reported in dual fuel mode operation (relative to the diesel baseline) when considering the syngas composition.
- The use of EGR in dual fuel syngas-diesel combustion appears to further reduce NO<sub>x</sub> emissions in dual fuel mode [161]. Supercharging the syngas addition leads to increases in NO<sub>x</sub> emission in dual fuel mode when compared to premixed addition, reduces CO emissions, and improves the BTE data [111].
- The PM emissions decrease in dual fuel mode; the methods of determination used to conclude this vary from study to study.

A summary of the trends arising from syngas-diesel dual fuel combustion is shown in Table 2.6. This Table was generated from the literature reviewed in this subsection which is summarised in Tables 2.7 and 2.8.

**Table 2-6 Summary of the trends reported for syngas/diesel dual fuel combustion relative to the diesel baseline**

<b>Parameter</b>	<b>Increase in DF mode</b>	<b>Decrease in DF mode</b>
<b>BTE</b>	RS [97, 159] SS [165]	SS [142, 145] RS [70, 92, 102, 111, 147, 152, 158, 160, 162] GSS [149, 150, 153]
<b>BSEC</b>	GSS [153] RS [70, 92, 102, 111, 152]	
<b>ID</b>	GSS [117, 150] SS [142], RS [163]	GSS [149, 151]
<b>Combustion duration</b>	GSS [117]	GSS [117]-at full load only. GSS [142, 149]
<b>Peak Pressure (P<sub>max</sub>)</b>	GSS [149, 150] SS [165]	SS [142] GSS [117], RS [163]
<b>Exhaust Gas Temperature (EGT)</b>	SS [142] RS [102, 111, 157]	
<b>Peak in-cylinder temperature</b>	SS [165]	GSS [117, 150, 153]
<b>HC/UHC</b>	SS [142] RS [147, 162] GSS [158]	
<b>CO</b>	SS [142, 165] RS [70, 92, 102, 111, 147, 152, 157-159, 162] GSS [149, 150, 153]	
<b>CO<sub>2</sub></b>	SS [165], RS [102, 152] GSS [151]	
<b>NO<sub>x</sub></b>	GSS [153] [151] SS [145, 146]	RS [70, 92, 111, 147, 159, 162], SS [142] GSS [149, 150, 158]
<b>NO</b>	SS [165]	
<b>NO<sub>2</sub>/NO<sub>x</sub> Ratio</b>	SS [145]	
<b>Particulate Matter (PM)</b>		RS -smoke density [102], GSS & RS -PM mass (g/kWh): [149, 150, 153, 161, 162] RS -PM concentration [161] SS – Reduction in PSD [131] SS- Soot emissions (% opacity) [146]

SS = Simulated Syngas, RS = Real Syngas, GSS = Gasifier Simulated Syngas

### **2.11.12 The impact of changing the H<sub>2</sub> content of the syngas on dual fuel engine combustion and emissions**

This subsection reviewed the literature concerning the impact of changing the hydrogen content of the syngas in dual fuel combustion for syngas-diesel.

Sahoo et al. [144] researched the effects of varying the H<sub>2</sub>/CO content on dual fuel combustion. Three fuel blends were examined: 100% hydrogen, syngas blends containing 75:25 H<sub>2</sub>/CO, and 50:50 H<sub>2</sub>/CO (volume ratio). Higher BTE values were reported with an increase in the H<sub>2</sub> content of the syngas at high loads. The BTE values decreased for all dual fuel modes relative to the diesel baseline. The highest in-cylinder pressures and combustion temperatures were reported for 100% H<sub>2</sub> resulting in higher NO<sub>x</sub> emissions and EGTs in comparison to the other gaseous fuels evaluated. The CO emissions increased when using syngas with a higher CO content in dual fuel mode. It was concluded that higher hydrogen content results in lower CO and HC emissions due to the higher flame speed. Also, a reduction in volumetric efficiency was noted in DF mode, this was said to be due to the displacement of sucked air by the syngas.

These same authors, Sahoo et al. [143] investigated syngas-diesel dual fuel combustion at various loads from the second law point of view using the same engine/equipment, whilst varying the H<sub>2</sub>/CO ratio of the simulated syngas. This study reported that increasing the hydrogen content of the syngas enhanced the cumulative work availability at higher loads in dual fuel mode, hence improved combustion was observed.

Bika et al. [145] also investigated the effects of differing amounts of hydrogen and CO content in simulated syngas in DF mode. These authors also suggested that the efficiency was higher when using higher hydrogen content syngas, this was supported by the reduction seen in the CO emissions. At 2 bar IMEP<sub>n</sub>, the NO<sub>x</sub> levels were unaffected by syngas composition and remained constant for all test conditions. At 4 bar IMEP<sub>n</sub>, at 40% gas substitution of diesel, increasing the hydrogen content of the syngas led to the NO<sub>x</sub> levels decreasing but remained higher than the diesel baseline.

Kousheshi et al. [128] investigated dual fuelling using a 2.44 L, single-cylinder RCCI engine via experimental numerical analysis to determine the effects of syngas on the engine exhaust emissions and performance.

This study evaluated three different syngas types whose composition was based on that typically produced by gasification containing varying amounts of H<sub>2</sub>, CO, CH<sub>4</sub>, CO<sub>2</sub>, N<sub>2</sub>, and C<sub>2</sub>H<sub>4</sub>/C<sub>2</sub>H<sub>6</sub>. These gases varied from each other in terms of the H<sub>2</sub>/CO ratio (% Vol). These gases were also compared to simulated syngas which contained 50:50 H<sub>2</sub> to CO. Kousheshi et al. [128] reported that using simulated gasifier syngas led to higher soot, CO, and unburnt hydrocarbons (UHCs) in comparison to the simulated syngas which contained just CO and hydrogen. Also, the peak pressure and maximum local temperatures increased significantly with an increasing ratio of H<sub>2</sub>. With the increase in hydrogen, a shorter ID, a sharper HRR, and reduced soot, CO, and UHC emissions were reported, alongside an increase in NO<sub>x</sub> emissions.

Guo et al. [150] also looked at the effect of hydrogen using simulated syngas blends. Syngas 1 had a composition representative of that typically produced from a downdraft air blown gasifier. Syngas 5 represented syngas 1 but with a different H<sub>2</sub> to CO ratio. This study concluded that increasing the hydrogen content lead to a reduction in the soot levels, the NO<sub>x</sub> levels were unaffected and the BTE increased.

The study by Guo et al. [150] and by Kousheshi et al. [128] are some of the few studies that looked at the impact of the hydrogen content of the syngas using gasifier based syngas (real or simulated). Both were conducted using slower speed engines ≤1,500 RPM.

Azimov et al. [148] also researched the impact of the H<sub>2</sub> content in dual fuel combustion using a four-stroke, single-cylinder, water cooled, 1,000 RPM speed engine equipped with a common rail injection system used. The engine was supercharged and utilised PREMIER combustion: PREmixed Mixture Ignition in the End-gas Region. This study reported that increasing the hydrogen content led to an increase in the combustion temperatures, P<sub>max</sub>, and efficiency, leading to higher NO<sub>x</sub> and a higher heat release rate. As a consequence of increasing the hydrogen content, the CO and HC emissions were reduced, as were the ID and the resulting main combustion duration.

Roy et al. [85] investigated the effects of changing the hydrogen content in the gasifier simulated syngas (based on an updraft gasifier) during syngas diesel dual fuel combustion. A four-stroke, single-cylinder, water cooled, DI, supercharged 1,000 RPM speed engine was used. The experimental work was conducted using constant injection pressure and injection quantities, and by utilising multiple injection timings.

It was concluded that as a result of increasing the hydrogen content, the flame speed, NO<sub>x</sub> emissions, BTE, and combustion temperatures all increased. As a direct consequence, the HC and CO emissions decreased, as did the main combustion duration.

To summarise, the majority of authors studying the impact of hydrogen on syngas/diesel dual fuel combustion concurred that as a result of increasing the hydrogen content, the ignition delay decreased [128, 144, 148], which resulted in reduced emissions. Also, the combustion duration was reduced [85, 148], therefore the diffusion combustion stage was also reduced, thus resulting in less mass of soot being produced [128, 150], which was supported by a reduction in the HC emissions [85, 128, 144, 148].

Furthermore, the CO emissions were reduced [85, 128, 144, 148], and this is due to the higher flame speed of hydrogen, as the laminar flame speed of hydrogen/CO/air mixture increases with increasing hydrogen fraction [85, 144], thus, leading to more complete combustion and better overall efficiencies as reflected by the increase in the BTE data [85, 144, 145, 148, 150]. The HRR increased with hydrogen fraction due to the role the hydrogen plays in the dominant pathway of the oxidation of the CO; this is accountable for a large fraction of the associated heat release [148, 169].

The  $P_{max}$  increased [128, 144], as did the cylinder temperatures [85, 144, 148], and the exhaust gas temperatures [144, 148]. Thus, it is expected that the NO<sub>x</sub> emissions would rise; this was the case as reported by the majority of the studies reviewed [85, 128, 144, 148].

Guo et al. [150] reported that the NO<sub>x</sub> emissions were unaffected by the hydrogen content of the syngas, as did Bika et al. [145] at 2 bar IMEP, but at 4 bar IMEP, at 40% gas substitution of diesel, increasing the hydrogen content of the syngas led to the NO<sub>x</sub> levels decreasing but remained higher than the diesel baseline. It is exceedingly difficult to infer the reasons why the NO<sub>x</sub> trend with increasing hydrogen content in the syngas was reported differently for these two studies. Different sizes, speeds, and designs of engines were used in each case, alongside syngas of different compositions. The CO<sub>2</sub> and nitrogen components of the syngas decrease the oxygen availability in the premixed air/syngas fuel mixture, therefore, this will affect the resulting combustion [128].

Guo et al. [150] used simulated syngas which had a composition reflective of that produced by gasification which included CO<sub>2</sub> and nitrogen. Bika et al. [145] used simulated syngas containing just CO<sub>2</sub> and H<sub>2</sub>, hence this highlights the problems when attempting to cross compare data across studies.

Overall, these studies report that the hydrogen content of the syngas is particularly important in controlling the resulting CO and HC emissions [85, 144, 145, 148, 150]. The engine types summarised in Table 2.8 all vary in terms of operational performance, design, and speed (910 to 1,825 RPM) as does the composition of the syngas used.

The summary in Table 2.8 shows that the only negative impact of increasing the hydrogen content in the syngas is the increase in NO<sub>x</sub> emissions in all these studies. However, this comes with the benefit of an increase in the BTE and reduced CO and HC emissions.

**Table 2-7 Literature review summary for syngas dual fuel combustion**

Year	Engine speed (RPM)	Syngas type	Reference	Engine particulars	Changes in the emissions & in the engine performance characteristics in dual fuel mode versus the diesel baseline
1989	1,500	RS	Parikh et al. [157]	DI single cylinder, water cooled, 3.7 kW	CO increased, higher EGT in DF
2004	1,500	RS	Uma et al. [92]	DI, 6 cylinders, 4-stroke, 77.2kW	CO, SEC increase, BTE, NO <sub>x</sub> and SO <sub>2</sub> decrease, PM remained unchanged, and HC levels changes are load dependent.
2005	1,500	GSS	Garnier et al. [151]	2.8kW, Lister-Petter engine, single-cylinder, 4-stroke.	NO <sub>x</sub> and CO <sub>2</sub> increased, ID decreased,
2006	1,500	RS	Ramadhas et al. [102]	4-stroke, DI, naturally aspirated, single-cylinder 5.5kW	CO, SEC, CO <sub>2</sub> and EGT are all higher in DF, BTE lower, decrease in smoke density
2008	1,500	RS	Ramadhas et al. [152]	4-stroke, naturally aspirated single-cylinder, 5.5 kW, DI	SEC, CO, CO <sub>2</sub> increased, BTE decreased
2011	1,800	RS	Silva et al. [156]	BRANCO, DI, 5.5kW	Diesel displacement rate of 57% at 3.5kW load
2011	1,800	RS	Dasaapa and Sridhar [70]	Naturally aspirated, six-cylinder, DI, 68.4kW	CO & SEC increase, NO <sub>x</sub> & BTE decrease, Diesel displacement rate of 64%
2011	1,600	RS	Hassan et al. [111]	Supercharged and premixed Dual Fuel evaluated v pure diesel, Yanmar, single-cylinder, DI, 4.9kW	BTE & NO <sub>x</sub> lower in DF. EGT, SEC, & CO higher in DF. BTE, NO <sub>x</sub> , EGT, & diesel displacement higher in supercharged v premixed. Diesel displacement rate: 48.3 to 68.2% in DF mode. CO, and SEC higher in Premixed v Supercharged.
2012	1,600	RS	Das et al. [160]	Four-stroke, single-cylinder, 5.25 kW	BTE decreased, ~63% diesel displacement rate
2013	1,500	RS	Shrivastava et al. [158]	Direct injection, single-cylinder, 4-stroke air cooled, 4.4kW	BTE and NO <sub>x</sub> decreased, CO and HC increased
2014	1,500	GSS	Tuan and Luong [153]	3-cylinder diesel engine, 8.75 kW	In-cylinder temperature & soot decreased, SEC, NO <sub>x</sub> , and CO increased, Rate of HRR in DF increased at fixed indicated mean effective pressure.
2014	1,500	RS	Hernandez et al. [161]	AVL 501 single-cylinder DI engine with EGR and common rail injection system	PM mass & concentration decreased, PM volatile fraction increased, Use of EGR reduces NO <sub>x</sub>
2015	1,500	RS	Dhole et al. [147]	62.5kW, turbocharged, 4-stroke, DI, 4-cylinder water-cooled engine, 13-80% loads tested with 0-50 gas substitution	CO and UHC increased, NO <sub>x</sub> and BTE decreased,
2015	1,500	RS	Hernandez et al. [162]	AVL 501 supercharged, common-rail injection, single-cylinder diesel engine with & w/o EGR	BTE, NO <sub>x</sub> , and PM mass decreased, CO, methane and HC increased
2016	910	GSS	Guo et al. [150]	74.6kW, single cylinder, simulated turbocharged, Port injection system for syngas.	ID, P <sub>max</sub> , and CO increased, BTE, Mass of soot, cylinder temperatures and NO <sub>x</sub> decreased
2016	1,500	RS*	Malik and Mohapatra [159]	Single-cylinder, 4-stroke, water cooled diesel engine, 3.5kW	SFC favourable, CO, BTE increased, NO <sub>x</sub> reduced (* RS~49% methane content)
2017	1,500	GSS	Feng [149]	18kW engine with a common rail injection system	ID & combustion duration, BTE, PM mass and NO <sub>x</sub> all reduced, Laminar flame speed, P <sub>max</sub> , and CO increased

2017	3,000	RS	<b>Rinaldini et al. [97]</b>	Turbocharged 2.8L diesel engine, 4-cylinder with a common rail injection system.	In-cylinder pressure does not change much, Diesel displacement rate of 60%, BTE increased at 27% gas substitution Higher rate of heat release rate for DF mode.
2020	3,000	RS	<b>Rith et al. [163]</b>	HRR study, 5.7kW, single-cylinder,4-stroke, single-cylinder, air cooled DI naturally aspirated engine	$P_{max}$ decreased and occurred later in DF mode. Net HRR lower in premixed stage, higher in diffusion combustion. Cumulative HR higher for DF during diffusion mode = less efficient combustion. Increased ID in DF mode.
2022	3,000	GSS	<b>Olanrewaju et al. [117]</b>	HRR study, 5.7kW, single-cylinder,4-stroke, single-cylinder, air cooled DI engine	HRR study. ID increased, PHRR was delayed, Flame, peak & in cylinder temp &, $P_{max}$ decreased, Combustion duration increased
2010	1,500	Varying H <sub>2</sub> /CO	<b>Sahoo et al. [142]</b>	Single cylinder, 4-stroke water cooled DI 5.2kW	BTE, NO <sub>x</sub> , $P_{max}$ , and combustion duration decreased, EGT, CO, HC, and ID increased
2011	1,825	Varying H <sub>2</sub> /CO	<b>Bika et al. [145]</b>	CR of 21.2:1, 2 bar and 4 bar net IMEP	BTE decreased in DF, NO <sub>x</sub> unaffected at 2 bar, Increase at 4 bar in DF, NO <sub>2</sub> /NO ratio increased in Dual fuel
2011	1,500	Varying H <sub>2</sub> /CO	<b>Sahoo et al. [143]</b>	Single cylinder, 4-stroke water cooled DI 5.2kW engine, 2nd law investigation	Hydrogen quantity of syngas increases the cumulative work availability and reduces the destroyed availability.
2017	1,300	50% CO/H <sub>2</sub>	<b>Chuahy and KokJohn[130]</b>	2.44L 9 bar IMEP	90% reduction in cylinder peak soot production
2018	2,450	Varying H <sub>2</sub> /CO	<b>Chuahy et al. [146]</b>	Multi-cylinder, turbocharged, light-duty engine + port fuel injection system (RCCI) as multi cylinders	Reduced soot emissions (AVL 439 Opacimeter) in dual fuel mode without NO <sub>x</sub> increasing noticeably for transient load changes
2021	2,000	H <sub>2</sub> /CO	<b>Mahmood et al. [165]</b>	Ricardo-Hydra, single-cylinder diesel, diesel-syngas fuel mixture with lambda of 1.6	$P_{max}$ , combustion chamber temperature, CO, NO, BTE, and CO <sub>2</sub> all increased
2021	1,300	50% CO/H <sub>2</sub>	<b>Chuahy et al. [131]</b>	Single-cylinder version of a Caterpillar C-15, 15L six-cylinder engine, 2.5L displacement, simulated turbocharger + port fuel injection system, RCCI mode.	Syngas addition changed the PSD, nucleation mode increased & accumulation mode decreased Soot surface chemistry unaffected, fuel stratification reduced, high $\phi$ lead to larger soot

**Table 2-8 Literature review summary for effects of varying the hydrogen content of the syngas on dual fuel combustion**

Engine speed (RPM)	Syngas type	Engine details	Reference	The effect of increasing the hydrogen content of the syngas:
1,300	GSS & SS	RCCI Engine- Numerical modelling study	<b>Kousheshi et al. [128]</b>	ID, Soot, CO and UHC decreased, Sharper HRR, $P_{max}$ , pressure rate rise & max local temperatures, $NO_x$ increased.
1,000	GSS	PREMIER COMBUSTION enabled engine, 4-stroke, single-cylinder, water cooled, 2 intake and exhaust valves. Common rail injection system used.	<b>Azimov et al. [148]</b>	CO, HC, ID, and main combustion duration decreased, BTE, $NO_x$ , HRR, flame speed, $P_{max}$ , and combustion temperatures increased.
1,500	Varying $H_2/CO$	A single-cylinder, water cooled, 5.2 kW, DI dual fuel engine	<b>Sahoo et al. [144]</b>	CO, HC, and ID decreased, BTE, combustion temperature & flame speed increased $P_{max}$ , $NO_x$ , EGT, diesel displacement rate increased. Volumetric efficiency increased in DF mode v diesel
1,825	Varying $H_2/CO$	CR of 21.2:1, 2 bar and 4 bar IMEP <sub>n</sub>	<b>Bika et al. [145]</b>	Higher BTE, $NO_x$ levels unaffected at 2 bar, increased at 4 bar
910	GSS	74.6kW, single cylinder, simulated turbocharged, Port injection system for syngas	<b>Guo et al. [150]</b>	Soot levels decreased, BTE increased. $NO_x$ levels were unaffected.
1,000	GSS: low and high $H_2$ content impact assessed	4-stroke, single-cylinder, water cooled DI engine, supercharged, two stage combustion engine.	<b>Roy et al. [85]</b>	HC (ppm), CO (ppm), and main combustion duration decreased. $NO_x$ (ppm), BTE, flame speed, and combustion temperatures increased
1,500	Varying $H_2/CO$	A single-cylinder, water cooled, 5.2 kW, DI dual fuel engine	<b>Sahoo et al. [143]</b>	Dual fuel had a better work availability at higher load v diesel baseline/ Increasing hydrogen enhanced the work availability in dual fuel mode.

**RS denotes Real Syngas**

**SS denotes Simulated Syngas ( $H_2$  and CO only)**

**GSS denotes Gasifier Simulated Syngas**

**DF denotes Dual Fuel**

**EGT denotes Exhaust Gas Temperature**

**BTE denotes Brake Thermal Efficiency**

**SEC denotes Specific Energy Consumption**

### **2.11.13 Summary of the syngas-diesel literature reviewed**

Overall, these studies vary in their research objectives and methodology, some being wholly numerical based, some a combination of experimental and modelling work, and others solely experimental based. In terms of emissions, there are very few studies that analyse the full range of emissions from dual fuel combustion. Further to this, the engine speed, size, type, design, operational parameters, et cetera, used are also variable across these studies.

The composition of the syngas used in these dual fuel combustion studies is variable. Also, the composition of the syngas produced from gasification itself can vary, (see Table 2.2). From the literature reviewed, the syngas produced from downdraft gasification can include oxygen which can vary in content from 0.6 to 1.6%. From the literature reviewed, aside from the co-authored study [117], only one other study used simulated syngas which was reported to contain a trace amount of oxygen (0.08%) [153]. For the majority of the studies reviewed which used real syngas, the oxygen content was not mentioned, this could be due to it not being present or not measured. Any increase in the fuel's oxygen content aids oxidation and improves combustion, hence, it is beneficial to include this when investigating dual fuel combustion using syngas derived from downdraft gasification. A further research gap highlighted here is the lack of NO, NO<sub>2</sub>, NO<sub>2</sub>/NO<sub>x</sub> ratio emission data in dual fuel operation relative to diesel.

The review of the syngas/diesel literature does well to highlight that there is no single comprehensive study that looks at the effect on the engine combustion performance together with the resulting emissions using 'gasifier' simulated syngas with a high-speed small engine. Rinaldi et al. [97], and Rith et al. [163] have done some studies using 3,000 RPM speed engines using real syngas; both these are partial studies in the sense that the emissions have not been studied.

The need to have one single comprehensive study is important as it is difficult to compare data across studies as there are too many variables that affect the resulting engine performance. Some examples include engine design, the operating parameters (such as speed, pilot fuel injection timing, pilot fuel mass, compression ratio, and inlet manifold conditions), as well as the gaseous fuel type [170]. For example, the study by Lal and Mohapatra [171] identified that changing the compression ratio changed the resulting emissions of a dual fuel engine that was run using biomass derived syngas, thus illustrating the difficulty in comparing data across studies.

One study reviewed in this thesis has evaluated the particle number and particle size distribution for syngas-diesel dual fuel combustion using gasifier simulated syngas with a 1,500 RPM speed engine equipped with EGR [161]. The syngas used in this study contained CO, H<sub>2</sub>, CO<sub>2</sub>, CH<sub>4</sub>, N<sub>2</sub>, and C<sub>2</sub>H<sub>6</sub>, and analysed the particle number and particle size distribution using an SMPS analyser which has a limited particle size diameter measurement range (up to 100 nm). Therefore, there is a need to investigate the impact of dual fuel combustion using syngas-diesel in a higher speed (3,000 RPM) diesel genset engine.

Half of the studies reviewed here investigated the impact of changing the hydrogen content or the H<sub>2</sub>/CO ratio of the syngas composition on the engine combustion performance and emissions used syngas that contained only CO and hydrogen [143-145]. This is not beneficial as the impact of the diluent gases such as CO<sub>2</sub> cannot be considered on the resulting NO<sub>x</sub> emissions. Also, the PM data will be potentially lower; Kousheshi et al. [128] reported that the CO, UHC, and PM mass emissions from syngas containing just CO and hydrogen are lower than when using real syngas (simulated or direct from gasification). The remaining three studies which assessed the impact of changing the hydrogen content of the syngas on dual fuel mode combustion all used slower speed engines ≤1,500 RPM, and were as follows:

- Guo et al. [150] used a turbocharged engine and only investigated two different hydrogen concentrations, however, these authors also changed the % of CO present in the syngas at the same time as changing the % of hydrogen, therefore evaluating the H<sub>2</sub>/CO ratio as a whole. Hence, any changes in combustion performance and emissions cannot be wholly attributed to the change in hydrogen content alone.
- The numerical modelling study conducted by Kousheshi et al. [128] researched the impact of increasing hydrogen content in syngas. Again, the % CO content was simultaneously changed with the hydrogen content. Hence, the impact of the change in the ratio of H<sub>2</sub>/CO has been evaluated. Furthermore, the other components in the syngas have also been changed in the composition alongside such as the methane, ethane, and ethene content. Therefore, any changes in combustion performance and emission cannot be wholly attributed to the change in hydrogen content alone.

- The final study by Roy et al. [85] investigated the effects of changing the hydrogen content in the gasifier simulated syngas (based on an updraft gasifier) during syngas diesel dual fuel combustion. This was the only study reviewed that looked at the direct impact of changing the hydrogen content of the syngas only. Here, the composition of the other gases was kept constant (CO, methane, and CO<sub>2</sub>), with the balance being nitrogen. Hence, any changes in combustion performance and the resulting emissions could be directly attributed to the hydrogen content of the syngas. It is worth noting that syngas from updraft gasification is not recommended for use in dual fuel diesel combustion.

In summary, there is a gap in the literature where there is a need to compare the impact of changing the hydrogen content of the syngas on dual fuel combustion which considers both combustion performance and a full range of emissions using an engine speed of 3,000 RPM. In terms of emissions, in particular, the impact of changing the hydrogen content on the particle number and particle size distribution emissions when using gasifier-based syngas (real or gasifier based simulated syngas).

## **2.12 Engine performance & emission studies for biogas/diesel**

The literature reviewed for biogas-diesel dual fuel combustion for this thesis involved biogas with varying methane content, engine speeds varying from 1,000 to 1,750 RPM, variable engine sizes and designs, as well as technologies, this is summarised in Table 2.9.

In some of the studies reviewed, the biogas was added via the air intake manifold [135, 136, 138, 139], in other studies, an air-biogas mixer was installed at the air intake manifold to aid mixing before entering the engine [137, 140]. The resulting trends will be discussed and compared from these studies.

### **2.12.1 Particulate Matter (PM) emissions for biogas-diesel**

The particulate matter (PM) arising from biogas-diesel dual fuel combustion was measured using various techniques. Overall, a reduction in the PM was reported in dual fuel mode using biogas/diesel relative to the diesel baseline. The PM was measured and expressed in various ways: PM SE (g/kWh), smoke emissions (expressed as an opacity number), and as a concentration in mg/m<sup>3</sup> [135, 136, 138, 139]. It is reported that the opacity number/smoke opacity decreased with increasing biogas flow rate [135, 138].

Ambarita [138] reported that as the methane concentration of the biogas increased, further reductions in the opacity number were noted as the increasing methane content of the biogas displaced more diesel.

Smoke emissions or the related reductions in PM mass are due to the biogas containing fewer aromatic compounds compared to diesel fuel, thus displacement of diesel led to these reductions [138]. Also, in dual fuel mode, a reduction in the flame temperature is noted in the combustion chamber, and an increase in the O and OH radicals (from the CO<sub>2</sub>) around the flame promotes the oxidation of soot and its precursors in the soot forming areas, thus leading to a reduction in PM [135, 139].

### **2.12.2 Brake Thermal Efficiency (BTE) for biogas-diesel**

Various authors reported a reduction in the BTE data when using biogas-diesel in dual fuel mode relative to diesel [135, 137, 140]; this is similar to that reported for syngas dual fuel combustion (see subsection 2.11.4), with BTE decreasing with increasing biogas flow [135, 137].

The theory for a reduction in the BTE in dual fuel mode is that when biogas is added, the air is displaced, hence oxygen availability decreases leading to incomplete combustion and reduced efficiencies. A further explanation given for the reduction of BTE for biogas/diesel given by some authors [135, 137, 138] is that CO<sub>2</sub> prevents fast burning of the mixture, thus decreasing the flame propagation speed and combustion temperatures. The increase in the negative compression work is caused by the intake of higher flow rates of biogas added in dual fuel mode [135].

Other authors reported dual trends for BTE in dual fuel mode, Ambarita [138] reported that the BTE value relative to the diesel baseline was dependent on the flow rate of the biogas, i.e. the amount of biogas added. At a lower substitution ratio of biogas, a higher BTE value was observed; at higher biogas substitution ratios, a lower BTE value was obtained relative to the diesel baseline.

Ambarita [138] concluded that the maximum BTE achievable was dependent on the engine speed, and the BTE increased with engine speed (1,000 and 1,500 RPM were compared), load, and methane concentration.

Aklouche et al. [136] reported an increase in the BTE during biogas diesel dual fuel combustion when using a fixed energy input into the engine and utilising 60% biogas energy substitution at 80% load. Hence, there may be an optimum BTE value during biogas/diesel dual fuel combustion which is dependent on the engine speed, load, and biogas energy substitution value. This may have not been identified by other researchers due to the limits of their experimental parameters. These authors reported an increase in the energy specific fuel consumption (in MJ/kWh) in dual fuel mode relative to diesel, which is contradictory as one would expect that if the BTE is higher in dual fuel mode, the BSEC data would decrease.

Mustafi et al. [139] reported no significant change in BSEC data in DF mode versus diesel, thus it can be inferred similar BTE values for both modes of combustion were obtained. A slightly faster speed engine of 1,750 RPM was used in this study in comparison to the rest.

Various studies have reported that the BSFC increased for DF combustion relative to diesel [137, 139, 140]. This was expected as this was calculated using the combined mass of both fuels and not represented as an energy term which is more useful when being compared to BTE data.

Overall, this review shows varying trends in terms of BTE in dual fuel mode when using biogas/diesel relative to the diesel baseline. It is difficult to determine the reason for the variability in the BTE trends reported during biogas/diesel operation versus the diesel baseline. This could be due to the difference in operational parameters used, engine types, and designs, as well as the composition of the biogas used and the potential of the BTE being sensitive to the flow rates used.

### **2.12.3 Carbon monoxide (CO) emissions for biogas-diesel**

The CO emissions in dual fuel mode are expected to increase relative to the diesel baseline due to incomplete combustion which results in lower thermal efficiency. This was the consensus in the literature reviewed whereby the majority of authors reported an increase in the CO emissions during dual fuel combustion relative to the diesel baseline, with increasing CO emissions with increasing biogas addition [135-140]. The incomplete combustion was caused by a reduction in oxygen availability, caused by the displacement of air when biogas was added [135, 137, 138].

Furthermore, the CO<sub>2</sub> content of the biogas acts as a diluent, therefore the pilot fuel flame formed in the ignition region is suppressed (lower flame speed) until the biogas-air mixture reaches its autoignition temperature [135, 140]. This is supported by the longer IDs seen in DF mode. Biogas has a higher specific heat value compared to diesel [137]. This combined with the reduction of air/oxygen from the addition of biogas results in increased CO emissions. Flame quenching may also result in increased CO emissions [139].

According to Ambarita [138], the CO emissions were not greatly affected by a change in the engine speed, nor an increase in the methane concentration of the biogas. Salve et al. [140] reported that increasing the compression ratio led to reductions in CO emissions, and this serves well to reiterate the difficulty in comparing emission data across studies that are based on different engine sizes, designs, and specifications.

#### **2.12.4 Hydrocarbon (HC) emissions for biogas-diesel**

As per CO emissions, due to incomplete combustion occurring in biogas-diesel dual fuel combustion, it is expected that the hydrocarbon (HC) emissions would also increase. HCs are formed in rich areas of the combustion chamber where the fuel remains unburnt. The majority of studies reviewed here all reported a significant increase in HC emissions in dual fuel combustion [135-138, 172]. The resulting HC emissions increased with engine speed, load, and with increasing biogas flow rate [137-139]. The increase in HC emissions was attributed to a lower flame velocity present during dual fuel combustion [137]. Barik and Murugan [135] further postulated that the HC emissions increased due to incomplete combustion of any unburnt fuel/air mixture which was trapped in the crevices of the combustion chamber during the compression stroke. The increase in HC emissions with increasing biogas flow rate was said to be caused by a reduction in the air intake which in turn resulted in a richer mixture in the cylinder, thus favouring incomplete combustion [137].

Sahoo et al. [170] state that in dual fuel mode combustion, if the CO<sub>2</sub> content of the biogas is high, then it behaves as an inert diluent, thus, the introduction of biogas with a high CO<sub>2</sub> content does not dissociate, rather it promotes incomplete combustion and increases the HC emissions.

However, at lower concentrations, CO<sub>2</sub> dissociates into CO and oxygen. As CO is relatively fast burning, this speeds up the burning rate, and this dissociation increases the oxygen availability, hence, reducing IDs and improving the combustion of UHCs and other particulates. The dissociation is initiated by the high flame temperature of diesel.

Ambarita [138] also looked at the effect of the methane concentration of the biogas on the resulting emissions. This author reported that at low engine loads, increasing the methane content of the biogas/reducing the CO<sub>2</sub> content simultaneously, increased the HC emissions. Consequently, at higher loads, increasing the methane content or decreasing the CO<sub>2</sub> content of the biogas (by 10%) did not lead to significant increases in the HC emissions, hence, the dissociation of CO<sub>2</sub>, alongside higher combustion temperatures may have kept the resulting HC emissions down at higher engine loads.

Mustafi et al. [139] reported that increasing the CO<sub>2</sub> content of the biogas/ whilst decreasing the methane content leads to an increase in the UHC emissions. These authors looked at a 22% change in the CO<sub>2</sub>/CH<sub>4</sub> content, potentially the CO<sub>2</sub> behaved predominantly as a diluent in this study which explains the increase in the UHC emissions.

### **2.12.5 Nitrogen oxides (NO<sub>x</sub>) emissions for biogas diesel**

Lower NO emissions were reported in dual fuel mode for biogas-diesel relative to diesel baseline; higher levels were reported at higher loads [135]. This was expected as NO is favoured by higher combustion temperatures, and the CO<sub>2</sub> fraction of the biogas not only reduces the oxygen availability, but it also lowers the cycle temperature, acting like an EGR strategy. This, combined with the fact that CO<sub>2</sub> has a higher molar specific heat value thereby the compressed air and fuel in the cylinder is diluted, and the cycle temperature is lowered again resulting in lower NO formation [135]. As 90% of NO<sub>x</sub> emissions are made up of NO,[167], if the concentration of NO is expected to decrease in dual fuel mode, then so will NO<sub>x</sub> emissions.

NO<sub>x</sub> emissions were also said to decrease in dual fuel mode (relative to the diesel baseline) and with increasing biogas addition [136, 137, 139, 140]. NO<sub>x</sub> emissions in dual fuel mode (as seen in pure diesel baseline), are lower at lower loads due to lower combustion temperatures.

At higher biogas flow rates, more air is displaced and oxygen is further reduced, thus the temperature decreases in the combustion chamber, thereby reducing NO<sub>x</sub> formation [137]. Also, at higher biogas flow rates, lower peak cylinder temperatures are obtained, further hindering NO<sub>x</sub> formation [137].

The high CO<sub>2</sub> content of the biogas acts as a diluent, it has a high molar specific heat capacity, thus lowering the combustion chamber temperature [139, 140]. This was confirmed by Mustafi et al. [139] who reported that when the CO<sub>2</sub> concentration of the biogas was increased, the NO<sub>x</sub> emissions were reduced further in DF mode, thereby confirming that CO<sub>2</sub> does act as a diluent, thus reducing oxygen availability and cycle temperature due to its high molar specific heat capacity.

### **2.12.6 Carbon dioxide (CO<sub>2</sub>) emissions for biogas-diesel**

Lower CO<sub>2</sub> emissions were reported in dual fuel mode than diesel combustion [135, 140]; in dual fuel mode, this was due to less diesel being combusted. The 27-35% CO<sub>2</sub> content of the biogas was not considered to play a factor in the resulting CO<sub>2</sub> emissions in these studies.

In contrast, Leykun and Mekonen [137] reported an increase in CO<sub>2</sub> emissions in DF mode relative to the diesel baseline, the CO<sub>2</sub> emissions were said to increase with an increasing biogas flow rate. This was attributed to the high CO<sub>2</sub> content of the biogas, whereas, other studies stated these emissions were similar for both combustion modes [136].

It is difficult to cross compare CO<sub>2</sub> emissions across studies due to the multiple factors which affect this as discussed above, alongside the variations in the in-cylinder temperature, the CO<sub>2</sub> content of the biogas, differences in the engines used, and the oxygen concentrations, all affect the resulting emissions [167].

The EGTs were marginally lower in dual fuel mode [135] caused by incomplete combustion as a result of the reduced flame propagation speed of diesel which is hindered by the CO<sub>2</sub> content of the biogas.

Overall, the presence of the CO<sub>2</sub> content in the biogas leads to a reduction in the overall cycle temperature, a reduction in the rate of oxidation reactions, and NO<sub>x</sub> formation [135, 148].

### **2.12.7 Diesel displacement rate for biogas-diesel**

Generally, as reported for syngas-diesel mode combustion, the diesel displacement rate increased with increasing biogas flow rate [135, 137, 138]. Also, the diesel displacement rate decreased with increasing methane concentration of the biogas [138]. The % mass of diesel displaced as a result of biogas-diesel dual fuel combustion varied in the literature reviewed from 15% to 87.5% [138].

### **2.12.8 Biogas-diesel Heat Release Rate (HRR) studies**

Three heat release studies were reviewed for dual fuel combustion using biogas-diesel [136, 139, 140]. All these studies agreed that the ID was found to increase in dual fuel mode when using biogas-diesel relative to diesel. This was thought to be caused by the delay in the autoignition of the pilot diesel due to the addition of biogas in the cylinder. Biogas has a higher autoignition temperature related to the CO<sub>2</sub> content of the biogas [135, 136]. A further contributing factor is a reduction in pressure and temperature during the start of the ignition of the fuel/air mixture due to methane having a higher heat capacity than air. Thus, a change in the composition of the biogas, in terms of a reduction in the methane content/increasing the CO<sub>2</sub> content would expect the ID would increase further, this was indeed the case as reported in the studies that looked at biogas with varying compositions [135, 139].

A reduction in the volumetric efficiency in dual fuel mode was found relative to the diesel baseline [135, 136], which caused a reduction in the pressure at the start of the compression stroke in dual fuel combustion.

The reduction in  $P_{max}$  is typically expected in dual fuel mode when considering that biogas and air are compressed together in the compression stroke. Biogas has a higher specific heat than air [136], hence the in-cylinder temperatures are lower, and therefore, the compression pressure is lower [167], combined with the fact that the CO<sub>2</sub> content of the biogas hinders burning during the early stage of combustion. Hence, overall, a lower  $P_{max}$  is achieved in dual fuel mode relative to diesel, which is reported in the studies reviewed [136, 140].

However, Mustafi et al. [139] reported that a similar  $P_{max}$  was obtained for diesel and DF mode, but the  $P_{max}$  was delayed due to the increase in the ID.

A further study by Barik and Murugan [135] reported the  $P_{\max}$  to increase in all dual fuel mode operations relative to diesel; also, the  $P_{\max}$  was found to occur later into the expansion stroke, as noted by others [139]. This increase in the  $P_{\max}$  data is rather contradictory as the corresponding temperatures in dual fuel mode in this study have been reported to have decreased relative to the diesel baseline, those being a lower cycle temperature, reduced local flame temperature, exhaust gas temperature, and a lower combustion chamber temperature, alongside reduced NO formation which is a direct result of combustion temperature [135]. Hence, the increase in  $P_{\max}$  remains unclear in DF mode for this study but could be linked to rapid heat release in the premixed combustion phase occurring near TDC [135, 167, 173].

Salve et al. [140] reported that the  $P_{\max}$  increases with increasing compression ratio at a fixed speed in all combustion modes.

Conflicting trends have been reported when considering the change in the  $P_{\max}$  data in DF relative to diesel, which is not dissimilar to that reported for syngas-diesel dual fuel combustion (see Table 2.6).

With an increase in ID in dual fuel mode using biogas-diesel [135, 136, 139], the  $P_{\max}$  is said to have occurred later (in crank angle degree) towards the expansion stroke [135, 136], thus, it is to be expected that the HRR would be delayed in DF mode. The HRR studies reviewed reported this delay in dual fuel mode [136].

Overall, as a result of an extended ID, this allows the accumulation of more fuel and more premixing in dual fuel mode relative to diesel, thus when combustion starts in the first phase, more fuel is burnt thus more heat is released. Hence, it is expected that dual fuel combustion would produce a higher peak of heat release rate for DF mode relative to diesel, as was reported for the HRR studies reviewed [135, 136, 139]. In terms of the combustion duration in dual fuel mode relative to diesel, the HRR studies reviewed reported a shorter duration of combustion [136, 139], this was due to a reduction in the diesel consumption in dual fuel mode, alongside a higher premixed combustion rate and a shorter diffusion combustion period [139, 174]. The overall maximum net heat release rate was reported to be higher in dual fuel mode than that of diesel by one study [139], whereas the study by Salve et al. [140] reported that the net heat release rate of diesel was higher; full combustion performance and heat release analysis has not been reported in this study; it appears incomplete, hence this contradiction remains unexplained. Overall, the cumulative heat release was reported to be lower in DF mode, alongside more rapid combustion in DF combustion [139].

### **2.12.9 Summary of the biogas-diesel literature reviewed**

This subsection of this literature review has investigated the effects of dual fuel combustion using biogas-diesel using slow speed engines ranging from 1,000 to 1,750 RPM. There is no single study for dual fuel biogas-diesel combustion which uses a 3,000 RPM speed engine. The summarised findings from this literature review are provided in Table 2.9.

The source and the composition of the biogas used in these dual fuel combustion studies are variable, as illustrated in Table 2.9. Some studies have used simulated biogas and others have used real biogas produced from AD. In addition, the methane and CO<sub>2</sub> content of the biogas used are variable.

The study by Ambarita [138] reported that a change in the methane concentration of the biogas affects the BTE, smoke emissions (opacity number), and HC emissions at low loads. Hence, it is difficult to compare data across studies, in addition, the engine speed, size, type, design, operational parameters, et cetera, used are also variable across these studies.

Overall, the literature reviewed indicated that the trend regarding BTE in dual fuel mode using biogas-diesel combustion relative to the diesel baseline is inconclusive. In some studies, this is higher, in some is unaffected, and in others, it is lower relative to pure diesel.

There is good agreement in the literature whereby the PM mass or smoke number decreases for all biogas-diesel dual fuel combustion studies reviewed relative to diesel. However, there is a gap in the literature when considering the impact of biogas-diesel dual fuel combustion on the resulting emissions which considers the particle number and particle size distribution when using simulated biogas.

The consensus in the literature reviewed was that the majority of authors reported an increase in the ID, HC, and CO emissions in dual fuel combustion relative to the diesel baseline.

Lower NO<sub>x</sub> emissions were reported in dual fuel mode for dual fuel mode relative to the diesel baseline; higher levels were reported at higher loads. However, a research gap highlighted here is the lack of NO, NO<sub>2</sub>, NO<sub>2</sub>/NO<sub>x</sub> ratio emission data in dual fuel operation relative to diesel baseline. The study by Barik and Murugan [135] is the only one that reported NO emissions but did not report NO<sub>x</sub> emissions alongside this.

**Table 2-9 Summary of the literature reviewed for various biogas-diesel dual fuel combustion studies**

Engine speed (RPM)	Biogas	Engine particulars	Reference	Results in DF mode relative to diesel	Other information
1,000 & 1,500	Enriched biogas: 70% CH <sub>4</sub> , 30% CO <sub>2</sub> Raw biogas: 60% CH <sub>4</sub> , 40% CO <sub>2</sub>	Single cylinder, 4-stroke, water cooled, DI, 4.4 kW. Compression ratio: 23	<b>Ambarita [138]</b>	HC, CO, & SFC increase  Smoke: opacity number ↓, Low biogas flow rate ↑BTE High biogas flow rate ↓BTE	Two biogas compositions compared, as CH <sub>4</sub> content increases:  BTE ↑, CO unaffected, opacity number ↓, HC ↑ at low loads & is unaffected at high loads.
1,500	Biogas (~73% CH <sub>4</sub> )	Single cylinder, 4-stroke, air cooled, DI, 4.4 kW. Compression ratio 17.5	<b>Barik &amp; Murugan [135]</b>	Lower smoke opacity. Higher BSFC, CO, and HC Lower, BTE, NO, CO <sub>2</sub> & Volumetric efficiency	↑P <sub>max</sub> , ID & combustion duration increase. P <sub>max</sub> and HRR delayed. Higher PoHRR in DF mode. Lower: cylinder, flame, & combustion chamber temperature, Lower cycle and exhaust gas temperature
1,500	Raw biogas: 44.5% CH <sub>4</sub> , 10.7% CO <sub>2</sub> , 8.7% O <sub>2</sub>	Single cylinder, 4-stroke, naturally aspirated, DI, 2.2 kW Compression ratio 21	<b>Leykun &amp; Mekonen [137]</b>	Lower BTE, HC, and NO <sub>x</sub> ,  Higher: BSFC, CO CO <sub>2</sub> ↑	
1,500	Simulated Biogas: 60% CH <sub>4</sub> , 40% CO <sub>2</sub>	Lister Petter, single cylinder, 4-stroke, naturally aspirated, DI, 4.5kW	<b>Aklouche et al. [136]</b>	↑ BTE, ↑SEC, ↑CO, ↑HC CO <sub>2</sub> unaffected.  ↓NO <sub>x</sub> , ↓soot conc. ↓volumetric efficiency	Increase in ID & PoHRR. ↓in duration of combustion, ↓ P <sub>MAX</sub> , HRR & P <sub>max</sub> delayed, Higher peak for premixed combustion phase, Load kept constant, air intake modified using throttle, fuel masses not changed so different φ investigated
1,750	Simulated Biogas of varying % CH <sub>4</sub> /CO <sub>2</sub> content: 80/20, 67/33, 58/42	Lister Petter, single cylinder, 4-stroke, water cooled, DI, Compression ratio 16.5.	<b>Mustafi et al. [139]</b>	↑ID, ↑UHC, ↑BSFC, ↑CO  ↓NO <sub>x</sub> , ↓PM mass emissions. No significant change in BSEC	P <sub>max</sub> did not change, shorter combustion duration, P <sub>max</sub> delayed, Cumulative heat release lower in DF mode.  Higher peak of heat release rate in DF mode Net heat release rate higher in DF mode
1,500	Simulated biogas 65% CH <sub>4</sub> , 35% CO <sub>2</sub>	3.5 kW single cylinder, direct injection, water cooled. Variable compression ratio: 15 and 18 used.	<b>Salve et al. [140]</b>	↓BTE, ↓P <sub>max</sub> , ↓CO <sub>2</sub> , ↓NO <sub>x</sub> .  ↑BSFC, ↑CO higher	Net heat release rate lower in DF mode

## 2.13 Knowledge gaps

The above literature review highlights that although biomass waste resource assessments do exist, many of these do not quantify all four waste biomass residues of interest, especially for Tanzania. The biomass waste streams of interest are those arising from agriculture, forestry, livestock, and urban human waste. Furthermore, there is little or no work that assesses if the biomass residues in Tanzania/ Uganda have sufficient energy potential to produce renewable electrical energy for small-scale electricity generation using off-grid diesel generators coupled with anaerobic digestion (AD) and/or gasification (dual fuel combustion).

Furthermore, when considering utilising the gaseous fuel produced from either gasification and/or anaerobic digestion in a dual fuel high-speed diesel genset, the existing dual fuel combustion studies all vary in their research objectives, methodology, engine types, and the syngas/biogas composition; all these make any cross comparison of data difficult (as summarised in sections 2.11.3 and 2.12.9). There is limited data on the engine performance and emissions when using a small-sized 3,000 RPM speed diesel genset in dual fuel mode for small-scale electricity generation based on gasification derived syngas and or simulated biogas.

Thus, in conclusion, it is difficult to find a single comprehensive study that looks at engine combustion performance and the full range of resulting emissions for dual fuel combustion using simulated syngas and/or biogas, as well as the effects of changing the hydrogen content of the simulated syngas.

## **2.14 Research questions**

This literature review has looked at the most relevant studies for the areas of interest of this thesis. The research questions to be addressed are:

1. What is the net electrical generating potential (when considering utilising gasification and AD) coupled with a diesel genset of the selected biomass waste streams identified in The United Republic of Tanzania and Uganda, in comparison to their national electricity production?
2. How does syngas-diesel dual fuel combustion affect engine performance and emissions, when compared to diesel?
3. What is the impact of changing the hydrogen content of the simulated syngas on the engine performance and emissions?
4. How will biogas-diesel dual fuel combustion affect engine performance and emissions, when compared to diesel?
5. Are there any GHG savings (CO<sub>2</sub> equivalent) arising from the optimum dual fuel combustion conditions identified from the reduction in diesel fuel usage?

## **2.15 Refined aims and objectives**

The refined research aims and objectives for this thesis, when considering the identified research gaps are outlined here.

### **2.15.1 Overall aim**

The overall aim of this study is to further research means of increasing electrification rates in the developing world, specifically, in rural areas where small-scale electricity generation is currently carried out using diesel gensets. In particular, the focus is on the utilisation of biomass residues that are available in this region.

By utilising these residues in thermal conversion techniques such as gasification and/or biological conversion like anaerobic digestion, a gaseous fuel (syngas/biogas) can be produced. This gaseous fuel can be used to substitute diesel in modified diesel genset engines to operate as a dual fuel engine to generate more affordable, renewable small-scale electricity. This study undertaken seeks to investigate the impact of dual fuel combustion using either syngas and/or biogas.

### **2.15.2 Specific objectives**

The following specific objectives were defined to achieve the aim of this thesis which are as follows:

1. Investigate the energy potential of the combined biomass waste streams identified for Tanzania and Uganda.
2. Investigate the electricity generating potential of the biomass waste streams identified in Tanzania and Uganda.
3. Investigate the impact of syngas-diesel dual fuel combustion relative to diesel.
4. Investigate the effect of changing the hydrogen content of the simulated syngas in dual fuel combustion.
5. Investigate the impact of biogas-diesel dual fuel combustion relative to diesel.
6. Investigate the impact of diesel consumption in dual fuel combustion when considering greenhouse gas emissions (CO<sub>2</sub> equivalent).

## Chapter 3 Methodology for Engine Testing

### 3.1 Introduction

This chapter summarises the methodology, equipment, and fuels used to assess the impact of using the selected gaseous fuels within a diesel genset in dual fuel combustion, specifically, the engine performance and emissions.

### 3.2 Fuels for testing

#### 3.2.1 Red Diesel

Ultra-Low Sulfur Diesel fuel (ULSD/red diesel) was used for this study which was purchased from Crown Oil. The fuel was compliant with BS 2869: Part 2: 2010 classification class A2. Proximate analysis was conducted on this fuel using the instrument 'Shimadzu TGA 50' to conduct Thermogravimetric Analysis (TGA). Ultimate/elemental analysis was conducted on the fuel for carbon, hydrogen, nitrogen, and sulfur content. The calorific value was also determined using the bomb calorimeter (instrument PARR6200). The results (obtained from the direct analysis) are summarised in Table 3.1 and compared alongside the specifications from the red diesel fuel supplier.

**Table 3-1 Results of the analysis of red diesel**

Parameter	Lab Results	EN590 Gas oil (red diesel) [175]
Density at 15 °C (kg/m <sup>3</sup> )	0.84	0.820 minimum
HHV (MJ/kg)	45.63	45.4 (typical)
LHV (MJ/kg)	44.19	N/A
Carbon (% m/m)	85.07	87 % (typical)
Hydrogen (% m/m)	14.10	12.75 % (typical)
Nitrogen (% m/m)	0.53	0.01-0.05 % (typical)
*Oxygen	0.30	N/A
Cetane Number (CN)	N/A	45 (minimum), 48 (typical)

*\*Calculated by difference*

#### 3.2.2 Simulated syngas

Simulated syngas was used for the dual fuel testing whereby the composition mimicked 'clean' syngas (after removal of tar/particulates and other impurities) produced from using waste biomass as a feedstock in a downdraft gasifier.

Three different simulated syngas blends were evaluated for this study. These blends were purchased from BOC and labelled as syngas A (SGA), syngas B (SGB), and syngas C (SGC).

The quality and composition of any syngas produced from a typical downdraft gasifier are variable as it is dependent on many factors. These include the design and operation of the gasifier, the type of biomass feedstock, and its physical and chemical properties. This is discussed in more detail in the literature review (see Chapter 2, subsection 2.5.4). As a result, the syngas composition quoted in the literature is variable as it is based on many factors which differ from study to study. Hence, data from the open literature was researched and collated on typical syngas composition produced from downdraft gasification using various waste biomass residues as feedstock [62, 81, 82, 84, 86, 87, 90, 91, 100-109] (see Table 3.2). From this, average values and ranges were determined for the individual gas components to produce simulated Syngas A. Thus, a composition for production was requested from BOC. Due to economic limitations associated with including the hydrocarbons ( $C_nH_m$ ), these were excluded, instead, the  $CH_4$  content was increased to 4% with slight other changes being incorporated. However, the final composition of the SGA purchased, and the subsequent syngas blends purchased (SGB and SGC), all were within the compositional range of each gas component as reported in the literature by other researchers. This is summarised again in Table 3.2.

**Table 3-2 Summary of the compositional variability of the syngas from the literature review**

Species:	CO	H <sub>2</sub>	CH <sub>4</sub>	C <sub>n</sub> H <sub>m</sub>	O <sub>2</sub>	N <sub>2</sub>	CO <sub>2</sub>	LHV (MJ/m <sup>3</sup> )
% Range	9.4-29.6	7-24.8	0.1-8.21	0.2-2.4	0.61-1.61	34.1-60.8	8.9-36.4	3.8 - 10.6
% Average	19.7	14.8	2.7	1	0.95	54.2	12.2	5.2
% Requested from BOC	20	15	3	1	1	48*	12	
SGA (%) purchased	20	15	4	N/A	0.98	48.02	12	

*\*Balance being nitrogen gas*

After testing SGA, it was decided to evaluate the impact of changing the composition of hydrogen whilst keeping the composition of the remaining gases the same.

The literature review (see Chapter 2, section 2.11.12) discusses the impact of the hydrogen content of the syngas composition on the engine combustion performance. Thus, a further two syngas compositions were ordered for testing: SGB and SGC, both with different hydrogen content.

Table 3.3 summarises the composition of the gases purchased from BOC. Table 3.4 shows the calculation of the density for each syngas mixture and biogas. This has been calculated by multiplying the molar fraction of each gas component by the density value of each gas ( $\text{kg/m}^3$ ). The sum of the density fractions is the calculated density for that gaseous fuel.

Table 3.5 shows the calculated LHV data. This has been calculated by multiplying the mass fraction of each gas component by the LHV for each gas ( $\text{MJ/kg}$ ). The sum of the LHV fractions is the calculated LHV in  $\text{MJ/kg}$ .

**Table 3-3 Summary of the composition of the syngas/biogas purchased**

Composition (mol fraction)							
	CH <sub>4</sub>	H <sub>2</sub>	CO	O <sub>2</sub>	CO <sub>2</sub>	N <sub>2</sub>	Total
Syngas A (SGA)	0.04	0.15	0.2	0.0098	0.12	0.48	1.0
Syngas B (SGB)	0.04	0.20	0.2	0.0098	0.12	0.43	1.0
Syngas C (SGC)	0.04	0.25	0.2	0.0098	0.12	0.38	1.0
Biogas (BG)	0.50				0.50		1.0

**Table 3-4 Summary of the density values calculated for each gaseous fuel**

Density contribution (based on mol fraction)							
	CH <sub>4</sub>	H <sub>2</sub>	CO	O <sub>2</sub>	CO <sub>2</sub>	N <sub>2</sub>	Calculated $\rho$ ( $\text{kg/m}^3$ )
$\rho$ values ( $\text{kg/m}^3$ ) [176]	0.668	0.0899	1.165	1.331	1.842	1.165	
SGA	0.027	0.013	0.233	0.013	0.221	0.559	1.0667
SGB	0.027	0.018	0.233	0.013	0.221	0.501	1.0130
SGC	0.027	0.022	0.233	0.013	0.221	0.443	0.9592
Biogas	0.334	0	0	0	0.921	0	1.2550

**Table 3-5 Summary of the LHV calculated for each gaseous fuel**

LHV contribution (based on mass fraction)							
	CH <sub>4</sub>	H <sub>2</sub>	CO	O <sub>2</sub>	CO <sub>2</sub>	N <sub>2</sub>	Calculated
LHV ( $\text{MJ/kg}$ )	50.05 [177]	119.96 [177]	10.112 [178]				LHV ( $\text{MJ/kg}$ )
SGA	1.25	1.42	2.21				4.89
SGB	1.32	1.99	2.33				5.64
SGC	1.40	2.63	2.46				6.49
Biogas	13.37	0	0				13.37

### 3.2.3 Biogas

The typical composition of biogas (BG) produced depends on the feedstock and the production method. The methane content can vary between 45% to 75% by volume. The remainder is predominantly CO<sub>2</sub>, with a small number of impurities [71, 179].

The simulated biogas purchased from BOC contained only CH<sub>4</sub> and CO<sub>2</sub>; this composition represented 'clean' biogas that was free of any impurities. The composition, the calculated LHV, and the density value are given in Tables 3.3 to 3.5 for the simulated biogas purchased.

### 3.3 Engine testing lab

This work was carried out in the engine testing lab and this section will cover the instrumentation and equipment used. For the experimental combustion testing, the following genset was used: MG6000 SSY (MHM plant, UK) 6 kVA. This incorporated a 5.7kW rated single-cylinder, naturally aspirated diesel engine without any EGR capability. This engine was adapted for dual fuel use (gas-diesel). A single-phase 50Hz generator (socket 230V, 32A) was connected to the load bank. Fig. 3.1 depicts the overall schematic for the genset engine, and the related instrumentation used to measure the gaseous emissions and the engine performance.

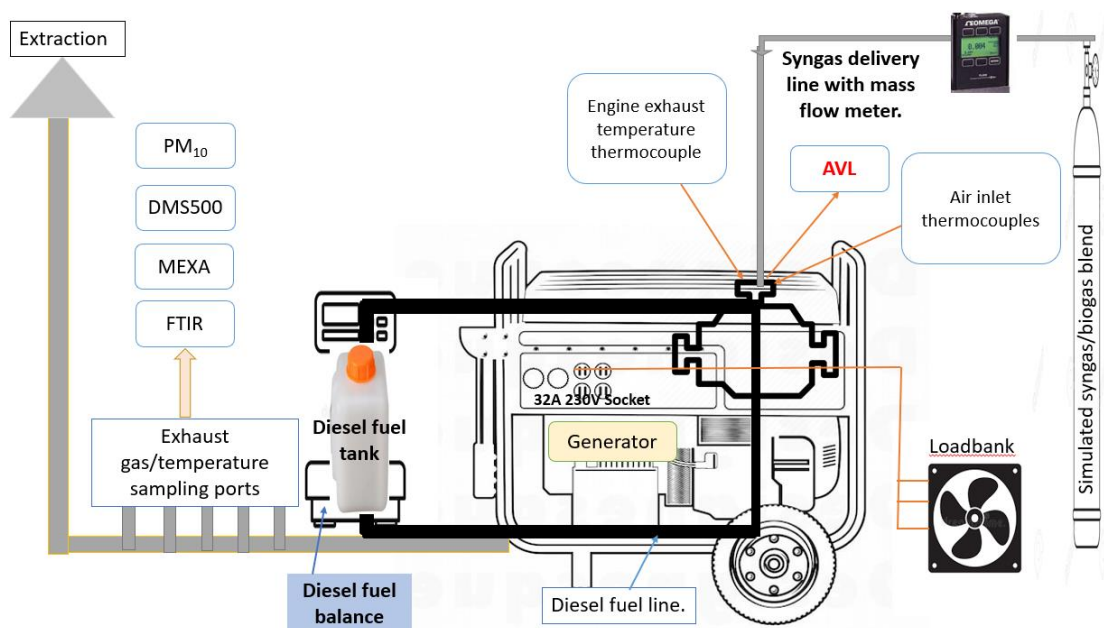


**Figure 3-1 The overall schematic for the genset engine and the related instrumentation**

### 3.3.1 Engine specification

The specifics of the engine are summarised in Table 3.6.

**Table 3-6 Engine specifications**

Parameter	Specification
Manufacturer/Model	Yanmar LV Series, 2019 Model, L100V5
Compliance	EU Stage V emission compliant
Type	4-stroke, single-cylinder, air-cooled
Rated power	5.7 kW
Speed	3,000 RPM
Bore x Stroke	86 mm x 75 mm
Compression Ratio	20.9:1
Total cylinder volume	457.55 cm <sup>3</sup>
Displacement	435.66 cm <sup>3</sup>
Injection pressure	19.6 MPa
Injection timing	13.5° before Top Dead Centre (bTDC)
Injector type	FB (5 holes, ~185 nm width, 150° cone angle)
Engine oil capacity	1.7 L
Starting system	Electric start/recoil start

This diesel engine was adapted for dual fuel mode to enable gaseous addition. This was done by the cylinder head on the genset engine being drilled and a thread tapped directly above the inlet port to allow the syngas/biogas ‘injector’ to inject as close to the inlet valve as possible (to reduce the potential of a build-up of a flammable gas). The delivery of the gaseous fuel was controlled by an omega mass flow meter. The bottled gas was piped through stainless-steel pipework equipped with a two-stage regulator and a stainless-steel flashback arrester. Reactivity Control Compression Ignition (RCCI) technology often uses multiple injection timing and a high level of premixing which is achieved by utilising port fuel injection systems to control and optimise the combustion process when using two different fuel types (as discussed in Chapter 2). In the current setup, some level of premixing was achieved, especially at high flow rates, however, at low loads and low gas flow rates, it is debatable whether this setup /adaption fully utilised RCCI technology.

Fig. 3.2 depicts the syngas delivery configuration and Fig. 3.3 shows the syngas injection point on the cylinder head of the engine.

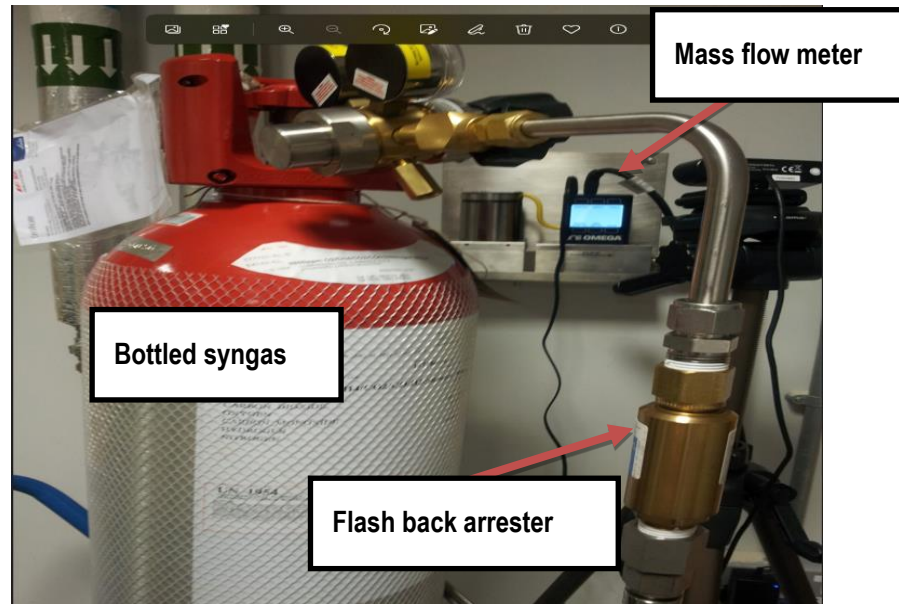


**Figure 3-2 Syngas cylinder configuration**

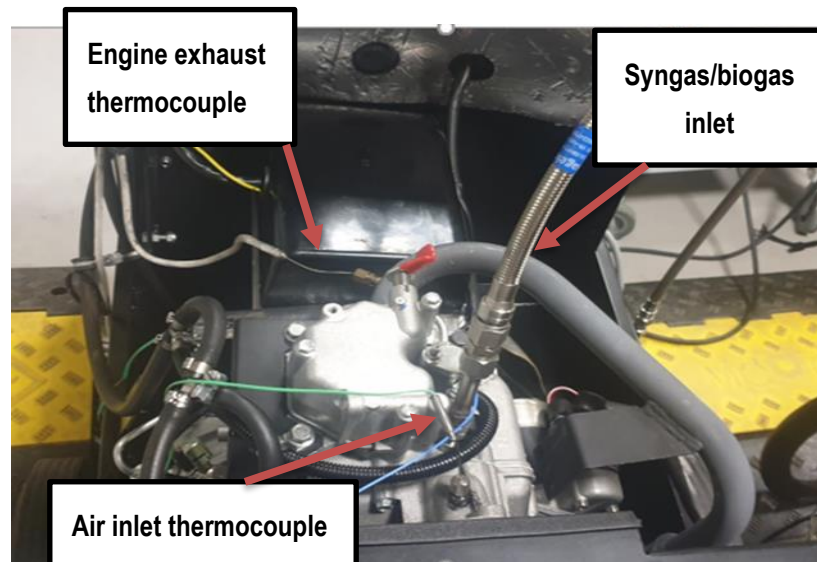


**Figure 3-3 The modified cylinder head to incorporate syngas/biogas**

### **3.3.2 Engine-related instrumentation**

Various equipment and software were used for data collection during the testing from the genset engine. The temperature was measured at various points from the engine exhaust system using thermocouples. In particular, the temperature data was analysed from the thermocouple measuring the temperatures of the engine oil, the exhaust air (directly leaving the engine from the engine exhaust manifold), and the engine inlet air (see Fig. 3.3). The engine itself was connected to a digital fuel balance which monitored diesel fuel usage in increments of 10g.

The gaseous fuel was metered into the engine on a volume basis using an omega mass flow meter. The omega flow meter used (FMA-2613A-V2) had an accuracy of  $\pm 0.8\%$  reading,  $+0.2\%$  full scale, with the capacity of delivering 4 to 1000 standard litres per minute.

The electrical socket of the engine generator was connected to the load bank. The load bank resistors were cooled with a fan incorporated at the front of the unit. The load bank created an electrical sink which enabled the load on the engine to be changed. The resistance of the load bank was controlled in the control room via remote control. The software supplied with this logged the voltage/current and frequency every second; this was connected to the computer in the control room using the intranet via an ethernet connection.

The in-cylinder pressure was measured using a pressure transducer connected to the Flexifem charge amplifier, this converted the charge into a voltage. This had a measuring range from 0 to 250 bar, with a sensitivity of 19 pico coulomb/bar. The RPM was calculated from the pressure data (360 pulses/rotation) by using the initial crankshaft point of rotation when the piston is at the top dead centre (at peak pressure), and by assuming a constant angular velocity. This provided the time interval for four strokes, hence the average interval between ten of these events was used to calculate the RPM. The crank angle degree (CAD) was also determined using the pressure sensor and was detected when  $\sim 20$  bar pressure was reached on the compression stroke. This is before combustion has begun and occurs at the same angle, i.e., when the TDC pressure equates to zero CAD. The algorithm to calculate the RPM and CAD was previously written into the LabView software. The CAD was measured at a resolution of 0.5 CAD.

Data from the engine, pressure sensor, thermocouples, fuel balance, and gas flow meter fed into the 8-slot CompactRio chassis (National Instruments), this was connected to a computer via an Ethernet port in the control room. Data logging and visualising were conducted in the control room using an in-house program written into the LabView software. Table 3.7 presents the specifications of the genset/load bank and other engine-related instrumentation used.

**Table 3-7 Other engine-related instrumentation**

Parameter	Specification
Cylinder pressure	AVI FlexIFEM Indi 601 (2 chanel), AVL GH14D transducer [180]
Fuel usage	Digital Scales- ADAM (CPW plus-35)
Syngas/Biogas flow	Omega FMA-2613A-V2 Mass flow meter
Temperature	K-type thermocouples (x6)
Data logging & visualisation	LabView Software
Load output	Hillstone HAC2410-10. Single phase resistive load bank [181]
Alternator	Linz E1C10M H [182]

### 3.3.3 Analytical instrumentation and analysis

Various analytical techniques were employed to determine the engine performance and emissions during the testing procedure. This sub-section explains the instruments used.

#### 3.3.3.1 Particulate analysis

##### *a) DMS500 for particle size distribution measurement*

The particle size distribution was measured during the engine runs using the DMS500 MKII Fast Particle Analyser (from Cambustion). This instrument measures particle size between 5 -1,000 nm and has an integrated two-stage dilution system.

Engine exhaust gas passes through a heated line (set at 55°C) connected to the instrument; a remote cyclone is integrated at the start of this line. The exhaust gas passes through the remote in-line cyclone (at ~8l/min) whereby the primary diluter is incorporated. Here, any larger particles above 1,000 nm are removed. Compressed air was used to achieve a dilution factor of up to 5:1 for the first diluter. The exhaust gas then passes through a secondary cyclone to further remove any large particles. The gas is then diluted further by the rotating disc diluter to ensure the secondary dilution factor remains at around 20:1.

This secondary dilution factor is variable and was monitored during the experiment, if required, it was adjusted accordingly by the operator (researcher). This was achieved by ensuring that the visual display of the 'signal strength indicator bar' on the 'Cambustion' software remained within the green zone (to achieve a good signal-to-noise ratio). The particle number concentration (/cm<sup>3</sup>) and the particle size distribution were measured in real-time at a frequency 2Hz.

The operating principle of the DMS500 are as follows [183]:

- The particles enter the classifier section of the instrument via a silicon tube that contains a unipolar corona charge which positively charges the particles relative to their surface area (which is relative to their size).
- Charged particles then enter the classifier alongside the sheath flow air and are repelled by the positive high voltage provided by the central electrode towards the electrometer detectors.
- The particles impact, the impaction is based on momentum and the electrical charge, which is a direct function of the particle size.
- Smaller particles have higher mobility and are more easily deflected.
- The software provided by Cambustion uses the signals detected from the detectors to calculate the particle size distribution in real time.

*b) Andersen Cascade (AC) impactor for size segregated PM<sub>10</sub>*

The Andersen cascade impactors were used to measure particulate mass emissions below 10µm (PM<sub>10</sub>). This technique was only used for high load runs (4kW generator output /~ 96% engine load), for the diesel baseline, 10 and 22% syngas (A/B & C) substitution runs as outlined in subsection 3.6.2 of this chapter. This testing was limited to high load conditions due to the limited supply of gaseous fuels.

The Andersen cascade unit comprises a pre-separator with an air inlet cone, followed by eight impaction stages and a final stage (backup filter). The pre-separator collects any particulates greater than 10µm in size. The sample exhaust gas was drawn into the top of the unit at a constant rate of 28.3 l/min (as recommended by the manufacturer) using a vacuum pump and a calibrated gas meter. The unit and any associated pipework were maintained at a temperature of 55°C, ± 5°C (as per the temperature of the DMS heated line) using an electric heating blanket/tape and lagging. A thermocouple was fitted at the top of the unit to measure and control the inlet exhaust gas temperature.

Typically, when testing for PM<sub>10</sub> mass for emission standards, the exhaust PM<sub>10</sub> is collected from diluted and cooled exhaust gas streams (around 47°C, ± 5°C). In contrast, the analysis for this thesis has deviated from the standard methods used for emission testing as the PM<sub>10</sub> mass was collected from the raw undiluted exhaust gas stream. Also, the exhaust gas was maintained at a higher temperature of 55°C. Preliminary screening experiments highlighted temperature control issues when trying to maintain the temperature at 47°C, ± 5°C for every engine load and testing condition. Increasing the temperature enabled better control across all engine testing conditions. This small increase should not affect the results as the temperature remained uniform across all the tests.

The filter paper(s) used to collect the impacted particulates were eight GF/A filter papers (Whatman Glass fibre 'A' grade), and one GF/F filter paper (Whatman Glass microfibre filter) for the backup filter; all 81mm in diameter. All the filter papers were dried to a constant weight in a desiccator before and after use for a minimum of 24 hours before the final mass was recorded. During engine testing, the exhaust sample gas was drawn in from the engine exhaust system through a stainless-steel line into the top of the inlet cone where it travelled through the impaction stages.

Each stage contains multiple precision-drilled holes. As it travels down the stages 0 to 7, the orifice velocities increase. This is due to the size of the orifices decreasing per stage. Impaction at each stage is dependent on the aerodynamic dimension. Smaller particulates are captured at the later stages, with the backup filter collecting particulates smaller than 0.4 µm.

Each test run using the Andersen impactor was tested for 45 minutes to ensure sufficient PM was collected. All experiments involving PM mass collection using the Andersen cascade impactor were analysed in duplicate for all test conditions (diesel baseline and syngas-diesel dual fuel mode combustion). The total volume of gas flow that passed through the unit was recorded per experiment using a calibrated gas meter. Table 3.8 shows the particle size distribution across the Andersen cascade impactor.

**Table 3-8 Particle size distribution of each impactor stage**

Stage	0	1	2	3	4	5	6	7	Backup
Size (µm)	>9.0	5.8-9.0	5.8-4.7	4.7-3.3	3.3-2.1	2.1-1.1	1.1-0.7	0.7-0.4	<0.4

The PM collected from stage 7 and the backup filter from the Andersen cascade experiments were analysed further. These stages were chosen for further analysis as they contained the bulk mass of the PM collected which ranged from 60 to 68% of the total PM mass (see Chapter 7, section 7.3). The characterisation analysis conducted on the collected PM mass is discussed as follows:

#### *Scanning Electron Microscope (SEM) & Energy Dispersive X-Ray (EDX)*

SEM and EDX analysis was conducted on the PM collected from the Andersen cascade impactor at the Leeds Electron Microscopy and Spectroscopy centre. The instrument used was a Hitachi SU8230: high-performance cold field emission SEM with Oxford Instrument Aztec Energy EDX system with an 80mm X-Max silicon drift detector. In terms of the EDX analysis, this technique was used to provide qualitative compositional elemental analysis. The SEM images produced were compared; the size and shape of the individual particles were studied.

#### *TGA analysis of particulates*

Proximate analysis was conducted on the PM samples collected from the Andersen testing (using the instrument NETZSCH STA 449F3, type ASCII). The PM collected from the backup filter and stage 7 was analysed. Filter paper discs, 13mm diameter in size containing the impacted PM were weighed and analysed using the following procedure:

- The sample was heated up to 100°C in an inert atmosphere of nitrogen and then held for 10 minutes. This weight loss for this section of the heating profile corresponded to the moisture content of the sample.
- Next, the sample was heated from 100°C to 550°C and held for 10 minutes; the corresponding weight loss for this stage represented the volatile organic fraction (VOF).
- The final heating stage involved changing the gas from nitrogen to air, and then was held at 550° C for 20 minutes; the corresponding weight loss for this stage represented the fixed carbon content.
- Any residual mass that remained corresponded to the ash content of the sample, this was calculated by difference.

### 3.3.3.2 Gaseous emission analysis

#### *Use of the Horiba MEXA stack gas analyser (raw emissions)*

Gaseous emissions were analysed using the Horiba MEXA-7100D automobile emission analysers which allow the analysis of numerous gases using various analytical techniques. The exhaust gases were analysed on a dry (non-condensable) basis.

The exhaust sample was drawn in from the engine exhaust system through a heated line set at 191°C. Data logging was automated using the DSG (Dynamometer Services Group) software in the control room using a dedicated computer. The data was logged every 10 seconds. NO<sub>x</sub> and NO were analysed using a chemiluminescence detector (CLD). Carbon dioxide (CO<sub>2</sub>), and carbon monoxide were analysed using Non-Dispersive Infrared Spectroscopy (NDIR). Oxygen content was measured using a paramagnetic sensor that uses Magneto-pneumatic Detection (MPD). The Total Hydrocarbons (THCs) were analysed using flame ionisation detection (FID) technique. High purity calibration gases were used for the daily calibration of the gases being analysed in the exhaust stream. Table 3.9 summarises the gases analysed, the method of detection, and the measuring and calibration range of the Horiba MEXA 7100D.

**Table 3-9 MEXA: Principles of analysis & the measuring range per gas**

<b>Component</b>	<b>Detection method</b>	<b>Measuring range</b>	<b>Calibration gas range</b>
NO/ NO <sub>x</sub>	CLD	0- 10,000 ppm	457 ppm NO, 459 ppm NO <sub>x</sub>
CO <sub>2</sub>	NDIR	0 -20 % Vol	6.93 % Vol
CO	NDIR	0 -12 % Vol	2.08 % Vol
THC's	FID	0- 50,000 ppm C	465 ppm (C <sub>1</sub> )
O <sub>2</sub>	MPD	0- 25 % Vol	Calibrated by air

#### *FT-IR Gasmet DX4000*

Gaseous emissions were also measured in real-time using the GASMET DX400 Fourier Transform Infrared (FT-IR) analyser. This analytical technique analyses wet exhaust gas using infrared radiation. During operation, the engine exhaust gas was drawn through a heated line (at 180°C), directly into the sampling unit which incorporated a glass fibre filter on entry.

Daily calibrations of the zirconia sensor were conducted by measuring the oxygen concentration inside the sampling unit. The instrument itself was zeroed daily before testing using pure high-grade nitrogen gas. Spectra were recorded after every 7 seconds for SGA, and every 20 seconds for the remaining gaseous fuels evaluated. This difference in the frequency of testing was unplanned, it arose from an operational change in the FT-IR software library used during the testing. However, this change did not affect the results generated.

Each gaseous chemical species analysed is made up of various individual types of elements and bond types/lengths. Hence, each compound will undergo molecular vibrations in the infrared region; due to its unique structure, it will have a characteristic absorption frequency. This intensity of absorption when correlated corresponds to the concentration of the compound. Infrared radiation is passed through the sample exhaust gas through the interferometer and finally to the detector. The signal is then amplified, converted, and decoded to produce a spectrum. The spectrum produced is compared to the 'Calcmel' software library database which identifies and quantifies the gas species present.

The raw emissions analysed directly from the FT-IR and MEXA (in ppm) were compared. In addition, the gaseous emissions corresponding to the methane, oxygen, CO, CO<sub>2</sub>, THC, and all NO<sub>x</sub>-related species were converted to emission index (EI) values expressed in g/kg fuel. To allow cross comparison of fuel blends, these EI values were further converted to EI values whereby they were expressed as g/MJ fuel.

Specific emissions (SE) were also calculated which were expressed as g/kWh which allowed comparison of data across engine loads. The equations used for this are discussed in subsection 3.5.9 of this chapter. Table 3.10 summarises the gas species analysed from the FT-IR analysis.

**Table 3-10 Gaseous species analysed using the FT-IR with the detection limits**

Component	Formula	Measuring unit	Calibration gas composition
Oxygen	O <sub>2</sub>	% Vol	0 - 25
Water vapour	H <sub>2</sub> O	% Vol	25
Carbon dioxide	CO <sub>2</sub>	% Vol	20
Carbon monoxide	CO	ppm	10,000
Nitrous oxide	N <sub>2</sub> O	ppm	500
Nitrogen monoxide	NO	ppm	500
Nitrogen dioxide	NO <sub>2</sub>	ppm	1,000
Sulfur dioxide	SO <sub>2</sub>	ppm	1,000
Ammonia	NH <sub>3</sub>	ppm	500
Hydrogen chloride	HCl	ppm	500
Hydrogen fluoride	HF	ppm	100
Methane	CH <sub>4</sub>	ppm	500
Ethane	C <sub>2</sub> H <sub>6</sub>	ppm	100
Ethylene/Ethene	C <sub>2</sub> H <sub>4</sub>	ppm	100
Propane	C <sub>3</sub> H <sub>8</sub>	ppm	100
Hexane	C <sub>6</sub> H <sub>14</sub>	ppm	100
Formaldehyde	CHOH/HCHO	ppm	200
Benzene	C <sub>6</sub> H <sub>6</sub>	ppm	100
Acetylene	C <sub>2</sub> H <sub>2</sub>	ppm	200
Acetic acid	C <sub>2</sub> H <sub>4</sub> O <sub>2</sub>	ppm	100
Furfural	C <sub>5</sub> H <sub>4</sub> O <sub>2</sub>	ppm	100
Terpinen-4-ol	C <sub>10</sub> H <sub>18</sub> O	ppm	100
Hydrogen cyanide	HCN	ppm	100
Ethanol	C <sub>2</sub> H <sub>6</sub> O	ppm	100
* <sup>1</sup> NO <sub>x</sub> as NO <sub>2</sub>		ppm	
* <sup>2</sup> N Species		ppm	
* <sup>3</sup> VOCs		ppm	
* <sup>4</sup> Non methane VOCs		ppm	

\*<sup>1</sup> NO<sub>x</sub> as NO<sub>2</sub> represents the sum of NO<sub>2</sub> and NO.

\*<sup>2</sup> N species reports the sum of N<sub>2</sub>O, NO, NO<sub>2</sub> and Ammonia

\*<sup>3</sup> Volatile organic compounds (VOCs) were calculated as the sum of the concentration of the following species: methane, ethane, ethylene, propane, hexane, formaldehyde, benzene, acetylene, furfural, terpinene-4-ol, and ethanol.

\*<sup>4</sup> Non-methane VOCs are reported as the concentration of the VOCs minus the methane concentration.

### **3.4 Health and Safety**

During the testing of the syngas/biogas, in addition to the existing gas monitoring detectors present, additional CO and H<sub>2</sub> portable monitors were used in the lab and the control room. The portable monitors were Crowcon Gasman rechargeable units capable of detecting within the ranges of 0 - 2,000 ppm of hydrogen, and 0-1,500 ppm of carbon monoxide.

### **3.5 Data Analysis**

#### **3.5.1 Conversion of genset output to engine output power**

The current lab setup shows the power output (as controlled by the load bank remote) for the overall generator output. This is not the actual engine power as losses have occurred which are associated with the alternator. The generator used (MG6000 SSY,6 kVA) is coupled with a resistive load bank with a power factor (PF) of one. The PF of this alternating current power system represents the ratio of the real power, expressed as Kilowatt-electric (kWe) flowing to the load versus the apparent power in kilo-volt-ampere (kVA) in the electrical circuit [184]. However, the difference in power output between the generator and the engine is due to the efficiency of the alternator. To determine the actual engine power output, the generator power is divided by the alternator efficiency, this alternator efficiency value is load dependent.

For the current alternator in use in the lab, model type: Linz E1C10M H [182], only a partial efficiency data set was provided from the manufacturer, that being for full and 75% load. To determine the alternator efficiency values for the remaining engine loads (50 and 25%), the full efficiency dataset was obtained from the same manufacturer for a similar-size alternator with matching characteristics [185].

This full dataset (of engine load versus alternator efficiency) was studied; in particular, the trends between the coefficient data for 50, and 25%. From this, the data for the missing alternator efficiency corresponding to engine loads of 50, and 25% was generated. This full data set was then plotted, and polynomial regression was conducted. This curve was then used to determine the alternator efficiency values for the experimental data.

As the data fitting was done for a minimum engine load of 25%, the lowest engine experimental load evaluated was 21%, hence there is a slight gap in the experimental data versus the modelled data.

Fig. 3.4 depicts the calculated efficiency data from this regression analysis, alongside experimental data values plotted which indicate a good fit.

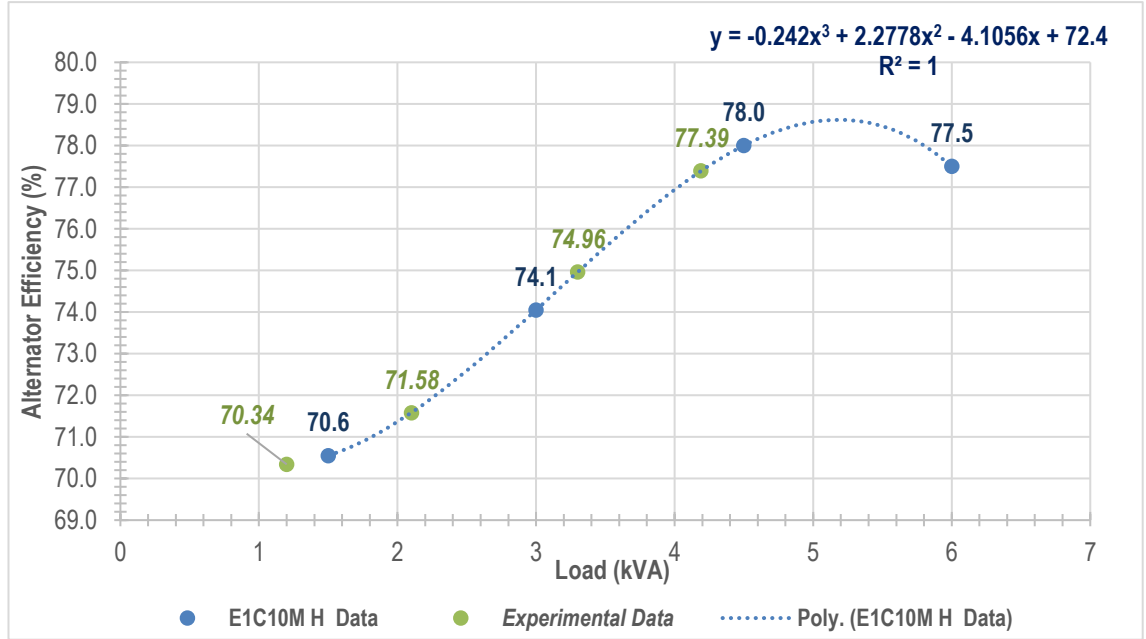


**Figure 3-4 Regression analysis results for the alternator efficiency calculations at various kVA values**

Hence, all subsequent calculations, (BSFC, BTE, AFR, et cetera), are based on the calculated engine load (kW) after accounting for the alternator efficiency at the load used.

### 3.5.2 Brake Thermal Efficiency (BTE)

The brake thermal efficiency (BTE in %) for dual fuel mode was calculated using Eq. 3.1, and the BTE for diesel baseline was calculated using Eq. 3.2.

$$BTE (\%) = \frac{BP}{m_{pd} \times LHV_d + m_g \times LHV_g} \times 100 \quad (3.1)$$

$$BTE (\%) = \frac{BP}{m_d \times LHV_d} \times 100 \quad (3.2)$$

Where  $m_{pd}$  is the mass flow rate of pilot diesel in dual fuel mode (kg/s), the  $m_d$  is the mass flow rate of diesel for diesel baseline (kg/s),  $m_g$  is the mass flow rate of the gaseous fuel (kg/s), BP is the engine brake power output (kW),  $LHV_d$  is the LHV of diesel, and  $LHV_g$  is the LHV of the gaseous fuel (both in KJ/kg).

### 3.5.3 Brake Specific Fuel Consumption (BSFC)

The brake specific fuel consumption (BSFC) for the diesel baseline was calculated using Eq. 3.3.

$$BSFC = \left( \frac{m_d}{BP} \right) \quad (3.3)$$

In Eq. 3.3, the BSFC is the brake specific fuel consumption for diesel baseline (g/kWh),  $m_d$  is the mass flow rate of diesel for diesel baseline (g/h), and BP is the engine brake power output (kW).

### 3.5.4 Brake Specific Energy Consumption (BSEC)

The brake specific energy consumption (BSEC in MJ/kWh) was calculated on an energy basis to allow values to be cross compared across the various gas/diesel blends evaluated. The BSEC for dual fuel mode was calculated using Eq. 3.4, and for diesel baseline using Eq. 3.5.

$$BSEC_{dual\ fuel} = \frac{(m_{pd} \times LHV_d) + (m_g \times LHV_g)}{BP} \quad (3.4)$$

$$BSEC_{diesel} = \frac{(m_d \times LHV_d)}{BP} \quad (3.5)$$

In Eq. 3.4, the  $m_{pd}$  is the mass flow rate of pilot diesel in dual fuel mode (kg/h),  $LHV_g$  is the calculated LHV for the gaseous fuel (MJ/kg),  $m_g$  is the mass flow rate of the gas (kg/h),  $LHV_d$  is the LHV of diesel (MJ/kg), and BP is the engine brake power output (kW).

In Eq. 3.5, the  $m_d$  is the mass flow rate of diesel for the baseline (kg/h),  $LHV_d$  is the LHV of diesel (MJ/kg), and BP is the engine brake power output (kW).

The mass flow rate of the gaseous flow rate was calculated by multiplying the volumetric gas flow rate with the corresponding density values which have been calculated as shown in Table 3.4.

### 3.5.5 Air to Fuel Ratio

During all of the analysis, the MEXA 7100D contained standard diesel fuel parameters as inputs, thus enabling the instrument to calculate the *Air to fuel ratio* (AFR) value using the inbuilt software program based on the Bretttschneider/Spindt equation [186]. As the mass of the air intake was not measured directly, the AFR for dual fuel runs ( $AFR_{df}$ ) was calculated.

First, the mass of the direct air ( $m_{DBL\ air}$ ) was calculated using diesel baseline data at each condition using Eq. 3.6.

$$m_{DBL\ air} = (AFR_{DBL} \times m_d) \quad (3.6)$$

In Eq. 3.6, the  $m_{DBL\ air}$  is the mass of the air intake in pure diesel mode (kg/h),  $AFR_{DBL}$  is the air to fuel ratio as calculated by the MEXA instrument for diesel baseline, and  $m_d$  is the mass flow rate of the diesel used for diesel baseline (kg/h).

Next, it was assumed that the addition of the gaseous fuel would directly displace the air, thus reducing the mass of air in dual fuel mode. The mass of the air intake in dual fuel mode was calculated using Eq. 3.7.

$$m_{df\ air} = (m_{DBL\ air} - m_g) \quad (3.7)$$

Where,  $m_{df\ air}$  is the mass of air intake in dual fuel mode (kg/h),  $m_{DBL\ air}$  is the mass of air intake in pure diesel mode (kg/h), and  $m_g$  is the mass flow rate of gas (kg/h). The dual fuel air to fuel ratio ( $AFR_{df}$ ) was calculated using Eq. 3.8. The dual fuel mass was taken as the combined mass of both fuels.

$$AFR_{df} = \left( \frac{m_{df\ air}}{m_{pd} + m_g} \right) \quad (3.8)$$

Where,  $AFR_{df}$  is the air to fuel ratio by mass in dual fuel mode,  $m_{df\ air}$  is the mass of air intake in dual fuel mode (kg/h),  $m_g$  is the mass flow rate of gas (kg/h), and  $m_{pd}$  is the mass flow rate of pilot diesel in dual fuel mode (kg/h).

### 3.5.6 Diesel displacement rate (Z)

The diesel displacement rate (Z) was calculated using Eq. 3.9. Where,  $m_d$  is the mass flow rate of diesel for diesel baseline runs (kg/h), and  $m_{pd}$  is the mass flow rate of pilot diesel in dual fuel mode (kg/h).

$$Z (\%) = \frac{m_d - m_{pd}}{m_d} \times 100 \quad (3.9)$$

### 3.5.7 Equivalence ratio ( $\phi$ )

The  $\Phi$  in dual fuel mode was calculated using Eq. 3.10, and for DBL this was calculated using Eq. 3.11.

$$\phi_{df} = \frac{(m_{pd} \times AFR_{stoich-diesel}) + (m_g \times AFR_{stoic-gas})}{m_{df\ air}} \quad (3.10)$$

$$\phi_{DBL} = \frac{m_d \times AFR_{stoich-diesel}}{m_{DBL\ air}} \quad (3.11)$$

In Eqs. 3.10- 3.11,  $\phi_{df}$  is the equivalence ratio in dual fuel mode,  $\phi_{DBL}$  is the equivalence ratio for diesel baseline,  $m_{pd}$  is the mass flow rate of pilot diesel in dual fuel mode (kg/h),  $m_g$  is the mass flow rate of the gaseous fuel (kg/h),  $m_d$  is the mass flow rate of diesel used for diesel baseline (kg/h). The  $AFR_{stoich-diesel}$  is the stoichiometric air to flow mass ratio of diesel, and the  $AFR_{stoich-gas}$  is the stoichiometric air to flow mass ratio of gaseous fuel. The  $m_{df\ air}$  is the mass of the air intake in dual fuel mode, and  $m_{DBL\ air}$  is the mass of the air for the diesel baseline.

The  $AFR_{stoich-gas}$  data was calculated for each syngas blend whereby one mole of syngas was used as the basis. The following values were used: SGA (1.316), SGB (1.527), SGC (1.763), biogas (4.574), and diesel (14.6).

### 3.5.8 Peak pressure and ignition delay

The average peak pressure ( $P_{max}$ ) was determined from the pressure crank angle (P-CAD) plots generated from one hundred cycles of P-CAD data.

#### *Start of Combustion (SoC)*

The SoC was determined from the 1<sup>st</sup> and 2<sup>nd</sup> derivative plots of the P-CAD average data. The SoC was identified at the point whereby the pressure was the minimum of the 2<sup>nd</sup> derivative curve and the start point of the continuous rise in pressure from the first derivative curve, as done by other researchers [116, 117], as illustrated in Fig. 3.5.

#### *Ignition Delay (ID)*

The ID was calculated in CAD and milliseconds (ms). The ID in CAD was calculated by using Eq. 3.12, by adding together the identified SoC crank angle to the Start of Injection (Sol) crank angle. The ID was expressed in milliseconds (ms) using Eq. 3.13 with the inputs being the engine speed (in RPM) and the ID (in CAD) [116].

$$ID\ (CAD) = SoC\ (CAD) + SoI\ (13.5^\circ\ bTDC) \quad (3.12)$$

$$ID\ (ms) = \frac{ID\ in\ CAD}{RPM \times \left(\frac{min}{60\ s}\right) \times \frac{360^\circ}{rev}} \times 1,000 \quad (3.13)$$

An example of a P-CAD plot generated during dual fuel combustion at 4kW/full engine load is shown in Fig. 3.5; the SoC is identified at seven CAD.

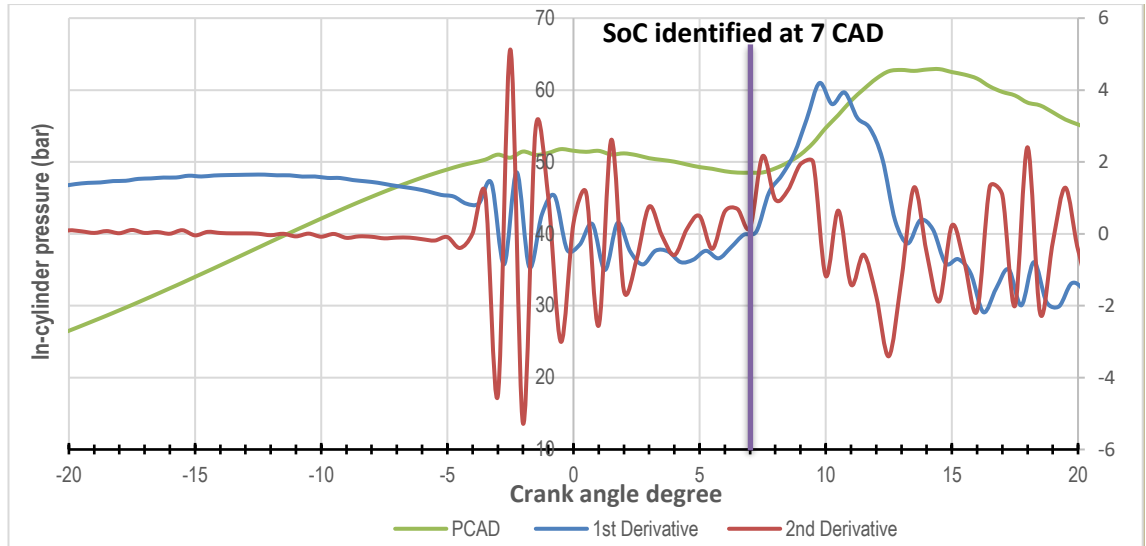


**Figure 3-5 A typical P-CAD plot generated at full load during dual fuel combustion with the identified SoC**

### 3.5.9 Emission Index for gaseous emissions

Raw gaseous emission was measured using the MEXA (in % or ppm). This data for each test condition was converted into emission index values (EI) which enable emission comparisons to be made across similar-sized engines. The EI (expressed as g/kg fuel) was calculated using Eq. 3.14 [187].

$$EI = k_{gas} \times C_i \times (1 + AFR) \times 1,000 \quad (3.14)$$

In Eq. 3.14,  $k_{gas}$  represents the conversion coefficient of the gaseous pollutant being analysed. This is the ratio of the molecular weight of the gaseous emission/pollutant over the exhaust gas molecular weight. These coefficients for the gaseous pollutants analysed are fixed values:  $k_{CO} = 0.971$ ,  $k_{CO_2} = 1.526$ ,  $k_{THC} = 0.555$  (HC measured as methane equivalent),  $k_{NO_x} = 1.595$  (all  $NO_x$  is counted as  $NO_2$ ),  $N_2O = 1.526$ , and  $CO_2 = 1.526$ .

The  $C_i$  is the concentration of a gaseous pollutant (in ppm or %). If the concentration is measured in ppm, the equation is multiplied by  $10^{-6}$ , if measured in % then the equation is multiplied by  $10^{-2}$ . The AFR is either  $AFR_{DBL}$  or  $AFR_{df}$  depending on if this data is calculated for the diesel baseline or dual fuel mode.

The EI (g/kg fuel) was converted further and expressed in units of g/MJ fuel by dividing the existing calculated EI value (in g/kg fuel) by the LHV of the dual fuel, as shown in Eq. 3.15.

$$EI (g|MJ \text{ fuel}) = \left( \frac{EI \text{ in } \frac{g}{kg} \text{ fuel}}{LHV_{df \text{ blend}}} \right) \quad (3.15)$$

In Eq. 3.15, EI is the emission index value for each pollutant (g/MJ fuel), the EI is the emission index value for each pollutant (g/kg fuel), and the LHV<sub>df blend</sub> is the LHV of the combined fuel i.e., the pilot diesel and gas (MJ/kg). The LHV<sub>df blend</sub> was calculated using Eq. 3.16.

$$LHV_{df \text{ blend}} = \left( \frac{m_{pd}}{m_{pd} + m_g} \times LHV_d \right) + \left( \frac{m_g}{m_g + m_{pd}} \times LHV_g \right) \quad (3.16)$$

In Eq. 3.16, the LHV<sub>df blend</sub> is the combined LHV of the pilot diesel and the gaseous fuel (MJ/kg). The m<sub>pd</sub> is the mass flow rate of pilot diesel in dual fuel mode (kg/h). The m<sub>g</sub> is the mass flow rate of the gaseous fuel (kg/h), the LHV<sub>d</sub> is the LHV of diesel (MJ/kg), and LHV<sub>g</sub> is the LHV of the gaseous fuel (MJ/kg).

### 3.5.10 Specific Emissions for gaseous emissions

To compare the emission data across engine loads, the EI data was converted and expressed as specific emission data (SE), in g/kWh. This was done using Eq. 3.17 whereby EI is the emission index value for each pollutant (in g/MJ fuel), and BSEC is the brake specific energy consumption for dual fuel mode (MJ/kWh).

$$SE = EI \left( \frac{g}{MJ} \right) \times BSEC \quad (3.17)$$

### 3.5.11 Particulate Matter Emission Index (PM EI)

The PM mass collected from the PM<sub>10</sub> analysis using the Andersen impactor was expressed in g/m<sup>3</sup> by dividing by the total mass collected by the exhaust gas flow rate measured per experiment. This PM mass concentration is abbreviated as C<sub>par</sub>. This PM mass concentration was then expressed as a 'particulate matter emission index' (PM EI) using Eq. 3.18 [188] as g/kg fuel.

$$PM \text{ EI} = \frac{C_{par}}{1.18} \times (1 + AFR) \times 10^{-3} \quad (3.18)$$

In Eq. 3.18, the C<sub>par</sub> value is divided by a factor of 1.18 which is the exhaust density (at the pressure and temperature of the constant volume flow meter) [188]. The AFR is either AFR<sub>DBL</sub> or AFR<sub>df</sub> depending on if this data is calculated for the diesel baseline or dual fuel mode.

The PM EI (g/kg fuel) was converted further and expressed as PM EI in units of g/MJ fuel. This was done by dividing the existing calculated PM EI value (in g/kg fuel) by the LHV of the dual fuel, as shown in Eq. 3.19.

$$PM EI (g/MJ) = \left( \frac{PM EI \text{ in } \frac{g}{kg} \text{ fuel}}{LHV_{df \text{ blend}}} \right) \quad (3.19)$$

In Eq. 3.19, PM EI is the emission index value for the mass of the PM collected (g/MJ fuel), and PM EI is the emission index value of the PM mass (g/kg fuel). The  $LHV_{df \text{ blend}}$  is the LHV of the pilot diesel and gas (MJ/kg) which was calculated as previously shown using Eq. 3.16.

### 3.5.12 Particulate Matter Specific Emissions (PM SE)

The PM EI data was converted and expressed as specific emission data (PM SE), in g/kWh. This was done using Eq. 3.20 whereby the BSEC is the brake specific energy consumption for dual fuel mode (MJ/kWh).

$$PM SE = PM EI \left( \text{in } \frac{g}{MJ} \right) \times BSEC \quad (3.20)$$

### 3.5.13 Methane slippage

The methane slippage, i.e., the % of methane that had passed through into the exhaust, unburnt, versus the input, was calculated.

To calculate the mass rate of the methane added, the ideal gas law was applied whereby it was assumed that one mole of an ideal gas occupied 24.45 litres at standard ambient temperature and pressure (at 25°C and one atmosphere). The methane volume fraction of all the syngas blends was 0.04, and for biogas was 0.50 (see Table 3.3). The mass rate of methane added (in g/min) was calculated using Eq. 3.21.

$$CH_4 \text{ input mass rate } (g/min) = \left( \frac{V_g \times \text{vol fraction of } CH_4}{24.45} \right) \times 16.04 \quad (3.21)$$

In Eq. 3.21,  $V_g$  is the volumetric flow rate of the gaseous fuel added (l/min).

The volume fraction of the  $CH_4$  is based on the composition of the gaseous fuel (see Table 3.3), 24.45 is the conversion factor when applying ideal gas law (at 25°C and one atm), and 16.04 is the molecular weight of methane.

Next, the concentration of the methane found in the exhaust gas was calculated (in g/m<sup>3</sup>) using Eq. 3.22.

$$\mathbf{CH_4\ conc. (g/m^3) = \left( \frac{C_i\ for\ methane}{1,000} \right) \times \frac{16.04}{24.45}} \quad (3.22)$$

In Eq. 3.22, C<sub>i</sub> is the methane concentration as measured by the FT-IR (in ppm), 24.45, and 16.04 are the conversion factors used, as described earlier for use in Eq. 3.21.

To calculate the next stage, the mass of the total exhaust flow was necessary. This was calculated by applying the law of conservation of mass whereby it can be assumed that the mass of the exhaust gas in dual fuel mode would be equal to the sum of all the reactants: the diesel fuel, gaseous fuel, and the air intake (minus the mass displaced during dual fuel addition). For the standard diesel baseline runs, this was taken as the sum of the mass of the diesel and the air intake.

The mass of the exhaust flow (in kg/h) was divided by the density of the diesel exhaust (using a value of 1.2 [188]) to calculate the volumetric exhaust flow, as shown in Eq. 3.23.

$$\mathbf{Exhaust\ flow\ rate\ (m^3/h) = \frac{mass\ of\ exhaust\ flow}{1.2}} \quad (3.23)$$

The exhaust flow rate was then converted into m<sup>3</sup>/min by dividing this by 60 as shown in Eq. 3.24.

$$\mathbf{Exhaust\ flow\ rate\ (m^3/min) = \frac{Exhaust\ flow\ rate\ (m^3/h)}{60}} \quad (3.24)$$

To calculate the methane mass rate present in the exhaust gas, the concentration of the methane found in the exhaust gas (as calculated by Eq. 3.22) was multiplied by the exhaust gas flow rate in m<sup>3</sup>/min (as determined using Eq.3.24).

The equation for the methane output concentration rate is shown in Eq. 3.25.

$$\mathbf{CH_4\ output\ mass.\ rate\ (g/min) = CH_4\ conc.\ (g/m^3) \times Exhaust\ flow\ rate\ \left( \frac{m^3}{min} \right)} \quad (3.25)$$

Finally, once both the methane concentration rate (in g/min) had been calculated for the input (see Eq. 3.21), and for the output, (see Eq. 3.25), the % methane slippage was calculated using Eq. 3.26 as shown below.

$$\% \text{CH}_4 \text{ slippage} = \frac{\text{CH}_4 \text{ output mass. rate}}{\text{CH}_4 \text{ input mass. rate}} \times 100 \quad (3.26)$$

## 3.6 Experimental procedure

### 3.6.1 Preliminary screening tests

Initial screening tests were conducted using SGA at a range of % 'gas energy fraction' (GEF) substitution values of diesel to determine the best range for testing. The limiting factors assumed when calculating the maximum amount of % SGA substitution viable was based on the minimum diesel fuel consumption achievable (based on the BSFC for diesel at idle load running conditions). These preliminary screening experiments were conducted as trial and error, whilst observing various engine performance parameters.

The SGA screening testing was conducted at various load outputs at the following % GEF diesel substitution values of approximately 5, 10, 14, 22, 38, and 45%. Tests ran at 5% did not show a reduction in diesel fuel consumption. From these preliminary screening tests, future experimental testing conditions were defined.

The % gas energy fraction value (% GEF) of diesel was energy-based and was calculated using Eq. 3.27.

$$\text{GEF} (\%) = \frac{(m_g \times \text{LHV}_g)}{(m_{pd} \times \text{LHV}_d + m_g \times \text{LHV}_g)} \quad (3.27)$$

Where in Eq. 3.27,  $m_g$  is the mass flow rate of the gaseous fuel (kg/h),  $\text{LHV}_g$  is the calculated LHV for the gaseous fuel (MJ/kg),  $\text{LHV}_d$  is the LHV of diesel (MJ/kg), and  $m_{pd}$  is the mass flow rate of pilot diesel in dual fuel mode (kg/h).

### 3.6.2 List of experimental tests conducted

The experiments ran in terms of generator output load (kW), % engine load, and % syngas/biogas energy fraction substitution value, are summarised in Table 3.11.

**Table 3-11 Summary of the experiments conducted and the test conditions**

Generator load (kW)	% Engine load	% Syngas/biogas energy fraction substitution				
		0/DBL	10	22	38	46
4	96	0/DBL	10	22	38	46
3	77	0/DBL	10	22	38	
2	53	0/DBL	10	22		
1	30	0/DBL	10	22		

Experiments using high ‘% GEFs’ were only evaluated at high loads, as typically a genset engine is run for better efficiency at higher loads. Also, experiments using a % GEF of greater than ~22% were not conducted at lower output loads, this was due to a limited supply of syngas/biogas.

The PM<sub>10</sub> Andersen particulate collection testing was only conducted for 96% engine load (4kW) using 10 and 22 % GEF of SGA, SGB, and SGC. Full engine load, (~96% engine load) condition was selected for PM<sub>10</sub> as this represents typical genset running conditions and higher BTE values. GEF values of 10 and 22% were explored only using the Andersen impactor due to the limited supply of syngas. Longer run times are needed for this analysis to collect a sufficient mass of particulate matter.

The experimental range of the % GEF values used, and the generator output/engine load are shown in Table 3.12. The PM<sub>10</sub> was not analysed for dual combustion for biogas-diesel due to time limitations and economic constraints.

**Table 3-12 Summary of the experimental testing ranges (for engine load and % GEF)**

The testing range for all gases				
<b>Generator output load (kW)</b>	4.20 ± 0.2	3.3 ± 0.20	2.2 ± 0.2	1.20 ± 0.2
<b>Approx. Engine load (%)</b>	96	77	53	30
<b>% GEF Testing range</b>	*10.0 ± 1.0	23 ± 2	39 ± 2.5	46.5 ± 2.5
<b>Average % GEF value used</b>	10	22	38	46

*\*Except for biogas at an engine load of ~30%. The gas flow meter was unable to deliver a gas flow rate of <4 l/min as required, hence the minimum flow rate used equated to a GEF of ~12% in this case, rather than the required 10%.*

### 3.6.3 Lab testing procedure

Before the testing of any syngas/biogas, initial baseline tests were conducted to determine diesel baseline values. These were conducted in each case before experimenting with any syngas/biogas, usually commencing with lower engine loads. This generated four diesel baseline data sets (SGA, SGB, SGC, and BG), This was done due to the stop/start nature of the lab experimental timeline. Long delays were experienced in between testing of different gas types due to issues with instrumentation, including delayed calibration requirements because of Covid-19. Each experimental condition typically was repeated three times (twice as a minimum) for accuracy.

Before conducting any tests, the engine was warmed up using red diesel fuel until the engine oil temperature reached a minimum of 50°C. The analytical instruments in use (DMS/MEXA and FT-IR), were warmed up and calibrated as necessary according to the operating instructions in preparation for testing. Once the engine was warm, the required testing load was selected using the remote controller. The engine was allowed to stabilise at the selected load for a minimum of 5 minutes whilst using diesel.

Once the engine was deemed stable, testing with syngas/biogas commenced. Datalogging of the LabView software, MEXA, FT-IR, DMS500, and PM<sub>10</sub> analysis (if being conducted) was commenced. For every % GEF assessed, the typical protocol followed once data logging at been started was as follows:

- The engine was run using solely diesel to generate 'diesel baseline' data at the required load for a minimum of 10 minutes. Diesel baseline data was generated in terms of ID,  $P_{max}$ , BSFC, AFR, FT-IR, MEXA, load bank, and DMS.
- After this period, the clock time was recorded, and the gaseous fuel addition commenced.
- The engine was allowed to equilibrate for 3-5 minutes in dual fuel mode at the inputted gas flow. The data generated during this period was not used for any analysis from any instrument.
- After 3-5 minutes (or when the engine and related instrumentation had stabilised), the clock time was recorded, and the engine ran in dual fuel mode for a further 10 minutes. The data generated here forth was used for data analysis.

- Between every increase/change in the gas flow rate, the engine was allowed to equilibrate for a minimum of 3-5 minutes in dual fuel mode at the inputted gas flow. Again, this part of the data was not analysed analysis from any instrument.
- At every load change, the engine was allowed to stabilise at that power output for ~5 minutes. Once deemed stable, data logging was commenced using diesel only to provide a diesel reference point for every test condition before any gaseous fuel addition.

## **Chapter 4 An Assessment of the Energy and Power Generation Potential from Biomass Residues**

The first section of this chapter looks at the methodology used for the quantification of the raw energy potential from the four biomass residues streams selected per country. From this, the electrical generating potential is calculated using a series of assumptions and equations. The second half of this chapter reports the findings of the assessment of the energy & power generation potential from the biomass residues for both countries.

This paper published titled '*Increasing Access to Electricity: An Assessment of the Energy and Power Generation Potential from Biomass Waste Residues in Tanzania*' was based on the dataset for the base year of 2018 using the same methodologies as described in this chapter [59]. The candidate, (Z. Aslam) was the lead author of this paper. Since this publication, more current data became available, hence this thesis contains more up to date results using the base year of 2019.

### **4.1 Methodology for the biomass resource assessment**

The two countries of interest chosen for quantification purposes were the United Republic of Tanzania (referred to as just Tanzania in this study), and Uganda. These countries represent some of the least electrified Sub-Saharan countries in the world [12]. This work is part of two funded projects (as mentioned earlier in Chapter 2) that involved collaborative research in this region. The four developing countries of focus for these projects were: The Republic of Congo, Tanzania, Uganda, and Indonesia. For this study, Tanzania and Uganda were selected as there was more data available in comparison to the remaining two.

Firstly, the methodology used to quantify the gross energy potential from the biomass residues from both countries is described. Lastly, the methodology used to calculate the net electrical generating potential from these waste streams is described. For this study, the year 2019 dataset was chosen as the base year as it represented the most recent year where a complete data set was available. This whole process is summarised using Fig. 4.1.

### 4.1.1 Quantification of the gross energy potential

The biomass waste considered for this study was from the following streams: agricultural, forestry, livestock, and urban human waste. This sub-section discusses the methodology used to quantify the raw energy potential of each waste stream.

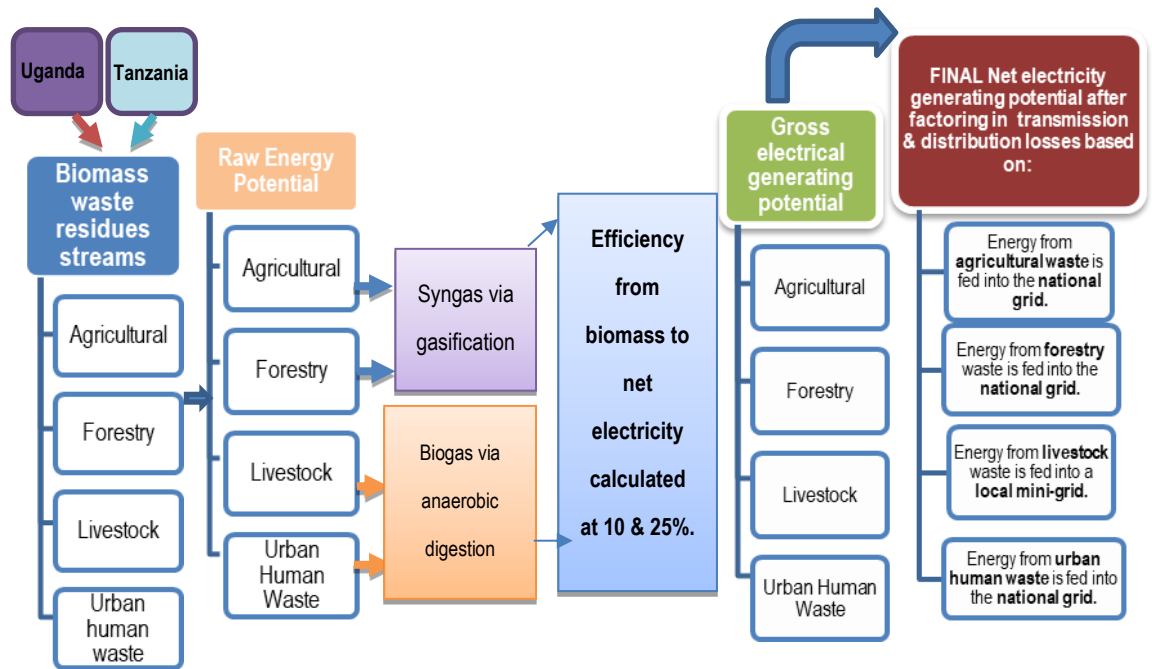


**Figure 4-1 A visual summary of the biomass resource assessment**

#### 4.1.1.1 Agricultural residues

For this calculation, values for the residue to product ratio (RPR), moisture content (MC), fraction availability (FA), and lower heating values (LHVs) were obtained for the crops of interest [189]. The RPR is dependent on many variables which include processing and harvesting techniques, type/variety of the crop, growing conditions such as the amount of water, nutrients, and fertiliser used, et cetera. Hence, the values quoted in the open literature vary from study to study. As with other biomass assessment studies available in the open literature, the more commonly used figure from the literature was used. Furthermore, not all the agricultural residues produced can be used or are available for bioenergy purposes due to competing uses such as animal bedding, fodder, fertiliser, briquette manufacture, et cetera. Again, literature sources quote variable figures for the % availability or a FA factor. For this study, the most common/utilised FA figure for this region was used.

To calculate the energy potential of these residues, data from the FAO database was collected for the base year of 2019 [190]. Some crops have been excluded as either small quantities were produced, insufficient information was available in the literature for the values of RPR, MC, FA, LHV, or lack of information regarding the extraction methodology (for oilseed crops).

Agro-based woody crop residues have also been excluded such as pruning's from various trees. The data used for calculations for the energy potential arising from key agricultural, perennial plantation and oilseed crops are shown in Tables 4.1 to 4.3. For reference, sisal is a plant that yields a tough fibre that has a myriad of uses which include textiles and the construction industry.

**Table 4-1 Perennial plantation crop residue data**

Crop	Type	RPR	FA	MC (%)	LHV (MJ/kg)
Cashew	Husks	2.10 [51, 191]	0.17 [51]	6.5 [51, 191]	14.9 [51, 191]
Cocoa	Dry pods	150kg/ha [192, 193]	0.9 [46, 192, 194]	16.1 [195]	15.12 [46, 192, 194]
Coffee	Husks	0.25 [51, 191]	1.0 [51]	15 [191, 193]	12.38 [191, 193]
Coconut	Husks	0.419 [191, 193]	0.884 [48]	10.3 [191, 193]	18.62 [191, 193]
Coconut	Shells	0.12 [191, 193]	0.75 [46, 191, 196]	8.7 [191, 193]	18.09 [191, 193]
Oil, Palm	Shell	0.065 [193, 197]	0.625 [48]	10 [193, 197]	18.83 [193, 197]
Oil, Palm	Fibre	0.13 [193, 197]	0.80 [46, 192, 197]	40 [193, 197]	11.34 [193, 197]
Oil, Palm	Empty bunches	0.23 [193, 197]	0.614 [48]	50 [193, 197]	8.16 [193, 197]
Soybean	Straw	2.5 [191, 193]	0.767 [48]	15 [191, 193]	12.38 [191, 193]
Soybean	Pods	1 [191, 193]	0.767 [48]	15 [191, 193]	12.38 [191, 193]
Sorghum	Straw	1.25 [191, 193]	0.766 [48]	15 [191, 193]	12.38 [191, 193]
Seed cotton	Stalk	3.743 [46, 191]	0.8[198]	12 [46, 191]	13.07 [48]
Sisal	Pulp	24 [51, 191, 199]	1[51]	91 * [51, 191]	14.4 [51, 191]
Sisal	Ball/fibre	3.55 * [47]	1 ** [51]	71 ***[199]	14.4 ** [51, 191]

\* Average value used. \*\* Assumed as per sisal pulp. \*\*\* Assumed (by difference).

**Table 4-2 Agricultural crop residue data**

Crop	Type	RPR	FA	MC (%)	LHV (MJ/kg)
Cassava	Stalks	0.062 [191, 193, 200]	0.2 [46, 201]	15 [191, 193]	17.5 [191, 193]
	Peelings	0.25 [200]	0.3 [200]	50 [193]	10.61 [200]
Groundnuts including shells	Shells	0.477 [191, 193]	1.0 [200]	8.2 [191, 193]	15.66 [191, 193]
	Straw	2.3 [193, 200]	0.5 [46, 202, 203]	15 [193]	14.4 [200]
Maize	Straw/stalk	2.0 [46, 193, 202]	0.7 [46, 193, 202]	15 [46, 193, 202]	19.66 [46, 193, 202]
	Cob	0.273 [191, 193]	0.863[48]	7.53 [191, 193]	16.28 [191, 193]
	Husk	0.2 [46, 193, 200, 204]	0.6 [46, 200, 204]	11.11 [46, 200, 204]	15.56 [46, 200, 204]
Millet	Straw/stalk	1.75 [191, 193]	0.8 [46, 191]	15 [191, 193]	12.39 [191, 193]
Rice, paddy	Straw	1.757 [191, 193]	0.684 [48]	12.71[191, 193]	16.02 [191, 193]
	Husk	0.267 [191, 193]	1.0 [48]	12.37 [191, 193]	19.33 [46, 191]
Sugar	Top & leaves	0.30 [193, 205]	0.986 [48]	10 [46, 205]	15.81[46, 193, 205]
	Bagasse	0.29 [191, 193]	0.8 [46, 191]	50 [46, 191, 201]	18.10 [191, 193]

**Table 4-3 Oilseed crop residue data**

Oilseed Crop	% Oil from Seed	Waste Type	Waste (based on % of seed/bean)	LHV (MJ/kg)
Sesame	50 [206]	Cake	35 * [207]	9.54 ** [208-210]
		Hull	15 [207, 211]	18.22 [212]
Cotton	12 [198]	Cake	50 [198]	18.6 [213]
		Hull	26 [198]	18.01 [214, 215]
Sunflower	40 [216]	Cake	35 [217]	15.86 [216]
		Hull	25 [217]	19.5 [218]
Soyabean	18.4 [219]	Meal	57.4 [219]	15.4 [220]

\* Assumed (by difference). \*\* Average value calculated from the sources.

The energy potential of the agricultural residues ( $EP_{\text{residue}}$ ) was calculated using the method by Bhattacharya et al. [221] as shown in Eqs. 4.1 and 4.2. In Eq. 4.1, ARG is the amount of residue generated annually on a dry basis ( $\text{t yr}^{-1}$ ), and AH is the annual harvest of the crop or product (t). In Eq. 4.2, the  $EP_{\text{residue}}$  represents the total energy potential of each residue ( $\text{J t}^{-1}$ ), the sum of the SAF and EUF correlates to the fractional availability, whereby SAF represents the surplus availability factor, and the EUF represents the energy use factor. Both factors are dimensionless.

$$ARG = \sum(RPR \times AH) \quad (4.1)$$

$$EP_{residue} = ARG \times (SAF + EUF) \times LHV_{residue} \quad (4.2)$$

#### 4.1.1.2 Forestry residues

The logging industry produces significant residues, some of which are considered waste and are usually left to decompose. Some of the forestry residues have competing uses and are therefore unavailable for bioenergy purposes. Thus, a fraction availability factor (FA) is applied when carrying out the potential energy calculations as quoted in the literature [46, 193]. The energy potential was considered from the forestry industry residues using production data from the FAO database [222].

This data from the FAO database is quoted in volume (solid volume), and for the energy potential calculations, a mass value is required. Thus, to convert into mass, a basic density value for each type of residue stream was required. The basic density figure for the residues arising from the solid wood and plywood was calculated based on an oven-dried (od) weight over a green volume.

This average basic density was calculated based on the following facts for Tanzania [223]:

- The most important industrial plantation species are various species of pines, cypress, eucalyptus, and teak.
- Commercial wood (~85%) is dominated by softwoods.
- Softwood plantations cover approximately 85% of the gross plantation area which is dominated by various species of pines.
- The remainder (15%) is assumed to be made of various hardwood species.

Thus, an average figure for the overall basic density was calculated using known density values of the tree species of interest present in Tanzania [223]. These density values are shown in Appendix A, Tables A.1 & A.2 [224-243].

The average figure calculated for the basic density of solid wood available in Tanzania was 471 kg/m<sup>3</sup>, this was based on a ratio of 0.85:0.15 being applied (of softwood to hardwoods).

For Uganda, the average basic density was calculated based on the following:

- According to Kaboggoza [244], at the end of 2010, the government owned 23% of forest plantations with the remainder being privately owned (77%).
- The tree species distribution differed slightly for the two plantations, this variation is shown in Appendix A, Tables A.3 and A.4.

Thus, an average figure for the overall basic density was calculated using known values for each tree species based on the tree type distribution spread in each of the two plantations [226, 227, 231, 238, 241, 242, 245-247]. As a result, the average figure calculated for the basic density of solid wood available in Uganda was 497 kg/m<sup>3</sup>.

For the sawdust residues, a fixed value of 220 kg/m<sup>3</sup> was used for both countries. This is the basic density (od/green volume) data for the sawdust residues derived from a mixture of pine and hardwood [248]. LHV figures on a dry ash-free (LHV<sub>daf</sub>) used in the calculation were obtained from the literature [249-253] as shown in Table 4.4 In some cases, a range was used for the calculations due to the range of values quoted in the literature.

**Table 4-4 LHV data used for the EP calculation of the forestry residues**

Type	Residue	LHV Data Source	LHV <sub>daf</sub> (MJ/kg)
Logging and Sawmilling	Solid Wood	[249, 253]	18.89 20.69
Logging, Sawmilling, and Plywood	Dust	[250]	18.46
Plywood	Solid Wood	[251, 252]	18.06 20.34

#### 4.1.1.3 Livestock residues

Energy potential from the animal waste produced from five key animals was considered for this study: cattle, goats, chickens, pigs, and sheep. Collecting and processing such livestock waste via AD allows the organic content of the waste to be realised via the production of biogas. The biogas produced can be burnt directly to produce energy or can be upgraded/cleaned to remove any unwanted gases and impurities to produce biomethane. The data regarding the number of live animals for the base year of 2019 was obtained from the FAO database [254].

Data from the open literature for Tanzania suggests that the population of dairy cattle corresponds to 3.24% of the total cattle population [255], for Uganda, this is 5.6% [256]; these values were incorporated in the calculations.

According to Sajjakulnukit et al. [48], the cattle type influences the amount of manure produced, dairy cattle produce three times more daily waste than beef or buffalo. The energy potential from the animal manure that is recoverable ( $EP_{manure}$ ) was calculated using Eqs. 4.3 – 4.5 as shown below [221].

In Eq. 4.3, the  $APB_{manure}$  is the amount of biogas from recoverable manure ( $Nm^3/yr$ ),  $EP_{manure}$  is the energy potential of the recoverable manure ( $J/yr$ ) and the LHV biogas represents the lower heating value of biogas ( $J/m^3$ ). In Eq. 4.4, DMR represents the amount of dry matter recoverable from a type of animal manure ( $kg\ DMR/yr$ ), the *vs.* is the fraction of volatile solids in dry matter ( $kg\ vs.\ kg^{-1}\ DM$ ), and  $Y_{biogas}$  is the biogas yield ( $Nm^3\ kg^{-1}\ VS$ ). In Eq. 4.5, the DM is the amount of dry matter ( $kg/head/day$ ), NA represents the number of animals, and FR is the fraction of animal manure recoverable.

$$EP_{manure} = APB_{manure} \times LHV_{biogas} \quad (4.3)$$

$$APB_{manure} = \sum(DMR \times vs. \times Y_{biogas}) \quad (4.4)$$

$$DMR = DM \times NA \times FR \times 365 \quad (4.5)$$

The quantity and quality of manure produced are dependent on numerous variables which include the quality and quantity of nutrition supplied to the animal, the live weight of the animal, et cetera. Data used in terms of the amount of manure produced per animal ( $kg/head/day$ ) is as follows: It was assumed that the beef cattle produced a value of 5, dairy cattle 15, chickens 0.03, and the pigs/native swine 1.2 [48]. The data for the sheep was assumed to be the same as that of a goat, which was 1  $kg/head/day$  [257].

Data used for the volatile solid/dry matter ratio (VS/DM), for all the animals, was assumed, as quoted by Bhattacharya et al. [258]. The remaining data used to calculate the  $EP_{manure}$  from the cattle waste, was as quoted by Sajjakulnukit et al. [48]. For the chicken and pig calculations, all the remaining data used (FA, % DM, and the biogas yield) was from Sajjakulnukit et al. [48] and Bhattacharya et al. [258]. For the sheep and goats, the FA used was as quoted by Simonyan and Fasina [46], the DM content as per Ozcan et al. [259], and the biogas yield data from Bhattacharya et al. [258]. All the data used to calculate the  $EP_{manure}$  from the livestock waste is summarised in Appendix A, Table A.5.

It is assumed that the LHV of the biogas produced from both livestock and human waste is 20 MJ/m<sup>3</sup> (as used in various other studies for the same purpose [52, 260, 261]).

#### **4.1.1.4 Urban human waste**

The energy potential from urban human waste (UHW) was calculated based on the urban population figures for 2019 for both countries [262, 263]. The following assumptions were used: an average dry matter of 0.090 (kg/head/day) [46, 258], a VS/DM ratio of 0.667, and an average biogas yield of 0.20 m<sup>3</sup>/kg vs. [258].

#### **4.1.2 Net electrical generating potential of the biomass waste**

Based on the literature reviewed for this study, we calculated the overall efficiency of these dual fuel systems (from biomass to net electricity) at a lower and upper end. Overall efficiency values for this were chosen at 10 and 25% based on the values quoted in the open literature, as discussed in the literature review (Chapter 2, section 2.5.1). This range is also suitable for power generation when processing biomass waste using AD. Dual fuel operation diesel/biogas engines have a thermal efficiency of 23% [67].

Transmission and distribution (T & D) losses were also factored in. It was assumed that any energy generated from agricultural, forestry, and urban human waste residues would be fed into the national grid. Hence, national transmission and distribution losses were accounted for in Tanzania at 16.9% for 2018 [22, 59]. This was the most current available figure, and based on the previous year's data, it did not change significantly. For Uganda, the 2019 figure was used which was 20.4% [264, 265].

It is proposed that the electricity produced from the biogas (from livestock waste) will be fed into a local grid. Electrical losses do occur within mini/microgrids and are dependent on the size and the type of the grid, as well as the age of the equipment. Hirsch et al. [266] state that these losses can vary from 5 to 15% depending on the number of conversions between AC and DC modes. For this calculation, an average loss figure of 10% was utilised.

Hence, to calculate the final “*Net GWh<sub>e</sub>*” value for the agricultural, forestry, and urban human waste streams, Eq. 4.6 was used. For the livestock waste stream, (which incorporates microgrid losses), Eq. 4.7 was used.

$$Net\ GWh_e = Gross\ GWh_e \times \left( \frac{overall\ efficiency}{100} \right) \times \left( \frac{100 - \% T \& D\ losses}{100} \right) \quad (4.6)$$

$$Net\ GWh_e = Gross\ GWh_e \times \left( \frac{overall\ efficiency}{100} \right) \times \left( \frac{100 - \% microgrid\ losses}{100} \right) \quad (4.7)$$

## 4.2 The energy potential of the agricultural residues

The annual energy potential arising from the agricultural crop residues for Tanzania is summarised in Fig. 4.2 and Table 4.5. For Uganda, the annual energy potential arising from the agricultural crop residues is illustrated in Fig. 4.3 and Table 4.6. Figs. 4.2 and 4.3 show the % of the total energy potential available from each crop type, in each country. This is calculated by dividing the energy potential (in PJ) of each crop residue by the total EP<sub>residue</sub> available from all the agricultural crop residues. Tables 4.7 and 4.8 summarise the electrical generation potentials from this waste stream for each country. The electrical energy generating potential for all the waste streams was calculated using overall efficiencies of 10 and 25% (as discussed in Chapter 2, section 2.5), before and after transmission and distribution losses.

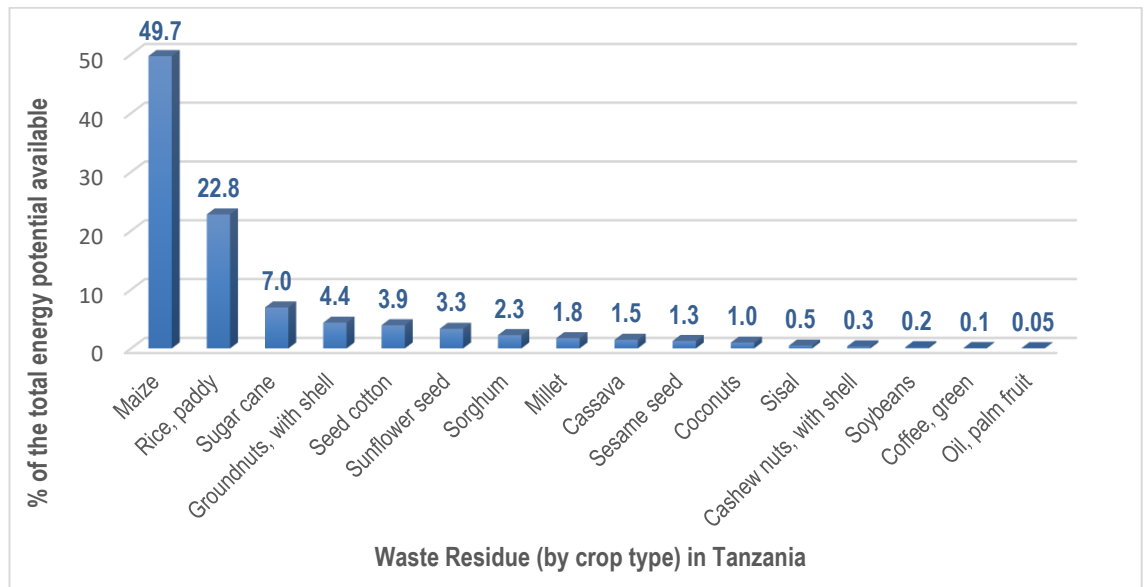


**Figure 4-2 The % of the total EP available by crop type in Tanzania**

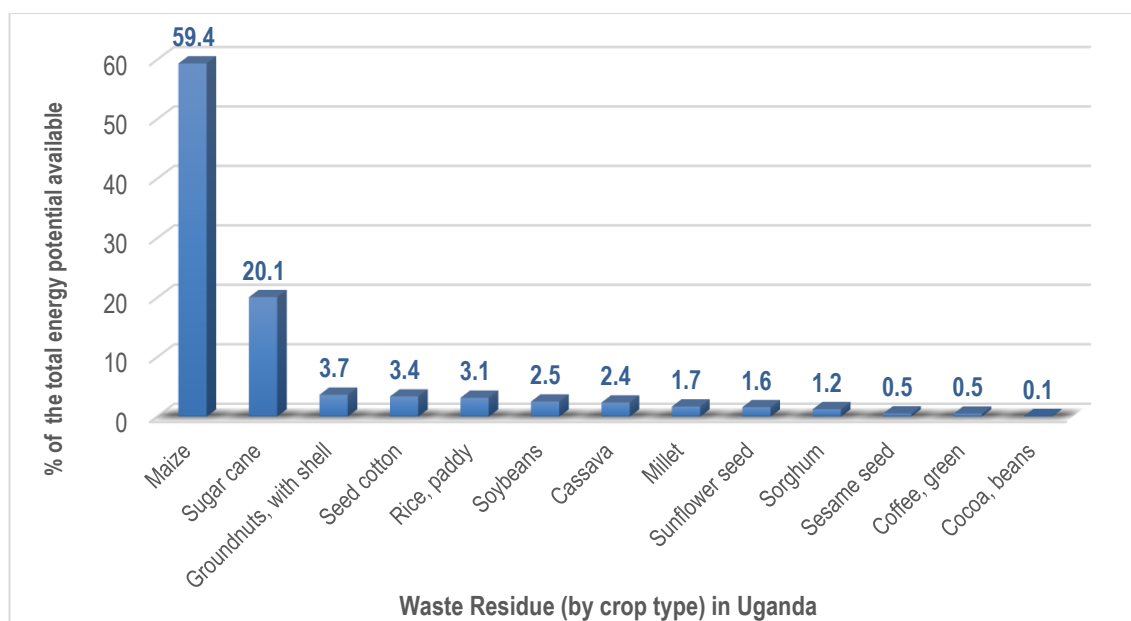


**Figure 4-3 The % of the total EP available by crop type in Uganda**

**Table 4-5 The EP arising from agricultural residues in Tanzania**

Crop	Amount (t)	Residue Type	Dry Residue (t)	EP <sub>residue</sub> (PJ)	The % of the total EP <sub>residue</sub>
Cashew nuts, with shell	225,106	Husks	75,139.3	1.12	0.3
Cassava	8,184,093	Stalks & peelings	393,163.8	4.77	1.5
Coconuts	419,916	Husks & shells	174,019.6	3.22	1.0
Coffee, green	68,147	Husks	14,481.2	0.18	0.1
Groundnuts, with shell	680,000	Shells & Straw	962,462.5	14.23	4.4
Maize	5,652,005	Straw/stalk, cobs & husk	8,560,110.8	161.66	49.7
Millet	385,962	Straw	459,294.8	5.69	1.8
Oil, palm fruit	76,506	Shells, fibre & empty bunches	12,973.3	0.15	0.05
Rice, paddy	3,474,766	Straw & husks	4,458,169.4	74.11	22.8
Seed cotton	264,495	*Straw/cake/hull	897,979.6	12.81	3.9
Sesame seed	680,000	*Cake & hull	340,000.0	4.13	1.3
Sisal	33,271	Pulp & ball/fibre	106,117.9	1.53	0.5
Sorghum	731,877	Straw	595,656.4	7.37	2.3
Soybeans	22,953	Straw & pods	52,374.7	0.65	0.2
Sugar cane	3,589,459	Tops/leaves & bagasse	1,371,963.0	22.64	7.0
Sunflower seed	1,040,000	*Cake & hull	624,000.0	10.84	3.3
<b>TOTAL</b>			<b>19,097,906</b>	<b>325.1</b>	

\* Includes residues arising from oilseed crops.

**Table 4-6 The EP arising from agricultural residues in Uganda**

Crop	Amount (t)	Residue Type	Dry Residue (t)	EP <sub>residue</sub> (PJ)	The % of the total EP <sub>residue</sub>
Cassava	6,983,000	Stalks & peelings	335,463.3	4.07	2.4
Cocoa, beans	*72,247	Dry pods	8,183.1	0.12	0.1
Coffee, green	312,601	Husks	66,427.7	0.82	0.5
Groundnuts, with shell	302,000	Shells & Straw	427,446.6	6.32	3.7
Maize	3,588,000	Straw/Stalk, cobs & husks	5,434,120.7	102.62	59.4
Millet	196,000	Straw	233,240.0	2.89	1.7
Rice, paddy	255,000	Straw & husks	327,168.3	5.44	3.1
Seed cotton	120,000	**Straw/cake/hull	407,408.6	5.81	3.4
Sesame seed	144,000	**Cake & hull	72,000.0	0.87	0.5
Sorghum	211,000	Straw	171,727.6	2.13	1.2
Soybeans	117,000	Straw, pods & **meal	334,131.5	4.34	2.5
Sugar cane	5,500,000	Tops/leaves & bagasse	2,102,210.0	34.70	20.1
Sunflower seed	260,000	**Cake & hull	156,000.0	2.71	1.6
<b>TOTAL</b>			<b>10,075,527</b>	<b>172.8</b>	

\*Area harvested (ha), \*\* Includes residues arising from oilseed crops.

**Table 4-7 Summary of the electrical generation potential of the agricultural residues in Tanzania**

Data for Tanzania	GWh Equivalent
Gross (100% efficiency)	90,308
Overall efficiency based on 10% (before T&D) losses	9,031
Net GWh <sub>e</sub> (for an efficiency based on 10% after T&D losses)	7,503
Overall efficiency based on 25% (before T&D) losses	22,577
Net GWh <sub>e</sub> (for an efficiency based on 25% after T&D losses)	18,758

National electricity generated in 2019 in Tanzania = 7,865 GWh [267].

**Table 4-8 Summary of the electrical generation potential of the agricultural residues in Uganda**

Data for Uganda	GWh Equivalent
Gross (100% efficiency)	48,013
Overall efficiency based on 10% (before T&D) losses	4,801
Net GWh <sub>e</sub> (for an efficiency based on 10% after T&D losses)	3,822
Overall efficiency based on 25% (before T&D) losses	12,003
Net GWh <sub>e</sub> (for an efficiency based on 25% after T&D losses)	9,555

National electricity generated in 2019 in Uganda = 4,415 GWh [268].

Tanzania produced ~19,098 kt of total solid biomass residue from this waste stream, with a total calculated energy potential of 325 PJ. Uganda produced ~10,076 kt of total solid biomass residue from this waste stream, with a total calculated energy potential of ~173 PJ.

In Tanzania, these residues can potentially produce between 7,503 and 18,758 GWh of electricity, after incorporating transmission and distribution losses. This stream is theoretically capable of generating 0.95 to 2.38 times the equivalent of the annual electricity produced in 2019. In Uganda, these residues can potentially produce between 3,822 and 9,555 GWh of electricity, after incorporating transmission and distribution losses. This stream is theoretically capable of generating 0.87 to 2.16 times the equivalent of the annual electricity produced in 2019.

For both countries, the agricultural waste stream has a large energy potential and is reflective of the large agricultural sector (in comparison to the other three waste streams assessed in this study). In both countries, the crop residues with the highest energy potential are maize and sugar cane, as typically seen by other researchers when conducting similar studies in these regions [51, 52]. Some of these waste residues have alternate uses, including use in energy cogeneration from sugar and sisal production [54, 199]. However, overall, a large amount remains underutilised [40, 52, 54, 199]. It is recognised that in Tanzania and Uganda alike, the potential for utilising such residues to produce more sustainable power/electricity is high but underexploited [40, 52, 54, 199]. Furthermore, low grass productivity combined with high fertiliser costs produce challenging conditions for farmers, hence using crop residues for farming purposes such as fodder or fertiliser remains a priority for many farmers [199, 269]. In addition, the availability of these crop residues varies regionally in each country. For example, the study by Okello et al. [52] showed that the Mubende district in the central region of Uganda had the highest crop residue availability with the lowest being in Kampala. In Tanzania, the cultivation of sugar cane is concentrated in three main regions [51]. Hence, the decision to utilise agricultural residues for producing small-scale electricity versus the competing uses must be considered regionally, on a case-by-case basis, with careful consideration based on the type of crop residue.

Due to the high volumes of agricultural residues available, theoretically, these residues could be utilised for large-scale energy generation; however, there are issues associated with the cost of transportation from the agricultural centres to the large power generation plants. The cost issues lie with the transportation of the low bulk density of these residues. Furthermore, the availability of these crop residues is seasonal; hence there will be periods when the supply is intermittent.

Utilising these residues locally as an energy source for small-scale energy generation avoids these issues mentioned. For the small-scale applications, as considered in this study, it is feasible to utilise/store these residues in bulk near the point of consumption. Ideally, such residues should be stored close to the gasification unit coupled with an ICE/diesel generator (which is linked to either the national grid or a local mini/microgrid).

### 4.3 The energy potential of the forestry residues

The energy potential of the forestry residues has been calculated based on LHVs from the literature. In some cases where the LHVs from the literature vary, a high and low energy potential value (PJ<sup>1</sup> and PJ<sup>2</sup>) has been calculated to reflect this variation. This data is shown in Table 4.9 for Tanzania, and in Table 4.10 for Uganda. Tables 4.11 and 4.12 summarise the electrical generation potential from the forestry residues for each country.

**Table 4-9 The EP arising from the forestry residues in Tanzania**

Type	Residue	% Fraction available [46, 193]	Residues		Energy Potential	
			m <sup>3</sup>	OD* (t)	PJ <sup>(1)</sup>	PJ <sup>(2)</sup>
Logging	Solid Wood	40	646,400	304,454	5.75	6.30
	Dust	20	323,200	71,104	1.31	1.31
Sawmilling	Solid Wood	38	614,080	289,232	5.46	5.98
	Dust	12	193,920	42,662	0.79	0.79
Plywood	Solid Wood	45	11,250	5,299	0.10	0.11
	Dust	5	1,250	275	0.01	0.01
<b>TOTAL</b>			<b>1,790,100</b>	<b>713,026</b>	<b>13.4</b>	<b>14.5</b>

*\*Where OD denotes 'oven dried'*

**Table 4-10 The EP arising from the forestry residues in Uganda**

Type	Residue	% Fraction Available [46, 193]	Residues		Energy Potential	
			m <sup>3</sup>	OD* (t)	PJ <sup>(1)</sup>	PJ <sup>(2)</sup>
Logging	Solid Wood	40	710,800	352,945	6.67	7.30
	Dust	20	355,400	78,188	1.44	1.44
Sawmilling	Solid Wood	38	675,260	335,297	6.33	6.94
	Dust	12	213,240	46,913	0.87	0.87
Plywood	Solid Wood	45	40,500	20,110	0.36	0.41
	Dust	5	4,500	990	0.02	0.02
<b>TOTAL</b>			<b>1,999,700</b>	<b>834,443</b>	<b>15.7</b>	<b>17.0</b>

\*Where OD denotes 'oven dried'

**Table 4-11 Summary of the electrical generation potential from the forestry residues in Tanzania**

Data for Tanzania	GWh Equivalent Based on PJ <sup>(1)</sup>	GWh Equivalent Based on PJ <sup>(2)</sup>
Gross (100% efficiency)	3,727	4,027
Overall efficiency of 10%, before T&D losses	373	403
Net GWh <sub>e</sub> (for an efficiency of 10%), after T&D losses	310	335
Overall efficiency based on 25%, before T&D losses	932	1,007
Net GWh <sub>e</sub> (for an efficiency of 25%), after T&D losses	774	836

National electricity generated in 2019 in Tanzania = 7,865 GWh [267]

**Table 4-12 Summary of the electrical generation potential from the forestry residues in Uganda**

Data for Uganda	GWh Equivalent Based on PJ <sup>(1)</sup>	GWh Equivalent Based on PJ <sup>(2)</sup>
Gross (100% efficiency)	4,359	4,716
Overall efficiency of 10%, before T&D losses	436	472
Net GWh <sub>e</sub> (for an efficiency of 10%), after T&D losses	347	375
Overall efficiency based of 25%, before T&D losses	1,090	1,179
Net GWh <sub>e</sub> (for an efficiency of 25%), after T&D losses	867	938

National electricity generated in 2019 in Uganda = 4,415 GWh [268]

Forestry residues in Tanzania have a calculated mean energy potential of ~14 PJ. These residues can produce on average between 323 and 805 GWh of electricity after incorporating transmission and distribution losses; it is assumed this energy will be fed into the national grid.

The energy potential from this stream is relatively small; it is only capable of generating at best, 10.6% of the annual electricity produced in 2019.

Forestry residues in Uganda have a calculated mean energy potential of ~17 PJ. These residues can produce on average between 361 and 903 GWh of electricity after incorporating transmission and distribution losses. The energy potential from this stream is greater than that calculated for Tanzania (when compared to the national electricity generated in 2019). It can generate ~21% of the annual electricity produced in 2019.

#### 4.4 The energy potential arising from the livestock residues

The amount of biogas was calculated from the recoverable manure and expressed as ABP<sub>manure</sub>. In addition, the energy potential of the manure (EP<sub>manure</sub>) was also calculated from the livestock data and expressed in PJ; this data is shown in Tables 4.13 - 4.14.

Figs. 4.4 - 4.5 show the % of the total energy potential available from each animal type for each country. This is calculated by dividing the energy potential calculated from each animal waste (in PJ) by the sum/total EP<sub>manure</sub> available from all the livestock waste residues.

Tables 4.15 and 4.16 summarise the total electrical generation potential arising from the livestock residues for each country.

**Table 4-13 The EP arising from the livestock residues in Tanzania**

Animal	NA (head)	FA	DM (%)	DMR (kt DM/yr)	VS/DM	Biogas Yield (m <sup>3</sup> /kg VS)	ABP <sub>manure</sub> (Mm <sup>3</sup> /yr)	EP <sub>manure</sub> (PJ)
Beef cattle	26,915,552	0.5	17.44	4283.3	0.934	0.307	1228.2	24.56
Dairy cattle	901,265	0.8	17.44	688.5	0.934	0.307	197.4	3.95
Chickens	38,369,000	0.8	33.99	114.2	0.465	0.18	9.6	0.19
Pigs/swine	519,256	0.8	35.22	64.1	0.893	0.217	12.4	0.25
Sheep	7,322,018	0.3	25	200.4	0.912	0.31	56.7	1.13
Goats	18,387,640	0.4	25	671.1	0.598	0.31	124.4	2.49
<b>TOTAL</b>				<b>6022</b>			<b>1629</b>	<b>32.6</b>

**Table 4-14 The EP arising from the livestock residues in Uganda**

Animal	NA (head)	FA	DM (%)	DMR (kt DM/yr)	VS/DM	Biogas Yield (m <sup>3</sup> /kg VS)	ABP <sub>manure</sub> (Mm <sup>3</sup> /yr)	EP <sub>manure</sub> (PJ)
Beef cattle	14,247,463	0.5	17.44	2,267	0.934	0.307	650.1	13.00
Dairy cattle	845,189	0.8	17.44	645.6	0.934	0.307	185.1	3.70
Chickens	35,452,000	0.8	33.99	105.6	0.465	0.18	8.8	0.18
Pigs/swine	2,582,732	0.8	35.22	318.7	0.893	0.217	61.8	1.24
Sheep	1,986,416	0.3	25	54.4	0.912	0.31	15.4	0.31
Goats	15,022,873	0.4	25	548.3	0.598	0.31	101.7	2.03
<b>TOTAL</b>				<b>3,940</b>			<b>1023</b>	<b>20.5</b>

**Table 4-15 Summary of the electrical generation potential from the livestock residues in Tanzania**

Data for Tanzania	GWh Equivalent
Gross (100% efficiency)	9,048
For overall efficiency of 10%, before microgrid losses	905
<i>Net GWh<sub>e</sub> (for overall efficiency of 10%), after microgrid losses</i>	752
For overall efficiency of 25%, before microgrid losses	2,262
<i>Net GWh<sub>e</sub> (for overall efficiency of 25%), after microgrid losses</i>	1,879

*National electricity generated in 2019 in Tanzania = 7,865 GWh [267]*

**Table 4-16 Summary of the electrical generation potential from the livestock residues in Uganda**

Data for Uganda	GWh Equivalent
Gross (100% efficiency)	5,683
For overall efficiency of 10%, before microgrid losses	568
<i>Net GWh<sub>e</sub> (for overall efficiency of 10%), after microgrid losses</i>	452
For overall efficiency of 25%, before microgrid losses	1,421
<i>Net GWh<sub>e</sub> (for overall efficiency of 25%), after microgrid losses</i>	1,131

*National electricity generated in 2019 in Uganda = 4,415 GWh [268]*

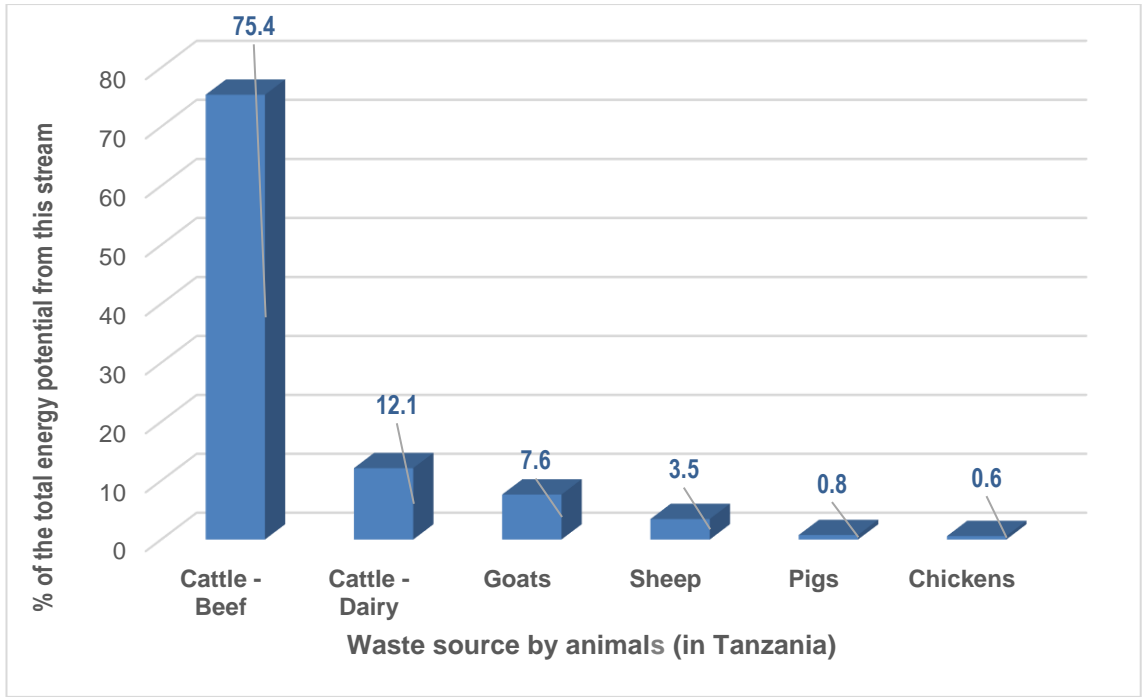


Figure 4-4 The % of the total EP available from each animal in Tanzania

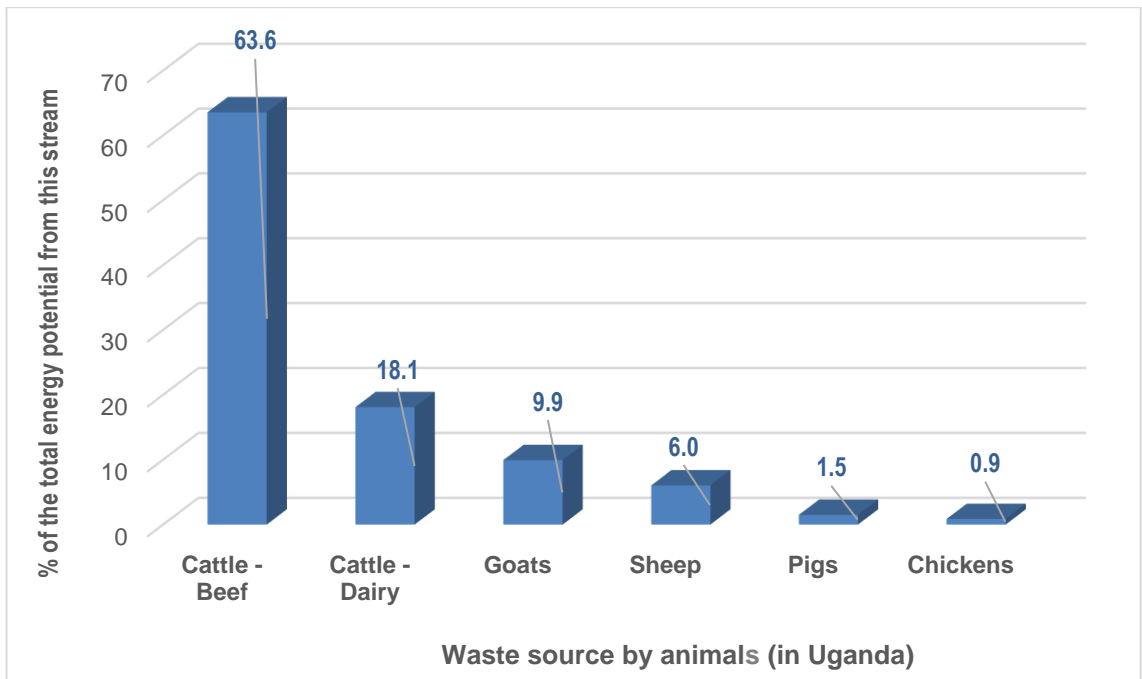


Figure 4-5 The % of the total EP available from each animal in Uganda

This data shows that there is significant energy potential from the collection of animal manure to produce biogas in both countries, equivalent to 32.6 PJ in Tanzania, and 20.5 PJ in Uganda with the leading source being cattle waste.

In Tanzania, these residues from this stream can produce between 752 to 1,879 GWh of electricity after incorporating microgrid transmission and distribution losses. This is equivalent to generating approximately 9.6 to 23.9% of the annual electricity produced in 2019.

In Uganda, these residues from this stream can produce between 452 to 1,131 GWh of electricity after incorporating microgrid transmission and distribution losses. This is equivalent to generating approximately 10.2 to 25.6% of the annual electricity produced in 2019.

The utilisation of this technology is highly feasible in both countries. In Tanzania, most of the livestock/animals are concentrated in certain regions of the country in the arid/semi-arid regions. In Uganda, a high density of cattle is identified in a specific region of the country, often referred to as the '*cattle corridor*' [52]. Mwakaje [270], identifies that southwest Tanzania has a high potential to develop biogas technology due to its high population density (high demand), with a large number of indoor-fed cattle and/or pigs. The major constraints identified by Mwakaje [270] and Okello et al. [52] in these regions were cost/affordability, water scarcity, an existing pastoralism system (in Uganda), and a lack of technical support.

Rupf et al. [57] echoed this by reiterating that various factors need consideration for the usage of biodigesters in Africa. These include feedstock availability, water supply, energy demand, local materials, and labour, as well as the level of commitment required to operate and maintain the biodigester effectively. Other factors that may affect uptake are the local culture and the location [271]. Roopnarain [74] identified further barriers as cost implications, lack of communication, lack of ownership, and the negative image of the technology caused by past failures.

In addition, the livestock numbers may vary from household to household and over an annual period [271]. The benefits of establishing communal biogas digesters include the reduction or shared costs among householders, as well as providing a more continuous feedstock [271]. The biogas produced could be piped/distributed within small communities to produce electricity using dual fuel engines. Existing diesel genset engines can be converted to run on dual fuel mode to utilise this biogas.

## 4.5 The energy potential & biogas yield from the urban human waste

The biogas yield and the energy potential (EP) available from the urban human waste residues are shown in Table 4.17 (for Tanzania), and Table 4.18 (for Uganda). Tables 4.19 and 4.20 summarise the electrical generation potential from the urban human waste (UHW) stream for each country.

**Table 4-17 The biogas potential and energy potential available from urban human waste residues in Tanzania**

Item	Value
Tanzanian urban population in 2019 [263]	20,011,884
Average dry matter production, (kg/head/day) [46, 258]	0.09
Total dry matter/year, (tonnes)	657,390
Total Biogas produced (Mm <sup>3</sup> in 2019)	87.7
LHV of biogas (MJ/m <sup>3</sup> )	20.00
Biogas yield, (Biogas m <sup>3</sup> /kg VS) [258]	0.20
<b>Total EP (PJ) in 2019</b>	<b>1.75</b>

**Table 4-18 The biogas potential and energy potential available from urban human waste residues in Uganda**

Item	Value
Urban population in Uganda in 2019 [262]	10,784,514
Average dry matter production, (kg/head/day)[46, 258]	0.09
Total dry matter/year, (tonnes)	354,271
Total Biogas produced (Mm <sup>3</sup> in 2019)	47.3
LHV of biogas (MJ/m <sup>3</sup> )	20.00
Biogas yield, (biogas m <sup>3</sup> /kg VS) [258]	0.20
<b>Total EP (PJ) in 2019</b>	<b>0.95</b>

**Table 4-19 Summary of the electrical generation potential from the urban human waste residues in Tanzania**

Data for Tanzania	GWh Equivalent
Gross (100% efficiency)	487
Overall efficiency of 10%, before T&D losses	49
<i>Net GWh<sub>e</sub> (for efficiency based on 10% after T&amp;D losses)</i>	40
Overall efficiency based on 25%, before T&D losses	122
<i>Net GWh<sub>e</sub> (for efficiency based on 25% after T&amp;D losses)</i>	101

*National electricity generated in 2019 in Tanzania = 7,865 GWh [267]*

**Table 4-20 Summary of the electrical generation potential from the urban human waste residues in Uganda**

Data for Uganda	GWh Equivalent
Gross (100% efficiency)	263
Overall efficiency of 10%, before T&D losses	26
<i>Net GWh<sub>e</sub> (for efficiency based on 10% after T&amp;D losses)</i>	21
Overall efficiency based on 25%, before T&D losses	66
<i>Net GWh<sub>e</sub> (for efficiency based on 25% after T&amp;D losses)</i>	52

*National electricity generated in 2019 in Uganda = 4,415 GWh [268]*

Tanzania has a biomass energy potential that can be generated by processing urban human waste using AD which has been estimated at 1.75 PJ. The residues from this stream can produce between 40 and 101 GWh of electricity depending on the overall efficiency of the processes/conversions involved after incorporating national transmission and distribution losses. The energy potential from this stream is very small due to the low level of urbanisation; in 2019 approximately 65.5% of the total Tanzanian population lived in rural regions [15]. Hence, this waste stream can generate at best, only 1.3% of the annual electricity produced in 2019 (after losses).

In comparison, the biomass energy potential that can be generated by processing urban human waste using AD in Uganda is estimated at 0.95 PJ of energy. The residues from this stream can produce between 21 and 52 GWh of electricity depending on the overall efficiency of the processes/conversions involved after incorporating national transmission and distribution losses. The energy potential from this stream is very small due to a lower level of urbanisation in 2019 (compared to Tanzania), whereby approximately 75.6% of the total Ugandan population lived in rural regions [18]. Hence, this waste stream can generate at best, only 1.2% of the annual electricity produced in 2019 (after losses).

## **4.6 The combined energy potential of all four waste streams**

### **4.6.1 Tanzania**

Fig. 4.6 shows the raw EP of each waste stream, this illustrates that approximately 87.1% of all the raw EP arises solely from agricultural residues. Table 4.21 shows that when all the residues are combined for 2019, Tanzania has a huge net energy-generating potential.

Calculations show that the net electricity generation potential from these combined residues is equivalent to generating approximately 1.1 to 2.7 times the total electrical energy generated in 2019. This range quoted is based on the overall efficiencies from biomass to net electricity, whereby in the worst-case scenario, a figure of 10% was used, and in the best case, 25% was used.

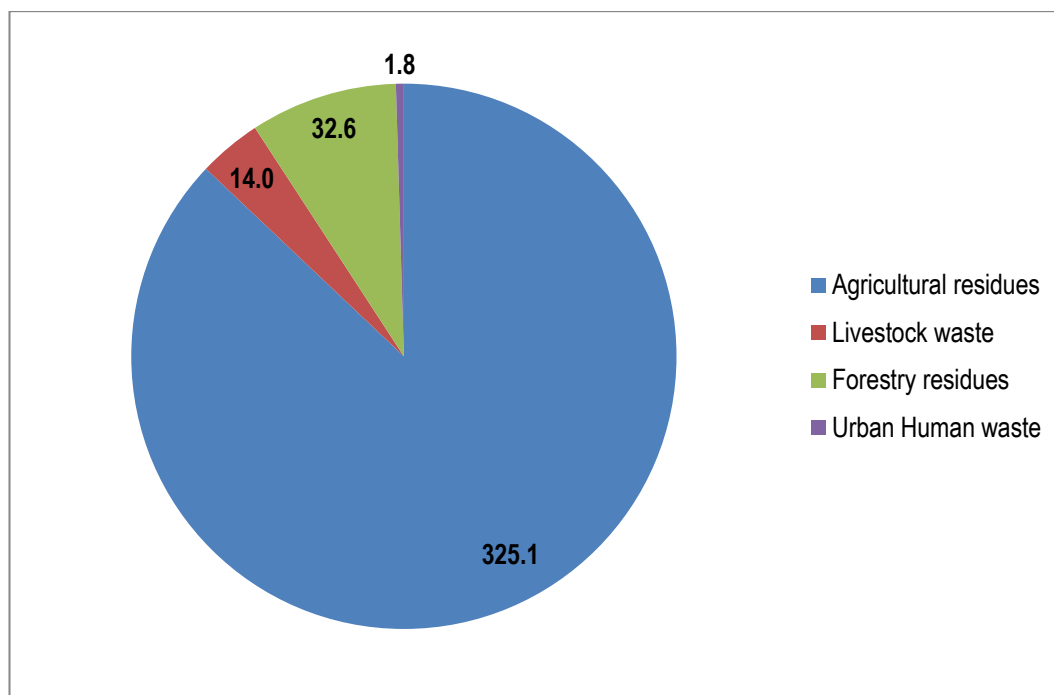


**Figure 4-6 The raw energy potential (PJ) of each waste stream in Tanzania**

**Table 4-21 Summary of the biomass assessment results for Tanzania**

Residue:	Gross GWh <sub>e</sub> at 100% efficiency	GWh <sub>e</sub> for overall efficiencies of:			
		10% before losses	25% before losses	10% after losses	25% after losses
Agricultural	90,308	9,031	22,577	7,503	18,758
*Forestry	3,877	388	969	322	805
Livestock	9,048	905	2,262	752	1,879
Urban Human Waste	487	49	122	40	101
<b>TOTAL</b>	<b>103,720</b>	<b>10,372</b>	<b>25,930</b>	<b>8,617</b>	<b>21,544</b>
% Of the electricity generation capacity possible (2019)	1,319	132	330	110	274

\*Average value used. Electricity generated in 2019 = 7,865 GWh [267]

## 4.6.2 Uganda

Fig. 4.7 shows the raw EP of each waste stream and combined they have an energy potential of 210.5 PJ for the base year of 2019. Okello et al. [52] conducted a similar biomass resources assessment for the year 2008. There were slight variations in the choice of crop residue streams selected but the study showed an annual energy potential of 260 PJ, which is within a similar range to these findings. Approximately, 82.1% of all the raw EP arises solely from agricultural residues. Okello et al. [52] also reported that the biomass residues with the greatest energy potential were those arising from crops (~58%). Interestingly, there is an 11-year span between the two studies, and the gross/raw energy potential calculated has not increased as expected with population growth. There are slight variations in the methodology and assumptions used between the study by Okello et al. [52] and the work presented in this thesis. For example, Okello et al. [52] did not differentiate between cattle types, i.e., beef cattle and dairy cattle. As mentioned earlier (in section 4.1.1.1.3), dairy cattle produce three times more daily waste than beef. In summary, Uganda also has a considerable net energy-generating potential. Calculations show that the net electricity generation potential from these combined residues is equivalent to generating 1.05 to 2.6 times the total electrical energy generated in 2019. As mentioned earlier, this range quoted is based on the overall efficiencies from biomass to net electricity, whereby in the worst-case scenario, a figure of 10% was used, and in the best case, 25% was used.

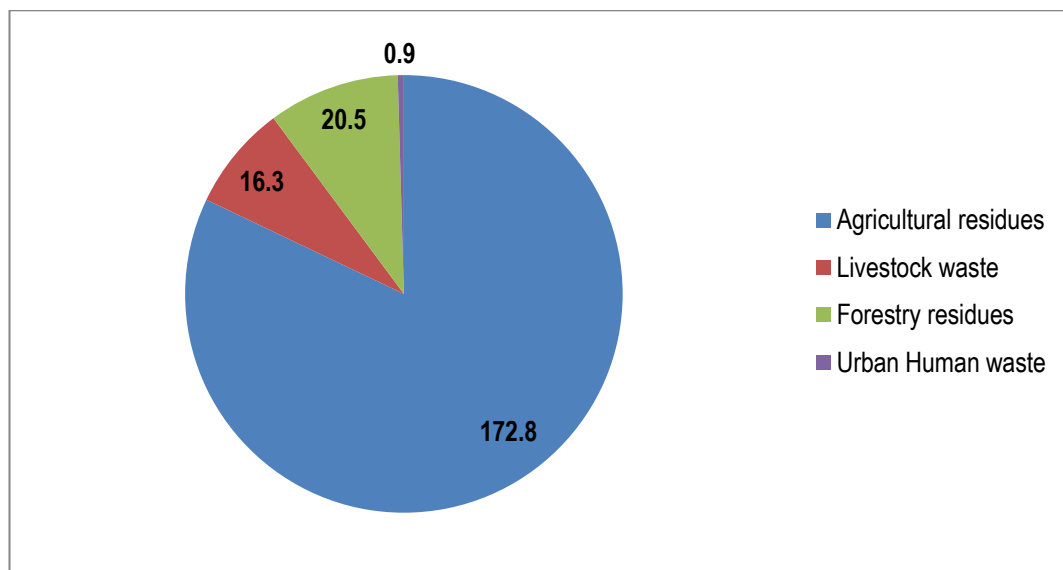


**Figure 4-7 The raw energy potential (PJ) of each waste stream in Uganda**

**Table 4-22 Summary of the biomass assessment results for Uganda**

Residue:	Gross GWh <sub>e</sub> at 100% efficiency	GWh <sub>e</sub> for overall efficiencies of:			
		10% before losses	25% before losses	10% after losses	25% after losses
Agricultural	48,013	4,801	12,003	3,822	9,555
*Forestry	4,537	454	1,134	361	903
Livestock	5,683	568	1,421	452	1,131
Urban Human Waste	263	26	66	21	52
<b>TOTAL</b>	<b>58,496</b>	<b>5,850</b>	<b>14,624</b>	<b>4,656</b>	<b>11,641</b>
% Of the electricity generation capacity possible (2019)	1,325	132	331	105	264
*Average value used. Electricity generated in 2019 = 4,415 GWh [268]					

For both countries, these residues have seasonal and regional availability, hence, to ensure a continuous supply, the usage of the residues will require some management. Utilising AD for livestock and urban human waste slurries is technically feasible; however, there are many barriers to overcome to make this a reality in many rural locations, as discussed earlier. Some of these barriers include the large fixed capital costs required for setting up, and the lack of technical expertise [54, 56, 74]. To overcome some of the socio-economic barriers linked to the uptake of these technologies, community involvement is important [33]. Governmental subsidies and interventions are required to provide training, and this needs to be promoted by favourable governmental policies.

This technology becomes more feasible in a centralised village location scenario, whereby the costs and feedstocks can be shared. This also enables a more continuous supply of biogas to be generated which can be transported via a network to a larger number of users.

## 4.7 Summary

Both countries have the highest estimated energy potential arising from agricultural waste residues, with the smallest being from the urban human waste stream.

However, overall, combined these residues in Tanzania have a huge energy potential of 374 PJ which is generated from approximately 26,490 kilotonnes of dry waste.

This energy potential and dry tonnage of biomass residue values are similar to those calculated for the base year of 2018 for Tanzania, as reported by the authored publication which is based on the methodologies used here [59].

In Uganda, combined, these residues have an energy potential of ~211 PJ which is generated from 15,204 kt of dry waste.

This study shows that renewable and sustainable energy can be generated from these residues in both countries. The net electricity generation potential from these combined residues (after accounting for transmission and distribution losses) in Tanzania is equal to 1.1 to 2.7 times the total electrical energy generated nationally in 2019.

In Uganda, the net electricity generation potential from these combined residues (after accounting for transmission and distribution losses) is equal to 1.05 to 2.6 times the total electrical energy generated nationally in 2019.

Utilising these residues using gasification or anaerobic digestion to produce a gaseous fuel to operate an existing diesel gensets in dual fuel mode can lead to a reduction in the usage and dependency on fossil fuels, whilst widening fuel choices. However, it is more economical and practical to utilise these residues on a village scale using small gasifiers near the point of production/storage. This entails the residues being stored near the gasification unit coupled with an ICE/diesel generator (linked to either the national grid or a local mini/microgrid). The gas produced can be fed into the air intake of an existing ICE and be used to produce small-scale electricity.

Utilising these waste residues offers further advantages which benefit the environment as the usual disposal/waste management techniques associated with these waste streams such as open field burning et cetera, are avoided [41, 42]. To use these waste streams using the technologies discussed in this thesis, it is particularly important to match supply with demand whilst considering the seasonal and regional availability of the feedstock. Further work is required to determine which communities would benefit from which technology based on the local availability/supply logistics of these waste residue streams, any competing uses, the population density, and any government incentives which can influence the uptake in this region.

# Chapter 5 Dual Fuel Engine Combustion Performance Analysis

## 5.1 Introduction

Following the methodologies described in Chapter 3, data was collected from the engine and analysed for combustion performance. This chapter discusses the engine combustion performance results. The first section focuses on brake specific fuel consumption (BSFC), brake specific energy consumption (BSEC), and brake thermal efficiency (BTE) data. The second section summarises the ignition delay (ID), start of combustion (SoC), Peak Pressure ( $P_{max}$ ), and peak pressure location data findings. The final subsection looks at the air to fuel ratio (AFR), the equivalence ratio ( $\phi$ ), and the engine exhaust gas temperatures (EGTs). In all cases, when analysing the data,  $\pm$  one standard deviation was used to represent the error bars (derived from repeat experimental work).

## 5.2 Brake Thermal Efficiency, Brake Specific Fuel Consumption, and the Brake Specific Energy Consumption data

The BTE data at the various % GEFs evaluated are summarised in this section across all loads. The corresponding BSEC data is also summarised in this section per gaseous fuel type, expressed as MJ/kWh. Using an energy-based unit (rather than mass) allows this data to be cross-compared across different dual fuel types as seen in the literature [170]. In the BSEC comparison graphs, the x-axis shows the % gas energy fraction (GEF) versus the BSEC value.

### 5.2.1 Diesel baseline data

For reference, the average diesel baseline (DBL) data (average data from all diesel data sets) shows the optimum BTE lies at a generator output load between 3.2 to 4.2 kW (between 76% and full engine load) as shown in Fig. 5.1. The corresponding BSFC and the BSEC data are also plotted alongside and are expressed as g/kWh and MJ/kWh, respectively.

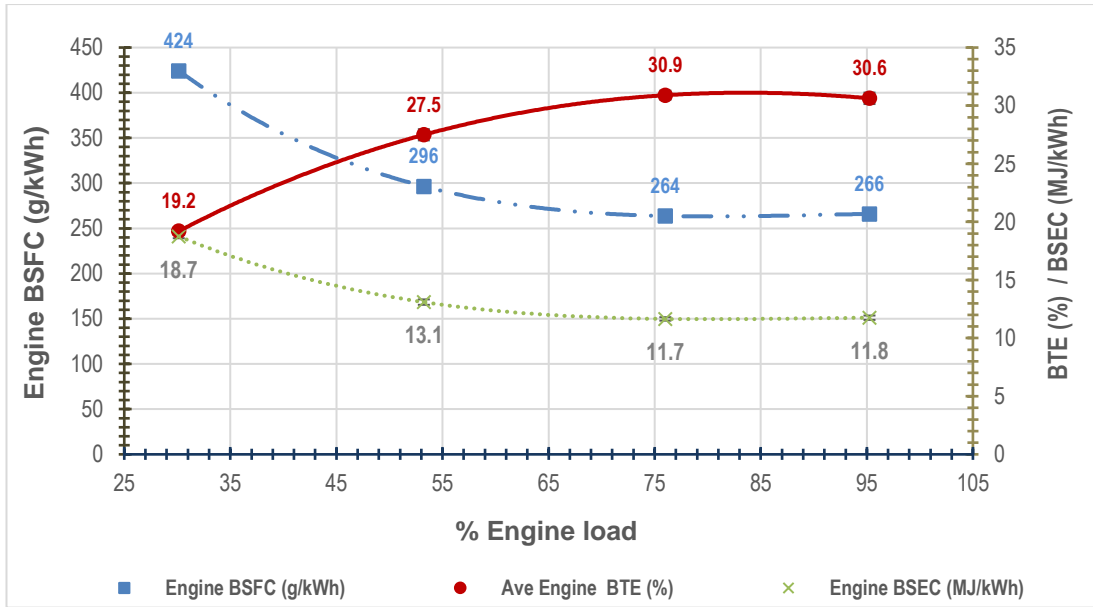


Figure 5-1 The diesel baseline data for BSFC, BSEC, and BTE

### 5.2.2 Syngas A

Figs. 5.2 and 5.3 illustrate the BTE and BSEC trends for syngas A (SGA). Fig. 5.2 shows that as the % of SGA is increased, the BTE reduces across all loads when compared to SG0 (DBL value) as a reference point.

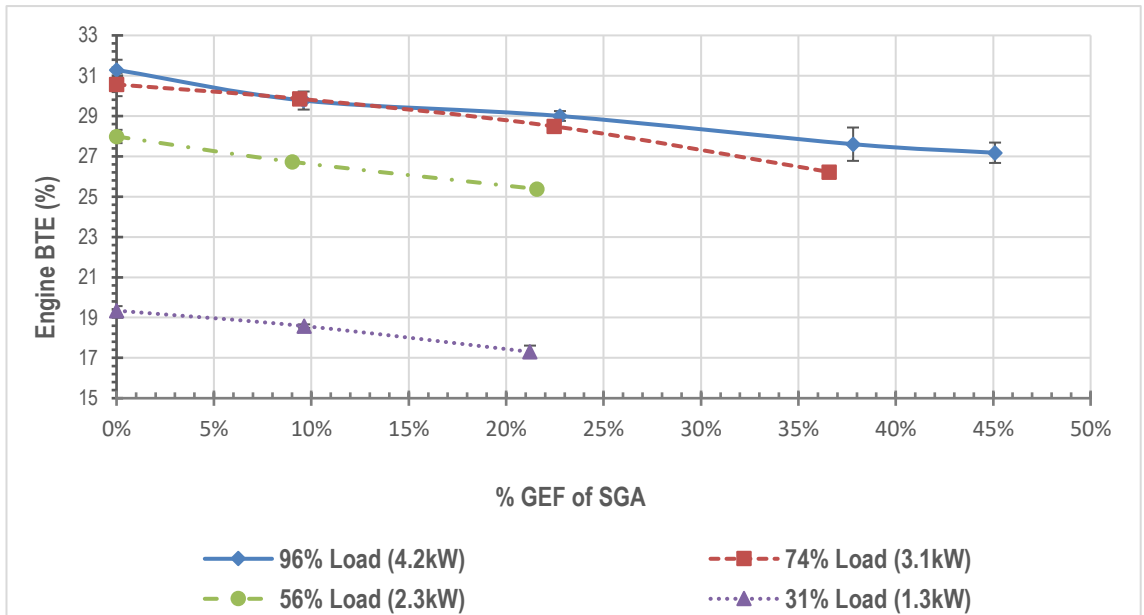
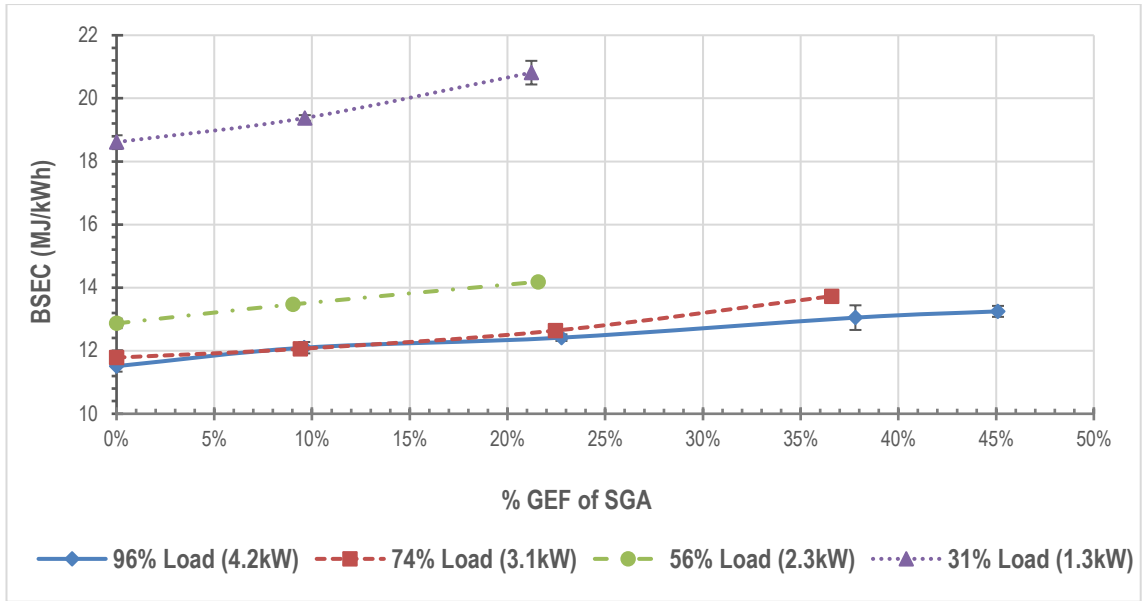


Figure 5-2 BTE versus increasing % GEF of SGA



**Figure 5-3 BSEC data versus increasing % GEF of SGA**

Fig. 5.3 shows the BSEC data (MJ/kWh) calculated at the various engine loads and at the % GEF values tested. This graph shows that the BSEC value increases with increasing SGA across all loads. There is a minimal difference between the BSEC data between 74 and 96% engine load when using a % GEF value of 10 and 22; this also corresponded to a minimal change in the BTE data at these test conditions. The BTE values show the largest % decrease at lower loads, also, the corresponding BSEC increased the most at these conditions.

### 5.2.3 Syngas B

Figs. 5.4 and 5.5 illustrate the BTE and BSEC trends for syngas B (SGB). Fig. 5.4 shows that as the % of SGB is increased, the BTE is reduced across all loads when compared to SG0 (DBL value) as a reference point.

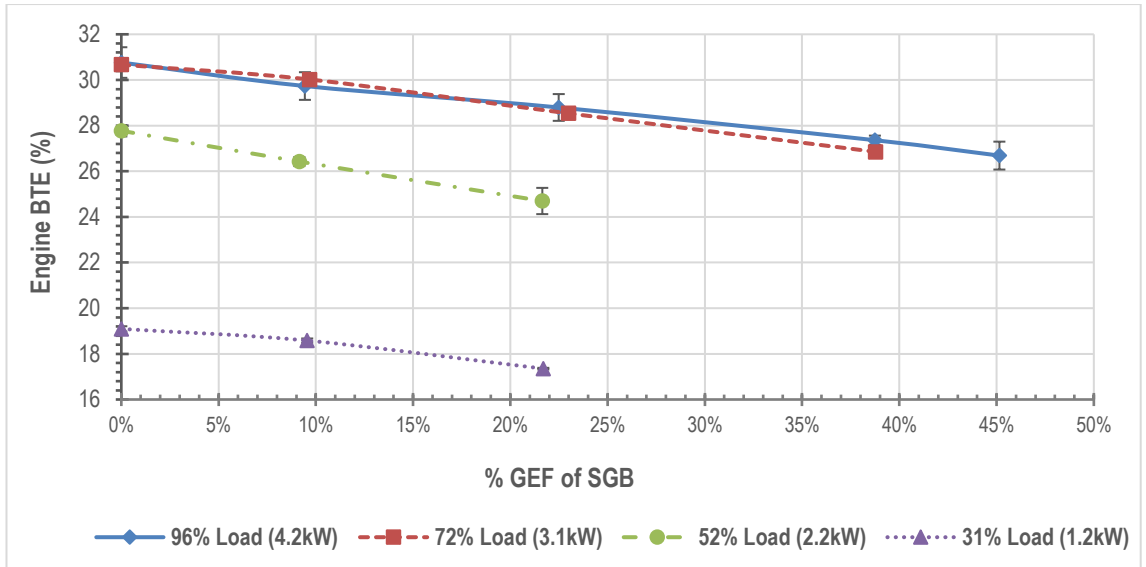


**Figure 5-4 BTE data versus increasing % GEF of SGB**

Fig. 5.5 shows the BSEC data (MJ/kWh) calculated at the various engine loads and at the % GEF values tested. This graph shows a trend whereby BSEC increases with increasing SGB at all loads. There is minimal difference between the 72% and full engine load BSEC data. The BTE values show the largest decrease at lower loads, the corresponding BSEC data also increases the most at these conditions.

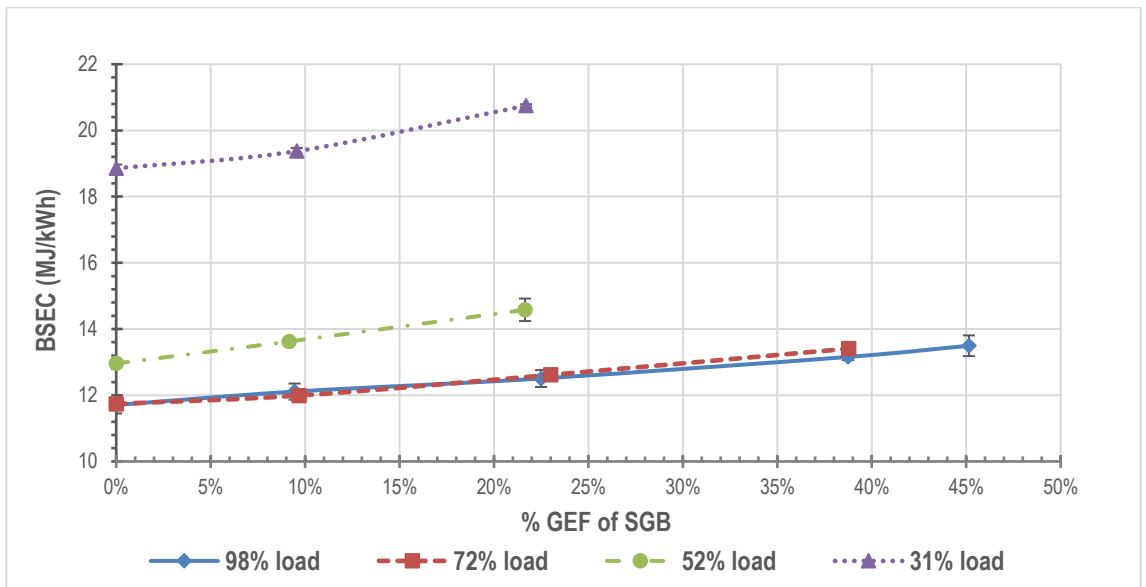


**Figure 5-5 BSEC data versus increasing % GEF of SGB**

## 5.2.4 Syngas C

Figs. 5.6 and 5.7 illustrate the BTE and BSEC trends for syngas C (SGC). Fig. 5.6 shows that as the % of SGC is increased, BTE is reduced across all loads when compared to SG0 (DBL value) as a reference point.

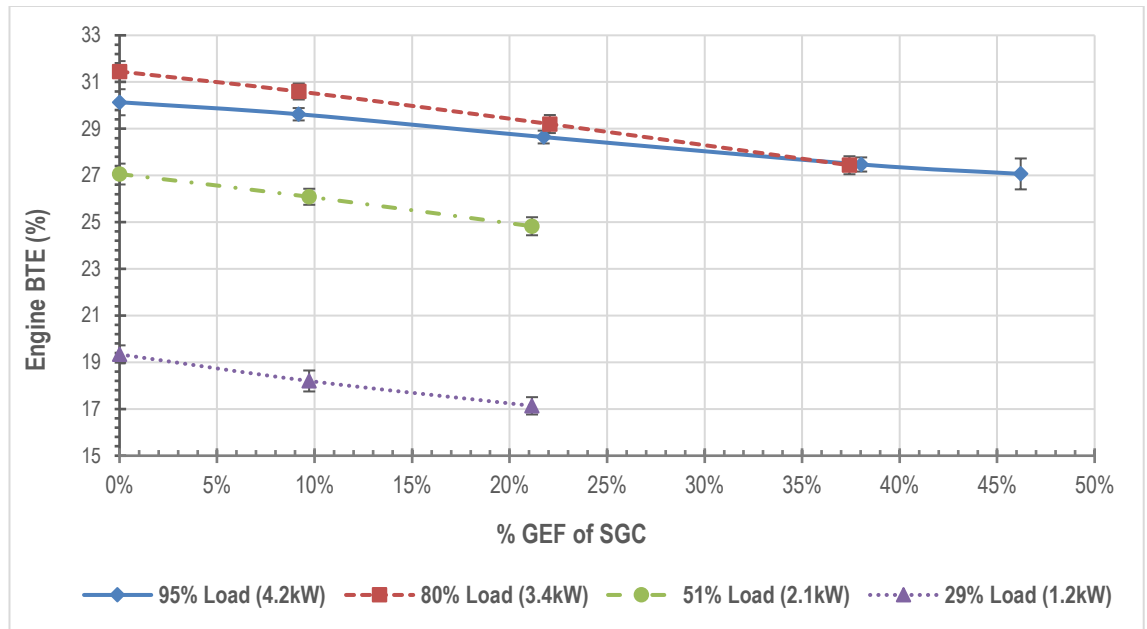


**Figure 5-6 BTE data versus increasing % GEF of SGC**

Fig. 5.7 shows the BSEC data (MJ/kWh) calculated at the various engine loads and at the % GEF values tested. This graph shows a trend whereby BSEC increases with increasing SGC at all loads. As per SGB, there is minimal difference between the BSEC data between 80% and full engine load.

Fig. 5.6 shows that the BTE values show the largest decrease at lower loads with corresponding increases in the BSEC data also noted at these conditions.

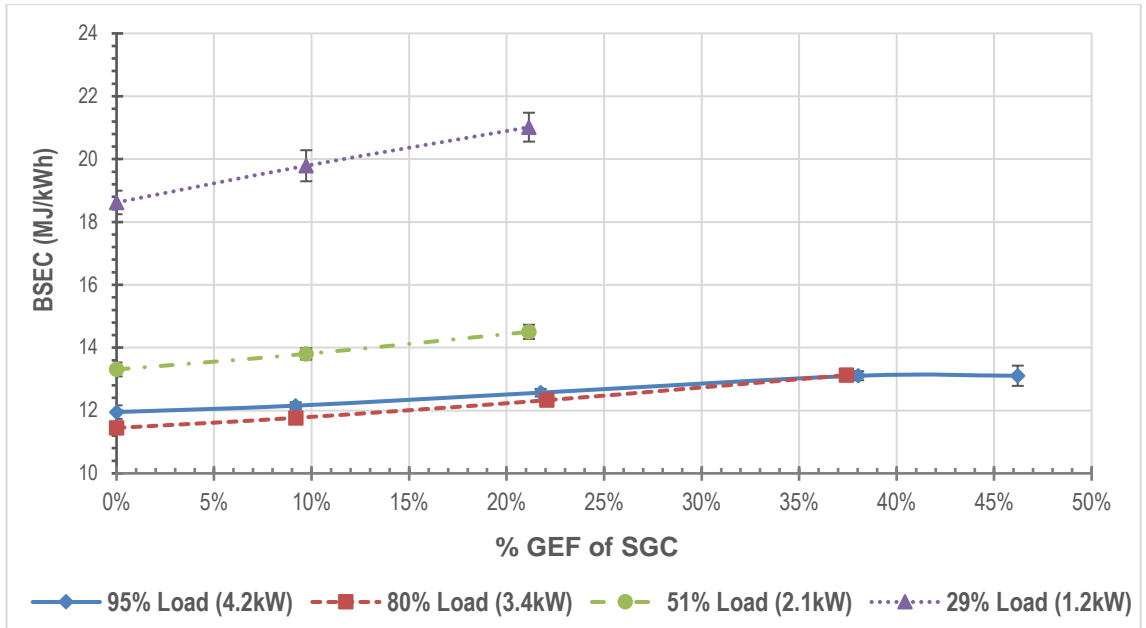


Figure 5-7 BSEC data versus increasing % GEF of SGC

### 5.2.5 Biogas

Figs. 5.8 and 5.9 illustrate the BTE and BSEC trends for the biogas/diesel experimental runs. Fig. 5.8 shows that as the % of biogas is increased, the BTE is reduced across all loads relative to the diesel baseline.

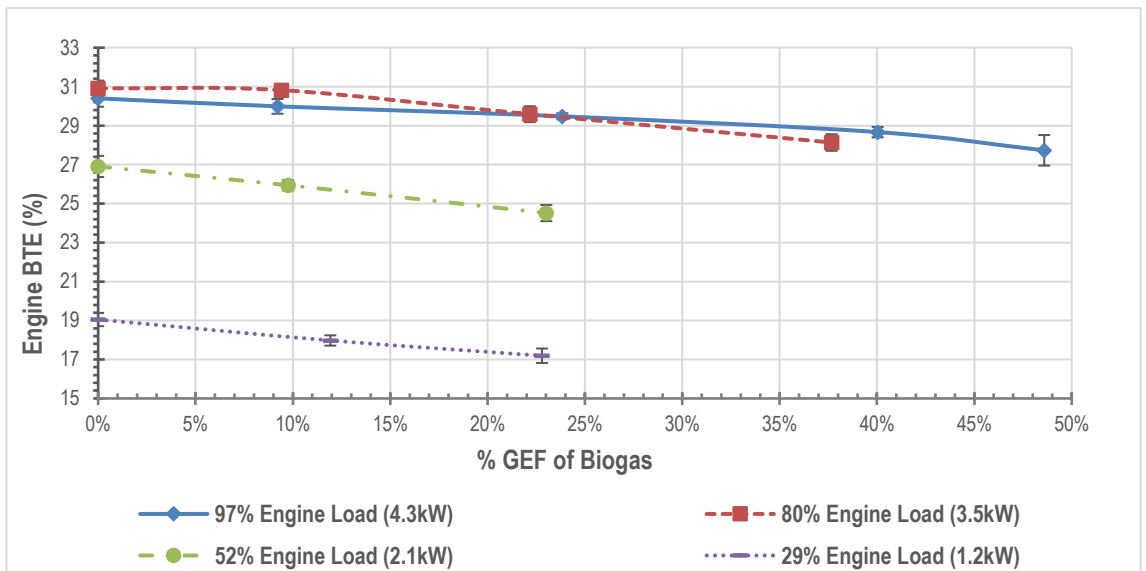
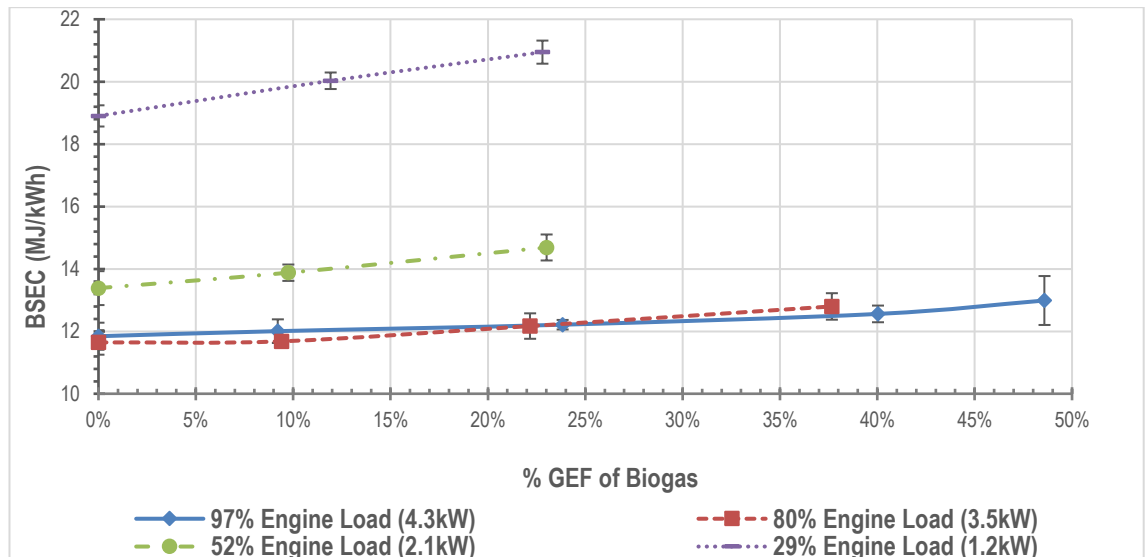


Figure 5-8 BTE data versus increasing % GEF of biogas

Fig. 5.9 shows the BSEC data (MJ/kWh) calculated at the various engine loads and at the % GEF values tested. This graph shows that the BSEC increases with increasing biogas at all loads. As per syngas blends, there is minimal difference between the BSEC data between 80% and full engine load. The BTE values show the largest decrease at lower loads; also, the corresponding BSEC increases the most at these conditions.



**Figure 5-9 BSEC data versus increasing % GEF of biogas**

### 5.2.6 Discussion of the Brake Thermal Efficiency and the Brake Specific Energy Consumption results

Comparing dual fuel engine combustion performance data reported in this research with the literature should be done with caution as the composition of the gaseous fuels, the engine design, speed, et cetera, will affect the resulting performance [170], as discussed in the literature review (see section 2.11).

For all the syngas fuels tested, as the % GEF values increased, the % BTE values decreased. This was expected as seen by many other researchers when using syngas/dual fuel blends [69, 88, 92, 102, 142, 145, 147, 149, 150, 152, 153, 158, 160, 162]. However, a small minority of researchers have reported the opposite trend; an increase in the efficiency in dual fuel mode, with increasing syngas replacement of diesel [97, 159, 165]. In the case of Mahmood et al. [165], these authors studied the combustion characteristics of syngas-diesel dual fuelling using numerical simulations. This study was based on a different engine type and associated equipment (fixed speed of 2,000 RPM), as well as the composition of the syngas used for testing, which was 50:50 hydrogen to CO (% mass fraction based).

The other two syngas-diesel dual fuel combustion studies that reported an increase in the BTE data in dual fuel mode [97, 159] used different specifications of engines, also both were directly coupled with gasification units. Any change in the composition of the syngas during the testing experimental procedure could potentially lead to inaccurate BTE data.

For biogas diesel, this study showed a decrease in BTE with an increasing % of biogas; this was in line with that reported by many other researchers [135, 137, 140]. Contrary to this, Ambarita [138] reported that BTE values for biogas/diesel in dual fuel mode are dependent on the biogas flow rate, hence BTE may increase or decrease, their work was carried out on a 4.41 kW rated variable speed engine. This dual trend in the reported BTE was not noted in the biogas-diesel findings reported in this thesis.

In dual fuel mode combustion, a lower BTE is produced due to the lower energy content of the gaseous fuel relative to diesel, coupled with a reduction in the oxygen availability as the gaseous fuel displaces the air, resulting in poorer combustion performance which is more evident at lower loads [135, 142, 144]. A lack of oxygen leads to incomplete combustion and an increase in BSEC. Other explanations for the lower BTE values in dual fuel mode seen here can be linked to slower burning rates and lower  $P_{max}$  cylinder pressures [142].

The reduction of BTE for biogas/diesel combustion is also attributed to the  $CO_2$  content of the biogas which is said to restrict the rapid burning of the mixture during combustion, thereby affecting the burning speed, causing a reduction in flame propagation, thus resulting in a lower energy conversion efficiency during biogas-diesel runs [135, 137, 138].

It is expected that if poorer combustion has occurred, this will be evident by the presence of unburnt fuel in the exhaust gases, in particular, the CO levels at lower loads [145, 150]. The presence of CO and HC in the exhaust gases are both direct indicators of incomplete combustion occurring due to a lack of oxygen and a rich fuel-air mixture [138].

This reduction in BTE observed for all gas/diesel blends corresponds to an increase in BSEC data (MJ/kWh) due to the inverse relationship. This increases across all syngas and biogas dual fuel operational modes at all loads. Overall, the reduction in the BTE is said to be caused by a reduction in the combustion efficiency in dual fuel mode [142] and this is seen from the analysis of the gaseous emissions (see Chapter 6).

It is widely accepted that to improve the BTE of syngas-diesel dual fuel combustion, an increase in the hydrogen fraction is beneficial. In addition, improving the H<sub>2</sub>/CO ratio, especially in the lean mixture condition is recommended [142, 143].

The fractions of H<sub>2</sub> and CO significantly affect combustion due to their different combustion characteristics. CO can affect the reactivity of a syngas mixture; oxidation of CO with H<sub>2</sub> present is known to affect the syngas oxidation mechanism as more reactive radicals are available to oxidise CO with a higher hydrogen content [148]. Also, the CO in the syngas becomes trapped in the crevices within the combustion chamber, away from the flame, thereby remaining unburnt and present in the exhaust gases [128].

Thus, increasing the H<sub>2</sub> content of the syngas should result in a higher cylinder pressure as H<sub>2</sub> has a higher flame speed and a higher calorific value when compared to the other gases present in the syngas [149]. A study that focuses on the laminar flame speed of hydrogen/carbon monoxide/air mixtures determined that the laminar flame speed of an H<sub>2</sub>/CO/air mixture increases with an H<sub>2</sub> fraction [272]. A higher flame speed arising from the increased hydrogen content could potentially force the flame near the crevice regions [128], thus reducing the CO content present from incomplete combustion in the exhaust gases.

Hence, as the H<sub>2</sub> content and the H<sub>2</sub>/CO ratio of the three syngas varies, the next section will investigate if the composition of the gaseous fuels (the change in the H<sub>2</sub> content) affects the BTE data.

### **5.2.7 Brake Thermal Efficiency data: cross-comparison**

The BTE results that are in section 5.2 show that the BTE decreases as the % GEF values are increased for all the gaseous fuels evaluated. In this section, the BTE data was cross compared across the gases evaluated to determine if the decrease in BTE observed is affected by gas type/compositions. These findings are summarised in Table 5.1.

When cross comparing the syngas types assessed for combustion performance, the findings for engine loads <50% (2 and 1kW generator output) cannot be wholly attributed to the H<sub>2</sub>/CO composition, other factors are potentially responsible for the change.

Sahoo et al. [144] state that at part engine loads (20 and 40%), there is a minor influence of H<sub>2</sub>/CO composition on efficiency. However, above 50% load, it is stated that the BTE is enhanced by increasing the H<sub>2</sub> content, thus increasing the H<sub>2</sub>/CO ratio which results in a significant improvement in the combustion efficiency. This is attributed to the faster combustion rate of H<sub>2</sub> and CO, and a higher level of premixing associated with higher loads.

**Table 5-1 Summary of the effect of the gaseous fuel composition on BTE**

Engine load /( <b>kW</b> )	% <b>GEF</b>	Trend for <b>SGA v SGB v SGC</b>	Position of Biogas
96% (4.2 kW)	46	No trend	No trend
96% (4.2 kW)	39	No trend	Highest <i>BTE</i> of all gas fuels
96% (4.2 kW)	23	No trend	Highest <i>BTE</i> of all gas fuels
96% (4.2 kW)	9	No trend	No trend
76% (3.3kW)	38	SGC has the highest <i>BTE</i> value	Highest <i>BTE</i> of all gas fuels
76% (3.3kW)	22	SGC has the highest <i>BTE</i> value	Highest <i>BTE</i> of all gas fuels
76% (3.3kW)	9	SGC has the highest <i>BTE</i> value	Highest <i>BTE</i> of all gas fuels
54% (2.2kW)	22	SGA has marginally higher <i>BTE</i> , with SGB/SGC/BG being comparable	
54% (2.2kW)	9	SGA has marginally higher <i>BTE</i> , with SGB/SGC/BG being comparable	
30% (1.2kW)	21	No trend	No trend
30% (1.2kW)	10	No trend	No trend

Cross-comparison of SGA/SGB/SGC BTE data shows at an engine load of 96% (4.2kW), the BTE values are unaffected by the gaseous composition at various % GEF values; there is no difference in the values obtained. However, enhanced combustion performance was noted at full load when comparing parameters of ID and P<sub>max</sub> for SGC relative to the other syngas blends (see subsection 5.3.7). The positive effect of the increased hydrogen may not translate into higher BTE values for SGC relative to the other syngas blends as the combustion temperature are consistently high for all syngas blends at full engine load. Additionally, at full load, at GEFs of 23 and 39%, the highest BTE value is obtained using biogas/diesel as a dual fuel mixture versus the other gaseous fuels evaluated.

At 76% engine load, at all % GEF values evaluated, SGC produces higher BTE values in comparison to the other two syngas types. It can be deduced that the faster burning rate of H<sub>2</sub> promoted the combustion of the mixture at a medium-high load (76% engine load) [144]. Fig. 5.10 illustrates this by comparing the average BTE values obtained at a GEF value of ~10%.

Also, at 76% engine load, the highest BTE value is obtained using biogas/diesel as a dual fuel versus the other gaseous fuels at all the GEFs evaluated. Data analysis of BTE data generated at an engine load of 54% (2kW generator load) shows that the SGA has a marginally higher BTE value when compared to the remaining gas fuels assessed. At 30% engine load, there is no difference in the BTE values obtained from the different gaseous fuels tested.

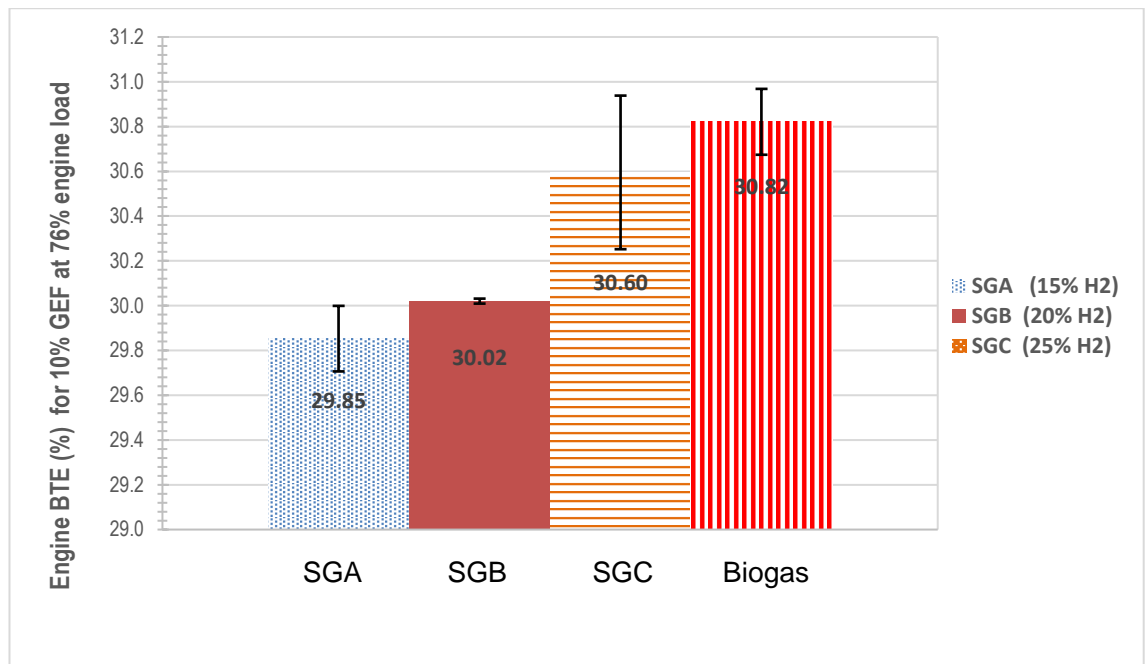


**Figure 5-10 A comparison of the BTE values obtained for the different gaseous fuels evaluated at 10% GEF at 76% engine load**

At 76% engine load (3kW generator load), the BTE data obtained for all % GEF values (for SGA, SGB, and SGC) was plotted against the H<sub>2</sub> content present in the composition of the individual syngas blends, this is depicted in Fig. 5.11.

Fig. 5.11 shows that the highest BTE value seen in SGC could be attributed to the higher H<sub>2</sub> content and H<sub>2</sub>/CO ratio of the syngas. This affirms what has been reported by other researchers; increasing the hydrogen content and H<sub>2</sub>/CO ratio of syngas leads to improved combustion performance and efficiency [85, 143, 145, 148].

Sahoo et al. [144] explain the increase in the H<sub>2</sub>/CO ratio leads to improved BTE due to a faster rate of combustion of H<sub>2</sub> and CO and increased premixing.

Fig. 5.11 also shows that at an engine load of 76%, the highest GEF value evaluated of 38% is more sensitive to changes in the hydrogen content of the syngas as the BTE values change more dramatically when compared to 10 or 22%. This is potentially due to the higher syngas flow rate used, thereby increasing the H<sub>2</sub> content of the syngas/air mixture. For reference, at a similar engine load, the diesel baseline data produced an average BTE value of 30.9% (as shown in Fig. 5.1).

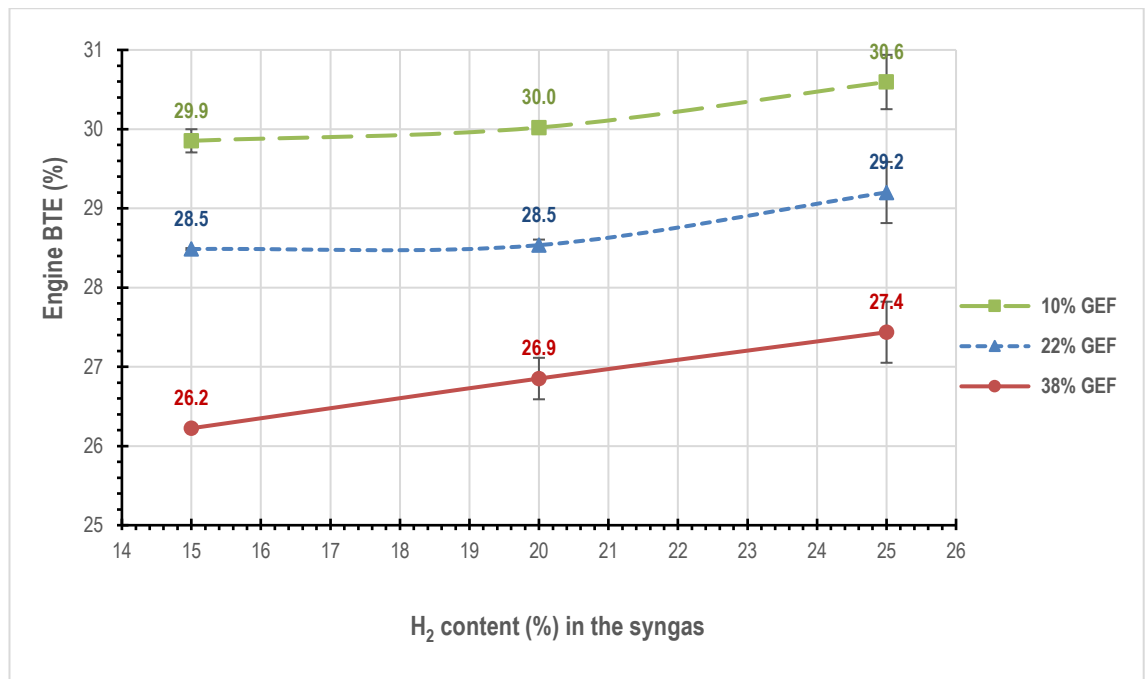


**Figure 5-11 BTE data versus the H<sub>2</sub> content at 76% engine load**

Overall, dual fuel operation leads to a reduction in the BTE values relative to the diesel baseline. For all three syngas blends assessed, an average 12% reduction in BTE was calculated at full engine load using the maximum syngas fraction of 46%. At an engine load of 76% load using the maximum syngas fraction evaluated (38%), a 13% reduction in BTE was calculated.

Similarly, for biogas dual fuel mode, at full engine load and 76% load, at the maximum gas fractions evaluated (46, and 38% respectively), a reduction of 9% in BTE was calculated for both cases, relative to the diesel baseline.

## 5.2.8 Brake Specific Energy Consumption data: cross-comparison

The BSEC data was cross compared across the different gas/diesel blends evaluated. This was done to determine if this data is influenced by the composition of the gaseous fuel tested. These findings are summarised in Table 5.2. Cross-comparison of the BSEC data across the three syngas types shows at an engine load of 96%, and at all % GEF values tested, the BSEC values are unaffected by the gaseous composition (as was observed for the BTE cross-comparison data).

**Table 5-2 Summary of the effect of the BSEC data versus gaseous fuel type**

Engine load (kW)	% GEF	BSEC data comparison for SGA v SGB v SGC	Position of Biogas
96% (4.2 kW)	46	No apparent	No trend
96% (4.2 kW)	39	No apparent	Lowest of all four gases
96% (4.2 kW)	23	No apparent	Lowest of all four gases
96% (4.2 kW)	9	No apparent	No trend
76% (3.3kW)	38	SGC is the lowest	Lowest of all four gases
76% (3.3kW)	22	SGC is the lowest	Lowest of all four gases
76% (3.3kW)	9	SGC is the lowest	Lowest of all four gases
54% (2.2kW)	22	SGA is the lowest	No trend
54% (2.2kW)	9	SGA is the lowest	No trend
30% (1.2kW)	21	No trend	No trend
30% (1.2kW)	10	No trend	No trend

However, when considering biogas/diesel, at full load (at GEF values of 23 and 39%), this fuel blend had the lowest BSEC consumption of all the gas/diesel blends evaluated, this is also supported by the highest corresponding BTE data. This suggests better combustion is seen under these experimental conditions for biogas/diesel blends, this is reflected by the CO emissions as reported in Chapter 6 (see Table 6.5).

At 76% engine load, at all % GEF values evaluated, SGC produced the lowest BSEC values, coupled with higher BTE data (in comparison to the other two syngas types). Fig. 5.12 compares the average BSEC values obtained at 76% engine load at the various % GEF values tested and confirms that the higher H<sub>2</sub> content in the syngas results in enhanced combustion performance at this engine load. For reference, at this load, the diesel baseline data produced an average BSEC value of 11.65 MJ/kWh (as shown in Fig. 5.1).

At 54% engine load, SGA has the lowest BSEC and marginally higher BTE data at both GEFs in comparison to the other two blends. A comparison of the THC and CO EI emissions (in g/MJ fuel) showed that SGA did not exhibit lower emissions at this load in comparison to the other syngas blends (see Chapter 6, section 6.3.6).

At 30% engine load, there was no discernible difference in the BSEC data between any of the four gaseous fuels tested.

Fig. 5.12 also shows that at 76% engine load, the GEF value of 38% is more sensitive to changes in the hydrogen content of the syngas, as the BSEC values decrease more dramatically when compared to 10 or 22%. This has been explained earlier, as seen for 76% load SGC BTE data. This is due to the higher flow rates of syngas used; thus, the impact of the hydrogen content is increased.

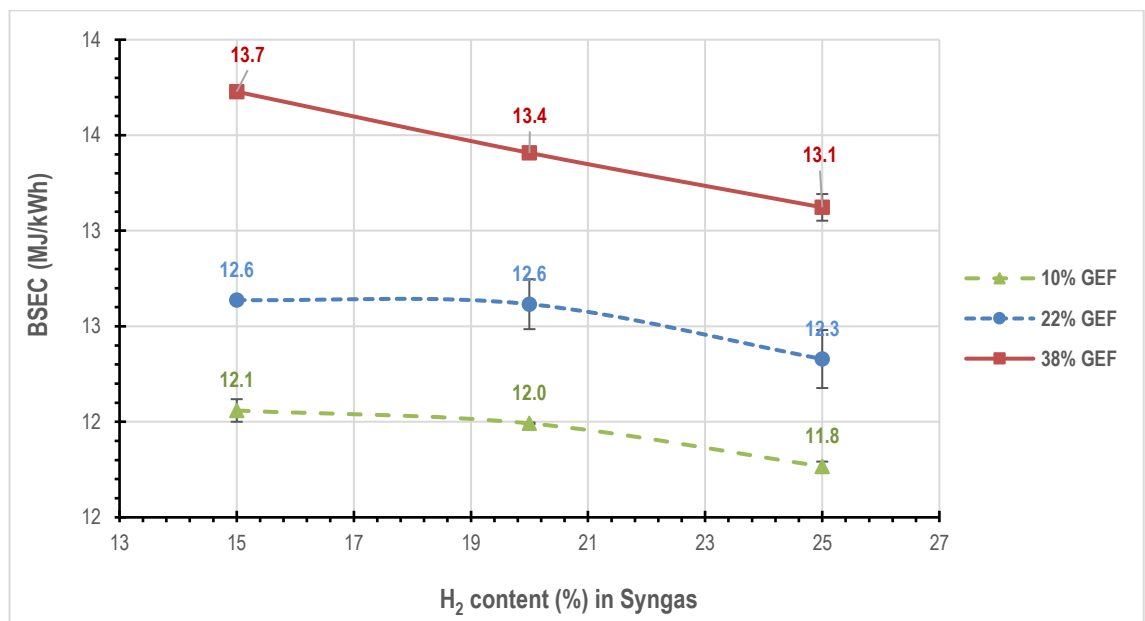


**Figure 5-12 BSEC data at 76% engine load versus the syngas H<sub>2</sub> content of the syngas blends**

### 5.3 In-cylinder pressure and ignition delay

This section summarises the findings in terms of the in-cylinder pressure, SoC, and ID data. The cyclic variability was calculated from ~ 100 cycles of the P-CAD data. An average relative standard deviation value of 4.3% was calculated for all modes of combustion (pure diesel and dual fuel mode), across all % gas energy fractions and engine loads tested. Close analysis of the P-CAD plots (direct pressure data, first derivative, and second derivative data) was carried out near TDC. From these plots, the following data was calculated (as per the methodology described in section 3.5.8):

- The crank angle degree (CAD) corresponding to the SoC
- The ID (in CAD and ms)
- Peak pressure expressed as  $P_{max}$  (bar)
- Location of  $P_{max}$  (in CAD)

The average calculated data for all four gaseous fuels tested at all % GEFs and engine loads is presented in the following subsections.

#### 5.3.1 Diesel baseline

For reference, the average diesel baseline data (average data from all the diesel data sets) was summarised and displayed in Table 5.3. This shows the SoC, ID,  $P_{max}$ , and  $P_{max}$  location.

**Table 5-3 The SoC, ID, RPM, and  $P_{max}$  data for the diesel baseline**

Genset load (kW)	% Engine load	RPM	SoC in CAD ( $\pm 0.5$ )	ID in CAD ( $\pm 0.5$ )	ID (ms)	$P_{max}$ (bar)	$P_{max}$ location in CAD ( $\pm 0.5$ )
1.2	30.3	3116	5.3	18.84	1.01	61.22	11.08
2.2	55.4	3101	5.3	18.84	1.01	64.03	11.00
3.3	77.2	3075	5.2	18.67	1.01	65.86	11.36
4.2	95.2	3045	5.4	18.89	1.03	66.75	11.80

Typically, the ID (measured in CAD) decreases in diesel engines with increasing load. However, we are not seeing this trend with this engine. The resolution of the measurement is 0.5 CAD, which when converted into ID is equivalent to 0.027 ms (based on a fixed engine speed of 3,000 RPM, as per engine specification). Hence, in conclusion, there is also no change in ID with increasing load for the diesel baseline data. The in-cylinder peak pressure ( $P_{max}$ ) shows an increase with load, which is expected at higher loads as more fuel is injected and combusted, thus producing higher  $P_{max}$  values.

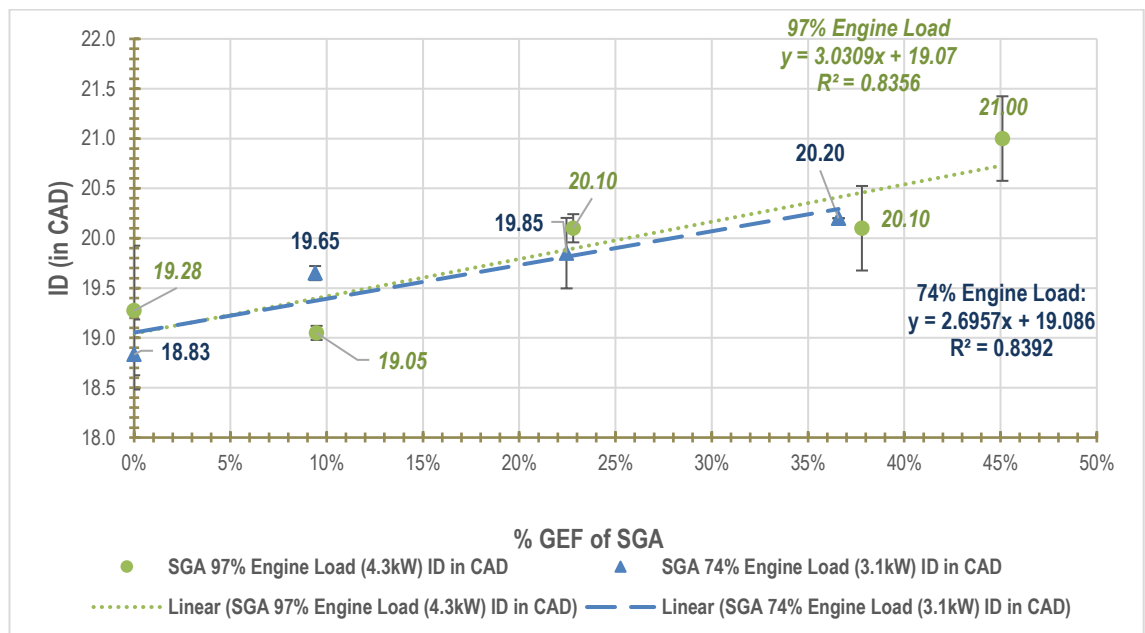
### 5.3.2 Syngas A

Table 5.4 summarises the calculated data for peak pressure ( $P_{max}$ ), SoC, and ID for SGA experiments.

**Table 5-4 The data for SoC, ID, and  $P_{max}$  data for SGA-diesel**

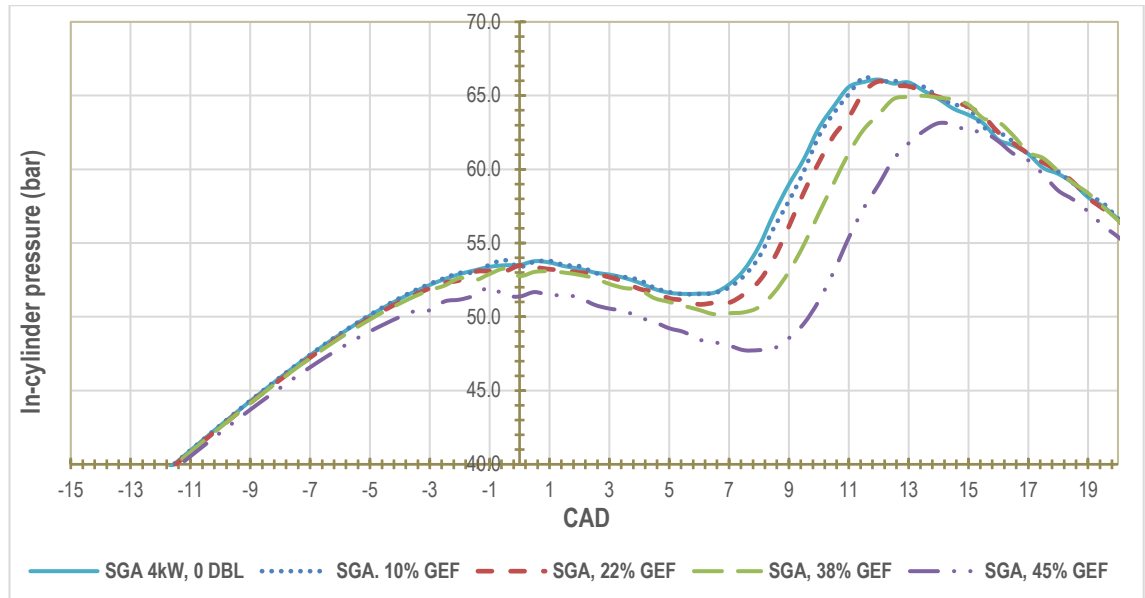
Engine load (%)	%GEF	SoC	ID (CAD)	ID (ms)	$P_{max}$ (bar)	$P_{max}$ location (CAD)
97	0	5.8	19.28	1.05	66.20	11.75
	9	5.6	19.05	1.04	66.20	12.00
	23	6.6	20.10	1.09	65.97	12.00
	38	6.6	20.10	1.08	65.10	12.75
	45	7.5	21.00	1.13	63.13	14.00
74	0	5.3	18.83	1.02	65.08	11.83
	9	6.2	19.65	1.06	64.64	11.75
	22	6.4	19.85	1.07	63.52	12.50
	37	6.7	20.20	1.08	61.54	13.00
56	0	5.6	19.09	1.01	63.60	11.50
	9	5.6	19.07	1.02	62.84	11.33
	21	5.9	19.37	1.03	62.17	11.83
32	0	5.4	18.86	1.01	60.65	11.20
	10	5.6	19.07	1.02	60.83	11.67
	21	5.7	19.18	1.02	59.59	11.75

Table 5.4 shows that the ID increases with increasing SGA across every load. This increase is more profound at higher loads, this is shown graphically in further detail in Fig. 5.13.



**Figure 5-13 The ID at full and 74% engine load versus % GEF of SGA**

Table 5.4 also shows that the peak pressure decreases with increasing % SGA and the  $P_{max}$  location (in terms of CAD) is delayed (moves away from TDC). Both changes are more noticeable at higher loads than at lower loads. Fig. 5.14 shows the P-CAD plots for SGA at full engine load at the various % GEFs evaluated.



**Figure 5-14 P-CAD data for SGA at full engine load at various % GEFs**

Both these findings are supported by the findings reported by Olanrewaju et al. [117] who studied the heat release rate (HRR) and combustion behaviour of SGA using the same instrumentation and equipment.

This co-authored study showed that as the % GEF of SGA was increased, the HRR profile shifted to the right of the diesel baseline profiles, thus concluding that an increase in ID was observed alongside a reduction in  $P_{max}$ . The HRR graphs produced by Olanrewaju al. [117] for generator loads of 4 and 3kW (full and 76% engine load) that depict the effect of syngas concentration on the combustion behaviour of SGA-diesel dual fuel combustion are shown in Figs. 5.15 and 5.16.

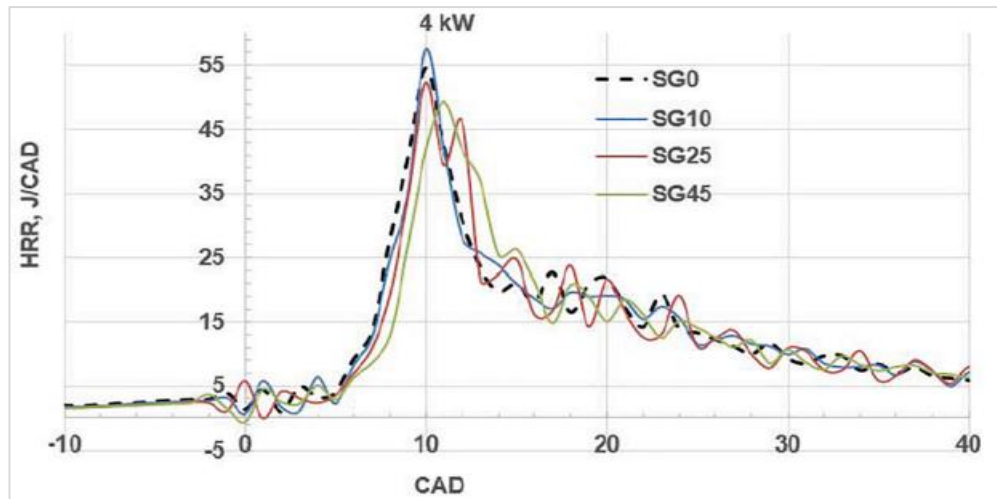


Figure 5-15 HRR profile for 4kW SGA at various % GEF values [117]

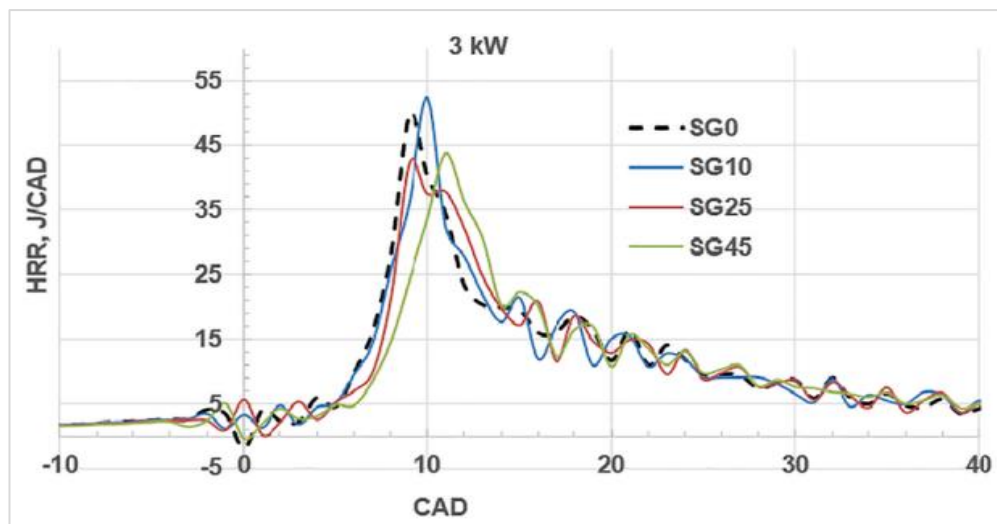


Figure 5-16 HRR profile for 3kW SGA at various % GEF values [117]

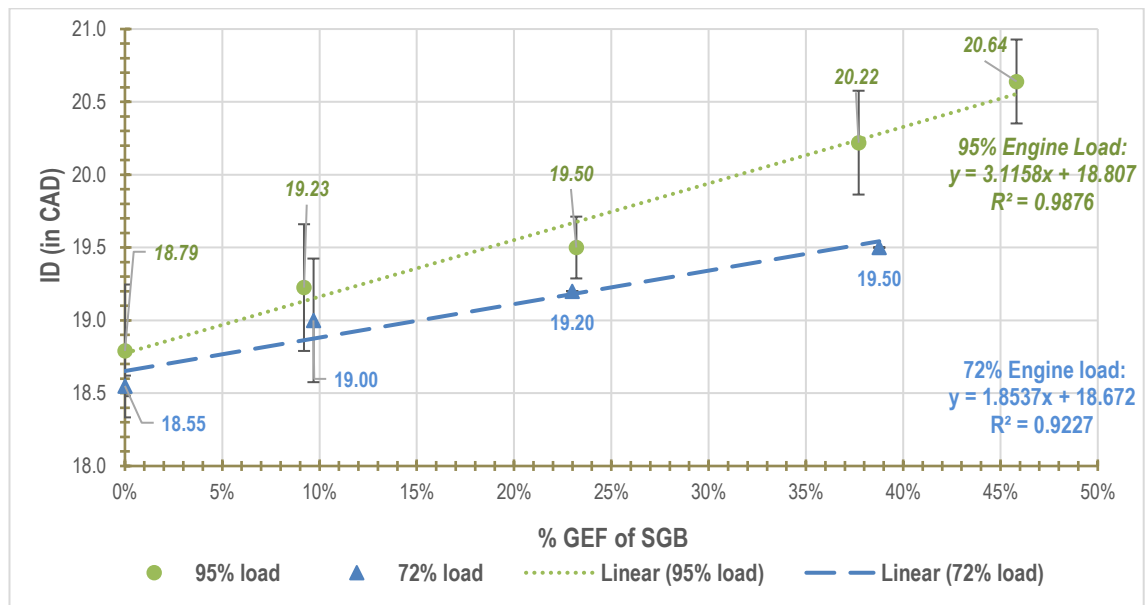
### 5.3.3 Syngas B

Table 5.5 summarises the average peak pressure ( $P_{max}$ ), SoC, and ID data for the SGB experiments. This data shows that the ID increases as the % GEF values of SGB increase across all engine loads. The increase in ID is greater at higher engine loads of 72 and 95%, and this change is illustrated using Fig. 5.17.

Table 5.5 also shows that with increasing SGB, the peak pressure decreases, and the  $P_{max}$  location (in terms of CAD) is increasingly delayed (moves away from TDC). Again, these changes are more noticeable at higher loads than at lower loads. This is depicted in Fig. 5.18 which shows the P-CAD plots at full engine load at the various % GEF values of SGB evaluated.

**Table 5-5 The data for SoC, ID, and P<sub>max</sub> data for SGB-diesel**

Engine load (%)	% GEF	SoC	ID (CAD)	ID (ms)	P <sub>max</sub> (bar)	P <sub>max</sub> location (CAD)
95	0	5.3	18.79	1.02	66.81	11.60
	9	5.7	19.23	1.05	66.36	11.75
	23	6.0	19.50	1.07	65.52	11.80
	38	6.7	20.22	1.09	64.76	12.50
	46	7.1	20.64	1.11	65.68	13.10
72	0	5.1	18.55	1.00	65.06	10.75
	10	5.5	19.00	1.03	63.89	11.75
	23	5.7	19.20	1.03	62.61	12.25
	39	5.8	19.50	1.04	61.30	12.50
54	0	5.2	18.68	1.00	64.84	10.75
	9	5.2	18.70	1.00	63.94	11.75
	22	5.3	18.80	1.01	63.52	11.75
30	0	5.6	19.10	1.02	62.09	11.00
	10	5.6	19.10	1.02	61.82	11.50
	22	5.7	19.24	1.03	60.93	12.00



**Figure 5-17 The ID at full and 72% engine loads versus % GEF of SGB**

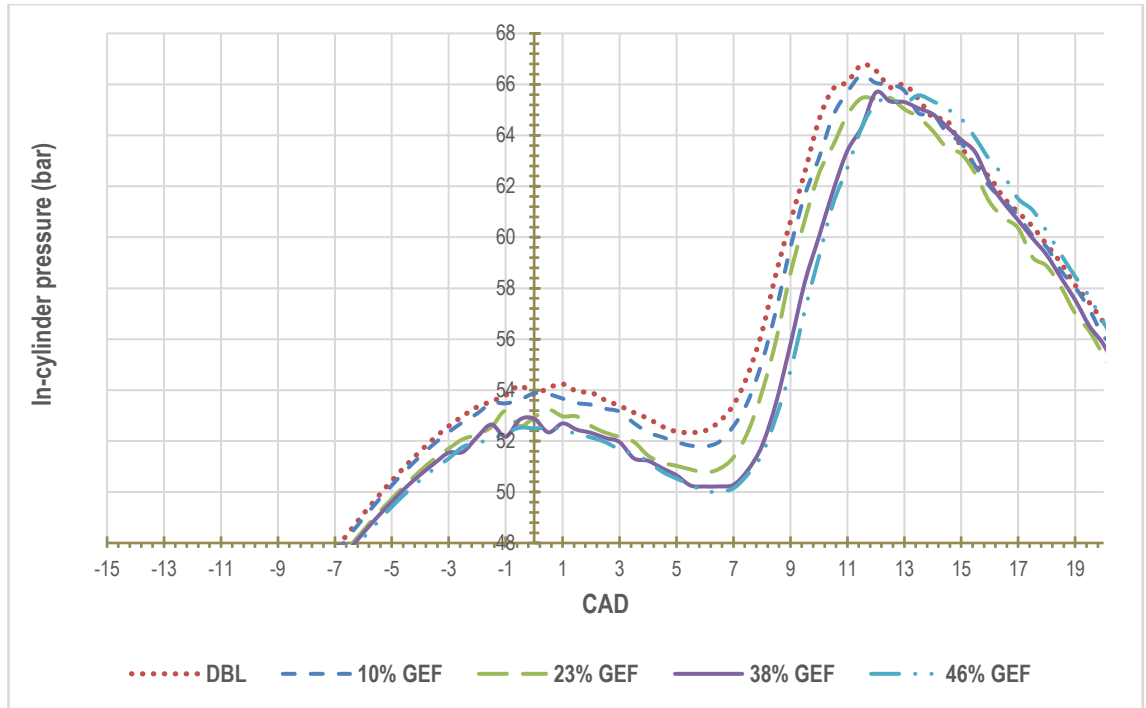


**Figure 5-18 P-CAD data for SGB at full engine load at various % GEFs**

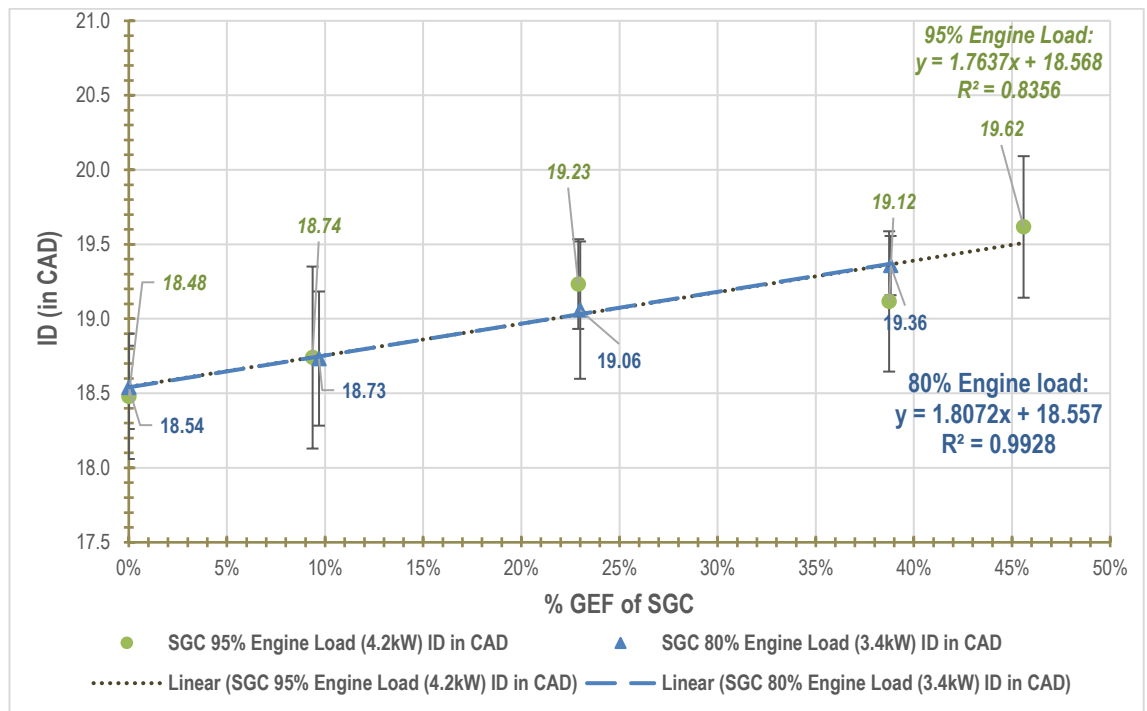
### 5.3.4 Syngas C

Table 5.6 summarises the average data calculated in terms of peak pressure ( $P_{max}$ ), SoC, and ID data for all SGC dual fuel combustion experiments. This data shows that the ID increases as the % GEF values of SGC increase at engine loads of 95 and 80%, as shown in Fig. 5.19. At 51% engine load, there is a minimal change in ID, and at 30% engine load, there is no change in the ID with increasing gas energy fraction.

The peak pressure decreases with increasing SGC at engine loads of 30 to 80%. At full engine load, there is a minor increase seen in the  $P_{max}$  as the SGC is increased, as seen in Fig. 5.20. This change has not been noted with the other syngas types being tested and is further discussed in section 5.3.7. In terms of  $P_{max}$  location, (expressed as CAD), as the % SGC is increased, this shifts to the right, away from TDC, i.e., is increasing delayed and this delay is more noticeable at higher loads than lower loads. This is depicted in Fig. 5.20 which shows the P-CAD plots for SGC at full engine load at the various %GEF values evaluated.

**Table 5-6 The data for SoC, ID, and P<sub>max</sub> data for SGC-diesel**

Engine load (%)	% GEF	SoC	ID (CAD)	ID (ms)	P <sub>max</sub> (bar)	P <sub>max</sub> location (CAD)
95	0	5.0	18.48	1.00	67.00	11.80
	9	5.4	18.74	1.01	67.30	11.75
	23	5.7	19.23	1.05	66.74	11.75
	39	5.6	19.12	1.05	67.43	11.92
	46	6.1	19.62	1.07	68.76	12.75
80	0	5.0	18.54	1.00	66.21	11.20
	10	5.2	18.73	1.02	66.07	11.25
	23	5.6	19.06	1.02	65.41	11.33
	39	5.9	19.36	1.04	64.72	11.71
51	0	5.1	18.57	1.00	64.21	10.83
	9	5.2	18.72	1.01	62.72	10.92
	22	5.4	18.89	1.01	62.10	11.29
30	0	5.0	18.47	0.99	61.42	10.83
	10	4.7	18.15	0.97	61.19	11.30
	22	4.9	18.35	0.97	61.07	11.42



**Figure 5-19 The ID at full & 80% engine loads versus % GEF of SGC**

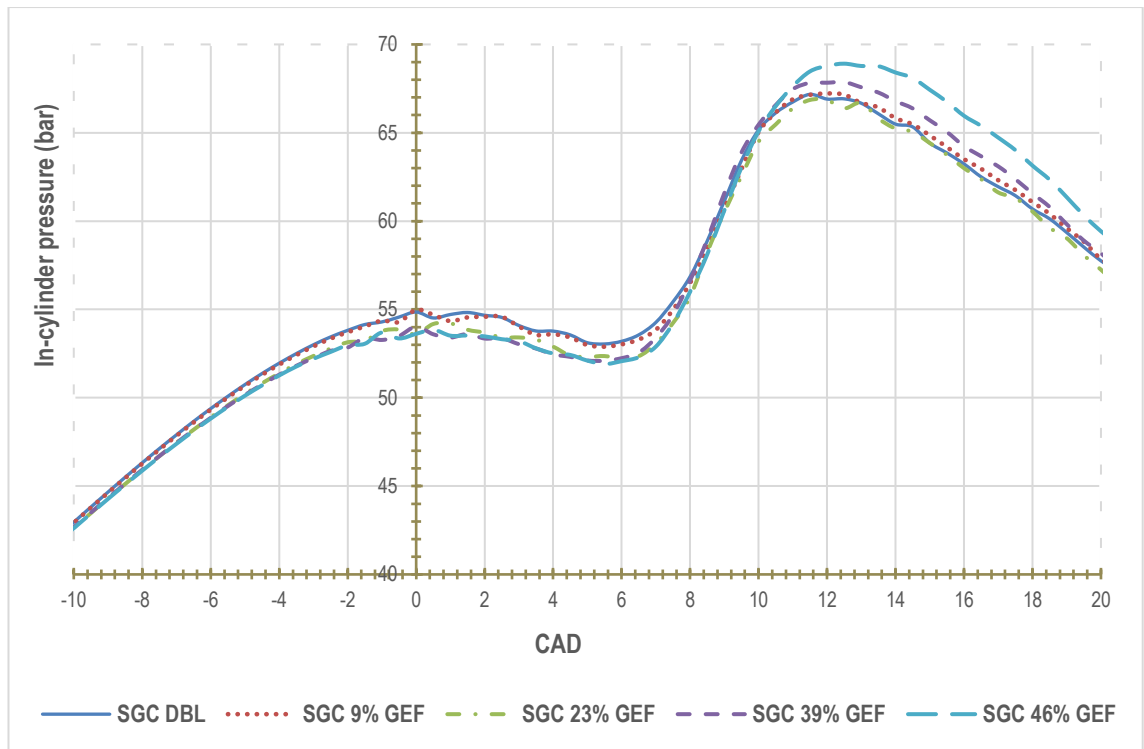


**Figure 5-20 P-CAD data for SGC at full engine load at various % GEFs**

### 5.3.5 Biogas

Table 5.7 summarises the average data in terms of peak pressure ( $P_{max}$ ), SoC, and ID data for all the biogas experiments. This data shows that the SoC increases with increasing biogas substitution (compared to BG0 diesel) across all engine loads. This is attributed to the higher autoignition temperature of biogas [135]. Hence, the ID increases with an increasing GEF of biogas.

This is most apparent for higher engine loads of 97 and 81%, as shown in Fig. 5.21. At lower engine loads of 51 and 31%, there is a minimal change in the ID (when considering the resolution of  $\pm 0.5$  CAD).

The peak pressure decreases with increasing biogas at all engine loads (as seen in Fig. 5.22). In terms of the  $P_{max}$  location, (in CAD), this shifts to the right or is increasingly delayed (moves away from TDC) as the % biogas is increased. At full engine load, a shift of  $>2$  CAD is noted, and at 80% and 51% engine load, this shift is  $>1$  CAD; at 30% engine load, there is minimal change. The change in the P-CAD profile around TDC is depicted in Fig. 5.22 which shows the data for biogas at full engine load at the various % GEF values of biogas evaluated.

**Table 5-7 The data for SoC, ID, and P<sub>max</sub> data for biogas-diesel**

Engine load (%)	% GEF	SoC	ID (CAD)	ID (ms)	P <sub>max</sub> (bar)	P <sub>max</sub> location (CAD)
97	0	5.6	19.05	1.04	66.94	12.00
	9	5.9	19.43	1.06	66.80	12.00
	24	6.3	19.80	1.07	66.60	11.88
	40	6.5	19.96	1.08	64.87	12.75
	48	6.9	20.40	1.10	63.43	14.13
81	0	5.4	18.85	1.02	67.11	11.25
	9	5.7	19.18	1.04	66.38	11.13
	22	5.4	19.07	1.03	64.75	11.88
	38	5.9	19.41	1.04	62.93	12.50
51	0	5.4	18.90	1.02	63.76	10.67
	10	5.4	18.90	1.02	62.74	11.13
	23	5.7	19.16	1.02	61.24	11.88
30	0	5.5	19.02	1.02	61.46	11.17
	<b>*BG 12</b>	5.2	18.70	1.00	60.73	11.50
	23	5.7	19.23	1.03	59.93	11.63

\*The % GEF value used here for 30% load was slightly higher due to the actual minimum flow rate possible versus the required gas flow rate.

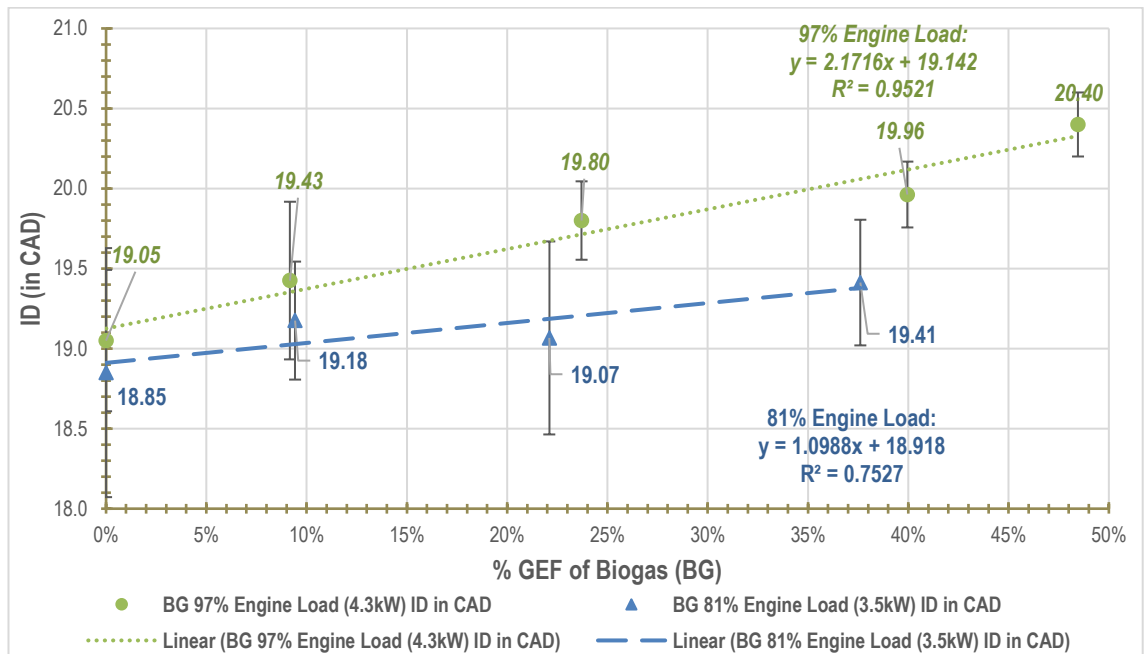


**Figure 5-21 ID at full & 80% engine loads versus %GEF of biogas**

The ID increases with increasing GEF, more so at higher loads. For biogas this is due to an increased flow rate of biogas being added at higher loads which increases the CO<sub>2</sub> amount being added, hence there is a greater diluent effect as the CO<sub>2</sub> changes the charge mixture, which results in a reduction in the in-cylinder temperature and pressure resulting in slower ignition.

Also, the higher cetane number of the biogas will change the autoignition properties and result in longer IDs [135, 140].

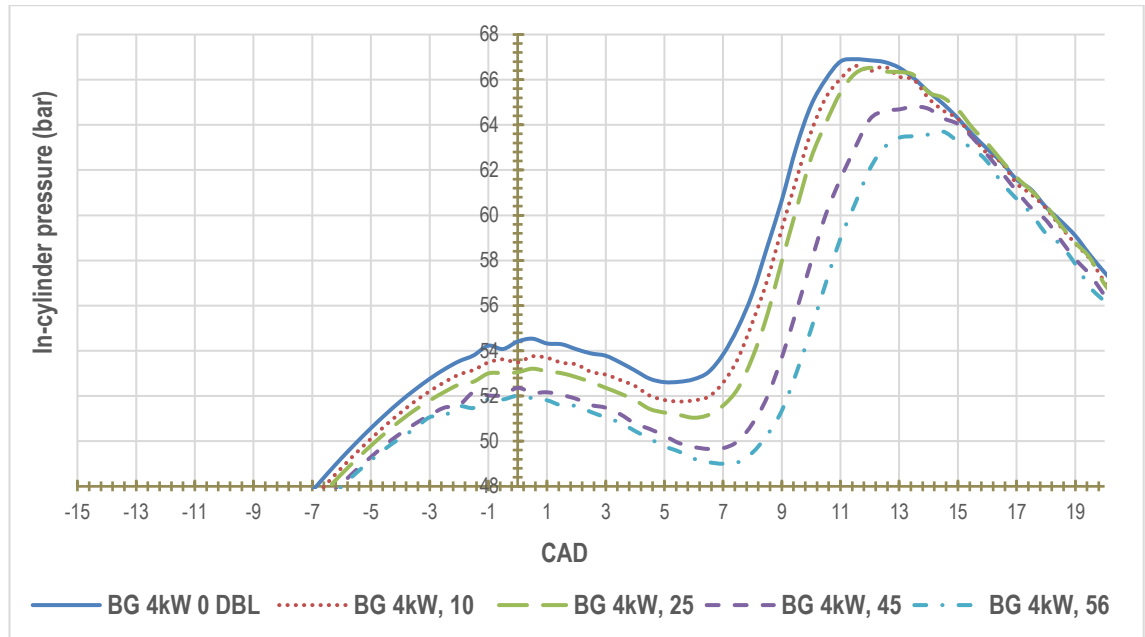


**Figure 5-22 P-CAD data for biogas at full engine load at various %GEF**

### 5.3.6 Discussion of the ignition delay and peak pressure findings

The effect on ID as a result of increasing syngas substitution in dual fuel mode reported in the literature varies, as does the methodology used to calculate this. Moreover, most of the researchers reported an increase in the ID with increasing substitution of syngas/ biogas when in dual fuel mode [117, 135, 136, 139, 144]. The studies that have reported a decrease in the ID in dual fuel mode combustion are few [149, 151], both of these have calculated the ID from modelling work which appears not to have been validated with further experimental work, hence there is a greater degree of uncertainty related to such data.

Again, contrary to this, some studies have reported an increase in  $P_{max}$  with increasing syngas fraction in syngas/diesel dual fuel mode [149, 150, 165]. Similarly, this is also the case for biogas/diesel dual fuel operation whereby the  $P_{max}$  value has been reported as being higher relative to the diesel baseline [135]. In other studies, it was reported that the  $P_{max}$  value remained unaffected by dual fuel operation when using both syngas and biogas [97, 139].

The  $P_{\max}$  value is typically reported to decrease in dual fuel mode versus pure diesel [117, 136, 140, 142, 164, 170]. More importantly, the co-authored HRR study which involved using the same syngas (SGA) and engine equipment also reported a decrease in the  $P_{\max}$  values, delayed  $P_{\max}$  values away from TDC, and an increase in the ID for dual fuel mode combustion using SGA-diesel [117]. The basis for calculating the ID was the SoC which was identified from the P-CAD and HRR curves. Overall, there is conflicting data available in the literature on the effect of the  $P_{\max}$  value in dual fuel mode using syngas or biogas relative to pure diesel, as discussed in Chapter 2.

The shift or delay in  $P_{\max}$  location (in CAD) seen here in dual fuel mode using either syngas or biogas relative to pure diesel is affected by the longer ID experienced. A longer ID shifts the  $P_{\max}$  location away from TDC, towards the expansion stroke resulting in a reduction of the in-cylinder peak pressure [142], hence combustion is occurring later in the expansion stage.

For biogas dual fuel combustion, it is expected that the  $P_{\max}$  value would reduce in dual fuel mode. This is because when the biogas and air are compressed together in the compression stroke, the biogas has higher specific heat than air [136], hence the in-cylinder temperatures are reduced, thereby reducing the corresponding compression pressure [167]. This factor combined with the fact that the  $\text{CO}_2$  content of the biogas hinders burning all lead to a reduction in the  $P_{\max}$  value.

The P-CAD traces produced in this study confirm this; Fig. 5.22 indicates that at TDC the pressure for the biogas/air mixture is lower than that recorded for the diesel baseline. This phenomenon is also noted for syngas/diesel P-CAD trends although it is less apparent for the syngas blends, with SGC being the least affected (see Figs. 5.14 for SGA, Fig. 5.18 for SGB, and Fig. 5.18 for SGC). This decrease in pressure is not related to combustion as this has not yet commenced. This decrease can be explained by the higher specific heat capacity ( $C_p$ ) of the gaseous fuels. Biogas has a higher  $C_p$  value than air [136], this absorbs more heat in the cylinder, which results in a reduction in the  $P_{\max}$  values at around TDC.

The increase in ID can be explained as the addition of biogas/syngas into the cylinder causing a delay in the autoignition of the pilot diesel fuel [136]. In dual fuel mode, the diesel pilot spray is not surrounded solely by air, instead, it is surrounded by a mixture of air and the gaseous fuel injected.

The reaction between the pilot diesel and this gas-air mixture delays the ignition of the pilot diesel fuel causing longer IDs [144]. This could be caused by the reduction of oxygen in the combustion chamber as the gaseous fuel has substituted the air, hence altering the pre-ignition properties [135]. In addition, the CO<sub>2</sub> content acts as a diluent which results in the pilot fuel flame formation being suppressed until the biogas-air mixture reaches autoignition temperature which results in longer IDs [135, 140].

In summary, the ID is significantly affected by oxygen availability and by the autoignition property of the fuel [135]. In both cases (biogas/syngas), the increase in ID leads to a delay in the P<sub>max</sub> location (in terms of CAD), thus shifting the P<sub>max</sub> further away from TDC. The increase in ID shifts the overall combustion to the expansion stroke leading to a drop in P<sub>max</sub> [144]. Also, the low cetane number of the gaseous fuels tested contributed to the longer IDs, which became more profound as the % GEF increased [117].

This study showed that for all the gaseous fuels tested, the ID values increased with increasing % GEFs when compared to the DBL data. This is reflective of that reported by many researchers as discussed earlier. For all the gaseous fuels tested, as the % GEF values were increased, generally, the peak in-cylinder pressure values decreased (except for SGC at full load). For SGC, this could be indicative of a higher burning rate caused by the higher hydrogen content in the syngas. Also, the location of P<sub>max</sub> location (in CAD) increased or was delayed; shifted away from TDC. This was observed for all dual fuel types, at all % GEF values across all engine loads. For syngas/biogas dual fuel blends, the reduction in P<sub>max</sub> can also be explained by the fact that dual fuel operation has a lower energy release rate when compared to diesel [142]. An HRR study of all the syngas dual fuel combustion data would be beneficial in increasing knowledge in this area. SGA-diesel HRR analysis was conducted [117], but this was not completed for the remaining syngas blends due to the time constraints of the project.

In summary, for all gas/diesel blends tested, the ID and P<sub>max</sub> location increased, whilst P<sub>max</sub> decreased with increasing % GEF at all engine loads and when compared to the DBL data. These findings agree directly with the co-authored study which determined the ID using a different methodology by analysing the HRR curves generated [117]. The changes in the ID and P<sub>max</sub> were more noticeable at higher loads than at lower loads. The increase in ID is caused by the alteration of the air/fuel ignition properties caused by the addition of syngas/biogas, and also the reduction in the availability of oxygen.

The late ID results in the combustion shifting into the expansion stroke thus causing a decrease in  $P_{max}$  in dual fuel mode.

### 5.3.7 Comparison of the ignition delay and the peak pressure data across gas blends

#### 5.3.7.1 Ignition delay data

The increase in the ID (in CAD) data was cross compared across gas types. This was done by calculating the % change in ID using the ID values from SG0-diesel and the highest % GEF evaluated at each load. The findings have been summarised in Table 5.8.

**Table 5-8 The % change in the ID for each gas fuel type between the highest % GEF and DBL data at all engine loads**

<b>% Change in ID (relative to DBL) for:</b>	<b>SGA</b>	<b>SGB</b>	<b>SGC</b>	<b>Biogas</b>
46% GEF at full engine load	8.95	9.85	6.15	7.09
38% GEF at 77% engine load	7.26	5.12	4.41	2.98
22% GEF at 53% engine load	1.46	0.67	1.72	1.39
22% GEF at 30% engine load	1.67	0.72	-0.63	1.10

The largest % change value calculated in Table 5.8 is an indication of inferior combustion performance, relative to the other gaseous fuels. This data shows that at engine loads of 96, 77, and 30%, SGC has the smallest increase in ID versus the other gaseous fuel types. At 53% engine load, SGB has the smallest % increase in ID.

To summarise, at 77% engine load, SGC has the highest BTE, lowest BSEC, the smallest decrease in peak pressure, the smallest shift in the  $P_{max}$  location, and the smallest increase in ID, thus confirming this syngas has superior combustion performance at this load in comparison to the other syngas blends.

#### 5.3.7.2 Peak pressure data

The % change in the average peak pressure ( $P_{max}$ ) was calculated to determine if the syngas composition affected the  $P_{max}$  value. The % change in  $P_{max}$  was determined between diesel (SG0 or BG0) and the highest % GEF value evaluated for all engine loads, this is cross compared and summarised in Table 5.9.

**Table 5-9 The % change in the  $P_{max}$  value for each gas blend**

<b>% Change in the <math>P_{max}</math> (relative to DBL) for:</b>	<b>SGA</b>	<b>SGB</b>	<b>SGC</b>	<b>Biogas</b>
46% GEF at full engine load	-4.63	-1.70	2.63	-5.25
38% GEF at 77% engine load	-5.43	-5.79	-2.25	-6.24
22% GEF at 53% engine load	-2.24	-2.03	-3.29	-3.96
22% GEF at 30% engine load	-1.74	-1.87	-0.57	-2.49

The most negative value of the ‘%  $P_{max}$  change’ shown in Table 5.9 represents the largest decrease in the  $P_{max}$  value (versus diesel baseline). When comparing the gaseous fuels tested, SGC experienced the lowest  $P_{max}$  drop/change at full load, 77%, and 30% engine load. Moreover, at full load for SGC, a pressure rise was seen. This data confirms that the higher hydrogen content in SGC enhanced the combustion performance at all engine loads except for 53%.

The P-CAD plots for each syngas blend at full engine load at a GEF of 46%, alongside a diesel baseline plot, are shown in Fig. 5.23; this shows the  $P_{max}$  increase of SGC relative to the SGA, SGB, and diesel baseline.

SGB had the smallest % change in  $P_{max}$  at an engine load of 53% in comparison to the other syngas blends. This data is also supported by this blend having the smallest change in the ID (relative to the diesel baseline) at this test condition. However, Fig 6.44, and Fig. 6.52 in Chapter 6 indicate that SGB does not have lower corresponding THC and CO emissions when compared to SGA/SGC at these test conditions.

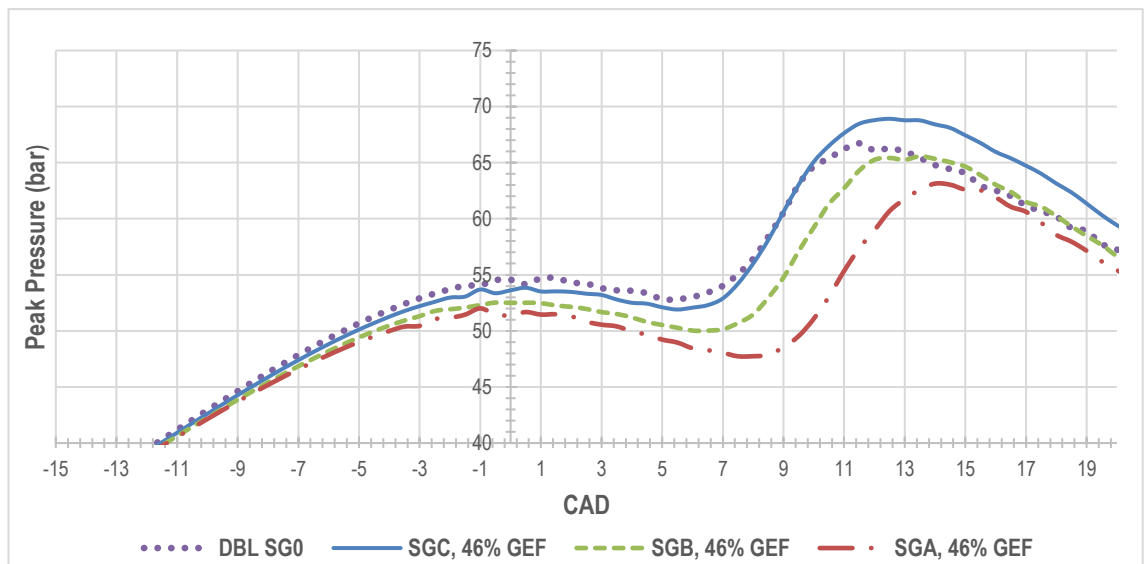


**Figure 5-23 P-CAD profiles per syngas blend at full engine load at 46 %GEF (with diesel baseline as a reference)**

The data from Table 5.9 showing the % change in  $P_{max}$  for the three syngas blends is illustrated in Fig. 5.24; this shows the effect of  $H_2$  content on the % change in  $P_{max}$  for various engine loads. This shows that as the load increases, the effect of a higher  $H_2$  content and  $H_2/CO$  ratio has a greater effect on the combustion performance, as seen earlier for BTE and BSEC. At full engine load, using a 46% substitution of syngas results in a sharp positive increase in the peak pressure.

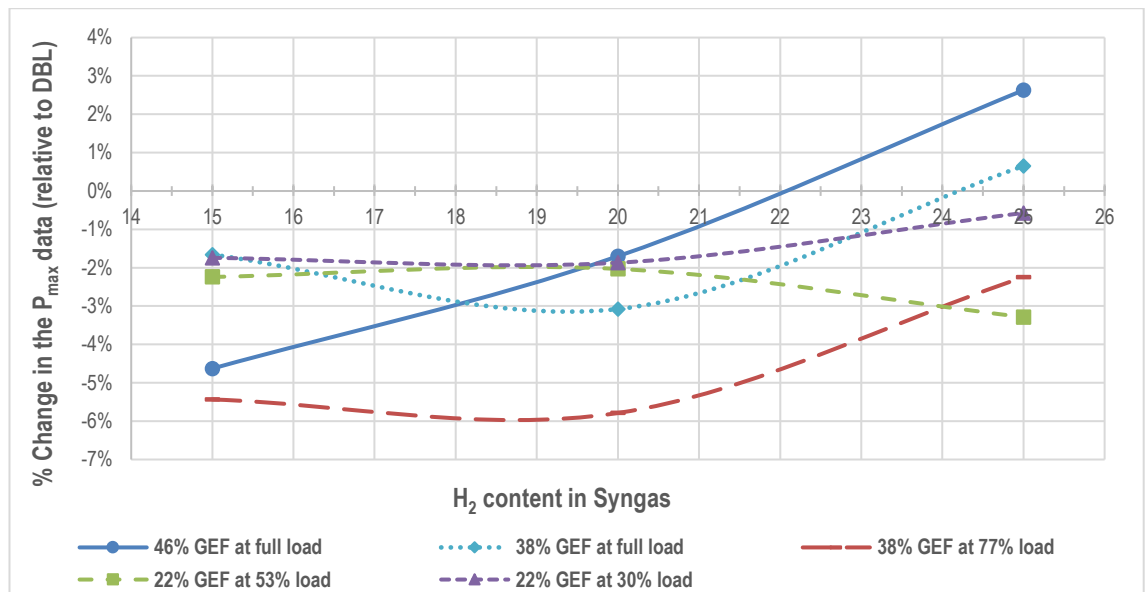


**Figure 5-24 The %  $P_{max}$  change versus the  $H_2$  content of the syngas**

Overall, this trend confirms that the change in  $H_2$  content and the  $H_2/CO$  ratio is affecting the combustion performance; better combustion performance is seen for SGC at engine loads > 50% (4 and 3kW generator loads). These findings tie in with that reported in the literature as discussed in section 2.11.12. At lower loads (<50% engine load) the  $H_2/CO$  composition of the syngas is said to have a reduced impact on the overall efficiency and combustion performance. In this study, this is evident in the plots for 30, and 53% engine loads as shown in Fig. 5.24.

These findings are consistent with that reported by other researchers [128, 148] who reported a decrease in the ID, an increase in  $P_{max}$ , local temperatures, and heat release, as the ratio of  $H_2$  mass in the syngas was increased. Hydrogen-rich mixtures are desired as they improve combustion efficiency. When considering the  $H_2:CO$  ratio of the three syngas blends tested (mole %ratio of  $H_2:CO$  in SGA is 0.75:1, SGB: 1 to 1, and for SGC 1.25:1), not only does SGC have a higher  $H_2$  content, but it also has a higher  $H_2:CO$  ratio which is associated with enhanced combustion performance.

This explains the higher BTE and lower BSEC data, and the smallest % reduction in  $P_{max}$  values of the three syngas blends at full and 77% engine loads.

### 5.3.7.3 Peak pressure location

The change in the average peak pressure ( $P_{max}$ ) location data (expressed as CAD) derived from the P-CAD plots was cross compared across gas types. The change in the CAD value of the  $P_{max}$  location was calculated by subtracting the  $P_{max}$  location (in CAD) at that test condition from the diesel baseline data (generated from that specific dataset). The findings have been summarised in Table 5.10.

**Table 5-10 The change in the  $P_{max}$  location (in CAD) for each gas fuel type between the highest and lowest % GEF value evaluated across all engine loads**

Change in the $P_{max}$ location in CAD (relative to DBL) for:	Change in $P_{max}$ (in CAD)			
	SGA	SGB	SGC	Biogas
46% GEF at full engine load	2.25	1.50	0.95	2.13
38% GEF at 77% engine load	1.17	1.75	0.51	1.25
22% GEF at 53% engine load	0.33	1.00	0.45	1.21
22% GEF at 30% engine load	0.55	1.00	0.58	0.46

The greater the change/value calculated in Table 5.10, the greater the effect the ID has had on that test condition. The data in Table 5.10 shows that at higher loads (full and 77% engine loads), SGC has the lowest change in  $P_{max}$  location versus the other syngas blends; only a marginal shift/change is observed at an engine load of 77%.

As discussed earlier, the higher  $H_2$  content of SGC, coupled with the higher  $H_2:CO$  ratio produces a smaller increase/shift of  $P_{max}$  value. Hence, the combustion rate of  $H_2$  and  $CO$  is faster with more premixing being achieved, coupled with a smaller increase in ID sees a smaller shift of the combustion phase into the expansion stroke (when compared to SGB/SGA) therefore resulting in better combustion performance.

It should also be noted that SGA has the lowest shift or delay of the  $P_{max}$  in CAD shift at 53 and 30% engine loads.

## 5.4 Exhaust gas temperature, air-fuel ratio, and the equivalence ratio ( $\phi$ )

The average EGT and AFR for diesel baseline and dual fuel mode, alongside the  $\phi$ , were calculated for each dual fuel run at each % GEF value evaluated across all engine loads. The results are summarised based on the gas type alongside the diesel baseline (as a reference point).

### 5.4.1 Diesel baseline

For reference, the  $\phi$  and the EGT data generated from all the diesel baseline runs (averaged from all diesel data sets) were summarised and are depicted in Fig. 5.25.

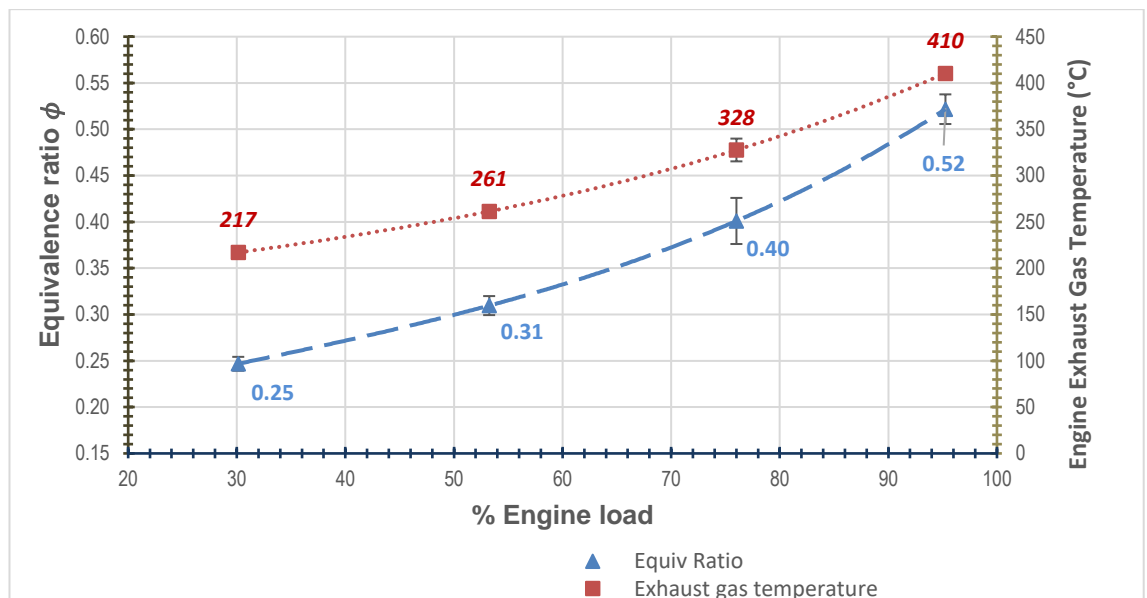


**Figure 5-25 The exhaust gas temperature and  $\phi$  for the diesel baseline**

The data shows that for pure diesel, as the engine load increases so does the engine exhaust gas temperature and the  $\phi$ . This is expected as fuel consumption increases with load, hence the mixture becomes richer.

### 5.4.2 Syngas A

The data for the engine exhaust gas temperature, AFR, and the  $\phi$  are tabulated in Table 5.11 for SGA.

**Table 5-11 The engine EGT, AFR, and the  $\phi$  for SGA-diesel**

Generator Load (kW)	% Engine load	% GEF	*AFR	$\phi$	Engine EGT (°C)
4.3	96	0	28.5	0.51	406
4.2		10	15.1	0.53	413
4.2		23	8.8	0.56	429
4.3		38	5.3	0.63	459
4.3		45	4.1	0.71	482
3.1	74	0	37.3	0.39	321
3.1		9	19.9	0.41	322
3.1		22	11.7	0.43	332
3.1		37	7.2	0.48	345
2.3	56	0	45.6	0.32	267
2.3		9	25.1	0.33	270
2.3		22	14.7	0.35	278
1.3	31	0	57.7	0.25	220
1.3		10	30.7	0.26	221
1.3		21	18.4	0.28	226

\*AFR represents either the  $AFR_{DBL}$  or the  $AFR_{df}$  depending on the combustion mode

Table 5.11 shows that as the % GEF value is increased, the engine exhaust gas temperature and the  $\phi$  increase, whilst the AFR value decreases across all engine loads.

Olanrewaju et al. [117] reported that the calculated in-cylinder temperature (calculated as the flame temperature), and the peak temperature for SGA decreased below baseline diesel as the fraction of the syngas in the dual fuel was increased. Due to the differences in the method of calculating the syngas substitution fractions in this thesis and the study by Olanrewaju et al. [117], Table 5.12 shows the equivalent syngas fraction used in this thesis and the co-authored HRR study being discussed (as previously presented in Chapter 2, section 2.1).

**Table 5-12 The equivalent % GEFs used in the HRR study**

% Engine/ generator load (kW)	Syngas energy fraction in HRR study [117]	Equivalent % GEF from this thesis
96 (4kW)	10	10
76 (3kW)	24	22
54 (2kW)	45	38
30 (1kW)	Not evaluated	46

The HRR study looked at a maximum SGA substitution of 45% gas energy fraction (equivalent to 38% GEF) only. The change in the calculated cylinder temperature change was more apparent at low loads than at high. The modelled in-cylinder temperature curves for all the engine loads are depicted in Figs. 5.26 – 5.29.

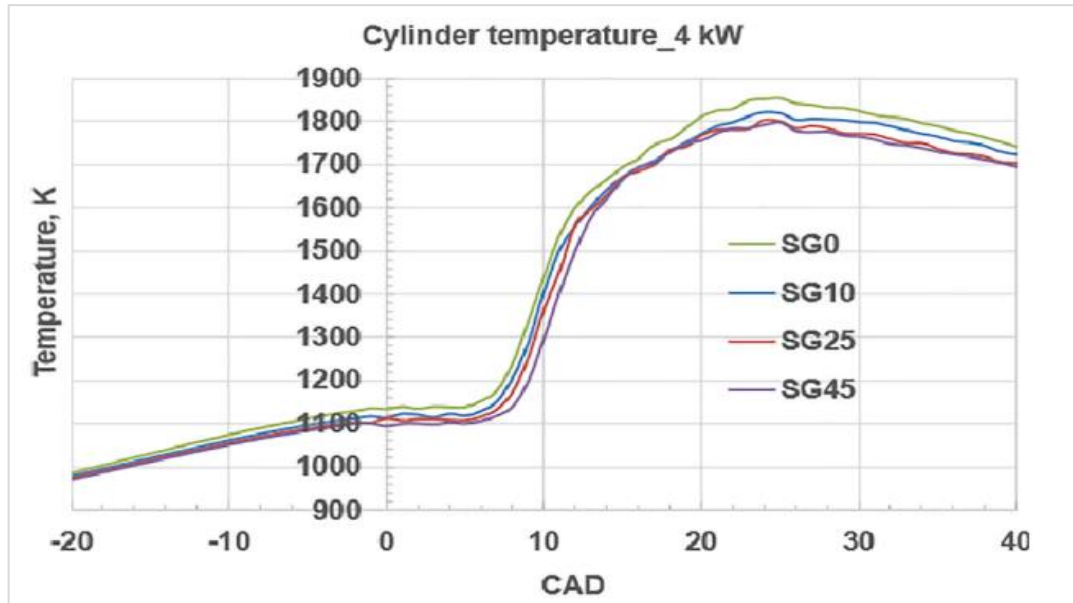


Figure 5-26 Modelled in-cylinder temperatures for SGA at full engine load [117]

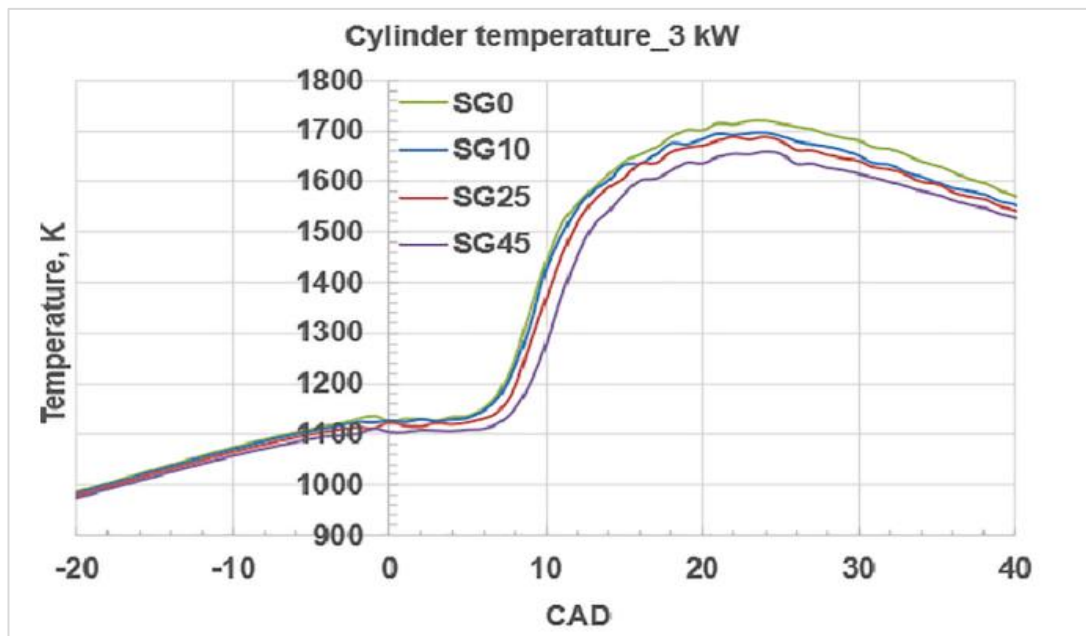
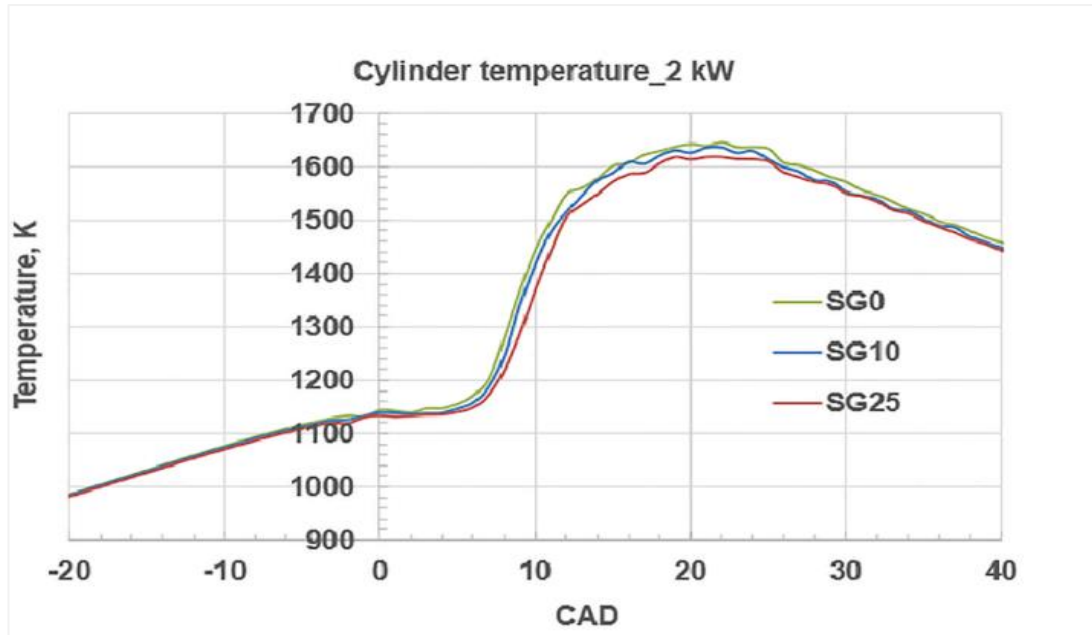
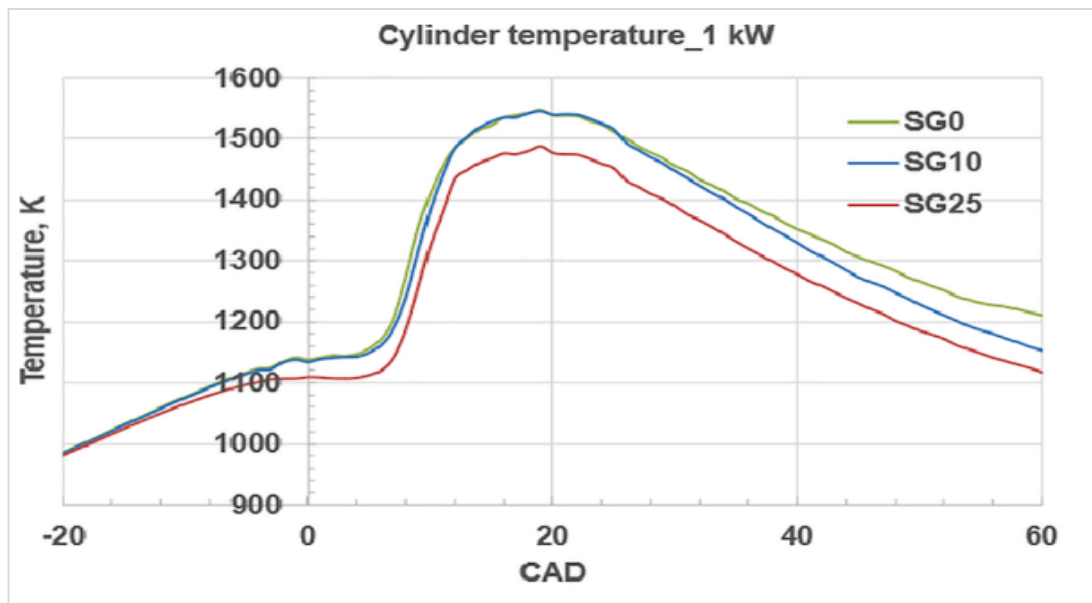


Figure 5-27 Modelled in-cylinder temperatures for SGA at 76% engine load [117]



**Figure 5-28 Modelled in-cylinder temperatures for SGA at 54% engine load [117]**



**Figure 5-29 Modelled in-cylinder temperatures for SGA at 30% engine load [117]**

It can be concluded from this HRR dual fuel study that as the SGA energy fraction increases, the EGTs increase, but the in-cylinder temperatures decrease at all engine loads, with a larger decrease noted at lower engine loads [117].

### 5.4.3 Syngas B

The data for the engine exhaust gas temperature, the AFR, and the  $\phi$  are tabulated in Table 5.13 for SGB.

**Table 5-13 The engine EGT, AFR, and the  $\phi$  for SGB**

Generator load (kW)	% Engine load	% GEF	*AFR	$\phi$	Engine EGT (°C)
4.1	96	0	28.7	0.51	403
4.2		9	16.0	0.54	420
4.2		22	9.8	0.57	430
4.1		39	6.3	0.60	450
4.3		45	5.0	0.65	474
3.0	72	0.0	39.0	0.37	314
3.1		10	22.3	0.39	320
3.1		23	13.2	0.41	331
3.1		39	8.4	0.44	345
2.2	54	0.0	49.0	0.30	261
2.2		9	28.1	0.31	265
2.2		22	17.1	0.33	272
1.2	31	0	61.4	0.24	215
1.2		10	35.7	0.24	217
1.2		22	21.8	0.26	220

\*AFR represents either the  $AFR_{DBL}$  or the  $AFR_{df}$  depending on the combustion mode

Table 5.13 shows that as the % GEF of SGB is increased, the EGT and the  $\phi$  increase, whilst the AFR value decreases across all engine loads.

### 5.4.4 Syngas C

The data for the engine exhaust gas temperature, the AFR, and the  $\phi$  are tabulated in Table 5.14 for SGC. The AFR represents either the  $AFR_{DBL}$  or the  $AFR_{df}$  depending on the combustion mode.

**Table 5-14 The engine EGT, AFR, and the  $\phi$  for SGC**

Generator Load (kW)	% Engine load	% GEF	*AFR	$\phi$	Engine EGT (°C)
4.2	95	0	28.1	0.52	416
4.2		9	17.7	0.53	424
4.2		22	10.9	0.57	443
4.2		38	7.0	0.60	467
4.2		46	6.1	0.60	473
3.4	80	0	36.0	0.41	337
3.4		9	22.1	0.42	346
3.4		22	13.9	0.44	357
3.4		37	9.0	0.48	373
2.1	51	0	47.9	0.30	260
2.1		9	29.6	0.32	264
2.1		23	18.0	0.34	270
1.2	29	0	60.0	0.24	217
1.2		10	35.6	0.26	219
1.2		20	22.9	0.28	222

Table 5.14 shows that as the % GEF value of SGC is increased, the engine EGT and the  $\phi$  increase, whilst the AFR value decreases across all loads.

### 5.4.5 Biogas

The data for the engine exhaust gas temperature, the AFR, and the  $\phi$  are tabulated in Table 5.15 for biogas.

**Table 5-15 The engine EGT, AFR, and the  $\phi$  for biogas.**

Generator Load (kW)	% Engine load	% GEF	*AFR	$\phi$	Engine EGT (°C)
4.2	97	0	26.8	0.54	417
4.2		9	21.5	0.56	424
4.3		24	15.7	0.60	431
4.4		40	12.1	0.65	456
4.4		49	10.4	0.67	464
3.4	81	0	33.7	0.43	339
3.5		9	27.1	0.44	342
3.5		22	20.6	0.47	352
3.5		38	15.4	0.51	363
2.1	52	0	46.3	0.32	259
2.1		10	37.3	0.33	261
2.1		23	27.2	0.35	266
1.2	30	0	57.8	0.25	216
1.2		12	43.1	0.27	216
1.2		23	33.6	0.29	219

\*AFR represents either the  $AFR_{DBL}$  or the  $AFR_{df}$  depending on the combustion mode

Table 5.15 shows that as the % GEF value of the biogas is increased, the engine EGT and the  $\phi$  increase, whilst the AFR value decreases across all engine loads.

#### **5.4.6 Discussion of the exhaust gas temperature data**

An increase in the temperature of the engine exhaust gases in pure diesel mode usually indicates better thermal efficiency/complete combustion, which is seen at higher loads, alongside an increase in fuel consumption (as shown in Fig. 5.1). For dual fuel (gas/diesel) combustion, an increase in exhaust gas temperature data is not necessarily indicative of better thermal efficiency, nor is it reflective of higher in-cylinder temperatures as reported by the HRR study of SGA-diesel whereby EGTs increased with increasing syngas fraction, however, the modelled in-cylinder temperatures decreased [117].

In dual fuel mode, using syngas/diesel, a reduction in the combustion efficiency results in an increase in the exhaust gas temperature, and this is typically accompanied by a decrease in the  $P_{max}$  value (versus pure diesel) [142]. The rise in the exhaust gas temperature seen in all the syngas-diesel blends tested can be attributed to a lack of adequate combustion time between diesel and syngas due to longer IDs [142].

In dual fuel mode using biogas/diesel, the increase in the engine exhaust gas temperatures also suggests a reduction in combustion performance (versus pure diesel). Typically in biogas/diesel blends, the in-cylinder and combustion temperatures are known to decrease in comparison to pure diesel [135] as discussed earlier due to the  $CO_2$  content of the gas acting as a diluent, thus, leading to reductions in the cycle temperature. Typically, the increase in the EGTs in dual fuel mode is reflective of later burning [157]

Dual fuel data reported here for all gas/blends evaluated, all show an increase in the engine exhaust gas temperature as shown in Table 5.11, and Tables 5.13 to 5.15. Taking this temperature rise into consideration alongside the reduced BTE, reduced in-cylinder temperatures [117], reduced  $P_{max}$ , delayed  $P_{max}$  location further away from TDC, increased BSEC, and ID data, it can be said that the combustion performance is adversely affected (with increasing % GEF) across all engine loads when using a gas/diesel blend in dual fuel mode versus pure diesel.

### 5.4.7 Cross-comparison of the exhaust gas temperature data

As stated earlier, in general, the increase in exhaust gas temperature in dual fuel mode is due to the lack of sufficient combustion time present between the syngas and diesel fuel [142].

In addition, the syngas with the highest H<sub>2</sub> content should have a reduced duration of combustion thereby increasing the average combustion temperature [19], leading to better combustion and therefore hotter exhaust gases in comparison to the other syngas blends.

In this study, the resulting exhaust gas temperatures are expected to increase when compared to the DBL data due to the dual fuel mode as discussed earlier. However, the magnitude of the increase will be influenced by the hydrogen content of the syngas as hydrogen produces higher flame speeds and temperatures. Thus, when cross-comparing engine exhaust gas temperature data across syngas types, it is envisaged that SGC will produce hotter exhaust gases at engine loads >50% (3 and 4kW generator loads).

To compare engine exhaust gas temperatures, temperature data from the thermocouple inserted into the exhaust manifold was utilised. This was averaged for each testing condition and then normalised to account for the slight variation/change in the diesel baseline start temperature for each gas/diesel blend testing condition. The normalised engine exhaust gas temperature plots for all engine loads at all % GEF values evaluated are shown in Figs. 5.30 - 5.33 (whereby 1.0 represents diesel baseline values).

At full engine load, this normalised data shows that there is no discernible difference in the engine exhaust gas temperatures between the syngas blends except for 46% GEF whereby SGC has the lowest value. Biogas-diesel combustion produced the lowest normalised engine exhaust gas temperatures at full engine load at GEF >10% as shown in Fig. 5.30.

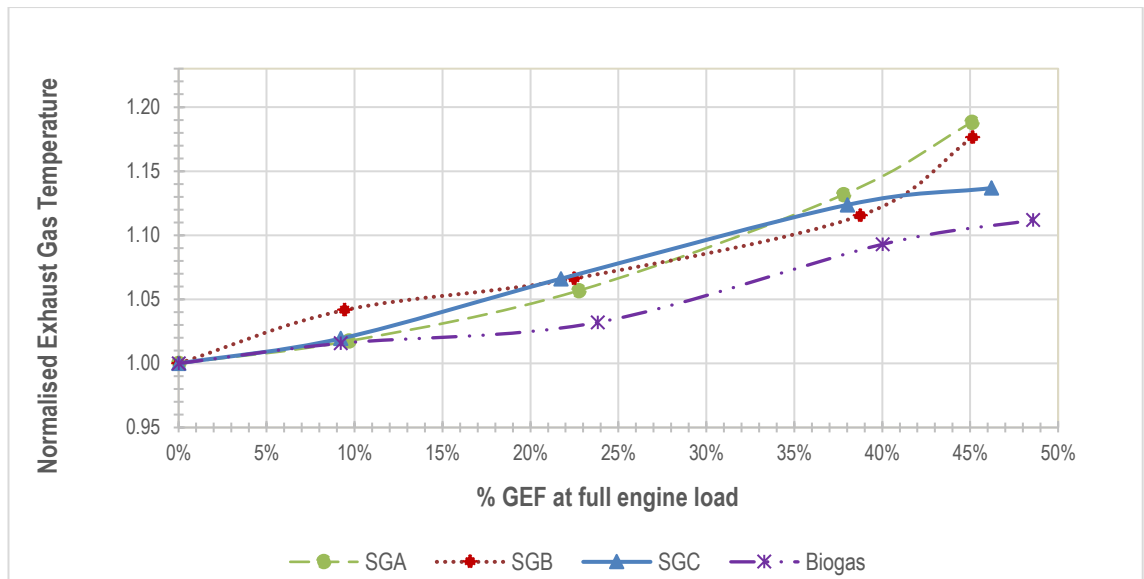


**Figure 5-30 Normalised EGT data comparison at full engine load across the dual fuel gas types at all the % GEF values tested**

At an engine load of 77% (see Fig. 5.31), the normalised engine exhaust gas temperatures are higher for SGC versus all the other gaseous fuels tested with SGA exhibiting the lowest exhaust gas temperatures of the three syngas blends. These findings can be explained as the effect of temperature reduction related to dual fuel operation is offset by the fact that the higher H<sub>2</sub> content has led to an increase in the average combustion temperature [273], thereby producing hotter exhaust gases. SGC had the lowest change in P<sub>max</sub> location versus the other syngas types at full and 77% engine load. The P<sub>max</sub> occurred closer to TDC at these engine loads compared to the other syngas blend. A delay in the location of the P<sub>max</sub> is indicative of late combustion. Hence, it can be postulated that increasing the hydrogen content of the syngas has reduced combustion duration because the P<sub>max</sub> occurs earlier in SGC relative to the other syngas blends at full and 77% engine load conditions. Due to the impact of Covid-19, the HRR study was not completed for SGB and SGC, so no comparisons can be made regarding the difference in the duration of combustion.

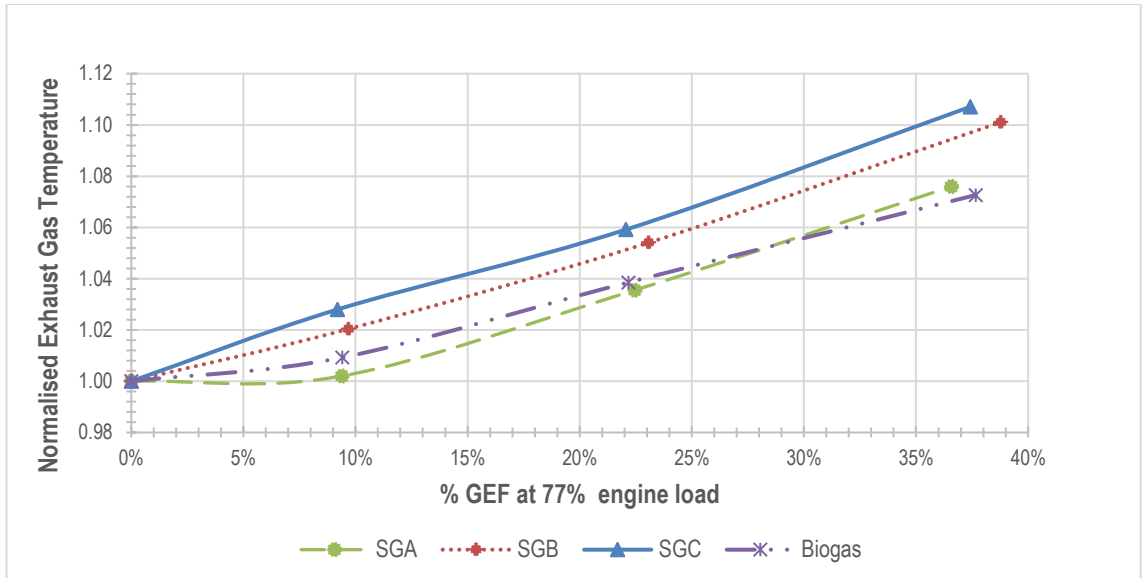


**Figure 5-31 Normalised EGT data comparison at 77% engine load of the various dual fuel gas types with increasing % GEF**

At 54 and 30% engine loads, (see Figs. 5.32 - 5.33), the normalised data plots show that overall, all three syngas blends have similar exhaust gas temperature profiles, with the exception of 10% GEF where SGA has the lowest EGT value. Overall, at lower engine loads the data suggests that the hydrogen content of the syngas is not affecting the resulting exhaust gas temperatures. Also, in dual fuel mode combustion, biogas-diesel combustion produces the coolest EGTs.

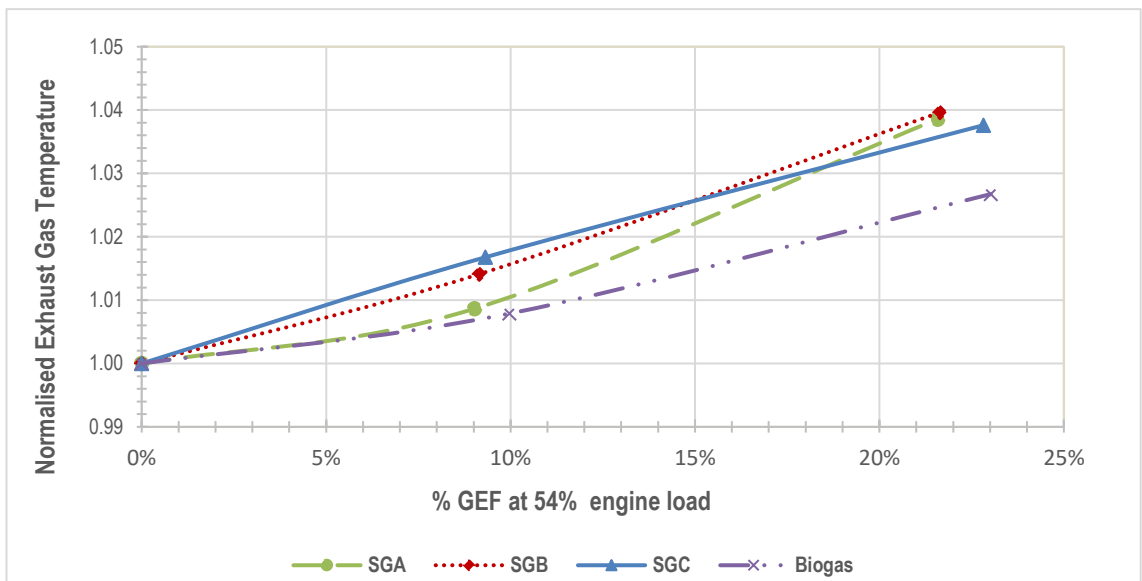


**Figure 5-32 Normalised EGT data comparison at 54% engine load of the various dual fuel gas types with increasing % GEF**

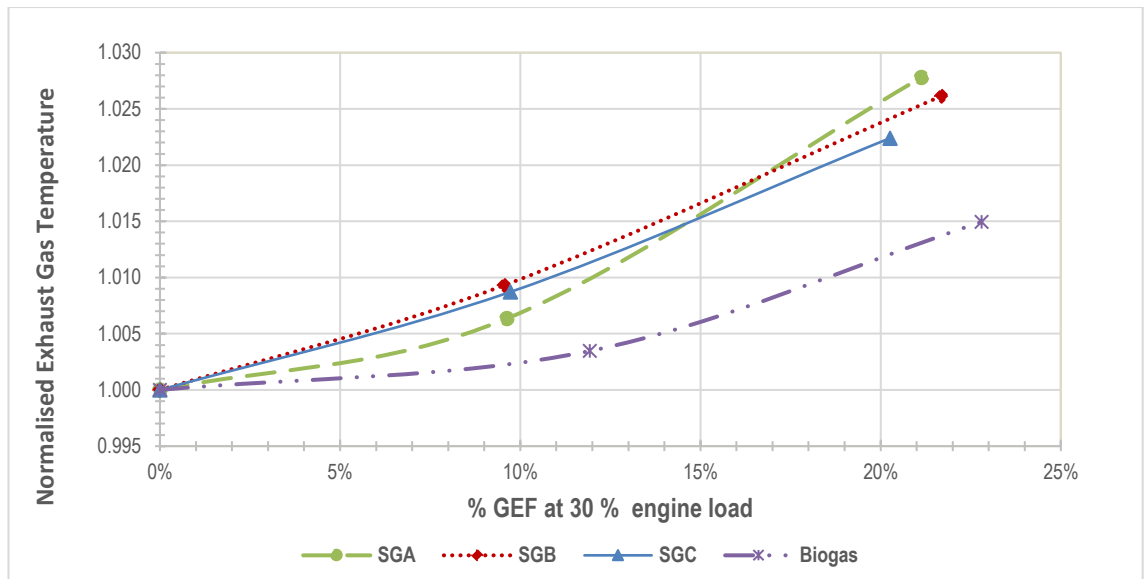


**Figure 5-33 Normalised EGT data comparison at 30% engine load of the various dual fuel gas types with increasing % GEF**

## 5.5 Summary

As syngas/biogas % GEFs are increased across all engine loads, the general trends noted (in comparison to the diesel baseline) were as follows:

- An increase in BSEC, and a decrease in the BTE
- A decrease in  $P_{max}$
- An increase in ID
- An increase in the location of  $P_{max}$  (in CAD) away from TDC
- A decrease in the AFR
- An increase in the  $\phi$
- An increase in the engine exhaust gas temperature
- A decrease in the flame temperature as calculated by the HRR co-authored study using SGA [117]

Overall, this leads to a reduction in combustion efficiency in dual fuel mode for reasons elaborated earlier. In terms of gas composition, the conclusions drawn when comparing the three syngas blends are summarised in Table 5.16.

**Table 5-16 Summary of the trends noted when cross-comparing data across the syngas blends evaluated**

Parameter	Best performing syngas at engine load:			
	Full load	76%	54%	30%
Highest <i>BTE</i>	No trend	<b>SGC</b>	SGA	No trend
Lowest <i>BSEC</i>	No trend	<b>SGC</b>	SGA	No trend
Smallest $P_{max}$ decrease	<b>SGC</b>	<b>SGC</b>	SGB	<b>SGC</b>
Smallest $P_{max}$ location delay	<b>SGC</b>	<b>SGC</b>	SGA	SGA
Smallest increase in <i>ID</i>	<b>SGC</b>	<b>SGC</b>	SGB	<b>SGC</b>
Highest <i>EGT</i>	No trend	<b>SGC</b>	No trend	No trend

Hence, Table 5.16 illustrates that when considering the various parameters evaluated, SGC displays superior combustion performance due to the higher hydrogen ( $H_2$ ) content and  $H_2/CO$  ratio, at engine loads  $\geq 76\%$ . At engine loads of 54 and 30%, any differences in the combustion parameters noted cannot necessarily be attributed to the difference in the  $H_2$  content, hence at these loads, a syngas blend rich in hydrogen or with a high  $H_2/CO$  ratio is not necessarily beneficial in terms of combustion performance.

At an engine load of 54%, SGA performs better than SGB for three out of the six parameters evaluated; SGA has a higher *BTE*, lower *BSEC* values, and the smallest delay in the  $P_{max}$  location. From this data, it can be concluded that SGA exhibits better combustion performance at this load based on the parameters stated compared to the other gas types. The next chapters will discuss emission performance and will determine if the emission findings correlate with these findings. At an engine load of 30%, SGC still shows enhanced combustion parameters in terms of *ID*, the lowest *BSEC* for one data point, and the lowest decrease in  $P_{max}$ . Also, at 30% engine load, it can be inferred that SGA exhibits better combustion performance than SGB on the basis that it produces the smallest delay in the  $P_{max}$  location.

Thus, at high loads, using SGC preferentially over the other syngas types is proven beneficial due to its higher  $H_2$  content and  $H_2/CO$  ratio. The higher  $H_2$  content increases the ignitability of the fuel and produces more stable combustion and higher efficiencies. This is said to be due to the increased hydrogen content enhancing the lean limit of the mixture [148], and also producing a higher flame speed and temperatures [128], thus enhancing combustion performance.

For optimum combustion performance, this data shows that using SGC/diesel as a fuel mixture at an engine load of 77%, at GEF values of up to 38% (as opposed to full load) is not detrimental to the overall efficiency. At an engine load of ~77%, this syngas blend exhibits superior combustion performance: the smallest decrease in peak in-cylinder pressure, the smallest shift in  $P_{max}$ , the smallest increase in ID, higher BTE values as well as hotter exhaust gas temperatures, compared to the other syngas types (when using diesel as a baseline).

In terms of engine operational combustion performance, if there was a choice between biogas or the syngas blends assessed in this study for the dual fuel option with this diesel engine, biogas outperforms the syngas blends tested here when comparing BTE and BSEC parameters only. This can be explained simply by the higher calorific value of biogas in comparison to the syngas types assessed. Biogas performs better, specifically in terms of the following (when compared to the three syngas types tested):

- Highest BTE & lowest BSEC at full engine load using GEF values of 22 and 38%.
- Highest BTE & lowest BSEC at 76% engine load at all % GEF values tested.

However, biogas combustion performance is inferior to syngas when considering parameters such as the ID,  $P_{max}$  value, and  $P_{max}$  location.

The next chapters will explore the results in terms of gaseous emissions.

## Chapter 6 Gaseous Emission Analysis

### 6.1 Introduction

This chapter looks at the gaseous emissions from the analysis of the engine exhaust gas using the MEXA 7100D and the FT-IR. Gaseous emissions analysed from the MEXA are initially shown as raw emissions (ppm), then are further expressed as SE and EI data to allow comparisons to be made across other studies, loads, and fuel blends. Where raw emission data has been displayed graphically, the error bars are based on  $\pm$  one standard deviation derived from repeat experimental data. The FT-IR was used to provide additional analysis of the gaseous species present in the exhaust gases, especially needed for dual fuel runs. The findings from each gas blend type have been summarised, as well as cross-comparison across syngas blends.

### 6.2 Raw emission analysis using MEXA 7100D

#### 6.2.1 Diesel baseline data

The diesel baseline data (averaged from all DBL runs from all datasets) is shown for all the species analysed using the MEXA in Table 6.1. The  $\text{NO}_2$  has been calculated by subtracting  $\text{NO}_x$  from the NO concentration. The  $\text{NO}_2/\text{NO}_x$  ratio is simply the % ratio of these species. The equivalence ratio ( $\phi$ ) is as reported in Chapter 5.

**Table 6-1 Raw emission analysis from MEXA for the diesel baseline runs**

Generator load (kW)	% Engine load	% Vol		(ppm)					% Ratio	AFR	$\phi$
		$\text{CO}_2$	$\text{O}_2$	CO	THC	$\text{NO}_x$	NO	$\text{NO}_2$			
1.2	30	4	16	565	229	244	186	58	23.8	59	0.25
2.2	53	5	15	468	197	325	282	43	13.4	47	0.31
3.3	78	6	13	347	129	470	458	12	2.5	36	0.40
4.2	95	8	11	247	125	611	603	8	1.2	28	0.52

The diesel baseline data shows the  $\text{CO}_2$  increases with load, as more fuel is being combusted. The CO and THC both decrease as load increases due to improved brake thermal efficiencies, higher combustion temperatures, and more complete combustion. The  $\text{NO}_x$  increases with load due to the higher combustion temperatures seen at higher loads. The  $\text{NO}_2$  content reported here is predominantly influenced by two factors: the excess oxygen availability and the NO concentration in the combustion chamber [274].

At lower engine loads, as there is more oxygen available (as shown by the AFR and  $\phi$  data), an increase in NO<sub>2</sub> is seen which results in a corresponding rise in the NO<sub>2</sub>/NO<sub>x</sub> ratio. Also, lower speeds promote the formation of NO<sub>2</sub> as there is more time for this to be formed [274], however, this will have a minimal impact here due to the minor variations in the RPM in this fixed speed engine used in this study. For the RPM data generated from the diesel baseline runs, see Chapter 5, Table 5.3.

## 6.2.2 Syngas A

The raw emissions (in ppm) from SGA-diesel combustion are shown in Table 6.2, alongside the corresponding diesel baseline data.

**Table 6-2 Raw emission analysis for SGA-diesel**

Engine load (%)	GEF (%)	CO <sub>2</sub> O <sub>2</sub>		CO	THC	NO <sub>x</sub>	NO	NO <sub>2</sub>	NO <sub>2</sub> /NO <sub>x</sub> (% Ratio)	$\phi$
		(% Vol)								
96 (*4.2)	0	8	11	260	155	605	601	4	0.6	0.51
	10	8	11	1,536	259	543	528	15	2.7	0.53
	23	9	10	3,124	441	485	471	15	3.0	0.56
	38	11	8	4,431	600	410	412	ND	ND	0.63
	45	12	6	4,393	659	362	364	ND	ND	0.71
74 (*3.1)	0	6	13	392	148	455	421	33	7.3	0.39
	9	6	13	1,832	353	407	332	75	18.5	0.41
	22	7	12	3,806	642	359	282	77	21.5	0.43
	37	8	12	6,037	1,008	292	243	49	16.7	0.48
56 (*2.3)	0	5	15	490	211	344	290	54	15.7	0.32
	9	5	15	1,983	435	317	224	93	29.4	0.33
	21	5	14	4,134	784	276	174	102	37.1	0.35
31 (*1.2)	0	4	16	590	247	234	186	48	20.6	0.25
	10	4	16	2,184	497	229	132	97	42.4	0.26
	21	4	15	4,393	901	200	98	103	51.3	0.28

\* Equivalent generator load in kW. ND denotes 'none detected.'

Table 6.2 shows that overall, the THC and CO levels show an increase as the % GEF of SGA is increased across all loads. The NO<sub>2</sub> concentration increases at all engine loads upon initial introduction of the syngas, relative to the diesel baseline data. The NO<sub>2</sub> concentration is higher at lower engine loads of 56, and 31%, and increases with increasing syngas fraction.

At 74% engine load, an increase is seen in the NO<sub>2</sub> concentration up to a GEF of 22%, after which, further increases in the GEF result in a decrease in the NO<sub>2</sub> emissions.

At full engine load, the NO<sub>2</sub> concentration increases with the initial introduction of syngas, between GEF of 10 and 23% the NO<sub>2</sub> concentration does not change, after 23% GEF any further increases in the GEF result in a decrease of the NO<sub>2</sub> concentration resulting in zero emissions. The formation of NO<sub>2</sub> is dependent on the concentration of the NO, which is dependent on three factors: combustion temperature,  $\phi$  (oxygen availability), and the retention time (time the gases spend in the reaction zone) [275].

The NO concentration decreases in dual fuel mode, and this is as expected as the NO dominantly contributes to the total NO<sub>x</sub>, this reduction in NO is due to the reduction in the flame temperature [117] and pressure (as discussed in Chapter 5). As the NO concentration reduces with increasing gas fraction, it is expected that the NO<sub>2</sub> concentration would follow the same trend. This appears to not be the case for all the engine loads evaluated.

The initial increase seen in NO<sub>2</sub> emissions upon the initial introduction of the gaseous fuel is suggesting that the introduction of the gaseous fuel potentially encourages the formation of NO<sub>2</sub>. This initial increase is also noted for biogas dual fuel combustion, hence, cannot be attributed to the oxygen content of the syngas. Subsequent reductions in the NO<sub>2</sub> levels with increasing GEF and full and 74% engine load are more likely to be linked with the change in the  $\phi$  which increases with increasing GEF, thus limiting the oxygen availability and reducing NO<sub>2</sub> formation. At higher loads, although the combustion temperatures are higher, the engine is running richer. This explanation is supported by plotting the NO<sub>2</sub> raw emissions at each load as a function of  $\phi$  for SGA-diesel, as shown in Fig. 6.1. Also, the concentration of the radicals involved in the oxidation of the NO to NO<sub>2</sub> [274] may change with the GEF and  $\phi$ , hence this could impact the resulting NO<sub>2</sub> concentration.

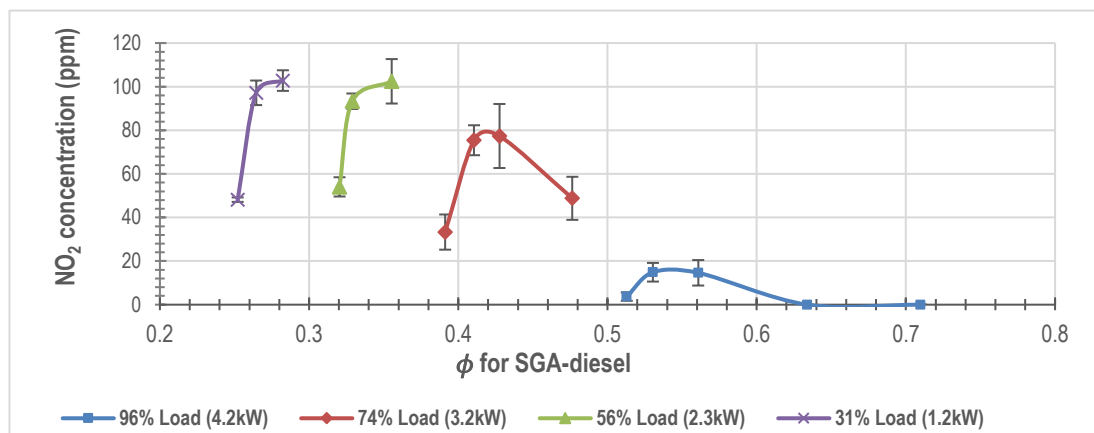


**Figure 6-1 Raw NO<sub>2</sub> emission data for SGA-diesel versus  $\phi$  per load**

The O<sub>2</sub>, NO<sub>x</sub>, and NO all show a steady decrease as the % GEF is increased, at all loads. The  $\phi$  increases more noticeably at higher loads as the % GEF is increased, thus the engine is running richer, hence less oxygen is available.

This data also shows that the CO increases at each load with increasing % GEF, and the CO content is higher at lower loads; this is linked to reduced combustion efficiency. The overall trend seen with increasing % GEF at each load for the raw CO emissions data is depicted in Fig. 6.2.

This data also shows that the CO<sub>2</sub> concentration increases whilst the oxygen concentration decreases simultaneously with increasing syngas addition at full, and 74% engine load. CO<sub>2</sub> is a product of complete combustion; hence this suggests that more combustion of carbon species is occurring in dual fuel mode. From a syngas compositional point of view, this can only arise from the methane and the carbon monoxide components of the syngas. It should be noted that although the syngas has a CO<sub>2</sub> component in the composition that will pass into the exhaust, increasing the CO<sub>2</sub> concentrations, this would not cause the resulting oxygen concentration to decrease simultaneously. This data also shows that at lower loads, there is a slight reduction in the oxygen levels, but the CO<sub>2</sub> concentration remains unchanged with increasing syngas addition.

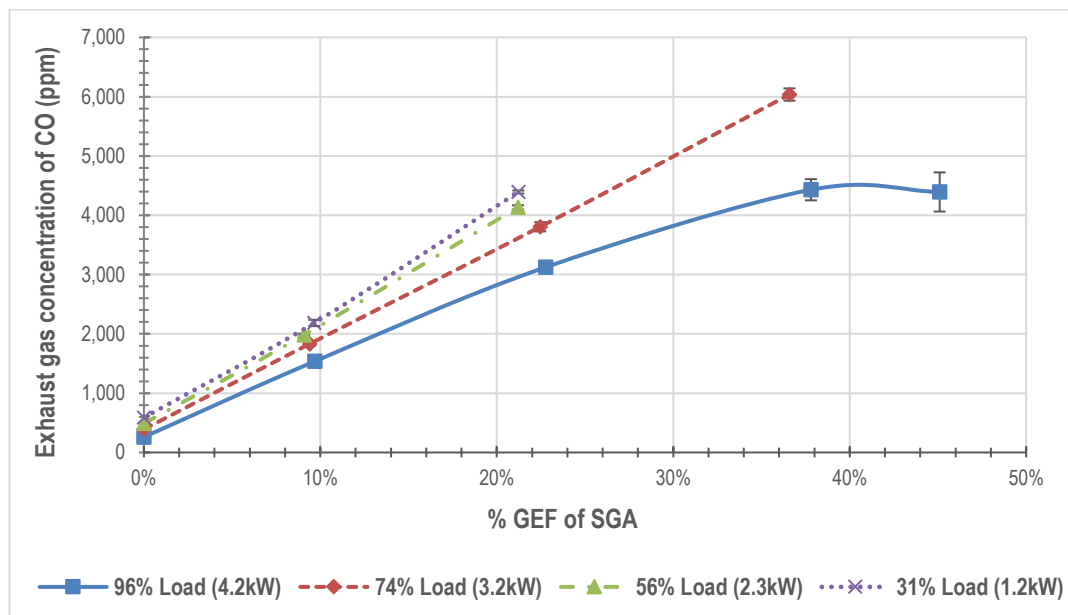


**Figure 6-2 Raw CO emission data for SGA-diesel at various engine loads**

At full engine load, between 38 and 45% GEF, the increase in CO concentration appears to be levelling off.

This lack of change could be potentially explained by the fact that the limiting equivalence ratio has been reached whereby the resulting CO and unburnt methane emissions are unaffected by the pilot diesel quantity due to successful flame propagation being achieved [170, 276]. Further work is required to corroborate these findings by studying and comparing the HRR at full engine load which includes the highest GEF evaluated.

The HRR study conducted by Olanrewaju et al. [117] for SGA-diesel did not include the highest GEF where this phenomenon has been noted. If the lack of change in the THC and CO emissions between these two high GEFs at full engine load is due to the limiting equivalence ratio being achieved as a result of successful flame propagation being achieved, this will be apparent in the HRR profiles. If this has occurred, then it is postulated that the second and third energy release phases will merge thereby reflecting more stable flame propagation [110].

Badr et al. [276] studied the effects on the exhaust emissions as a function of  $\phi$  when using varying quantities of pilot diesel fuel using a single-cylinder direct injection diesel engine fuelled with pure methane at a speed of 1,000 RPM. The maximum engine power rating is not stated. According to Badr et al. [276], in dual fuel combustion, at low loads, the engine reaches an optimum or limiting equivalence ratio beyond which the CO and unburnt methane emissions remain unaffected by the pilot diesel quantity. It is stated that this point is a direct indication of the  $\phi$  limit for successful flame propagation from the pilot ignition centres [276]. The plots as shown by Badr et al. [276] which depict the methane and CO concentration as a function of the total  $\phi$  are shown in Fig. 6.3.

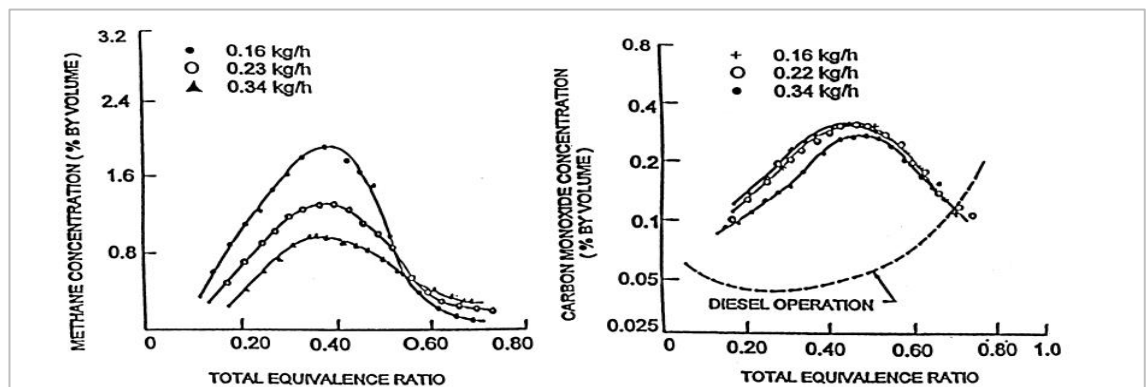


**Figure 6-3 The effect on the dual fuel emissions as a function of the total  $\phi$  at variable pilot diesel quantities [276]**

Although this research mentions this phenomenon at light loads, it is potential this has been reached at full engine load when using the highest % GEF for this study. Figs. 6.4 and 6.5 show the THC and CO concentration (in ppm) as a function of  $\phi$  at full engine load for SGA. Fig. 6.5 shows more clearly than Fig. 6.4, that the emission concentration does not change once a certain  $\phi$  is reached (which is richer), for SGA at maximum engine load, hence, the limiting  $\phi$  may have been reached, thereby the resulting CO and THC emissions are not affected.

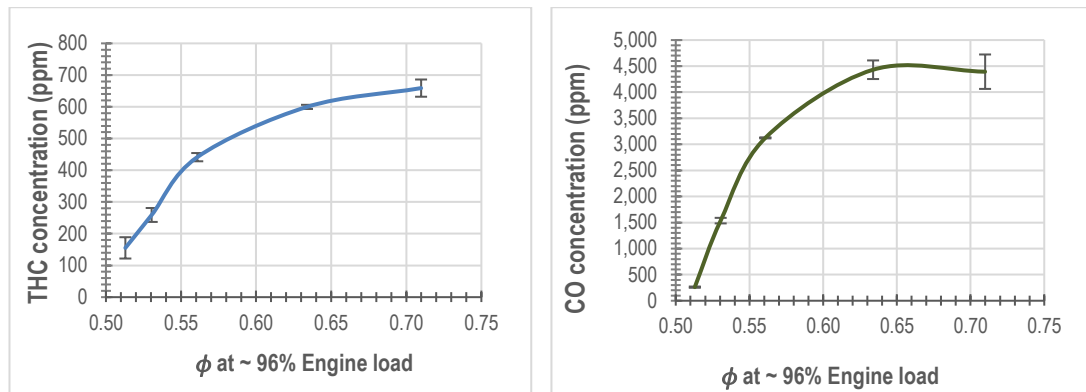


**Fig 6-4 SGA: THC levels at full load    Fig 6-5 SGA: CO levels at full load**

Also, the  $\phi$  value corresponding to the highest % GEF at maximum load is the highest calculated in this study (across all the dual fuel blends).

### 6.2.3 Syngas B

The raw emission results obtained from the analysis of the exhaust gas from SGB-diesel are shown in Table 6.3.

As seen for SGA, the  $\text{NO}_2$  concentration increases at all engine loads upon initial introduction of the syngas, relative to the diesel baseline data. The  $\text{NO}_2$  concentration is higher at lower engine loads.

At an engine load of 76%, an increase is seen in the  $\text{NO}_2$  concentration up to a GEF of 23%, after which further increases in the GEF result in a decrease in the  $\text{NO}_2$  emissions.

At full engine load, the  $\text{NO}_2$  concentration increases with increasing GEF up to 39%, after which, a further increase in the syngas fraction leads to a sharp decrease in the  $\text{NO}_2$  concentration. The  $\text{NO}_2$  raw emissions at each engine load as a function of  $\phi$  for SGB-diesel, are expressed in Fig. 6.6.

**Table 6-3 Raw emission analysis for SGB-diesel**

Engine load (%)	GEF (%)	CO <sub>2</sub> (% Vol)	O <sub>2</sub> (% Vol)	CO (ppm)	THC (ppm)	NO <sub>x</sub> (ppm)	NO (ppm)	NO <sub>2</sub> (ppm)	NO <sub>2</sub> /NO <sub>x</sub> (% Ratio)	φ
96 (*4.2)	0	8	10	258	120	602	585	17	2.8	0.51
	9	8	10	1,405	232	583	561	22	3.8	0.54
	22	9	10	2,625	344	532	501	31	5.9	0.57
	39	11	9	4,189	533	460	410	49	10.7	0.60
	45	12	6	4,262	508	428	425	3	0.7	0.65
76 (*3.2)	0	6	14	354	123	457	389	68	14.8	0.37
	10	6	14	1,684	304	416	345	71	17.1	0.39
	23	7	13	3,472	615	382	297	85	22.1	0.41
	39	8	12	5,742	924	301	229	73	24.1	0.44
54 (*2.2)	0	5	16	457	197	334	287	47	14.2	0.30
	9	5	16	1,919	416	311	217	93	30.1	0.31
	22	5	15	3,956	722	284	175	109	38.5	0.33
30 (*1.2)	0	4	17	563	235	242	189	53	21.8	0.24
	10	4	17	2,099	483	228	132	96	42.0	0.24
	22	4	17	4,185	850	207	97	110	53.3	0.26

\* Equivalent generator load in (kW).

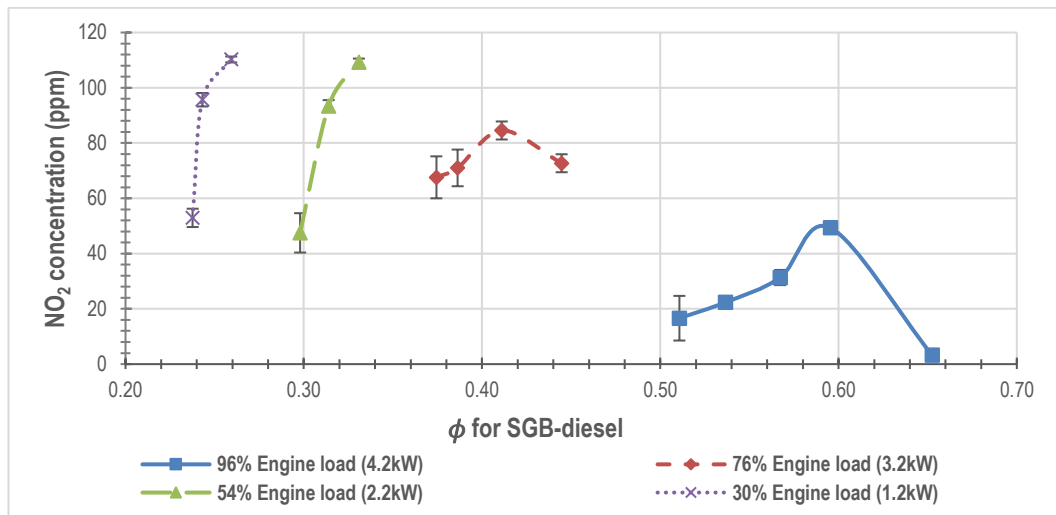


**Figure 6-6 NO<sub>2</sub> v φ levels for SGB-diesel at various engine loads**

As discussed for SGA, the initial increase seen in the NO<sub>2</sub> emissions in dual fuel mode is favoured by dual fuel combustion. Subsequent changes in the NO<sub>2</sub> levels with increasing GEF are possibly linked with the change in the φ which increases with increasing GEF, in doing so this limits the oxygen availability, thus reducing the formation of NO<sub>2</sub>. At higher loads, although the combustion temperatures are higher, the engine is running richer, hence less NO<sub>2</sub> is formed.

As per SGA, the SGB data also shows that the CO<sub>2</sub> concentration increases whilst the oxygen concentration decreases simultaneously with increasing syngas addition at full, and 76% engine load. At lower loads, there is a slight reduction in the oxygen levels, but the CO<sub>2</sub> concentration remains unchanged with increasing syngas addition. The reason for this has been discussed earlier for SGA, (see section 6.2.2).

The trends seen in the raw CO emissions data per load are depicted in Fig. 6.7. At full engine load, between GEF of 39 and 45%, the increase in CO appears to be levelling off; this value does not increase significantly.

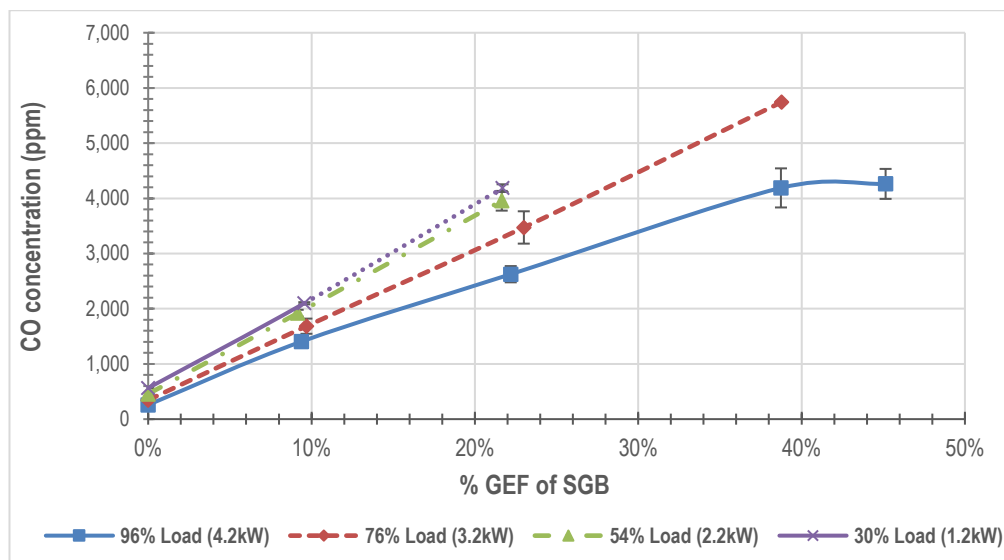


**Figure 6-7 CO emission data for SGB-diesel at various engine loads**

The same CO trend was observed for SGA-diesel at the same load and GEF condition, whereby one possible explanation is that the limiting equivalence ratio has been reached whereby the resulting CO and THC emissions are no longer affected by the pilot diesel quantity [170]. As mentioned for SGA, an HRR study for full engine load at these GEFs would help corroborate these findings. To determine if this explanation is plausible for the lack of change in the CO and THC concentration (in ppm), these values were plotted as a function of  $\phi$  at full engine load for SGB and are shown in Figs. 6.8 and 6.9.

The trends depicted in Figs. 6.8 and 6.9 both show that potentially the limiting  $\phi$  has been reached, thereby the resulting emissions are unaffected.

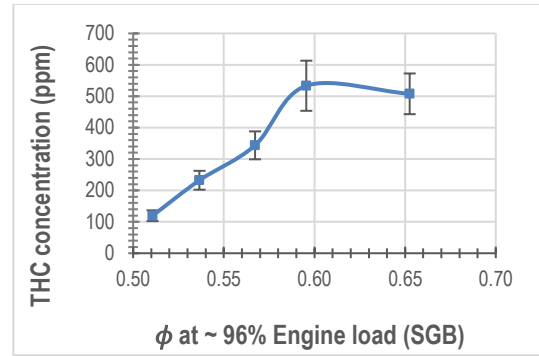
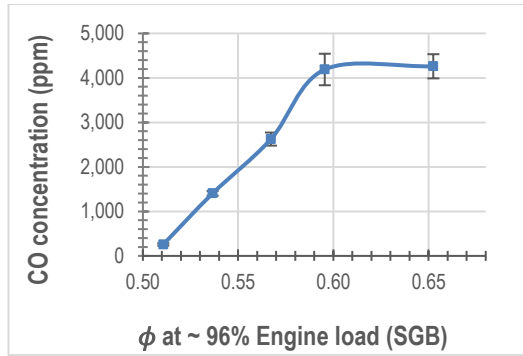


**Fig 6-8 CO v  $\phi$  for SGB-diesel**

**Fig 6-9 THC v  $\phi$  for SGB-diesel**

Table 6.3 also shows that the THC and CO levels all increase with increasing % GEF of SGB at all engine loads. A larger increase in the THC and CO levels are observed at lower loads. At all engine loads, the  $\text{NO}_x$  and NO all show a steady decrease as the % GEF is increased. The  $\phi$  increases substantially at higher loads, especially for higher % GEF values, thus indicating the engine is running richer.

## 6.2.4 Syngas C

The raw emission results obtained from the analysis of the exhaust gas from SGC-diesel are shown in Table 6.4 alongside the corresponding diesel baseline data.

**Table 6-4 Raw emission analysis for SGC-diesel**

Engine load (%)	GEF (%)	CO <sub>2</sub> (% Vol)	O <sub>2</sub> (% Vol)	CO (ppm)	THC (ppm)	NO <sub>x</sub> (ppm)	NO (ppm)	NO <sub>2</sub> (ppm)	NO <sub>2</sub> /NO <sub>x</sub> (% Ratio)	$\phi$
95 (*4.2)	0	8	11	235	100	616	601	14	2.3	0.52
	9	8	11	1,282	213	597	563	34	5.7	0.53
	22	9	10	2,452	328	568	547	21	3.7	0.57
	38	10	9	3,474	415	533	518	16	2.9	0.60
	46	11	9	3,750	423	522	506	16	3.0	0.60
79 (*3.4)	0	6	13	312	125	495	464	31	6.3	0.41
	9	7	13	1,480	280	473	381	92	19.4	0.42
	22	7	12	3,017	456	430	344	85	19.8	0.44
	37	8	12	4,805	686	390	316	74	19.1	0.48
51 (*2.1)	0	4	15	445	181	325	268	57	17.5	0.30
	9	5	15	1,858	394	306	206	100	32.6	0.32
	23	5	14	3,782	661	282	171	112	39.6	0.34
29 (*1.2)	0	4	16	543	203	245	186	59	24.0	0.24
	10	4	16	1,975	424	231	130	101	43.9	0.26
	21	4	16	3,804	731	214	100	114	53.4	0.28

\* Equivalent generator load in (kW).

Table 6.4 shows that as per other syngas blends, the CO<sub>2</sub> concentration notably increases whilst the oxygen concentration decreases simultaneously with increasing syngas addition at full, and 79% engine load. The reason for this has been discussed earlier for SGA (see section 6.2.2).

Table 6.4 also shows that the CO and THC levels increase at each load with increasing SGC, a larger increase is noted at lower loads. The trends seen in the raw CO emissions data per load are shown in Fig. 6.10.

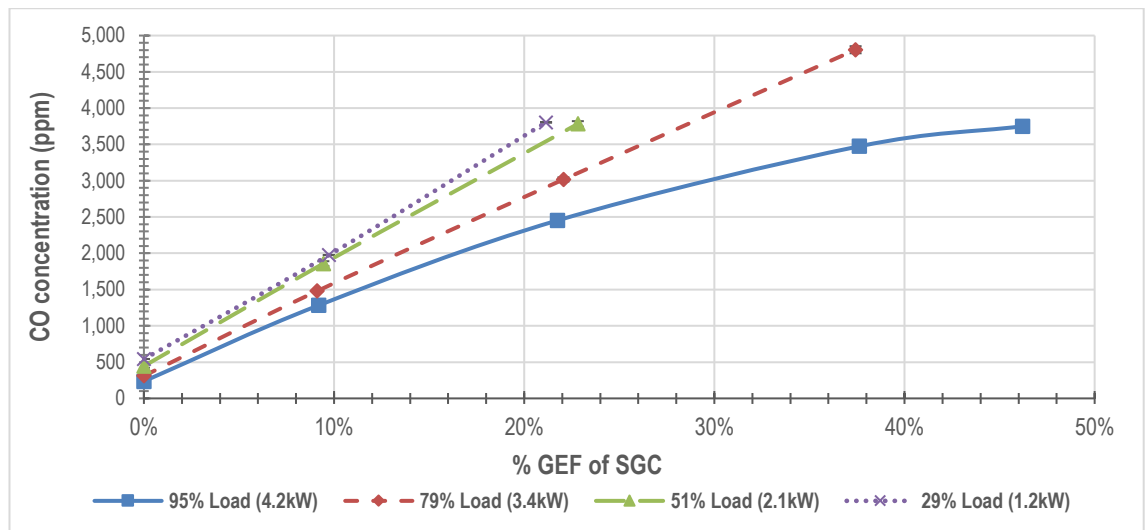


**Figure 6-10 CO emission data for SGC-diesel at various engine loads**

Fig. 6.10 shows that the CO concentration at full engine load for SGC continues to increase between GEF of 38 and 46%, albeit at a slower rate, whereas for SGA and SGB the concentration of CO remained steady between these two data points. This suggests that for this syngas blend, at these test conditions, the limiting  $\phi$  has not been reached. Regardless, in comparison, the CO concentration for SGC, at the highest % GEF evaluated at full engine load, is still lower than the values obtained for SGA and SGB.

At full engine load, the NO<sub>2</sub> concentration shows a slight increase upon initial introduction of SGC, subsequent increases in the GEF beyond 9% results in the NO<sub>2</sub> concentration falling back to diesel baseline levels. At 79% engine load, there is a sharper increase in NO<sub>2</sub> seen upon the initial introduction of SGC, but as the % GEF of SGC increases further beyond 9%, the NO<sub>2</sub> levels decrease slightly. At lower engine loads (51, and 29%), the NO<sub>2</sub> levels increase with increasing levels of SGC. The notable difference here for SGC versus the other two syngas blends is that the NO<sub>2</sub> concentration levels start to reduce quicker, i.e., at an earlier gas energy fraction of 9% for both full and 79% engine loads.

As discussed for SGA/B, the NO<sub>2</sub> trend noted here is similar, hence the same explanation is employed: the initial increase seen in the NO<sub>2</sub> emissions in dual fuel mode is favoured by dual fuel combustion, and at lower loads, increasing the GEF also increases NO<sub>2</sub> levels as the  $\phi$  remains very lean.

Subsequent changes in the NO<sub>2</sub> levels with increasing GEF, specifically at higher loads are linked with an increase in the  $\phi$  which further limits the oxygen availability, thus reducing the formation of NO<sub>2</sub>.

At higher loads, although the combustion temperatures are higher, the engine is running richer, hence less NO<sub>2</sub> is formed. This explanation is supported by plotting the NO<sub>2</sub> raw emissions at each load as a function of  $\phi$  for SGC-diesel, as shown in Fig. 6.11.

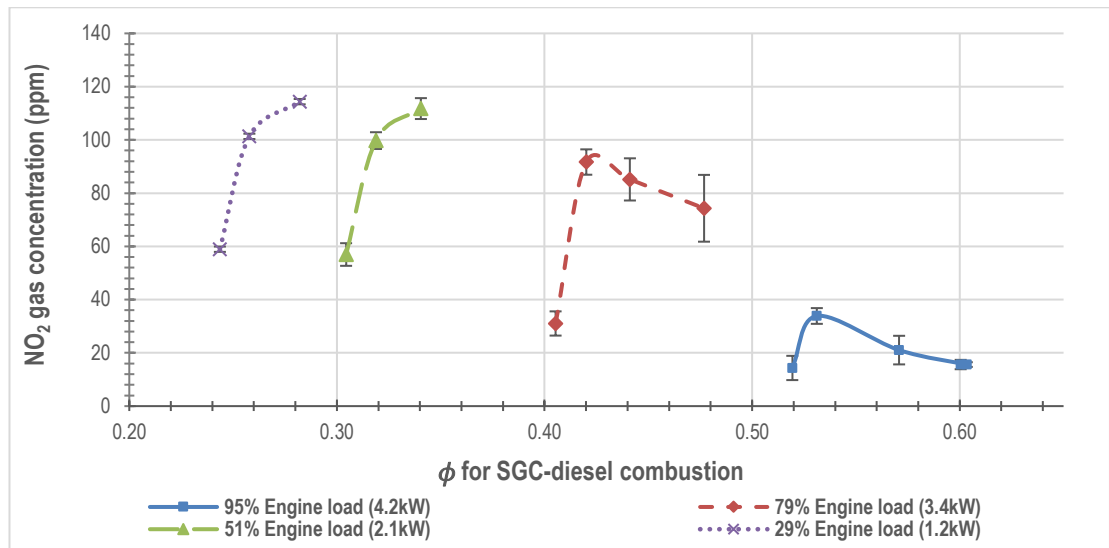


**Figure 6-11 NO<sub>2</sub> emission data v  $\phi$  for SGC-diesel at various engine loads**

Also, at lower engine loads of 51, and 29%, the NO<sub>x</sub> and NO both show a steady decrease as the % GEF increases. The  $\phi$  increases at higher loads at higher % GEF values, thus indicating the engine is running richer.

### 6.2.5 Biogas

The raw emission results obtained from the analysis of the exhaust gas from biogas-diesel are shown in Table 6.5. This data shows that the CO<sub>2</sub> concentration increases whilst the oxygen concentration decreases simultaneously with increasing biogas addition at full, and 80% engine load. At lower loads, there is a slight reduction in the oxygen levels, but the CO<sub>2</sub> concentration remains unchanged with increasing gas addition.

This increase in CO<sub>2</sub> combined with a decrease in the O<sub>2</sub> can be linked to more combustion occurring in dual fuel mode. For biogas, the complete combustion of methane produces additional CO<sub>2</sub> which explains the cause of this trend.

As noted previously, although the biogas contains 50% CO<sub>2</sub> which will directly pass into the exhaust causing an increase in the CO<sub>2</sub> concentrations, this would not cause the resulting oxygen concentration to decrease.

At lower loads, there is a slight reduction in the oxygen levels, but the CO<sub>2</sub> concentration remains unchanged with increasing biogas addition.

**Table 6-5 Raw emission analysis for biogas-diesel**

Engine load (%)	GEF (%)	CO <sub>2</sub> (% Vol)	O <sub>2</sub> (% Vol)	CO (ppm)	THC (ppm)	NO <sub>x</sub> (ppm)	NO (ppm)	NO <sub>2</sub> (ppm)	NO <sub>2</sub> /NO <sub>x</sub> (% Ratio)	φ
97 (*4.3)	0	8	10	241	120	626	626	0	0	0.54
	9	9	10	637	838	582	575	8	1.3	0.56
	24	9	9	1,164	2,015	516	511	5	1.0	0.60
	40	11	8	1,685	3,377	442	433	10	2.2	0.65
	49	11	8	1,888	4,195	410	391	19	4.6	0.67
80 (*3.5)	0	6	12	334	115	494	478	16	3.2	0.43
	9	7	12	734	1,074	448	395	52	11.7	0.44
	22	7	12	1,176	2,445	396	329	67	17.0	0.47
	38	8	11	1,697	4,531	332	272	59	17.9	0.51
52 (*2.1)	0	5	15	473	200	323	277	46	14.3	0.32
	10	5	14	901	1,525	284	206	79	27.6	0.33
	23	5	14	1,365	3,471	244	158	87	35.5	0.35
30 (*1.2)	0	4	16	555	239	237	180	57	24.1	0.25
	12	4	16	1,050	1,996	207	121	86	41.5	0.27
	23	4	16	1,402	3,687	187	94	93	49.7	0.29

\* Equivalent generator load in (kW).

Table 6.5 shows that the CO and THC levels increase at each load with increasing % biogas addition; in terms of the THC levels, larger increases are noted at lower loads. The trends seen in the raw CO and THC emissions are depicted in Figs. 6.12 and 6.13, respectively.

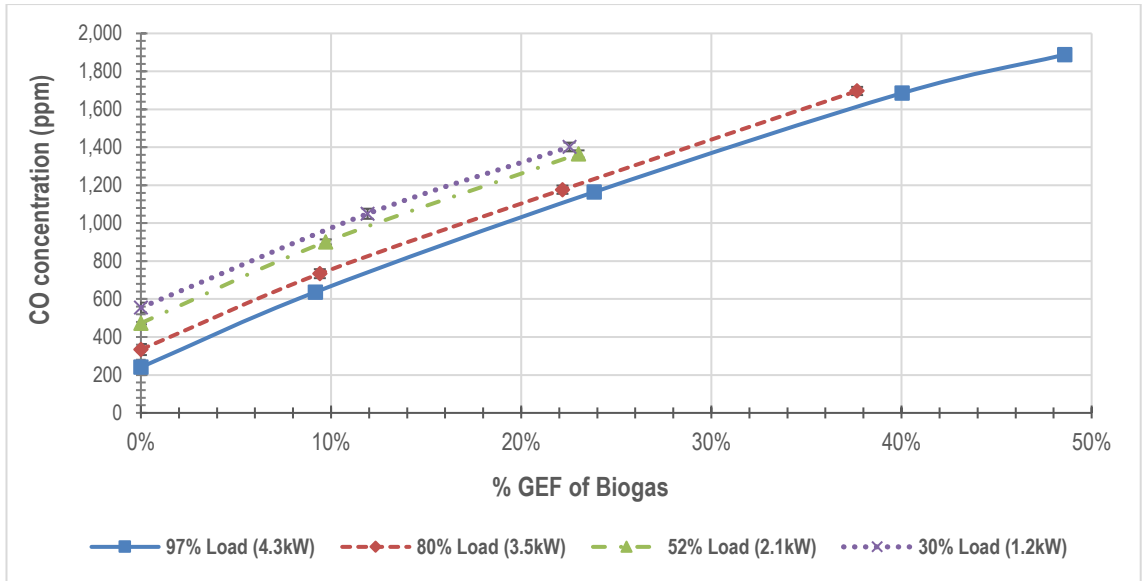


**Figure 6-12 CO data for biogas-diesel at various engine loads**

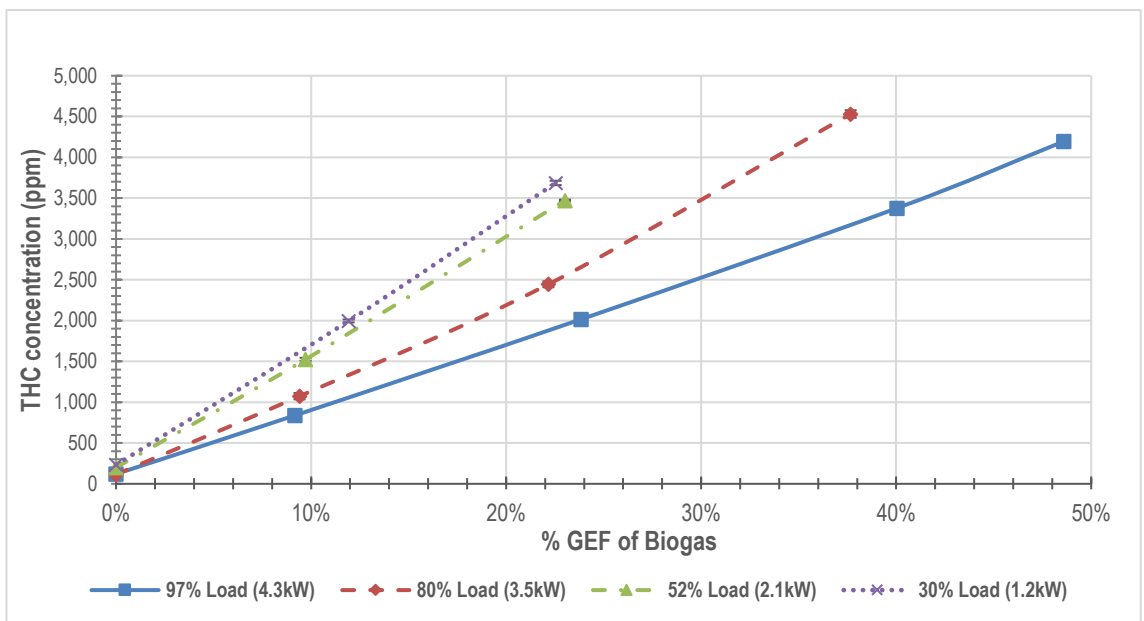


**Figure 6-13 THC data for biogas-diesel at various engine loads**

Both NO<sub>x</sub> and NO show a steady decrease as the % GEF increases at all loads. The  $\phi$  increases at higher loads and with higher % GEF values.

The initial increase seen in the NO<sub>2</sub> emissions in dual fuel mode is favoured by dual fuel combustion. At lower loads (52 and 30%), increasing the GEF also increases NO<sub>2</sub> as the  $\phi$  remains very lean, thus these conditions promote the formation of NO<sub>2</sub>.

At 80% engine load, the NO<sub>2</sub> levels peak at a GEF of 22%, increasing the GEF beyond this results in a decrease in the NO<sub>2</sub> levels. One explanation for this trend is associated with the  $\phi$  which reaches a limiting point at a GEF of 22% whereby the oxygen availability becomes critical, hence any further increases in the biogas addition limits the NO<sub>2</sub> formation. At full engine load, the NO<sub>2</sub> concentration only increases marginally in dual fuel mode (a 19ppm increase is noted between DBL to ~49% GEF).

Subsequent changes in the NO<sub>2</sub> levels with increasing GEF, specifically at higher loads are linked with an increase in the  $\phi$  which further limits the oxygen availability, thus reducing the formation of NO<sub>2</sub>. At higher loads, although the combustion temperatures are higher, the engine is running richer, hence less NO<sub>2</sub> is formed. The trend of the NO<sub>2</sub> raw emissions at each load as a function of  $\phi$  for biogas-diesel, as shown in Fig. 6.14.

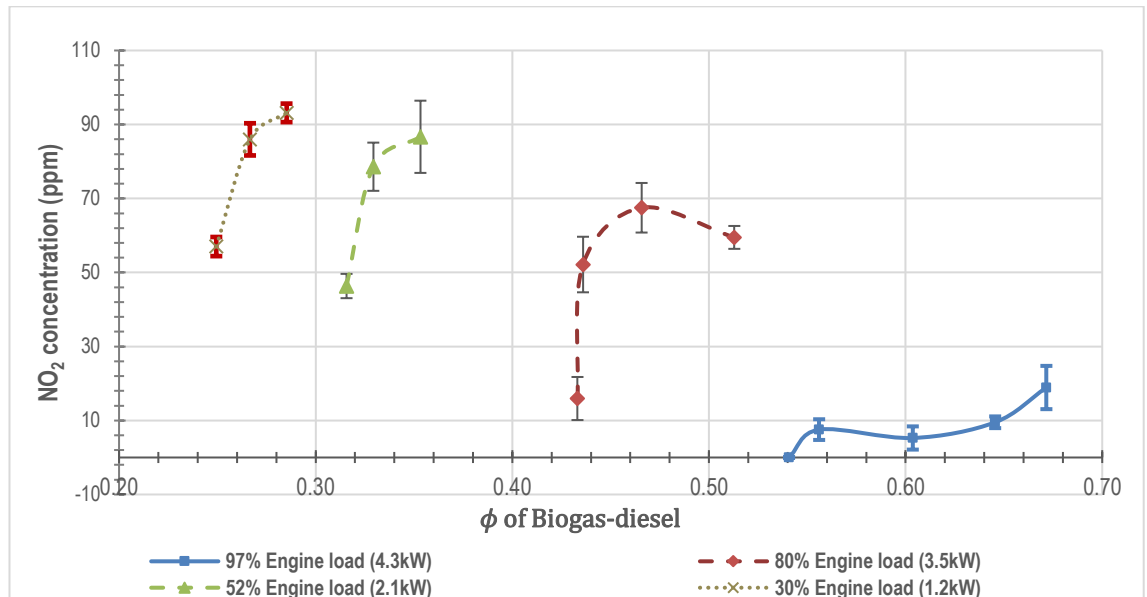


**Figure 6-14 NO<sub>2</sub> emission data as a function of  $\phi$  for biogas-diesel**

The trends seen in the raw methane emissions are illustrated in Fig. 6.15. This data was obtained from the FT-IR analysis but has been included here to allow direct comparisons to be made. Fig. 6.15 shows that at engine loads of 52, and 30%, the CH<sub>4</sub> levels increase with increasing levels of biogas. However, at full engine load, the methane concentration increases up to an optimum GEF of ~40%, after which any further increase in the biogas leads to a reduction in concentration. At 80% load, a similar trend is observed, however, the optimum GEF occurs earlier at 22%, after which a further increase in biogas leads to this concentration not changing.

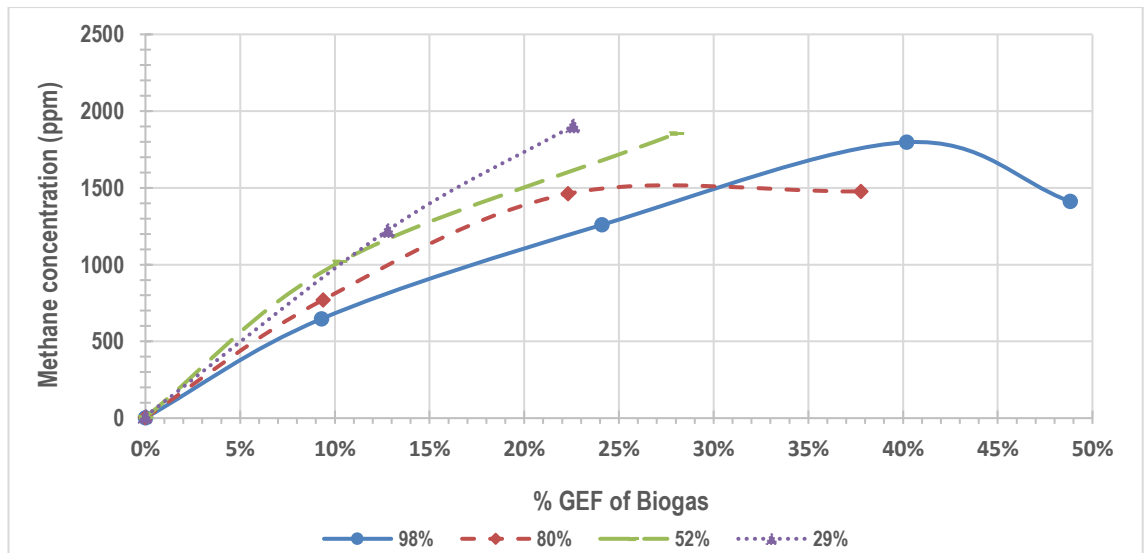


**Figure 6-15 CH<sub>4</sub> emission data for biogas-diesel at various engine loads**

### 6.2.6 Raw emission trends during dual fuel combustion

In dual fuel mode, for all gas-diesel blends evaluated, the CO<sub>2</sub> levels increase as the % syngas/biogas is increased, and this is more evident at higher loads. This is due to the higher efficiency associated with the combustion of the gaseous fraction. Complete combustion of the methane and CO present in the syngas/biogas will produce additional CO<sub>2</sub> as evident in the exhaust gases. This is not noticeable at lower engine loads of 53 and 30% dual fuel combustion due to lower brake thermal efficiencies of syngas/biogas relative to diesel. In addition, the CO<sub>2</sub> content of the syngas/biogas will pass directly into the exhaust system.

All CO and THC increases are a direct result of incomplete combustion. The CO present in the dual fuel exhaust stream suggests unburnt CO is passing through from the gaseous fuel due to incomplete combustion. In dual fuel mode, the contributing factors for CO emissions include the lower heating value, lower adiabatic flame temperatures (as seen for SGA [117]), and lower mean effective pressures [170]. Thus, it is expected that the CO and THC emissions in dual fuel mode would be higher than in pure diesel, as reported by other researchers [138, 145, 150, 170].

For all gas-diesel blends, the THC and CO emissions observed in this study were significantly higher for engine loads of ~53 and 30%. This was as expected as at lower loads dual fuel engines are known for their lower combustion efficiency and higher unburnt percentage of gaseous fuel [170].

This can be further explained that at lower loads dual fuel engines have a longer combustion duration [170], this was indeed the case for SGA as reported in the co-authored study [117]. This leads to insufficient combustion time, resulting in incomplete combustion and raised emissions [144], as indicated by the lower engine exhaust gas temperatures, especially, at lower loads (see Chapter 5, subsection 5.4.6.2)

In terms of CO emissions, in dual fuel mode, incomplete combustion is most likely caused by a lower in-cylinder temperature which in turn is caused by a lower in-cylinder pressure [166]. Sahoo et al. [170] suggested that a lower engine load limit when operating in syngas-diesel mode would be beneficial to control CO emissions. When considering the data from this study, it would be advantageous in more than one aspect to implement this in dual fuel mode, especially when considering the engine combustion parameters such as BTE and BSEC (as discussed in Chapter 5).

Furthermore, it was found that at ~4kW (~95% engine load), increasing the syngas fraction from ~38 to 45% did not significantly increase the CO emissions for SGA and SGB (not for SGC), potentially due to the limiting  $\phi$  being reached whereby the resulting CO and UHC emissions are unaffected by the pilot diesel quantity (as discussed earlier). HRR studies of these dual fuel combustion conditions are recommended to aid further understanding in this area.

The data for all gaseous fuel blends also suggests that the CO and THC emissions are encouraged by a rich fuel mixture [166, 170], and the highest readings obtained in all cases correspond to the highest  $\phi$  values at each load, as shown in Tables 6.2 – 6.5. This data (in Tables 6.2 – 6.5) shows that the THC emissions in dual fuel mode decreased as the load increased. This increase is due to higher combustion temperatures which enable the oxidation of unburnt hydrocarbons (UHC) [170], thereby reducing the THC emissions in the exhaust gases. This data is also supported by the higher in-cylinder pressures data as discussed in Chapter 5.

Typically, for the formation of thermal NO, high oxygen levels and combustion temperatures are required [112, 170, 274], and it is from this, that NO<sub>2</sub> is formed. NO<sub>x</sub> on the other hand is dependent on the presence of the gaseous fuel-air mixture, the flame temperature [170], as well as oxygen concentration and combustion duration [147].

Additionally, it is stated that in dual fuel mode the  $\text{NO}_x$  formation is also dependent on the diesel pilot spray region [147]. Hence, in dual fuel mode versus diesel, a reduction in  $\text{NO}_x$  is expected due to a lower flame temperature and a lower rate of premixed controlled combustion [170].

Contradictory results were reported by Bika et al. [145] whereby research was conducted using a single-cylinder dual fuel diesel engine at a fixed speed of 1,800 RPM using simulated syngas substitution (syngas being simulated of varying  $\text{H}_2/\text{CO}$  proportions). These authors reported that the effect on the  $\text{NO}_x$  emissions was dependent on the net IMEP. As the syngas substitution was increased, at 2 bar the  $\text{NO}_x$  remains remained unchanged, and at 4 bar the  $\text{NO}_x$  emissions increased, this increase was explained by an increase in the flame temperature of the diesel fuel flame jet.

This is contradictory to the remainder of the other findings present in the open literature as discussed in Chapter 2 (see subsection 2.11.7); the effects of the other components of syngas must be considered on the resulting  $\text{NO}_x$  emissions rather than just  $\text{H}_2$  and  $\text{CO}$ .

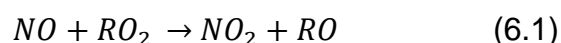
For all dual fuel bends tested in this study, the trend seen was that as the % GEF increased the  $\text{NO}_x$  and  $\text{NO}$  decreased across all loads. This can be explained by various factors which include a lower flame temperature [117], lower  $P_{\text{max}}$  values (as discussed in Chapter 5), a reduction in the oxygen availability (as indicated by the calculated  $\phi$  values) caused by the displacement of the air from the gas addition, and the impact of the  $\text{CO}_2$  component of the gaseous fuel which acts as a diluent.

It was noted by Sahoo et al. [142] that a larger %  $\text{NO}_x$  reduction (based on raw ppm emissions) was observed at lower engine loads (20 to 60%) with syngas-diesel. Hence, the %  $\text{NO}_x$  reduction data from this study was calculated between the diesel baseline and 22% GEF data across all engine loads using raw emissions (in ppm). The %  $\text{NO}_x$  reductions did mirror the findings as reported by Sahoo et al. [142] for biogas-diesel combustion whereby the optimum  $\text{NO}_x$  reductions occurred at 52% engine load. For SGA, and SGB the optimum  $\text{NO}_x$  reductions occurred at 75% engine load (~3kW generator load), and for SGC, the optimum %  $\text{NO}_x$  reductions occurred at either 78, or 52% engine load, as the calculated values at both these engine loads were similar.

At lower loads (<55% engine load), for all syngas/biogas-diesel blends tested, typically the NO<sub>2</sub> concentration and the NO<sub>2</sub>/NO<sub>x</sub> ratio increased as % GEF was increased. This was thought to be due to an increase in the radicals which promoted the oxidation of NO to NO<sub>2</sub>.

In a diesel engine, the NO<sub>2</sub> formation is dependent on the concentration of the NO species and the quantity of excess oxygen available in the chamber, and NO<sub>2</sub> is derived solely from NO [274]. Also, in cooler temperature regions the NO is more likely to convert back into NO<sub>2</sub> [112]. Based on this, in dual fuel mode at engine loads of 53 and 30%, the lowest levels of NO are present at the highest % GEF values, which should correlate to the highest NO<sub>2</sub> emissions. However, the dual fuel data for engine loads <55% does not correlate with this. Higher levels of NO<sub>2</sub> are formed from lower levels of NO. The  $\phi$  only changes marginally with increasing GEF values at lower loads, therefore, is still considerably lean.

Hence, the mechanism of NO<sub>2</sub> formation must be considered in laminar flames, which is expressed in Eq. 6.1 [145, 274, 277].



In Eq. 6.1, The R in RO<sub>2</sub> can represent a hydrocarbon radical (alkyl peroxy radical) [274] or a hydrogen atom (hydroperoxy radical - HO<sub>2</sub>) [278], both of which, can oxidise the NO to produce NO<sub>2</sub>. An increase in the RO<sub>2</sub> concentration would lead to an increase in NO<sub>2</sub>. It is postulated that these peroxy radicals are relatively stable and higher concentrations can build up nearer cooler regions of the flame [274]. However, the mechanism for the formation of this radical is based on the oxidation of an alkane; this is associated with cooler flames and lower ignition temperature in engines [278], lower than those seen in this study.

Hence, the concentration of the peroxy radical cannot explain why higher levels of NO<sub>2</sub> were found at lower engine loads (<55%) with lower corresponding NO emissions. These were noted with increasing gas energy fractions (with higher corresponding  $\phi$ ). Further work is required to understand the kinetic mechanism of the oxidation of NO which results in the formation of NO<sub>2</sub>, especially at lower engine loads when using higher gas energy fractions.

## 6.2.7 Cross-comparison of raw emissions for syngas blends

In terms of raw emissions, the data was cross compared across the three syngas blends at all loads and % GEF values. The findings are shown in Table 6.6, whereby after cross-comparison, the syngas producing the highest and lowest emissions has been summarised for THC, CO, CH<sub>4</sub>, NO<sub>x</sub>, and NO<sub>2</sub>.

Methane, although analysed by the FT-IR, has also been included here for cross-comparison. The cross-comparison graphs and data for methane can be found in section 6.4 and Figs. 6.80-6.81.

**Table 6-6 Cross-comparison of raw emission data (in ppm)**

Engine load (%)	Syngas	CH <sub>4</sub>	THC	CO	NO <sub>x</sub>	NO
~96	Highest syngas	*SGA	SGA	SGA	SGC	SGC
	Lowest syngas	<b>SGC</b>	<b>SGC</b>	<b>SGC</b>	SGA	SGA
~77	Highest syngas	*SGA	SGA	SGA	SGC	SGC
	Lowest syngas	<b>SGC</b>	<b>SGC</b>	<b>SGC</b>	No clear trend for both	
~53	Highest syngas	*SGA	SGA	SGA	No clear trend for both	
	Lowest syngas	<b>SGC</b>	<b>SGC</b>	<b>SGC</b>	No clear trend for both	
~30	Highest syngas	*SGA	SGA	SGA	No clear trend for both	
	Lowest syngas	<b>SGC</b>	<b>SGC</b>	<b>SGC</b>	No clear trend for both	

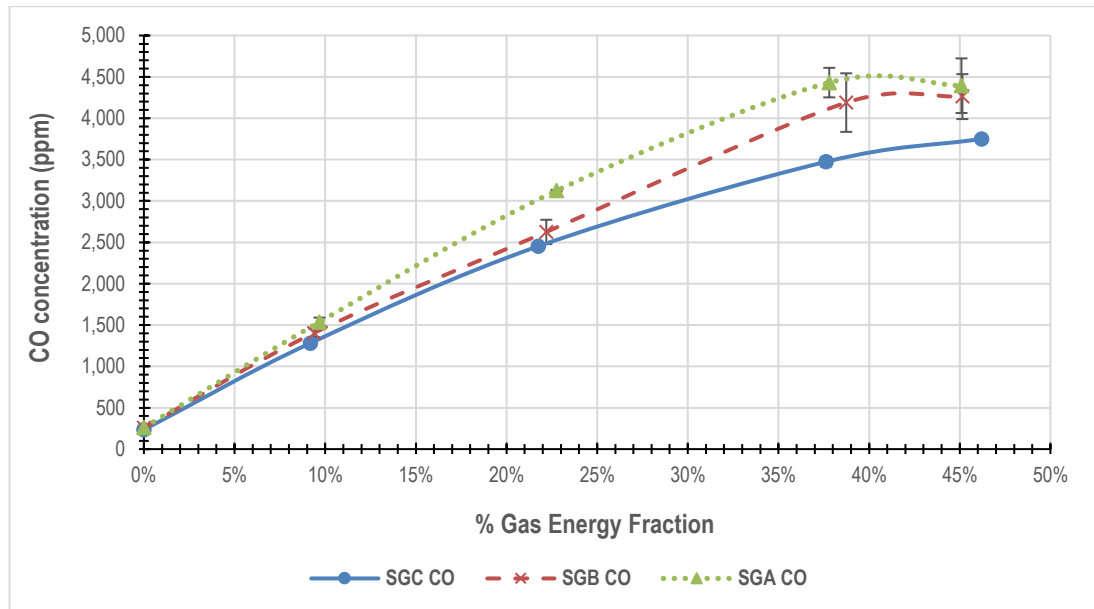
\*SGA was only compared for the raw CH<sub>4</sub> emissions up to a maximum GEF of ~22%

Table 6.6 clearly shows that the raw emissions of CO, CH<sub>4</sub>, and THC for SGC were the lowest of all syngas types across all the loads tested. This reinforces the engine combustion performance data from Chapter 5 and highlights that the higher H<sub>2</sub> content and H<sub>2</sub>/CO ratio leads to enhanced combustion performance resulting in less CO passing through into the exhaust as unburnt gas.

The average raw CO emission data was plotted for all three gases at ~96% engine load (4.2 kW), across various % GEF values and this is compared in Fig. 6.16 which shows that the exhaust gases produced from SGC dual fuel mode contain the lowest CO levels at % GEF values >23%. For values < 22% GEF, there is no noticeable difference between the syngas blends. This confirms the findings discussed in Chapter 5.

SGC had the highest NO<sub>x</sub> and NO emissions at full and 77% engine load. As discussed in Chapter 5, the normalised engine exhaust gas temperature data showed higher values for SGC at 77% engine load which help explain these findings.

SGA had the highest CO, CH<sub>4</sub>, and THC emissions across all loads assessed which are as expected when considering it has the lowest H<sub>2</sub> and H<sub>2</sub>/CO ratio of the three syngas types. In addition, for SGA, the marginally higher BTE as well as the lowest BTE/BSEC data at 10% GEF did not result in lower THC and CO emissions (in ppm) compared to the other syngas blends.



**Figure 6-16 Raw CO emission data for all syngas blends at 96% load**

As there is a slight load output variation across the dual fuel datasets, further in-depth cross-comparison of the gaseous emissions produced from these dual fuel runs will be compared using specific emission (SE) data expressed in g/kWh (see section 6.3.7).

### 6.3 Specific Emissions, and Emission Index data

The raw emission data (in ppm) from the MEXA 7100D, and the methane results from the FT-IR, were converted into SE and EI values for NO<sub>x</sub>, CO<sub>2</sub>, THC, CH<sub>4</sub>, CO<sub>2</sub>, and CO using the equations as discussed in Chapter 3 (see section 3.5). To avoid repetition, the CO<sub>2</sub> SE emission trend graphs for syngas blends are not reported in this section; instead, they are cross compared later in subsection 6.3.6.

#### 6.3.1 Syngas A

The EI in g/kg fuel is summarised in Table 6.7. From this, the calculated EI data in g/MJ fuel, and the SE in g/kWh are summarised for SGA in Table 6.8.

**Table 6-7 Emission Index (EI) data (in g/kg fuel) for SGA-diesel**

% Engine load	% GEF	EI (g/kg fuel)				
		THC	CH <sub>4</sub>	NO <sub>x</sub>	CO	CO <sub>2</sub>
96 (*4.2)	0	2.4	0.03	28	7	3,382
	10	2.2	1.53	14	25	1,993
	23	2.4	1.94	8	29	1,362
	38	2.1	No data	4	27	1,059
	45	1.8	No data	3	23	929
74 (*3.1)	0	3.1	0.09	28	15	3,509
	9	4.1	2.41	14	37	1,914
	22	4.5	3.54	7	47	1,353
	37	4.6	No data	4	48	1,007
56 (*2.3)	0	5.4	0.15	26	22	3,415
	9	6.4	3.03	14	51	2,004
	21	6.6	4.47	5	60	1,091
31 (*1.2)	0	7.5	0.21	24	34	3,491
	10	8.7	4.45	12	68	1,897
	21	9.7	6.46	6	83	1,196

**Table 6-8 EI (g/MJ fuel) and SE (g/kWh) data for SGA-diesel**

% Engine load	% GEF	EI (g/MJ fuel)					SE (g/kWh)				
		THC	CH <sub>4</sub>	NO <sub>x</sub>	CO	CO <sub>2</sub>	THC	CH <sub>4</sub>	NO <sub>x</sub>	CO	CO <sub>2</sub>
96	0	0.1	<0.01	0.64	0.2	77	0.7	0.01	7.4	1.9	878
	10	0.1	0.1	0.56	1.0	81	1.1	0.7	6.7	12.0	954
	23	0.2	0.1	0.49	1.9	87	1.8	1.5	5.8	22.4	1,041
	38	0.2	*	0.38	2.5	97	2.5	*	4.9	32.4	1,263
	45	0.2	*	0.31	2.4	97	2.5	*	4.1	31.6	1,289
74	0	0.1	<0.01	0.63	0.3	79	0.8	0.02	7.4	3.9	936
	9	0.2	0.1	0.54	1.5	76	2.0	1.2	6.5	17.8	917
	22	0.3	0.2	0.46	3.0	86	3.6	2.8	5.8	37.6	1,086
	37	0.4	*	0.34	4.3	90	5.7	*	4.7	59.2	1,233
56	0	0.1	<0.01	0.6	0.5	77	1.6	0.04	7.5	6.5	1,021
	9	0.2	0.1	0.5	2.0	78	3.2	1.6	7.1	26.8	1,051
	21	0.5	0.3	0.3	4.5	82	5.8	3.9	5.7	52.4	1,138
31	0	0.2	<0.01	0.5	0.8	79	3.3	0.1	10.4	15.0	1,576
	10	0.3	0.2	0.5	2.7	76	6.8	3.4	9.1	53.2	1,492
	21	0.6	0.4	0.4	5.1	72	12.3	8.2	7.9	105.2	1,496

*\*At these datapoints, the FT-IR was unavailable, hence the data set is incomplete.*

This SE data for CO, CH<sub>4</sub>, and THCs all show an increase with load and with increasing % GEF. Steeper increases are seen at lower loads due to the lower efficiencies. However, at full engine load increasing the GEF from 38 to 45% does not increase the NO<sub>x</sub>, CO, or THC emissions. As discussed earlier (see section 6.2.2), the specific emissions for CO and NO<sub>x</sub> decrease.

For reference, only a 0.52% reduction is noted in the BTE data between these two % GEF testing values.

The SE  $\text{NO}_x$  data shows a reduction with increasing % GEF of SGA across every load. The trends seen in the SE data for CO, THC,  $\text{NO}_x$ , and  $\text{CH}_4$  are shown in Figs. 6.17- 6.20.

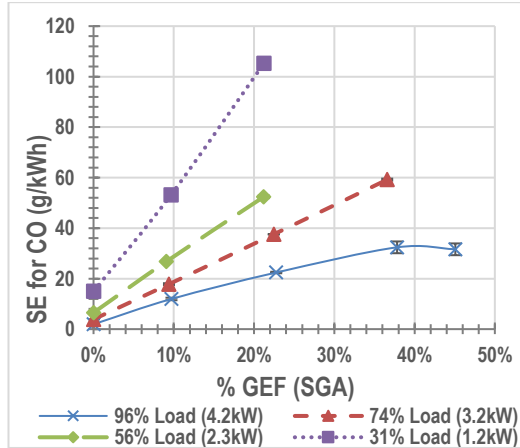


**Fig 6-17 SE CO for SGA**

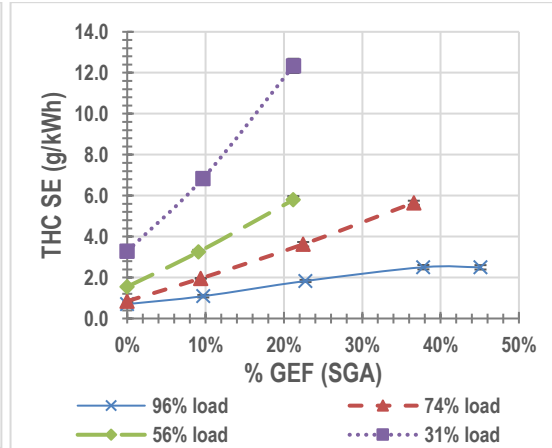


**Fig 6-18 SE THC for SGA**

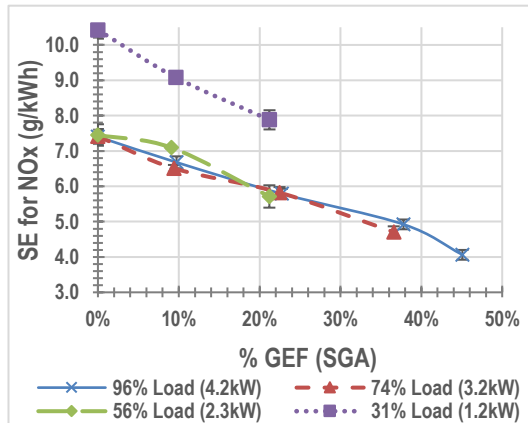


**Fig 6-19 SE  $\text{NO}_x$  for SGA**

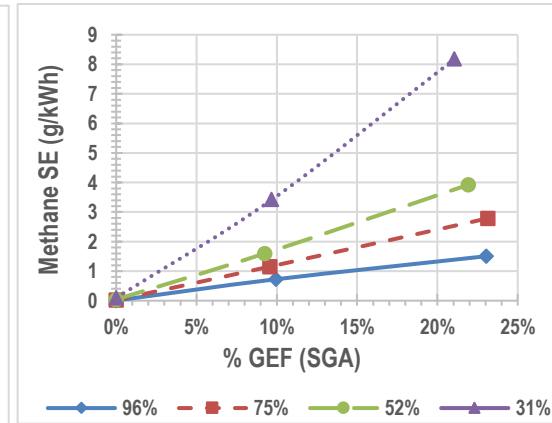


**Fig 6-20 SE  $\text{CH}_4$  for SGA**

### 6.3.2 Syngas B

The EI in g/kg fuel is summarised in Table 6.9 for SGB-diesel. From this, the further calculated data showing the EI in g/MJ fuel and the SE in g/kWh is summarised in Table 6.10, alongside the corresponding diesel baseline data.

**Table 6-9 Emission Index (EI) data (in g/kg fuel) for SGB-diesel**

(%) Engine load	(%) GEF	EI (g/kg fuel)				
		THC	CH <sub>4</sub>	NO <sub>x</sub>	CO	CO <sub>2</sub>
96 (*4.2)	0	1.9	0.02	29	7	3,568
	9	2.4	1.11	16	24	2,180
	22	2.3	1.37	9	30	1,502
	39	2.2	1.37	5	30	1,121
	45	1.6	1.23	4	26	1,062
76 (*3.2)	0	2.6	0.05	27	15	3,579
	10	4.4	1.80	14	41	2,138
	23	4.9	2.43	8	50	1,522
	39	4.8	2.69	5	52	1,106
54 (*2.2)	0	5.4	0.12	27	22	3,518
	9	6.7	3.19	15	53	2,224
	22	7.1	4.69	8	68	1,382
30 (*1.2)	0	8.0	0.21	24	34	3,811
	10	9.8	4.45	13	74	2,240
	22	10.6	6.45	8	92	1,392

**Table 6-10 EI (g/MJ fuel) and SE (g/kWh) data for SGB-diesel**

(%) Engine load	(%) GEF	EI (g/MJ fuel)					SE (g/kWh)				
		THC	CH <sub>4</sub>	NO <sub>x</sub>	CO	CO <sub>2</sub>	THC	CH <sub>4</sub>	NO <sub>x</sub>	CO	CO <sub>2</sub>
96	0	0.04	<0.01	0.65	0.2	81	0.5	0.01	7.5	2.0	946
	9	0.09	0.04	0.6	0.9	79	1.1	0.5	7.2	11.0	962
	22	0.14	0.08	0.52	1.7	88	1.7	1.0	6.4	21.1	1,093
	39	0.17	0.11	0.4	2.5	91	2.1	1.4	5.8	30.2	1,207
	45	0.15	0.11	0.4	2.4	95	2.0	1.5	5.4	32.6	1,283
76	0	0.06	<0.01	0.61	0.3	81	0.8	0.01	7.1	4.0	973
	10	0.16	0.07	0.54	1.5	80	2.0	0.8	6.5	18.4	964
	23	0.28	0.13	0.46	2.9	88	3.6	1.7	5.8	37.0	1,116
	39	0.40	0.19	0.4	4.3	91	5.3	2.8	5.0	57.8	1,223
54	0	0.12	<0.01	0.6	0.5	80	1.7	0.04	8.0	6.5	1,119
	9	0.25	0.12	0.5	2.0	82	3.3	1.7	7.4	26.7	1,114
	22	0.40	0.28	0.5	3.8	77	5.8	4.0	6.9	55.4	1,130
30	0	0.18	<0.01	0.6	0.8	85	3.5	0.09	10.4	14.7	1,626
	10	0.37	0.16	0.5	2.8	84	7.1	3.1	9.7	53.9	1,623
	22	0.60	0.37	0.4	5.2	78	12.4	7.6	8.8	106.9	1,622

\* Equivalent generator load in kW

This SE data for CO, CH<sub>4</sub>, and THCs all show an increase with load and with increasing % GEF. Steeper increases are seen at lower loads due to the lower combustion efficiencies.

However, at full engine load, increasing the SGB from 39 to 45 % does not significantly change/increase the specific emission data for CH<sub>4</sub>, NO<sub>x</sub>, or THC. For reference, a 0.75% reduction is noted in the BTE data between these two % GEF testing values.

The SE NO<sub>x</sub> data shows a reduction with increasing % GEF of SGB across every load. The trends seen in SE data CO, THC, NO<sub>x</sub>, and CH<sub>4</sub> are shown in Figs. 6.21- 6.24.

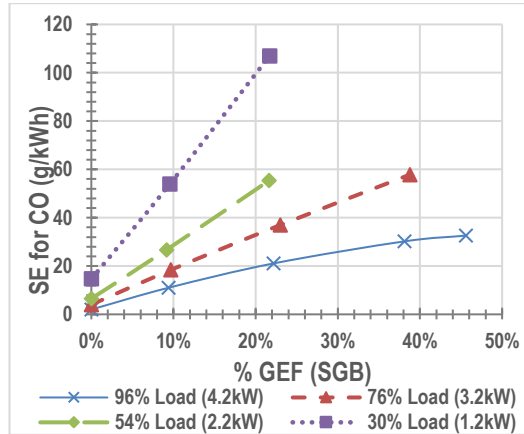


Fig 6-21 SE CO for SGB

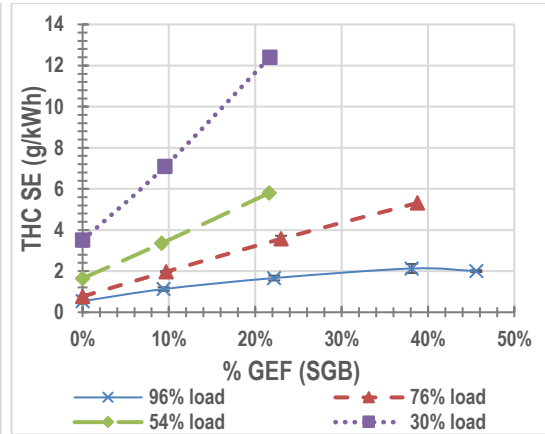


Fig 6-22 SE THC for SGB

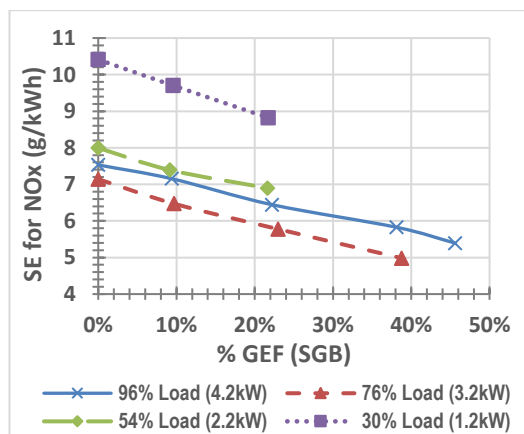


Fig 6-23 SE NO<sub>x</sub> for SGB

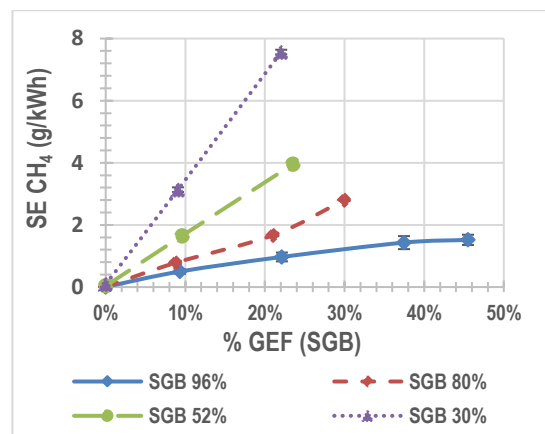


Fig 6-24 SE CH<sub>4</sub> for SGB

### 6.3.3 Syngas C

The EI in g/kg fuel is summarised in Table 6.11 for SGC-diesel. From this, the calculated data showing the EI in g/MJ fuel and the SE (g/kWh) is summarised in Table 6.12.

**Table 6-11 Emission Index (EI) data (in g/kg fuel) for SGC-diesel**

(%) Engine load	(%) GEF	EI (g/kg fuel)				
		THC	CH <sub>4</sub>	NO <sub>x</sub>	CO	CO <sub>2</sub>
95 (*4.2)	0	1.5	0.03	28	7	3,557
	9	2.1	1.18	18	23	2,302
	22	2.2	1.49	11	28	1,645
	38	1.8	1.42	7	27	1,268
	46	1.7	1.23	6	26	1,194
79 (*3.4)	0	2.4	0.05	28	11	3,391
	9	3.5	1.96	17	34	2,392
	22	3.7	2.90	10	44	1,597
	37	3.8	3.16	6	47	1,222
51 (*2.1)	0	4.9	0.13	25	21	3,106
	9	6.4	3.28	15	55	2,298
	23	6.8	4.79	8	69	1,430
29 (*1.2)	0	6.9	0.22	23	30	3,504
	10	8.6	4.36	13	70	2,233
	21	9.8	6.53	8	88	1,463

**Table 6-12 EI (g/MJ fuel) and SE (g/kWh) data for SGC-diesel**

(%) Engine load	(%) GEF	EI (g/MJ fuel)					SE (g/kWh)				
		THC	CH <sub>4</sub>	NO <sub>x</sub>	CO	CO <sub>2</sub>	THC	CH <sub>4</sub>	NO <sub>x</sub>	CO	CO <sub>2</sub>
95	0	0.03	<0.01	0.64	0.2	80	0.4	0.01	7.7	1.8	962
	9	0.07	0.04	0.61	0.8	80	0.9	0.5	7.5	9.8	969
	22	0.11	0.08	0.55	1.4	84	1.4	1.0	6.9	18.2	1,053
	38	0.13	0.10	0.49	1.9	91	1.8	1.3	6.4	25.4	1,205
	46	0.14	0.10	0.49	2.1	99	1.8	1.3	6.5	28.5	1,337
79	0	0.05	<0.01	0.64	0.2	77	0.6	0.01	7.4	2.9	878
	9	0.12	0.07	0.60	1.2	86	1.4	0.8	7.1	13.7	1,008
	22	0.19	0.15	0.50	2.3	81	2.4	1.8	6.2	27.9	1,001
	37	0.27	0.23	0.42	3.4	86	3.6	3.0	5.5	44.3	1,132
51	0	0.11	<0.01	0.56	0.5	70	1.4	0.04	7.4	6.2	938
	9	0.23	0.12	0.51	1.9	80	3.1	1.7	6.9	26.3	1,106
	23	0.36	0.27	0.44	3.6	75	5.2	4.0	6.4	52.7	1,089
29	0	0.15	<0.01	0.51	0.7	79	2.7	0.1	9.5	12.9	1,548
	10	0.30	0.16	0.45	2.5	79	6.0	3.0	9.0	48.8	1,546
	21	0.49	0.34	0.39	4.5	74	10.3	7.1	8.3	93.7	1,525

This SE data for CO, CH<sub>4</sub>, and THC again, all show an increase with load and with increasing % GEF. Steeper increases are seen at lower loads due to the lower combustion efficiencies.

At full engine load, as the GEF is increased from 38 to 46%, the THC, CH<sub>4</sub>, and NO<sub>x</sub> levels remain unaffected. Again, as per other syngas types, the SE NO<sub>x</sub> data shows a reduction with increasing % GEF of SGC across every load. The trends seen in the SE data for the CO, THC, NO<sub>x</sub>, and CH<sub>4</sub> are shown in Figs. 6.25-6.28.

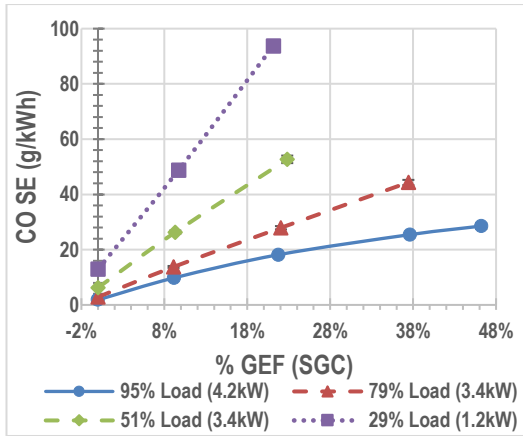


Fig 6-25 SE CO for SGC

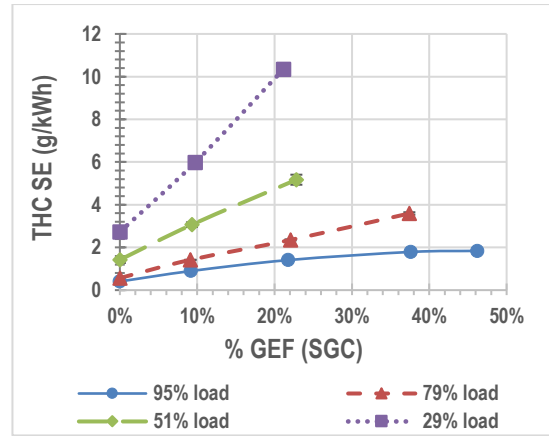


Fig 6-26 SE THC for SGC

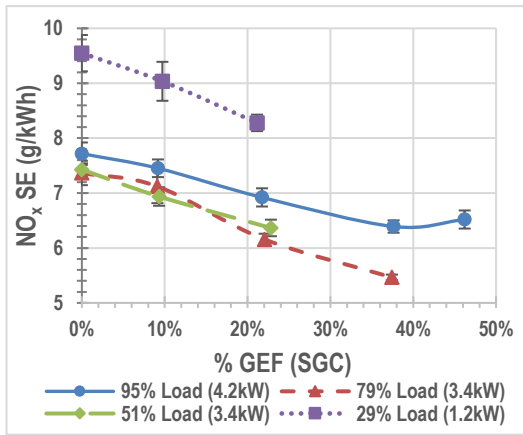


Fig 6-27 SE NO<sub>x</sub> for SGC

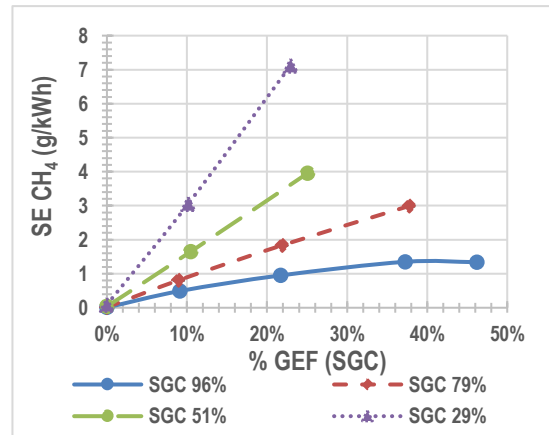


Fig 6-28 SE CH<sub>4</sub> for SGC

### 6.3.4 Biogas

The EI in g/kg fuel is summarised in Table 6.13. From this, the further calculated data showing the EI in g/MJ fuel and the SE in g/kWh is summarised for biogas-diesel in Table 6.14, alongside the corresponding diesel baseline data.

**Table 6-13 Emission Index (EI) data (in g/kg fuel) for biogas-diesel**

% Engine load	% GEF	EI (g/kg fuel)				
		THC	CH <sub>4</sub>	NO <sub>x</sub>	CO	CO <sub>2</sub>
97	0	2.4	0.03	28	6	3,418
	9	10.6	7.9	21	14	3,070
	24	18.7	11.5	14	19	2,319
	40	24.2	12.6	9	22	2,156
	49	26.6	8.7	7	21	1,945
80	0	2.2	0.1	27	11	3,211
	9	16.2	11.6	20	19	3,056
	22	29.2	16.9	13	24	2,343
	38	42.2	13.1	9	27	2,038
52	0	5.5	0.2	24	22	3,380
	10	31.9	20.7	17	33	2,881
	23	56.0	30.9	11	38	2,154
30	0	7.6	0.4	22	32	3,603
	12	49.1	30.1	15	44	2,706
	23	68.7	35.2	10	47	2,092

**Table 6-14 EI (g/MJ fuel) and SE (g/kWh) data for biogas-diesel**

% Engine load	% GEF	EI (g/MJ fuel)					SE (g/kWh)				
		THC	CH <sub>4</sub>	NO <sub>x</sub>	CO	CO <sub>2</sub>	THC	CH <sub>4</sub>	NO <sub>x</sub>	CO	CO <sub>2</sub>
97	0	0.1	<0.01	0.6	0.1	77	0.6	0.01	7.4	1.7	917
	9	0.3	0.2	0.6	0.4	84	3.5	2.6	6.8	4.6	1,010
	24	0.7	0.4	0.5	0.7	81	8.0	4.9	5.9	8.1	994
	40	1.1	0.6	0.4	0.9	94	13.2	6.9	5.0	11.8	1,152
	49	1.3	0.4	0.3	1.0	93	17.0	5.3	4.5	13.4	1,221
80	0	0.05	<0.01	0.6	0.2	73	0.6	0.02	7.2	2.8	849
	9	0.5	0.3	0.6	0.5	84	5.4	3.7	6.6	6.2	981
	22	1.0	0.6	0.5	0.8	80	12.2	7.1	5.6	10.0	971
	38	1.8	0.6	0.4	1.1	86	22.8	7.1	4.6	14.3	1,099
52	0	0.1	<0.01	0.6	0.5	76	1.7	0.05	7.4	6.6	1,022
	10	0.9	0.6	0.5	0.9	80	12.1	7.6	6.4	12.4	1,090
	23	2.0	1.1	0.4	1.3	75	27.4	13.8	5.5	19.0	1,096
30	0	0.2	<0.01	0.5	0.7	82	3.2	0.2	9.4	13.7	1,534
	12	1.4	0.9	0.4	1.3	79	27.3	16.4	8.1	25.2	1,516
	23	2.4	1.2	0.4	1.6	73	50.2	25.5	7.3	33.7	1,528

This SE data for CO and THC both show an increase with load and with increasing % GEF. The SE data for methane shows that at low engine loads (52, and 30%), these emissions increase with increasing GEF. However, at higher engine loads (full and 80%), the methane emissions reach an optimum level, after which further increases in biogas result in these emissions falling.

Steeper increases of CO and THC are seen at lower loads due to lower efficiencies. Again, as per other syngas types, the SE NO<sub>x</sub> data shows a reduction with increasing % GEF of biogas across every load. The CO<sub>2</sub> SE trend shows an increase in CO<sub>2</sub> emissions with increasing biogas at loads of 80 and 97%. For lower loads (<55%), the CO<sub>2</sub> emissions do not significantly change with increasing biogas fraction. The trends seen in the SE data for CO, THC, NO<sub>x</sub>, CH<sub>4</sub>, and CO<sub>2</sub> are shown in Figs. 6.29-6.33.

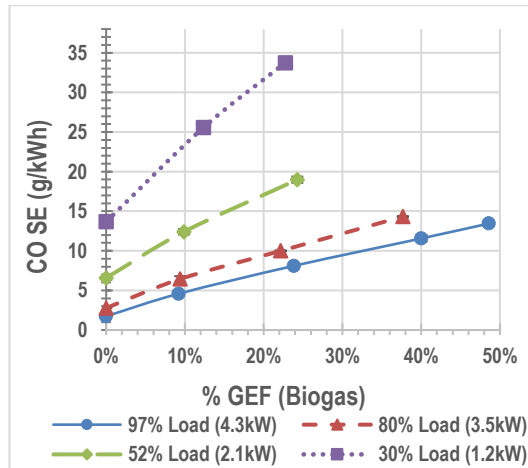


Fig 6-29 SE CO (Biogas)

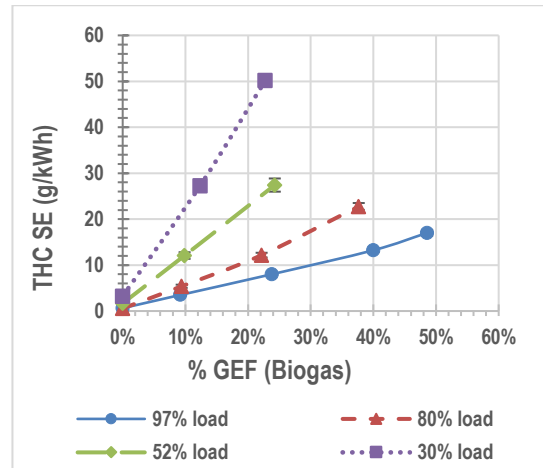


Fig 6-30 SE THC (Biogas)

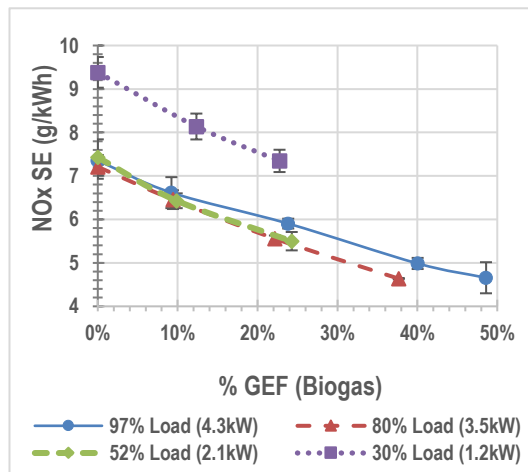


Fig 6-31 SE NO<sub>x</sub> (Biogas)

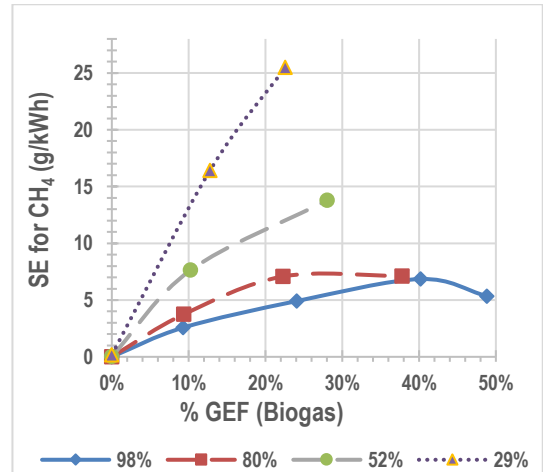
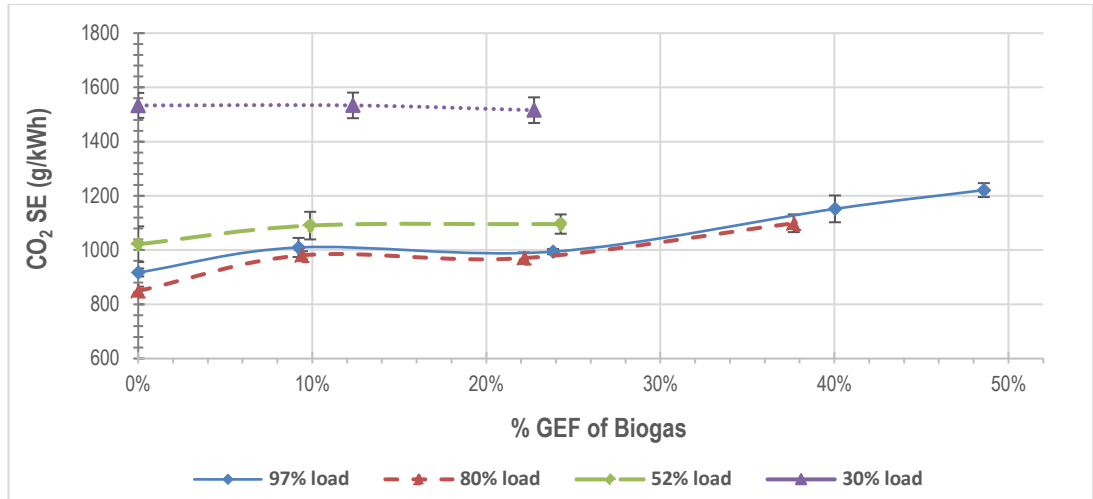
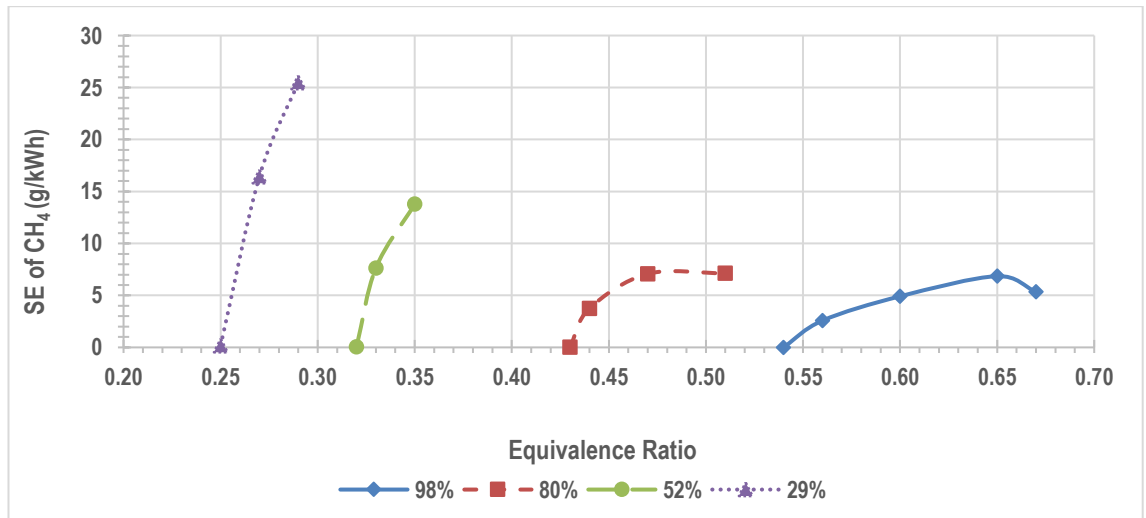


Fig 6-32 SE CH<sub>4</sub> (Biogas)



**Figure 6-33 CO<sub>2</sub> SE data for biogas-diesel at various engine loads**

The trend in the methane emissions was further explored by plotting this data as a function of  $\phi$ , this is depicted in Fig. 6.34. This graph shows that the potential reason for the methane emissions not increasing beyond a certain point at full and 80% engine load is because the limiting  $\phi$  has been potentially reached [276] ( as discussed earlier see section 6.2.2).



**Figure 6-34 SE of CH<sub>4</sub> versus  $\phi$  for biogas-diesel**

Interestingly, although the methane emissions are affected by the  $\phi$ , the THC emissions appear to be unaffected by this. The emissions classified as THC detected by the FID technique includes unburnt hydrocarbons and partially oxidised hydrocarbons, in other words, the total volatile hydrocarbon content is measured. Methane is a component of the total THC measured as the FID flame oxidises all the hydrocarbon compounds passing through.

Hence, the THC data is always greater than the methane data, the THCs represent a mixture of components all with different characteristics so will behave differently.

### **6.3.5 Specific Emission and Emission Index (g/MJ fuel) trends during dual fuel combustion**

#### **6.3.5.1 Specific Emission (SE in g/kWh) trends**

The general trends seen for the SE of THC and CO are similar to the raw CO and THC emissions (see subsection 6.2), whereby generally an increase of these emissions is observed with increasing % GEF of all gas/diesel fuel blends across every load; also, larger increases are seen at lower loads. This reduction at higher engine loads is associated with higher brake thermal efficiencies which are indicative of higher combustion efficiencies.

However, for THC emissions expressed as SE, it has been noted that at full engine load, when the GEF value is increased from ~39 to 46%, for all syngas fuels tested, the THC SE value remains unchanged, or shows a slight decrease (for the case of SGB). The graphs illustrating the THC trends were shown earlier, see Figs. 6.18, 6.22, and 6.26 which correspond to full engine loads trends for SGA, SGB, and SGC, respectively.

Similarly, for CO emissions expressed as SE, it has been noted that at full engine load, when the GEF value is increased from ~39 to 46%, we see a small decrease or no change in the CO SE levels for SGA and SGB. The potential reasoning for this has been discussed earlier (see subsection 6.2.2 -6.2.3). For the CO SE graphs, Figs. 6.17, 6.21, and 6.25 correspond to full engine loads trends for SGA, SGB, and SGC, respectively.

The study conducted by Guo et al. [150] looked at the effect of using simulated syngas in dual fuel mode in a diesel engine (maximum power rating of 74.6 kW, and speed of 910 RPM). They looked at the effects of various emissions at 25 and 50% engine load using syngas fractions of 25 and 50%, with their 25% being equivalent to approximately 23% in this study. BMEP values of 4.05 and 8.10 bar were used, the intake temperature was fixed at 40°C, and the combustion phasing (the CA position at which 50% cumulative heat release was reached, was fixed at 4 CAD after the top dead centre).

Their 'syngas 1' was similar to the SGA used in this study in terms of the LHV value and H<sub>2</sub>/CO ratio which was 0.72:1. (SGA has an H<sub>2</sub>/CO ratio of 0.75:1).

Guo et al. [150] reported similar findings whereby after experiencing increases in CO emissions (in g/kWh) at medium loads, further increases in syngas fractions did not significantly affect the CO emissions. Potentially this could be explained by the limiting equivalence ratio being reached, hence the CO emissions remain unaffected by the pilot diesel quantity during dual fuel combustion [276] (see subsection 6.2).

In terms of the biogas, the SE data for the THC emissions was consistently higher for the biogas-diesel dual fuel mode than any syngas-diesel blend, this is due to the high methane content of the biogas which is passing through as unburnt fuel due to the lower combustion efficiency. Comparatively, the SE emissions of CO were consistently lower for biogas-diesel than any syngas-diesel dual fuel, this is due to the biogas not containing any CO in its composition, thus cannot pass into the exhaust as unburnt fuel.

Again, the trend noted for the SE of NO<sub>x</sub> is as discussed in subsection 6.2.6, whereby the NO<sub>x</sub> levels decreased across all loads as the % GEF increased.

The trend noted for the SE of CO<sub>2</sub> for all dual fuel blends evaluated was that at 30% engine load, there is minimal change in the SE of CO<sub>2</sub> with increasing syngas fraction. At 54% engine load, there is no change noted again for SGB, whereas the remaining gas-diesel blends all saw a slight increase in the SE CO<sub>2</sub> data with the increasing addition of gas. At 76% and full engine loads, an increase was noted for all gas-diesel blends evaluated with increasing % GEF values. The CO<sub>2</sub> EI values have been cross compared for the three syngas types, see subsection 6.3.6.4 for further discussion. The CO<sub>2</sub> trend graphs showing the SE emissions for all the syngas-diesel blends are illustrated using Figs. 6.63, 6.65, 6.67, and 6.69 for all four engine loads assessed.

Comparing SE values from one study to another is tricky in literature as there are many variables to consider which will affect the resulting emissions: engine size, speed, and design, changes in injecting timing, and the composition of the syngas used to name a few.

The study carried out by Guo et al. [150], (as mentioned earlier) used syngas that did not contain any methane or oxygen. Hence, the NO<sub>x</sub> and CO data corresponding to 2kW (~55% engine load) and a GEF of 22% from this study were compared to SE data published by Guo et al. [150] obtained in dual fuel mode when using a 25% syngas fraction.

The following was summarised:

- NO<sub>x</sub> (g/kWh) as reported by Guo et al. [150] were ~6.4 (for 4.05 bar) and 6.6 (for 8.10 bar) versus 5.8 g/kWh for SGA.
- CO SE (in g/kWh) as reported by Guo et al. [150] were ~36 (for 4.05 bar) and ~11.4 (for 8.10 bar) versus 52 g/kWh for SGA.

Hence, the NO<sub>x</sub> data is roughly comparable, however, the CO data from this study is almost double. There are many reasons for this difference in the data such as larger engines having better thermal efficiency and the difference in the engine speed which affects the combustion duration. Also, the composition of the syngas. The syngas used in the study by Guo et al. [150] did not contain any methane, hence there would be no additional CO being produced from the partial oxidation of the methane component of the syngas which could contribute to the lower emissions reported. This comparison illustrates typical issues when trying to compare this data to literature across studies.

### 6.3.5.2 Emission index (in g/MJ fuel) trends

The emission index (EI) data produced from each gas-diesel blend was studied. EI plots for the gases were generated using error bars corresponding to  $\pm$  one standard deviation derived from repeat experimental data. The graphs depicting the EI trends (g/MJ fuel) for the syngas blends are shown in the next section, (subsection 6.3.6) for CO, THC, NO<sub>x</sub>, and CH<sub>4</sub> emissions. The EI plots for the biogas-diesel are shown in Figs. 6.35-6.38 for the CO, THC, NO<sub>x</sub>, and CH<sub>4</sub> emissions.

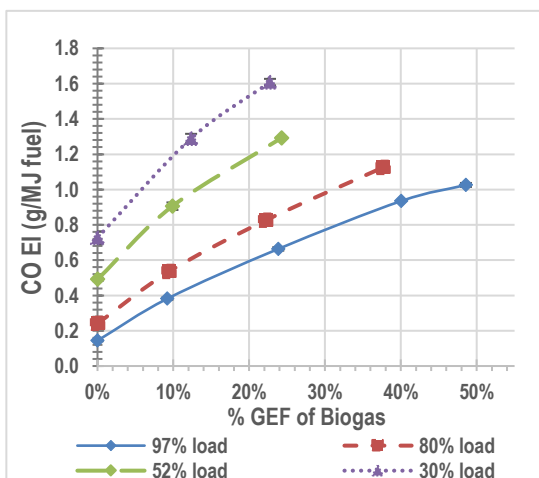


Fig 6-35 EI CO (Biogas)

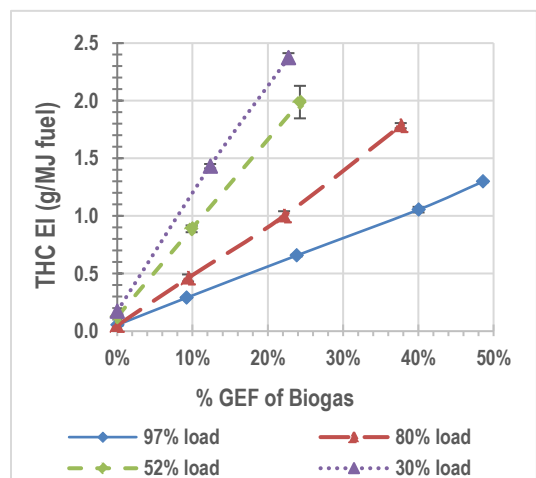
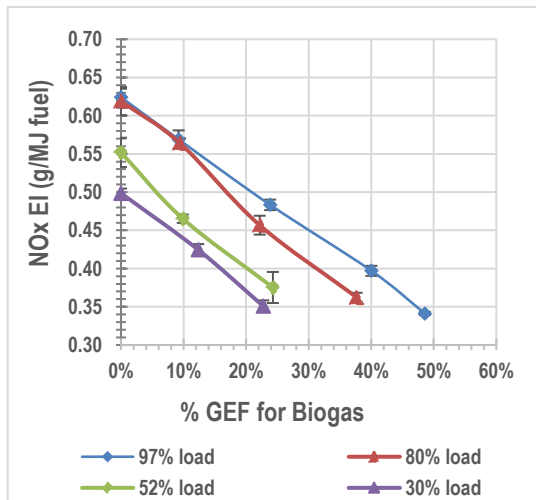
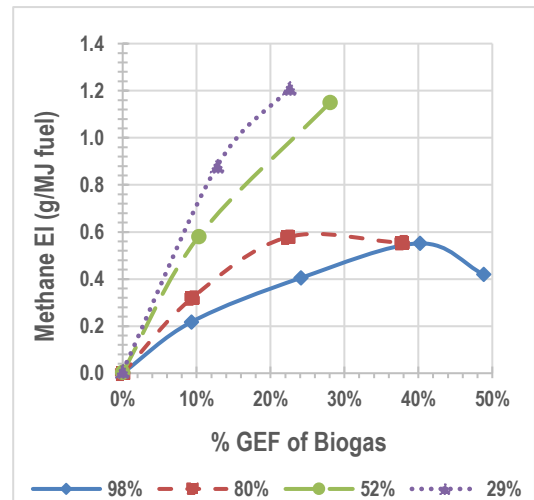


Fig 6-36 EI THC (Biogas)



**Fig 6-37 EI NO<sub>x</sub> (Biogas)**



**Fig 6-38 EI CH<sub>4</sub> (Biogas)**

The general trends summarised from the EI plots are as follows:

- The EI for THC increases as the % GEF is increased across all gas-diesel blends evaluated at all engine loads except for full engine load,
- At full engine load, the THC emissions increase with increasing biogas addition.
- However, at full engine load, for all syngas types, the THC emissions increase with increasing gas up to a GEF of ~38%, further addition of syngas above 38% GEF leads to a reduction or no further change in the THC values.

The increase in the THC EI data observed at lower engine loads (~53 and 30%), is due to the reduction in BTE with increasing gas fraction. This indicates a reduction in the combustion efficiency, which is shown by the increase in the UHCs due to incomplete combustion, thus this data reflects this. At 76% and full engine load, the THC emission trend can be explained similarly due to reduced combustion efficiency.

At 30 and 52% engine loads, as the biogas fraction is increased, this results in increasing THC EI emissions due to the reduction in efficiency and associated incomplete combustion of biogas.

A reduction in dual fuel brake thermal efficiency results in incomplete combustion, hence a reduction is noted in the combustion efficiency which also leads to unburnt CO passing into the exhaust gases. The CO in the exhaust could have originated from either the raw unburnt fraction of CO from the syngas or the partial oxidation of methane present in the biogas and syngas.

The general trend seen for CO emissions expressed as EI in g/MJ fuel, (when error bars are considered) is as follows:

- The EI data for CO increases as the % GEF is increased across all gas-diesel blends evaluated across all generator loads, with one exception,
- At full engine load, for SGA/SGB, the CO EI levels do not increase when the syngas is substituted above 38%, further addition of syngas leads to a slight reduction or no change in these levels.

For biogas, the CH<sub>4</sub> EI trend (see Fig. 6.38) shows that at lower engine loads (52, and 30%), the emissions increase with increasing GEF. However, at higher engine loads (full and 80%), the methane emissions reach an optimum level, after which further increases in biogas addition results in these emissions falling. For 80% engine load, this corresponds to a GEF of 22%, and for the full engine load, this occurs at a GEF of 40%. One possible explanation for this is that limiting  $\phi$  has been reached [276]. Further work is required to research this fully.

The EI methane graphs for syngas blends have not been included in this thesis as they mirror the trends seen for the SE of methane. The EI methane data are tabulated per syngas blend in Tables 6.8, 6.10, 6.12, and 6.14.

### **6.3.6 Cross-comparison of Specific Emission and Emission Index trends across syngas types**

#### **6.3.6.1 Total hydrocarbon (THC)**

The cross-comparison THC EI and SE data for the three syngas types tested are depicted in Figs. 6.39 to 6.46 which shows the data across all the loads per dual fuel gas blend.

This data shows that at every load assessed, generally, the THC SE and EI emission data is lower for SGC than the other syngas types. The syngas with the highest H<sub>2</sub> content and H<sub>2</sub>/CO ratio results in the cleanest combustion with respect to THC emissions at all loads tested (relative to the other syngas blends).

Analysis of the engine combustion parameters (as shown in Chapter 5) also supports that SGC dual fuel THC data should be the lowest of the three syngas types tested, especially at high loads (3kW and above, equivalent to  $\geq \sim 72\%$  engine load).

At these loads, the data shows that SGC is associated with higher brake thermal efficiency, higher engine exhaust temperatures, (specifically at 3kW), better combustion performance (in terms of the lowest value of the ID, highest  $P_{max}$ , and the smallest shift in  $P_{max}$  location), in comparison to SGA and SGB. All such conditions help promote better combustion and promote oxidation of UHCs, thus reducing the THC levels in the exhaust.

At lower engine loads of 53 and 30%, the reason for SGC having the lowest THC levels relative to the other syngas types is unclear. This is not directly evident in better engine combustion performance as judged by the parameters analysed in Chapter 5. However, this is possibly linked to its composition (higher  $H_2$  content and  $H_2/CO$  ratio), as there is a minor impact of the  $H_2/CO$  composition on the brake thermal efficiency at part-loads which were defined as 20-40% loads [144]. Further work is required to determine the cause of this; however, this will be discussed further when discussing the CO emissions in the next section (6.3.7.2).

Also, as mentioned in the summary of Chapter 5, SGA exhibited slightly better combustion characteristics at 54% load in terms of BTE and a smaller delay in the  $P_{max}$  location. However, from the THC emission comparison, as shown in Fig. 6.44, this did not translate to lower THC emissions in comparison to the other syngas blends.

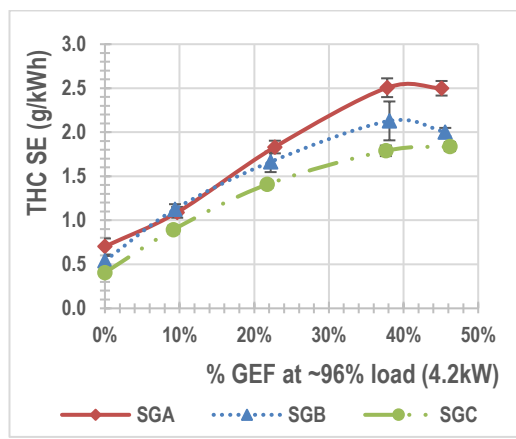


**Fig 6-39 SE THC (96% load)**

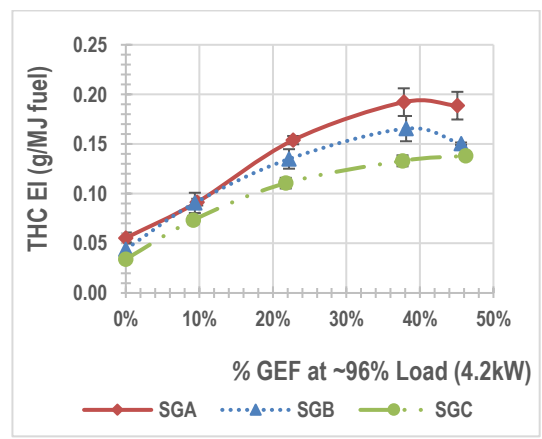


**Fig 6-40 EI THC (96% load)**

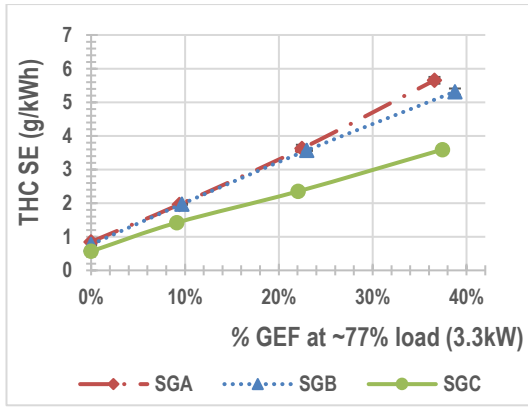


Fig 6-41 SE THC (77% load)

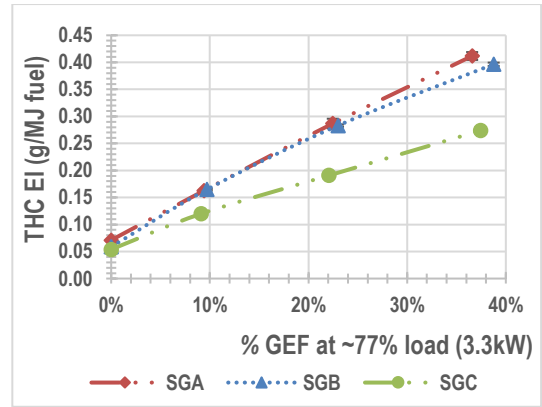


Fig 6-42 EI THC (77% load)

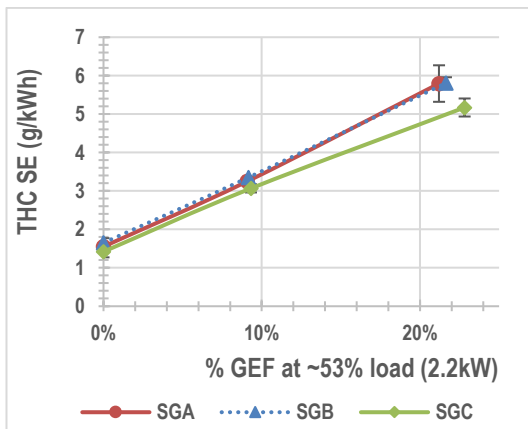


Fig 6-43 SE THC (53% load)

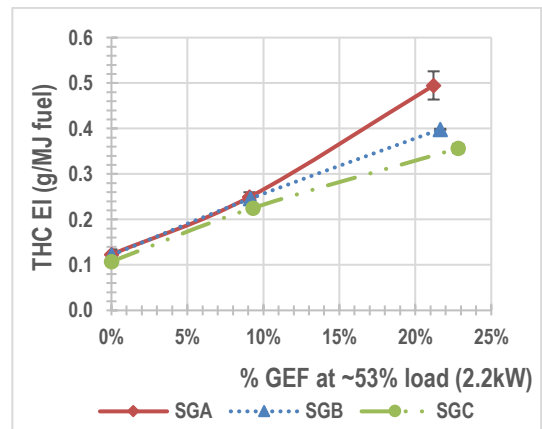


Fig 6-44 EI THC (53% load)

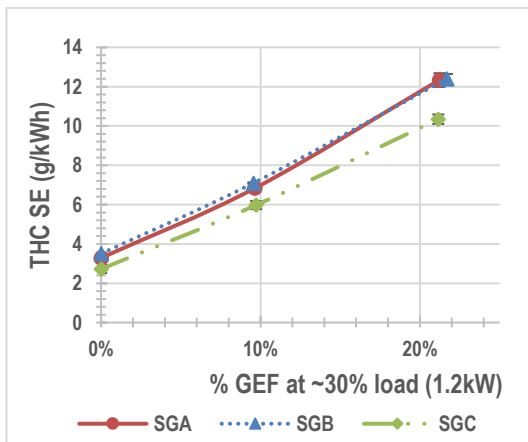


Fig 6-45 SE THC (30% load)

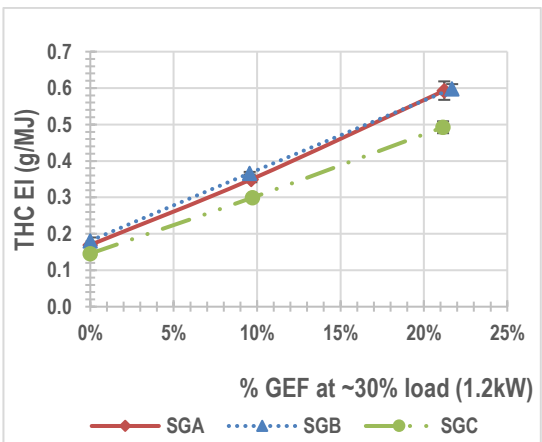


Fig 6-46 EI THC (30% load)

### 6.3.6.2 Carbon monoxide (CO)

The cross-comparison carbon monoxide (CO) EI and SE data for the three syngas types tested are depicted in Figs. 6.47 to 6.54 which shows the data across all the loads per dual fuel gas-type.

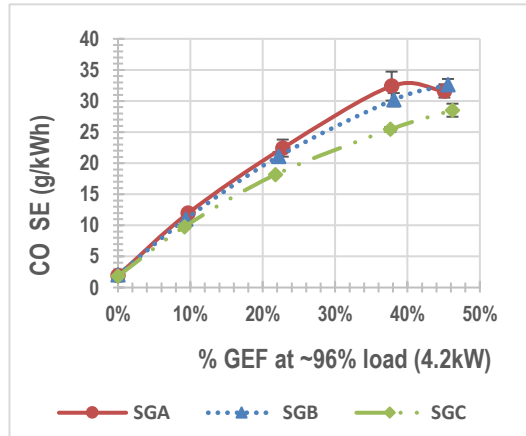


Fig 6-47. SE CO (96% load)

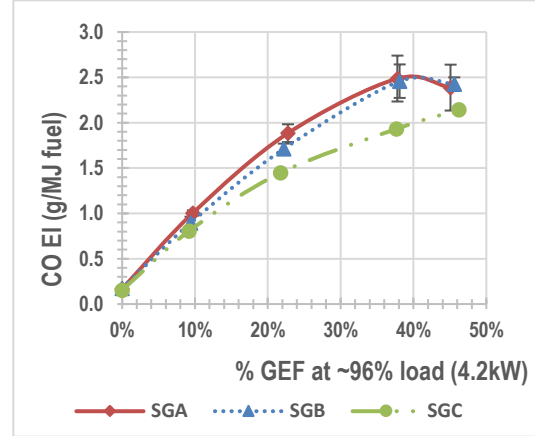


Fig 6-48. EI CO (96% load)

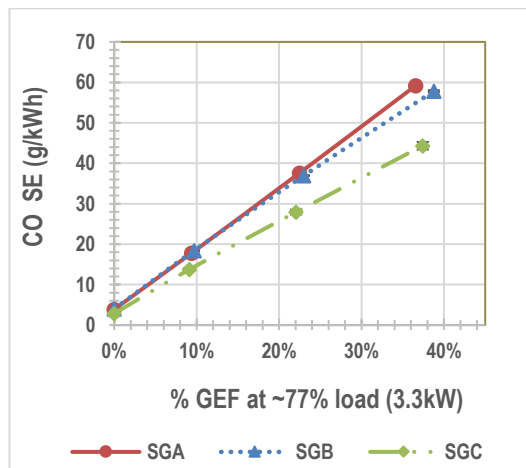


Fig 6-49 SE CO (77% load)

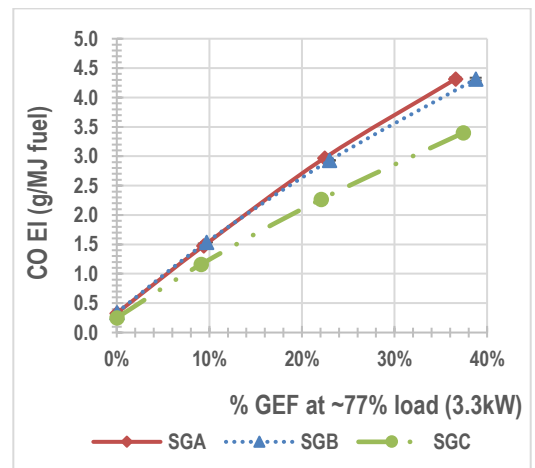
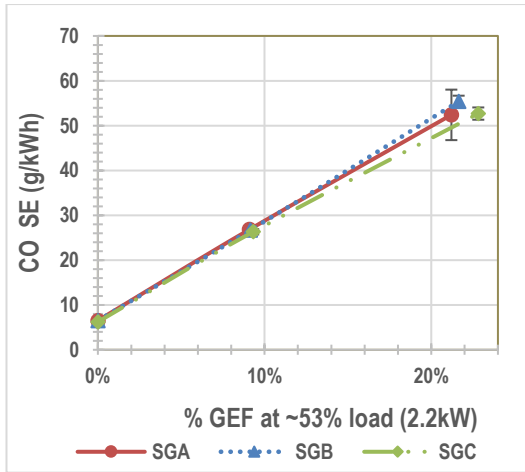
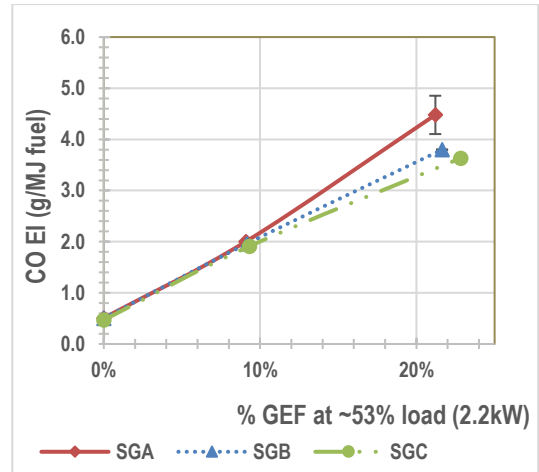


Fig 6-50 EI CO (77% load)



**Fig 6-51 SE CO (53% load)**



**Fig 6-52 EI CO (53% load)**

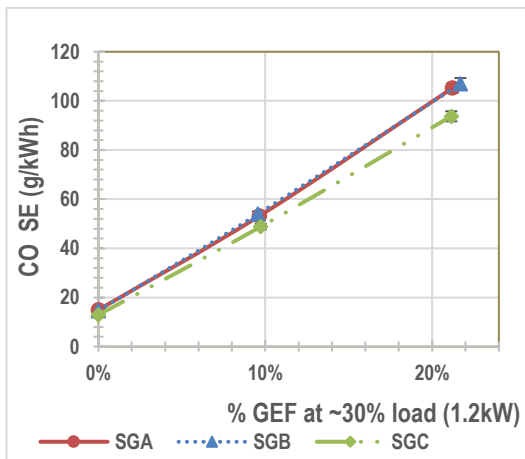


**Fig 6-53 SE CO (30% load)**

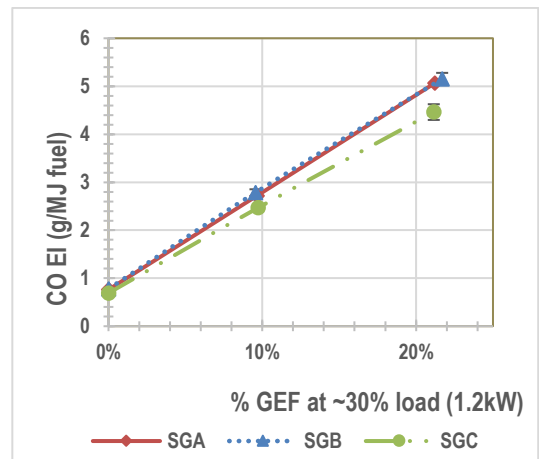


**Fig 6-54 EI CO (30% load)**

Both the SE and EI data for CO show that at full load, 77% and 30% engine load, at all % GEF tested, SGC produced the lowest CO emissions compared to the other syngas-diesel blends tested. At 53% engine load, SGC produced the lowest CO SE and EI levels at % GEF  $\geq$  22. This mirrors the exact findings seen for the THC SE and EI data for SGC (as discussed earlier, see section 6.3.6.1).

As the CO content in each syngas did not change, rather, the hydrogen content was increased (thus increasing the H<sub>2</sub>/CO ratio), therefore, any changes in the CO emission data are not due to the change in the CO composition of the syngas.

The most logical explanation is the enhanced combustion efficiency caused by higher H<sub>2</sub> content in SGC which leads to reduced CO emissions, as seen by other researchers [128].

Also, CO emissions are boosted by fuel-rich mixtures. Of all syngas types tested, SGC has the highest LHV, therefore requiring lower flow rates to obtain the same energy content in comparison to SGA and SGB. Hence, when using SGC, lower flow rates meant less displacement of air/oxygen, thus in theory this mixture was always leaner. The calculated  $\phi$  data from high loads (~96%) for SGC is leaner than that for SGA and SGB. For the remaining loads, this is not that apparent. In addition, the faster flame velocity of hydrogen helps to burn the CO trapped within the crevices of the combustion chamber thus reducing CO emissions [128]. Consequently, a combination of these effects leads to cleaner combustion in terms of CO and THC emissions.

As mentioned in the summary of Chapter 5, SGA exhibited slightly better combustion characteristics at 54% engine load in terms of BTE and a smaller delay in the P<sub>max</sub> location. However, from the CO emission comparison, as shown in Fig. 6.52, this did not translate to lower emissions in comparison to the other syngas blends.

### **6.3.6.3 Nitrogen oxides (NO<sub>x</sub>)**

The cross-comparison nitrogen oxides (NO<sub>x</sub>) EI and SE data for the three syngas types tested are depicted in Figs. 6.55 to 6.62, these plots show the data across all the engine loads tested. Overall, the NO<sub>x</sub> emissions decreased with increased syngas/biogas addition.

Figs. 6.55 and 6.56 show that SGC has the highest NO<sub>x</sub> SE and EI values at 96% engine load, followed by SGB, with SGA having the lowest. Figs. 6.57 and 6.58 show that at 77% engine loads, SGC still has the highest NO<sub>x</sub> SE and EI values, SGA and SGB having similar profiles except for the last GEF evaluated whereby SGA has a lower value. At lower engine loads (53 and 30%), SGB has the highest NO<sub>x</sub> SE and EI values; the remaining blends: SGA and SGC have similar profiles except for at 53% load where SGA has a lower value at the highest GEF evaluated.

At engine loads  $\geq 72\%$ , higher NO<sub>x</sub> emissions are produced from the syngas with the highest H<sub>2</sub> content and the H<sub>2</sub>/CO ratio.

Other findings in the literature support this whereby higher NO<sub>x</sub> emissions have been reported for fuels with higher H<sub>2</sub> content due to higher in-cylinder pressure and combustion temperatures [85, 128, 144, 147].

Engine performance analysis conducted in Chapter 5 has also reported higher in-cylinder pressures and higher engine exhaust gas temperatures for SGC at full load and at 78% engine load relative to the rest of the syngas types which indicate higher combustion temperatures, thus validating these findings.

However, for lower loads ( $\leq 55\%$  engine load), the higher H<sub>2</sub> content of the syngas does not appear to result in higher NO<sub>x</sub> values. One plausible explanation for this is that at these load conditions the benefits of the faster flame velocity of H<sub>2</sub> are lost due to the lower combustion temperatures. Instead, SGB (which contains equal amounts of H<sub>2</sub>/CO or a 1:1 ratio) produced the highest NO<sub>x</sub> levels at engine loads  $<55\%$ .

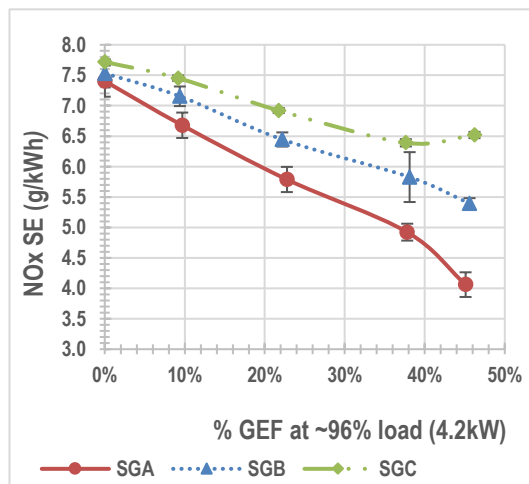


Fig 6-55 SE NO<sub>x</sub> (96% load)

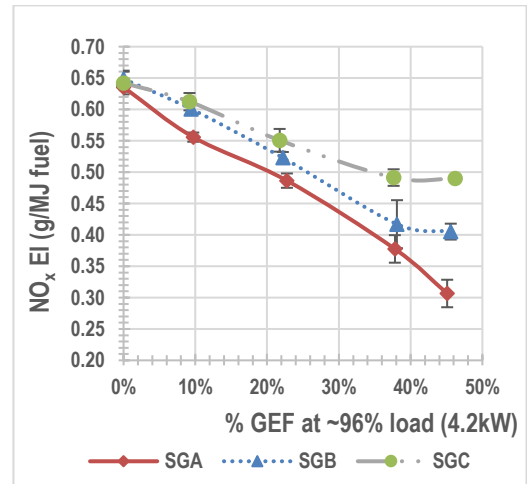


Fig 6-56 EI NO<sub>x</sub> (96% load)

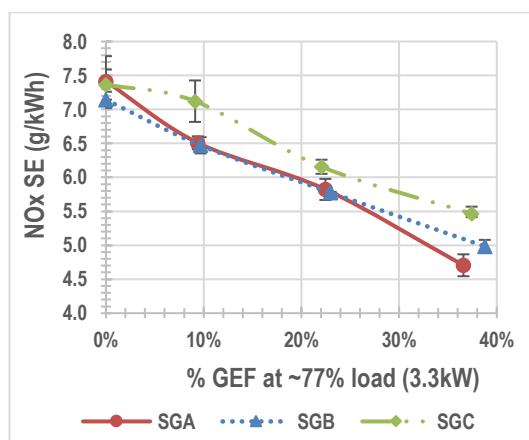


Fig 6-57 SE NO<sub>x</sub> (77% load)

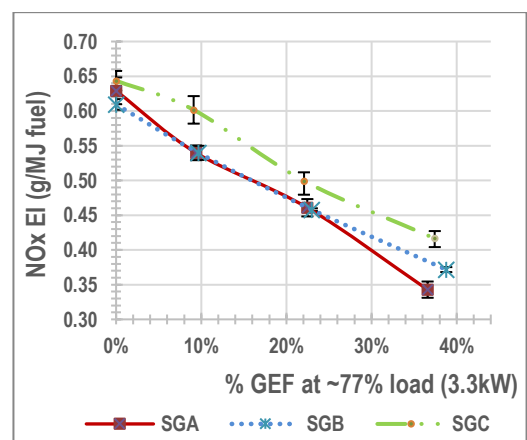


Fig 6-58 EI NO<sub>x</sub> (77% load)

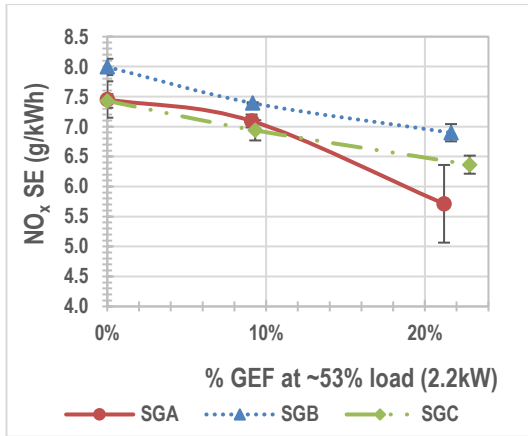


Fig 6-59 SE NOx (53% load)

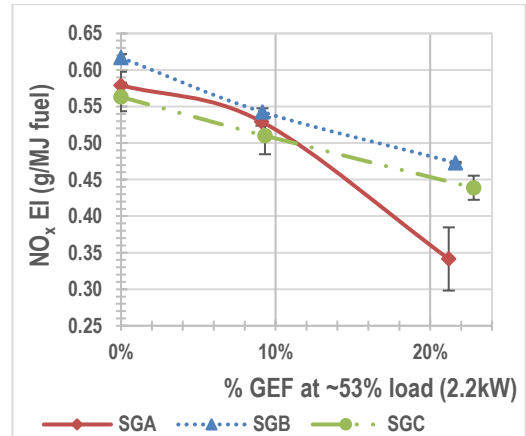


Fig 6-60 EI NOx (53% load)

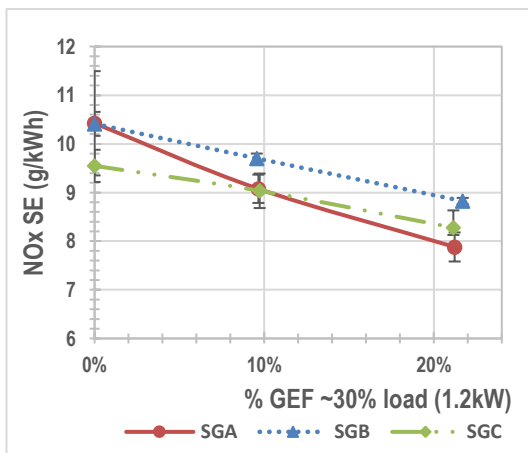


Fig 6-61 SE NOx (30% load)

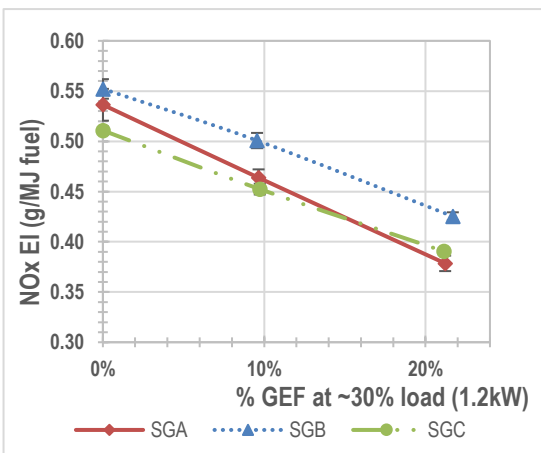


Fig 6-62 EI NOx (30% load)

### 6.3.6.4 Carbon dioxide (CO<sub>2</sub>)

The cross-comparison carbon dioxide (CO<sub>2</sub>) EI and SE data for the three syngas types tested are depicted in Figs. 6.63 to 6.70 which shows the data across all the loads.

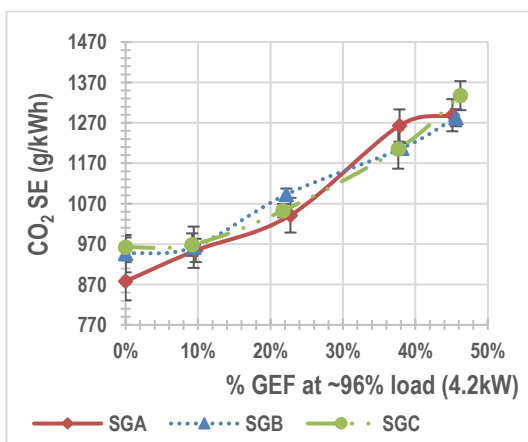


Fig 6-63 SE CO<sub>2</sub> (96% load)

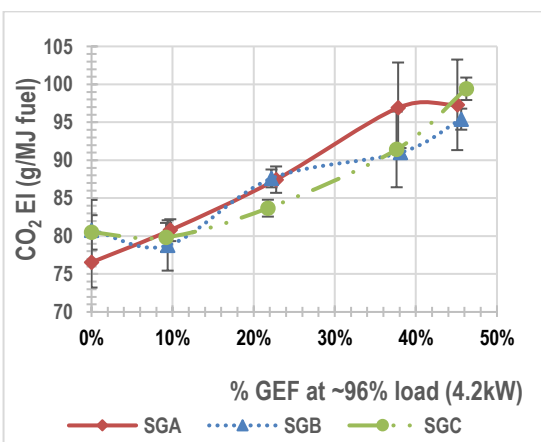
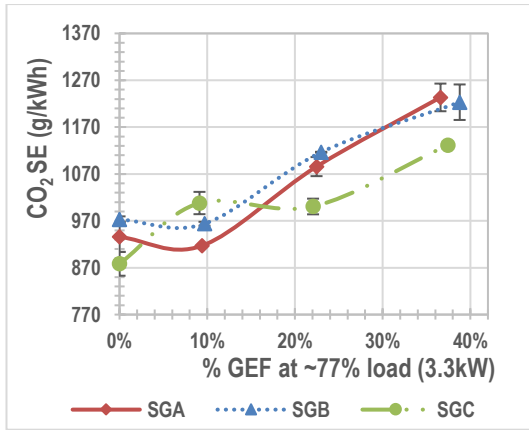
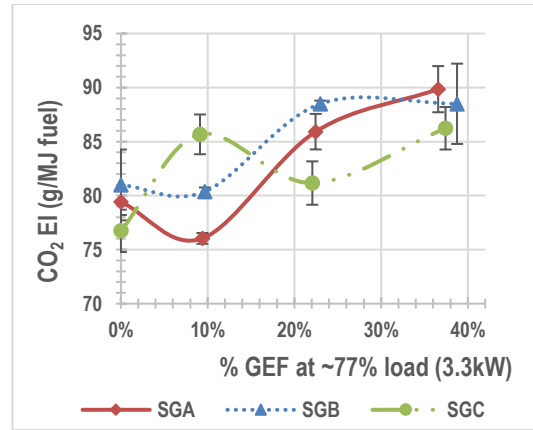


Fig 6-64 EI CO<sub>2</sub> (96% load)



**Fig 6-65 SE CO<sub>2</sub> (77% load)**



**Fig 6-66 EI CO<sub>2</sub> (77% load)**

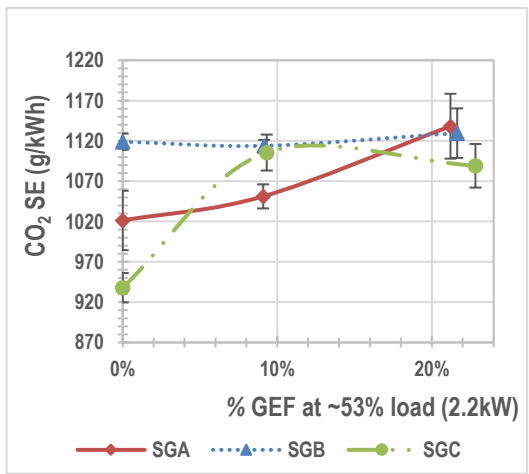


**Fig 6-67 SE CO<sub>2</sub> (53% load)**

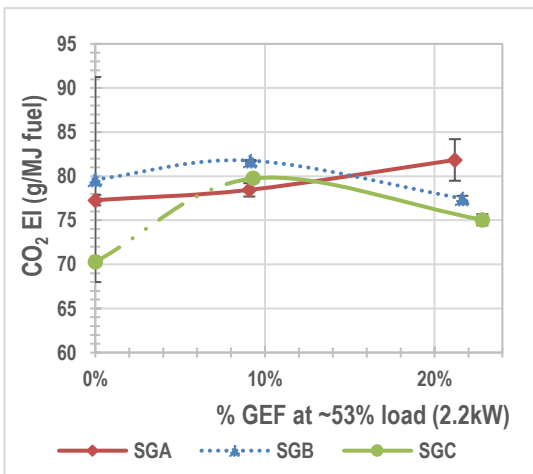


**Fig 6-68 EI CO<sub>2</sub> (53% load)**

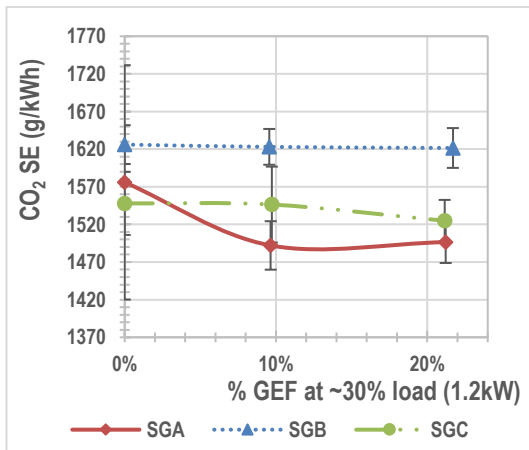


**Fig 6-69 SE CO<sub>2</sub> (30% load)**

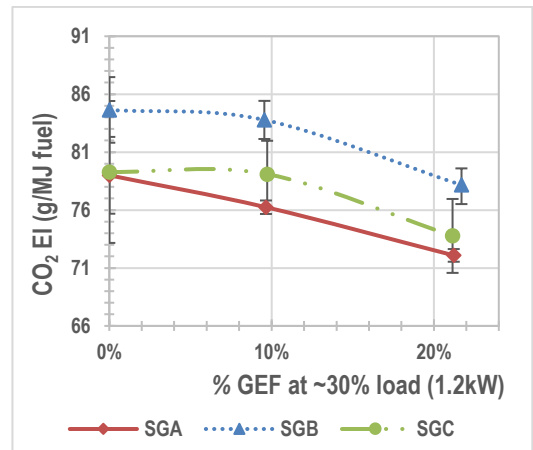


**Fig 6-70 EI CO<sub>2</sub> (30% load)**

Figs. 6.63 to 6.66 show that all three syngas types produce similar CO<sub>2</sub> emissions at full and 77% engine load. Thus, the combustion product, i.e., CO<sub>2</sub> does not appear to be affected by the syngas composition at these loads.

Fig. 6.67 shows that at 53% engine load, for SGA and SGC, the CO<sub>2</sub> SE values increase with increasing % syngas, whereas for SGB the CO<sub>2</sub> emissions stay static. Fig. 6.68 shows that at 53% engine load there is no clear trend between the syngas types in terms of CO<sub>2</sub> EI data.

Fig. 6.69 shows that at 30% engine load, SGB has the higher CO<sub>2</sub> SE values, with SGA the lowest. Increasing the % syngas fraction does not equate to an increase in the SE of CO<sub>2</sub> at 30% engine load. These findings are confirmed by the EI data shown in Fig. 6.70, which shows that at 30% engine load, SGB has the higher CO<sub>2</sub> EI value and SGA the lowest, these values decrease with increasing % syngas addition for all the fuel blends assessed.

#### **6.4 Speciation of gaseous emissions using the FT-IR**

For the dual fuel analysis, the focus of this analysis was to determine the speciation of the gaseous emissions, in particular the hydrocarbons present. Also, for ease of comparison, and to avoid repetition, some species which have already been analysed by the MEXA (CO<sub>2</sub>, CO, O<sub>2</sub>, and all NO<sub>x</sub> related species) have been omitted from these dual fuel FT-IR results. For reference, a good correlation was found between the oxygen, CO, and NO<sub>x</sub> data using both modes of analysis. For the diesel baseline runs, the full range of analysis results are shown in Table 6.1 (p178 for MEXA) and Table 6.15 (p221 for FT-IR).

For the FT-IR results presented, only the species detected above the detection limit have been reported. There are some slight variations in the experimental parameters (% engine load/ % GEF) presented between the FT-IR and MEXA datasets as the FT-IR was not used alongside the MEXA in every case. To determine trends in terms of the concentration of the species as a function of % GEF, the average concentrations from repeat measurements at each condition were reported. The concentration graphs for each species detected were generated (with error bars based on  $\pm$  one standard deviation derived from repeat experimental work).

These graphs are not shown due to the high volume, instead, a summary table is provided in each case to illustrate the effect on the concentration with increasing % GEF, alongside the actual data values.

### 6.4.1 Diesel baseline data

The diesel baseline data (averaged from all the diesel baseline FT-IR runs) is shown for all the species detected above the detection limit in Table 6.15.

**Table 6-15 FT-IR emission data for diesel baseline runs**

Species	Unit	Generator Load (Engine load %)			
		4.2 kW (96%)	3.4kW (79%)	2.1kW (52%)	1.2kW (30%)
Oxygen	% Vol	10	13	15	17
Carbon dioxide (CO <sub>2</sub> )	% Vol	8	7	6	6
Water vapor (H <sub>2</sub> O)	% Vol	7	6	5	4
Carbon monoxide (CO)	ppm	236	304	448	560
Nitrogen monoxide (NO)	ppm	573	436	248	167
Nitrogen dioxide (NO <sub>2</sub> )	ppm	0	0	19	23
Methane (CH <sub>4</sub> )	ppm	1	3	5	7
Ethane (C <sub>2</sub> H <sub>6</sub> )	ppm	4	3	6	8
Ethylene/Ethene (C <sub>2</sub> H <sub>4</sub> )	ppm	6	7	6	6
Hexane (C <sub>6</sub> H <sub>14</sub> )	ppm	13	12	23	24
Formaldehyde (HCHCO)	ppm	5	6	13	17
Ethanol	ppm	12	19	32	37
NO <sub>x</sub> as NO <sub>2</sub>	ppm	573	436	267	190

### 6.4.2 Syngas A

The FT-IR was not available to analyse exhaust gas emissions at full load and 77% engine loads when testing SGA at GEF values of 38 and 46%. The species of interest and the average concentrations analysed during the SGA-diesel dual fuel runs by the FT-IR are summarised in Table 6.16.

**Table 6-16 FT-IR emission data for SGA-diesel runs**

Generator load kW	Engine load %	% GEF	(Concentration in ppm)						
			THC (MEXA)	CH <sub>4</sub>	Ethane	Ethylene	Hexane	HCHO	Ethanol
4.2	95	0	149	ND	5	6	14	4	14
4.2	96	10	259	155	5	ND	14	11	16
4.3	97	23	441	325	5	ND	14	18	21
3.4	79	0	148	4	5	10	19	8	20
3.1	73	10	353	192	5	ND	17	15	23
3.2	74	23	642	473	5	ND	17	23	26
2.2	54	0	211	5	7	5	28	15	46
2.1	52	9	435	217	8	ND	26	20	46
2.1	51	22	784	535	11	ND	26	28	47
1.2	31	0	247	7	8	4	25	17	48
1.2	31	10	497	242	11	8	27	25	47
1.3	31	21	901	579	16	6	29	34	50

ND denotes none detected (i.e., below the detection limit of 3 ppm)

### 6.4.3 Syngas B

The species of interest and the average concentrations analysed during the SGB-diesel dual fuel runs by the FT-IR are summarised in Table 6.17.

**Table 6-17 FT-IR emission data for SGB-diesel runs**

Generator load (kW)	Engine load %	% GEF	(Concentration in ppm)						
			THC (MEXA)	CH <sub>4</sub>	Ethane	Ethylene	Hexane	HCHO	Ethanol
4.2	96	0	120	1	6	4	10	4	13
4.2	96	9	232	117	6	5	9	10	17
4.3	96	22	344	232	5	4	5	14	16
4.3	97	38	533	343	6	5	5	19	15
4.3	97	45	508	361	6	6	4	22	19
3.4	79	0	123	3	ND	6	10	6	18
3.4	80	9	304	155	ND	4	11	11	19
3.4	80	21	615	334	ND	5	11	17	20
3.5	80	30	924	574	ND	6	11	25	27
2.1	52	0	197	4	ND	ND	21	11	33
2.1	52	10	416	214	ND	ND	22	18	35
2.1	52	23	722	528	ND	ND	21	25	37
1.2	30	0	235	6	ND	ND	23	16	36
1.2	30	9	483	233	6	ND	26	24	37
1.2	30	22	850	564	11	ND	30	32	38

*ND denotes none detected (i.e., below the detection limit of 3 ppm)*

### 6.4.4 Syngas C

The species of interest and the average concentrations analysed during the SGC-diesel dual fuel runs by the FT-IR are summarised in Table 6.18.

**Table 6-18 FT-IR emission data for SGC-diesel runs**

Generator load (kW)	Engine load %	% GEF	(Concentration in ppm)						
			THC (MEXA)	CH <sub>4</sub>	Ethane	Ethylene	Hexane	HCHO	Ethanol
4.2	95	0	100	2	6	6	14	5	6
4.2	95	9	213	113	7	4	14	9	7
4.2	96	22	328	222	6	3	9	13	8
4.3	96	37	415	319	3	5	9	19	11
4.3	97	46	423	323	3	6	7	19	12
3.4	79	0	125	2	ND	5	12	5	15
3.4	79	9	280	148	ND	3	12	10	17
3.4	79	22	456	338	ND	3	12	16	19
3.4	79	38	686	551	8	3	11	24	21
2.1	51	0	181	5	8	6	25	12	32
2.1	51	10	394	196	9	8	26	18	34
2.1	51	25	661	471	9	6	26	24	37
1.2	29	0	203	6	10	7	26	15	34
1.2	29	10	424	209	11	7	27	21	38
1.2	29	23	731	489	11	7	28	28	40

*ND' denotes none detected (i.e., below the detection limit of 3 ppm)*

## 6.4.5 Biogas

The species of interest and the average concentrations analysed during the biogas-diesel dual fuel runs by the FT-IR are summarised in Table 6.19.

**Table 6-19 FT-IR emission data for biogas-diesel runs.**

Generator load (kW)	Engine load %	% GEF	(Concentration in ppm)						
			THC (MEXA)	CH <sub>4</sub>	Ethane	Ethylene	Hexane	HCHO	Ethanol
4.3	96	0	120	2	5	5	15	4	13
4.3	96	9	838	647	18	9	13	36	15
4.3	98	24	2,015	1,259	94	15	ND	70	20
4.4	99	40	3,377	1,797	189	21	ND	128	22
4.4	100	49	4,195	1,411	76	32	ND	151	9
3.4	79	0	115	4	3	4	6	6	23
3.4	80	9	1,074	771	25	6	9	41	28
3.5	80	22	2,445	1,462	117	12	ND	75	31
3.5	80	38	4,531	1,477	73	20	ND	143	15
2.1	52	0	200	6	5	ND	21	12	42
2.1	52	10	1,525	1,017	52	ND	15	53	42
2.1	52	28	3,471	1,855	179	16	ND	100	43
1.2	30	0	239	12	7	4	24	19	47
1.2	30	13	1,996	1,224	82	12	16	59	48
1.2	30	23	3,687	1,905	189	22	4	106	47

*ND denotes none detected (i.e., below the detection limit of 3 ppm)*

## 6.4.6 Methane slippage in the exhaust gases in dual fuel mode

The % methane slippage was calculated from the exhaust gas, based on the methane input from the gaseous fuel using equations as described in Chapter 3 (see subsection 3.5.13). The trends seen per load for each gas-diesel blend are shown in Figs. 6.71-6.74 for SGA, SGB, SGC, and biogas, respectively.

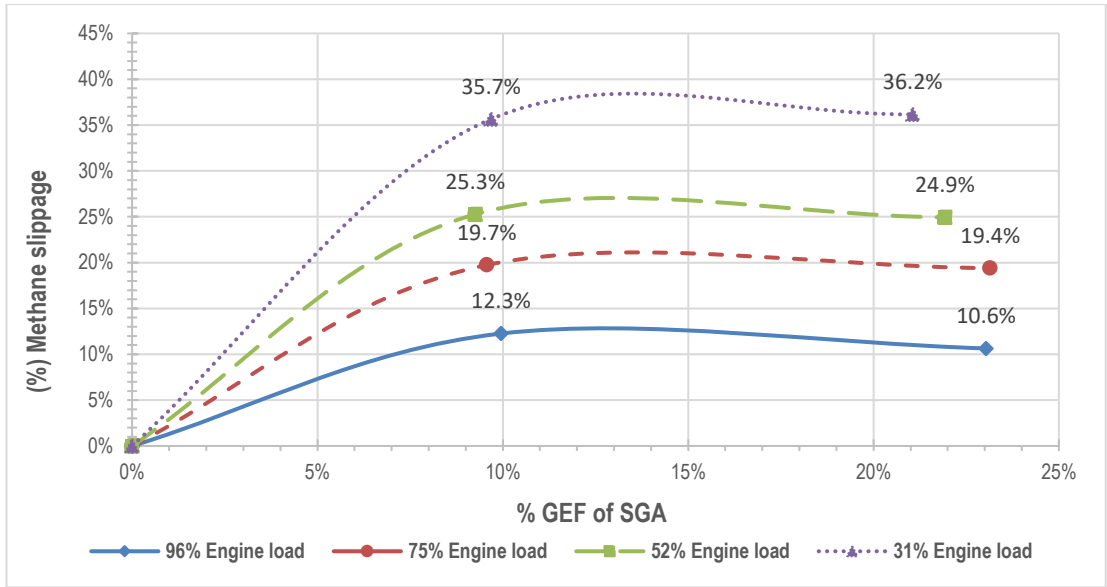


**Figure 6-71 Methane slippage (%) for SGA-diesel**

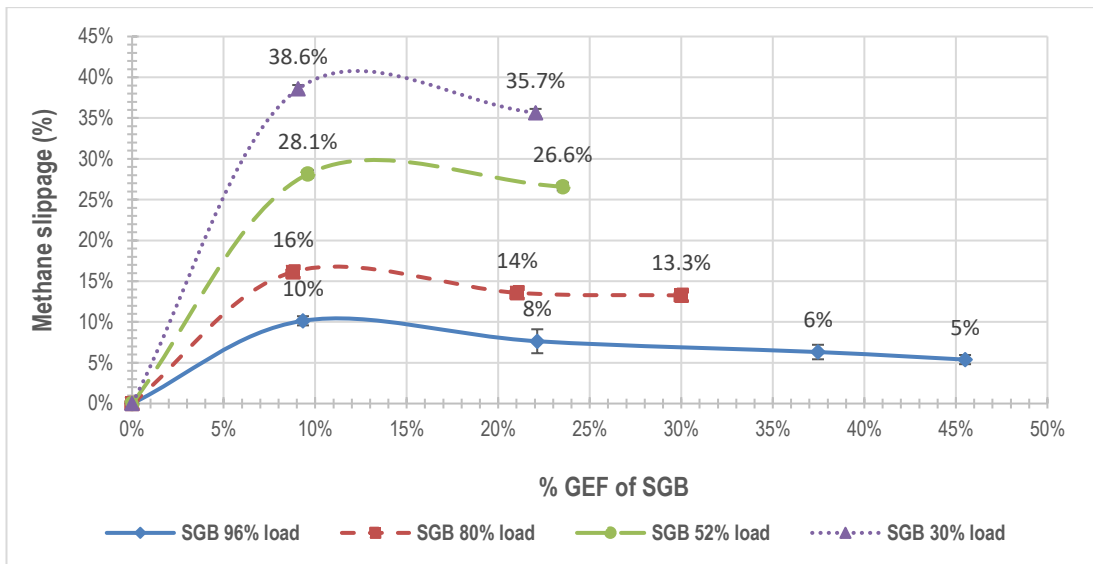


**Figure 6-72 Methane slippage (%) for SGB-diesel**

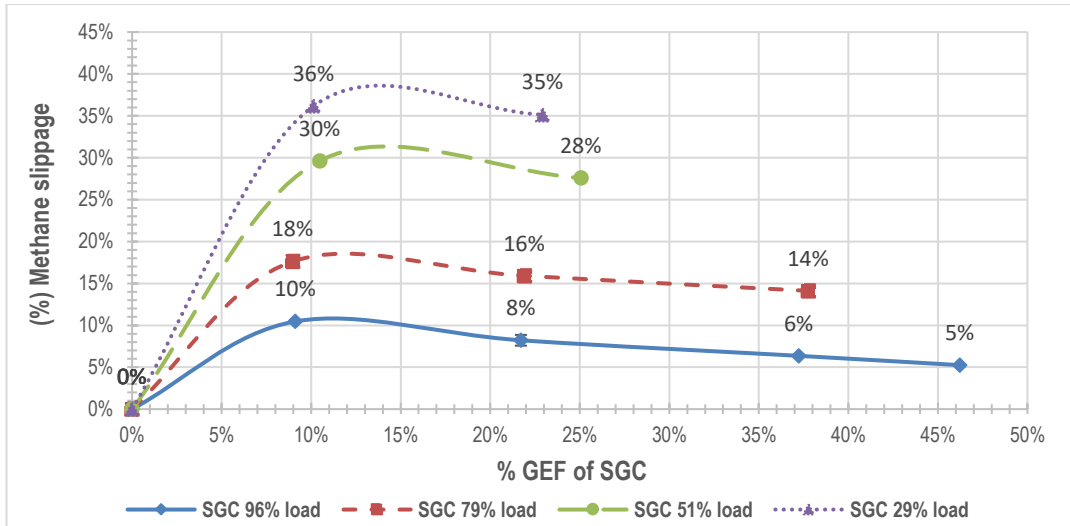


**Figure 6-73 Methane slippage (%) for SGC-diesel**

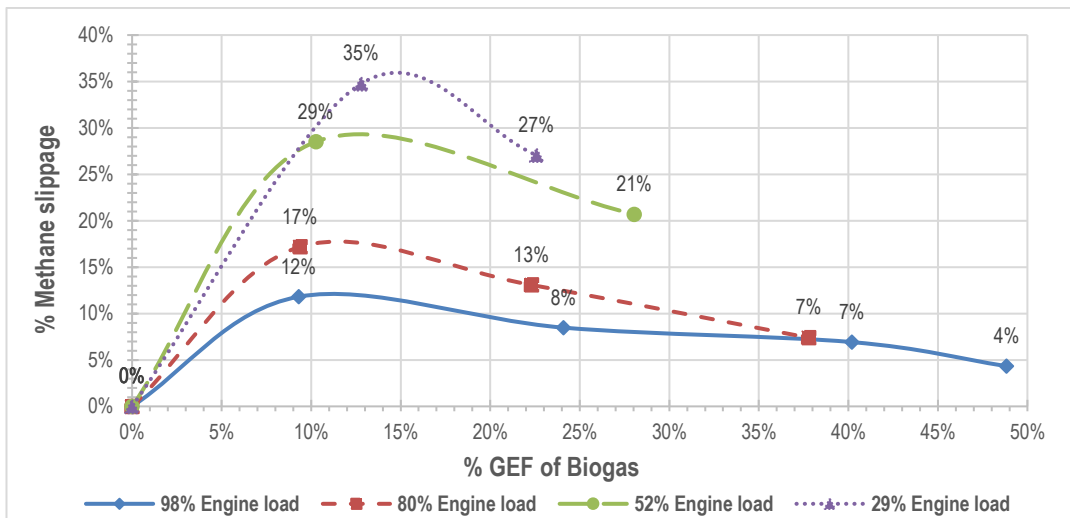
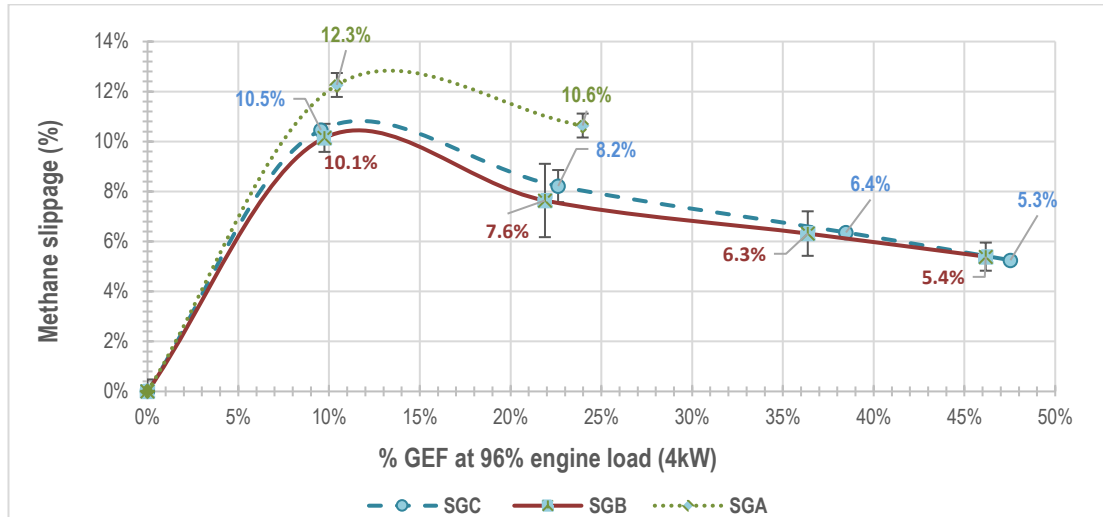


**Figure 6-74 Methane slippage (%) for biogas-diesel**

For all gas-diesel blends evaluated, the methane slippage is lower at higher engine loads due to higher combustion efficiencies, this generally increases as load decreases. In terms of the methane slippage (%) at a fixed load, the maximum % methane slippage is experienced at ~10% addition of gaseous fuel. Subsequent addition of any gaseous fuel leads to methane slippage decreasing. Hence, in terms of minimising the methane slippage, it is preferential to run at higher gas substitutions and at higher loads for all the syngas/biogas blends evaluated. At the highest engine load, and the highest GEF evaluated (48% GEF), a methane slippage of ~5% was experienced for all the gaseous fuels evaluated.

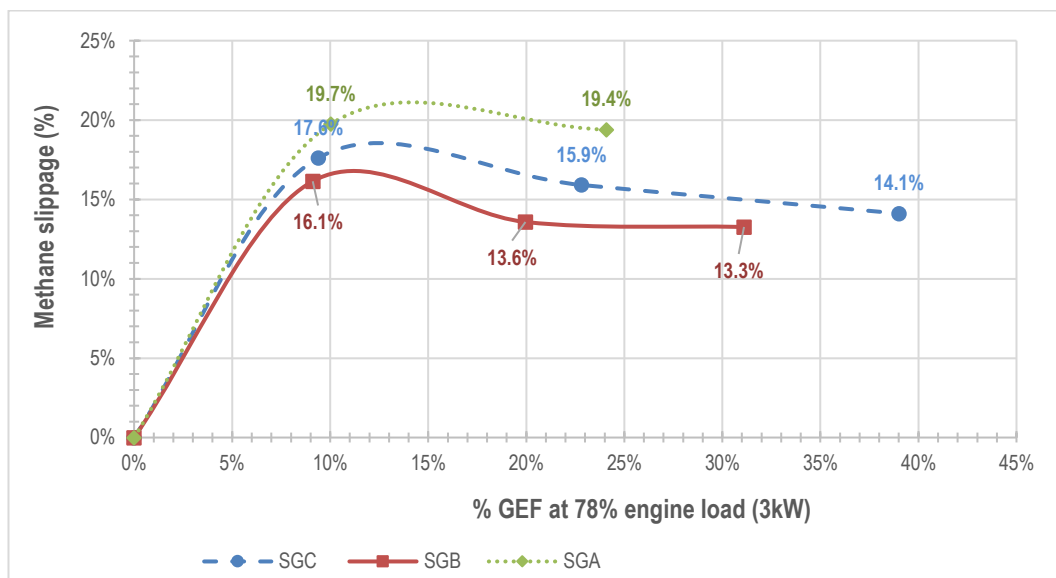
### 6.4.6.1 Cross-comparison of the methane slippage for syngas

The cross-comparison of the methane slippage data (%) for the three syngas types evaluated are depicted in Figs. 6.75 to 6.78 which shows the methane slippage data compared at each engine load assessed. For SGA, limited FT-IR data was produced as all the GEF values have not been evaluated for full and ~78% engine load, therefore, cannot be fully cross compared.



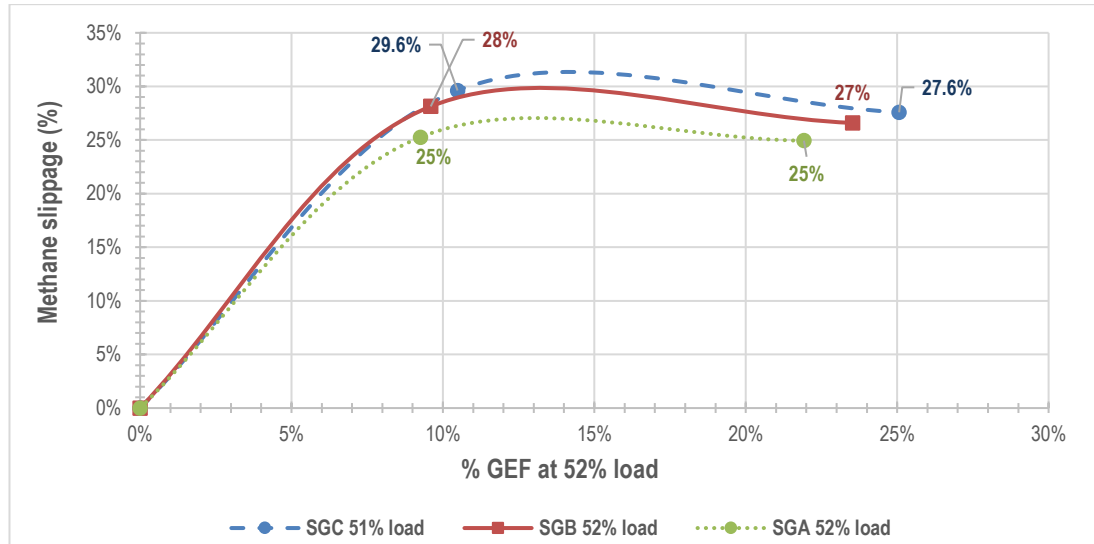
**Fig 6-75 The methane slippage (%) at full load for all syngas blends**

Fig. 6.75 illustrates that the methane slippage profile is similar for SGB and SGC. SGA experiences slightly higher methane slippages at full engine load at the limited GEF evaluated.



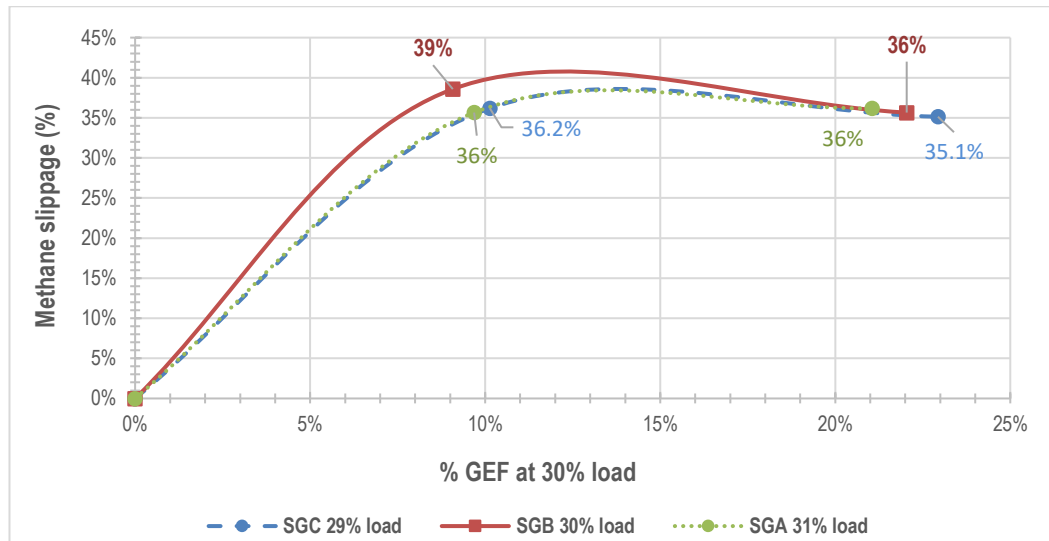
**Fig 6-76 The methane slippage (%) at ~78% load for all syngas blends**

Fig. 6.76 shows that SGB has the lowest methane slippage in comparison to the other two syngas blends. At full engine load, SGB and SGC had a similar profile, but at 78% engine load, the gap widens between these two blends. SGA remains experiencing slightly higher methane slippages at 78% engine load at the maximum GEF evaluated (up to ~22% GEF).



**Fig 6-77 The methane slippage (%) at ~52% load for all syngas blends**

Fig. 6.77 shows that at 52% engine load SGA has the lowest methane slippage at the GEFs evaluated in comparison to the other syngas blends, with SGC experiencing marginally higher methane slippage.



**Fig 6-78 The methane slippage (%) at 30% load for all syngas blends**

Fig. 6.78 shows that SGA and SGC have similar methane slippage profiles which are the lowest for all GEFs evaluated at a 30% engine load.

SGB has the highest methane slippage value at 10% GEF only, at 22% GEF there is no difference between the three syngas blends.

In summary, the syngas with the highest hydrogen content does not experience the lowest methane slippage. The best syngas to use at each engine load for the lowest methane slippage is summarised in Table 6.20.

**Table 6-20 Summary of the cross-comparison methane slippage data from syngas-diesel dual fuel combustion**

Engine load (%)	Generator load (kW)	Highest methane slippage	Lowest methane slippage
~96	~ 4.2	SGA (up to 22% GEF)	SGB/SGC
~77	~3.3	SGA (up to 22% GEF)	SGB
~53	~2.2	SGC (at 22% GEF only)	SGA
~30	~1.2	SGB (at 10% GEF only)	No difference

#### 6.4.7 Summary of the FT-IR trend data

The trends seen for all the species of interest detected by the FT-IR with increasing % GEF per gaseous fuel are summarised in Tables 6.21 to 6.24.

**Table 6-21 Summary of the FT-IR trends for SGA-diesel**

(Effect on concentration with increasing SGA addition from 0 to 22 % GEF)				
Species	4.2kW (96%)	3.2kW (75%)	2.1kW (52%)	1.2kW (31%)
Methane	↑	↑	↑	↑
Ethane	NC	NC	↑	↑
Ethylene (Ethene)	↓	↓	↓	↓
Hexane	NC	NC	↓	↑
Formaldehyde	↑	↑	↑	↑
Ethanol	↑	↑	↑	↑

*'NC' denotes no change*

**Table 6-22 Summary of the FT-IR trends for SGB-diesel**

(Effect on concentration with increasing SGB addition from 0 to the maximum % GEF at each load)				
Species	4.3kW (96%)	3.4kW (80%)	2.1kW (52%)	1.2kW (30%)
Methane	↑	↑	↑	↑
Ethane	NC	ND	ND	↑
Ethylene (Ethene)	NC	NC	ND	ND
Hexane	↓	NC	NC	↑
Formaldehyde	↑	↑	↑	↑
Ethanol	NC	NC	↑	↑

*'NC' denotes no change and 'ND' denotes non-detected*

**Table 6-23 Summary of the FT-IR trends for SGC-diesel**

Species	(Effect on concentration with increasing SGC addition from 0 to the maximum % GEF at each load)			
	4.2kW (96%)	3.4kW (79%)	2.1kW (51%)	1.2kW (29%)
Methane	↑	↑	↑	↑
Ethane	↓	↑	↑	↑
Ethylene (Ethene)	NC	↓	NC	NC
Hexane	↓	↓	↑	↑
Formaldehyde	↑	↑	↑	↑
Ethanol	↑	↑	↑	↑

*'NC' denotes no change*

**Table 6-24 Summary of the FT-IR trends for biogas-diesel**

Species	(Effect on concentration with increasing biogas addition from 0 to the maximum % GEF at each load)			
	4.3kW (98%)	3.4kW (80%)	2.1kW (52%)	1.2kW (30%)
Methane	↑ then ↓	↑ then NC	↑	↑
Ethane	↑ then ↓	↑ then ↓	↑	↑
Ethylene (Ethene)	↑	↑	↑	↑
Hexane	↓	↓	↓	↓
Formaldehyde	↑	↑	↑	↑
Ethanol	↑ then ↓	↑ then ↓	NC	NC

*'NC' denotes no change*

#### 6.4.7.1 Ethanol

During lab testing, the lab atmosphere contained background levels of ethanol (as shown in the DBL FT-IR data in Table 6.15). Regardless, all syngas dual fuel combustion showed an increase in the ethanol concentration at higher loads (>70%). SGA and SGB levels remained relatively stable at loads <55%, whereas SGC observed a slightly smaller increase at engine loads <55%. The higher hydrogen content of SGC could have potentially caused this.

For biogas, at engine loads <55%, the ethanol concentration remained unchanged with the addition of biogas. However, at ~78% engine load, (as per the trend seen for methane and ethane), the ethanol concentration shows an increase up to a GEF of 22%, after which further increases in the biogas fraction led to a reduction in the ethanol concentration. Similarly, for full engine load, (as noted for methane and ethane levels), the ethanol concentration increased up to a GEF of 38%, after which any further increase in biogas fraction led to a reduction in the ethanol concentration.

The increase in the ethanol concentration observed with increasing % GEF during dual fuel combustion requires further investigation as the cause remains unclear.

This could be linked to the accuracy of the FT-IR instrument when identifying ethanol. Given the time constraints of this project, it was not possible to investigate this further.

### 6.4.7.2 Formaldehyde

The formaldehyde content increased across all the engine loads with an increasing biogas/syngas fraction. This increase noted is linked to the oxidation of methane which is a common component in all the gaseous fuels tested in this study. Typically, the oxidation of methane involves various complex reactions, whereby formaldehyde forms as an intermediate, which is further oxidised to CO and finally into carbon dioxide and water [279]. Hence, oxidation of methane in the syngas and biogas will most likely proceed via formaldehyde, and incomplete combustion will result in this passing out into the exhaust gases.

Higher values were seen at lower loads than higher loads due to lower combustion efficiencies. Also, when testing at each engine load, as the GEF was increased at that load, the formaldehyde increased with an increasing gas fraction (as the  $\phi$  value increased as the mixture got richer). This increase is due to the partial oxidation of the methane content in richer combustion conditions. The increase in the formaldehyde concentration with increasing GEFs is illustrated in Fig. 6.79 which shows the formaldehyde concentration at various engine loads for SGA.

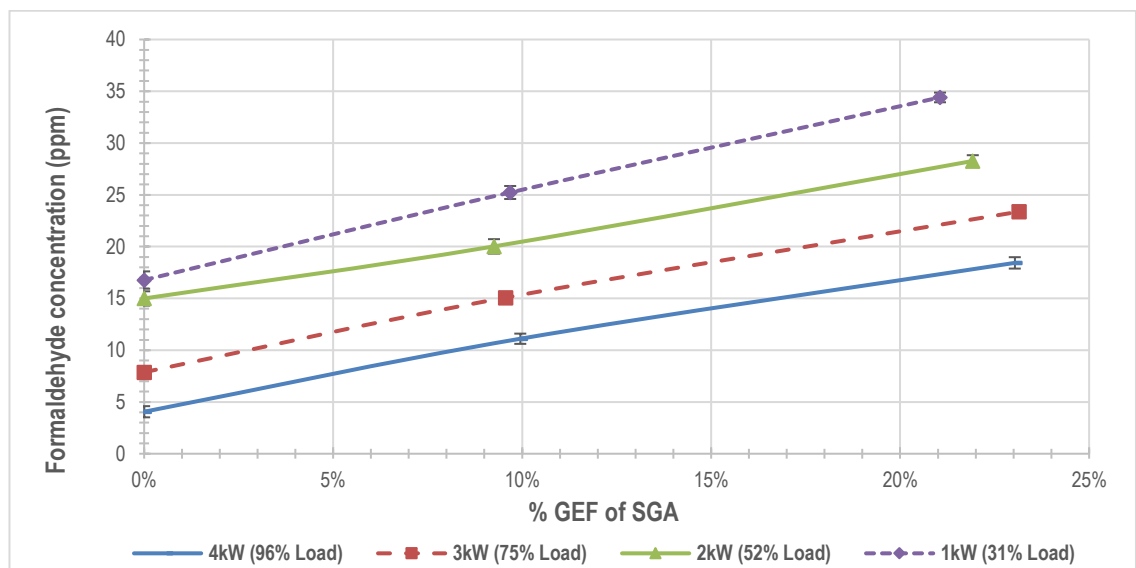


**Figure 6-79 The formaldehyde concentration for SGA-diesel at various engine loads**

### 6.4.7.3 Hexane

All syngas-diesel blends observed a reduction or no change in the concentration of hexane with increasing % GEF at engine loads >70%, this is as expected with the reduction in diesel consumption. At an engine load of ~52%, and with increasing syngas using SGA, the hexane levels fell (by 2 ppm), for SGB there was no change noted, and for SGC a marginal increase in the hexane levels was noted (of 1ppm). At the lowest engine load, with increasing % GEF, an increase in the hexane concentration of 4, 7, and 22 ppm was noted for SGA, SGB, and SGC, respectively.

It can be deduced that at <55% engine load (2 and 1kW generator loads), the increase in hexane concentration can be attributed to a reduction in the brake thermal efficiency in dual fuel mode coupled with lower  $P_{max}$  values and combustion temperatures, more incomplete combustion, and cracking. Also ~at 30% engine load, the engine performance is more variable as is unstable at low loads. In addition, there is the impact of the reduction in pilot diesel fuel to consider, which is discussed in subsection 6.4.7.6.

For biogas, the trend seen in the hexane concentration is consistent; a reduction is seen with increasing biogas use. This is as expected as this is derived from the incomplete combustion of diesel, thus with reduced diesel consumption, this decreases proportionately. However, we are not seeing the increase in hexane content at lower loads as we are seeing with syngas-diesel, this is attributed to the characteristics related to syngas-diesel combustion.

### 6.4.7.4 Ethane

An increase in the ethane content was observed at engine loads <55% with increasing % GEF for all dual fuel modes. This can be explained as follows: although the amount of diesel being used is reduced, the brake thermal efficiency is further reduced in dual fuel mode thereby leading to lower  $P_{max}$  values and combustion temperatures, more incomplete combustion, and cracking thereby leading to an increase in ethane/UHCs. Moreover, at 30% engine load, caution should be taken when interpreting this data as at this low load the engine combustion is unstable, hence such small variations in the concentration could be due to variable engine performance.

At higher loads (full and 79% engine load), for SGA and SGB there was no change in ethane concentration with increasing % GEF.

At full engine load, for SGC, the ethane concentration showed a small reduction (of ~3ppm) with increasing addition of syngas. At 79% engine load (3.4kW), a small increase was noted instead. However, in both cases, the concentration levels are close to the detection limit, therefore, care should be taken at the importance exacted to this trend.

For biogas, the ethane concentration increases with increasing biogas at engine loads <55%. However, at higher engine loads (> 73%), an initial increase is noted followed by a reduction at the final increase of biogas addition. The reason for the initial increases could be related to the reduction in combustion efficiency, thus increasing UHCs, however, the reason for the final decrease in the ethane concentration remains unknown but could be linked to the methane slippage.

#### **6.4.7.5 Ethylene (ethene)**

For SGA, with increasing % GEF, the ethylene content decreases, and this is the same across all loads.

For SGB, the ethylene concentration at higher loads is low and remains unaffected by the addition of the syngas. At engine loads <55%, the ethylene concentration was deemed 'non-detected' as was below the detection limit.

For SGC, this concentration remains low and relatively stable at all engine loads and is unaffected by the addition of syngas. Thus, overall, the ethylene content remains unaffected by the increasing addition of SGC across all engine loads.

For biogas, a clear trend is observed whereby the ethylene concentration increases across all loads, with increasing biogas addition. The reason for this was explained earlier, as per ethane: as the brake thermal efficiency is further reduced in dual fuel mode thereby leading to lower  $P_{max}$  values and combustion temperatures, more incomplete combustion and cracking occur thereby leading to an increase in ethane/UHCs.

#### **6.4.7.6 Increase in hydrocarbons at loads <55% in dual fuel mode**

The increase in the hexane/ethane and ethylene content at engine loads <55% can be explained by the effect of the pilot fuel quantity at low loads during dual fuel combustion. Abd et al. [168] state that generally, a diesel fuel injection system is prone to '*poor atomization and combustion when the amount of fuel injected per cycle is reduced below 5–10% of the maximum design level*'. In the context of dual fuel engines, the important factor is the size of the combustion zone relative to the size of the pilot fuel zone [170]. A study conducted by Abd et al. [168] which involved the investigation of various pilot fuel quantities on the performance and resulting emissions of an indirect dual fuel gas/-diesel engine showed that at low loads when a small amount of the pilot diesel was used, higher CO and UHC emissions were experienced. The gaseous fuels used were either methane or propane. This was explained that under these conditions, the mixture is excessively lean, thus the pilot diesel flame is unable to propagate throughout the combustion chamber resulting in partial oxidation and higher emissions [168, 170]. In their study, the gas flow rates were fixed with a variable pilot diesel quantity; plots were produced comparing the total  $\phi$  versus CO and UHC emissions.

In comparison, in this study, at low loads and with increasing % GEF, the pilot diesel quantity is further reduced in a lean mixture. Hence, the increase in the hydrocarbons from the FT-IR analysis seen here at low loads could be further explained because of the pilot diesel quantity.

#### **6.4.8 Cross-comparison of the formaldehyde and methane emissions across syngas blends**

Key hydrocarbon species were cross compared across the three syngas blends to determine if the syngas composition affected the concentrations. The species of interest selected were methane and formaldehyde. The concentrations were cross compared across 96 and 78% engine loads. Figs. 6.80 and 6.81 depict the change in methane concentration with increasing syngas addition at 96 and 78% engine load for each gas type.

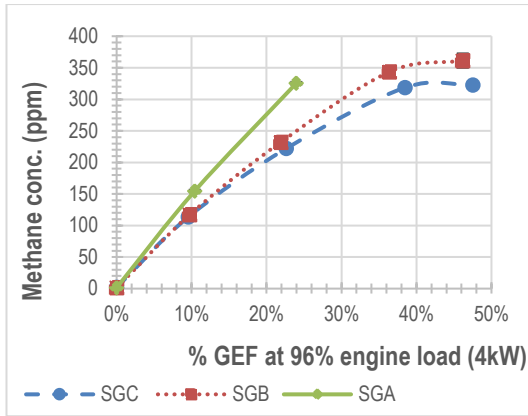


**Fig 6-80 CH<sub>4</sub> conc. (96% load)**

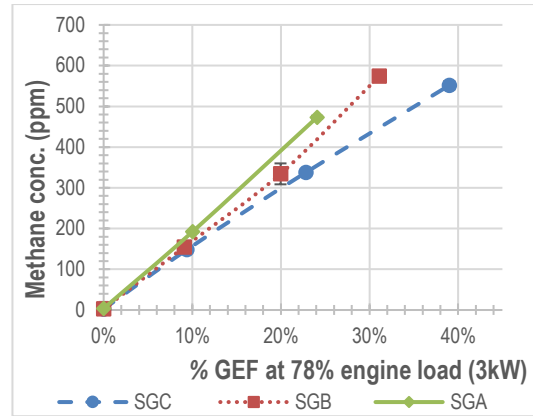


**Fig 6-81 CH<sub>4</sub> conc. (78% load)**

Figs. 6.80 and 6.81 both show that the methane levels are lower for SGC, notably when GEF  $\geq 22\%$  are utilised at both engine load conditions. This is attributed to the higher H<sub>2</sub> content and the faster flame rate which is helping the combustion of the methane. Interestingly, this does not translate into SGC having the lowest methane slippage as discussed earlier in section 6.4.6. SGA has the highest methane concentration, the lowest hydrogen content, and the highest methane slippage as shown in Figs. 6.75-6.76 at both engine loads (full and 78%) at GEFs up to  $\sim 22\%$ .

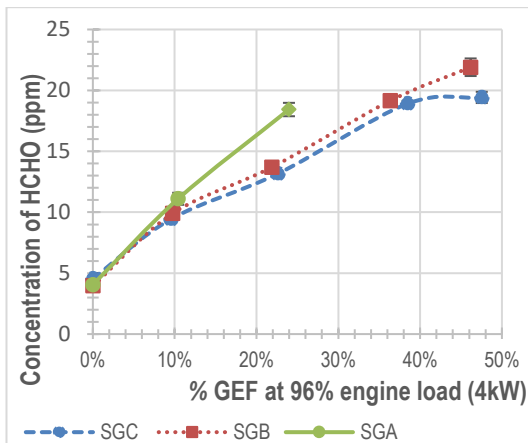


**Fig 6-82 HCHO conc. (96% load)**

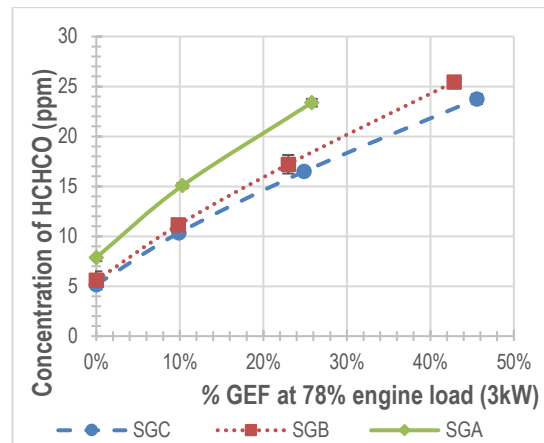


**Fig 6-83 HCHO conc. (78% load)**

Fig. 6.82 shows that the formaldehyde (HCHO) content for SGB and SGC is remarkably similar at full engine load, apart from one datapoint that represents the maximum % GEF value; at this point, the concentration level drops for SGC. Fig. 6.83 shows that the formaldehyde concentration is typically lower for SGC, especially at higher GEFs at an engine load of 78%.

Both the reduction in the methane and formaldehyde content can be attributed to the higher H<sub>2</sub> content and the faster flame speed which is helping the combustion of the methane. Sattarzadeh et al. [141] state that gases with higher hydrogen exhibit hydrogen characteristics which allow the hydrogen flame to get closer to low temperature regions within the RCCI engine, thus enabling better combustion of methane, thus reducing the potential formaldehyde formation from incomplete oxidation of methane.

## 6.5 Summary

Syngas and biogas dual fuel combustion data has shown that running at engine loads <55% is not recommended from a combustion efficiency perspective based on the gaseous emissions results. In addition, typically for power generation purposes, a genset such as this is not usually run at low load conditions. Hence, the resulting emission and BTE data will be considered for engine loads ( $\geq 72\%$ ) for this conclusion. To evaluate the optimum % GEF (at full and at 79% engine load), the % change in SE data (g/kWh) has been calculated relative to the diesel baseline and compared alongside the corresponding % methane slippage, % mass reduction in diesel consumption, equivalence ratio, and the BTE data. This has been summarised for SGC and biogas in dual fuel mode in Tables 6.25 and 6.26.

SGC was chosen as the emissions, and engine combustion performance data (in Chapter 5) indicated that this syngas presented superior combustion performance relative to the other syngas blends evaluated.

**Table 6-25 Overall trend summary for SGC-diesel at high loads**

Load %	% GEF comparison versus DBL	BTE	Methane slippage	Mass diesel reduction	THC	NO <sub>x</sub>	CO	CO <sub>2</sub>	$\phi$
					% Change in SE (g/kWh) data				
96	10	29.6	10	8	120	-3	436	1	0.52
	22	28.6	8	17	247	-10	894	9	0.53
	38	27.5	6	31	341	-17	1,293	25	0.57
	46	27.1	5	39	353	-16	1,462	39	0.60
79	9	30.6	18	6	150	-3	381	15	0.60
	22	29.2	16	16	315	-16	878	14	0.41
	37	27.4	14	28	534	-26	1,452	29	0.42

Table 6.25 shows that at 96% engine load, the optimum GEF value is either 38 or 46%, and the choice between the two GEF values depends on the focus.

At both these % GEF values, similar % NO<sub>x</sub> reductions, BTE, and methane slippage values are observed. The disadvantage of increasing to 46% GEF is that the THC and CO values increase. However, the advantage is the lower diesel consumption at the maximum GEF value which helps broaden fuel choices as it reduces the reliance on fossil diesel, whilst promoting the use of solid biomass waste. In terms of the other emissions, there is no increase noted in the formaldehyde content as the % GEF is increased from 38 to 46% at full engine load as shown in Fig. 6.82.

At 79% engine load, running at the highest % GEF is preferential in terms of reduction in diesel consumption, NO<sub>x</sub> emissions, and reducing methane slippage. Again, the disadvantages are the corresponding increases in THC and CO emissions.

When choosing between the two loads at maximum % GEF values, there is no discernible difference in the BTE data, however running at maximum load is preferential due to the lower methane slippage, lower THC, and formaldehyde emissions, as well as a higher mass % diesel reduction.

### **Biogas summary**

To evaluate the optimum % GEF (at full and 80% engine load), for biogas-diesel, the corresponding data has been summarised in Table 6.26.

**Table 6-26 Overall trend summary for biogas-diesel at high loads**

Load %	GEF comparison versus DBL (%)	BTE (%)	Methane slippage (%)	Mass diesel reduction (%)	% Change in SE (g/kWh) data				$\phi$
					THC	NO <sub>x</sub>	CO	CO <sub>2</sub>	
97	9	30.0	12	8	458	-8	163	10	0.55
	24	29.5	8	20	1,177	-20	366	8	0.58
	40	28.7	7	34	2,009	-32	578	26	0.61
	49	27.6	4	42	2,609	-39	672	33	0.63
80	9	30.8	17	8	839	-9	125	15	0.43
	22	29.6	13	17	2,019	-23	260	14	0.46
	38	28.1	14	30	3,865	-36	415	29	0.48

Table 6.26 shows that when operating at full engine load (97%), the highest % GEF is beneficial as it produces the highest NO<sub>x</sub> reductions, lowest methane slippage, and maximum mass % diesel reductions.

When running at ~80% load, it is preferential to run at the maximum GEF (of the values evaluated in this study), for the same reasons discussed above, with the negative factors being the higher THC and CO emissions.

When choosing between the two loads at maximum % GEF values, running at maximum load is preferential due to lower methane slippages experienced at full engine load, alongside lower THC, and formaldehyde emissions, as well as the higher mass % diesel reductions.

***Dual fuel CO<sub>2</sub> reductions arising from reduced diesel consumption***

For both SGC and biogas, there are reductions in terms of the tailpipe CO<sub>2</sub> emissions that arise directly as a result of the reduction in diesel consumption as the syngas/biogas is added. In other words, the reduction of fossil fuel derived CO<sub>2</sub> emissions from reduced diesel consumption from dual fuel combustion. It is assumed that any CO<sub>2</sub> emissions produced from the combustion of the syngas and biogas count as zero as they are derived from waste biomass.

The kg of CO<sub>2</sub> produced is calculated based on the actual diesel usage directly measured during experimental runs and is calculated based on the fact that one litre of red diesel produces ~2.7kg of CO<sub>2</sub> [280]. The results are tabulated in Table 6.27 for SGC, and Table 6.28 for biogas.

**Table 6-27 A reduction in the CO<sub>2</sub> emissions arising from the reduced diesel consumption during SGC-diesel mode**

% GEF	% Engine load	Diesel usage (l/h)	kg CO <sub>2</sub> eq produced	kg CO <sub>2</sub> eq reduction	% CO <sub>2</sub> eq kg reduction (relative to diesel baseline)
0	96	1.73	4.7	N/A	N/A
9		1.60	4.4	0.4	8
22		1.44	3.9	0.8	17
38		1.20	3.3	1.5	31
46		1.05	2.9	1.9	39
0	79	1.39	3.8	N/A	N/A
9		1.30	3.5	0.2	6
22		1.17	3.2	0.6	16
37		1.01	2.7	1.1	28

**Table 6-28 A reduction in the CO<sub>2</sub> emissions arising from the reduced diesel consumption in biogas-diesel mode**

% GEF	% Engine load	Diesel usage (l/h)	kg CO <sub>2</sub> eq produced	kg CO <sub>2</sub> eq reduction	% CO <sub>2</sub> eq kg reduction (relative to diesel baseline)
0	97	1.74	4.7	N/A	N/A
9		1.60	4.4	0.4	8
24		1.40	3.8	0.9	20
40		1.14	3.1	1.6	34
49		1.01	2.8	2.0	42
9	80	1.42	3.9	N/A	N/A
10		1.31	3.6	0.3	8
22		1.18	3.2	0.7	17
38		0.99	2.7	1.2	30

Table 6.27 and Table 6.28 both show that the reduction in diesel consumption leads to a reduction in the amount of kg of CO<sub>2</sub> produced, the % reduction is higher at higher engine loads with higher GEF values.

However, when considering the total amount of CO<sub>2</sub> produced from dual fuel combustion, which accounts for the combustion of diesel, methane, and CO, the CO<sub>2</sub> produced (expressed as EI g/MJ fuel) does increase relative to diesel (as shown in Tables 6.14 and 6.12). Hence, theoretically, any CO<sub>2</sub> reduction seen arising from the reduction in diesel consumption is off set by the increase in CO<sub>2</sub> emissions in dual fuel mode.

However, the CO<sub>2</sub> increase from the syngas/biogas combustion can be considered 'carbon-neutral' due to it originating from biomass residues. Additionally, if the biomass residues were not used in this manner, they would have been disposed of using other methods which are detrimental to the environment.

Further work is required here to quantify the carbon footprint from this whole dual fuel small-scale electricity generating process which incorporates gasification and anaerobic digestion. In addition, economic analysis is required to determine the cost of producing small-scale electricity in this manner when utilising waste biomass residues.

## Chapter 7 Particulate Emissions

### 7.1 Introduction

This chapter looks at the particle number emissions measured via the DMS500 for all gas-diesel dual fuel combustion at all the GEFs evaluated across all engine loads. The particulate matter (PM) mass was also collected using the Andersen cascade impactor at full engine load testing conditions of DBL, 10, and 22% GEFs using SGA, SGB, and SGC. The collected PM was characterised further using TGA, SEM, and EDX.

### 7.2 Particle number emissions

DMS500 data was averaged to produce the peak particle diameter and the Total Particle Number Concentration (TPNC) for each load and test condition. The % TPNC change at each % GEF was also calculated relative to the corresponding DBL run for each gas blend. This data is summarised for each syngas blend in Tables 7.1 to 7.4. Examples of the typical particle number sized distribution (PNSD) trends from each load/condition are also included.

#### 7.2.1 Syngas A

Table 7.1 shows that at all loads (except for 31%), there is a reduction in the TPNC as a result of increasing syngas addition. At 31% engine load, the TPNC increases with syngas addition.

**Table 7-1 SGA-diesel particle emission data**

Engine Load	% GEF	Peak particle diameter (nm)	TPNC	% TPNC change
<b>96%</b>	<b>DBL/0</b>	<b>64.94</b>	1.19E+08	
	9	64.94	1.13E+08	-5%
	23	64.94	1.10E+08	-7%
	38	64.94	1.03E+08	-14%
	45	64.94	9.93E+07	-17%
<b>74%</b>	<b>DBL/0</b>	<b>64.94</b>	<b>1.03E+08</b>	
	9	64.94	9.60E+07	-6%
	22	56.23	7.71E+07	-25%
	37	56.23	5.78E+07	-44%
<b>56%</b>	<b>DBL/0</b>	<b>56.23</b>	<b>1.00E+08</b>	
	9	56.23	9.09E+07	-9%
	23	48.70	6.32E+07	-37%
<b>31%</b>	<b>DBL/0</b>	<b>48.70</b>	8.92E+07	
	9	15.40	1.10E+08	23%
	21	15.40	1.16E+08	30%

Examples of the PNSD trends observed for each load are depicted in Figs 7.1 to 7.4 at the various GEFs evaluated. At full engine load, the PNSD shape remains unchanged with one exception: at 45% GEF, as shown in Fig. 7.1. This is likely to have been caused by the change in the DMS500 instrument, this GEF was analysed individually after the DMS500 instrument had been returned after maintenance work, hence, the slight change in the PNSD between 5 to 31nm is a direct result of this. It is anticipated that had this GEF been analysed at the same time as the others at full load, the PNSD curve would have mirrored the other GEFs.

At 74% engine load, the PNSD curve shape remains unchanged with increasing GEF as shown in Fig. 7.2.

Fig. 7.3 shows that at 56% engine load, the shape of the PNSD curves started to change with increasing syngas addition whereby a bimodal distribution becomes more pronounced. The particle concentration in the nucleation mode shows an increase, whereas the particle concentration related to the accumulation mode decreases with increasing syngas addition.

The PNSD depicted in Fig. 7.4 for a 31% engine load shows a change in the PNSD whereby a dominant bimodal distribution becomes clearer with increasing GEF. Also, a shift is noted in the peak particle diameter size into the nanoparticle range (nucleation mode). The change in the PNSD profile as depicted in Fig. 7.4 is due to the nanoparticle concentration increasing; these particles were not destroyed by either combustion or agglomeration at low load conditions.

Various factors could have caused this in dual fuel combustion at a low engine load. This could be due to the lower combustion temperature, the change in the fuel to air ratio, and the effect of the syngas in the combustion chamber, alongside a reduced pilot diesel flame. At higher loads, (as seen in Fig. 7.1 and 7.2), these nanoparticles are burnt out, hence, are absent from the exhaust stream. This increase of nanoparticles at 31% engine load in dual fuel combustion results in an increase in the TPNC at this condition.

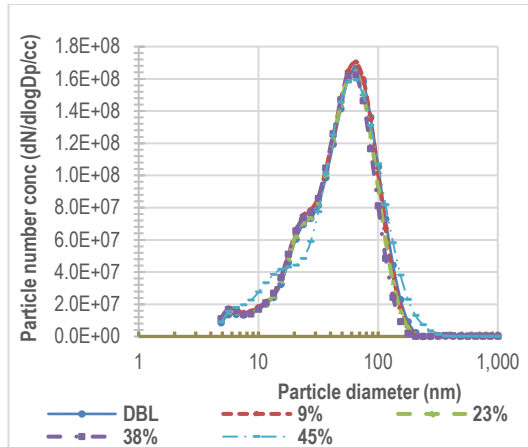


**Fig 7-1 PNSD (full load) SGA**

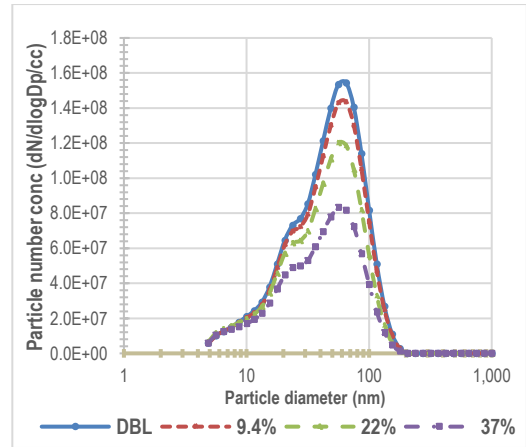


**Fig 7-2 PNSD (74% load) SGA**

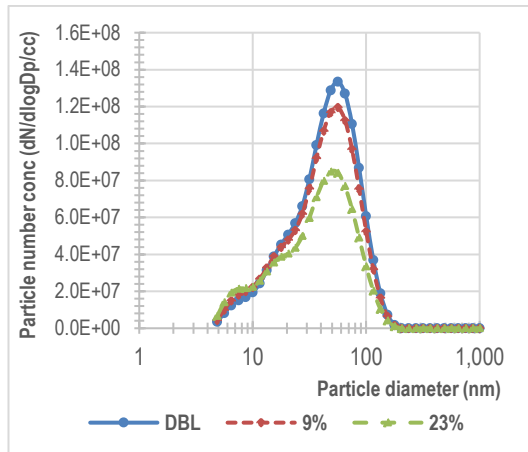


**Fig 7-3 PNSD (56% load) SGA**

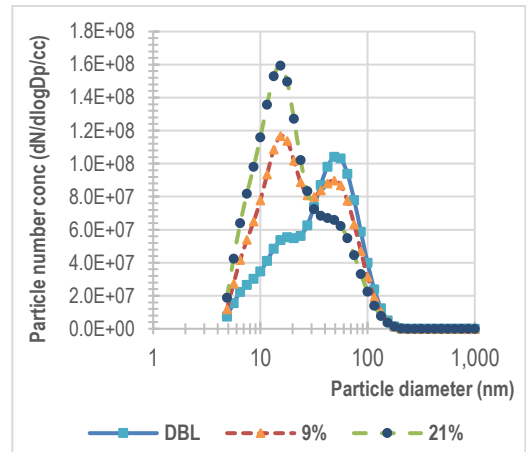


**Fig 7-4 PNSD (31% load) SGA**

## 7.2.2 Syngas B

Table 7.2 shows that at all engine loads (except for 30%), there is a reduction in the TPNC as a result of increasing syngas. At 30% engine load, the TPNC increases with syngas addition. Typical PNSD curves for SGB at each load are depicted using Figs. 7.5 to 7.8. At full and 76% engine load, the PNSD curve shape remains unchanged with increasing syngas additions as shown by Figs. 7.5 -7.6.

At 54% engine load, Fig. 7.7 shows that the PNSD curves start to change with increasing syngas addition, whereby a bimodal distribution is noted at the highest GEF evaluated of 22%. At 22% GEF, the particle concentration in the nucleation mode has increased, whereas the particle concentration related to the accumulation mode has decreased, with increasing syngas addition.

Fig. 7.8 shows that at 30% load, a change is noted in the PNSD with increasing syngas addition, however, the bimodal distribution seen at 54% load is no longer apparent. A clear PNSD trend is not apparent, it is envisaged that the nucleation mode particles have increased significantly and have merged with the accumulation mode particles resulting in a large broad peak. The highest GEF of 22% presents a monomodal trend at this load. This increase in the nanoparticles results in an increase in the TPNC, hence at this load, the dual fuel combustion conditions favour the formation of nucleation particles.

**Table 7-2 SGB-diesel particle emission data**

Load	% GEF	Peak particle diameter (nm)	TPNC	% TPNC change
96%	DBL/0	64.94	1.12E+08	
	9	64.94	1.09E+08	-2%
	22	64.94	1.01E+08	-10%
	39	56.23	8.54E+07	-24%
	46	64.94	9.11E+07	-18%
76%	DBL/0	56.23	8.74E+07	
	10	56.23	8.39E+07	-4%
	22	56.23	7.06E+07	-19%
	39	56.23	4.98E+07	-43%
54%	DBL/0	56.23	8.95E+07	
	9	56.23	8.18E+07	-9%
	22	56.23	7.42E+07	-17%
30%	DBL/0	17.78	2.29E+08	
	9	20.54	3.13E+08	37%
	22	23.71	5.08E+08	122%

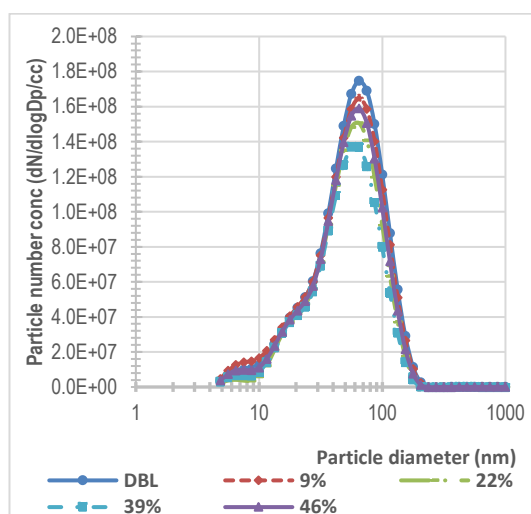


**Fig 7-5 PNSD (full load) for SGB**

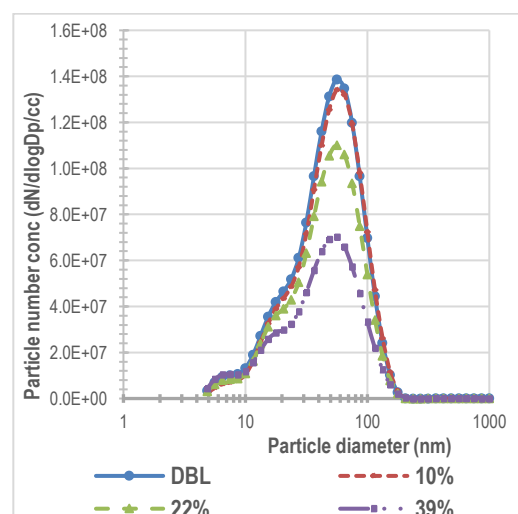


**Fig 7-6 PNSD (76%load) for SGB**

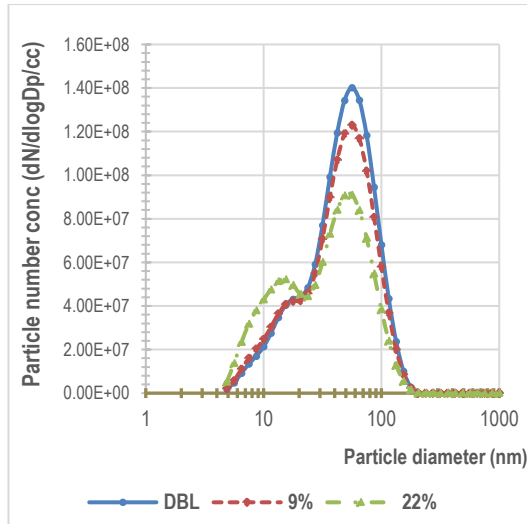


**Fig 7-7 PNSD (54% load) SGB**

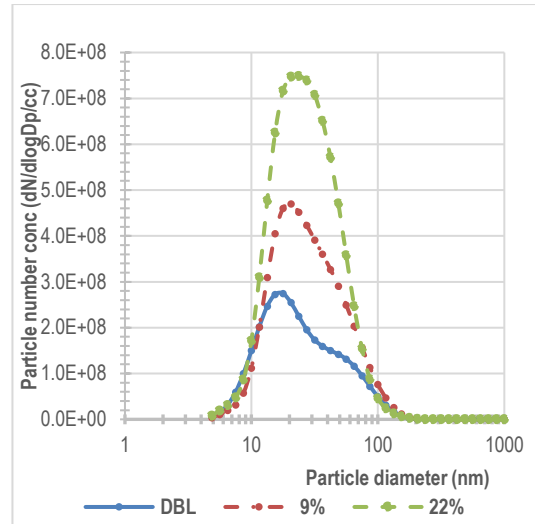


**Fig 7-8 PNSD (30% load) SGB**

### 7.2.3 Syngas C

Table 7.3 shows that at all engine loads (except for 29%), there is a reduction in the TPNC as a result of increasing syngas addition. At 29% load, the TPNC increases with syngas addition. Typical PNSD curves for SGC at each load are depicted using Figs. 7.9 to 7.12.

At full and 80% engine load, the shape of the PNSD curve remains unchanged with increasing syngas addition as shown in Figs. 7.9 and 7.10, respectively.

At 51% engine load, the PNSD curves start to change with increasing syngas addition, whereby a bimodal trend is noted, this becomes more defined with increasing GEF as shown in Fig. 7.11. This is due to the particle concentration in the nucleation mode increasing, whereas the particle concentration related to the accumulation mode decreases with increasing syngas addition.

At 29% engine load, a change is noted in the PNSD with increasing syngas addition which is apparent when compared to the DBL PNSD curve. However, a clear bimodal trend is not apparent as it is at 51% load. As previously discussed, (for SGB at this test condition), it is possible that due to the significant increase in the nucleation mode particles, this nucleation mode has merged with the accumulation mode particles resulting in a large single broad peak. The highest GEF evaluated (22%) presents a monomodal trend at this load. The increase in the nanoparticles results in an increase in the TPNC at this load as shown in Fig. 7.12. As seen for all three syngas blends; the dual fuel combustion conditions at this load boost the formation of nucleation particles.

**Table 7-3 SGC-diesel particle emission data**

Load	% GEF	Peak particle diameter (nm)	TPNC	% TPNC change
95%	DBL/0	<b>64.94</b>	<b>1.10E+08</b>	
	9	64.94	9.64E+07	-12%
	22	64.94	1.01E+08	-7%
	37	64.94	9.73E+07	-11%
	46	64.94	9.62E+07	-12%
80%	DBL/0	<b>64.94</b>	<b>9.38E+07</b>	
	9	56.23	8.58E+07	-9%
	22	56.23	8.01E+07	-15%
	38	56.23	6.27E+07	-33%
51%	DBL/0	<b>56.23</b>	<b>9.48E+07</b>	
	9	17.78	7.72E+07	-19%
	23	17.78	6.00E+07	-37%
29%	DBL	<b>48.70</b>	<b>6.11E+07</b>	
	10	17.78	3.22E+08	426%
	22	17.78	3.25E+08	432%

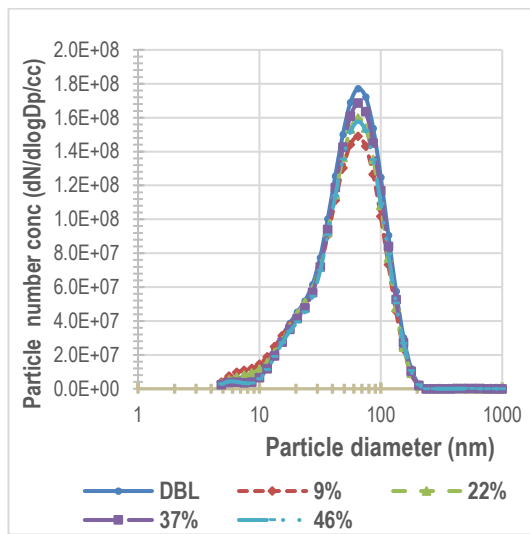


**Fig 7-9 PNSD (full load) SGC**

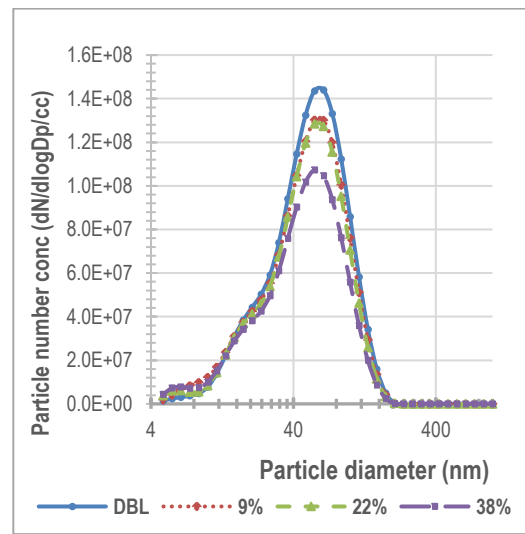


**Fig 7-10 PNSD (80% load) SGC**

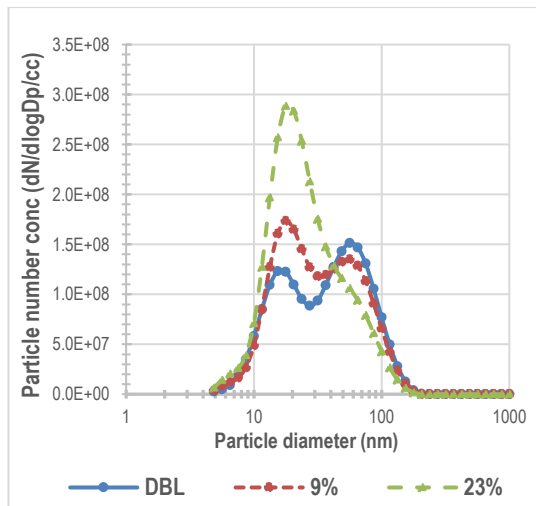


**Fig 7-11 PNSD (51% load) SGC**

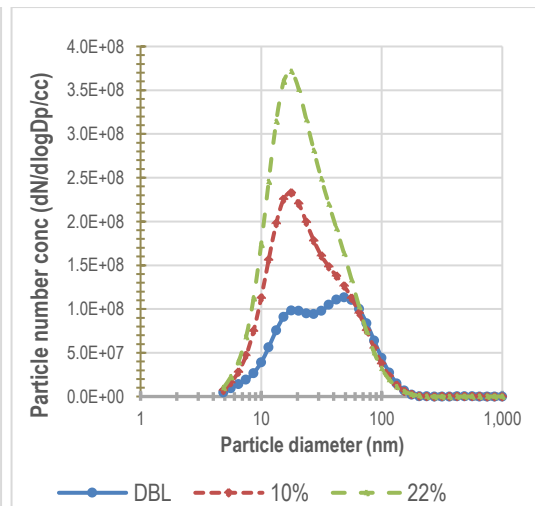


**Fig 7-12 PNSD (29% load) SGC**

### 7.2.4 Biogas

Table 7.4 shows that at all engine loads (except for 30%), there is a reduction in the TPNC as a result of increasing biogas addition. At 30% engine load, the TPNC increases with biogas addition. Examples of the PNSD curves for biogas-diesel at each load are depicted using Figs. 7.13 to 7.16.

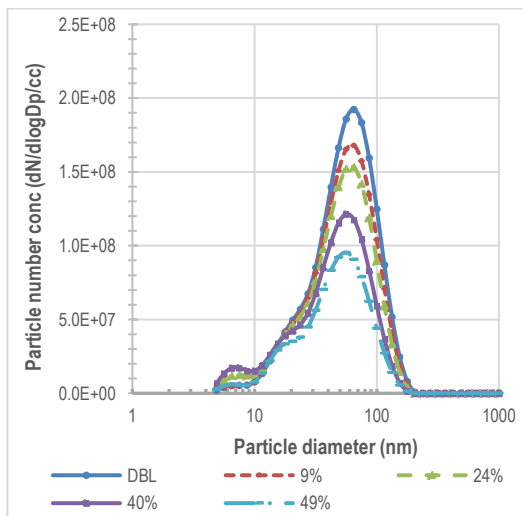
At full and 80% engine load, the shape of the PNSD curve remains unaffected with increasing biogas addition as shown in Figs. 7.13 and 7.14.

Fig. 7.15 illustrates the PNSD curves generated at 52% engine load. This shows that the PNSD curve changes with increasing biogas addition whereby a bimodal trend is noted: the particle concentration in the nucleation mode increases, whereas the particle concentration related to the accumulation mode decreases. This also results in a slight decrease in the peak particle diameter relative to the diesel baseline.

At 30% engine load, as depicted in Fig. 7.16, the PNSD changes with increasing biogas addition, however, a bimodal trend is not noted as it is seen at 52% load. The highest GEF presents a monomodal trend at this load. As seen for syngas-diesel, at this load, the increase in the nanoparticles increases the TPNC. This increase is not attributed to the gaseous fuel composition as this phenomenon is observed for all syngas/biogas fuels evaluated and is linked to fuel/air mixing.

**Table 7-4 Biogas-diesel particle emission data**

Load	% GEF	Peak particle diameter (nm)	TPNC	% TPNC change
97%	DBL/0	64.94	1.17E+08	
	9	64.94	1.03E+08	-12%
	24	64.94	9.60E+07	-18%
	40	56.23	8.12E+07	-31%
	49	56.23	6.08E+07	-48%
80%	DBL/0	56.23	9.08E+07	
	9	56.23	8.73E+07	-4%
	22	56.23	7.40E+07	-19%
	38	56.23	5.26E+07	-42%
52%	DBL/0	56.23	9.21E+07	
	10	48.70	7.45E+07	-19%
	23	48.70	5.85E+07	-37%
30%	DBL/0	17.78	1.42E+08	
	12	17.78	2.02E+08	43%
	23	20.54	2.85E+08	101%



**Fig 7-13. PNSD (full load) Biogas**

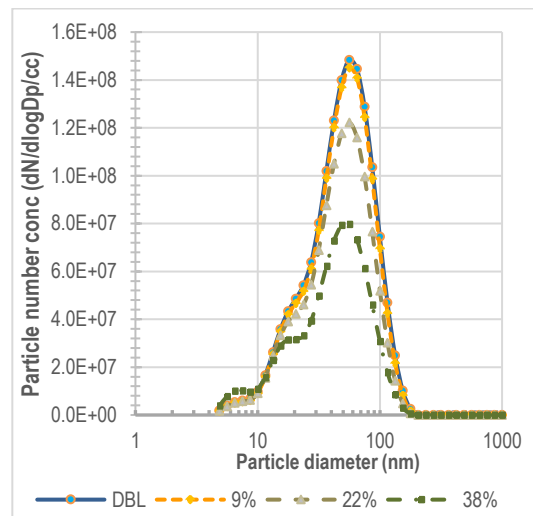


**Fig 7-14 PNSD (80% load) Biogas**

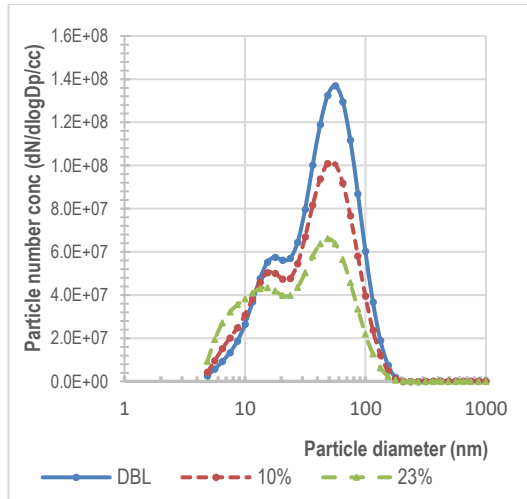


**Fig 7-15 PNSD (52% load) Biogas**

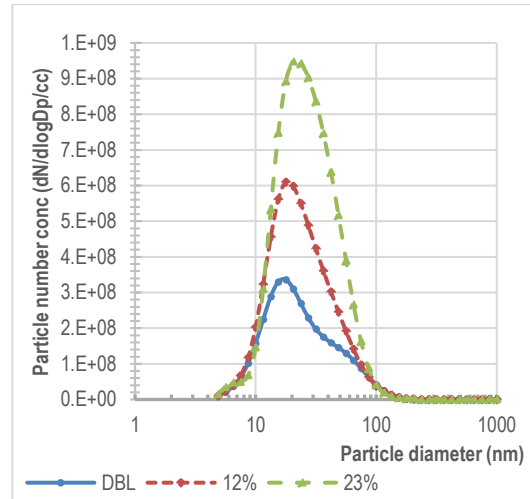


**Fig 7-16 PNSD (30% load) Biogas**

### 7.2.5 Cross-comparison of the Total Particle Number Concentration (TPNC) data

The % change in the TPNC data was calculated between the value obtained at the maximum GEF evaluated at that load, relative to the diesel baseline data, this is summarised for all gas dual fuel modes in Table 7.5. Comparison of the % change in the TPNC data across different gas blends should be done with caution as there were slight variations in the engine testing loads which will affect the comparison data.

Chuahy et al. [131] looked at the effects of hydrogen concentration/syngas composition on the particle size distribution (PSD) when using syngas (containing H<sub>2</sub> and CO only). They reported a reduction in the total particle concentration for both particle diameter ranges with decreasing hydrogen content [131], however, overall, they stated that changes in the H<sub>2</sub> concentration did not affect the PSD curve shapes as the overall riding effect resulting in the decrease of accumulation mode particles was the reduction in diesel consumption; syngas compositional changes related to hydrogen were stated to play a minor role.

Hence, the % change in the TPNC has been calculated and presented in Table 7.5, but no firm conclusions have been drawn regarding the performance of the syngas blends relative to each other. Notably, SGA had the smallest TPNC increase at 30% engine load.

**Table 7-5 The % change in the TPNC data (relative to diesel baseline) per gas/diesel blend**

The % change in the TPNC data (relative to DBL) for:	SGA	SGB	SGC	Biogas
46% GEF at full engine load	-17%	-18%	-12%	-48%
38% GEF at 77% engine load	-44%	-43%	-33%	-42%
22% GEF at 53% engine load	-37%	-17%	-37%	-37%
22% GEF at 30% engine load	+30%	+122%	+432%	+101%

**7.2.5.1 TPNC versus diesel consumption**

The TPNC data was plotted for each syngas/biogas blend as a function of pilot diesel brake specific fuel consumption (BSFC in kg/kWh) at each testing condition for each engine load. BSFC was used rather than direct diesel usage to account for any load variations. This was plotted to determine if the reduction in the TPNC data is a direct result of the reduction in diesel fuel with increasing GEF. Linear regression analysis was conducted for each gas/diesel blend at each load to determine the effects of the relationship between the diesel consumption and the TPNC data. For full engine load, the TPNC versus diesel consumption is shown using Fig. 7.17. For medium-high load (~77% engine load), this is illustrated using Fig. 7.18, and for 53% load using Fig. 7.19.

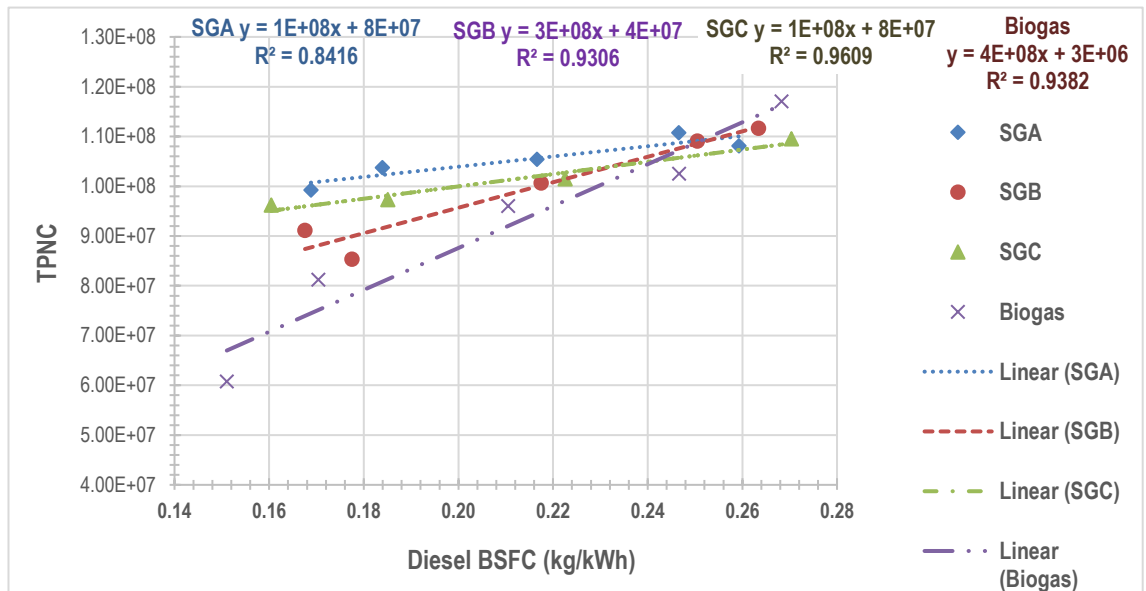


**Fig 7-17 TPNC versus diesel BSFC at full load for all gas/diesel blends**

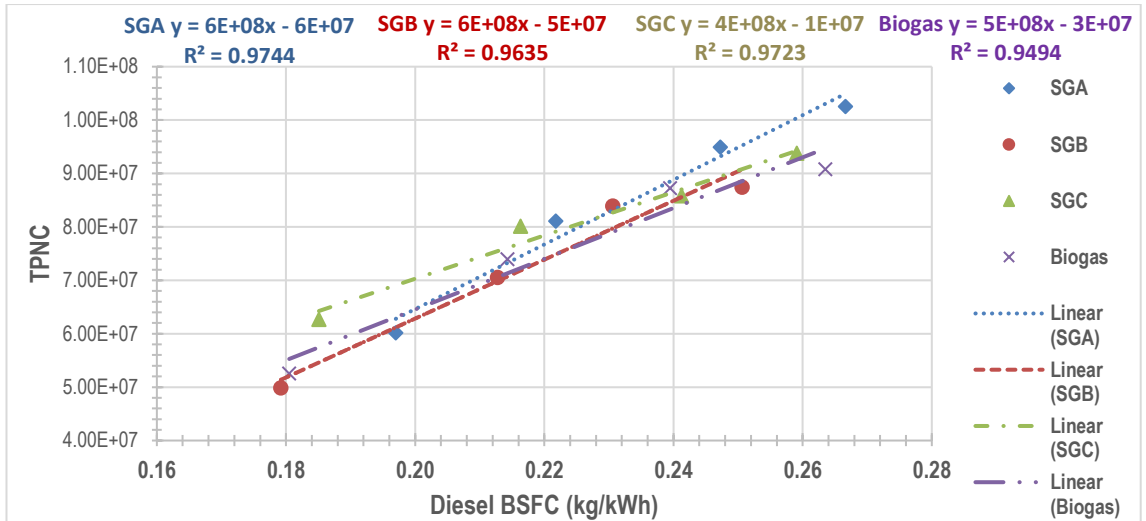


**Fig 7-18 TPNC versus diesel BSFC at 77% load for all gas/diesel blends**

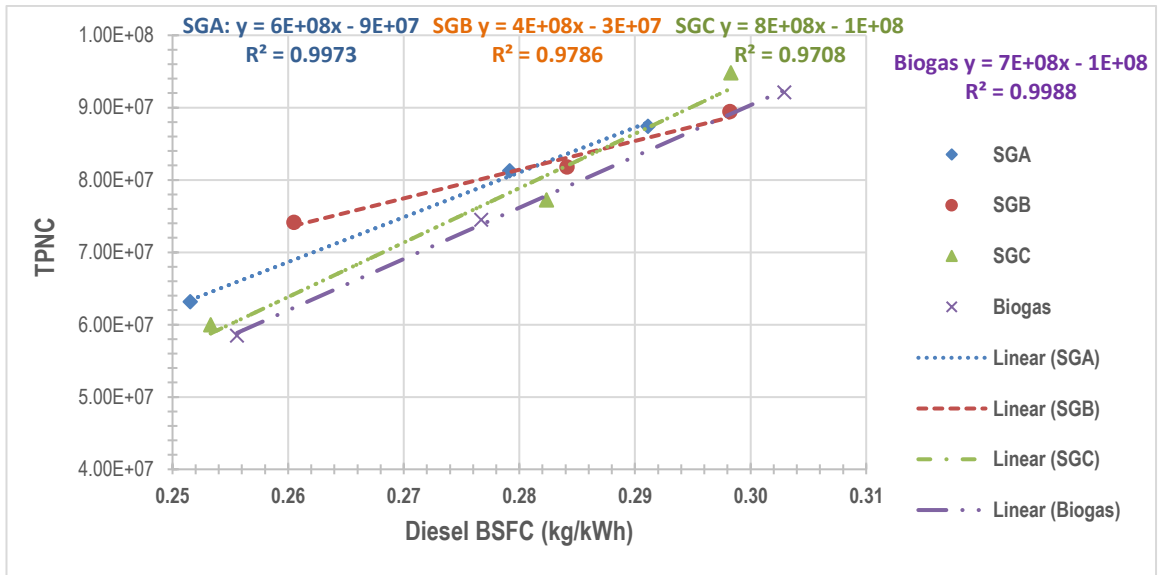


**Fig 7-19 TPNC versus diesel BSFC at 53% load for all gas/diesel blends**

Linear regression analysis results indicate that at full engine load, there is a direct correlation between the reduction in diesel BSFC and the corresponding reduction in the TPNC data as shown in Fig. 7.17;  $R^2$  values for all gas/diesel combustion of  $> 0.93$  were obtained except for SGA which had an  $R^2$  value of 0.84. As all the other gas blends produced a higher  $R^2$  value than SGA, the slightly lower value for SGA was not deemed problematic.

At medium-high load ( $\sim 77\%$ ), a stronger relationship was found with minimum  $R^2$  values being calculated of  $> 0.96$ , apart from biogas, which was found to be slightly lower at  $\sim 0.95$ , as shown in Fig. 7.18. At  $\sim 53\%$  engine load, a good correlation was found, all  $R^2$  values were  $> 0.97$ , as shown in Fig. 7.19.

Hence, it can be concluded that the reduction in the TPNC is a direct result of the reduction of diesel fuel consumption with increasing gas energy fraction.

### **7.2.6 Particle emissions summary during dual fuel mode**

The TPNC levels reduce in dual fuel mode at all engine loads (except for ~30%). This reduction is due to the decrease in diesel consumption, thereby resulting in lower particulates which arise predominantly from the incomplete combustion of diesel fuel [161]. Linear regression analysis using the BSFC of diesel versus the TPNC data showed a good correlation at engine loads greater than >50%.

At 30% engine load, an increase was noted in the TPNC data which was shown by the increase in the particle concentration corresponding to the nuclei mode for all gas/diesel combustion with increasing gas fraction. Notably, SGA showed the smallest increase in TPNC at this load, and SGC was the highest compared to the other syngas blends as shown in Table 7.5.

The overall increase of the TPNC data in dual fuel mode at this low load was thought to be due to lower combustion temperatures resulting in more incomplete combustion and partial oxidation of PM [139]. This is linked to the pilot diesel fuel flame in dual fuel mode, whereby the pilot diesel flame is unable to propagate throughout the combustion chamber resulting in higher emissions and partial oxidation [168]. Hence, at such a low load, this leads to an increase in volatile precursors thus leading to an increase in the nuclei mode particles.

In all cases of dual fuel combustion, at full and medium-high engine loads, the shape of the PNSD curves remains unchanged with increasing gas addition.

At ~53% engine load, for all dual fuel combustion testing, there is a reduction in the particle number concentration with increasing gas addition, however, the change in the PNSD curves observed varies and is dependent on the gas blend evaluated. For SGA and biogas, there is only a slight shift in the PNSD curve, and a bimodal trend in the PNSD curve is not as pronounced. However, for SGB and SGC, the bimodal trend is clearly defined: there is a clear increase in the particles in the nucleation mode and a reduction in the particles in the accumulation mode, similar to that reported by Chuahy et al. [131]. These changes in the PNSD were attributed to reductions in fuel stratification and not due to changes in the soot surface chemistry [131].

The PNSD curve at ~30% engine load shows a bimodal trend for SGA only, for the remaining gas blends evaluated, there is a change in the PNSD curves with increasing gas addition, but a bimodal trend in PNSD is not noted. A large increase in the particles in the nuclei mode is observed. For SGB, SGC, and biogas, it is postulated that the nucleation mode particles increase significantly and merge with the accumulation mode particles resulting in a single large broad peak that presents as a monomodal trend. This increase of nanoparticles at 30% engine load in dual fuel combustion results in an increase in the TPNC.

### 7.3 Andersen cascade impactor data

#### 7.3.1 PM<sub>10</sub> mass data from the impactor

The PM collected by the Andersen cascade (AC) impactor was quantified for the stages in terms of the mass collected corresponding to PM<sub>0.4</sub>, PM<sub>2.1</sub>, and the total PM<sub>10</sub> (in mg/m<sup>3</sup>) for diesel baseline, 10, and 22% GEF for each syngas blend. The graphs for each syngas blend showing the mass of particulate matter collected at each particle size are shown for SGA, SGB, and SGC using Figs. 7.20 to 7.22, respectively.

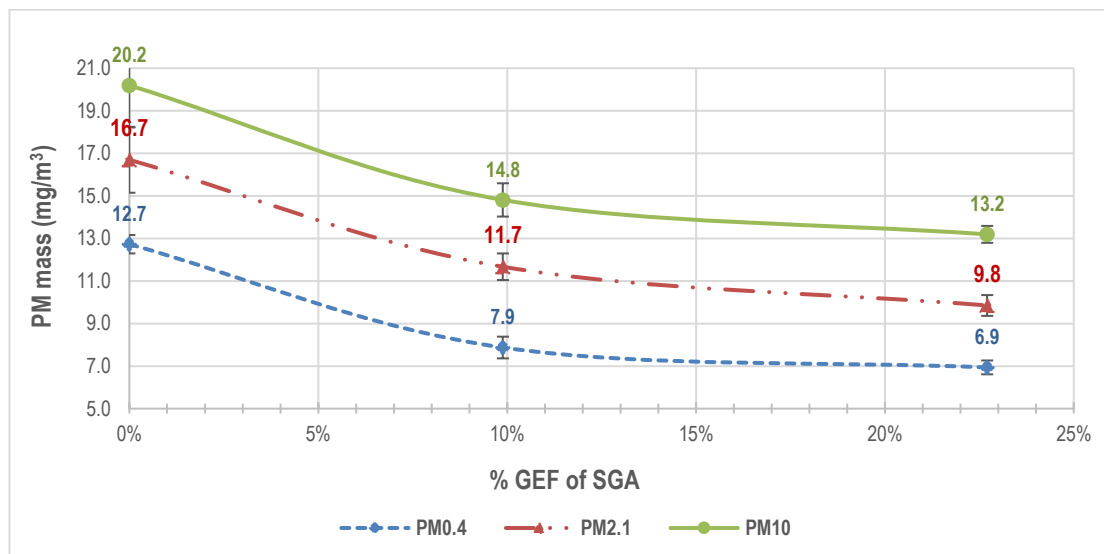
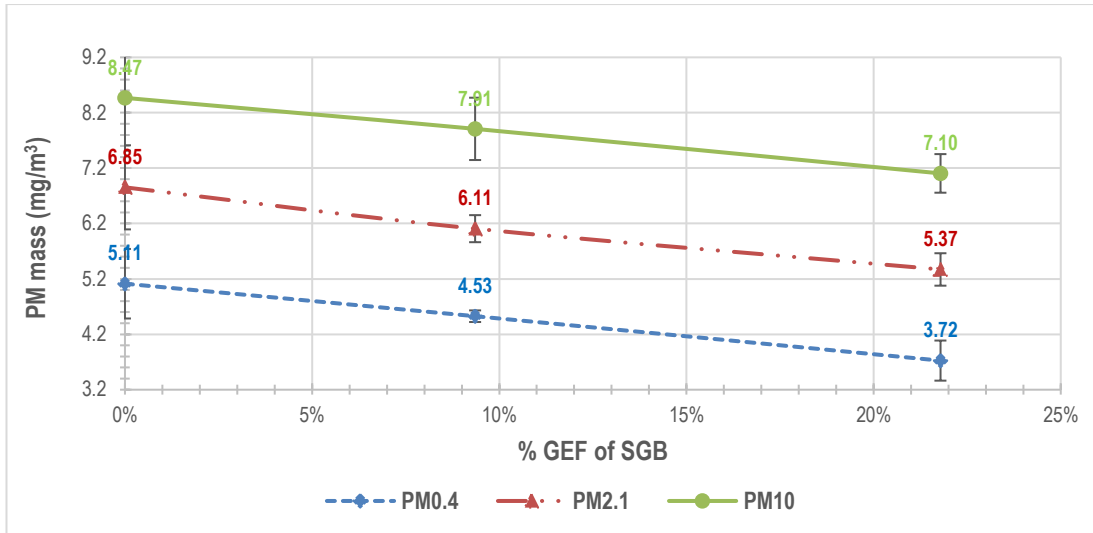
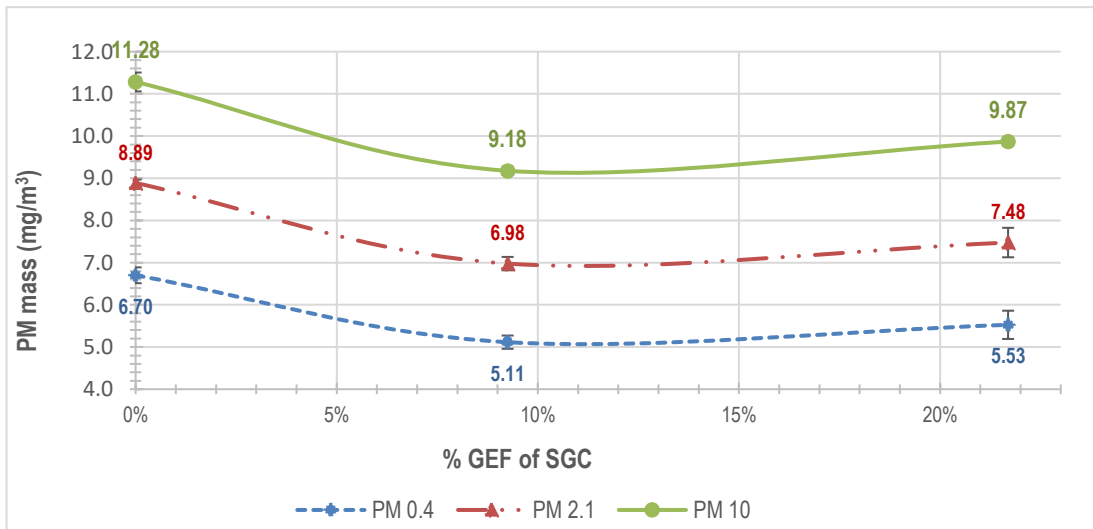


Figure 7-20 Mass of PM collected at various sizes for SGA



**Figure 7-21 Mass of PM collected at various sizes for SGB**



**Figure 7-22 Mass of PM collected at various sizes for SGC**

For SGA and SGB, the amount of PM collected (of all PM sizes, expressed as mg/m<sup>3</sup>) decreases with increasing syngas addition, with the lowest amount collected at 22% GEF as illustrated in Figs. 7.20 and 7.21. However, for SGC, an initial reduction is seen in the PM mass for all sizes as SGC is introduced, however, as the GEF is increased from 10 to 22%, the mass collected remains stable; increasing the syngas fraction does not decrease the PM mass collected any further as shown in Fig. 7.22.

The decrease in the mass of PM collected with increasing syngas fraction is due to the reduction in diesel usage which leads to fewer particulates being formed from incomplete combustion [139, 161].

In dual fuel combustion, soot/PM is known to form in fuel rich areas at higher temperatures with the source being the liquid droplets of hydrocarbon based fuels, i.e. diesel [139].

The mass of the PM is expected to decrease in dual fuel combustion due to a reduction in diesel consumption with increasing GEF [161]. According to Mustafi et al. [139], dual fuel combustion resulted in reduced PM emissions due to shorter combustion durations as the combustion diffusive phase was reduced. In addition, the reduction in the particle concentration in dual fuel mode in the combustion chamber could also reduce the likelihood of collisions [161]. A linear trend was reported earlier with the TPNC and diesel consumption in dual fuel mode (see section 7.2.5.1). Also, a longer ID in dual fuel combustion results in a more homogeneous fuel-air mixture, which results in a reduction in PM formation [281].

In this study, for all gas/diesel dual fuel combustion, longer IDs were experienced in dual fuel mode (as reported in Chapter 5). Notably, the duration of combustion and the flame temperatures were reduced in dual fuel mode at full engine load for SGA as reported by the co-authored study [117]. Hence, a combination of these factors resulted in a decrease in the mass of the PM emissions in dual fuel mode with increasing GEF. However, for SGC, the mass of PM collected does not decrease with a further increase in the syngas fraction from 10 to 22% GEF. This is not due to temperature; the engine exhaust temperature does increase between these two points. The ID does not increase between these two points. The change in the  $\phi$  between these two points is comparable to that observed for SGA and SGB which both saw a reduction in the PM mass between these two data points, hence, this is possibly due to the syngas composition. Further work is required to determine the cause, it is recommended that the HRR study is completed to enhance understanding of any combustion phase changes across the different syngas blends.

It is worth noting that the amount of PM<sub>10</sub> collected at the diesel baseline for each syngas blend is variable, for SGA this is almost double the amount collected. This variation is possibly due to the variation in the engine performance as during the testing of the SGA blend, the engine was in the 'run-in' period after installation from new. Also, the stainless-steel pipes leading to the Andersen cascade impactor were clean and new, hence, less particulate matter may have been lost to wall deposition. Overall, the exact reason is unknown.

Hence, to accurately compare the PM across syngas blends, the % reduction of the PM has been considered relative to the corresponding diesel baseline data for each syngas blend. The amount of PM corresponding to PM<sub>10</sub> was quantified by using the Andersen cascade impactor by adding up the soot/PM collected in all the stages. This was first calculated as PM<sub>10</sub> EI expressed as g/kg (using equation 3.26 in Chapter 3), and then converted into PM<sub>10</sub> EI expressed as g/MJ fuel. This was then expressed as PM<sub>10</sub> SE by multiplying the PM EI (in g/MJ fuel) by the BSEC (in MJ/kWh). The equations corresponding to these calculations are found in Chapter 3, (see section 3.5).

The % reduction in the PM mass relative to the corresponding DBL data was calculated for each syngas at full load using 10 and 22% GEF in terms of PM<sub>2.1</sub> mass (mg/m<sup>3</sup>), PM<sub>10</sub> EI (in g/MJ), and PM<sub>10</sub> SE (in g/kWh). These results have been tabulated in Tables 7.6 to 7.8.

**Table 7-6 The % reduction of PM<sub>2.1</sub> per syngas at 10 & 22% GEF**

The % reduction in PM <sub>2.1</sub> mass (mg/m <sup>3</sup> ) relative to DBL for:	10% GEF	22% GEF
SGA	30%	41%
SGB	11%	22%
SGC	21%	16%

**Table 7-7 % Reduction of PM<sub>10</sub> EI (g/MJ) per syngas at 10 & 22% GEF**

The % reduction in EI (g/MJ fuel) for:	10% GEF	22% GEF
SGA	29%	40%
SGB	4%	17%
SGC	20%	8%

**Table 7-8 % Reduction of PM<sub>10</sub> SE (g/kWh) per syngas at 10 & 22% GEF**

The % reduction in SE (g/kWh) for:	10% GEF	22% GEF
SGA	27%	35%
SGB	2%	12%
SGC	19%	15%

The comparison of the % reduction in the mass of PM<sub>2.1</sub> data for all syngas blends in Table 7.6 shows that SGA dual fuel combustion results in the largest decrease at both GEFs assessed.

Tables 7.7 and 7.8 show that the largest % reduction in the PM<sub>10</sub> EI and SE data was observed for SGA at both GEFs assessed. The PM<sub>10</sub> mass, expressed as EI was reduced by ~40% at a GEF of 22%.

Also, for SGA and SGB, increasing the GEF from 10 to 22% further reduced the PM<sub>10</sub> EI and SE data, whereas for SGC, increasing the GEF from 10 to 22% did not lead to a further reduction in the PM<sub>10</sub> SE and EI data.

Hernández et al. [161] stated that a higher H<sub>2</sub>/CO ratio in the syngas composition would result in lower soot emissions due to the increased presence of the OH radical which plays a crucial role in the oxidation of soot and its precursors [139, 161]. Guo et al. [150] also stated that a higher H<sub>2</sub>/CO ratio in the syngas would lead to lower soot emissions.

Hence, it is expected that SGC dual fuel combustion would lead to a greater reduction in the mass of soot collected relative to the diesel baseline when cross comparing the three syngas blends. However, when cross comparing the PM<sub>10</sub> reduction data in terms of PM EI using Table 7.7, SGA shows the largest decrease/reduction in the PM<sub>10</sub> at 10 and 22% GEF and not SGC.

The reason for this remains unclear and is either associated with the PM mass collection. SGA DBL produced a higher PM mass, this could be due to the engine run-in period/ soot wall deposition on the new stainless-steel pipes associated with the Andersen cascade impaction collection unit, or the influence of the higher H<sub>2</sub> content of SGC was not realised at full engine load at these % GEFs. Further investigative work was required to explore these findings, but due to the impact of Covid-19, this was not possible due to time constraints.

### **7.3.2 PM<sub>10</sub> Particle Mass Size Distribution**

The average Particle Mass Size Distribution (PMSD) data was compared across the various % GEFs evaluated per syngas blend. This was expressed as % cumulative weight gain as a function of particle size (PS) related to each Andersen impactor stage, as well as the mass collected at each stage (expressed as a mass % of the total PM mass collected, as shown in the bars of the graphs). This was graphically represented for each syngas blend in Figs. 7.23 to 7.25.

#### **7.3.2.1 Syngas A**

The PMSD and the % cumulative weight gain as a function of the particle size are depicted in Fig. 7.23 for SGA. This graph shows that DBL runs produced a larger amount of ultrafine particulate matter (0 - 0.43 μm), ~63% of the total mass is collected at this stage.

In comparison to dual fuel combustion, 53.1 and 52.6 % of the total mass is collected, there is a minor decrease with increasing SGA addition. Hence, by deduction, dual fuel mode produces a greater number of larger particulate matter between 10 and 0.4 $\mu\text{m}$ .

When comparing the % mass collected at each particle size stage, dual fuel combustion does indicate that larger sized particulate matter is produced in dual fuel combustion, this mass increases with increasing SGA addition up to the impaction stage corresponding to 3.3-2.1 $\mu\text{m}$ . Impaction stages smaller than this showed no clear trend with increasing SGA.

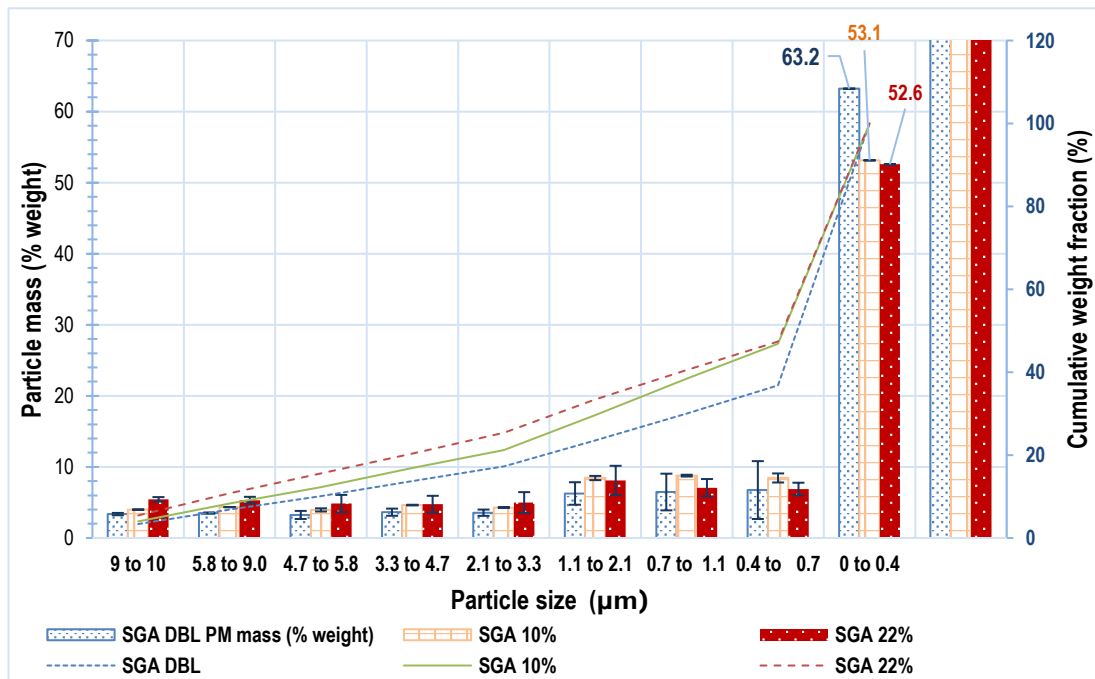


**Figure 7-23 The PMSD and the cumulative weight gain up to PM<sub>10</sub> for SGA**

### 7.3.2.2 Syngas B

The PMSD and the % cumulative weight gain as a function of particle size related to each Andersen impactor stage are depicted using Fig. 7.24 for SGB. Again, (as per SGA), this shows that DBL runs produced a larger mass of fine particulate matter (0- 0.43  $\mu\text{m}$ ) equivalent to ~60% of the total mass, and as the GEF is increased, this mass decreases.

Again, this indicates that dual fuel combustion produces a larger amount of larger sized particulate matter ranging in size between 10 and 0.4 $\mu\text{m}$ . However, individual analysis data from each impaction stage does not clearly show this trend as shown in Fig. 7.24.

Only at one impaction stage: 3.3 - 4.7  $\mu\text{m}$ , it can be concluded that the diesel baseline produces a small mass of particulate matter, and the mass of particulate matter collected increases with syngas addition. This trend is potentially lost due to the error related to this experimental work. The error bars are based on  $\pm$  one standard deviation derived from repeat experimental work.

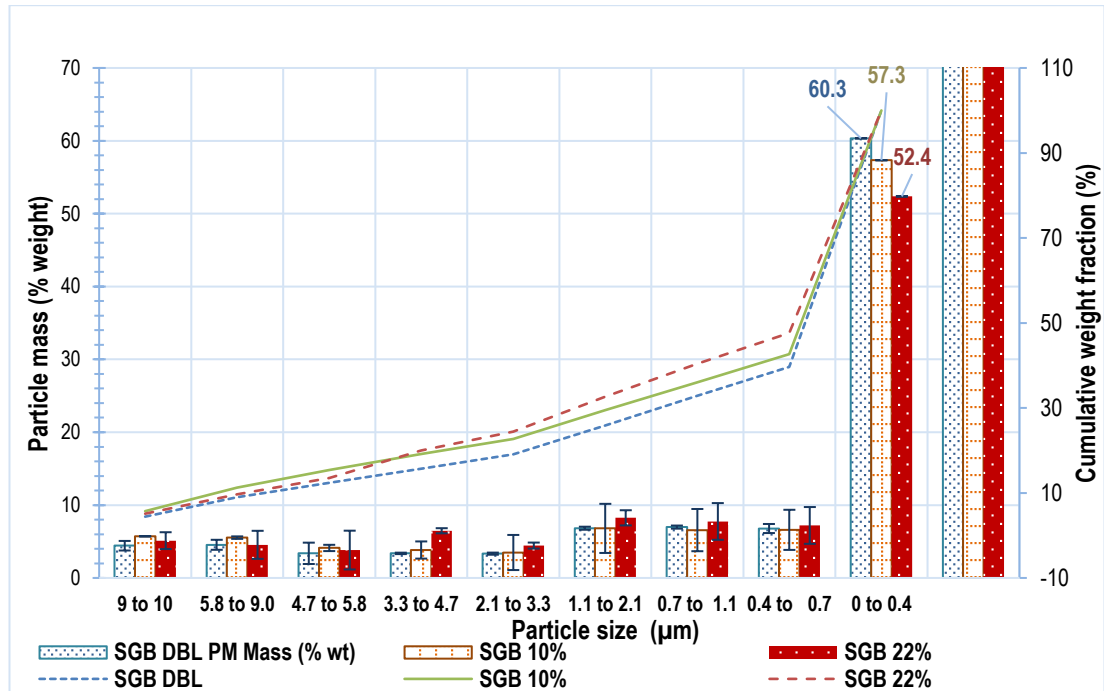


**Figure 7-24 The PMSD and the cumulative weight gain up to PM<sub>10</sub> for SGB**

### 7.3.2.3 Syngas C

The PMSD and the % cumulative weight gain as a function of particle size related to each Andersen impactor stage are depicted using Fig. 7.25 for SGC. Again, this graph shows that the DBL run produces a larger mass of fine particulate matter (0-0.4  $\mu\text{m}$ ) equivalent to ~59% of the total mass. In dual fuel mode combustion, as the GEF is increased from 10 to 22%, the % mass (as a % of the total) does not change.

This again indicates that dual fuel combustion produces a larger amount of larger sized particulate matter ranging in size from 10 and 0.4 $\mu\text{m}$ . However, individual analysis data from each impaction stage does not clearly show this trend due to potential experimental error. Hence, no further conclusions can be drawn regarding the PMSD of SGC-diesel versus diesel baseline.

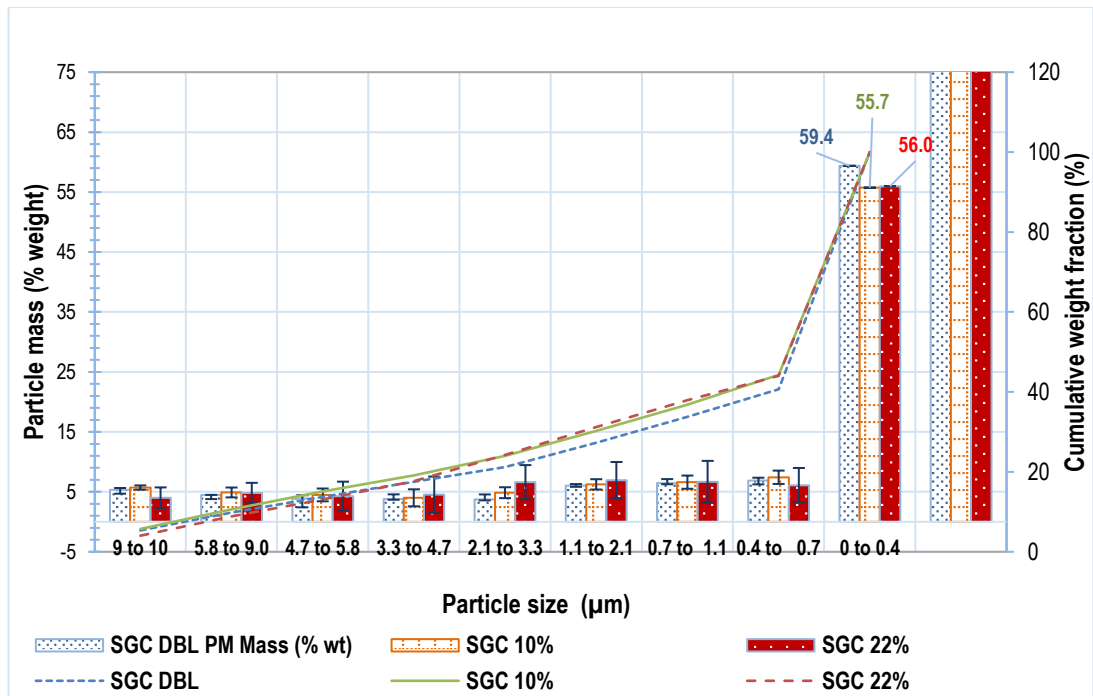


**Figure 7-25 The PMSD and the cumulative weight gain up to PM<sub>10</sub> for SGC**

### 7.3.3 Summary of the PM<sub>10</sub> Andersen cascade data

In summary, when considering the particulate matter corresponding to the mass of the PM<sub>10</sub> collected, the following can be concluded:

- The mass of the PM collected for all PM fractions (PM<sub>0.4</sub>, PM<sub>2.1</sub> and PM<sub>10</sub>), all decreased in dual fuel mode relative to DBL due to the reduction in diesel fuel usage and hotter engine exhaust temperatures in dual fuel mode (see Chapter 5, section 5.4).
- SGA had the largest reduction in PM<sub>10</sub> EI data at both % gas energy fractions assessed, and not SGC as expected. This was potentially due to the influence of the higher hydrogen content of SGC not being realised at these testing conditions.
- In terms of PM<sub>10</sub> PMSD: DBL produced a larger mass of ultrafine particulate matter in comparison to all syngas dual fuel combustion. This indicates that dual fuel mode combustion produces a larger amount of particulate matter ranging from 10 to 0.43µm in size.
- The PMSD as a function of particle size related to each Andersen impactor stage showed that for SGA, the cumulative weight gain of mass of particulate matter also increased across all particle sizes with increasing GEF.

## 7.4 Characterisation of PM<sub>10</sub>

It was calculated that ~ 68% of the total mass of the PM was collected in both the backup filter (0-0.43  $\mu\text{m}$ ) and the last Andersen impactor stage (0.43 to 0.65 $\mu\text{m}$ ) when running using pure diesel. For syngas-diesel combustion, this corresponded to 63% of the total PM mass collected for 10% GEF, and 60% of the total PM mass for 22% GEF. Hence, as the bulk of the PM mass was collected at these two stages, the PM collected from both these stages was further characterised using Thermogravimetric analysis (TGA), Scanning Electron Microscope (SEM), and Energy Dispersive X-Ray (EDX) techniques.

### 7.4.1 Thermogravimetric Analysis (TGA)

For the TGA analysis, any contribution from the blank filter paper which may affect the results was compensated for by analysing blank filter samples alongside the soot samples and these values were then deducted. From the TGA analysis, the following was calculated: the total mass of the PM collected at the specific Andersen stage, and the mass of PM (in  $\text{mg}/\text{m}^3$ ) corresponding to the volatile organic fraction (VOF), carbon (C), and ash fraction. The ash fraction was calculated by difference (100 minus the sum of the volatile organic fraction and carbon fraction). Due to this method of this calculation, there is a larger degree of error associated with the ash data.

For both impaction stages, the mass concentration (in  $\text{mg}/\text{m}^3$ ) is expressed for the following fractions: total PM mass, C, VOF, and ash. The mass concentration corresponding to these fractions (in  $\text{mg}/\text{m}^3$ ) was also converted to PM EI and PM SE data for the last impaction stage corresponding to the particle size of 0-0.43  $\mu\text{m}$ . This was only calculated for this stage as it collected the bulk of the PM mass from the PM<sub>10</sub> (~61% of the total PM mass).

For all syngas blends, to compare the trend in the mass concentration (in  $\text{mg}/\text{m}^3$ ), the mass data was normalised whereby the corresponding diesel baseline value represented a value of 1.0, thus allowing the comparison of the VOF fraction, C fraction, and the total mass fraction together. The ash fraction was not illustrated as this has been calculated by difference.

### 7.4.1.1 Syngas A: Thermogravimetric analysis data

A summary of the TGA results for SGA dual fuel combustion with increasing % GEF has been tabulated in Table 7.9.

**Table 7-9 Summary of the mass of PM (mg/m<sup>3</sup>) equivalent to the various mass fractions at the two particle size ranges for SGA**

	Mass of PM (mg/m <sup>3</sup> ) collected at PS 0-0.43µm				Mass of PM (mg/m <sup>3</sup> ) collected at PS 0.43-0.65µm			
	Total mass	VOF fraction	C fraction	Ash fraction	Total mass	VOF fraction	C fraction	Ash fraction
<b>0/DBL</b>	12.73	0.26	0.23	12.24	1.38	0.006	0.003	1.37
<b>10% GEF</b>	7.87	0.07	0.12	7.68	1.25	0.010	0.005	1.23
<b>22% GEF</b>	6.94	0.05	0.10	6.79	0.91	0.004	0.002	0.91

The PM EI (mg/MJ fuel) and PM SE (in mg/m<sup>3</sup>) values of the PM mass fraction collected at this impaction stage (0 - 0.43 µm) are summarised in Table 7.10.

**Table 7-10 Summary of the PM EI and PM SE data for the various SGA mass fractions equivalent to the particle size of 0-0.43µm**

	PM EI (mg/MJ fuel)			PM SE (mg/kWh)		
	Total mass	VOF	C	Total mass	VOF	C
<b>DBL</b>	7.47	0.15	0.14	86	1.73	1.59
<b>10%</b>	4.46	0.04	0.07	53	0.45	0.82
<b>22%</b>	3.77	0.03	0.05	47	0.34	0.64

Table 7.10 shows the corresponding PM EI and PM SE data for each fraction of the PM collected at this impaction stage. In all cases, the PM EI and the PM SE decreased with increasing SGA.

The results for the normalised mass concentration plots for the total mass, the mass of the VOF, and the C fraction at the Andersen stage corresponding to a PS of 0-0.43µm is depicted using Fig. 7.26, and for the Andersen stage corresponding to a PS of 0.43 - 0.65 µm are depicted using Fig. 7.27.

Table 7.9 and Fig. 7.26 both show that in terms of the mass concentrations of the VOF, C, and total PM fractions at this impaction stage (0-0.43µm), all these decreased sharply when syngas was introduced, Between GEF additions of 10% and 22% of SGA a small further decrease was noted.

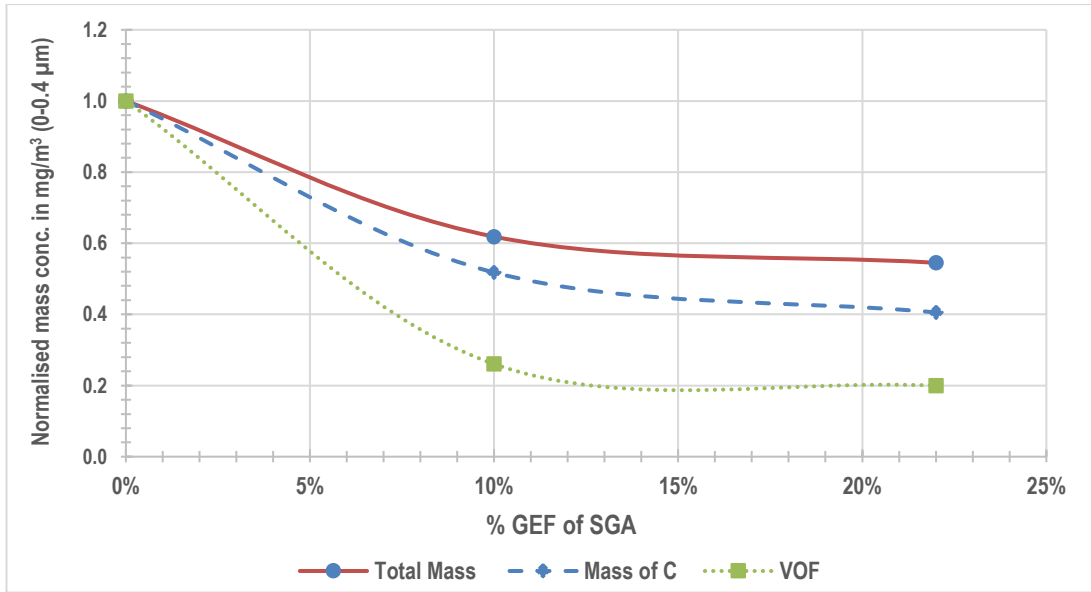


**Figure 7-26 Mass conc. (relative to DBL) of the various fractions collected (PS  $\leq 0.43\mu\text{m}$ ) v GEF of SGA-diesel**

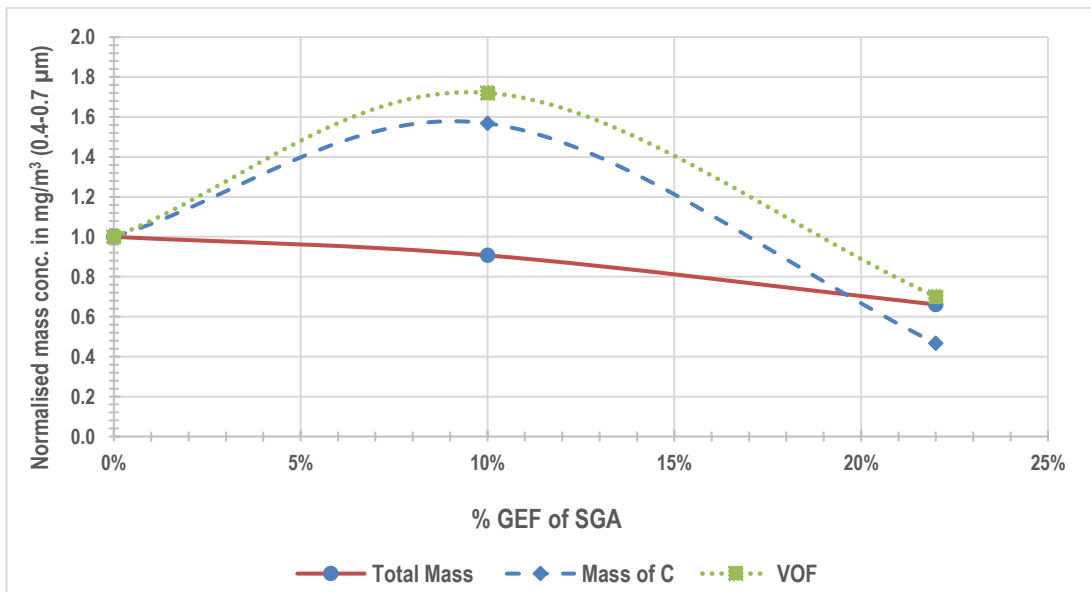


**Figure 7-27 Mass conc. (relative to DBL) of the various fractions collected (PS 0.43 – 0.65 µm) v GEF of SGA-diesel**

Fig. 7.27 shows that the total mass concentration of the PM collected at the Andersen impactor stage corresponding to a particle size of 0.43-0.65 µm decreases with increasing SGA fraction. For the mass concentration of the C and the VOF, both increase at a GEF of 10% (relative to the DBL), then decrease as the GEF is increased from 10% to 22% to values below the diesel baseline.

#### 7.4.1.2 Syngas B: Thermogravimetric analysis data

A summary of the TGA results for SGB dual fuel combustion with increasing % GEF has been tabulated in Table 7.11.

**Table 7-11 Summary of the mass of PM (mg/m<sup>3</sup>) equivalent to the various mass fractions at the two particle size ranges for SGB**

	Mass of PM (mg/m <sup>3</sup> ) collected at PS 0-0.43µm				Mass of PM (mg/m <sup>3</sup> ) collected at PS 0.43-0.65µm			
	Total mass	VOF fraction	C fraction	Ash fraction	Total mass	VOF fraction	C fraction	Ash fraction
<b>0/DBL</b>	5.11	0.06	0.03	5.07	0.57	0.004	0.003	0.57
<b>10% GEF</b>	4.53	0.05	0.04	4.44	0.52	0.002	0.001	0.52
<b>22% GEF</b>	3.72	0	0.03	3.70	0.51	0.005	0.002	0.50

The PM EI (mg/MJ fuel) and PM SE (in mg/m<sup>3</sup>) values of the PM mass fractions collected at this impaction stage (0-0.43µm) are summarised in Table 7.12.

**Table 7-12 Summary of the PM EI and PM SE data for the various SGB mass fractions equivalent to the particle size of 0-0.43µm**

	PM EI (mg/MJ fuel)			PM SE (mg/kWh)		
	Total mass	VOF	C	Total mass	VOF	C
<b>DBL</b>	2.75	0.03	0.016	33	0.35	0.19
<b>10%</b>	2.36	0.02	0.021	29	0.31	0.26
<b>22%</b>	1.87	0.00	0.016	24	0.00	0.21

Table 7.12 shows the corresponding PM EI and PM SE data for each fraction of the PM collected at this impaction stage ( $\leq 0.43\mu\text{m}$ ). In all cases, the PM EI decreased with increasing SGB except for the C fraction whereby a very minor increase was noted between DBL and 10% GEF, as the GEF was increased further from 10% to 22%, the PM EI for the C fraction decreased back to baseline levels.

In terms of the PM SE data for this impaction stage, the total mass, and VOF decreased with increasing GEF. However, the C fraction showed an initial increase at 10% GEF, followed by a decrease when the SGB GEF was increased from 10 to 22%. The normalised mass concentration plots for the various fractions at the Andersen stage corresponding to a PS of 0-0.43µm are depicted using Fig. 7.28, and for the Andersen stage corresponding to a PS of 0.43-0.65 µm are depicted using Fig. 7.29.

Fig. 7.28 shows that the total PM mass and the VOF mass fraction collected at this impaction stage decreased with increasing SGB addition. However, the C mass fraction increased at a GEF of 10% (relative to DBL) and then decreased as the GEF increased from 10% to 22%.

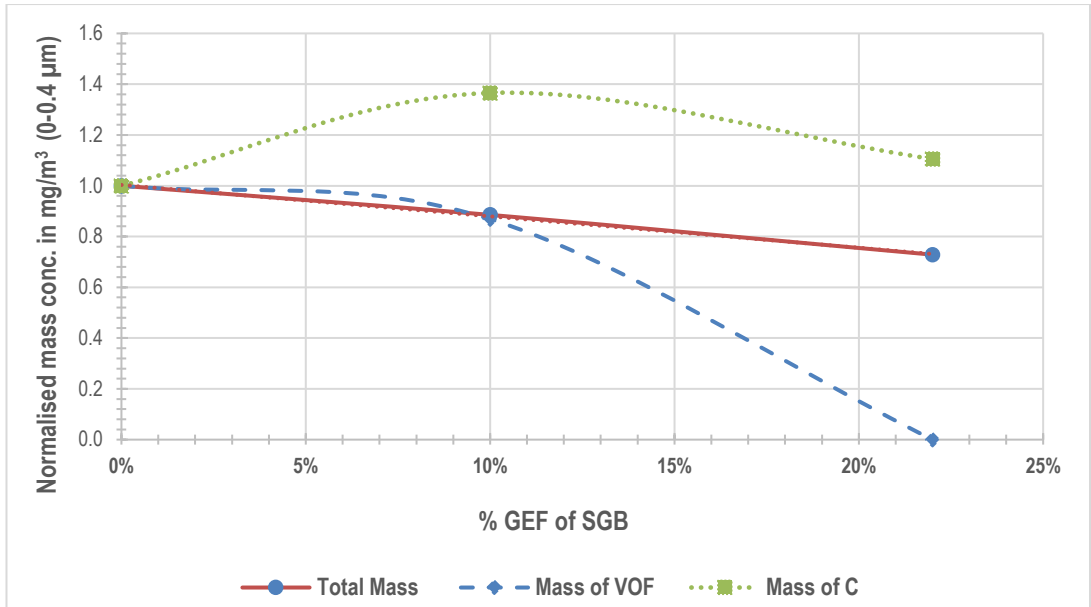


**Figure 7-28 Mass conc. (relative to DBL) of the various fractions collected (PS  $\leq 0.43\mu\text{m}$ ) for SGB-diesel**

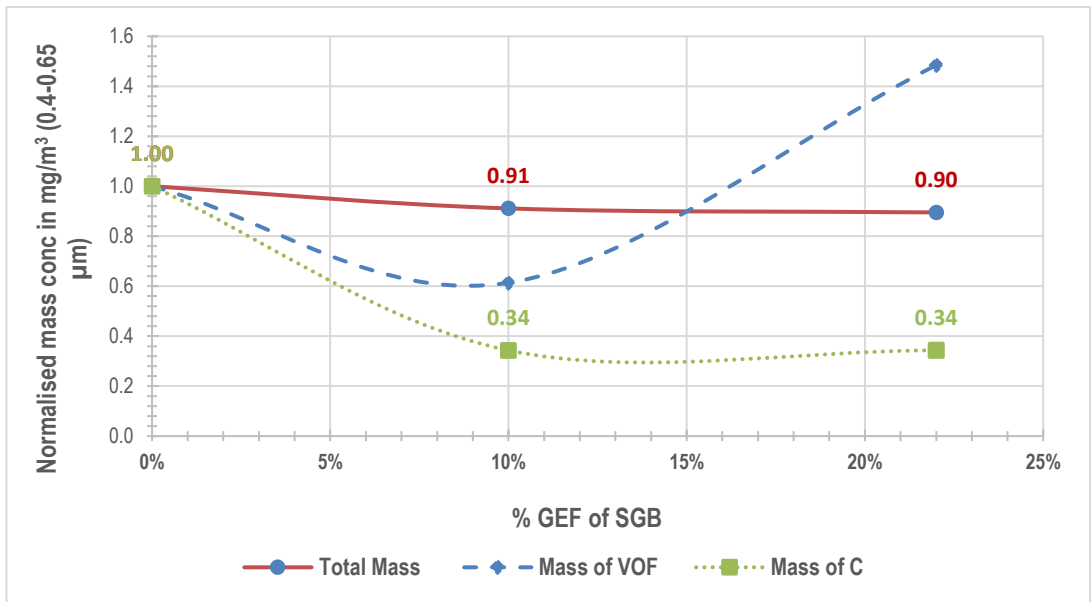


**Figure 7-29 Mass conc. (relative to DBL) of the various fractions collected (PS 0.43 – 0.65 μm) for SGB-diesel**

Fig. 7.29 shows that a decrease was seen in the total mass of the PM with increasing SGB addition at the Andersen impactor stage corresponding to the particle size range of 0.43-0.65 μm. The mass of the C fraction also reduced upon the initial introduction of SGB, however, no further notable reduction was observed when the SGB fraction was increased further from 10% to 22%. For the VOF mass fraction, this decreased between baseline and a GEF of 10% and then increased as the GEF was increased from 10% to 22%.

### 7.4.1.3 Syngas C: Thermogravimetric analysis data

A summary of the TGA data for SGC dual fuel combustion with increasing % GEF has been tabulated in Table 7.13.

**Table 7-13 Summary of the mass of PM (mg/m<sup>3</sup>) equivalent to the various mass fractions at the two particle size ranges for SGC**

	Mass of PM (mg/m <sup>3</sup> ) collected at PS 0-0.43µm				Mass of PM (mg/m <sup>3</sup> ) collected at PS 0.43-0.65µm			
	Total mass	VOF fraction	C fraction	Ash fraction	Total mass	VOF fraction	C fraction	Ash fraction
<b>0/DBL</b>	6.70	0.022	0.10	6.58	0.78	1.2 x10 <sup>-3</sup>	9 x10 <sup>-4</sup>	0.77
<b>10% GEF</b>	5.11	0.05	0.04	5.03	0.68	1.3 x10 <sup>-3</sup>	9 x10 <sup>-4</sup>	0.68
<b>22% GEF</b>	5.53	0.02	0.07	5.43	0.60	7 x10 <sup>-4</sup>	9 x10 <sup>-4</sup>	0.60

The PM EI (mg/MJ fuel) and PM SE (in mg/m<sup>3</sup>) values of the PM mass fractions collected at this impaction stage (0-0.43 µm) are summarised in Table 7.14.

**Table 7-14 Summary of the PM EI and PM SE data for the various SGC mass fractions equivalent to the particle size of 0-0.43µm**

	PM EI (mg/MJ fuel)			PM SE (mg/kWh)		
	Total mass	VOF	C	Total mass	VOF	C
<b>DBL</b>	3.60	0.012	0.055	43	0.14	0.66
<b>10%</b>	2.71	0.026	0.019	33	0.32	0.24
<b>22%</b>	2.78	0.012	0.037	35	0.15	0.47

Table 7.14 shows that the PM EI values for the C and total mass fraction decreased from 0 to 10% GEF, and then increased when the GEF was increased from 10% to 22%. The PM EI data for the VOF fraction increased from 0 to 10% GEF, and then as the GEF of SGB was increased from 10 to 22%, this value decreased back to diesel baseline levels.

In terms of the PM SE from this impaction stage (≤0.43µm), the overall trend is that the total mass and the mass of the C fraction decreased upon initial introduction of SGC, and then both increased as the GEF was increased from 10-22%. However, the PM SE values corresponding to the VOF fraction showed an initial increase at 10% GEF, followed by a decrease back to approximate diesel baseline values when the SGC was increased from 10 to 22%.

The normalised mass concentration plots for the various fractions at the Andersen stage corresponding to a PS of 0-0.43µm are depicted using Fig. 7.30, and for the Andersen stage corresponding to a PS of 0.43 - 0.65 µm are depicted using Fig. 7.31.

Fig. 7.30 shows that in terms of the total PM mass collected at the Andersen impaction stage corresponding to a particle size of 0-0.43  $\mu\text{m}$ , this decreased initially when SGC was introduced, however, when the SGC fraction was increased from 10 to 22% no further reduction was noted

The C fraction decreased in the initial dual fuel mode but then increased slightly from 10 to 22% GEF addition. In comparison, the VOF mass fraction increased initially in dual fuel mode, but then decreased with increasing SGC addition. The reason for this increase and decrease remains unclear.

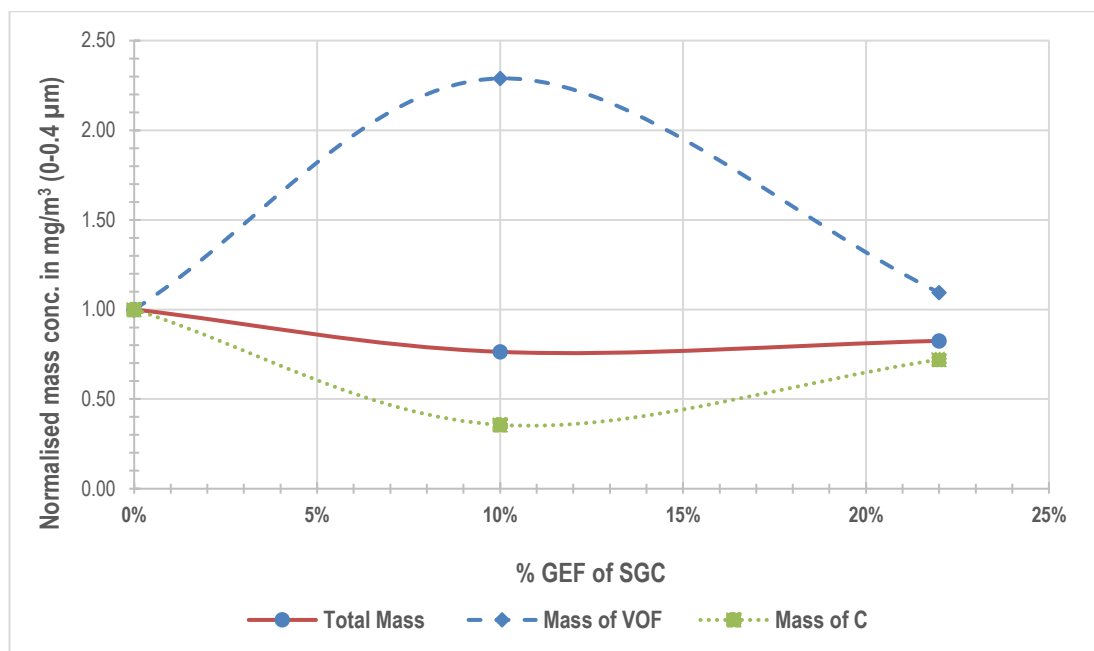


**Figure 7-30 Mass conc. plots (relative to DBL) of the various fractions collected ( $PS \leq 0.43\mu\text{m}$ ) for SGC-diesel**

Fig. 7.31 shows an overall decrease was noted in the total mass of PM with increasing SGC usage, this mass being the PM collected at the Andersen impactor stage corresponds to the particle size range of 0.43-0.65  $\mu\text{m}$ .

Fig. 7.31 also shows that the C fraction mass decreases from DBL to 10%, and then as the GEF is increased from 10 to 22%, this increased back to values close to diesel baseline levels. The VOF mass fraction increased initially in dual fuel mode but then decreased significantly with increasing SGC addition. The reason for this increase and decrease also remains unclear.

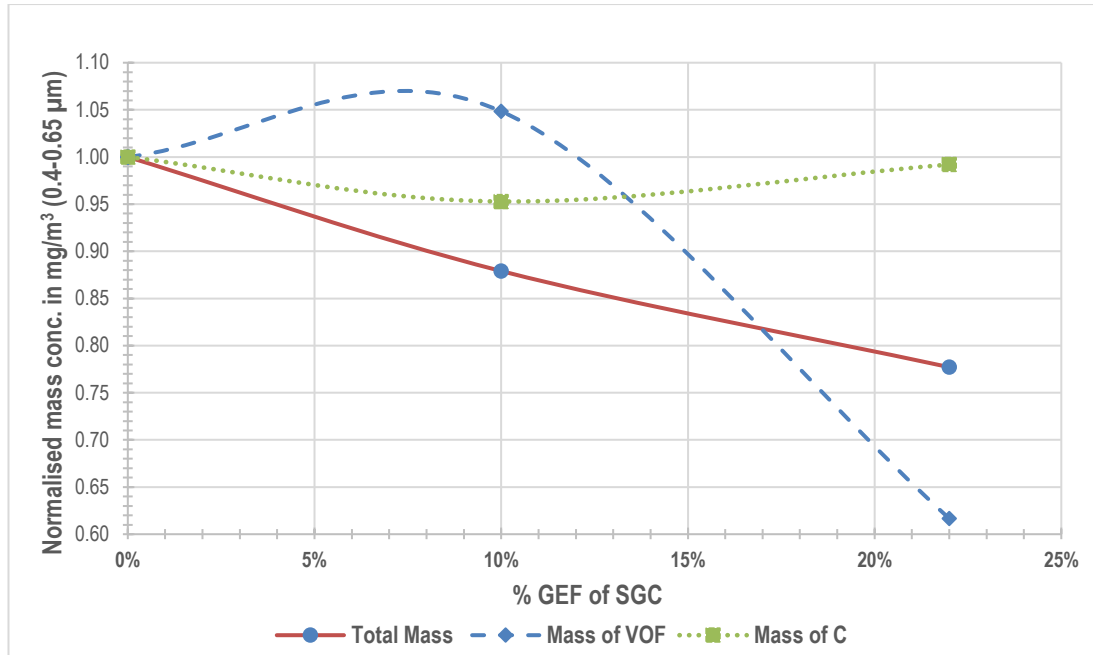


**Figure 7-31 Mass conc. plots (relative to DBL) of the various fractions collected (PS 0.43-0.65µm) for SGC-diesel**

#### 7.4.1.4 Thermogravimetric analysis trend summary

At the Andersen stage whereby the PM mass has been collected corresponding up to 430nm, this covers the nanoparticle range (up to ~50nm) with the rest being the accumulation mode which covers the particle size range approx. 50 to 1,000nm [125]. It is widely accepted that most of the mass is due to the particles in the accumulation mode, and these particles are comprised of carbon based soot agglomerates which are formed during the combustion process [125], with volatile matter adsorbed onto their surface [282].

The only fuel which contributes to the unburnt hydrocarbons and resulting PM formation is diesel [172], hence, as discussed earlier, as the diesel consumption is reduced, it is expected that the mass of soot collected at the Andersen impaction stage up to 430nm/0.43µm would also reduce accordingly, as would the VOF fraction. The hydrogen content in the syngas also plays a role in reducing the mass of the soot (as discussed earlier). This is because hydrogen produces OH radicals which enhance the oxidation of soot and its precursors [105, 283].

For all syngas dual fuel blends, the PM mass collected at this stage reduced accordingly as expected. However, the VOF fraction only showed a reduction for SGA and SGB.

For SGC, the mass of this fraction increased initially (relative to diesel) at 10% GEF, then as the GEF was increased further from 10% to 22%, the VOF fraction reduced significantly. The cause of this increase and decrease remains unclear but could be linked to the hydrogen content. The initial increase remains unexplained, however, as with increasing gas substitution, (from 10 to 22%), an overall reduction in the VOF was noted.

#### **7.4.1.5 Cross-comparison of the Thermogravimetric Analysis results across syngas blends**

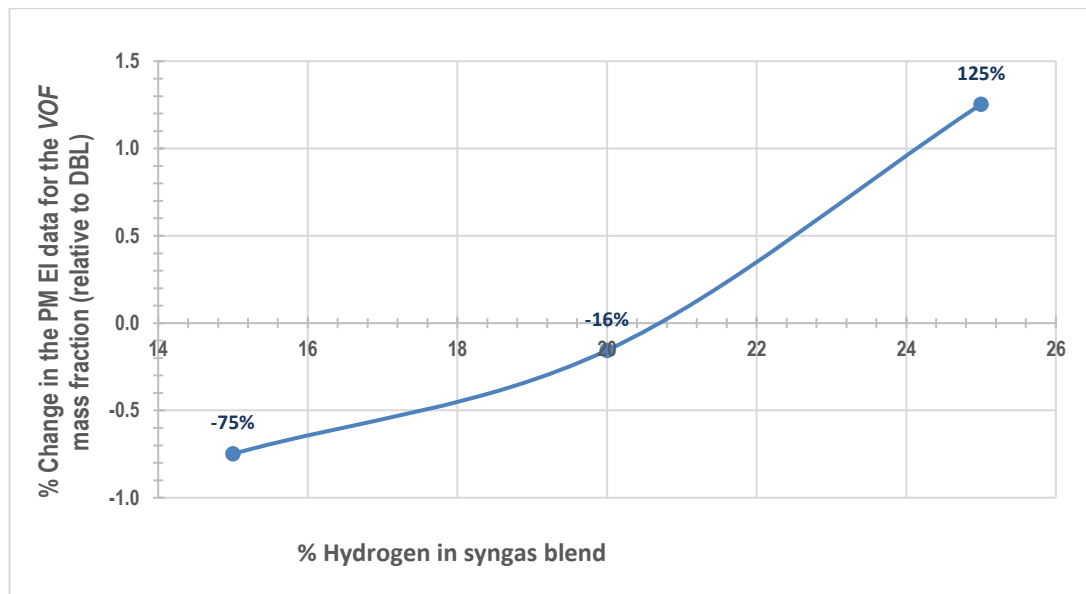
The % changes in the mass fractions of the PM collected at the Andersen impactor stage corresponding to a particle size range of 0-0.43  $\mu\text{m}$  were cross compared across syngas blends. This stage was chosen for cross-comparison as it had the largest amount of PM mass collected compared to the other impaction stages (as mentioned earlier). The data used for cross-comparison was the calculated PM emission index values (expressed in mg/MJ fuel) for the VOF and C mass fraction. The PM EI data used here was previously shown in Tables 7.10 (SGA), Table 7.12 (SGB), and Table 7.14 (SGC). The % change in the PM EI for each fraction was calculated relative to each diesel baseline value from each dataset.

The cross-comparison results for the backup filter (particle size 0-0.43  $\mu\text{m}$ ) at 10% GEF for the % change in the VOF fraction as a function of hydrogen content in the syngas blend is shown using Fig. 7.32, and the % change in the C fraction is shown using Fig. 7.33.

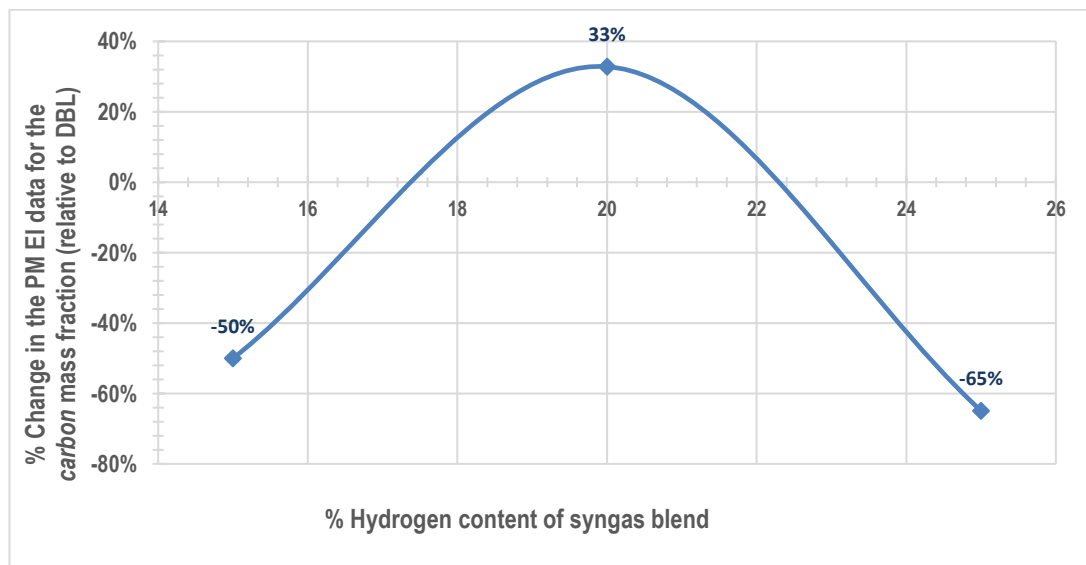
The cross-comparison results for the backup filter at 22% GEF for the % change in the VOF fraction as a function of the hydrogen content in the syngas blend is shown using Fig. 7.34, and the % change in the C fraction is shown using Fig. 7.35.

Fig. 7.32 shows that at 10% GEF, SGA produced the highest % reduction in the VOF fraction relative to the diesel baseline, whereas SGC resulted in an overall increase in the VOF mass fraction, further work is required to investigate the cause. Notably, SGA also had the largest reduction in the total PM<sub>10</sub> EI (g/MJ fuel) as shown in Table 7.7.

Fig. 7.33 shows that SGC produced the highest % reduction in the C fraction of the PM collected, followed by SGA, moreover, SGB saw an increase in the C fraction relative to the diesel baseline. The reason for the reduction in the C fraction of the PM collected for SGC could be due to the effect of the higher hydrogen content which results in a higher concentration of the OH radicals resulting in better oxidation of the soot, resulting in a lower C fraction engine [161] in comparison to the other syngas blends.



**Figure 7-32 The % change in the PM EI (mg/MJ fuel) data of the VOF mass fraction at 10% GEF as a function of the H<sub>2</sub> content of the syngas**



**Figure 7-33 The % change in the PM EI (mg/MJ fuel) data of the C mass fraction at 10% GEF as a function of the H<sub>2</sub> content of the syngas**

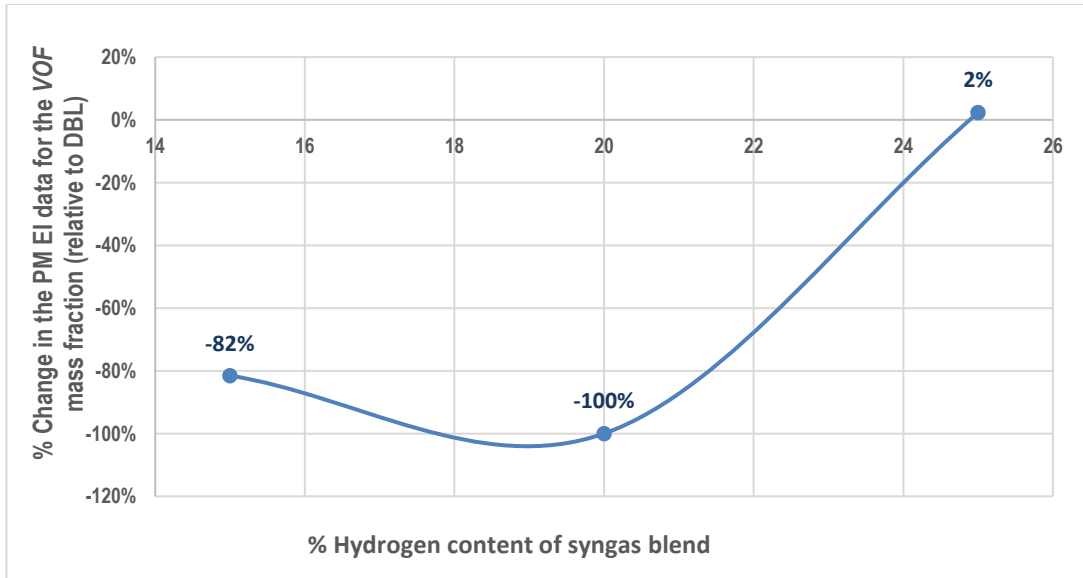


**Figure 7-34 The % change in the PM EI (mg/MJ fuel) data of the VOF mass fraction at 22% GEF as a function of the H<sub>2</sub> content of the syngas**

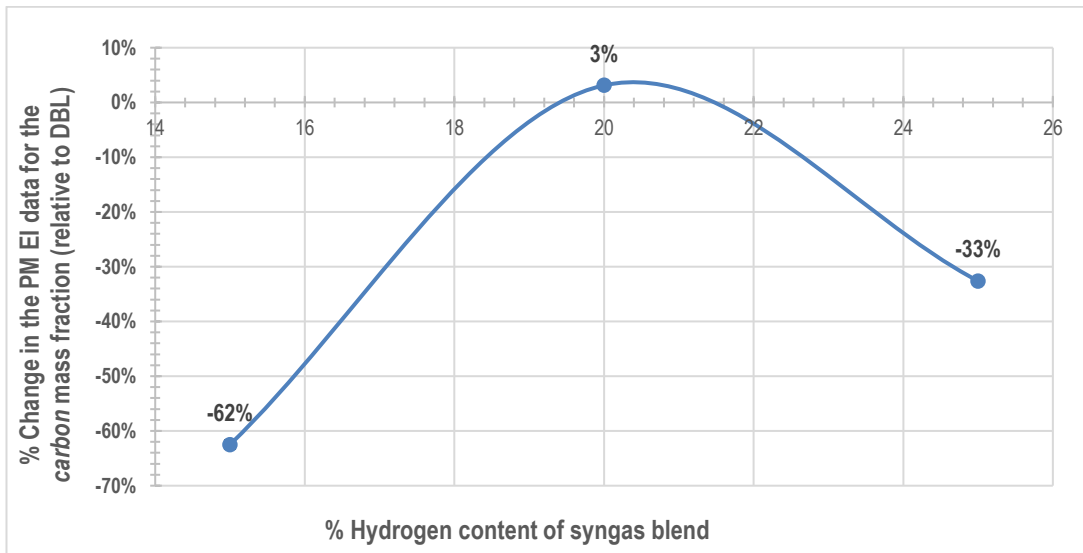


**Figure 7-35 The % change in the PM EI (mg/MJ fuel) data of the C mass fraction at 22% GEF as a function of the H<sub>2</sub> content of the syngas**

Fig. 7.34 shows that SGB produced the highest % reduction in VOF matter relative to the diesel baseline, whereas SGC resulted in an increase in the VOF mass fraction (as seen earlier using a GEF of 10%).

Fig. 7.35 shows that SGA produced the highest % reduction in the C fraction of the PM collected, followed by SGC, moreover, SGB saw an increase in the C fraction relative to the diesel baseline. It appears that at this % GEF, the % reduction in the C fraction of the PM collected is not linked to the hydrogen composition of the syngas.

## 7.4.2 Energy Dispersive X-Ray (EDX) analysis

Energy Dispersive X-Ray (EDX) analysis of the PM collected at both impaction stages was used for qualitative purposes, hence the key inorganic species detected will be discussed. For both Andersen impaction stages, for all dual fuel combustion, the main component of the soot was dominated by carbon, the following species were also detected: oxygen, magnesium, aluminium, silicon, phosphorus, calcium, zinc, and barium.

For all these inorganic species detected, the origins were considered. Oxygen is derived from the air or the syngas itself. The remaining species can be derived from two potential sources: from direct wear of the engine components or the engine oil and its additives.

Typically, metals such as aluminium and magnesium are derived from the wear and tear of the metal engine components [284]. Other species detected include silicon, phosphorus, calcium, zinc, and barium, all are potentially derived from the additives added to the engine oil [285]. Silicon is added to engine oil as an antifoaming agent, zinc, and phosphorus are anti-wear/antioxidation additives. Calcium and barium are also derived from the additives in engine oil. The carbon itself is derived from the unburnt hydrocarbons from diesel fuel.

Fig. 7.36 shows a typical spectrum produced from the EDX analysis of the PM collected from the backup filter (0- 0.4 $\mu$ m) during dual fuel combustion using SGB at a GEF of 22%.

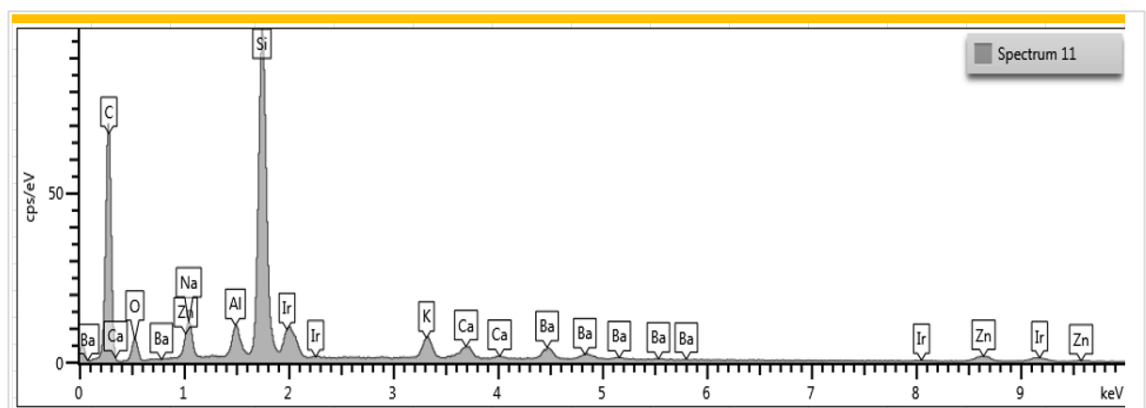


**Figure 7-36 An example of the EDX spectrum obtained from the analysis of the PM collected during dual fuel combustion**

### 7.4.3 Scanning Electron Microscope (SEM) analysis

#### 7.4.3.1 Diesel baseline SEM comparison

The images from the Scanning Electron Microscope (SEM) analysis were compared manually and not using typical software like 'ImageJ.' This was due to lack of time, access to the labs, and lack of training as a direct impact of Covid-19. The typical diameter of primary individual particles was measured manually, by 'eye' from multiple SEM images generated of the PM collected at that load/condition. Hence, there is a degree of error associated with this manual technique. Therefore, the quoted individual primary particle size diameter range at the Andersen impaction stage should be considered as a guide only.

Testing of each syngas blend generated its unique diesel baseline data (due to the large time gaps between analysis). Hence, in total, six diesel baseline runs were evaluated for the Andersen testing (in duplicate for each syngas blend). All the images generated from the SEM analysis of the PM collected during the diesel baseline runs were collated and compared. The diameter of the individual primary particle was measured from the images generated. The individual primary particles used for measurements were those with clearly defined boundaries, which were circular shaped nucleation mode particles. These primary particles were randomly chosen for measurement (to remove bias) based on the above criteria. Examples of the individual primary particles selected for diameter measurement are shown in the SEM image depicted in Fig. 7.37.

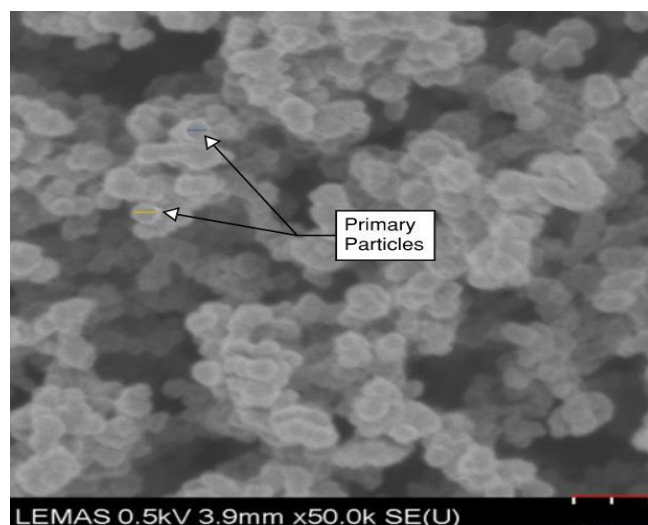


**Fig 7-37 Examples of some primary particles selected for diameter measurements from the SEM image of the particulate matter**

Diesel baseline images were produced for the particulate matter collected for the impactor stages corresponding to 0-0.43 $\mu$ m and 0.43-0.65 $\mu$ m. Examples of typical SEM images of the diesel particulate matter produced from the impactor size 0- 0.43 $\mu$ m are shown in Figs. 7.38 - 7.40. Typical SEM images of the diesel particulate matter produced from the impactor size 0.43 - 0.65  $\mu$ m are shown in Figs. 7.41- 7.43. For reference, the impactor size is given in brackets underneath each image.

All the SEM images for the DBL runs show that the primary particles are roughly spherical and typically clustered together to form agglomerate shaped clusters. The SEM image which depicts the SGA DBL soot collected for the Andersen stage equivalent to particle size ranging from 0.43-0.65 $\mu$ m (Fig. 7.41) stands out as the primary particles here appear more globular in shape, however, the resolution of the image is not so clear.

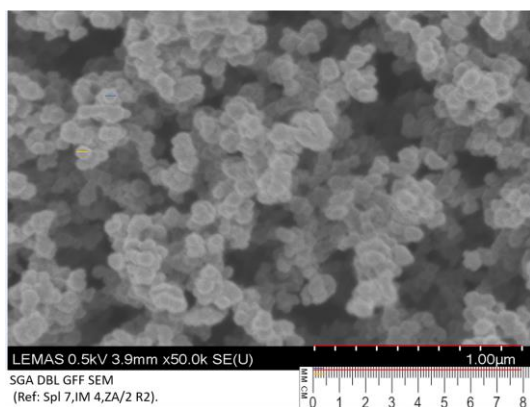


**Fig 7-38 SEM ( $\leq 0.43\mu$ m) SGA DBL**

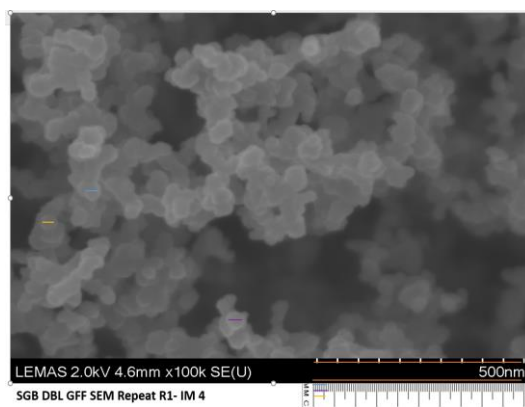


**Fig 7-39 SEM ( $\leq 0.43\mu$ m) SGB DBL**

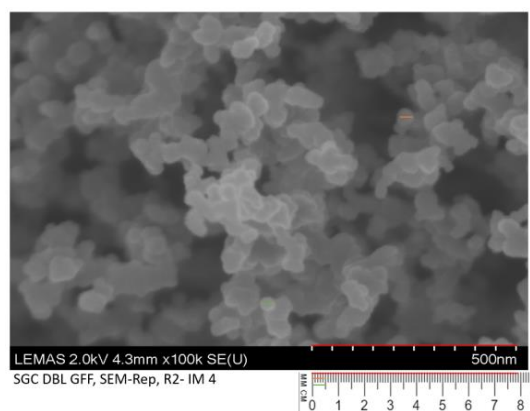


**Fig 7-40 SEM ( $\leq 0.43\mu$ m) SGC DBL**

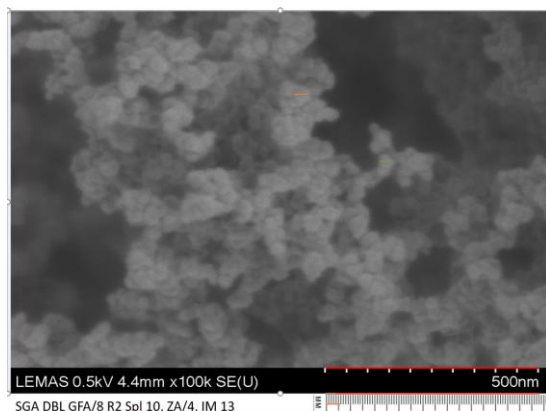


**Fig 7-41 SEM (0.43-0.65 $\mu$ m) SGA DBL**

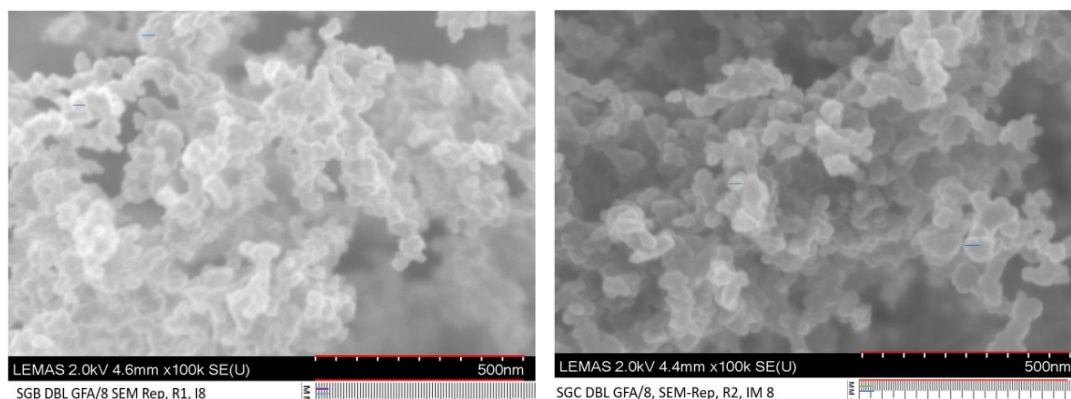


**Fig 7-42 SEM (0.43-0.65 $\mu$ m) SGB DBL Fig 7-43 SEM (0.43-0.65 $\mu$ m) SGC DBL**

The range of the diameter of the primary particles measured from the SEM images at each impaction stage for each diesel baseline run for each syngas blend has been summarised in Table 7.15.

**Table 7-15 Summary of the range of the measured diameter of the individual primary particle for DBL at each impaction stage per syngas blend**

	Andersen stage: 0 -0.43 $\mu$ m	Andersen stage: 0.43 -0.65 $\mu$ m
<b>The diameter range of the primary particle size (nm) impacted</b>		
<b>SGA</b>	44 - 60	26 -69
<b>SGB</b>	30 - 44	30 - 42
<b>SGC</b>	29 - 44	30 - 42

It is expected that the typical particle size range of the primary particle measured at the impaction stage of 0.43-0.65 $\mu$ m would see a larger diameter in comparison to the stage of 0-0.43 $\mu$ m, however, this is not the case as shown in Table 7.15. This could be due to the level of error/uncertainty associated with the SEM technique in terms of scanning a representative sample, (especially at the impaction stage of 0.43-0.65 $\mu$ m where less mass was collected), in addition, the error associated with the manual measurement. Hence, the quoted individual primary particle size diameter range at the Andersen impaction stage should be considered as a guide only.

Table 7.15 also shows that the diesel baseline data for SGA in terms of the diameter range of the primary particle collected at each impaction stage of interest covers a wider size range at both stages in comparison to the other two syngas blends. This, alongside the difference in PM<sub>10</sub> mass collected for SGA, is potentially linked. The reason for this is unknown and could be linked to the run-in period of the newly installed engine, or the use of fresh lubricating oil for SGA.

The SEM images corresponding to the diesel baseline runs (as depicted in Figs. 7.38- 7.43) all show that the individual particles have agglomerated to form clusters. The diameter of the clusters was not reported; trial and error during the analysis stage revealed that defining the boundaries of a cluster was very subjective using the manual technique employed here. Regardless, the diameter of these clusters is clearly <650 nm, as expected, based on the corresponding Andersen impaction stages. Also, regarding the DMS particle number size distribution data for the diesel baseline, the peak particle diameter quoted in Tables 7.1-7.3 is ~65nm. This corresponds to the primary particle diameter size calculated from these SEM images (as shown in Table 7.15) which quotes a range of 26-69 nm, hence showing a correlation.

#### 7.4.3.2 SEM particle size range comparison for dual fuel combustion

The diameter range of the primary particle measured using the SEM images at each impaction stage has been summarised in Tables 7.16 - 7.18 per syngas blend. As discussed earlier, this data should be used as a general guide only.

**Table 7-16 The diameter range of the primary particle for SGA**

Andersen stage:	The diameter range of the primary particle (nm) at GEF:		
	0/DBL	10%	22%
0 - 0.43 $\mu$ m	44-60	43-64	41-67
0.43 -0.65 $\mu$ m	26-69	31-42	34-49

**Table 7-17 The diameter range of the primary particles for SGB**

Andersen stage:	The diameter range of the primary particle (nm) at GEF:		
	0/DBL	10%	22%
0 - 0.43 $\mu$ m	30-44	32-51	32-43
0.43 -0.65 $\mu$ m	30-42	40-48	34-52

**Table 7-18 The diameter range of the primary particles for SGC**

Andersen stage:	The diameter range of the primary particle (nm) at GEF:		
	0/DBL	10%	22%
0 - 0.43 $\mu$ m	29-44	33-43	30-44
0.43 -0.65 $\mu$ m	30-42	24-47	23-45

At both Andersen impaction stages; the diameter of the primary particle size is not affected by increasing syngas with one exception: SGA. For SGA, at the Andersen impaction stage of 0.43-0.65 $\mu\text{m}$ , the size of the primary particle diameter is reduced in dual fuel mode. Typical SEM images from DBL, 10, and 22% GEF have been compared for SGA for both Andersen impaction stages in Figs. 7.44 -7.49.

Figs. 7.44 -7.49 show that the morphology of the individual primary particle appears unaffected with increasing SGA addition at the impaction stage of  $\leq 0.43\mu\text{m}$ . However, at the impaction stage which covers the particle size of 0.43-0.65 $\mu\text{m}$ , the individual primary particle diameter particle appears to reduce and become more spherical as a result of the introduction of SGA, this is reflective of the typical diameter size ranges quoted in Table 7.16 which ranges from 26-69 nm.

The diameter of the clusters apparent on the SEM images for all dual fuel combustion (see Figs. 7.44 - 7.61) was not measured for the same reason mentioned earlier for the diesel baseline images. This was due to the subjective definition of the boundaries of the clusters evident. However, it is visible that the overall diameter of these clusters is  $<650$  nm as expected, based on the associated Andersen impaction stages.

Also, regarding the DMS PNSD data for SGA, SGB, and SGC (see Tables 7.1 – 7.3), the peak particle diameter quoted is  $\sim 65$  nm at these testing conditions. This broadly corresponds to the primary particle diameter size calculated from the SEM images (as shown in Tables 7.16 -7.18) which ranges from 23-69 nm, thus showing a degree of correlation.

### 7.4.3.3 Morphology of the PM collected at each Andersen impaction stage

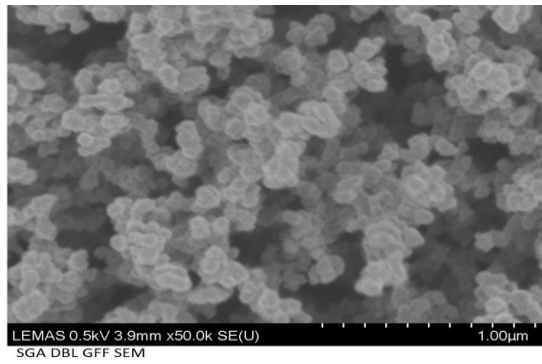


Fig 7-44. DBL SGA (≤0.43μm)

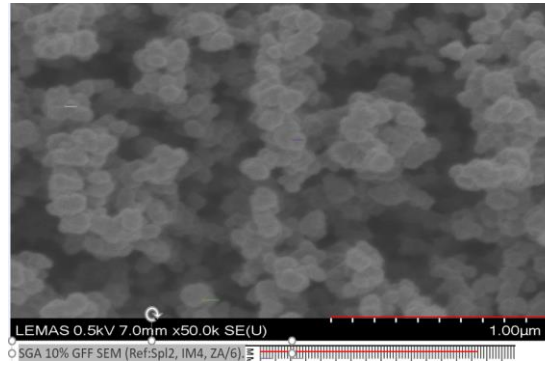


Fig 7-45 10% GEF SGA (≤0.43μm)

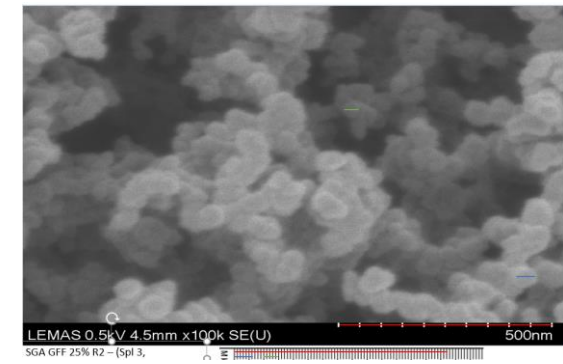


Fig 7-46 22% GEF SGA (≤0.43μm)

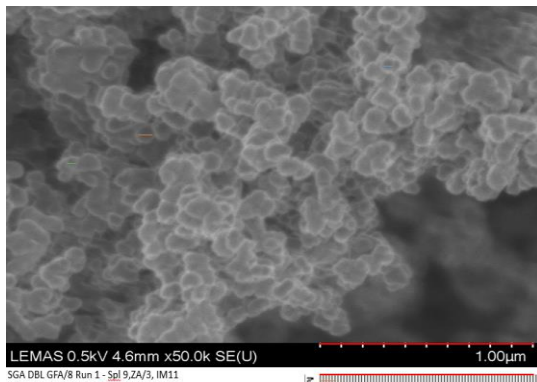


Fig 7-47 DBL SGA (0.43-0.65μm)

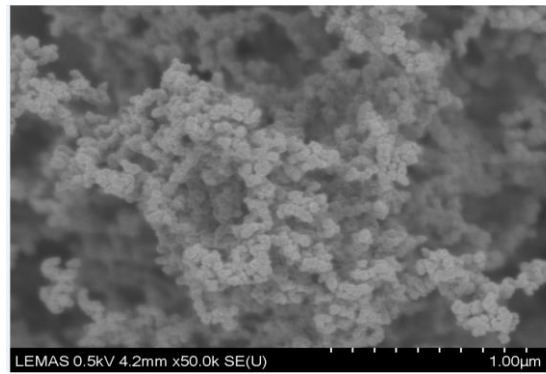


Fig 7-48 10% GEF SGA (0.43-0.65μm)

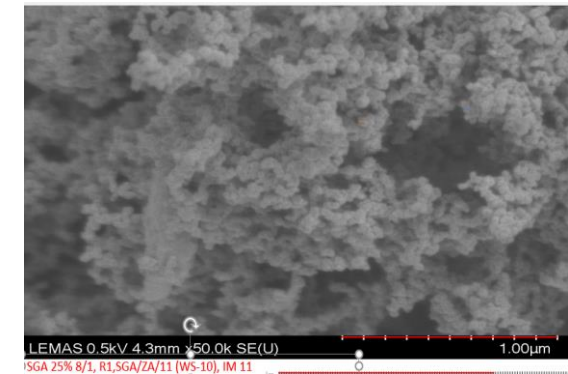
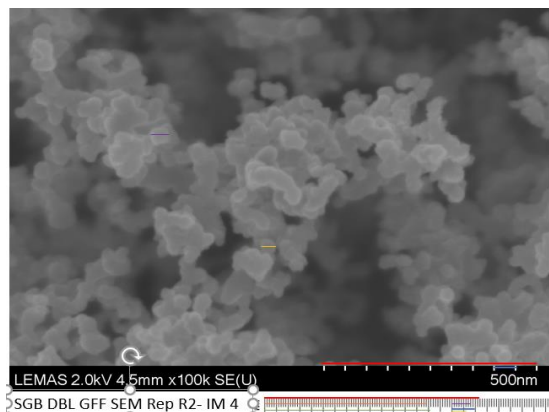
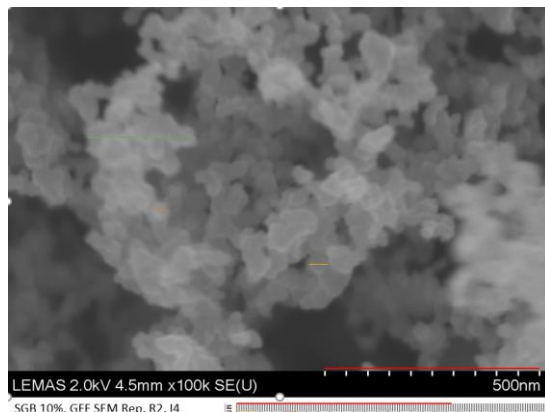


Fig 7-49 22% GEF SGA (0.43-0.65μm)

Typical SEM images from DBL, 10, and 22% GEF have been compared for SGB for both Andersen impaction stages in Figs. 7.50 -7.55.



**Fig 7-50 DBL SGB ( $\leq 0.43\mu\text{m}$ )**



**Fig 7-51 10% GEF SGB ( $\leq 0.43\mu\text{m}$ )**

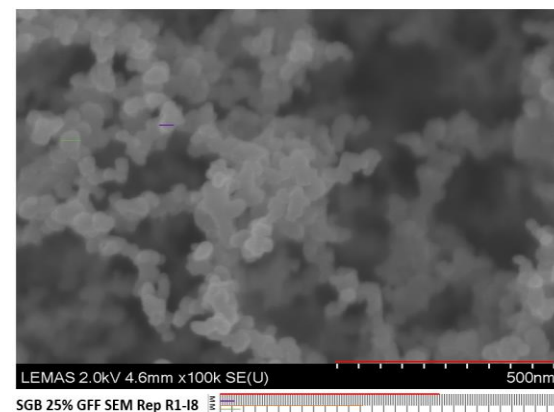


**Fig 7-52 22% GEF SGB ( $\leq 0.43\mu\text{m}$ )**

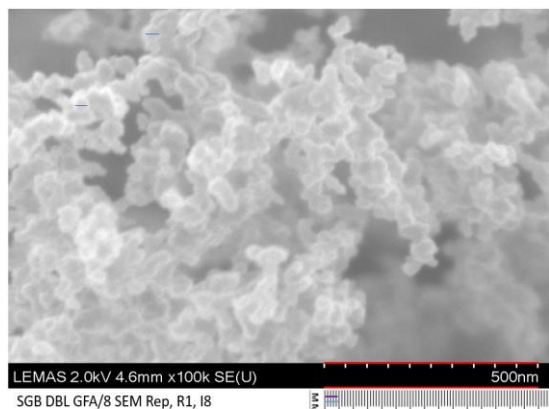


**Fig 7-53 DBL SGB (0.43-0.65 $\mu\text{m}$ )**

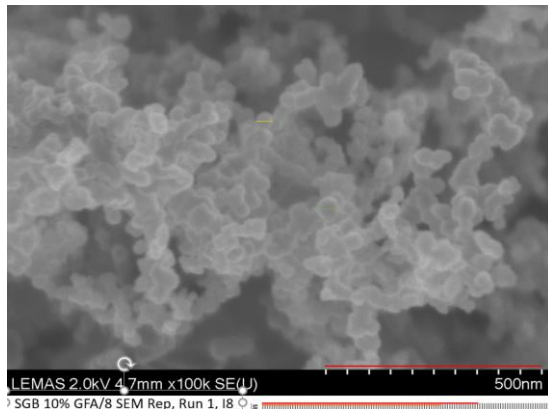


**Fig 7-54 10% GEF SGB (0.43-0.65 $\mu\text{m}$ )**

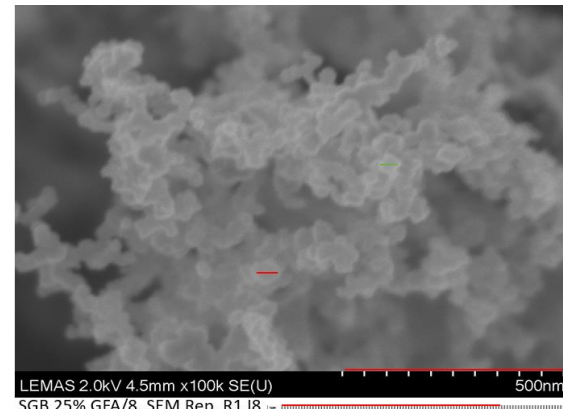


**Fig 7-55 22% GEF SGB (0.43-0.65 $\mu\text{m}$ )**

The shape and the size of the individual primary particle appear unaffected with increasing SGB addition at both Andersen impaction stages, this is reflective of the primary particle diameter range quoted in Table 7.17. Typical SEM images from DBL, 10, and 22% GEF have been compared for SGC for both Andersen impaction stages in Figs. 7.56 -7.61.

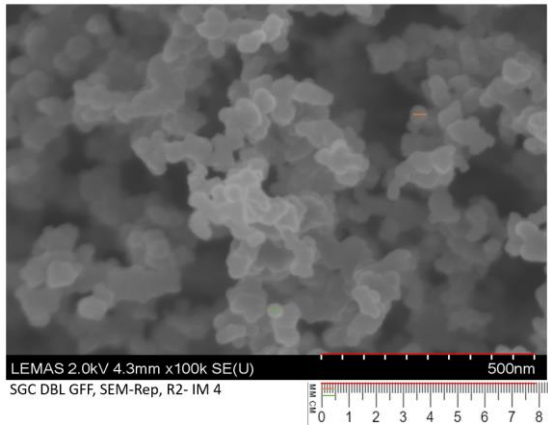


**Fig 7-56 DBL SGC (0-0.43µm)**

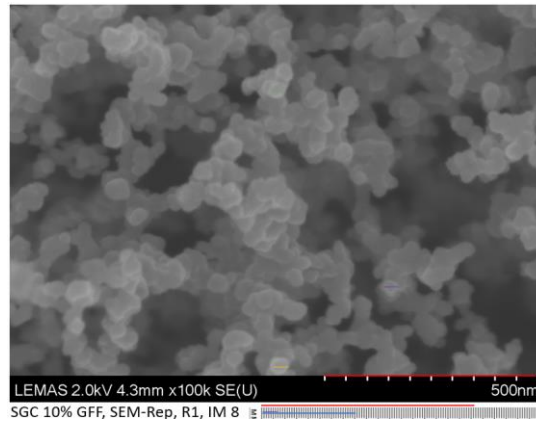


**Fig 7-57 10% GEF SGC (0-0.43µm)**

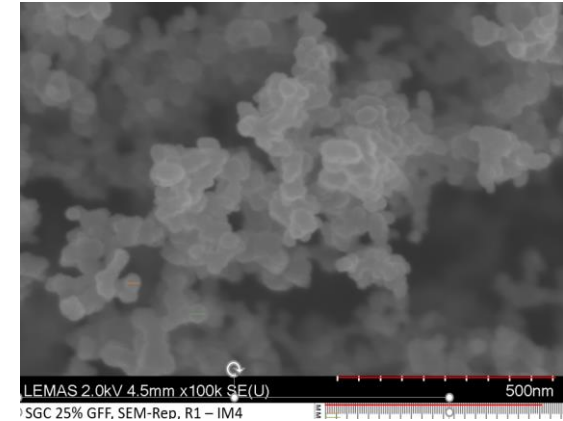


**Fig 7-58 22% GEF SGC (0-0.43µm)**

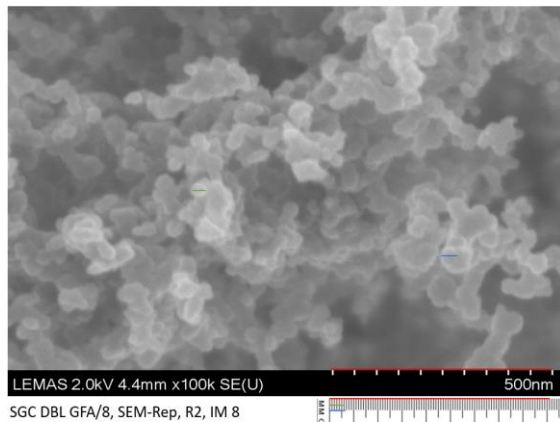


**Fig 7-59 DBL SGC (0.43-0.65µm)**

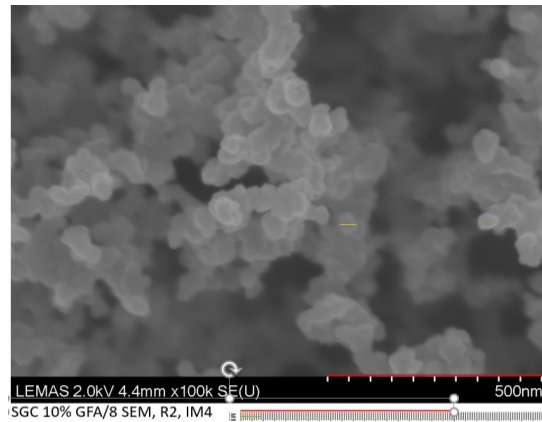


**Fig 7-60 10% GEF SGC (0.43-0.65µm)**

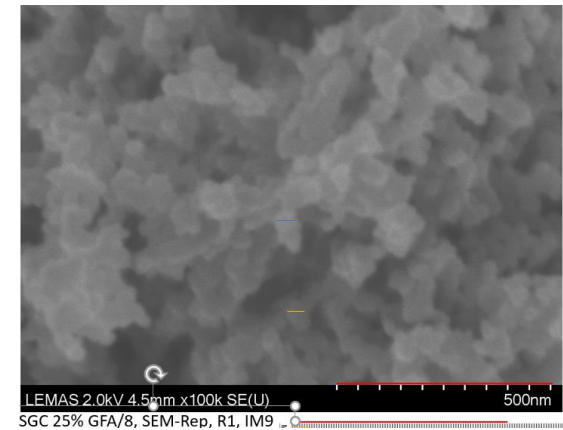


**Fig 7-61 22% GEF SGC (0.43-0.65µm)**

The morphology of the individual primary particle appears unaffected with increasing SGC addition at both the Andersen impaction stages, this is reflective of the typical diameter size ranges quoted in Table 7.18.

## 7.5 Overall summary

From the analysis of the PM mass and emissions in this chapter, the following can be summarised:

- At all engine loads, apart from 30%, there is a reduction in the TPNC in dual fuel mode.
- At 30% engine load, the TPNC increases for all dual fuel modes evaluated due to the increase of nanoparticles.
- At full engine load, at 46% GEF, the TPNC is reduced by 12 to 18% for syngas-diesel combustion, and biogas, by 48%.
- Linear regression analysis indicates that there is a strong correlation between the TPNC and the diesel fuel BSFC (in kg/kWh) at engine loads greater than >50%. The lower the BSFC, the lower the corresponding TPNC data.
- The patterns of the PNSD profiles remain unaffected with increasing GEF at full and medium-high engine loads.
- At 53% engine load, the PNSD curve changes shape, this change is dependent on the gas/diesel blend used. A bimodal PNSD trend is first seen at this load whereby a reduction in the accumulation mode particles is seen alongside an increase in the nucleation mode particles.
- At 30% engine load, the PNSD changes for all dual fuel blends were evaluated. The change in the shape and the trend are dependent on the gas/diesel blend evaluated. For SGA, a clear bimodal trend becomes apparent with increasing GEF. For SGB, SGC, and biogas, any bimodal trend seen at an earlier engine load is lost, and a monomodal trend results potentially due to the large increase in the nucleation mode particles which causes the two modes to merge to produce a large single broad peak.
- The mass concentration ( $\text{mg}/\text{m}^3$ ) of the PM collected for all PM fractions all decreased in dual fuel mode relative to the diesel baseline due to the reduction in the diesel fuel and the longer ID experienced in dual fuel combustion.
- SGC did not result in the largest reduction in the  $\text{PM}_{10}$  EI mass data at both % gas energy fractions assessed potentially due to the influence of the higher hydrogen content of SGC not being realised at these testing conditions.

- The range of PM<sub>10</sub> PM EI reductions (g/MJ fuel) seen for syngas-diesel combustion ranged from 8 to 40% at a full engine load, using a GEF of 22%.
- In terms of PM<sub>10</sub>, syngas-diesel fuel combustion produced a smaller mass of ultrafine particulate matter in comparison to diesel.
- TGA data showed that for all syngas dual fuel blends evaluated, the PM mass collected at the backup filter stage (particle size 0-0.43µm) reduced accordingly, as expected.
- Cross-comparison of the % change in TGA data showed that at 10% GEF, SGA had the highest % reduction in the VOF fraction, and at 22% GEF, SGB did. Further work is required to determine the cause.
- EDX qualitative analysis showed the soot to contain (aside from C), species that are derived from the engine oil and the engine wear and tear.
- SEM analysis showed that for the impaction stage correlating to the particle size range of ≤0.43µm, the morphology of the individual primary particle appears unaffected with increasing syngas addition.
- SEM analysis showed that for the impaction stage correlating to the particle size range of 0.43 to 0.7µm, the morphology of the individual primary particle appears unaffected with increasing syngas addition for SGB and SGC. However, for SGA, the SEM analysis of the individual primary particle diameter particle appears to reduce and become more spherically shaped upon the introduction of SGA.

## Chapter 8 Conclusions

### 8.1 Major findings from this study

The work conducted for this thesis covered two aspects: calculation of the net electricity generation potential from the biomass residues for the United Republic of Tanzania (Tanzania), and Uganda, for the base year of 2019.

The second focussed on investigating the impact of dual fuel combustion when using either syngas/biogas with diesel in a dual fuel engine when considering engine combustion performance and emissions. The objective of this work was to answer the research questions that were previously summarised in Chapter 2 (see p82), these are reiterated below.

1. What is the net electrical generating potential (when considering utilising gasification and AD) coupled with a diesel genset of the selected biomass waste streams identified in The United Republic of Tanzania and Uganda, in comparison to their national electricity production?
2. How does syngas-diesel dual fuel combustion affect engine performance and emissions, when compared to diesel?
3. What is the impact of changing the hydrogen content of the simulated syngas on the engine performance and emissions?
4. How will biogas-diesel dual fuel combustion affect engine performance and emissions, when compared to diesel?
5. Are there any GHG savings (CO<sub>2</sub> equivalent) arising from the optimum dual fuel combustion conditions identified from the reduction in diesel fuel usage?

Research question 1 has been addressed in Chapter 4, and the remaining research questions (2 to 5), have been addressed in Chapters 5 to 7. A summary of the research findings and the contributions to this field are highlighted below, alongside a general conclusion that summarises the overall project.

### **8.1.1 Net electricity generation potential from biomass residues**

Chapter 4 investigated the net electricity generation potential from the biomass residues quantified from the biomass waste assessments conducted for Tanzania and Uganda for the base year of 2019. From these assessments, it was highlighted that both these countries had a huge energy potential available from 'dry' biomass waste, with the majority being derived from agricultural residues. This work found that both countries had a plentiful supply of biomass residues. For Tanzania, the biomass waste had an energy potential of 374 PJ; a value of 385 PJ was calculated for Tanzania for the base year of 2018 using the same methodology [59]. For Uganda, biomass waste was found to have an energy potential of 211 PJ. These findings were in line with most findings available in the open literature regarding the energy potential of waste biomass in this region which is considered underutilised and unexploited.

Next, detailed calculations were conducted to determine the net electricity generating potential from these biomass residues using conversion techniques of gasification and/or anaerobic digestion to generate a gaseous fuel that could be used to substitute diesel fuel in an adapted diesel genset engine for small-scale electricity generation. Conservative calculations showed that the net electricity generation potential from the combined biomass residues (after accounting for transmission and distribution losses) for both these countries exceeded their national electricity production for the base year of 2019 and ranged between 1.05 to 1.10. This highlighted that the biomass residues available in these countries are theoretically capable of generating sustainable energy which can lead to a reduction and dependency on fossil fuels, whilst providing an alternative waste management tool and increasing access to electricity by widening fuel choices. No comparable combined study such as this was available in the open literature for either of these two countries.

### 8.1.2 The impact of syngas-diesel dual fuel combustion

Chapters 5 to 7 considered the impact of dual fuel combustion when utilising syngas-diesel relative to diesel. The engine combustion performance and the resulting emissions in dual fuel mode were investigated at various engine loads and % syngas substitution values. The dual fuel combustion characteristics were compared to the diesel baseline engine combustion performance.

Chapter 5 of this thesis demonstrated that the engine combustion performance was adversely affected during dual fuel combustion relative to the diesel baseline. The BTE values decreased with increasing syngas fraction at all engine loads evaluated. At full engine load, at the maximum gas energy fraction (GEF) evaluated (which was 46%), a 10-13% reduction in BTE was noted in dual fuel mode relative to the diesel baseline (the reduction is syngas blend dependent). This trend of the reduced BTE for syngas-diesel dual fuel combustion was supported by higher BSEC values.

In addition, longer injection delays, lower peak cylinder temperatures [117], lower peak pressures, and delayed peak pressures (which occurred further away from the top dead centre in CAD) were experienced in dual fuel mode relative to the diesel baseline, all of which resulted in reduced efficiency.

Dual fuel operation produced higher exhaust gas temperatures relative to the diesel baseline which were indicative of a lack of adequate combustion time between diesel and syngas due to longer injection delays [142]. The reduced engine combustion performance and efficiency noted in dual fuel combustion were found to be broadly in line with most of the previous research conducted in this field.

Chapter 6 concluded that the specific emissions (SE) for the total hydrocarbons (THCs), methane (CH<sub>4</sub>), and carbon monoxide (CO), all increased considerably in dual fuel mode, whereas the benefits of dual fuel combustion were found in the reduction in the specific emissions of nitrogen oxides (NO<sub>x</sub>). A reduction ranging from 16 to 45% in the NO<sub>x</sub> SE data was noted in syngas-diesel consumption at a full engine load at the maximum GEF evaluated (46%). A range is quoted as this was syngas blend dependent. The raw emissions (in ppm) of nitrogen monoxide (NO) also decreased in dual fuel mode relative to pure diesel.

The other benefit of dual fuel mode combustion was the reduction in diesel fuel consumption. A 35-39% mass reduction of diesel was observed at maximum engine load at the maximum syngas substitution value evaluated (46%) relative to the diesel baseline (the range is syngas blend dependent). The other associated benefit of the reduction in diesel consumption was the corresponding reductions in GHG emissions (expressed as CO<sub>2</sub> equivalent).

The NO<sub>2</sub>/NO<sub>x</sub> ratio (based on raw emissions in ppm) was found to be unchanged/similar at full engine load for both modes of combustion. For the remaining engine loads evaluated, this ratio was always higher in dual fuel mode relative to the diesel baseline.

Specific emissions relating to CO<sub>2</sub> were found to be greater in syngas-diesel dual fuel mode relative to the diesel baseline. An increase in the range of 36 to 47% was noted at full engine load, at the maximum GEF evaluated (the range is syngas blend dependent). CO<sub>2</sub> is a product of the combustion of diesel, the syngas components: methane and CO, this combined with the CO<sub>2</sub> component of the syngas passing through, all resulted in an overall increase in the CO<sub>2</sub> emissions relative to the diesel baseline.

One other drawback of dual fuel mode combustion was found from the analysis of the exhaust gases using FT-IR. Small increases were observed in the ethanol and formaldehyde concentration in dual fuel mode relative to the diesel baseline. Also, the methane slippage calculated for syngas-diesel dual fuel combustion at full engine load using a GEF of 22% ranged between 8 to 11% (varied per syngas blend). This could not be compared at the highest GEF due to the lack of data arising from the FT-IR availability.

In terms of PM emissions, Chapter 7 concluded that dual fuel combustion produced lower particle number emissions expressed as total particle number concentration (TPNC) in units of dN/dlogDp, relative to the diesel baseline at engine loads >50%. At full engine load, and a GEF of 46%, using syngas-diesel led to a reduction ranging from 12 to 18% in the TPNC data relative to diesel (the range quoted is syngas blend dependent).

A linear relationship was found between the reduction of the TPNC data and the reduction in diesel fuel consumption in dual fuel combustion. The particle number size distribution (PNSD) profile of the particle number emissions also changed in dual fuel combustion at low loads (30 and 52% engine loads), for higher loads the PNSD profiles were unaffected.

Chapter 7 also concluded that syngas-diesel combustion produced a larger mass of particulate matter ranging in size from 10 – 0.43  $\mu\text{m}$  relative to the diesel baseline at a full engine load using a GEF of 22%. This was not evaluated at the highest GEF due to economic limitations associated with the project.

A further benefit of dual fuel combustion found was the reduction in the  $\text{PM}_{10}$  mass collected (which included  $\text{PM}_{10}$ ,  $\text{PM}_{2.1}$ , and  $\text{PM}_{0.4}$ ). The mass of the PM decreased with increasing syngas fraction. A reduction ranging between 12 and 35% was noted in the  $\text{PM}_{10}$  mass specific emission data (PM SE in g/kWh) at a full engine load using a GEF of 22% (the range is syngas blend dependent).

To the best of the author's knowledge, this is one of the first syngas-diesel dual fuel combustion study that includes a comprehensive study of the engine combustion parameters and analyses a full range of exhaust emissions using simulated syngas which mimics the composition of gasifier syngas in a 3,000 RPM speed engine and studies the impact of changing the hydrogen content of the syngas.

### **8.1.3 The impact of changing the hydrogen content of the syngas**

The impact of changing the hydrogen content of the syngas was also investigated in terms of engine combustion performance and emissions. It was found that the syngas with the highest hydrogen content (SGC, 25% vol  $\text{H}_2$ ), exhibited enhanced combustion performance in comparison to the other two syngas blends (SGA, 15% vol  $\text{H}_2$ , and SGB, 20% vol  $\text{H}_2$ ) at engine loads >55%.

SGC-diesel dual fuel combustion produced shorter ignition delays, higher peak pressures, and peak pressures that were less delayed, (i.e., closer to TDC) in comparison to the other syngas blends, as well as higher exhaust gas temperatures (at 77% engine load). At engine loads >55%, SGC had the lowest emissions expressed as EI for THC and CO but had the highest for  $\text{NO}_x$ . The  $\text{CO}_2$  emissions were found to be similar to the other two syngas blends evaluated.

The raw emissions of methane and formaldehyde (in ppm) were also found to be lower for SGC in comparison to the other two syngas blends at engine loads >55%. At engine loads <55%, SGC did not consistently exhibit improved combustion characteristics in comparison to the other syngas blends.

Chapter 7 demonstrated that at full load, SGC did not produce a lower amount of PM relative to the other syngas blends as expected based on the theory of a higher hydrogen content results in higher OH radical concentrations which promote the oxidation of PM. Further work is recommended to investigate this.

#### **8.1.4 The impact of biogas-diesel dual fuel combustion**

Chapter 5 of this thesis demonstrated that the engine combustion performance was adversely affected in dual fuel combustion when using biogas-diesel relative to pure diesel. Dual fuel mode reported lower BTE values which decreased with increasing biogas fraction at all engine loads evaluated. A 9% reduction in BTE was observed relative to the diesel baseline at a full engine load at the maximum GEF evaluated (48%). This reduction in BTE was similar to some of the trends reported in the literature and opposite to others.

However, a comparison of other engine performance parameters revealed that biogas-diesel combustion resulted in longer ignition delays, lower peak pressures, and delayed peak pressures which were further away from TDC, when compared to the diesel baseline, thus the reduction in the dual fuel BTE was more understandable.

The resulting emissions were compared in Chapter 6 and concluded that the specific emissions (SE) for THC and CO increased, as did the NO<sub>2</sub>/NO<sub>x</sub> ratio (based on ppm data) in dual fuel mode, whereas the benefits of dual fuel combustion were found in the reduction of SE of NO<sub>x</sub>, and the NO emissions (in ppm). A 39% reduction in the specific emissions of NO<sub>x</sub> was noted at full engine load at the maximum GEF evaluated (48% GEF). The other reported benefit of dual fuel mode combustion was the reduction in diesel fuel consumption and the associated CO<sub>2</sub> equivalent reductions arising from the reduced diesel consumption. A 42% mass reduction of diesel fuel was noted for biogas-diesel at a full engine load using a GEF of 48% relative to the diesel baseline.

The SE corresponding to the CO<sub>2</sub> was found to be higher in dual fuel produced from the combustion of diesel. The methane content of the biogas and the 50% CO<sub>2</sub> content of the biogas composition, all combined, contributed to this. A 33% increase in the SE CO<sub>2</sub> data was observed at a full engine load at a 48% GEF relative to the diesel baseline.

One other drawback of dual fuel mode combustion was found from the analysis of the exhaust gases using FT-IR. An increase was observed in the methane and formaldehyde concentration in dual fuel mode relative to the diesel baseline. The increase in the methane was a direct result of the methane slippage occurring which peaked between 10 - 13% GEF depending on the engine load. At full engine load at the maximum GEF evaluated, a 4% methane slippage was calculated.

Chapter 7 concluded that dual fuel combustion produced lower particle number emissions with a lower TPNC relative to the diesel baseline at engine loads >50%. A 48% reduction in TPNC was noted at full engine load using the maximum GEF evaluated. A linear relationship was found between the reduction of the TPNC data and the reduction in the diesel fuel consumption in dual fuel combustion for all engine loads except for 30%. The PNSD profiles of the particle number emissions also changed in dual fuel combustion at low loads (30 and 52% engine loads). Analysis of the PM mass was not assessed for biogas-diesel combustion due to the impact of Covid-19; this limited the scope of the experimental work.

To the best of the author's knowledge, this is one of the first dual fuel combustion studies using simulated biogas which includes a comprehensive study of the engine combustion parameters and analyses a full range of exhaust emissions in a 3,000 RPM speed engine, especially considering the particle number emissions.

## **8.2 Concluding remarks**

The United Republic of Tanzania and Uganda both have a plentiful supply of biomass residues that can be used to produce gaseous fuel using gasification and/or anaerobic digestion. When this gaseous fuel is used in a dual fuel diesel genset, (using simulated syngas or biogas), this led to a marked reduction in the BTE, which resulted in increased THC and CO emissions relative to the diesel baseline.

The advantage seen in both dual fuel modes was the reduction in the emissions of NO<sub>x</sub> and PM relative to the diesel baseline. Further advantages of dual fuel mode combustion were the marked reduction in diesel fuel consumption and the associated reduction in CO<sub>2</sub> emissions based on this diesel fuel reduction.

Any CO<sub>2</sub> arising directly from the syngas or biogas combustion was considered carbon neutral due to the gaseous fuel originating from biomass residues.

As stated in Chapter 1, the major emissions highlighted from using fossil fuel gensets for energy generation in Africa include NO<sub>x</sub>, (the most dominant emission), and PM<sub>2.5</sub>. This study has demonstrated that the PM<sub>10</sub> and PM<sub>2.1</sub> emissions are reduced in syngas-diesel dual fuel combustion, this was not assessed for biogas-diesel.

Also, in dual fuel combustion using syngas and biogas, the particle number emissions (in terms of TPNC) and the NO<sub>x</sub> emissions were reduced.

In conclusion, the utilisation of syngas or biogas in dual fuel combustion in diesel gensets helps to reduce the dominant NO<sub>x</sub> and PM emissions. The increase in the THC and CO emissions can be mitigated by using a DOC which can be retrofitted into diesel gensets to reduce these emissions. Alternatively, increasing the H<sub>2</sub> content of the syngas composition will also reduce the THC and CO emissions.

Overall, using a gaseous fuel derived from biomass residues, which when utilised in dual fuel mode in diesel gensets, leads to a widening of fuel choices, potentially leading to an increase in rural electrification rates as the access to energy is increased due to the reduced reliance on diesel fuel. Also, the biogas produced from biomass residues can be used as a cooking fuel, mitigating the health and pollution risks associated with the current problematic cooking fuel sources in this region.

### **8.3 Limitations and future work**

The limitations present in this project alongside recommendations for future work will be discussed here.

#### **8.3.1 Net electricity generating potential**

Various recommendations and assumptions were made when calculating the net electricity generating potential of the biomass residues and these are discussed in detail within Chapter 4.

However, to fully explore the potential of these findings reported in Chapter 4, i.e., to fully understand the viability of using these biomass residues in this manner, more work is required to fully understand the supply and demand of these biomass residues in this region.

Further research is required to determine which conversions technology (gasification / anaerobic digestion) will be best suited for which community based on the local availability/supply logistics of these biomass residue streams which takes into consideration any competing uses, the population density, any specific socio-economic barriers which may be region specific, and any government incentives available which can influence the uptake in this region.

### **8.3.2 Dual fuel combustion (syngas-diesel & biogas-diesel)**

It was envisaged that the HRR data would be calculated and studied for all the dual fuel combustion evaluated and compared to the diesel baseline data. As mentioned in the Covid-19 impact statement, due to the delay in the lab work, this was not completed due to time constraints. Hence, it is recommended that is completed for all syngas and biogas dual fuel combustion. This will allow the study of the in-cylinder combustion process and the various combustion phases, thus identifying the changes occurring as a result of the increasing hydrogen content of the syngas blends. Some work has been conducted on the HRR study of dual fuel combustion using SGA [117], but this did not include the highest GEF used at a full engine load of 48%.

The specific emissions corresponding to the CO<sub>2</sub> were found to be greater in dual fuel mode, however, the CO<sub>2</sub> arising directly from the syngas or biogas combustion is considered carbon neutral due to its origins; utilising these residues in this manner mitigates the emissions arising from the usual disposal methods. Further work is required to understand and quantify the carbon footprint of the whole dual fuel small-scale electricity generating process which encompasses both gasification and AD. Also, economic analysis is required to fully understand and compare the cost of producing electricity in this manner.

The ethanol emissions (in ppm) were found to be higher in dual fuel mode at higher loads for syngas-diesel dual fuel combustion, these were found to increase with increasing syngas addition. Further investigation is required to be able to understand the cause of this phenomenon observed. Ordinarily, this would have been investigated but due to the impact of Covid-19 and the resulting time reduction, this was not possible.

The effects on the PM mass emissions were only considered at full load using 10 and 22% GEF in syngas diesel fuel combustion. Further investigation is recommended in this area which involves evaluating the full impact of increasing gas energy fractions across all the GEFs evaluated, (including 38 and 46% GEF). This was not conducted due to the large volume of gas required for these tests, it was not economically viable given the financial restraints of this project. Conducting this further work may explain why SGA-diesel combustion saw the largest decrease in PM mass relative to the other syngas blends (and not SGC).

The PM mass testing should also have been conducted for biogas-diesel dual-fuel combustion at full load for the full range of gas energy fractions evaluated. This was not conducted due to the time constraints arising from Covid-19.

Exhaust gas speciation using FT-IR was conducted for dual fuel combustion. For SGA, the analysis conducted using this instrument was limited due to equipment availability and budget constraints during that period. Ideally, analysis of the exhaust gas emissions arising from SGA-diesel combustion should have been analysed using the FT-IR across the full range of gas energy fractions evaluated at full engine load; not just 10, and 22%. It is also recommended that the FT-IR findings from this study should be validated using standard calibration gas bottles to provide further assurance in addition to the existing FT-IR calibration data.

Further work is also required to explore the impact on the resulting THC and CO emissions from dual-fuel combustion using syngas and biogas with the use of a DOC present in the exhaust system.

The maximum gas energy fraction evaluated was limited by the high price of the simulated biogas/syngas. The maximum GEF whereby stable engine performance is achieved in dual fuel mode may be greater than the 46-48% range evaluated; further work is required to determine this.

Finally, the synthetic syngas used was free of tars, however, real syngas produced from the gasification process will contain a small concentration of residual tars, even after clean-up. Further work was planned to determine the impact of introducing 'synthetic tars' during dual fuel combustion on the resulting engine performance and emissions. Again, this was not conducted due to time constraints arising from Covid-19. Future work would be beneficial to determine the impact of synthetic tars on dual fuel combustion.

## Appendix A Data related to Chapter 4

**Table A-1 Raw data of the softwood tree species used for the basic density calculation for Tanzania**

Species Name (Common/Scientific)	OD wt/Green vol (g/cm <sup>3</sup> )	Source
Slash Pine/Pinus elliottii	0.54	[225]
Caribbean Pine/Pinus caribaea	0.51	[226]
Patula Pine/Pinus patula	0.45	[227]
Khasi Pine/Pinus kesiya	0.45	[228]
Radiata Pine/Pinus radiata	0.41	[229]
African Juniper/Juniperus procera	0.44	[230]
Mexican Cypress/Cupressus lusitanica	0.4	[231]
<b>Average SG</b>	<b>0.457</b>	

**Table A-2 Raw data of the hardwood tree species used for the basic density calculation for Tanzania**

Species Name (Common/Scientific)	OD wt/Green vol (g/cm <sup>3</sup> )	Source
Black Wattle/Acacia mearnsii	0.59	[232]
Australian Blackwood/Acacia melanoxylon	0.54	[233]
Sheaok/Casuarina spp	0.62	[243]
Spanish Cedar/Cedrela odorata	0.38	[234]
Camphor/Cinnamomum camphora	0.43	[235]
Iroko/Chlorophora regia	0.55	[224]
River Red Gum/Eucalyptus camaldulensis	0.67	[236]
Blue Gum/Eucalyptus maidenii	0.68	[237]
Rose Gum/Eucalyptus grandis	0.48	[238]
Southern Silky Oak/Grevillea robusta	0.49	[239]
Olive/Olea capensis	0.72	[240]
Idigbo/Terminalia ivorensis	0.43	[241]
Teak/Tectona grandis	0.55	[242]
<b>Average SG</b>	<b>0.548</b>	

**Table A-3 Raw data of the tree species used for the basic density calculation for government plantations in Uganda (23%)**

Species Name (Common/Scientific)	OD wt/Green Volume (g/cm <sup>3</sup> )	% Species	SG fraction	Source
Caribbean Pine/Pinus caribaea	0.51	<b>75</b>	<b>0.383</b>	[226]
Patula Pine/Pinus patula	0.45	<b>8</b>	<b>0.036</b>	[227]
Ocote Pine/Pinus oocarpa	0.55	<b>6.5</b>	<b>0.036</b>	[245]
Rose Gum/Eucalyptus grandis	0.48	<b>10.5</b>	0.050	[238]
Musizi/Umbrella tree	0.48		0.050	[247]
Mexican Cypress	0.40		0.042	[231]
Monkey puzzle, Chilean pine	0.46		0.048	[246]
Idigbo	0.43		0.045	[241]
Teak/Tectona grandis	0.55		0.058	[242]
Average SG (for 10.5%)	<b>0.47</b>	100		
SG fraction (for 10.5%)			<b>0.049</b>	
<b>Average SG of all the trees found in government plantations in Uganda (23%):</b>			<b>0.503</b>	

**Table A-4 Raw data of the tree species used for the basic density calculation for private plantations in Uganda (77%)**

Species Name (Common/Scientific)	OD wt/Green Volume (g/cm <sup>3</sup> )	% Species	SG fraction	Source
Caribbean Pine/Pinus caribaea	0.51	<b>54</b>	<b>0.2754</b>	[226]
Rose Gum/Eucalyptus grandis	0.48	<b>17</b>	<b>0.0816</b>	[238]
Musizi/Umbrella tree	0.48	<b>29</b>	0.1392	[247]
Patula Pine/Pinus patula	0.45		0.1305	[227]
Ocote Pine/Pinus oocarpa	0.55		0.1595	[245]
Mexican Cypress	0.4		0.116	[231]
Monkey puzzle, Chilean pine	0.46		0.1334	[246]
Idigbo/Terminalia ivorensis	0.43		0.1247	[241]
Teak/Tectona grandis	0.55		0.1595	[242]
Average SG (for 29%)	0.474	100		
SG fraction (for 29%)			<b>0.1375</b>	
<b>Average SG of all the trees found in private plantations in Uganda (77%):</b>			<b>0.495</b>	

**Table A-5 Data sources used for the calculation of the energy potential from livestock**

<b>Animal</b>	<b>FA</b>	<b>(%) DM</b>	<b>VS/DM Ratio</b>	<b>Biogas Yield (m<sup>3</sup>/kg VS)</b>
Cattle–Beef	0.5 [48]	17.44 [48]	0.934 [258]	0.307 [48]
Cattle–Dairy	0.8 [48]	17.44 [48]	0.934 [258]	0.307 [48]
Chicken	0.8 [48]	33.99 [48]	0.465 [258]	0.18 [258]
Pigs	0.8 [48]	35.22 [48]	0.893 [258]	0.217 [48]
Sheep	0.3 [46]	25 [259]	0.912 [258]	0.31 [258]
Goat	0.4 [46]	25 [259]	0.598 [258]	0.31 [258]

## List of References

1. United Nations, *World Population Prospects-Data Booklet*, S.D. Department of Economic and Social Affairs, Editor. 2017.
2. The World Bank. *Access to electricity (% of population)*. 2022 [cited 2022 May]; Available from: <https://data.worldbank.org/indicator/EG.ELC.ACCS.ZS>.
3. The World Bank, *Tracking SDG 7: The Energy Progress Report*, The World Bank Group, Editor. 2021, IRENA: Washington, D.C.
4. The World Bank. *Access to electricity, rural (% of rural population) - Sub-Saharan Africa*. World Bank Global Electrification Database from "Tracking SDG 7: The Energy Progress Report" 2022 [cited 2022 June]; Available from: Access to electricity, rural (% of rural population) - Sub-Saharan Africa World Bank Global Electrification Database from "Tracking SDG 7: The Energy Progress Report".
5. United Nations. *Goal 7: Ensure access to affordable, reliable, sustainable and modern energy for all*. 2019 [cited 2019 12 Jun. 2019]; Available from: <https://unstats.un.org/sdgs/report/2016/goal-07/>.
6. World Bank Group, *The Dirty Footprint of the Broken Grid*, in *The Impacts of Fossil Fuel Back-up Generators in Developing Countries*. 2019, International Finance Corporation, Washington, D.C.,.
7. Zebra, C., Windt, H., Nhumaiio, G., and Faaij, A., *A review of hybrid renewable energy systems in mini-grids for off-grid electrification in developing countries*. *Renewable & sustainable energy reviews*, 2021. **144**: p. 111036 DOI: 10.1016/j.rser.2021.111036.
8. Williams, N.J., Jaramillo, P., Taneja, J., and Ustun, T.S., *Enabling private sector investment in microgrid-based rural electrification in developing countries: A review*. *Renewable & sustainable energy reviews*, 2015. **52**: p. 1268-1281 DOI: 10.1016/j.rser.2015.07.153.

9. Ismail, M.S., Moghavvemi, M., Mahlia, T.M.I., Muttaqi, K.M., and Moghavvemi, S., *Effective utilization of excess energy in standalone hybrid renewable energy systems for improving comfort ability and reducing cost of energy: A review and analysis*. Renewable & sustainable energy reviews, 2015. **42**: p. 726-734 DOI: 10.1016/j.rser.2014.10.051.
10. Stecher, K., Brosowski, A., and Thran, D., *Biomass Potential in Africa*, IEA Bioenergy, Editor. 2013, IRENA, UAE, p. 44.
11. IRENA, *Biofuel Potential in Sub-Saharan Africa: Raising food yields, reducing food waste and utilising residues*, International Renewable Energy Agency, Editor. 2017: Abu Dhabi.
12. The World Bank. *Access to electricity (% of population) - Sub-Saharan Africa*. 2022; Available from: <https://data.worldbank.org/indicator/EG.ELC.ACCS.ZS?locations=ZG>.
13. United Nations Statistics Division. *Human Development Indices: A statistical update 2019 2022* [cited 2022 May 2022]; Available from: <http://data.un.org/DocumentData.aspx?id=419>.
14. The World Bank. *% of the population with access to electricity, total in Tanzania*. 2022 12 Jan.2022; Available from: <https://data.worldbank.org/indicator/EG.ELC.ACCS.ZS?locations=TZ>.
15. The World Bank. *Rural population (% of total population) in Tanzania*. 2022 1 March 2022; Available from: <https://data.worldbank.org/indicator/SP.RUR.TOTL.ZS?locations=TZ>.
16. The World Bank. *Access to electricity, rural (% of rural population) in Tanzania*. 2022 9 Jan 22; Available from: <https://data.worldbank.org/indicator/EG.ELC.ACCS.RU.ZS?locations=TZ>
17. The World Bank. *Access to electricity (% of population) - Uganda*. 2022; Available from: <https://data.worldbank.org/indicator/EG.ELC.ACCS.ZS?locations=UG>.

18. The World Bank. *Rural population (% of total population) in Uganda*. 2022 [cited 2022 1st March]; Available from: <https://data.worldbank.org/indicator/SP.RUR.TOTL.ZS?locations=UG>.
19. The World Bank. *Access to electricity, rural (% of rural population) - Uganda*. 2022 [cited 2022 May 2022]; Available from: <https://data.worldbank.org/indicator/EG.ELC.ACCS.RU.ZS?locations=UG>.
20. EU Energy Initiative, *Mini-grid Policy Toolkit. Policy and Business Frameworks for Successful Mini-grid Roll-outs.*, E. PDF, Editor. 2014: Germany.
21. Kakumba, M., R, *Despite hydropower surplus, most Ugandans report lack of electricity*, in *Afrobarometer Dispatch No. 441*, H. Consult, Editor. 2021, Afrobaromete.
22. International Energy Agency, *Africa Energy Outlook 2019*, in *World Energy Outlook Special Report*, IEA, Editor. 2019, IEA: France.
23. Ahlborg, H. and Hammar, L., *Drivers and barriers to rural electrification in Tanzania and Mozambique – Grid-extension, off-grid, and renewable energy technologies*. *Renewable Energy*, 2014. **61**: p. 117-124 DOI: 10.1016/j.renene.2012.09.057.
24. World Energy Council and Wyman, O., *World Energy-Trilemma Index*. 2021, World Energy Council,: London.
25. Mobarra, M., Rezkallah, M., and Ilinca, A., *Variable Speed Diesel Generators: Performance and Characteristic Comparison*. *Energies (Basel)*, 2022. **15**(2): p. 592 DOI: 10.3390/en15020592.
26. Bertheau, P., Cader, C., Müller, H., Blechinger, P., Seguin, R., and Breyer, C., *Energy Storage Potential for Solar Based Hybridization of Off-grid Diesel Power Plants in Tanzania*. 2014, Elsevier Ltd. p. 287-293.
27. African Development Bank Group, *Renewable Energy in Africa: TANZANIA Country Profile*. 2015, Immeuble du Centre de commerce International d'Abidjan - CCIA: Côte d'Ivoire.

28. Mpagi, M., E., *Assessing the use of power generation technologies in Uganda: A case study of Jinja Municipality*, in *KTH School of Industrial Engineering and Management* 2012, Division of Energy Technology , SE-100 44 STOCKHOLM Division of Energy Technology , SE-100 44 STOCKHOLM p. 80.
29. Eder, J.M., Mutsaerts, C.F., and Sriwannawit, P., *Mini-grids and renewable energy in rural Africa: How diffusion theory explains adoption of electricity in Uganda*. *Energy research & social science*, 2015. **5**: p. 45-54 DOI: 10.1016/j.erss.2014.12.014.
30. Felix, M. and Gheewala, S.H., *A Review of Biomass Energy Dependency in Tanzania*. *Energy Procedia*, 2011. **9**(C): p. 338-343 DOI: 10.1016/j.egypro.2011.09.036.
31. Moner-Girona, M., Ghanadan, R., Solano-Peralta, M., Kougias, I., Bódis, K., Huld, T., and Szabó, S., *Adaptation of Feed-in Tariff for remote mini-grids: Tanzania as an illustrative case*. *Renewable and Sustainable Energy Reviews*, 2016. **53**: p. 306-318 DOI: 10.1016/j.rser.2015.08.055.
32. Okello, G., Devereux, G., and Semple, S., *Women and girls in resource poor countries experience much greater exposure to household air pollutants than men: Results from Uganda and Ethiopia*. *Environment international*, 2018. **119**: p. 429-437 DOI: 10.1016/j.envint.2018.07.002.
33. Röder, M., Chong, K., and Thornley, P., *The future of residue-based bioenergy for industrial use in Sub-Saharan Africa*. *Biomass & bioenergy*, 2022. **159** DOI: 10.1016/j.biombioe.2022.106385.
34. Bede-Ojimadu, O. and Orisakwe, O.E., *Exposure to Wood Smoke and Associated Health Effects in Sub-Saharan Africa: A Systematic Review*. *Annals of global health*, 2020. **86**(1): p. 32 DOI: 10.5334/aogh.2725.
35. Titcombe, M. and Simcik, M., *Personal and indoor exposure to PM 2.5 and polycyclic aromatic hydrocarbons in the southern highlands of Tanzania: a pilot-scale study*. *Environmental Monitoring and Assessment*, 2011. **180**(1-4): p. 461-476 DOI: 10.1007/s10661-010-1799-3.
36. The United Republic of Tanzania, *Tanzania's SE4ALL Action Agenda*, in *Tanzania's SE4ALL Action Agenda*, UNDP, Editor. 2015, Ministry of Energy and Minerals: P.O. Box 2000. 11474 Dar es Salaam. Tanzania.

37. Teske, S., Morris, T., and Nagrath, K., *100% Renewable Energy For Tanzania- Access to renewable energy for all within one generation*, I.f.B.f.t. World, Editor. 2017: Sydney, Australia.
38. Buchholz, T. and Da Silva, I., *Potential of distributed wood-based biopower systems serving basic electricity needs in rural Uganda*. Energy for sustainable development, 2010. **14**(1): p. 56-61 DOI: 10.1016/j.esd.2010.01.002.
39. Rural Electrification Agency of Uganda. *The Rural Electrification Programme -Mini-Grids Project*,. [cited 2022 May 2022]; Available from: <http://www.rea.or.ug/index.php/portfolio/minigrids/>.
40. Kusekwa, M., *Biomass Conversion to Energy in Tanzania: A Critique, New Developments in Renewable Energy*, in *New developments in renewable energy*, H. Arman and I. Yuksel, Editors. 2013, IntechOpen.
41. Ferronato, N. and Torretta, V., *Waste Mismanagement in Developing Countries: A Review of Global Issues*. International journal of environmental research and public health, 2019. **16**(6) DOI: 10.3390/ijerph16061060.
42. Lebuhn, M., Munk, B., and Effenberger, M., *Agricultural biogas production in Germany - from practice to microbiology basics*. Energy, Sustainability and Society, 2014. **4**(1): p. 1-21 DOI: 10.1186/2192-0567-4-10.
43. Food & Agricultural Organisation. *Burning - Crop Residues*. 2022 [cited 2022 May 22]; Available from: <https://www.fao.org/faostat/en/#data/GB>.
44. Nicolás, M.C., Giselle, G., Carolina, M.M., Julia, K., and María, E.V., *Biomass Waste as Sustainable Raw Material for Energy and Fuels*. Sustainability (Basel, Switzerland), 2021. **13**(2): p. 794 DOI: 10.3390/su13020794.
45. Twaha, S., Ramli, M.A.M., Murphy, P.M., Mukhtiar, M.U., and Nsamba, H.K., *Renewable based distributed generation in Uganda: Resource potential and status of exploitation*. Renewable and Sustainable Energy Reviews, 2016. **57**: p. 786-798 DOI: 10.1016/j.rser.2015.12.151.
46. Simonyan, K.J. and Fasina, O., *Biomass resources and bioenergy potentials in Nigeria*. African Journal of Agricultural Research, 2013. **8**(40): p. 4975-4989.

47. Lyakurwa, F.S., *Assessment of the energy potential of crop residues and animal wastes in Tanzania*. Independent Journal of Management & Production, 2016. **7**(4): p. 1227-1239 DOI: 10.14807/ijmp.v7i4.473.
48. Sajjakulnukit, B., Yingyuad, R., Maneekhao, V., Pongnarintasut, V., Bhattacharya, S.C., and Abdul Salam, P., *Assessment of sustainable energy potential of non-plantation biomass resources in Thailand*. Biomass and Bioenergy, 2005. **29**(3): p. 214-224 DOI: 10.1016/j.biombioe.2005.03.009.
49. Milbrandt, A., *Assessment of Biomass Resources in Liberia (USAID) under LEAP*, Editor. 2009: Colorado, US.
50. Saeed, M.A., Irshad, A., Sattar, H., Andrews, G.E., Phylaktou, H.N., and Gibbs, B.M., *Agricultural Waste Biomass Energy Potential In Pakistan*. 2015.
51. Terrapon-Pfaff, J.C., *Linking Energy- and Land-Use Systems: Energy Potentials and Environmental Risks of Using Agricultural Residues in Tanzania*. SUSTAINABILITY, 2012. **4**(3): p. 278-293 DOI: 10.3390/su4030278.
52. Okello, C., Pindozi, S., Faugno, S., and Boccia, L., *Bioenergy potential of agricultural and forest residues in Uganda*. Biomass and Bioenergy, 2013a. **56**: p. 515-525 DOI: 10.1016/j.biombioe.2013.06.003.
53. Mensah, T.N.O., Oyewo, A.S., and Breyer, C., *The role of biomass in sub-Saharan Africa's fully renewable power sector – The case of Ghana*. Renewable energy, 2021. **173**: p. 297-317 DOI: 10.1016/j.renene.2021.03.098.
54. Okello, C., Pindozi, S., Faugno, S., and Boccia, L., *Development of bioenergy technologies in Uganda: A review of progress*. Renewable and Sustainable Energy Reviews, 2013b. **18**: p. 55-63 DOI: 10.1016/j.rser.2012.10.004.
55. Aberilla, J.M., Gallego-Schmid, A., and Azapagic, A., *Environmental sustainability of small-scale biomass power technologies for agricultural communities in developing countries*. Renewable Energy, 2019. **141**: p. 493-506 DOI: 10.1016/j.renene.2019.04.036.
56. Kemausuor, F., Adaramola, M.S., and Morken, J., *A Review of Commercial Biogas Systems and Lessons for Africa*. Energies, 2018. **11**(11): p. 2984 DOI: 10.3390/en11112984.

57. Rupf, G.V., Bahri, P.A., de Boer, K., and McHenry, M.P., *Broadening the potential of biogas in Sub-Saharan Africa: An assessment of feasible technologies and feedstocks*. Renewable and Sustainable Energy Reviews, 2016. **61**: p. 556-571 DOI: 10.1016/j.rser.2016.04.023.
58. Gebreegziabher, Z., Naik, L., Melamu, R., and Balana, B.B., *Prospects and challenges for urban application of biogas installations in Sub-Saharan Africa*. Biomass and Bioenergy, 2014. **70**: p. 130-140 DOI: 10.1016/j.biombioe.2014.02.036.
59. Aslam, Z., Li, H., Hammerton, J., Andrews, G., Ross, A., and Lovett, J., *Increasing Access to Electricity: An Assessment of the Energy and Power Generation Potential from Biomass Waste Residues in Tanzania*. Energies, 2021. **14**(6): p. 1793 DOI: 10.3390/en14061793.
60. Overend, R. *Status of biomass gasifier village systems*. in *Village Power '98*. 1988. Washington, DC. World Bank Headquarters: National Renewable Energy Laboratory.
61. Dasappa, S., *Potential of biomass energy for electricity generation in sub-Saharan Africa*. Energy for Sustainable Development, 2011. **15**(3): p. 203-213 DOI: 10.1016/j.esd.2011.07.006.
62. Martínez, J.D., Mahkamov, K., Andrade, R.V., and Silva Lora, E.E., *Syngas production in downdraft biomass gasifiers and its application using internal combustion engines*. Renewable Energy, 2012. **38**(1): p. 1-9 DOI: 10.1016/j.renene.2011.07.035.
63. Tinaut, F.V., Melgar, A., Horrillo, A., and Díez de la Rosa, A., *Method for predicting the performance of an internal combustion engine fuelled by producer gas and other low heating value gases*. Fuel Processing Technology, 2006. **87**(2): p. 135-142 DOI: 10.1016/j.fuproc.2005.08.009.
64. Garcia-Bacaicoa, P., Bilbao, R., Arauzo, J., and Luisa Salvador, M., *Scale-up of downdraft moving bed gasifiers (25–300 kg/h) — Design, experimental aspects and results*. Bioresource Technology, 1994. **48**(3): p. 229-235 DOI: 10.1016/0960-8524(94)90151-1.
65. Dogru, M., Howarth, C.R., Akay, G., Keskinler, B., and Malik, A.A., *Gasification of hazelnut shells in a downdraft gasifier*. Energy, 2002. **27**(5): p. 415-427 DOI: 10.1016/S0360-5442(01)00094-9.

66. Kirubakaran, V., Sivaramakrishnan, V., Nalini, R., Sekar, T., Premalatha, M., and Subramanian, P., *A review on gasification of biomass*. Renewable and Sustainable Energy Reviews, 2009. **13**(1): p. 179-186 DOI: 10.1016/j.rser.2007.07.001.
67. Tippayawong, N., Promwungkwa, A., and Rerkkriangkrai, P., *Long-term operation of a small biogas/diesel dual-fuel engine for on-farm electricity generation*. Biosystems engineering, 2007. **98**: p. 26-32.
68. Dasappa, S., Subbukrishna, D.N., Suresh, K.C., Paul, P.J., and Prabhu, G.S., *Operational experience on a grid connected 100 kWe biomass gasification power plant in Karnataka, India*. Energy for sustainable development, 2011. **15**(3): p. 231-239 DOI: 10.1016/j.esd.2011.03.004.
69. Dasappa, S., Sridhar, G., Sridhar, V., H., Rajan, N., Paul, J., P., and Upasani, A. *Producer Gas Engines– Proponent of Clean Energy Technology in 15th European Biomass Conference & Exhibition*,. 2007. Berlin, Germany.
70. Dasappa, S. and Sridhar, H.V., *Performance of a diesel engine in a dual fuel mode using producer gas for electricity power generation*. International Journal of Sustainable Energy, 2013. **32**(3): p. 153-168 DOI: 10.1080/14786451.2011.605945.
71. IEA. *Outlook for biogas and biomethane: Prospects for organic growth*. 2020 [cited 2022 10 Feb 22]; Biogas facts]. Available from: <https://www.iea.org/reports/outlook-for-biogas-and-biomethane-prospects-for-organic-growth>
72. Oishi, Y., Situmorang, R.S., Sembiring, R.A., Kawai, H., and Ambarita, H., *Performance, rate of heat release, and combustion stability of dual-fuel mode in a small diesel engine*. Energy science & engineering, 2019. **7**(4): p. 1333-1351 DOI: 10.1002/ese3.352.
73. LTS International Limited, Edinburgh, T.U.o., and E4tech, *Bioenergy for Sustainable Energy Access in Africa*, in *Project Completion and Handover Report*. 2017: Penicuik, United Kingdom.
74. Roopnarain, A. and Adeleke, R., *Current status, hurdles and future prospects of biogas digestion technology in Africa*. Renewable and Sustainable Energy Reviews, 2017. **67**: p. 1162-1179 DOI: 10.1016/j.rser.2016.09.087.

75. Laramee, J. and Davis, J., *Economic and environmental impacts of domestic bio-digesters: Evidence from Arusha, Tanzania*. Energy for Sustainable Development, 2013. **17**(3): p. 296-304 DOI: 10.1016/j.esd.2013.02.001.
76. McCord, A.I., Stefanos, S.A., Tumwesige, V., Lsoto, D., Kawala, M., Mutebi, J., Nansubuga, I., and Larson, R.A., *Anaerobic digestion in Uganda: risks and opportunities for integration of waste management and agricultural systems*. Renewable agriculture and food systems, 2019. **35**(6): p. 1-10 DOI: 10.1017/S1742170519000346.
77. Ruiz, J.A., Juárez, M.C., Morales, M.P., Muñoz, P., and Mendivil, M.A., *Biomass gasification for electricity generation: Review of current technology barriers*. Renewable & sustainable energy reviews, 2013. **18**: p. 174-183 DOI: 10.1016/j.rser.2012.10.021.
78. Chan Seung Park, Roy, P.S., and Kim, S.H., *Current Developments in Thermochemical Conversion of Biomass to Fuels and Chemicals, Gasification for Low-grade Feedstock*, in *Gasification-for-low-grade-feedstock*, Y. Yun, Editor. 2018, IntechOpen.
79. Bhattacharyya, S.C., *Viability of off-grid electricity supply using rice husk: A case study from South Asia*. Biomass and Bioenergy, 2014. **68**(44-54) DOI: 10.1016/j.biombioe.2014.06.002.
80. Patra, T.K. and Sheth, P.N., *Biomass gasification models for downdraft gasifier: A state-of-the-art review*. Renewable & sustainable energy reviews, 2015. **50**: p. 583-593 DOI: 10.1016/j.rser.2015.05.012.
81. Beohar, H., Gupta, B., Sethi, K., V., and Pandey, M., *Parametric Study of Fixed Bed Biomass Gasifier: A review*. International Journal of Thermal Technologies, 2012. **2**(1).
82. Olgun, H., Ozdogan, S., and Yinesor, G., *Results with a bench scale downdraft biomass gasifier for agricultural and forestry residues*. Biomass and Bioenergy, 2011. **35**(1): p. 572-580 DOI: 10.1016/j.biombioe.2010.10.028.
83. Luo, X., Wu, T., Shi, K., Song, M., and Rao, Y., *Biomass Gasification: An Overview of Technological Barriers and Socio-Environmental Impact*, in *Gasification for Low-grade Feedstock*, Y. Yun, Editor. 2018, IntechOpen: London.

84. Warnecke, R., *Gasification of biomass: comparison of fixed bed and fluidized bed gasifier*. Biomass and Bioenergy, 2000. **18**(6): p. 489-497 DOI: 10.1016/S0961-9534(00)00009-x.
85. Mohon Roy, M., Tomita, E., Kawahara, N., Harada, Y., and Sakane, A., *Performance and emission comparison of a supercharged dual-fuel engine fueled by producer gases with varying hydrogen content*. International journal of hydrogen energy, 2009. **34**(18): p. 7811-7822 DOI: 10.1016/j.ijhydene.2009.07.056.
86. Erlich, C. and Fransson, H., T., *Downdraft gasification of pellets made of wood, palm-oil residues respective bagasse: Experimental study*. Applied Energy, 2011. **88**(3): p. 899-908 DOI: 10.1016/j.apenergy.2010.08.028.
87. Kalbandhe, V., R; Deshmukh, S,S; Waghmare, S,S; Arfin, T, *Fabrication and Performance Analysis of Downdraft Biomass Gasifier using Sugarcane Industry Waste*. IJSRD - International Journal for Scientific Research & Development, 2015. **3**(10).
88. Hassan, S., Z.A, Z., and Miskam, M.A., *A Preliminary Investigation of Compressed Producer Gas from Downdraft Biomass Gasifier*. Journal of Applied Sciences, 2010. **10**: p. 406-412.
89. Patil, K., Bhoi, P., Huhnke, R., and Bellmer, D., *Biomass downdraft gasifier with internal cyclonic combustion chamber: Design, construction, and experimental results*. Bioresource technology, 2011. **102**(10): p. 6286-6290 DOI: 10.1016/j.biortech.2011.03.033.
90. Masmoudi, M., Griou, N., Sahraoui, M., and Halouani, K., *Experimental study of syngas generation from almond shell in a downdraft gasifier*, in *16èmes Journées Internationales de Thermique (JITH 2013)*, J. 2013, Editor. 2013, JITH 2013: Marrakech (Maroc).
91. Kumar, A.R., Ravindra, *Experimental Analysis of a Producer Gas Generated by a Chir Pine Needle (Leaf) in a Downdraft Biomass Gasifier*. Int. Journal of Engineering Research and Applications, 2014. **4**(10): p. 122-130.
92. Uma, R., Kandpal, T.C., and Kishore, V.V.N., *Emission characteristics of an electricity generation system in diesel alone and dual fuel modes*. Biomass & bioenergy, 2004. **27**(2): p. 195-203 DOI: 10.1016/j.biombioe.2004.01.003.

93. Umeda, K., Nakamura, S., Lu, D., and Yoshikawa, K., *Biomass gasification employing low-temperature carbonization pretreatment for tar reduction*. Biomass & bioenergy, 2019. **126**: p. 142-149 DOI: 10.1016/j.biombioe.2019.05.002.
94. Hasler, P. and Nussbaumer, T., *Gas cleaning for IC engine applications from fixed bed biomass gasification*. Biomass & bioenergy, 1999. **16**(6): p. 385-395 DOI: 10.1016/S0961-9534(99)00018-5.
95. Bhattacharya, S.C., Shwe Hla, S., and Pham, H.-L., *A study on a multi-stage hybrid gasifier-engine system*. Biomass & bioenergy, 2001. **21**(6): p. 445-460 DOI: 10.1016/S0961-9534(01)00048-4.
96. Sridhar, G., Paul, P.J., and Mukunda, H.S., *Biomass derived producer gas as a reciprocating engine fuel—an experimental analysis*. Biomass & bioenergy, 2001. **21**(1): p. 61-72 DOI: 10.1016/S0961-9534(01)00014-9.
97. Rinaldini, C.A., Allesina, G., Pedrazzi, S., Mattarelli, E., Savioli, T., Morselli, N., Puglia, M., and Tartarini, P., *Experimental investigation on a Common Rail Diesel engine partially fuelled by syngas*. Energy conversion and management, 2017. **138**: p. 526-537 DOI: 10.1016/j.enconman.2017.02.034.
98. Basu, P., *Biomass gasification and pyrolysis : practical design and theory*. 2010, Amsterdam ;: Elsevier/Academic Press.
99. Kumar, G.S., Gupta, A., and Viswanadham, M., *Design of lab-scale downdraft gasifier for biomass gasification*. IOP conference series. Materials Science and Engineering, 2018. **455**(1): p. 12051 DOI: 10.1088/1757-899X/455/1/012051.
100. Couto, N., Rouboa, A., Silva, V., Monteiro, E., and Bouziane, K., *Influence of the Biomass Gasification Processes on the Final Composition of Syngas*. Energy Procedia, 2013. **36**: p. 596-606 DOI: 10.1016/j.egypro.2013.07.068.
101. Kumar, S.S., N; Mohapatra, K, S, *Producer Gas Production from Cotton Stalk and Sugarcane Bagasse in a Downdraft Gasifier: Composition and Higher Heating Value Investigation*, J.o.B.a.A.E. Research, Editor. 2016, Journal of Basic and Applied Engineering Research, © Krishi Sanskriti Publications. p. 1034-1037.

102. Ramadhas, A.S., Jayaraj, S., and Muraleedharan, C., *Power generation using coir-pith and wood derived producer gas in diesel engines*. Fuel Processing Technology, 2006. **87**(10): p. 849-853 DOI: 10.1016/j.fuproc.2005.06.003.
103. Bridgwater, A.V., *Renewable fuels and chemicals by thermal processing of biomass*. Chemical engineering journal (Lausanne, Switzerland : 1996), 2003. **91**(2): p. 87-102 DOI: 10.1016/S1385-8947(02)00142-0.
104. Corella, J., Toledo, J.M., and Padilla, R., *Catalytic Hot Gas Cleaning with Monoliths in Biomass Gasification in Fluidized Beds. 1. Their Effectiveness for Tar Elimination*. Industrial & Engineering Chemistry Research, 2004. **43**(10): p. 2433-2445 DOI: 10.1021/ie0307683.
105. Lapuerta, M., Hernández, J.J., Pazo, A., and López, J., *Gasification and co-gasification of biomass wastes: Effect of the biomass origin and the gasifier operating conditions*. Fuel processing technology, 2008. **89**(9): p. 828-837 DOI: 10.1016/j.fuproc.2008.02.001.
106. Beenackers, A.A.C.M., *Biomass gasification in moving beds, a review of European technologies*. Renewable energy, 1999. **16**(1): p. 1180-1186 DOI: 10.1016/S0960-1481(98)00469-8.
107. Corella J, T.J., *Modelling a CFB biomass gasifier: Part I. Model formulation.*, in *Progress in thermochemical biomass conversion*, B. AV, Editor. 2001, Blackwell Science: Oxford, UK. p. 333-45.
108. Corella J, T.J., M.; Aznar M,P. . *Checking an advanced 6-lump model for the kinetics of the variation tar composition in its catalytic elimination in biomass gasification.* . in *Proceed. Of 12th EC Conference on biomass for energy*. 2002. Amsterdam (NL): In: Proceed. Of 12th EC Conference on biomass for energy.
109. Corella J, H.J., ;Toledo JM,; Gomez-Cívicos JI., *Modelling fluidized bed biomass gasifiers: Part II. Gasification with steam in a bubbling fluidized bed*, in *1st World Conference on biomass for energy and industry*, e.a. Kyritsis S, editors., Editor. 2001, Science Publishers: London, UK. p. 1971-5.
110. Karim, A., G, *Dual-Fuel Diesel Engines*, ed. s. Edition. 2015: CRC Press.

111. Hassan, S., Nor, M., Zainal, Z.A., and Miskam, A., M., *Performance and Emission Characteristics of Supercharged Biomass Producer Gas-diesel Dual Fuel Engine*. Journal of Applied Sciences, 2011. **11**: p. 1606-1611 DOI: 10.3293/jas.2011.1606.1611.
112. Heywood, J.B., *Internal combustion engine fundamentals*. McGraw-Hill series in mechanical engineering. 1988, New York ;: McGraw-Hill.
113. Proctor, C., Lafayette, Armstrong, and Van Horn, L. *The Diesel Engine* 2021; Available from: <https://www.britannica.com/technology/diesel-engine/Fuel-injection-technology>.
114. Kamimoto, T. and Kobayashi, H., *Combustion processes in diesel engines*. Progress in energy and combustion science, 1991. **17**(2): p. 163-189 DOI: 10.1016/0360-1285(91)90019-J.
115. Lakshminarayanan, P.A. and Aghav, Y.V., *Ignition Delay in a Diesel Engine*, in *Modelling Diesel Combustion*, P.A. Lakshminarayanan and Y.V. Aghav, Editors. 2010, Springer Netherlands: Dordrecht. p. 59-78.
116. Alagumalai, A., *Combustion characteristics of lemongrass (Cymbopogon flexuosus) oil in a partial premixed charge compression ignition engine*. Alexandria Engineering Journal, 2015. **54**(3): p. 405-413 DOI: 10.1016/j.aej.2015.03.021.
117. Olanrewaju, F., Li, H., Aslam, Z., Hammerton, J., and Lovett, J., *Analysis of the effect of syngas substitution of diesel on the Heat Release Rate and combustion behaviour of Diesel-Syngas dual fuel engine*. Fuel, 2022. **312**: p. 122842 DOI: 10.1016/j.fuel.2021.122842.
118. Mehta, P.S., Lahiri, D., and Bhaskar, T., *Evaluation of Role of Premixed Combustion on Diesel Engine Combustion and Emission Characterisitcs*. 1996.
119. Hamlin, M., *Large stationary diesel & all stationary dual fuel engines*, in *Emission Factor Documentation for AP-42 section 3.4*, Acurex Environmental Corporation, Editor. 1993, U.S. Environmental Protection Agency.
120. Reşitoğlu, İ.A., Altinişik, K., and Keskin, A., *The pollutant emissions from diesel-engine vehicles and exhaust aftertreatment systems*. Clean technologies and environmental policy, 2014. **17**(1): p. 15-27 DOI: 10.1007/s10098-014-0793-9.

121. Zheng, M., Mulenga, M.C., Reader, G.T., Wang, M., Ting, D.S.K., and Tjong, J., *Biodiesel engine performance and emissions in low temperature combustion*. Fuel (Guildford), 2008. **87**(6): p. 714-722 DOI: 10.1016/j.fuel.2007.05.039.
122. EPA. *Technical Overview of Volatile Organic Compounds*. 2022 [cited 2022 April]; Available from: <https://www.epa.gov/indoor-air-quality-iaq/technical-overview-volatile-organic-compounds#:~:text=A%20VOC%20is%20any%20organic,atmospheric%20pressure%20of%20101.3%20kPa>.
123. IPCC, *Climate Change 2007: Synthesis Report. Contribution of Working Groups I, II and III to the Fourth Assessment Report of the Intergovernmental Panel on Climate Change*, in *Climate Change 2007: Synthesis Report*, R.K. Pachauri and A. Reisinger, Editors. 2007: Geneva, Switzerland. p. 14.
124. Majewski, W. and Jääskeläinen, H. *Exhaust Particulate Matter*. DieselNet Technology Guide » What Are Diesel Emissions 2019 [cited 2022 April]; Available from: <https://dieselnet.com/tech/dpm.php>.
125. Kittelson, D.B., *Engines and nanoparticles: a review*. Journal of aerosol science, 1998. **29**(5): p. 575-588 DOI: 10.1016/S0021-8502(97)10037-4.
126. Kittelson, D., Watts, W., and Johnson, J., *DIESEL AEROSOL SAMPLING METHODOLOGY - CRC E-43*, in *Report for the Coordinating Research Council*,. 2002, University of Minnesota: Minneapolis, U.S.,
127. Kassa, M. and Hall, C., *Dual-Fuel Combustion*, in *The Future of Internal Combustion Engines*, P. Carlucci, A, Editor. 2018, Intechopen: France.
128. Kousheshi, N., Yari, M., Paykani, A., Saberi Mehr, A., and De La Fuente, G.F., *Effect of Syngas Composition on the Combustion and Emissions Characteristics of a Syngas/Diesel RCCI Engine*. Energies, 2020. **13**(1): p. 212 DOI: 10.3390/en13010212.
129. W.E.R.C. *Reactivity Controlled Compression Ignition (RCCI)*. 2022 [cited 2022 May 2022]; Available from: <https://www.w-erc.com/services/rcci/>.
130. Chuahy, F. and Kokjohn, S., *High efficiency dual-fuel combustion through thermochemical recovery and diesel reforming*. Applied energy, 2017. **195**: p. 503-522 DOI: 10.1016/j.apenergy.2017.03.078.

131. Chuahy, F., Strickland, T., Walker, R., N., and Kokjohn, S., *Effects of reformed fuel on dual-fuel combustion particulate morphology*. International journal of engine research, 2021. **22**(3): p. 777-790 DOI: 10.1177/1468087419879782.
132. Wheeler, R., K, *Efficient Operation of Diesel Generator Sets in Remote Environments*, in *Mech Eng*. 2017, Virginia Polytechnic Institute and State University: Blacksburg, VA.
133. Brown, N. and Haydock, L., *Full Integration of an Axial Flux Machine for Reciprocating Engine Variable Speed Generating Sets*. The Institution of Electrical Engineers, 2001.
134. Genpower Ltd t/a The Power Site. *Diesel Generator FAQ: 1500RPM and 3000RPM Differences*. 2018; Available from: <https://thepowersite.co.uk/blog/diesel-generators-faq-frequently-asked-questions-1500rpm-3000rpm/#:~:text=A%201500rpm%20generator%20will%20cost,cost-effective%20and%20sensible%20option>.
135. Barik, D. and Murugan, S., *Investigation on combustion performance and emission characteristics of a DI (direct injection) diesel engine fueled with biogas–diesel in dual fuel mode*. Energy (Oxford), 2014. **72**: p. 760-771 DOI: 10.1016/j.energy.2014.05.106.
136. Aklouche, F.Z., Loubar, K., Bentebbiche, A., Awad, S., and Tazerout, M., *Experimental investigation of the equivalence ratio influence on combustion, performance and exhaust emissions of a dual fuel diesel engine operating on synthetic biogas fuel*. Energy conversion and management, 2017. **152**: p. 291-299 DOI: 10.1016/j.enconman.2017.09.050.
137. Leykun, M.G. and Mekonen, M.W., *Investigation of the Performance and Emission Characteristics of Diesel Engine Fueled with Biogas-Diesel Dual Fuel*. Fuels, 2022. **3**(1): p. 15-30 DOI: 10.3390/fuels3010002.
138. Ambarita, H., *Performance and emission characteristics of a small diesel engine run in dual-fuel (diesel-biogas) mode*. Case studies in thermal engineering, 2017. **10**(C): p. 179-191 DOI: 10.1016/j.csite.2017.06.003.
139. Mustafi, N.N., Raine, R.R., and Verhelst, S., *Combustion and emissions characteristics of a dual fuel engine operated on alternative gaseous fuels*. Fuel (Guildford), 2013. **109**: p. 669-678 DOI: 10.1016/j.fuel.2013.03.007.

140. Salve, D., N., Kolekar, H., A., and Jadhav, M., K, *Experimental Evaluation of Dual Fuel CI Engine Using Synthesized Biogas*. International Engineering Research Journal (2016: p. 1223-1229.
141. Sattarzadeh, M., Ebrahimi, M., and Jazayeri, S.A., *A detail study of a RCCI engine performance fueled with diesel fuel and natural gas blended with syngas with different compositions*. International Journal of Hydrogen Energy, 2022 DOI: 10.1016/j.ijhydene.2022.03.088.
142. Sahoo, B.B., Sahoo, N., and Saha, U.K. *Assessment of a Syngas-Diesel Dual Fuelled Compression Ignition Engine*. in *ASME 2010 4th International Conference on Energy Sustainability*. 2010. DOI: 10.1115/es2010-90218.
143. Sahoo, B.B., Saha, U.K., and Sahoo, N., *Theoretical performance limits of a syngas–diesel fueled compression ignition engine from second law analysis*. Energy (Oxford), 2011. **36**(2): p. 760-769 DOI: 10.1016/j.energy.2010.12.045.
144. Sahoo, B.B., Sahoo, N., and Saha, U.K., *Effect of H<sub>2</sub>:CO ratio in syngas on the performance of a dual fuel diesel engine operation*. Applied thermal engineering, 2012. **49**: p. 139-146 DOI: 10.1016/j.applthermaleng.2011.08.021.
145. Bika, A.S., Franklin, L., and Kittelson, D., *Cycle Efficiency and Gaseous Emissions from a Diesel Engine Assisted with Varying Proportions of Hydrogen and Carbon Monoxide (Synthesis Gas)*. 2011, SAE International.
146. Dal Forno Chuahy, F., Olk, J., and Kokjohn, S., *Reformed Fuel Substitution for Transient Peak Soot Reduction*. 2018.
147. Dhole, A.E., Yarasu, R.B., Lata, D.B., Baraskar, S.S., and Shaw, D., *Mathematical modeling for the performance and emission parameters of dual-fuel diesel engine using producer gas as secondary fuel*. Biomass Conversion and Biorefinery, 2015. **5**(3): p. 257-270 DOI: 10.1007/s13399-014-0142-6.
148. Azimov, U., Tomita, E., Kawahara, N., and Harada, Y., *Effect of syngas composition on combustion and exhaust emission characteristics in a pilot-ignited dual-fuel engine operated in PREMIER combustion mode*. International journal of hydrogen energy, 2011. **36**(18): p. 11985-11996 DOI: 10.1016/j.ijhydene.2011.04.192.

149. Feng, S., *Numerical Study of the Performance and Emission of a Diesel-Syngas Dual Fuel Engine*. Mathematical problems in engineering, 2017. **2017**: p. 1-12 DOI: 10.1155/2017/6825079.
150. Guo, H., Neill, W.S., and Liko, B. *The Combustion and Emissions Performance of a Syngas-Diesel Dual Fuel Compression Ignition Engine*. 2016. American Society of Mechanical Engineers DOI: 10.1115/icef2016-9367.
151. Garnier, C., Bilcan, A., and Le Corre, O., *Characterisation of a Syngas-Diesel Fuelled CI Engine*. 2005, SAE International.
152. Ramadhas, A.S., Jayaraj, S., and Muraleedharan, C., *Dual fuel mode operation in diesel engines using renewable fuels: Rubber seed oil and coir-pith producer gas*. Renewable energy, 2008. **33**(9): p. 2077-2083 DOI: 10.1016/j.renene.2007.11.013.
153. Tuan, L.A. and Luong, H., *Simulation of a syngas - diesel dual fuel engine for small-scale power generator*. 2014. **100B**: p. 36-41.
154. Rajvanshi, A.K. and Joshi, M.S., *Development and operational experience with topless wood gasifier running a 3.75 kW diesel engine pumpset*. Biomass, 1989. **19**(1): p. 47-56 DOI: 10.1016/0144-4565(89)90005-X.
155. Wankhade, P.P., Jajoo, B.N., and Wankhade, R.P. *Performance Evaluation of Parameters for Biomass Gasifier-Diesel Engine Setup Using Woody Biomass (Subabool)*. IEEE DOI: 10.1109/ICETET.2009.175.
156. Silva, M.J., Souza, S.N.M.d., Ricieri, R.P., Souza, A.A., and Secco, D., *Microgeneration of electricity with producer gas in dual fuel mode operation*. Engenharia Agrícola, 2011. **31**(5): p. 879-886 DOI: 10.1590/S0100-69162011000500005.
157. Parikh, P.P., Bhave, A.G., Kapse, D.V., and Shashikantha, *Study of thermal and emission performance of small gasifier-dual-fuel engine systems*. Biomass, 1989. **19**(1): p. 75-97 DOI: 10.1016/0144-4565(89)90008-5.
158. Shrivastava, V., Jha, A.K., Wamankar, A.K., and Murugan, S., *Performance and Emission Studies of a CI Engine Coupled with Gasifier Running in Dual Fuel Mode*. Procedia engineering, 2013. **51**: p. 600-608 DOI: 10.1016/j.proeng.2013.01.085.

159. Malik, A. and Mohapatra, S.K., *Power generation using cotton stalk-derived producer gas in diesel engines*. Energy sources. Part A, Recovery, utilization, and environmental effects, 2016. **38**(19): p. 2816-2822 DOI: 10.1080/15567036.2015.1111957.
160. Das, D.K., Dash, S.P., and Ghosal, M.K., *Performance evaluation of a diesel engine by using producer gas from some under-utilized biomass on dual-fuel mode of diesel cum producer gas*. Journal of Central South University, 2012. **19**(6): p. 1583-1589 DOI: 10.1007/s11771-012-1180-5.
161. Hernández, J.J., Ballesteros, R., Barba, J., and Guillén-Flores, J., *Effect of the Addition of Biomass Gasification Gas on the PM Emission of a Diesel Engine*. SAE International Journal of Engines, 2014. **8**(1): p. 14-19 DOI: 10.4271/2014-01-2840.
162. Hernández, J.J., Lapuerta, M., and Barba, J., *Effect of partial replacement of diesel or biodiesel with gas from biomass gasification in a diesel engine*. Energy (Oxford), 2015. **89**: p. 148-157 DOI: 10.1016/j.energy.2015.07.050.
163. Rith, M., Bernard, B., Gitano-Briggs, H.W., and Jose Bienvenido Manuel, M.B., *Design and fabrication of a low-cost research facility for the study of combustion characteristics of a dual producer gas-diesel engine*. Engineering and Applied Science Research (EASR), 2020. **47**(4): p. 447-457 DOI: 10.14456/easr.2020.48.
164. Stewart, J. and Clarke, A., *A Three-Zone Heat-Release Rate Model for Dual-Fuel Combustion*. Proceedings of the Institution of Mechanical Engineers. Part C, Journal of mechanical engineering science, 2010. **224**(11): p. 2423-2434 DOI: 10.1243/09544062JMES1955.
165. Mahmood, H.A., Al-Sulttani, A.O., and Attia, O.H., *Simulation of Syngas Addition Effect on Emissions Characteristics, Combustion, and Performance of the Diesel Engine working under Dual Fuel Mode and Lambda Value of 1.6.*, in *IOP Conf. Series: Earth and Environmental Science*. 2021, IOP Publishing Ltd.
166. Wagemakers, A.M.L.M. and Leermakers, C.A.J., *Review on the Effects of Dual-Fuel Operation, Using Diesel and Gaseous Fuels, on Emissions and Performance*. 2012.

167. Wei, L. and Geng, P., *A review on natural gas/diesel dual fuel combustion, emissions and performance*. Fuel processing technology, 2016. **142**: p. 264-278 DOI: 10.1016/j.fuproc.2015.09.018.
168. Abd Alla, G.H., Soliman, H.A., Badr, O.A., and Abd Rabbo, M.F., *Effect of pilot fuel quantity on the performance of a dual fuel engine*. Energy conversion and management, 2000. **41**(6): p. 559-572 DOI: 10.1016/S0196-8904(99)00124-7.
169. Sung, C.-J. and Law, C.K., *Fundamental Combustion Properties of H<sub>2</sub>/CO Mixtures: Ignition and Flame Propagation at Elevated Pressures*. Combustion science and technology, 2008. **180**(6): p. 1097-1116 DOI: 10.1080/00102200801963169.
170. Sahoo, B.B., Sahoo, N., and Saha, U.K., *Effect of engine parameters and type of gaseous fuel on the performance of dual-fuel gas diesel engines—A critical review*. Renewable & sustainable energy reviews, 2009. **13**(6): p. 1151-1184 DOI: 10.1016/j.rser.2008.08.003.
171. Lal, S. and Mohapatra, S.K., *The effect of compression ratio on the performance and emission characteristics of a dual fuel diesel engine using biomass derived producer gas*. Applied thermal engineering, 2017. **119**: p. 63-72 DOI: 10.1016/j.applthermaleng.2017.03.038.
172. Mustafi, N.N. and Raine, R.R., *Electron Microscopy Investigation of Particulate Matter from a Dual Fuel Engine*. Aerosol science and technology, 2009. **43**(9): p. 951-960 DOI: 10.1080/02786820903067210.
173. Mohand Said, L., Loubar, K., Tarabet, L., Balistrrou, M., Niculescu, D.-C., and Tazerout, M., *Towards improvement of natural gas-diesel dual fuel mode: An experimental investigation on performance and exhaust emissions*. Energy (Oxford), 2014. **64**: p. 200-211 DOI: 10.1016/j.energy.2013.10.091.
174. Liu, Z. and Karim, G.A., *Simulation of combustion processes in gas-fuelled diesel engines*. Proceedings of the Institution of Mechanical Engineers. Part A, Journal of power and energy, 1997. **211**(2): p. 159-169 DOI: 10.1243/0957650971537079.

175. Crown Oil. *EN 590 Diesel Fuel Specifications (ULSD)*. 2022 [cited 2022 16th Feb 22]; Available from: <https://www.crownoil.co.uk/fuel-specifications/en-590/>.
176. Engineering ToolBox. *Engineering ToolBox*. 2003 16th Feb 2022]; Density of gases]. Available from: [https://www.engineeringtoolbox.com/gas-density-d\\_158.html](https://www.engineeringtoolbox.com/gas-density-d_158.html).
177. McAllister, S., Chen, J.-Y., and Fernandez-Pello, A.C., *Fundamentals of combustion processes*. Mechanical engineering series. 2011, New York ;: Springer.
178. Chemeurope.com. *Heat of combustion*. Publication de l'Institut Français du Pétrole 2022 [cited 2021 Dec]; LHV of CO]. Available from: [https://www.chemeurope.com/en/encyclopedia/Heat\\_of\\_combustion.html](https://www.chemeurope.com/en/encyclopedia/Heat_of_combustion.html).
179. Kriaučiūnas, D., Žvirblis, T., Kilikevičienė, K., Kilikevičius, A., Matijošius, J., Rimkus, A., and Vainorius, D., *Impact of Simulated Biogas Compositions (CH<sub>4</sub> and CO<sub>2</sub>) on Vibration, Sound Pressure and Performance of a Spark Ignition Engine*. *Energies*, 2021. **14**(21): p. 7037 DOI: 10.3390/en14217037.
180. AVL. *Pressure sensor for Combustion Analysis - Data Sheet*. 2011 [cited 2022 Feb 22]; GH14D TIGG1321A.01]. Available from: [https://www.avl.com/documents/10138/885983/AT3363E\\_GH14D.pdf](https://www.avl.com/documents/10138/885983/AT3363E_GH14D.pdf).
181. Hillstone Products Ltd. *HAC240 series – 3kW to 30kW Single Phase AC Load Banks*. 2012 [cited 2022 16 Feb 22]; Tech Summary Sheet, Issue 3,]. Available from: <https://www.hillstone.co.uk/loadbank/ac.html>.
182. Manel Service. *LINZ E1C10M H Single-phase alternator 115/230V 6 kVA 50 Hz Brushless synchronous alternator with capacitor - 2 poles*. 2022 [cited 2022 16 Feb 22]; ALTERNATOR E1C10M H, Technical Data Sheet]. Available from: <https://www.manelservice.com/en/alternators/linz-e1c10m-h-single-phase-alternator-115-230v-6-kva-50-hz-brushless>.
183. Cambustion. *DMS500 operating principles*. 2022 [cited 2022 14th Feb 22]; Available from: <https://www.cambustion.com/products/knowledgebase/dms-animation>.

184. Cummins Generator Technologies, *Application Guidance Notes: AGN 087 – Power Factor*, Cummins Generator Technologies, Editor. ND, Cummins Generator Technologies,.
185. Linz Electric S.P.A. *E1S/4 - 4 POLES COMPOUND*,. 2017 [cited 2022 Jan]; Alternator E1S13S B/4]. Available from: <https://www.linzelectric.com/index.cfm/en/products/three-phase-alternators/e1s-4-poles-with-brushes/>.
186. Silvis, M, W., *The Algorithmic Structure of the Air/Fuel Ratio Calculation*, in *Readout No 15*, H.T. Reports, Editor. 1997. p. 17-24.
187. Li, H., Ropkins, K., Andrews, G.E., Daham, B., Bell, M.C., and Tate, J.E., *Evaluation of a FTIR Emission Measurement System for Legislated Emissions Using a SI Car*. 2006: Society of Automotive Engineers.
188. Lea-Langton, A., Li, H., and Andrews, G.E., *Comparison of Particulate PAH Emissions for Diesel, Biodiesel and Cooking Oil using a Heavy Duty DI Diesel Engine*. 2008.
189. Eisentraut, A., *Sustainable Production of Second-Generation Biofuels: Potential and Perspectives in Major Economies and Developing Countries*. 2010, OECD Publishing
190. F.A.O. *Official Crops data*. 2022 8th Feb 22 [cited 2022; Available from: <http://www.fao.org/faostat/en/#data/QC>.
191. Bhattacharya, S.C., Pham, H.L., Shrestha, R.M., and Vu, Q.V. *CO2 Emissions due to Fossil and Traditional Fuels, Residues and Wastes in Asia*. in *Proceedings of AIT Workshop on Global Warming Issues in Asia*. 1993. Bangkok, Thailand: AIT.
192. Lim, K.O., *The energy potential and current utilization of agriculture and logging wastes in Malaysia*. *Renewable Energy Review*, 1986. **8**(2): p. 57-75.
193. Koopmans, A. and Koppejan, J. *Agricultural and Forest Residues -Generation, Utilization and Availability*. in *Regional consultation on modern applications of biomass energy*. 1997. Malaysia.
194. Quaak, P., Knoef, H., and Stassen, H.E., *Energy from biomass. A review of combustion and gasification technologies*. , in *Energy series*., World Bank Technical paper, Editor. 1999: Washington, D.C. p. 6.

195. Syamsiro, M., Saptoadi, H., and Tambunan H, B., *Experimental Investigation on Combustion of Bio-Pellets from Indonesian Cocoa Pod Husk*. Asian Journal of Applied Sciences, 2011. **4**(7): p. 712-719.
196. PCA, in *Technical data handbook on the coconut, its products and by-products*, P.C. Authority, Editor. 1979: Casein City. Philippines.
197. Ma, A.N. and Ong, A.S.H., *Biomass Energy from the Palm Oil Industry*, in *ASEAN Conference on Energy from Biomass*. 1986: Penang, Malaysia.
198. Kabissa, J., *Cotton and its by-products in the United Republic of Tanzania.*, in *UNCTAD/SUC/MISC/2017/1*, United Nations conference on Trade & Development, Editor. 2016, UNCTAD: Geneva, Switzerland.
199. Terrapon-Pfaff, J.C., Fishedick, M., and Monheim, H., *Energy potentials and sustainability—the case of sisal residues in Tanzania*. Energy for Sustainable Development, 2012. **16**(3): p. 312-319 DOI: 10.1016/j.esd.2012.06.001.
200. Jekayinfa, S.O. and Scholz, V., *Potential Availability of Energetically Usable Crop Residues in Nigeria*. Energy Sources, Part A: Recovery, Utilization, and Environmental Effects, 2009. **31**(8): p. 687-697 DOI: 10.1080/15567030701750549.
201. AIT-EEC., *Evaluation and selection of lingo-cellulose wastes which can be converted into substitute fuels.* , E.E. Community, Editor. 1983, AIT-EEC: Belgium.
202. Vimal, O.P. and Tyagi, P.D., *Energy from biomass- An Indian Experience*. 1984, New Delhi. India.: Agricole Publishing Academy.
203. Ryan, P. and Openshaw, K., *Assessment of biomass energy resources, a discussion on its need and methodology.* . 1991, The World Bank.
204. Vimal, O.P. *Residue utilization, management of agricultural and agro industrial residues of selected tropical crops (Indian experience).* . in *Proceedings of UNEP/ESCAP/FAO Workshop on Agricultural and Agro industrial residue utilization in Asia and Pacific region*. 1979.
205. USAID, *Baling sugarcane tops and leaves: The Thai experience.*, in *R and D/EI Report No 91-15*. 1989, Office of Energy and Infrastructure. R and D/EI Report No 91-15.

206. Şahin, S. and Elhussein, E.A.A., *Assessment of sesame (Sesamum indicum L.) cake as a source of high-added value substances: from waste to health*. *Phytochemistry Reviews*, 2018. **17**(4): p. 691-700 DOI: 10.1007/s11101-018-9554-4.
207. Yasothai, R., *Processing method and composition of sesame oil cake – A review*,. *International Journal of Science, Environment and Technology*,, 2014a. **3**(3): p. 993 - 996.
208. Yasothai, R., *Energy content and protein quality of sesame oil cake - A review*,. *International Journal of Science, Environment and Technology*,, 2014. **3**(3): p. 901-904.
209. Mehta, B.V., *Sea Millennium Handbook 2000*. Vol. 7. 1989, Mumbai, India: The Solvent Extractors Association of India.
210. Pathak, N.K. and Kamra, D.N., *A Text Book of Livestock Feeding in Tropics*. 1989, New Delhi, India: A Falcon Book from Cosmo Publications; Cosmo Publications. 246–257.
211. Swick, R., *Considerations in using protein meals for poultry*. *Poultry Fortune*, 2001. **2**(10): p. 30-38.
212. Ozyuguran, A., Akturk, A., and Yaman, S., *Optimal use of condensed parameters of ultimate analysis to predict the calorific value of biomass*. *Fuel*, 2018. **214**: p. 640-646 DOI: 10.1016/j.fuel.2017.10.082.
213. Heuzé V., Tran G., Hassoun P., Bastianelli D., and Lebas F., *Cottonseed meal*. 2019, Feedipedia, a programme by INRA, CIRAD, AFZ and FAO. .
214. Magasiner, N. and de Kock, J.W., *Design criteria for fibrous fuel fired boilers*. *Energy World* 1987, 1987. **8-9**: p. 4-12.
215. ECN. *Database for (Treated) Biomass, Algae, Feedstocks for Biogas Production and Biochar*,. 2022 27/3/2019 [cited Phyllis 2; Available from: <https://phyllis.nl/Browse/Standard/ECN-Phyllis#370>].
216. Gerçel, H.F., *The production and evaluation of bio-oils from the pyrolysis of sunflower-oil cake*. *Biomass and Bioenergy*, 2002. **23**(4): p. 307-314 DOI: 10.1016/S0961-9534(02)00053-3.
217. FAO, *Sunflower Crude and Refined Oils*, in *Agribusiness Handbook*, FAO, Editor. 2010, FAO Investment Centre Division: Rome, Italy.

218. ECN. *Database for (Treated) Biomass, Algae, Feedstocks for Biogas Production and Biochar*,. 2022 [cited Phyllis2 15 Jan 2019]; Sunflower seed husk (#378)]. Available from: <https://www.ecn.nl/phyllis2/Biomass/View/378>.
219. Sheehan, J., Camobreco, V., Duffield, J., Grabosk, M., and Shapouri, H., *Life Cycle Inventory of Biodiesel and Petroleum Diesel for Use in an Urban Bus*,, U.S. Department of Energy's Office of Fuels Development and U.S. Department of Agriculture's Office of Energy, Editor. 1998, U.S. Department of Energy: Colorado, U.S.
220. Patzek, T.W., *A First Law Thermodynamic Analysis of Biodiesel Production From Soybean*. Bulletin of Science, Technology & Society, 2009. **29**: p. 194 - 204.
221. Bhattacharya, S.C., Abdul Salam, P., Runqing, H., Somashekar, H.I., Racelis, D.A., Rathnasiri, P.G., and Yingyuad, R., *An assessment of the potential for non-plantation biomass resources in selected Asian countries for 2010*. Biomass and Bioenergy, 2005. **29**(3): p. 153-166 DOI: 10.1016/j.biombioe.2005.03.004.
222. Food & Agricultural Organisation. *Official Forestry Data*. 2022 7th Feb 2022 [cited 2022; Available from: <http://www.fao.org/faostat/en/#data/FO>
223. Ngaga, Y., *Forest plantations and woodlots in Tanzania*,, African Forest Forum, Editor. 2011: Nairobi KENYA.
224. The Wood Database. *Iroko | The Wood Database - Lumber Identification (Hardwood)*. . 2022 [cited 2022 Feb]; Available from: <http://www.wood-database.com/iroko/>
225. The Wood Database. *Slash Pine, The Wood Database, - Lumber Identification (Softwood)*. 2022 [cited 2022 Feb]; Slash Pine, The Wood Database, - Lumber Identification (Softwood)]. Available from: <http://www.wood-database.com/slash-pine/>.
226. The Wood Database. *Caribbean Pine, The Wood Database, - Lumber Identification (Softwood)*. 2022 [cited 2022 Feb]; Caribbean Pine, The Wood Database, - Lumber Identification (Softwood)]. Available from: <http://www.wood-database.com/caribbean-pine/>.
227. The Wood Database. *Patula Pine, The Wood Database, - Lumber Identification (Softwood)*. 2022 [cited 2022 Feb]; Patula Pine, The Wood Database, - Lumber Identification (Softwood)]. Available from: <http://www.wood-database.com/patula-pine/>.

228. The Wood Database. *Khasi Pine, The Wood Database, - Lumber Identification (Softwood)*. 2022 [cited 2022 Feb]; Khasi Pine, The Wood Database, - Lumber Identification (Softwood)]. Available from: <http://www.wood-database.com/khasi-pine/>.
229. The Wood Database. *Radiata Pine, The Wood Database, - Lumber Identification (Softwood)*. 2022 [cited 2022 Feb]; Radiata Pine, The Wood Database, - Lumber Identification (Softwood)]. Available from: <http://www.wood-database.com/radiata-pine/>.
230. The Wood Database. *African Juniper, The Wood Database, - Lumber Identification (Dense Softwood)*. 2022 [cited 2022 Feb]; African Juniper, The Wood Database, - Lumber Identification (Dense Softwood)]. Available from: <http://www.wood-database.com/african-juniper/>.
231. The Wood Database. *Mexican Cypress, The Wood Database, - Lumber Identification (Hardwood)*. 2022 [cited 2022 Feb]; Mexican Cypress, The Wood Database, - Lumber Identification (Hardwood)]. Available from: <http://www.wood-database.com/mexican-cypress/>.
232. The Wood Database. *Black Wattle, Lumber Identification (Hardwood)*. 2022 [cited 2022 Feb]; Black Wattle, Lumber Identification (Hardwood)]. Available from: <http://www.wood-database.com/black-wattle/>.
233. The Wood Database. *Australian Blackwood, Lumber Identification (Hardwood)*. 2022 [cited 2022 Feb]; Australian Blackwood, Lumber Identification (Hardwood)]. Available from: <http://www.wood-database.com/australian-blackwood/>.
234. The Wood Database. *Spanish Cedar, Lumber Identification (Hardwood)*. 2022 [cited 2022 Feb]; Spanish Cedar, Lumber Identification (Hardwood)]. Available from: <http://www.wood-database.com/spanish-cedar/>.
235. The Wood Database. *Camphor, Lumber Identification (Hardwood)*. 2022 [cited 2022 Feb]; Camphor, Lumber Identification (Hardwood)]. Available from: <https://www.wood-database.com/camphor/>.
236. The Wood Database. *River Red Gum, Lumber Identification (Hardwood)*. 2022 [cited 2022 Feb]; River Red Gum, Lumber Identification (Hardwood)]. Available from: <http://www.wood-database.com/river-red-gum/>.

237. The Wood Database. *Blue Gum, Lumber Identification (Hardwood)*. 2022 [cited 2022 Feb]; Blue Gum, Lumber Identification (Hardwood)]. Available from: <https://www.wood-database.com/blue-gum/>.
238. The Wood Database. *Rose Gum, Lumber Identification (Hardwood)*. 2022 [cited 2022 Feb]; Rose Gum, Lumber Identification (Hardwood)]. Available from: <http://www.wood-database.com/rose-gum/>.
239. The Wood Database. *Southern Silky Oak, Lumber Identification (Hardwood)*. 2022 [cited 2022 Feb]; Southern Silky Oak, Lumber Identification (Hardwood)]. Available from: <http://www.wood-database.com/southern-silky-oak/>.
240. The Wood Database. *Olive, Lumber Identification (Hardwood)*. 2022 [cited 2022 Feb]; Olive, Lumber Identification (Hardwood)]. Available from: <https://www.wood-database.com/olive/>.
241. The Wood Database. *Idigbo, Lumber Identification (Hardwood)*. 2022 [cited 2022 Feb]; Idigbo, Lumber Identification (Hardwood)]. Available from: <http://www.wood-database.com/idigbo/>.
242. The Wood Database. *Teak, Lumber Identification (Hardwood)*. 2022 [cited 2022 Feb]; Teak, Lumber Identification (Hardwood)]. Available from: <http://www.wood-database.com/teak/>.
243. The Wood Database. *Western Sheoak, Lumber Identification (Hardwood)*. 2022 [cited 2022 Feb]; Western Sheoak, Lumber Identification (Hardwood)]. Available from: <https://www.wood-database.com/western-sheoak/>.
244. Kaboggoza , J., *Forest plantations and woodlots in Uganda*, in *African Forest Forum Working Paper Series*, African Forest Forum 2011, Editor. 2011, African Forest Forum: Nairobi GPO KENYA.
245. The Wood Database. *Ocote Pine/Mexican Yellow Pine. Lumber Identification (Softwood)*. 2022 [cited 2022 Feb]; Ocote Pine/Mexican Yellow Pine. Lumber Identification (Softwood)]. Available from: <http://www.wood-database.com/ocote-pine/>.
246. The Wood Database. *Monkey Puzzle, Lumber Identification (Softwood)*. 2022 [cited 2022 Feb]; Monkey Puzzle, Lumber Identification (Softwood)]. Available from: <http://www.wood-database.com/monkey-puzzle/>.

247. ITTO. *Musizi (Maesopsis eminii) a.k.a Umbrella tree Wood Identification*. 2022 [cited 2022 Feb]; Musizi - Wood Identification]. Available from: <http://www.tropicaltimber.info/specie/musizi-maesopsis-eminii/#lower-content>.
248. Harris , R. and Phillips, D., *Density of selected wood fuels*, in *Georgia Forestry Commission*. 1986, Research Division, Georgia Forestry Commission: Georgia, U.S.
249. ECN. *Database for (Treated) Biomass, Algae, Feedstocks for Biogas Production and Biochar*,. 2022 Feb 2022 [cited Phyllis2 #3121]; Forest waste (#3121)]. Available from: <https://www.ecn.nl/phyllis2/Biomass/View/3121>
250. ECN. *Database for (Treated) Biomass, Algae, Feedstocks for Biogas Production and Biochar*,. 2022 Feb 2022 [cited Phyllis2 #657]; Industrial wood waste (#657)]. Available from: <https://www.ecn.nl/phyllis2/Biomass/View/>.
251. ECN. *Database for (Treated) Biomass, Algae, Feedstocks for Biogas Production and Biochar*,. 2022 Feb 2022 [cited Phyllis2 #1487]; wood, plywood (#1487) ]. Available from: <https://www.ecn.nl/phyllis2/Biomass/View/1487>
252. ECN. *Database for (Treated) Biomass, Algae, Feedstocks for Biogas Production and Biochar*,. 2022 16 Feb 2022 [cited Phyllis2 Wood, plywood scraps (#443) ]. Available from: <https://www.ecn.nl/phyllis2/Biomass/View/443>
253. ECN. *Database for (Treated) Biomass, Algae, Feedstocks for Biogas Production and Biochar*,. 2022 15 Jan 2022 [cited Phyllis2; Wood (#3116)]. Available from: <https://phyllis.nl/Browse/Standard/ECN-Phyllis#3116>.
254. Food & Agricultural Organisation. *Official live animal data*. 2022 7 Feb 22 [cited 2022; 2022:[Available from: <http://www.fao.org/faostat/en/#data/QA>
255. Njombe, A.P., Msanga, Y., and Mbwambo, N., *The Tanzania Dairy Industry: Status, Opportunities and Prospects*,, in *7th African Dairy Conference and Exhibition 2011*, Ministry of Livestock and Fisheries Development: MovenPick Palm Hotel, Dar es Salaam, Tanzania.
256. Agricultural and Rural Development Department of the World Bank, *Uganda Dairy Supply Chain Risk Assessment*. 2011.

257. Shane, A., Gheewala, S.H., and Phiri, S., *Rural domestic biogas supply model for Zambia*. Renewable and Sustainable Energy Reviews, 2017. **78**: p. 683-697 DOI: 10.1016/j.rser.2017.05.008.
258. Bhattacharya, S.C., Thomas, J.M., and Abdul Salam, P., *Greenhouse gas emissions and the mitigation potential of using animal wastes in Asia*. Energy, 1997. **22**(11): p. 1079-1085 DOI: 10.1016/S0360-5442(97)00039-X.
259. Ozcan, M., Öztürk, S., and Oguz, Y., *Potential evaluation of biomass-based energy sources for Turkey*. Engineering Science and Technology, an International Journal, 2015. **18**(2): p. 178-184 DOI: 10.1016/j.jestch.2014.10.003.
260. Msibi, S.S. and Kornelius, G., *Potential for domestic biogas as household energy supply in South Africa*. Journal of Energy in Southern Africa, 2017. **28**(2): p. 1-13 DOI: 10.17159/2413-3051/2017/v28i2a1754.
261. Perera, K.K.C.K., Rathnasiri, P.G., Senarath, S.A.S., Sugathapala, A.G.T., Bhattacharya, S.C., and Abdul Salam, P., *Assessment of sustainable energy potential of non-plantation biomass resources in Sri Lanka*. Biomass and Bioenergy, 2005. **29**(3): p. 199-213 DOI: 10.1016/j.biombioe.2005.03.008.
262. The World Bank. *Urban Population, total in Uganda*. 2022 7 Feb 22; Available from: <https://data.worldbank.org/indicator/SP.URB.TOTL?locations=UG>.
263. The World Bank. *Urban population total in Tanzania*. 2022 7 Feb 22; Available from: <https://data.worldbank.org/indicator/SP.URB.TOTL?locations=CG-TZ>
264. Electricity Regulatory Authority. *Energy Purchases Sales and Losses for Electricity distribution for Uganda*. 2018 [cited 2022 21st Feb 2022]; Electricity Distribution Losses for 2019]. Available from: <https://www.era.go.ug/index.php/stats/distribution-statistics/energy-purchases-sales-and-losses>.
265. Electricity Regulatory Authority. *Energy Purchases, Sales and Losses, Transmission Losses*. 2018 [cited 2022 21st Feb 2022]; Transmission Loss Data for 2019]. Available from: <https://www.era.go.ug/index.php/stats/transmission-stats/energy-purchases-sales-and-losses>.

266. Hirsch, A., Parag, Y., and Guerrero, J., *Microgrids: A review of technologies, key drivers, and outstanding issues*. Renewable and Sustainable Energy Reviews, 2018. **90**: p. 402-411 DOI: 10.1016/j.rser.2018.03.040.
267. IEA. *IEA - Statistics Search Tanzania, United Republic of Tanzania, United Republic* IEA Atlas of Energy 2022 [cited 2022 7 Feb 22]; Total Electricity Generation (TWh)]. Available from: <https://www.iea.org/fuels-and-technologies/electricity>.
268. ERA Electrical Regulatory Authority. *Energy Generated to the National Grid in Uganda*. Energy Generation Statistics 2022 [cited 2022 March]; Electrical energy generated 2019]. Available from: <https://www.era.go.ug/index.php/stats/generation-statistics/energy-generated>.
269. Benson, T. and Mogue, T., *Constraints in the fertilizer supply chain: evidence for fertilizer policy development from three African countries*. Food security, 2018. **10**(6): p. 1479-1500 DOI: 10.1007/s12571-018-0863-7.
270. Mwakaje, A.G., *Dairy farming and biogas use in Rungwe district, South-west Tanzania: A study of opportunities and constraints*. Renewable and Sustainable Energy Reviews, 2008. **12**(8): p. 2240-2252 DOI: 10.1016/j.rser.2007.04.013.
271. Orskov, E.R., Yongabi Anchang, K., Subedi, M., and Smith, J., *Overview of holistic application of biogas for small scale farmers in Sub-Saharan Africa*. Biomass and Bioenergy, 2014. **70**(C): p. 4-16 DOI: 10.1016/j.biombioe.2014.02.028.
272. Dong, C., Zhou, Q., Zhao, Q., Zhang, Y., Xu, T., and Hui, S., *Experimental study on the laminar flame speed of hydrogen/carbon monoxide/air mixtures*. Fuel (Guildford), 2009. **88**(10): p. 1858-1863 DOI: 10.1016/j.fuel.2009.04.024.
273. Hagos, F.Y., Aziz, A.R.A., and Sulaiman, S.A., *Trends of Syngas as a Fuel in Internal Combustion Engines*. Advances in mechanical engineering, 2014. **6**: p. 401587 DOI: 10.1155/2014/401587.
274. Rößler, M., Koch, T., Janzer, C., and Olzmann, M., *Mechanisms of the NO<sub>2</sub> Formation in Diesel Engines*. MTZ worldwide, 2017(7-8).

275. Semakula, M. and Inambao, F., *The Formation, Effects and Control of Oxides of Nitrogen in Diesel Engines*. International Journal of Applied Engineering Research, 2018. **13**: p. 3200-3209.
276. Badr, O., Karim, G.A., and Liu, B., *An examination of the flame spread limits in a dual fuel engine*. Applied thermal engineering, 1999. **19**(10): p. 1071-1080 DOI: 10.1016/S1359-4311(98)00108-2.
277. Hargeaves, K.J.A., Harvey, R., Roper, F.G., and Smith, D.B., *Formantion of NO<sub>2</sub> by laminar flames*. Symposium, International, on Combustion, 1981. **18**(1): p. 133-142 DOI: 10.1016/S0082-0784(81)80018-5.
278. Bierkandt, T., Oßwald, P., Gaiser, N., Krüger, D., Köhler, M., Hoener, M., Shaqiri, S., Kaczmarek, D., Karakaya, Y., Hemberger, P., and Kasper, T., *Observation of low-temperature chemistry products in laminar premixed low-pressure flames by molecular-beam mass spectrometry*. International journal of chemical kinetics, 2021. **53**(10): p. 1063-1081 DOI: 10.1002/kin.21503.
279. Karim, G.A., Ito, K., Abraham, M., and Jensen, L., *An Examination of the Role of Formaldehyde in the Ignition Processes of a Dual Fuel Engine*. SAE Transactions, 1991. **100**: p. 975-982 DOI: 10.2307/44553650.
280. U.K. Department for B.E.I.S. *Greenhouse gas reporting: conversion factors 2021*. 2021 [cited 2022 April]; Available from: <https://www.gov.uk/government/publications/greenhouse-gas-reporting-conversion-factors-2021>.
281. Smith, O.I., *Fundamentals of soot formation in flames with application to diesel engine particulate emissions*. Progress in energy and combustion science, 1981. **7**(4): p. 275-291 DOI: 10.1016/0360-1285(81)90002-2.
282. Liu W, Zhang W, LEI Zhu, Li X, and Huang Z, *Characteristics of ultrafine particle from a compression-ignition engine fueled with low sulfur diesel*. Chinese Sci Bull, 2009, , 2009. **54**: p. 4411—4417 DOI: 10.1007/s11434-009-0304-2
283. Schefer, W., Robert , White, C., and Keller, J., *Lean Hydrogen Combustion*, in *Lean Combustion*. 2008, Academic Press, : Burlington.

284. Omidvarborna, H., Kumar, A., and Kim, D.-S., *Characterization of particulate matter emitted from transit buses fueled with B20 in idle modes*. Journal of environmental chemical engineering, 2014. **2**(4): p. 2335-2342 DOI: 10.1016/j.jece.2014.09.020.
285. Noria Corp. *Lubricant Additives - A Practical Guide*. 2022 [cited 2022 May 2022]; Available from: <https://www.machinerylubrication.com/Read/242/open-gear-lubrication>.